ISSN 0288-4534
CODEN: KPPJAD

KONA Powder and Particle Journal

No.41 (2024)



Hosokawa Powder Technology Foundation

available online-www.kona.or.jp

About this Journal

KONA Powder and Particle Journal is an international, interdisciplinary, and Diamond Open-Access journal that focuses on publishing articles on powder and particle science and technology.

This journal is a refereed scientific journal with an annual publication history dating back to 1983. It is distributed free of charge to researchers, members of the scientific community, universities, and research libraries worldwide by the Hosokawa Powder Technology Foundation, established by the late Mr. Masuo Hosokawa in 1991.

The Chinese character "粉" featured on the cover of the journal is pronounced as "KONA" in Japanese and signifies "Powder." The calligraphy for this character is attributed to the late Mr. Eiichi Hosokawa, the founder of Hosokawa Micron Corporation.

About the Cover

Controlling the fate of free-charge carriers generated in colloidal semiconductor nanocrystals through the sequential absorption of photons at photoexcited conditions determines the device performances of various applications including light-emitting diodes, photodetectors, sensors and theranostic photothermal agents. Defects, usually as non-radiating channels generated during crystal growth, interfere with efficient energy conversion between absorbed energy and other forms such as luminescence, photocurrent, and heat. In this paper, we report on a reliable method to investigate the origin of defects for identification and to inactivate them with unique surface chemistry approaches and doping techniques to maximize device performance. Review on this topic is discussed on pp. 172–182. <https://doi.org/10.14356/kona.2024001>



Headquarters of Hosokawa Micron Corporation

Editorial Board

Editor-in-Chief
M. Naito (Osaka Univ., *Japan*)

Asian / Oceanian Editorial Board
X.S. Cai (Univ. of Shanghai for Sci. & Tech., *China*)
T. Charinpanitkul (Chulalongkorn Univ., *Thailand*)
Y.F. Chen (Chinese Academy of Sciences, *China*)
H. Choi (Changwon National Univ., *Korea*)
S. Das (Indian Institute of Technology, *India*)
M. Fuji (Nagoya Institute of Technology, *Japan*)
E. Iritani (Nagoya Univ., *Japan*)
H. Kage (Kyushu Institute of Technology, *Japan*)
A. Kawasaki (Tohoku Univ., *Japan*)
D.J. Lee (National Taiwan Univ., *Taiwan*)
J.H. Li (Chinese Academy of Sciences, *China*)
H. Makino (CRIEPI, *Japan*)
S. Matsusaka (Kyoto Univ., *Japan*)
T. Ogi (Hiroshima Univ., *Japan*)
K. Okuyama (Hiroshima Univ., *Japan*)
Y. Otani (Kanazawa Univ., *Japan*)
Y. Sakka (NIMS, *Japan*)
Y.-S. Shen (Univ. of New South Wales, *Australia*)
Y. Shirakawa (Doshisha Univ., *Japan*)
H. Takeuchi (Gifu Pharmaceutical Univ., *Japan*)
W. Tanthapanichakoon (The Royal Society of Thailand, *Thailand*)
C.H. Wang (National Univ. of Singapore, *Singapore*)
S. Watano (Osaka Metropolitan Univ., *Japan*)
Secretariat
T. Yokoyama (Hosokawa Powder Tech. Foundation, *Japan*)
S. Mukaigawara (Hosokawa Powder Tech. Foundation, *Japan*)
L. Cui (Hosokawa Micron Corp., *Japan*)

European / African Editorial Board
Chairman
A. Kwade (TU Braunschweig, *Germany*)
D. Barletta (Univ. of Salerno, *Italy*)
G. Biskos (The Cyprus Institute, *Cyprus*)
M.-O. Coppens (Univ. College London, *UK*)
A. Mainza (Univ. of Cape Town, *South Africa*)
M.G. Rasteiro (Univ. of Coimbra, *Portugal*)
D.L. Schott (Delft Univ. of Technology, *the Netherlands*)
Secretariat
S. Sander (KONA Europe e.V., *Germany*)
S. Wilk (KONA Europe e.V., *Germany*)

American Editorial Board
Chairman
B.M. Moudgil (Univ. of Florida., *USA*)
A.J. Hickey (Univ. of North Carolina, *USA*)
A. Misra (Univ. of Kansas, *USA*)
A.D. Rosato (New Jersey Institute of Technology, *USA*)
L.M. Tavares (UFRJ, *Brazil*)
W.N. Wang (Virginia Commonwealth Univ., *USA*)
Q. Zhang (Univ. of Manitoba, *Canada*)
Secretariat
C.C. Huang (Hosokawa Micron Intl. Inc., *USA*)

■ Publication Office
Hosokawa Powder Technology Foundation (www.kona.or.jp)
(in the headquarters building of Hosokawa Micron Corporation)
1-9, Shodaitajika, Hirakata-shi, Osaka 573-1132, Japan
E-mail: contact_zainq@hmc.hosokawa.com

■ Printing Office: Nakanishi Printing Co., Ltd., Japan

■ Publication Date: 10 January 2024



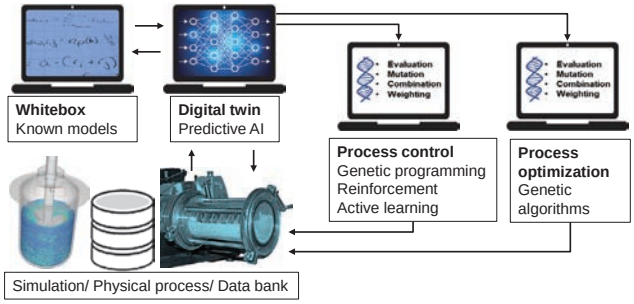
<Editorial>

1 Editor's Preface

<Review Papers>

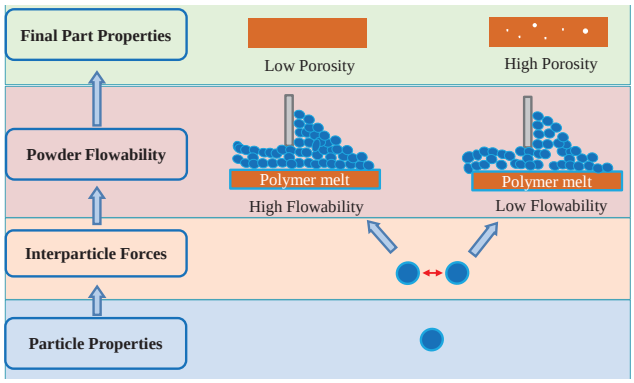
3 Artificial Intelligence and Evolutionary Approaches in Particle Technology

Christoph Thon, Marvin Röhl, Somayeh Hosseinhashemi, Arno Kwade and Carsten Schilde



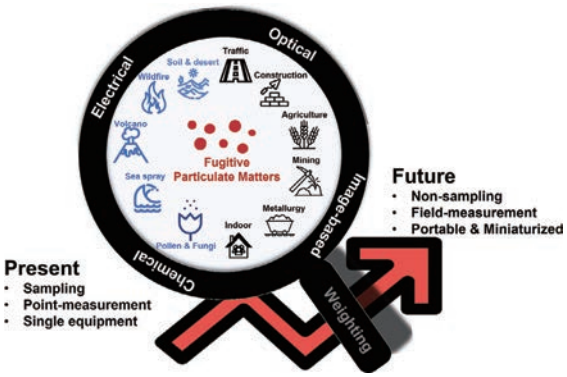
26 Role of Powder Properties and Flowability in Polymer Selective Laser Sintering—A Review

Xi Guo and Brij M. Moudgil



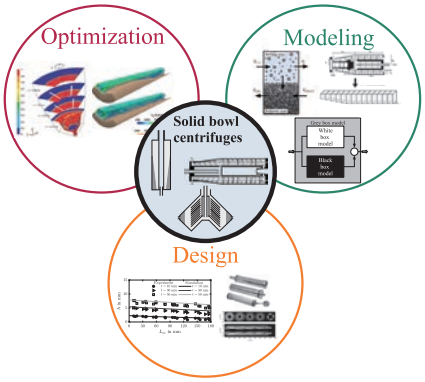
42 Measurement of Fugitive Particulate Matter Emission: Current State and Trends

Tianyi Cai and Wu Zhou



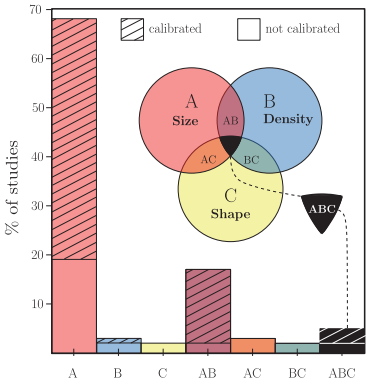
58 About Modeling and Optimization of Solid Bowl Centrifuges

Marco Gleiss and Hermann Nirschl



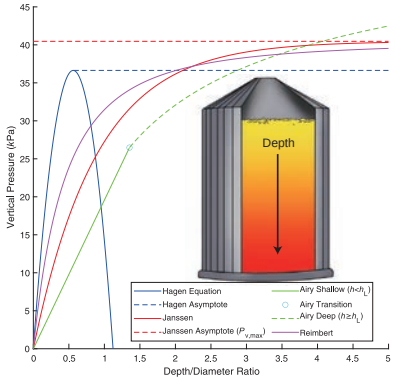
78 DEM Modelling of Segregation in Granular Materials: A Review

Ahmed Hadi, Raïsa Roeplal, Yusong Pang and Dingena L. Schott



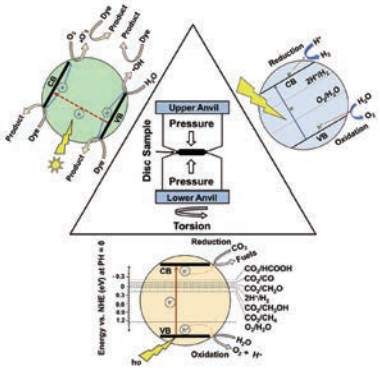
108 A Review of Analytical Methods for Calculating Static Pressures in Bulk Solids Storage Structures

George Dyck, Adam Rogers and Jitendra Paliwal



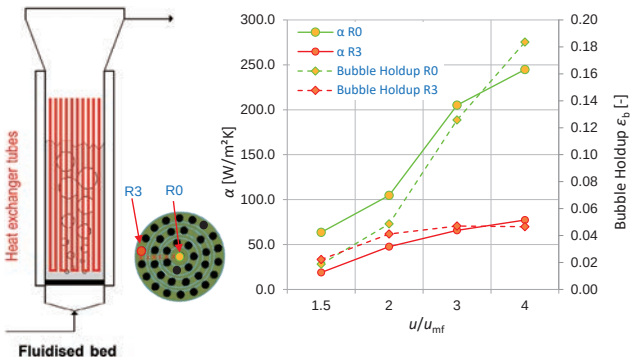
123 High-Pressure Torsion for Highly-Strained and High-Entropy Photocatalysts

Saeid Akrami, Parisa Edalati, Masayoshi Fuji and Kaveh Edalati



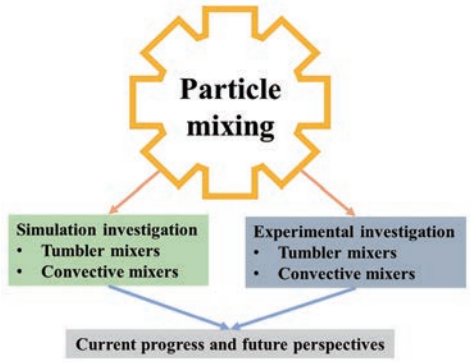
140 Applying Bubbling Fluidized-Bed Reactors for Strongly Exothermic Reactions: Focus on Methanation

Philipp Riechmann and Tilman J. Schildhauer



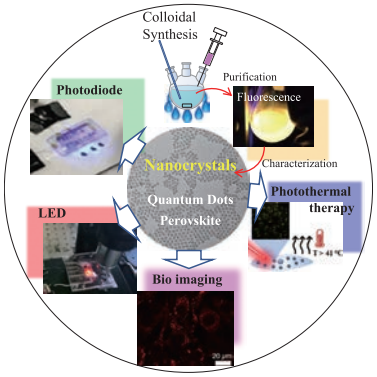
151 **Current Progress of Experimental and Simulation Work of Mixing Processes in Particulate Systems**

Xin Jin and Yansong Shen



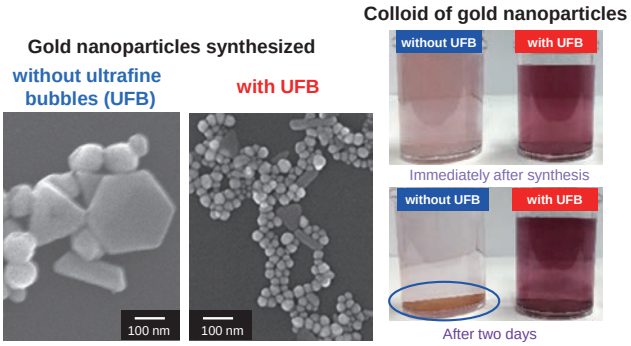
172 **Recent Progress in Controlled Nanostructure of Colloidal Nanocrystal Powders for Efficient Light Emission**

Naoto Shirahata



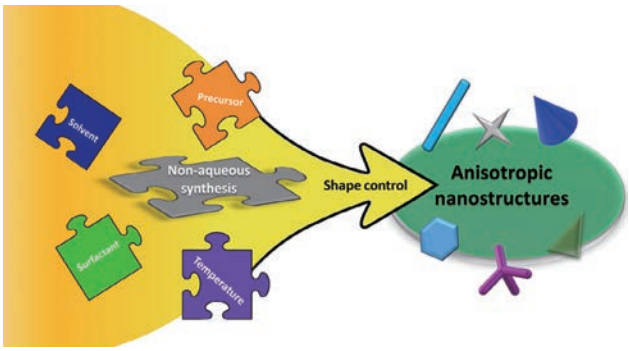
183 **Characteristics of Ultrafine Bubbles (Bulk Nanobubbles) and Their Application to Particle-Related Technology**

Keiji Yasuda



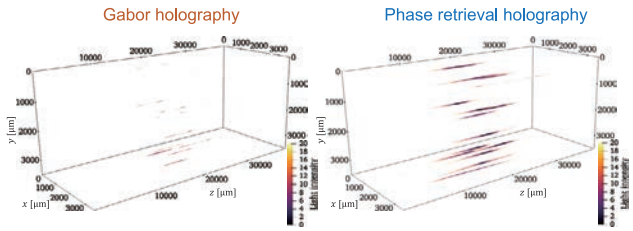
197 **Synthesis of Anisotropic Metal Oxide Nanoparticles via Non-Aqueous and Non-Hydrolytic Routes**

Sherif Okeil, Julian Ungerer, Hermann Nirschl and Georg Garnweitner



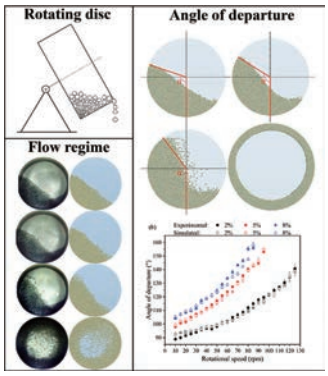
<Original Research Papers>

221 **Particle Size Measurement Using a Phase Retrieval Holography System with a GPU-Equipped SBC**



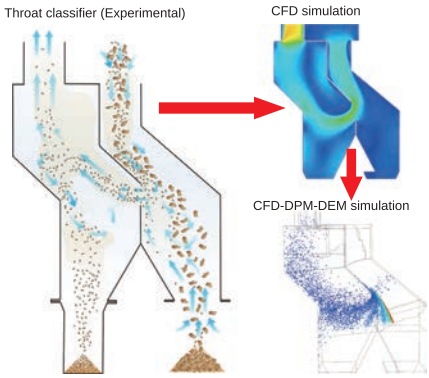
Yohsuke Tanaka and Dai Nakai

229 **Effects of DEM Parameters and Operating Conditions on Particle Dynamics in a Laboratory Scale Rotating Disc**



Rondinelli M. Lima, Gisele M. Souza, Rodolfo J. Brandão, Claudio R. Duarte and Marcos A.S. Barrozo

242 **Simulation of the Classification of Manufactured Sands in the Throat Air Classifier**



Horacio A. Petit and Edgardo Fabián Irassar

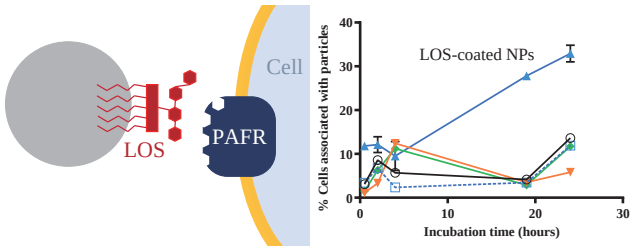
254 **The Mechanism behind Vibration Assisted Fluidization of Cohesive Micro-Silica**



Rens Kamphorst, P. Christian van der Sande, Kaiqiao Wu, Evert C. Wagner, M. Kristen David, Gabrie M.H. Meesters and J. Ruud van Ommen

265 **Lipooligosaccharide Ligands from Respiratory Bacterial Pathogens Enhance Cellular Uptake of Nanoparticles**

Mai H. Tu, Timothy M. Brenza, Margaret R. Ketterer, Morgan Timm, Benjamin M. King, Michael A. Apicella and Jennifer Fiegel



<Information Articles>

280 **The 55th Symposium on Powder Technology**

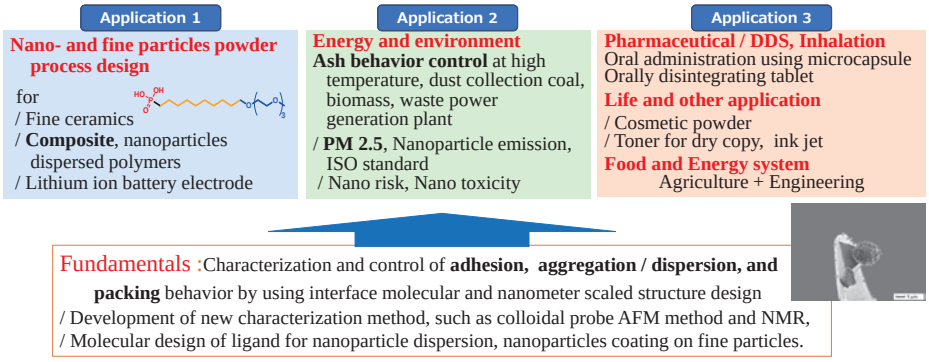
282 **4th International Hosokawa Powder Technology Symposium Held in Germany**

284 **The KONA Award 2022 (Awardees: Prof. Dr. Hidehiro Kamiya and Prof. Dr. Toshitsugu Tanaka)**

286 **General Information**

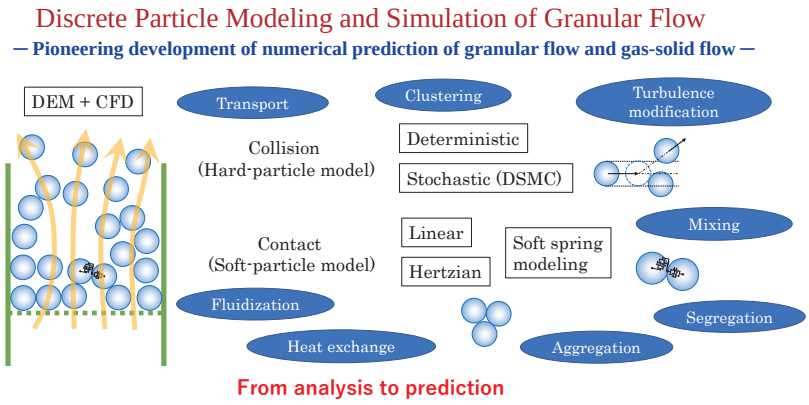






Selected research achievements for the KONA Award 2022 (Awardee: Prof. Dr. Hidehiro Kamiya): Particle adhesion and aggregation behavior characterization and control.





Selected research achievements for the KONA Award 2022 (Awardee: Prof. Dr. Toshitsugu Tanaka): Development of discrete particle modeling and simulations of gas-solid flows and granular flows.

Reviewer Appreciation

Makio Naito, *Editor-in-Chief*



I would like to express my sincere gratitude to the reviewers for their hard work for the KONA Powder and Particle Journal. Thanks to the generous contributions of the volunteer reviewers as well as the interest of researchers in our journal, the number of submissions to this journal has been increasing since its registration on major international journal platforms, and its level has been further improving. Thanks to their strong support and effort, I am pleased to inform you that the 2022 Impact Factor (JCR) of the KONA Powder and Particle Journal has increased to 4.1, with the CiteScore 2022 of 6.8. Because of the limited space of this annual journal, the number of papers published here is regrettably rather restricted. Therefore, only the papers of good quality will be selected for the journal and further improved and refined by the reviewing process. Moreover, we have created a channel on J-STAGE Data, to enable authors to deposit, share and link to the data within their papers that will be or were published in this journal. J-STAGE Data, which is the data repository provided by the Japan Science and Technology Agency (JST), enables KONA authors to contribute to the promotion of Open Science with reviewers and editors.

The editorial team of the KONA Journal would like to take this opportunity to gratefully acknowledge the reviewers here and deeply appreciate their valuable time and professional contributions to the KONA Journal. We apologize to any reviewers who may have been inadvertently omitted from this list. We are sincerely grateful to all who have been of any assistance to the publication of this journal.

BISKOS, George
BOURGEOIS, Florent
COPPENS, Marc-Olivier
GOTOH, Kuniaki
GRADON, Leon
HICKEY, Anthony
IRITANI, Eiji
ISHIMOTO, Takuya
KANIE, Kiyoshi
KANO, Junya
KWADE, Arno
MEESTERS, Gabriel
OKUYAMA, Kikuo
SAKKA, Yoshio
SASABE, Shuji
TAVARES, Luis Marcelo
YAMAMOTO, Hiromitsu
YOKOYAMA, Toyokazu
ZHANG, Qiang

Makio Naito
Professor Emeritus, Osaka University
October 2023

Copyright © 2024 The Author. Published by Hosokawa Powder Technology Foundation. This is an open access article under the CC BY license (https://creativecommons.org/licenses/by/4.0/).

Editor's Preface



Arno Kwade
Chairman of European/African Editorial Board
Technische Universität Braunschweig, Germany

It is a great honour for me to introduce KONA Powder and Particle Journal No. 41 as the recently appointed Chair of the European and African KONA Editorial Board and the successor of Gabrie Meesters, whom I would like to thank for his great commitment to KONA. Since my doctoral thesis on ultrafine wet milling over 40 years ago, I have been part of the journey of particle and powder technology. From predominantly basic research on unit operations of grinding, granulation, classification, and mixing, including powder flow and particle size characterization, the research focus has moved first to in-depth research on the behaviour and interaction of individual particles and more recently to the deep investigation of full process chains and the production of complex particulate products with optimized properties. During this journey, the design of functional particles and complex particle structures has become increasingly important, with strong interaction with materials science. An expression of this is the development of nanoparticle technology, especially in the first decade of this century, and the design of complex particle structures for energy storage, conversion, and generation, especially in recent years. Accordingly, my research has shifted from the production of nanoparticles to the processing and design of energy and pharmaceutical materials, always based on a deep understanding of particle behaviour within individual processes.

I am very happy that in the post-Corona period, we can meet again with our particle technology colleagues and friends around the world at conferences or KONA board meetings to further our common interests. It was a pleasure to meet so many colleagues and friends during 2022 at various conferences, especially the World Congress on Particle Technology in Madrid (Spain) and Chops in Salerno (Italy), although these conferences were still influenced by Corona as quite a few participants were infected at the conferences. In 2023, the European conference highlight was PARTEC 2023 in Nuremberg (Germany), with the overarching theme "Particle Technology for Sustainable Products", addressing the increasing importance of sustainability and circular economy due to climate change. As the PARTEC 2023 Chair, it was an honour and a pleasure for me to welcome over 500 colleagues from 25 countries, who enjoyed more than 300 plenary, keynote, regular and flash presentations and experienced the diversity of our research field. Overall, the presentations at PARTEC 2023 show the importance of particle technology across all industries. Today, particle technology plays an important role not only in classical industries such as chemical, pharmaceutical, food, and minerals industries but also in dynamically developing industries of energy transition with products such as batteries, solar panels, and fuel cells. Moreover, numerical simulation and digitalisation are becoming more and more important. Overall, I see a clear trend that particle technology is becoming increasingly interlinked with other technologies and communities:

First, the importance of design, synthesis, and processing of particulate energy materials rises significantly due to the global energy transition towards 100% use of renewable energy resources and minimisation of the CO_2 footprint. Even today, the production, processing, and recycling of active materials for lithium-ion batteries require in-depth knowledge of particle technology in addition to materials science, electrochemistry, and production engineering. Particle technology is even more important for solid-state batteries, which are the most promising new generation of

Copyright © 2024 The Author. Published by Hosokawa Powder Technology Foundation. This is an open access article under the CC BY license (https://creativecommons.org/licenses/by/4.0/).

batteries. Here, particulate solid electrolyte particles made of sulphides, halides, or oxides have to be produced and processed together with the active material particles and other components in such a way that high ionic conductivity and long cycle life are achieved.

Second, the production of innovative products such as battery cells, solid pharmaceuticals, functional coatings, and additively manufactured products requires close cooperation between particle technology and production engineering, as well as cooperation with relevant technology areas. A relatively new and emerging field is additive manufacturing, where particles need to be produced, tailored, e.g., with nanoparticle coatings, and recycled. In addition to metal- and polymer-based particles, mineral particles for additive manufacturing in construction are also current areas of research.

Third, for the numerical simulation and digitalisation of processes and products using particles, the Particle Technology Community works with scientists and experts from mathematics, physics and computer science. As a result, numerical simulation using discrete element methods (DEM) is becoming increasingly powerful and can now simulate even larger industrial problems. In addition, DEM is increasingly being combined with other simulation methods such as computational fluid dynamics and population balances. More recently, artificial intelligence methods have been used to predict process results and product properties based on relatively large datasets.

In addition to inter- and transdisciplinary collaborations, I see increasing international collaboration within our particle technology community as an important goal for the future, despite the increasing conflicts between countries that we see today. In addition to international conferences, the funding of joint research projects with partners from different countries is an important measure and should be strengthened in the future. There are also international organisations such as the International Fine Particle Research Institute (IFPRI) or more technology-oriented associations such as the Global Comminution Collaborative (GCC), the International Delegation on Filtration (INDEFI) or the Association pour l'Etude de la MicroMécanique des Milieux Granulaires (AEMMG). Such global scientific organisations not only promote international research cooperation but also an intensive exchange between science and industry, and a general understanding between nations.

This issue of KONA continues the trend of previous issues towards the publication of more high-quality review articles alongside forward-looking original articles from many countries. Accordingly, journal metrics such as the impact factor, which is now above 4, have developed very positively recently. The increased focus on high-quality review papers is sure to further enhance KONA's reputation. This issue contains 12 high-quality review papers and 5 original papers by 54 authors from 11 countries. Five papers focus on modelling and numerical simulation, 2 on energy materials, and one on additive manufacturing, the three emerging areas mentioned above. Further 5 papers focus on fundamental operations, including powder and multiphase flow, and 2 papers each on the characterisation and synthesis of particle systems.

Finally, I would like to thank all the authors and reviewers for their hard work in preparing and optimising the papers, as well as all those who have contributed to the realisation of this "KONA Powder and Particle Journal" Issue No. 41.

Arno KWADE
Chairman of European/African Editorial Board
Professor, Technische Universität Braunschweig
October, 2023

KONA Powder and Particle Journal

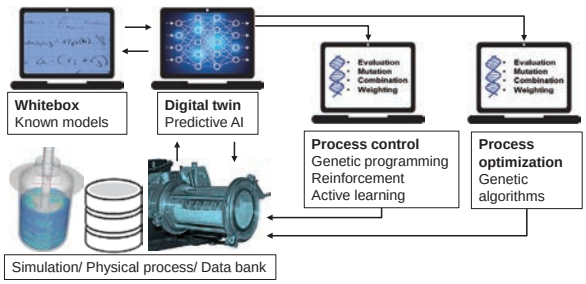
KONA Powder and Particle Journal No. 41 (2024) 3–25/https://doi.org/10.14356/kona.2024011 Review Paper

Artificial Intelligence and Evolutionary Approaches in Particle Technology †

Christoph Thon *, Marvin Röhl, Somayeh Hosseinhashemi, Arno Kwade and Carsten Schilde

Institute for Particle Technology (iPAT), Technische Universität Braunschweig, Germany

Since the early 2010s, after decades of premature excitement and disillusionment, the field of artificial intelligence (AI) is experiencing exponential growth, with massive real-world applications and high adoption rates both in daily life and in industry. In particle technology, there are already many examples of successful AI applications, for predictive modeling, process control and optimization, fault recognition, even for mechanistic modeling. However, in comparison to its still untapped potential and to other industries, further expansion in adoption rates and, consequently, gains in productivity, efficiency, and cost reduction are still possible. This review article is intended to introduce AI and its application scenarios and provide an overview and examples of current use cases of different aspects and unit operations in particle technology, such as grinding, extrusion, synthesis, characterization, or scale up. In addition, hybrid modeling approaches are presented with examples of the intelligent combination of different methods to reduce data requirements and achieve beneficial synergies. Finally, an outlook for future opportunities is given, depicting promising approaches, currently being in the conception or implementation phase.



Keywords: artificial intelligence, genetic algorithms, predictive modeling, hybrid modeling, particle technology

1. Introduction

Artificial intelligence (AI) has reached critical applicability rates in recent years as a consequence of algorithmic improvements, exponential gains in hardware and data generation, and increasing improvements in available infrastructure, such as the current focus on parallelization and dedicated hardware solutions (ASICs) (LeCun et al., 2015).

Consequently, AI is increasingly being adopted in all aspects of daily life and throughout industries. In particle technology, there are many areas in which AI techniques are already being applied, but dependent on the specific background such as the ability to rely on or generate large amounts of data, security aspects, availability of sensors, the ability to dynamically interact with processes, etc., which lead to varying rates of and requirements for the adoption of AI. Practical examples encompass a wide variety of areas within particle technology, such as predictive modeling of grinding results, kinetics, pathways, stability, mixing and quality, preprocessing of data, shape control in particle synthesis and parameter control in general, yield optimization, separation via machine vision, use as soft sensors, improvement of measurement results, surrogate modeling, etc.

Similarly, AI itself is an umbrella term. This review article builds on more general articles about AI in the context of process engineering (Thon et al., 2021; Pham and Pham, 1999; Linkens, 1990; Mavrovouniotis, 2012; Lee J.H. et al., 2018) and focuses on the context of particle technology specifically. Furthermore, general reviews exist, such as of mechanical engineering (Patel et al., 2021), electrical engineering (Sakunthala et al., 2017), material science (Pilania, 2021), and chemical engineering (Schweidtmann et al., 2021; Ashraf et al., 2021; Venkatasubramanian, 2019). On the other hand, focused review articles for specific subfields within particle technology exist, such as for related autonomous processes (Nirschl et al., 2022) or nanoparticle drug formulations (Uhlemann et al., 2021), although, to date, no conclusive overview of the field of particle technology has been provided, which is the focus of this review article.

In this paper, prominent techniques such as neural nets or evolutionary algorithms are discussed and an overview of hybrid modeling techniques and examples of ensemble methods (the intelligent combination of techniques) are provided.

In the following, based on a short summary of important AI methods, examples of applying AI to important aspects of particle technology, including unit operations such as grinding, synthesis, modification, or classification, as well

† Received 18 May 2022; Accepted 6 September 2022
J-STAGE Advance published online 15 July 2023
* Corresponding author: Christoph Thon;
Add: Volkmaroder Str. 5, D-38104 Braunschweig, Germany
E-mail: c.thon@tu-braunschweig.de
TEL: +49-531-391-65553 FAX: +49-531-391-9633

Copyright © 2024 The Authors. Published by Hosokawa Powder Technology Foundation. This is an open access article under the CC BY license (https://creativecommons.org/licenses/by/4.0/).

as particle analysis and scale up procedures, are reviewed. Finally, an overview is provided to depict near-term opportunities and untapped potentials.

2. Introduction into Artificial Intelligence

AI encompasses a wide spectrum of techniques like artificial neural networks (ANN), genetic algorithms (GA), Hidden Markov Models, and others. First introduced at the famous 1956 Dartmouth conference with the goal to emulate general human cognitive capabilities, AI experienced three major waves of enthusiasm and disillusionment as a consequence of initial hype and overestimations on one side and hardware and software limitations on the other. It was not until the early 2010s that AI experienced major breakthroughs in real-world applications and adoption rates, with the most common AI techniques used today being deep neural networks (DNNs) (Ongsulee, 2017).

Fig. 1 depicts the basic principle of ANNs. Being loosely inspired by the brain, the fundamental building blocks are neurons, which are connected. The neurons are arranged in layers, with the first layer being denoted as the input layer and the last one as the output layer. Each input and output node is a representation of an input and output, e.g., a parameter of a process, a pixel in an image, or a word in a text. Inputs can be binary, integers, or continuous values. Between these two layers are a number of hidden layers, in which the modeling is taking place. Between the neurons of neighboring layers, the different connections have dedicated weights associated with them.

As can be seen in the right part of **Fig. 1**, which is zoomed out for one representative neuron, inputs are multiplied with their respective weights and consequently summed. The summed weight is further processed via an activation function; the resulting value is then propagated forward to successive neurons of the following layer. Through different activation functions, linearities, non-linearities, or other patterns can be introduced, with the resulting behaviors of the overall system changing, such as spiking neural nets appearing, etc. Being a hierarchical statistical system, ANNs have generalizing capabilities because they process more complex patterns of a higher order on the basis of detected lower-order patterns of more limited complexity. The goal of AI training is the iterative optimization of connection weights in order to get correct outputs for given inputs based on training data. The classical approach for this is backpropagation in which after each iteration, a loss function is determined for the successive analytical approximation and adjustment of the weights. Specifically, for large AI systems with an abundance of training data, backpropagation is the classically used training approach, although it has a strong tendency toward overfitting in cases with limited data sets. Alternative systems exist, which are focused on training with more limited data, such as genetic reinforcement learning (GRL), which was described in greater detail in Thon et al. (2022b) and can be described as the training of AI via a genetic algorithm.

In addition, there exists a plethora of techniques to prevent overfitting, which can also be combined to achieve more general models, such as regularization, feature selection, early stopping, layer removal, or dropout. Regularization encompasses techniques to prevent the training of too complex models, e.g., through the use of penalties or changes in the neural network architecture upon training. L1 (Lasse regularization) and L2 (ridge regression) modify the penalties in training by adding an absolute value or the squared value of magnitude (Demir-Kavuk et al., 2011). In dropout, as another regularization method, neurons are randomly deactivated during training to prevent excessive co-adaptation (Srivastava et al., 2014). Feature selection is another method to prevent overfitting by restricting the training to only the most relevant features in case of

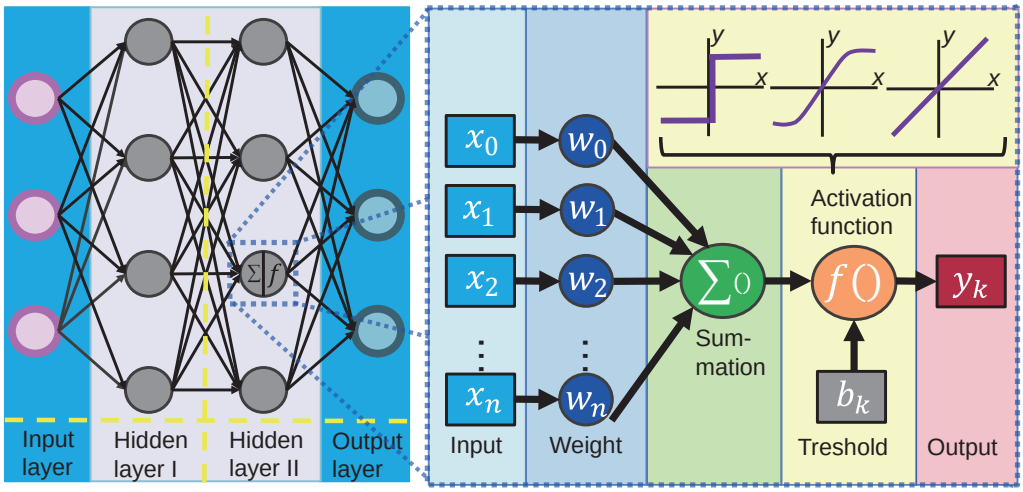


Fig. 1 Depiction of a neural net, with an input, an output, and two hidden layers. Connections between neurons of layers feature dedicated weights. Incoming inputs from former layer neurons are summed and multiplied according to an activation function, e.g., to introduce non-linearities.

the initial number of features in the data being too large (Hawkins, 2004). Early stopping describes the techniques of evaluating training over epochs with independent data (also termed “hold up”) to quit training once a degradation of the loss becomes detectable, indicating overfitting and a loss in generalizing capabilities (Ying, 2019). Cross-validation, as a more advanced version of hold up, allows for training and evaluation with independent data, with varying assignments of the data groups to train and test data, allowing all data to be used for training (Schaffer, 1993).

GAs are another tool often used, specifically for optimization tasks but also for modeling and regulatory applications. As shown on the left in **Fig. 2**, GAs are a population-based approach that mimics Darwinian evolution in biology.

As a starting point, a population of parameter sets (usually consisting of a fixed and, throughout the population, identical number of entries with variable values) is evaluated according to a stated goal. If, for instance, process parameters in a stirred media mill are to be optimized with regard to maximum energy efficiency, production yield, or the optimal combination of both KPI, measures for the optimization goal or for multiple goals are established, and the optimizable parameters are defined. Evaluation of the specified goals of initial parameter sets is performed for the selection of the most suitable parameter sets. A subsequent crossover of selected areas in the parameter space results in a new generation with mixed attributes from the previous generation. In addition, mutations are induced at specified rates to increase the “genetic” diversity of the population and to avoid optimization within local minima. Through iterative execution over multiple generations, eventually (under constant environmental conditions), a steady state is reached with ideally close to optimal parameter settings.

Genetic programming, shown on the right side of **Fig. 2**, applies the same steps for the iterative evolution of decision tree structures or decision trees. These tree structures can represent computer programs, with respective operators and numbers being the nodes in the tree, to automatically develop code. Alternatively, the trees can represent mathematical operators for the evolution of fitting equation systems for the description of data sets for modeling tasks. The technical term for genetic programming, when applied to formulas, is symbolic regression. In principle, all tree-based tasks can be optimized with genetic programming.

A more detailed summary of underlying AI techniques can be found in more general review papers (Krishna et al., 2018; Rupali and Amit, 2017; Raschka et al., 2020; Rahmani et al., 2021; Thon et al., 2021).

Key criticisms of AI are usually its inherent lack of transparency and its empirical nature. Different methods exist to address these issues including explainable AI (XAI), reverse engineering strategies, and hybrid or gray-box modeling. Often, respective disadvantages of different AI methods can be compensated for by the intelligent combination of different methods such as ensemble methods or hybrid approaches (Stosch et al., 2014). For instance, as seen in **Fig. 3**, predictive neural net modeling as a black box can be utilized in order to create a model with generalizing capabilities for the subsequent prediction of virtual training data for genetic programming.

The generalizing capabilities of genetic programming are more limited than those of neural nets. The technique is, however, intrinsically more transparent. In conjunction with additional methods, genetic programming even allows

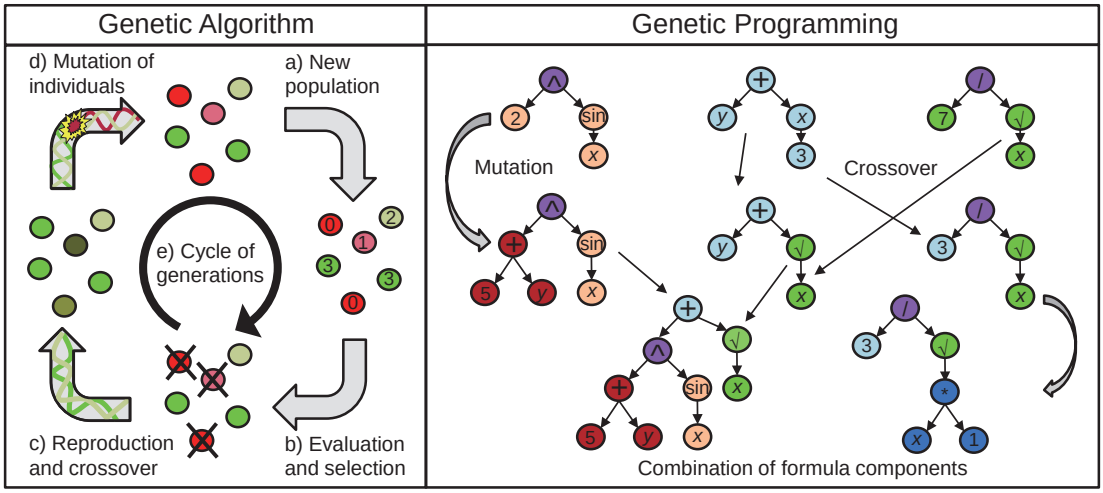


Fig. 2 Two common evolutionary algorithms, genetic algorithms and genetic programming, emulating Darwinian evolution on technical use cases. On the left, settings for a fixed set of parameters are optimized via successive generations of parameter mutations, crossover between candidates, and the evaluation and selection of suitable candidates in the population. On the right, the same principles are applied in genetic programming, but on the basis of decision trees of theoretically unconstrained complexity, representing computer code, rule sets, or mathematical equations, with the latter one called symbolic regression. Reprinted from Ref. (Thon et al., 2022b) under the terms of the CC-BY 4.0 license. Copyright: (2022) The Authors, published by Elsevier.

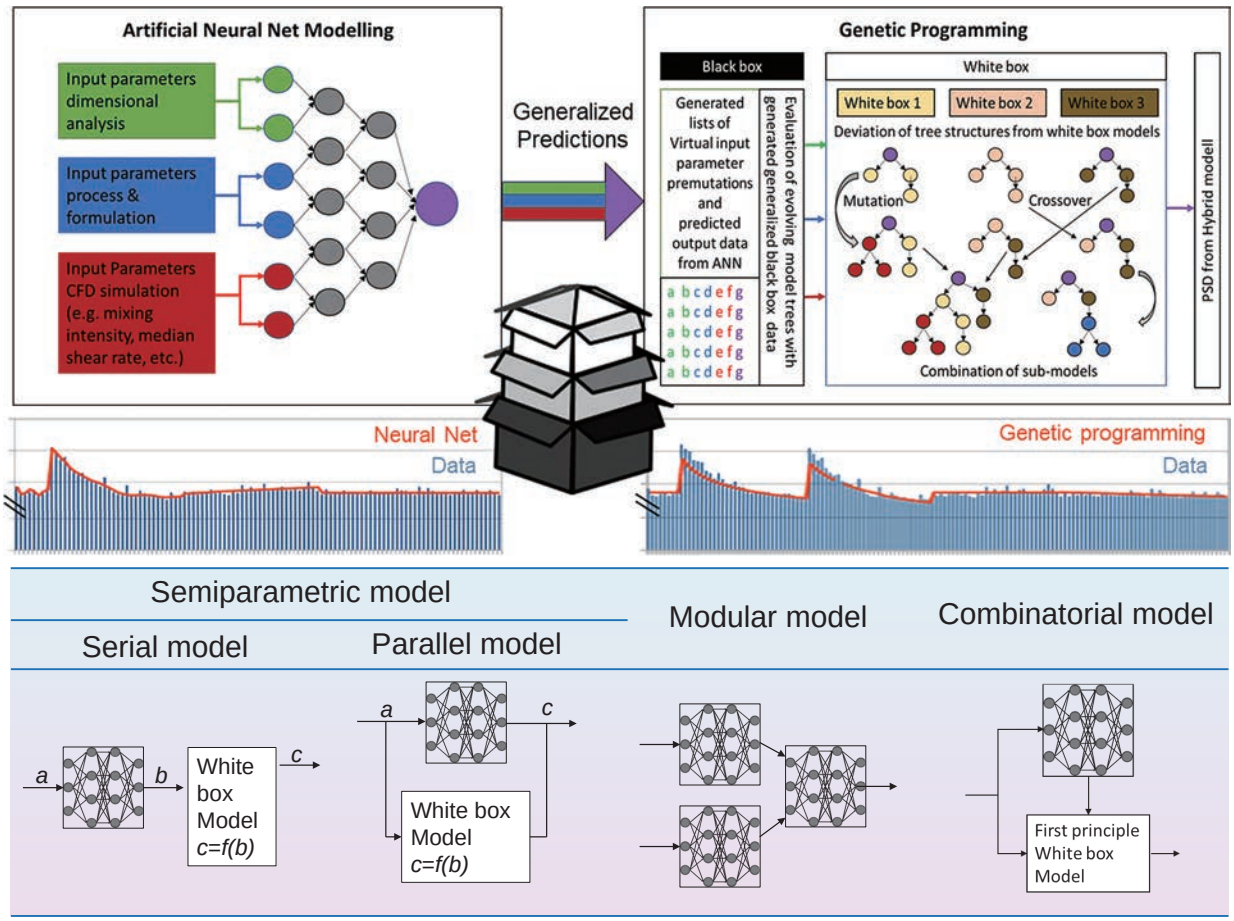


Fig. 3 A combination of predictive models based on neural nets to gain generalizing capabilities and genetic programming for the subsequent deduction of more transparent mathematical models, in which equation modeling is performed on the basis of predictions from the neural net model. Examples are provided for the results of both approaches, with blue columns marking training data and orange lines the respective model prediction. Furthermore, hybrid modeling approaches are depicted, as well as serial and parallel semi-parametric models, modular models, and a possible combinatorial approach.

for the incorporation of physical relations (Udrescu et al., 2020).

In addition, as can be seen in **Fig. 3**, for an exemplary data foundation (blue), the generated equation represents a simpler (more transparent), though still accurate, relation when compared to neural net predictions (orange lines).

Similarly, McKay et al. (1996) proposed a nonlinear dynamic model using two different paradigms. In this work, they tried to compare the recurrent neural network and the genetic programming algorithm to build a viscosity model. They showed that in this particular case, the genetic programming model has simpler transparency than neural networks.

Beyond the combination of neural nets and evolutionary approaches, hybrid models, shown in the lower part of **Fig. 3**, are well suited for mechanistic modeling and the incorporation of existing empirical or white-box models. In a serial approach, a white-box model can be applied to preprocessed data from AI or in a direction opposite to the preprocessed data based on known relations for subsequent AI modeling. Running in parallel, black-box AI models can be used to compensate for the shortcomings of existing white-box models by merely modeling the divergence between white-box model predictions and reality. The parallel AI can, for instance, be broken down again via genetic programming to iteratively extend the white-box model (Thon et al., 2021, 2022b; Evans et al., 2019). In modular hybrid models, an interconnected system of sub-AI models is set up to mirror the known structure of its physical counterpart and facilitate the modeling effort. Combinations of hybrid models are possible, such as a mixture of a serial and a parallel semiparametric model, as Psichigios and Ungar (1992) demonstrated.

In addition, a wide variety of reverse engineering strategies exist to deconstruct or deduce the inner workings of trained AI systems, such as sensitivity analysis, dropout, deconvolution, rationalization, LIME, GAM, gradient descent, neuron activation, etc.

3. Applications of AI in particle technology

Table 1 provides an overview of AI applications for various categories of particle technology unit processes.

Table 1 Overview (state July 2022) of some examples for AI in particle technology with the author, a broad description, the task, and used AI types, as well as the data foundation, sorted according to a classification scheme featuring unit operations, and tasks. Abbreviations are defined in the nomenclature before the references.

		Example	Description	Task (process and AI)	AI type	Data foundation
Operations	Grinding	Qu et al.	Fault recognition in the grinding process	Classification	ANNs: BP, LSTM, Auto-Encoder	Experiments
		Thon et al.	Predictive modeling of kinetic energies in a wet stirred media mill with subsequent mechanistic modeling via genetic programming	Predictive and mechanistic modeling	ANN, GA, GP	Simulation
		Dai et al.	Particle size estimation in grinding (ball mill, spiral classifier)	Predictive modeling	Hybrid; ANN: random vector functional-link network	NA
	Synthesis	Pellegrino et al.	Process parameter-dependent prediction of TiO_2 nanoparticle morphology, size, polydispersity, and aspect ratio in hydrothermal synthesis. Reverse engineering for optimal process conditions	Modeling and process optimization	NA	NA
		Li et al.	Identify likely synthesis patterns of gold nanoclusters	Process optimization	NA	NA
		Chen et al.	Prediction and classification of energy expressions on the basis of structure and energy in ZnO nanoparticle morphologies	Classification and predictive modeling	NA	NA
		Zhang et al.	Control particle distribution in a cobalt oxalate synthesis process	Hybrid model; process control	NA	NA
	Mixing	Ittiphalin et al.	Process control of fat addition for feed pellets for animals	Predictive modeling for process control	LLM, BPNN	Preexisting data base of case study
		Khaydarov et al.	Data rectification through image recognition of a physical stirred reactor coupled with a CFD simulation to act as the surrogate model for process control	Preprocessing and data rectification for process control	DNN (YOLO model); serial hybrid model	Mixed experimental and simulation setup
	Aggregation	Leal et al.	Prediction of chemical equilibrium states effecting precipitation	Predictive modeling	NA	Simulations
		Nielsen et al.	Prediction of process kinetics for flocculation, crystallization, and fracture to model the kinetics of nucleation, growth, shrinkage, fracture, and agglomeration	Hybrid based on preexisting process knowledge	NA	Experimental (sensor data)
	Classification/ Removal	Hoseinian et al.	Prediction of ion flotation-based Zn(II) removal	Hybrid ANN-GA; predictive modeling	ANN-GA	NA
		Dai et al.	Size estimation in classification via a classifier (ball mill, spiral classifier)	Predictive modeling	Hybrid; ANN: random vector functional-link network	Experiments
	Combined System	Tie et al.	Online soft sensor: Particle size estimation for hydrocyclone overflow, combined with ball mill and classifier	Predictive modeling and classification	Modular-hybrid: 2x ANN; radial basis function networks	NA
		Dai et al.	Size estimation in grinding (ball mill, spiral classifier)	Predictive modeling	Hybrid; ANN: random vector functional-link network	Experiments
Characterization/ analysis	Rheology	Finke et al.	Fit rheology model via a genetic algorithm	Mechanistic modeling; GA	GA	Experiments
		Sun et al.	Electron transfer properties (e.g., Femi energy) dependent on the structural and morphological features of silver nanoparticles	Predictive modeling	ANN (three layers)	Experiments

The four classical unit operations of grinding, separation/classification, mixing, and agglomeration/granulation are elaborated on later in this paper, as well as bottom-up methods such as particle synthesis and characterization methods, including rheology.

Unit operations in particle technology are sometimes applied in isolation. In industrial operations, however, they are often combined and interconnected in complex plants. Possible assemblies vary to a significant degree, with some being more prominent. As can be seen in **Fig. 4**, the characterization of educts, products, or intermediary products can accompany the entire production flow and is often performed online during processes, as is modeling and the scale-up of operational steps. Mixing is an important operation embedded in the beginning of a process, repeated throughout the process flow, or integrated into other unit operations. Grinding as a top-down approach and synthesis as a bottom-up approach are typical operations for the production of particles. Stabilization/functionalization, agglomeration, or precipitation are unit operations often performed successively after the production of primary particles, although integrative approaches such as parallel stabilization during grinding or synthesis are also often applied. After production, primary particles, agglomerates, or aggregates can be classified, e.g., according to their size, morphology, or other characteristics and can be further processed, e.g., via extrusion. This brief overview is intended as a simplified representation of inter-dependencies and how unit operations can be integrated and connected in practical applications. The individual unit operations and accompanying steps are discussed in regard to the application of AI and evolutionary approaches.

In this regard, descriptions are given together with the AI-specific tasks (predictive modeling, classification, optimization, etc.) and the used types of AI (ANNs, genetic, algorithms, and hybrid models, etc.), as well as the training data source (experiments, simulations, data banks, etc.). In the following, the respective examples for the different categories are described in more detail.

At the time of this review article, numerous works existed. However, distribution throughout the different tasks and unit operations is inhomogeneous, with many mostly small-scale academic applications and a much smaller number of practical industrial adoption cases for large connected systems or plants. Distribution between individual unit operations and accompanying steps is similarly inhomogeneous, with most publications focusing on initial unit operations such as grinding, while examples for later unit operations such as extrusion are rarer. Furthermore, most of the published works with real-world applicability are very recent since they became possible only in the last five years, with more publications appearing closer to the date of this review. This indicates that there is significant untapped potential in the field for the adoption of AI techniques and aligns well with adoption rates in most other industries, with some featuring more advanced adoption rates.

3.1 Grinding

A plethora of techniques for the creation of product particles exists, as is elaborated on in subsequent chapters. Grinding is the most widespread technique used throughout many industries for a large variety of materials and products. As a top-down approach, it is suitable to cost-effectively process large quantities of material. With a developmental history almost as old as human cultural history itself, starting with the grinding of grains, modern available equipment is well established, sophisticated, and available in a large variety for more specialized applications such as mechanochemical reactions.

AI-based preprocessing can, for instance, be applied as an initial step for predictive modeling. Going to more sophisticated systems, modular predictive models allow for the modeling of more complex plants, which can be aided by hybrid modeling and white-box model combinations. Based on this optimization, anomaly detection and mechanistic modeling can be utilized, and examples for these increasingly sophisticated models are provided.

Dimensionality reduction: As depicted in **Fig. 5**, one of the first possible tasks that can be performed in an AI process flows is data preprocessing and dimensionality reduction, for instance, through the use of auto encoders. With grinding, Qu et al. (2017) trained a hybrid

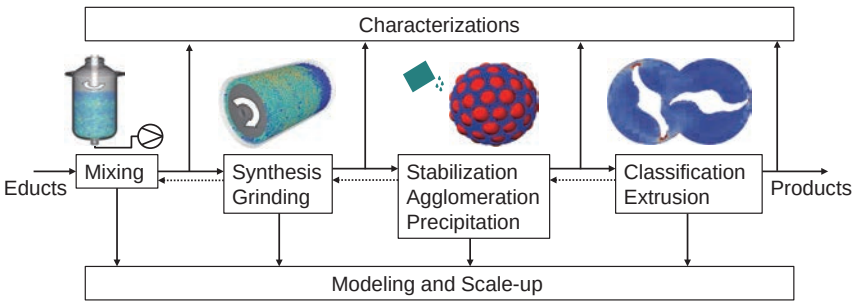


Fig. 4 Unit operations in particle technology.

auto-encoder-Softmax network and an RNN-LSTM network for fault recognition in a grinding system. One thousand experimentally gained data points were used, with 30 dimensional input features.

Via the reduction of the number of involved dimensions, the complexity of the data set can be drastically reduced, making successive conventional or AI modeling easier. In Qu et al., dimensionality can be reduced from 30 dimensions (such as temperatures, pressures, sounds, vibrations in different regions of the grinding system) to 24 (Qu et al., 2017). Input and output layers are set up identically. The encoder side is intended to reverse engineer and reconstruct the previously decoded representations from the input side as accurately as possible. The narrowing of intermediary hidden layers enforces more compact representations with reduced features.

Predictive modeling of single units: Based on experimental data, the authors of this review article trained predictive models (see **Fig. 6**), for grinding Quarz in a stirred media mill (PM1 from Bühler). Input process parameters such as tip speed, solid content, and fluid volume flow were varied, and additional values for torque and power were measured. An ANN was then optimized and trained.

The cumulative particle size distributions (PSD) were normalized and represented via a discretized grid, with the distribution curve being in a grid cell translating to a cell value of 1 or 0. The resulting binary values were assigned to the output nodes of the net. Consequently, for novel input parameter settings, heat-maps can be generated to mark the likelihood that the respective cumulative curve will pass through a cell. During post-processing, resulting scatter plots were derived and converted to approximation cumulative curves. In the right lower part of **Fig. 6**, predicted X_{50} (describing the particle size within the distribution, at which 50 percent of particles are smaller and 50 percent larger) values are depicted over the respective X_{50} values of the independent evaluation data points. The approach was further optimized for the prediction of fitting parameters, which is elaborated on later in the context of describing a predictive breakage tester AI.

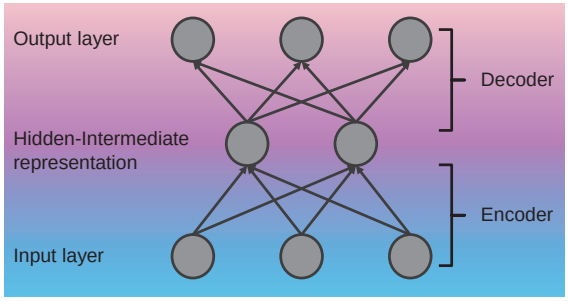


Fig. 5 Autoencoder networks with an encoder and a decoder side are often used for dimensionality reduction, as smaller hidden layers act as a bottleneck, forcing intermediary representations with narrower features.

Modular predictive hybrid modeling of plants: Dai et al. proposed a parallel semiparametric hybrid particle size estimation model, in combination with a random vector functional-link network (RVLFN), with the examined grinding circuit mainly consisting of an interconnected system comprising a ball mill and spiral classifier (see **Fig. 7**).

The ball mill's first principle model was based on population balance equations; the classifier was described by its own mechanistic model (Dai et al., 2015).

Based on these these underlying models, sensitivity

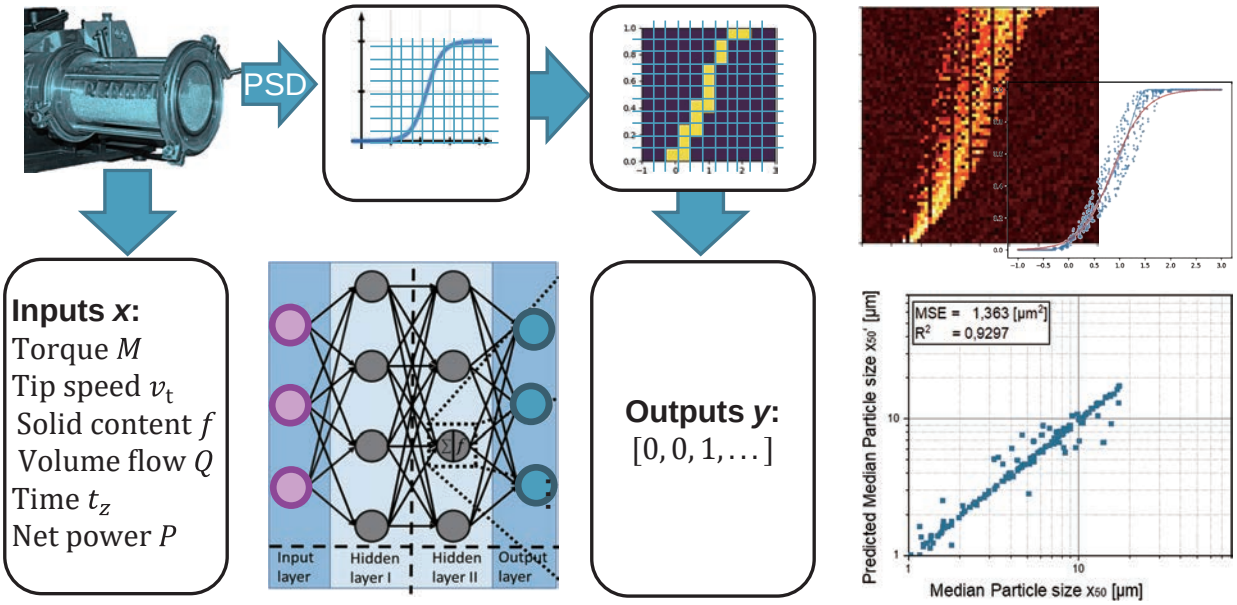


Fig. 6 Predictive model for experimental grinding results. For varied process parameters such as tip speed and solid content, resulting particle sizes were predicted, with one output for X_{50} (marking the particle size in the distribution, where 50 percent of the particles are smaller and 50 percent are larger) and the other a heat map for the representation of the entire particle size distribution (original work by author).

analysis and pre-predator optimization algorithms were utilized in order to reduce parameter optimization complexity. For the resulting error, the RVFLN was trained to compensate for the first principle method's error, resulting in an overall system with significantly higher accuracy (Dai et al., 2015).

Similarly, Tie et al. (2005) demonstrated PSD estimation via an on-line soft sensor for a setup consisting of a hydrocyclone overflow and a multitude of accompanying machines such as ball mills in two connected semi-circular grinding circuits, as shown in **Fig. 8**.

The underlying basic structures were divided utilizing a modular approach, while the classifier and hydrocyclone were described with respective ANNs.

The percentages of solids in the mass flow with diameters smaller than 75 µm, M_{75}, were modeled via AI in dependence of masses, concentrations, and respective flows for both the cyclone and spiral classifier. Mass percentage was furthermore modeled in dependence of multiple relevant parameters such as shaft power and recycle slurry flow rate. Sump modeling was based on a first principle population balance equation approach. The respective nets acting as functions in the overall setup ($f1$ for the cyclone and $f2$ for the classifier) were both radial basis function networks (RBF). In addition to the described models for the modeling of nominal process conditions, an adaptive neuro fuzzy inference system (ANFIS) model was trained for the upstream prediction of anomalies and malfunction, e.g., in case of excessive slurries. A subsequent fuzzy logic coordinator was applied for model connection (Tie et al., 2005).

Simulation-based modeling and breakdown for mechanistic modeling: AI modeling based on simulations is an approach with distinct advantages due to the coupling of two numerical approaches, as they can autonomously interact with one another unsupervised (for instance in active learning (AL), etc.). As an example, on the basis of two-way coupled computer fluid dynamics - discrete element method (CFD-DEM) simulations with Rocky DEM and Ansys Fluent, a representative slice of a wet operated stirred media mill was simulated with varying tip speeds and grinding bead diameters (Thon et al., 2022a; 2022b). Heatmaps were extracted, with each voxel representing the averaged values of relative velocities. **Fig. 9** depicts the results of the approach.

On the left side of **Fig. 9**, heatmaps for an independent test case not used in training are shown, with the prediction respectively depicted over the independent simulation result. Averaged values in 14 layers, as well as the density distribution of the entire domain for relative velocity, demonstrate the good fit of the result. The results also proved the advantages of GRL, as the models achieved significantly more accurate results in comparison to classical backpropagation. Finally, genetic programming was applied to identify a fitting equation to describe the relationship between the relative velocities 99 of colliding beads (99 percent had smaller energies) and the absolute tip speed of the stirrer. Depicted in the lower right corner of **Fig. 9**, parameter settings in random order are depicted, with red marking the equation and black the evaluation data.

The methodology was further improved and adapted to a vertical dry stirred media mill (original unpublished work by the author), demonstrating its universality, regardless of wet and dry states in grinding. In this case, a vertical mill was numerically investigated in Rocky DEM. Restitution coefficients and friction coefficients were determined and calibrated beforehand. Stirrer tip speed, grinding bead size, and grinding aids for the variation of powder flowability

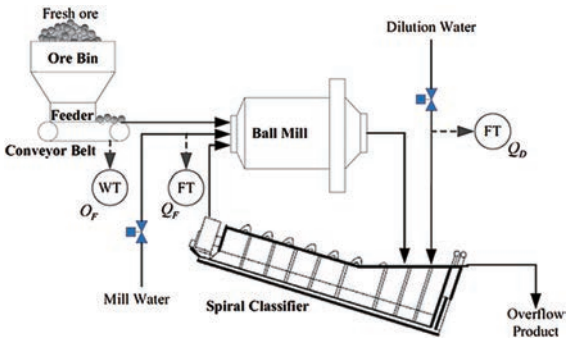


Fig. 7 Milling setup consisting of a bin, a feeder, the ball mill, and a spiral classifier. Reprinted with permission from: Ref. (Dai et al., 2015). Copyright: 2015 B.V.

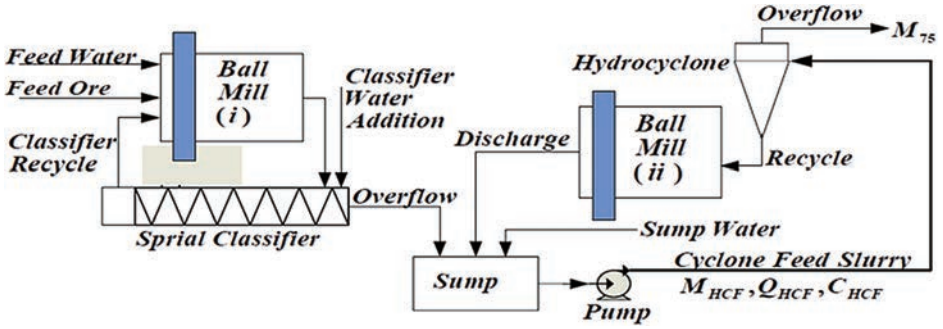


Fig. 8 Investigated connected setup with multiple machines used for PSD prediction with machine learning in a soft-sensor approach. Reprinted with permission from Ref. (Tie et al., 2005). Copyright: 2005 B.V.

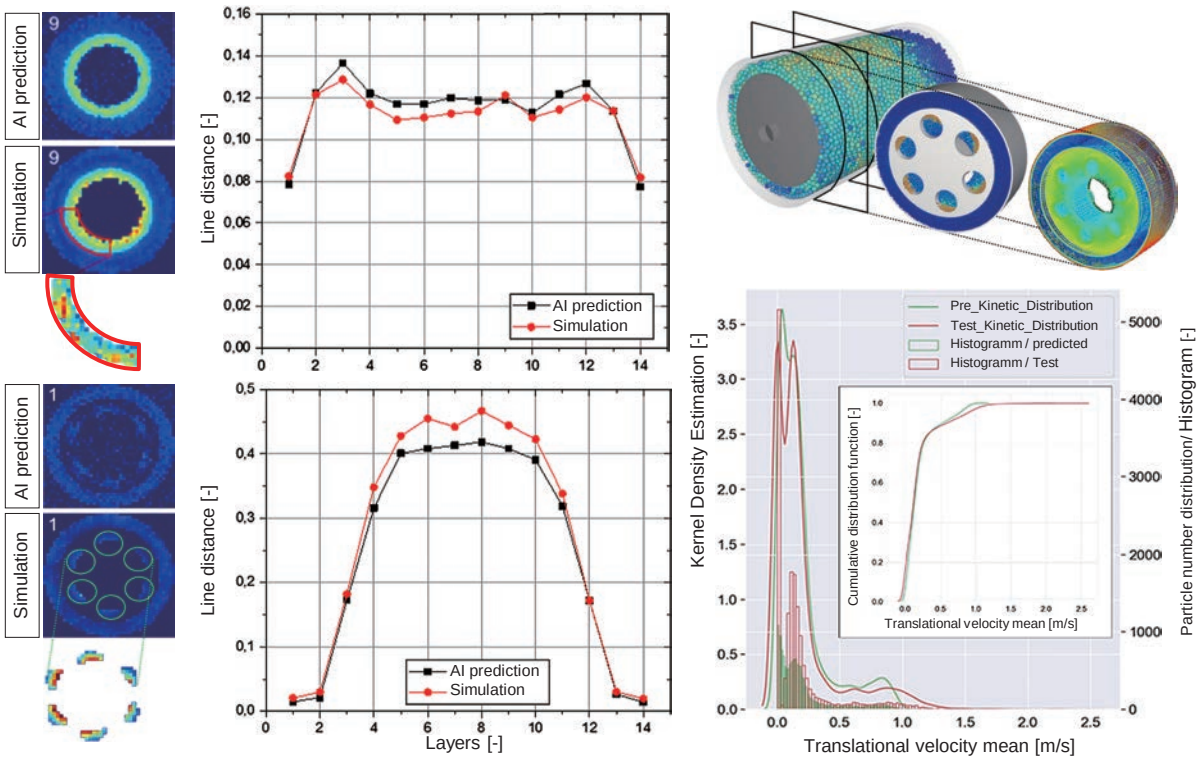


Fig. 9 A predictive mill model trained on the basis of a coupled CFD-DEM simulation. The simulation and prediction domain were discretized for the predictive modeling of the relative velocities of colliding beads as a measure of kinetic energy via heatmaps. Comparisons between AI predictions for independent simulation cases, not used for training, are depicted, showing good accuracy. Furthermore, a comparison of averaged values for characteristic regions in 14 layers of the mill, as well as for the entire domain, is provided. Finally, with genetic programming, a fitting equation describing the relationship of relative velocity 99 with tip speed was identified, being depicted for 22 parameter combinations in random order. Adapted from Ref. (Thon et al., 2022b) under the terms of the CC-BY 4.0 license. Copyright: (2022) The Authors, published by Elsevier.

(considered via the preliminary determined calibration parameters in the simulation) were chosen as input parameters, and the relative velocity voxels of the discretized mill domain (with a resolution in *x*, *y* and *z* of 46 × 22 × 22 voxels) were considered the output (see **Fig. 10**).

Adding to the previous approach, a convolutional neural net (CNN) was applied. CNNs are an approach often used in image recognition, in which pooling layers are introduced, with a sliding box sampling and condensing the features of a wider discretized domain, which can be seen in the upper part of **Fig. 10**. It can be seen that the predicted result comes close to the real values, which is also evident in the density distribution curve with close to convergent curves.

The main advantage of predictive AI as an intermediary modeling tool lies in its generalizing capabilities. Based on evaluated generalizing models, AI predictions can be obtained in inference for a large parameter space of high resolution whose systematic simulation, if performed completely, can take significantly longer. In the case of the wet mill simulation, systematic AI predictions were generated in the order of seconds, which would have taken time in the range of years with conventional CFD-DEM simulations (Thon et al., 2022a; 2022b).

3.2 Synthesis

AI can be used for the prediction of various particle properties and required synthesis pathways, as well as for the investigation of their correlations. Furthermore, AI can be used for synthesis control and optimization to achieve desired results.

Energy growth prediction: Chen and Dixon (2018) developed a machine learning (ML) approach to identify the relationships between the structure and surface and fragment energy in ZnO nanoparticle morphologies in bottom-up growth using nanoparticle fragments and derived means for the classification and energy expression of the nanoparticles. The focus was on the ML-based investigation of the stability, phase transition, and growth patterns of clusters, ultra-small nanoparticles, and bulk-sized particles based on fragment geometries and energy parameters.

Shape prediction: Pellegrino et al. (2020) demonstrated an ML approach for the predictive modeling of TiO_2 nanoparticle morphology, the size, polydispersity, and aspect ratio in dependence of process parameters such as the initial concentrations of Ti $(TeoaH)_2$, additive concentrations of $TeoaH_3$ as the shape controller, pH values, temperature in a hydrothermal synthesis process. Inversely, it can be used as a reverse-engineering approach to predict optimal process conditions for specific desired product

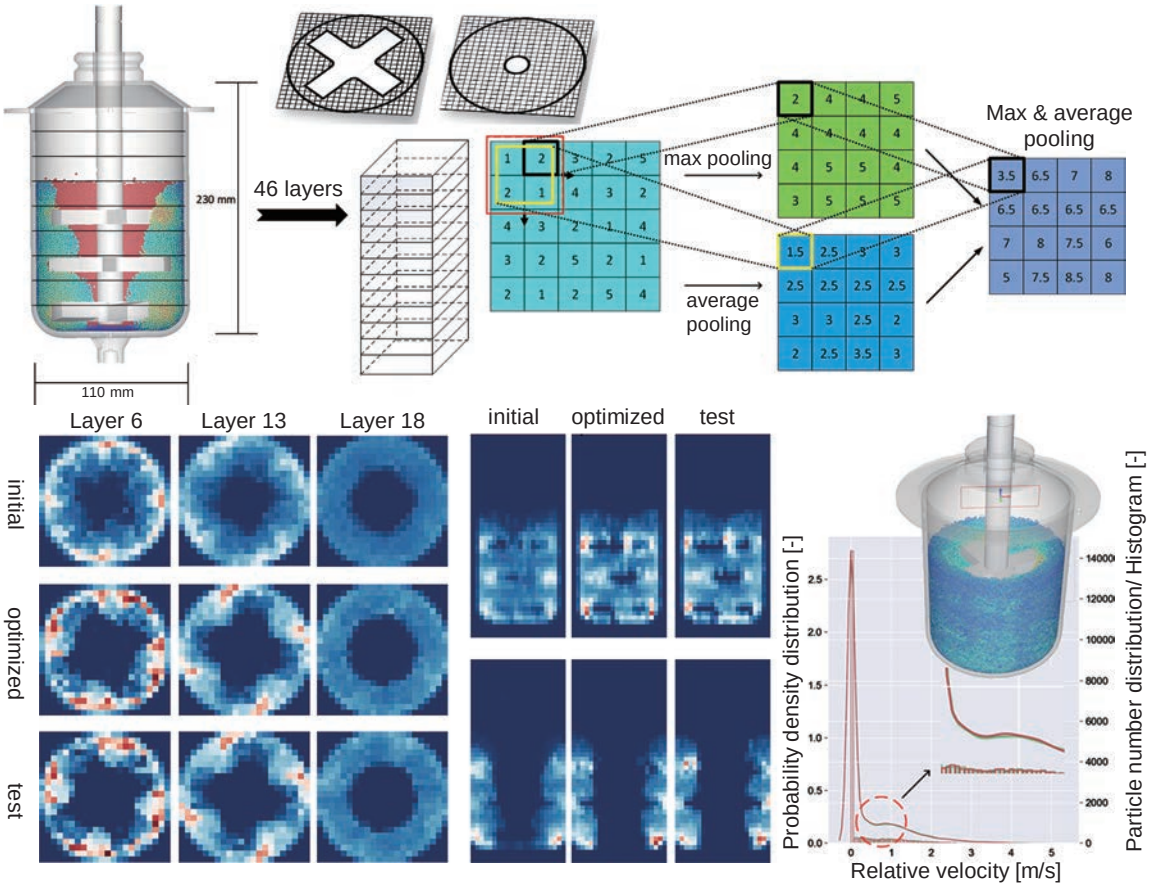


Fig. 10 Predictive models for relative velocities in a vertical dry stirred media mill with an improvement of the modeling approach by applying convolutional neural nets with integrated pooling layers. Very accurate models can be trained with heatmaps depicted for an independent evaluation case (test), with the initial prediction based on backpropagation and the final prediction following GRL. Both the side and top views of heatmaps and the whole domain density distribution show good alignment (original work by author).

characteristics in terms of aspect ratio, morphology, and size.

Process control for shape (hybrid): Zhang et al. (2012) demonstrated a hybrid model to control particle size distribution in a cobalt oxalate synthesis process, with the first principle model capturing the known process characteristics with a partial least-squares (PLS) regression ML model to compensate for its shortcomings, with the combined model being capable to model the PSD evolution. The reaction took place in a two-reactor system being connected in series, with the first acting as an ammonium oxalate dissolver and the second being responsible for the successive crystallization.

Process optimization for yield: Jose et al. (2021) demonstrated that AI in the form of multi-object ML optimization can also be used for the optimization of product yields with the example of ZnO nanoparticle synthesis. The optimization relied on high-yield microreactors and high-throughput analysis. In less than 100 experiments, optimization could be achieved, allowing for the continuous production of 1 kg per day. A scalability assessment of the approach was conducted.

Prediction, experimental planning, and synthesis-assistance: A dedicated review article that Tao et al. (2021) conducted focused on the use of AI in the specific context of nanoparticle synthesis. Examples were provided for the prediction of nanoparticle properties, the assistance of the synthesis, experimental planning, and data generation in the contexts of semiconductor, metal, carbon-based, and polymer nanoparticles. However, most current applications in the field focus on the identification and optimization of existing procedures, with some targeting the identification of novel particles and procedures.

3.3 Stabilization and Functionalization

After or during synthesis (e.g., during in-situ stabilization) and in the context of other unit operations (such as fine grinding, agglomeration, etc.), stabilization is required, as generated product particles would otherwise agglomerate uncontrollably. Identification of suitable stabilizers can be a laborious task, with the result and emerging properties often being unpredictable. Here, AI modeling can be a useful tool in predictive identification and the estimation of resulting properties in regard to solution or adsorption capabilities and resulting stability.

Prediction of solution capabilities: Astray et al. (2017)

showed an AI model to predict the solution properties of alkylammonium surfactants such as density, surface tension, and kinematic viscosity as functions of input parameters such as concentration, carbon number, and the molecular weight of surfactants, with an R^2 of 0.97.

Prediction of adsorption capabilities: Faghiri et al. (2019) trained an AI model based on least-square vector machines to predict the surfactant adsorption of sandstone in the context of oil recovery. Parameters were surfactant density, concentration, time, and kinetic adsorption density. Good predictive capability could be reached for kinetic adsorption density, with R^2 accuracies for independent testing data of around 0.96.

Prediction of final stability: Kundu et al. (2016) focused on stabilization in emulsions. A hybrid multiple inputs and multiple outputs (MIMO) ANN-GA model was used to predict the formation and stability of (o/w) petroleum emulsions during stirring, with parameters being oil and surfactant concentration, stirrer tip speed, and pH value. Prediction errors were at around five percent.

Li L. et al. (2020) modeled the stability of Al_2O_3-ethylene glycol nanofluids via an ANN in dependence of particle size distribution and velocity ratio (the ratio between Brownian particle velocity and gravitational settling velocity). The nanoparticles in ethylene glycol were magnetically stirred and positioned in an ultrasonic bath. Input parameters were thermal conductivity, viscosity, mass fraction, and temperature. R^2 accuracy ranged between 0.98 and 0.99.

3.4 Precipitation

Precipitation is an approach whereby the addition of agents or changes in other influencing parameters such as temperature in a solution can rapidly force specific materials out of the solution to form defined, mostly amorphous particles. In slower dissolution, the resulting particles crystalize. In both cases, the prediction of suitable conditions and the estimation of the result are difficult tasks, which usually involve much often intuitive manual experimentation to identify equilibrium states, resulting process kinetics, and the final amount of precipitate.

Equilibrium prediction: Leal et al. (2020) demonstrated an on-demand ML (ODML) algorithm to predict based on simulation results new chemical equilibrium states effecting precipitation in fluids on the basis of the already past chemical equilibrium states in reactive transport simulations to reduce computing costs based on simulation results.

Kinetics prediction: Nielsen et al. (2020) described an AI framework for modeling particle processes based on preexisting mechanistic process knowledge and sensor data to estimate underlying process kinetics. Three case studies of flocculation, crystallization, and fracture were described and modeled for the kinetics of different underlying processes such as nucleation, growth, shrinkage, fracture, and for agglomeration.

Final precipitate prediction: Hoseinian et al. (2020) demonstrated a hybrid neural network–genetic algorithm with first principle models for the prediction of ion flotation-based Zn(II) removal.

3.5 Mixing

Most processes require homogenous distributions, although on some occasions, controlled inhomogeneities can be desirable. Therefore, mixing is an important aspect, also due to energetic reasons. In particular, mixing parameters should be chosen to not exaggerate energy intake, which can cause inefficiencies, excess wear, or product degradation, etc. In addition to the modeling of the process, control modeling and monitoring are highly significant, as mixing is, in many processes, a highly influential parameter that often requires active and dynamic adaptations or continuous control during the process.

Qualitative and quantitative monitoring: Bowler et al. (2020) showed ML-based monitoring of a mixing process with ultrasonic sensors in which classification models were applied for the general mixing capabilities of materials and regression models for the progress monitoring for mixing time.

Predictive real-time digital twins: Khaydarov et al. (2020) demonstrated a hybrid surrogate model with bubble recognition and online video processing in a physical stirred tank reactor for the enhancement of a parallel-running AI-based surrogate model for a CFD simulation, as depicted in **Fig. 11**. The trained surrogate model could be implemented on a near real-time running edge-node, with online AR displaying the result for a human operator. As resource-efficient real-time modeling with direct feedback to human or machine interfaces is a desirable goal beyond mixing, the use case is interesting for other unit operations or plant operations. Furthermore, the given case demonstrates a quick mostly numerical AI-based digital twin for the real-time processing of the inner mechanisms of a parallel-running process, yet with periodic alignment to physical reality via direct measurement feedback (which can be a soft-sensor approach).

Mixing additive control prediction: Ittiphalin et al. (2017) demonstrated the addition of fat to a mixing process of feed pallets for animals. Among others, a backpropagation neural network was trained considering mold size, total percentage of fat, percentage of additional fat, percentage of fibers, and pallet shelf-life as inputs for the estimation of additional fat to be added. In order to achieve an optimum process for increasing the production rate and deteriorating pallet shelf-life with an increased fat content, optimal fat quantities can be added during the dynamic mixing process.

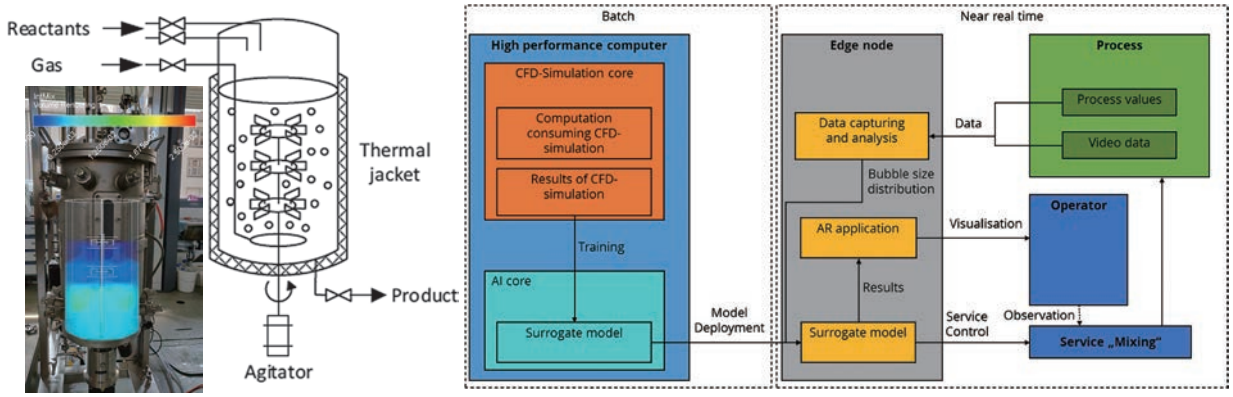


Fig. 11 Online surrogate modeling of a mixing process via a CFD surrogate model with direct feedback via an AR interface to a human operator running in near real time due to AI assistance. Feedback of the physical process was integrated into the approach via machine vision. Reprinted with permission from from Ref. (Khaydarov et at., 2020). Copyright 2020 B.V.

3.6 Aggregation

As described in precipitation and stabilization, primary particles can aggregate, agglomerate, or flocculate, which can be desirable under controlled circumstances. As in the previous operations, AI can assist in the prediction of suitable conditions and kinetics or the estimation or results. In addition to the prediction of specific given processes, it can also be used to identify suitable novel pathways within large parameter spaces.

Hybrid predictive kinetics modeling: Nielsen et al. (2020) described an AI framework for modeling particle processes based on preexisting mechanistic process knowledge and sensor data to estimate the underlying process kinetic rates of constitutive equations based on state variables and control actions. Depending on the investigated phenomena in the model, kinetic rates included one or more of the variables of nucleation, growth, shrinkage, agglomeration, and breakage. Three case studies, namely flocculation, crystallization, and fracture, were described and modeled for the kinetics of different underlying processes such as nucleation, growth, shrinkage, fracture, and agglomeration.

Aggregation pathway identification: Li J. et al. (2019) described the accelerated synthesis of gold nanoclusters with AU(III) to Au(I) reduction and subsequent coordination via thiolate ligands for complexation, considering all relevant parameters to identify likely patterns for the successful synthesis of nanoclusters using deep learning (DL).

Combined structure and pathway prediction: Wahl et al. (2021) demonstrated a ML-based approach to predict both the aggregate particles (polyelemental heterostructures) via colloidal self-assembly, as well as the way in which they formed, using a technique called a diffuse map. The approach proved capable of predicting many body phenomena and long-term assembly dynamics.

3.7 Extrusion

Another significant process in particle technology is extrusion. In this process, particles, and eventually, a fluid are first conveyed and then mixed. In the second step, the compression and shearing of a viscous mass under high pressure and temperature take place, then the mass is finally pressed through a shape-giving opening. The parameters are highly interdependent, and the selection of optimal operating conditions is usually time-consuming and increasingly costly. Consequently, the quality control of the extruded material is associated with various challenges, including the control of process parameters such as velocity and temperature or of the final product quality. Therefore, a more intelligent method needs to be developed. To achieve this goal, AI methods can be beneficial, in addition to being able to close the gap between often used simulations and accurate but costly experiments. In the following extrusion processes, pure polymers are described as the AI methods can be used similarly for particle-filled polymers.

Curing property prediction: Marcos et al. (2007) demonstrated the prediction of the extrusion properties of rubber, relying on compound composition and mixing conditions during extrusion. Despite being applied to molten rubber in this case, extrusion is often based on granular material, e.g., in many extrusion processes for battery production, wherefore the general approach is also of interest in the context of particle technology. Online information about specific curing properties can be predicted via integration into the process, eliminating waiting time for laboratory results and increasing product traceability.

Velocity control: Martínez-de-Pisón et al. (2010) presented a dynamic model for extrusion velocity control, which was capable of controlling manufacturing processes based on previously successful start-ups with data about pressure, temperature, and velocity. The complexity of this task was due to the open-loop control system and the constant alterations inherent to the process.

Temperature control: Taur et al. (1995) proposed a fuzzy PID temperature controller for the temperature control of the extruder cylinder using if-then rules and membership functions.

Tsai and Lu (1998) developed a predictive fuzzy PID controller with single-loop monitoring for extruder cylinder temperature control.

Quality control: Liu X. et al. (2012) proposed dynamic gray-box modeling based on a soft-sensor approach to control the quality of polymer extrusion. In this article, an attempt was made to use a gray box to provide real-time monitoring of the quality of the extrudate in order to reduce the setup time and improve the operation of the system. In this work, a soft-sensor structure was combined with a feedback observer to estimate the viscosity and control the final quality of the material.

Simulation-experiment translator: Bajimaya et al. (2007) used an ANN to predict the process parameters in extrusion. Simulation analyses are usually unable to take into account the boundary conditions of the manufacturing process, which is why their results remain mainly theoretical. On the other hand, conducting experiments is usually expensive and time-consuming, which is why the use of AI methods can reduce the gap between simulation and real data. The trained AI algorithm acted as a transfer tool to translate the theoretical variables gained from finite element method (FEM) simulations such as stress, strain, and shearing into realistic measures for extrusion pressure, temperature, and velocity.

3.8 Classification

Classification has many applications in particle technology that can be performed analytically to determine distributions or properties or as physical separation according to the respective properties. There exist many separation categories, with some being easier to implement, such as the classification of compact particles according to size, e.g., via sieving. For other aspects such as morphology or composition, sorting can be difficult. In such cases, manual human involvement or application-specific hardcoded automation is often required, but this can be expensive, unreliable, and inflexible and can limit the quantities that can be processed. Consequentially, the application of AI is a viable alternative in such instances.

Analytical classification with machine vision: Gonçalves et al. (2010) demonstrated an ANN-based technique of analytically classifying microscopic wear particles. Binarized particle images were obtained, and features such as area, perimeter, width, height, diameter, circularity, ferret diameter, elongation, and aspect ratio were obtained via ImageJ. Supervised classification reached accuracies of around 95 percent.

Massarelli et al. (2021) used computer vision and ML to analytically (i.e., with no physical separation involved) classify and count particles depending on dimensional size and morphology. The particles could be classified under supervision according to predetermined groups or without supervision to act as a measure for sample representativeness and in order to identify hidden features.

Physical separation: In addition to mere analytical classification, physical sorting can be performed, as Kattentidt et al. (2003) demonstrated, for the sorting of bulk solids. In an online operation, AI-based quality control was performed with two optical sensors for the separation of recycled glass. Distinguishing features were dimensionality, surface area and volume, texture, morphology, homogeneity, conductivity, and spectral reflection. Finally, a separation unit sorted the bulk material into dedicated fractions.

The AI-based sorting of particles, also in the context of recycling, has the potential to be a crucial pillar for a circular economy. For instance, Wilts et al. (2021) demonstrated AI-based waste sorting via a robotic arm and a sorting belt with a multitude of sensors (metal detector, high-resolution RGB camera, NIR sensor, VIS sensor).

Furthermore, Peršak et al. (2020) demonstrated the sorting of transparent plastic granulates based on computer vision and subsequent pneumatic air separation. The plastic particles had sizes of 2–4 mm, sorting accuracy for 9 classes equaled 90 percent, and for two classes, it was 100 percent.

3.9 Characterization and Analysis

In almost all cases, after or during unit operations, the characterization of properties and their distribution is required. Sometimes, these can easily be gathered, while in other cases, directly obtaining the required data can be challenging or impossible due to limitations in measurement equipment, physical constraints, accessibility during operations, etc. Often, analysis is possible but limited in regard to the executable quantity due to the nature of the measurement technique or the hardware. In all these cases, AI can be a useful technique to use with parallel running predictive or surrogate models, as these can be enriched by limited physical information, as previously shown in the case of mixing (Khaydarov et al., 2020). In addition to use in soft sensors, AI and evolutionary approaches can be used to enhance measurement results through post-processing or to derive mechanical descriptions of the measured properties and their influencing parameters.

AI as a soft sensor: Reliable predictive models can also be used to directly replace measurement, or as additional assistance in the context of soft sensors.

An important characterization method for particle breakage is the particle breakage function, which can be determined via a breakage tester, as described in Böttcher et al. (2021) (see **Fig.12**).

In the breakage tester, rotational velocity and gap size

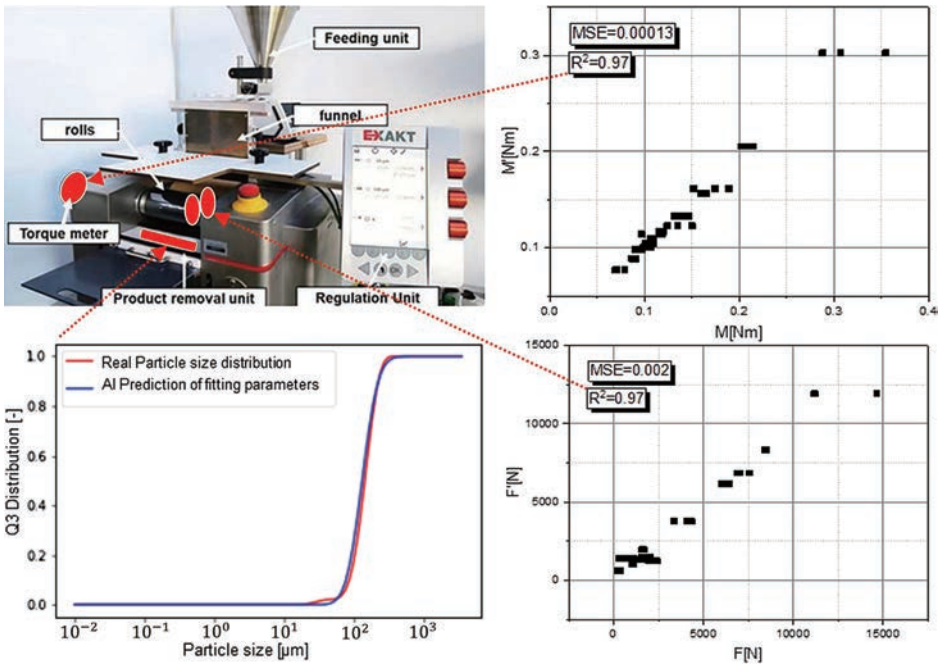


Fig. 12 A predictive model for a breakage tester to characterize the particle breakage function. Successful prediction capabilities were achieved for acting normal forces, power intake, and resulting particle size distribution. Further processing can be done for transference into existing breakage function models, with AI enabling reduction in the physical measurement effort (original work by author). Left upper picture reprinted with permission from Ref. (Böttcher et al., 2021). Copyright 2021 B.V.

can be adjusted, while torque and normal force between the rollers are measured. Based on GRL for rotational velocity, with gap size and initial particle size as input parameters, a predictive model was trained for the prediction of power, force, and resulting particle size via two fitting parameters. Both, the prediction of power and force achieved high accuracies, with an R^2 in both cases of 0.97.

Sun et al. (2017) successfully trained a three-layer neural net for the prediction of electron transfer properties such as the Femi energy of silver nanoparticles and successfully identified correlations with structural and morphological features.

Measurement improvement: Furat et al. (2022) applied generative adversarial networks (GANs) to retrospectively super-resolve images of particle based Li-ion electrodes for the quantification of features such as the identification of cracks in aged cathodes. Consequentially, the trade-off between resolution and field of view in the SEM imaging of bulk-pictures was significantly reduced.

Mechanistic analysis measure modeling: GAs provide another AI method that is often used for optimization tasks by mimicking the process of evolution involving the mutation, selection, and reproduction of system states and parameters. Finke et al. (2021) used a GA for the identification and optimization of suitable model parameters for a viscosity model of nanoparticulate suspensions.

3.10 Other Applications

A method with great potential for future applications is a combination of nature-based or mathematical algorithms and AI.

Drilling and blasting through hybrid models: One possible hybrid approach was introduced by Mojtahedi et al. (2019), which was developed for the prediction of particle size distribution in mining and is presented below.

Drilling and blasting are the most widely used methods in mining for rock crushing. In order to describe the fragmentation, the ANFIS method was combined with the firefly algorithm (FA). By extending a fuzzy inference system (FIS) with an artificial neural network (ANN), the system becomes self-learning and can solve nonlinear complex problems. In addition, the combination of ANFIS with the FA provides an ability to determine optimal values for complex nonlinear problems. More precisely, the FA describes a nature-based algorithm of firefly social behavior, where the convergence speed of the algorithm is high and the number of iterations for an optimal result is low. The objective of the ANFIS-FA was to predict the D_{80} (the 80 percent passing size at which 80 percent of the particles are smaller) value for different input parameters of the resulting particle distribution, using a data set from 88 blasting operations at the Shur river dam in Iran. For further validation of the predictions, the ANFIS-FA method was contrasted with linear multiple regression (LMR) methods alongside the test data set.

Six different hybrid models were created, each differing in the choice of input parameters used. Each of these models achieved higher R^2 values with a minimum of 0.856 in

predicting the D_{80} value than the LMR method, with 0.669 in relation to the test data set.

In summary, combining AI methods with existing algorithms has been demonstrated to significantly improve the accuracy of particle size predictions (Mojtahedi et al., 2019).

4. AI Surrogate Models

Sophisticated computer simulations are increasingly aiding particle technology in all covered domains. Depending on the time and length scale, different simulation techniques can be applied, such as the Finite Elements Method (FEM) for the investigation of the inner structural and mechanical behaviors of solid objects, Computer Fluid Dynamics (CFD) for the simulation of fluid flows, the Discrete Elements Method (DEM) for the investigation of the interactions among many particles and boundaries, or population balance simulations (PB) for the numerical modeling of particle-based processes. The methods can be coupled for multi-scale investigations or in CFD and DEM to investigate particulate systems within fluids, such as air or water. Interaction can be mono- or bidirectional, depending on the required accuracy and computational demands. Coupled CFD-DEM simulations are often used to numerically investigate particles in fluidic environments (Li J. and Tao J., 2018; Schrader et al., 2019; Zhu et al., 2020; Beinert et al., 2018; El-Emam et al., 2019). Such simulations are often demanding in terms of time and computing resources, limiting the space, time, or accuracy that can be investigated.

Predictive AI systems have the potential for massive savings in computing power and extensions of the investigable parameter space, yet they represent customized solutions that need to be performed repeatedly for new use cases, as was done for the dry operated vertical mill simulation after the modeling of the wet simulation.

More universally applicable AI solutions exist for some simulation methods in the form of surrogate models, although development is still in an early state. Calzolari et al., using tensor basis neural networks (TBNN) and CNNs (discussed in terms of the vertical mill), described CFD surrogate models (see left side of Fig. 13), demonstrating the time extrapolation of flow fields and AI upscaling based on previously learned physical data to derive super-resolved fields for low-resolution fields and physics-informed DL turbulence model enhancement (Calzolari and Liu, 2021).

For the discrete elements method, the authors (Thon and Schilde) are currently working on a surrogate model to train small-scale unit cells with particle positions and forces from DEM for incorporation in a respective small-scale unit cell surrogate model for later application on large domains. By discretizing the large domain cyclically and re-meshing the unit cell grid, the dynamics for larger domains are to be represented by the surrogate model and predicted as a new initialization state for subsequent iteration. The Initial training of output 3D particle positions over time is promising, with minuscule errors in individual time steps and a mean error of 0.5 percent per spatial dimension (0.1 nm error in a 20 × 20 × 20 nm unit cell).

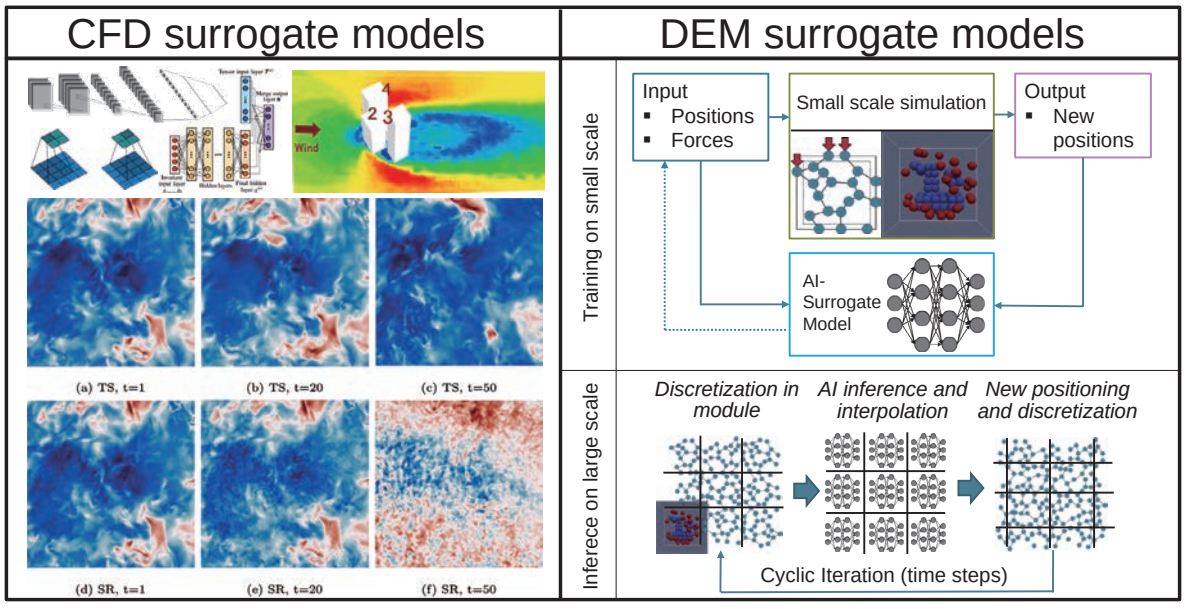


Fig. 13 Depiction of surrogate models for CFD simulations to quickly get accurate results, which would take unaided CFD significantly longer. On the right side, a current approach for a surrogate model for DEM is shown, in which a predictive model of a 3D tesseract is trained for a small-scale unit for later iterative inference in a larger discretized domain with remeshing. The left part is a reprint of Calzolari and Liu (2021) under the terms of the CC-BY 4.0 license. Copyright: (2021) The Authors, published by Elsevier. (The right part is an original work by the author).

5. AI-based design and scale-up

In addition to modeling, the optimization or control of individual processes such as synthesis, grinding, analysis etc., the design, modeling, and control of plants and complex networks as a whole, as well as layout and optimization, including the design of the underlying processes and units, is of major economic significance. Using AI for design, layout, optimization, or scale-up can lead to significant savings and improved efficiency.

Other than for the task or unit's specific applications, elaborated on earlier in the publication, adoption of AI in particle technology in this respect is still in an early stage. However, there are some examples, more advanced examples, and real-world applications in other fields, with the used approaches being transferable to particle technology, e.g., the use of GAs for the autonomous design of heat exchangers, which can be easily adopted for the design of milling geometries.

Generally, two major approaches can be distinguished, the design and optimization of dedicated production systems, processes, unit operations, plants, and logistics infrastructure for dedicated goals or the intelligent dynamic identification, connection, and management of suitable (potentially decentralized) infrastructure already in existence.

The former method of dedicated design tasks can be used for basic operations or if products will be required in the long term and in large quantities, making application-specific inflexible yet efficient high-throughput systems a suitable option.

With GAs, Wisniewske (2004) demonstrated an optimal design of reinforcing fibers within a composite, while Jatti et al. (2013) optimized the milling of aluminum alloys. For the design of process units, RatnaRaju and Nandi (2013) used GAs for the construction of heat exchangers while considering pressure drop and effectiveness.

In contrast to evolutionary techniques, Lee X.Y. et al. (2019) used deep reinforcement learning for microfluidic flow sculpturing, finding it to be superior to a GA approach. Similarly, with classical AI techniques such as neural nets, Sarkar et al. (2019) demonstrated an autonomous design of a compressor rotor and optimization through AL.

Specifically, GANs, in which two competing AIs train each other, are useful for the design process. In this approach, a generator learns from training examples in order to produce similar results, while a discriminator AI evaluates the results and learns through feedback to improve the accuracy of its evaluation. Being mostly known from deep fakes, the generation of realistic images, they can also be applied to generate solutions for given problems. Via the iterative interaction of generator and critique AI, the two networks improve each other's capabilities.

Chen and Fuge (2019) demonstrated GANs for design synthesis, the generation of hierarchical designs in conjunction with generative models. Similarly, Oh et al. (2019) applied GANs for the generation of 2D wheels. Nobari et al. (2021) demonstrated autonomous design synthesis for constrained 3D geometry generation for different purposes via deep generative models and constraint GANs.

In addition to the complete execution of the design process, AI can be used in a semi-automated manner to assist manual design endeavors. For instance, Khan et al. (2019) discussed iterative design adjustment in the construction endeavor in a loop with user feedback. Similarly, Deshpande and Purwar (2019) demonstrated the solution generation of mechanisms and synthesis for abstract inputs.

Raina et al. (2019) applied transfer learning to incorporate historical design strategies from past cases into AI systems. Combining these approaches in the future, a closed loop of adjustment with continued learning based on human feedback can be implemented.

Similarly, GA-, ANN-, and GAN-based design or the evolution of design strategies can be applied for processes or production units in particle technology, such as in the design of mill geometries and operating conditions or for the morphological features of product particles.

In regard to the second major variant in design, optimization and scale-up, the intelligent management and interconnection of existing infrastructures, units, systems, and processes, a key foundation are digital twins, which can be predictive AI models, as already discussed in this publication. Cyber-physical systems, which include sensors, communication, computation, and control elements, are closely associated with digital twins as virtual representations of physical systems. Ideally, they rely on a digital twin for monitoring, control, and autonomous decision-making (Lee E.A., 2008; Tao et al., 2019). Together with cloud computing, big data, and the internet of things (IoT) as the foundation, both cyber physical systems and digital twins, which can rely heavily on AI, are important components of the concept of smart factories and industry 4.0.

As already discussed, in a fixed production environment, management and control are vital for the dynamic interconnection and allocation of resources, units, processes, or entire plants in a decentralized (potentially global) manner while considering the available infrastructure and its flexibility, intelligent supply chain management and decision-making are of paramount importance. Toorajipour et al. (2021) performed a more detailed review of AI in supply chain management and successive decision-making, focusing on marketing (including sales, pricing, segmentation, consumer behavior, decision support, direct marketing, industrial marketing, new products, etc.), logistics (containing container terminal operations, inbound, logistics automation, sizing, etc.), production (assembly, integration, product driven control, etc.), and the supply chain itself (facility location, supplier selection, supply

chain network design, risk management, and inventory replenishment), with references to specific examples. Supply chain management and autonomous decision making are important aspects that mirror, to a large degree, process control in a fixed system, although challenges in a dynamic decentralized system can strongly outweigh those in a fixed system.

In terms of the online monitoring of large connected production systems, the company Hosokawa Alpine (2019) applies an ML-based platform intelligent software assistant (ISA) for the maximization of efficiency and quality.

Regarding the supply chain network design under consideration of profit maximization, Zhang et al. (2017) demonstrated a competition-based intelligent physarum solver.

Wang et al. (2012) demonstrated autonomous collaboration between heterogeneous actors (multi-robotic systems) and AI to solve complex formation performance in a dynamic environment.

In regard to the dynamics of product life-cycles and supply chain networks and the resulting inbound fluctuations, Knoll et al. (2016) demonstrated predictive inbound logistics planning.

Kwon et al. (2007) presented an integrated multi-agent framework to solve collaboration tasks in supply chain management in regard to supply and demand uncertainties.

In cases when human supervision is desired, Kasie et al. (2017) demonstrated a decision support system combining AI and discrete-event simulations (DES), as well as database management.

Applied to particle technology, the existing production sites addressed earlier in this review can be intelligently connected in a dynamic, decentralized, self-organizing structure based on digital twins and cyber physical systems. Based on AI market prediction, as well as autonomous real-time monitoring and decision making, the cost and efficiency benefits of smart factories and industry 4.0 can be adopted more progressively in the field of particle technology.

6. Conclusion

In conclusion, AI techniques are already used in all areas of particle technology. Predictive modeling, often the foundation for successive AI applications or conventional post-processing, is already universally represented for all process types, although the degree of adoption varies. AI methods or evolutionary approaches, which are often used in combination, are furthermore applied for the optimization or set up of process control.

AI can perform or assist in scale-up, as trained AI models can be transferred between different scales through pre-training. In regard to classical simulations such as DEM, FEM, or CFD, AI can aid in numerical investigation. Surrogate models are increasingly being investigated in various fields as quick-to-apply alternatives to classical simulations such as DEM for particulate systems. Often, the simulation counterpart is used as a training foundation for the training of surrogate models. Consequently, through surrogate models, the investigation of systems such as large stirred media mills with trillions or quadrillions of particles or more and their inner workings can be possible, orders of magnitudes being larger than what could be done with state-of-the-art simulations. Inversely, surrogate models can be performed significantly faster than real simulations, allowing for real-time or faster numerical investigations of parallel-running physical processes or plants, allowing for the predictive control of complex milling or reaction processes or of entire plants. Since simplifications or approximations need to be done often as compromises need to be made between accuracy and computing performance, e.g., simpler contact models or focusing on grinding beads without product particles, such simplifications can become unnecessary with surrogate models, allowing for greater transparency and realism.

Regarding the criticism of AI's black-box nature, there are techniques to increase the transparency of AI models, in particular the use of genetic programming (GP) or reverse-engineering strategies, to transfer AI models into more transparent representations to facilitate, among others, the mechanistic modeling endeavor in particle technology.

In summary, there are examples in most domains of particle technology, although widespread adoption has not yet been achieved. Based on the existing examples, ranging from proof of principles to successfully applied economic adoptions, with the exponential increase in general capability, AI adoption will be a major determinant of economic competitiveness and survivability in this and the following decade.

7. Outlook

Looking towards the future, the author sees promising areas and ideas to address untapped potential and remaining shortcomings.

In **Fig. 14**, a possible framework is depicted, extending a previously published hybrid modeling approach now called hybrid regression evolutionary network (HyREN) (Thon et al., 2022b).

1) HyREN: Being marked by the blue square, training data from either experiments or experimentally validated simulations (e.g., via DEM calibration or the execution and comparison of identical mill experiments and simulations) are used for parallel hybrid modeling, also called gray-box modeling. In this way, the parallel-running black-box AI only models the divergence between predefined white-box models, e.g., an existing physical or mechanistic model from the literature, and only compensates for the white-box model's shortcomings, with major tendencies being

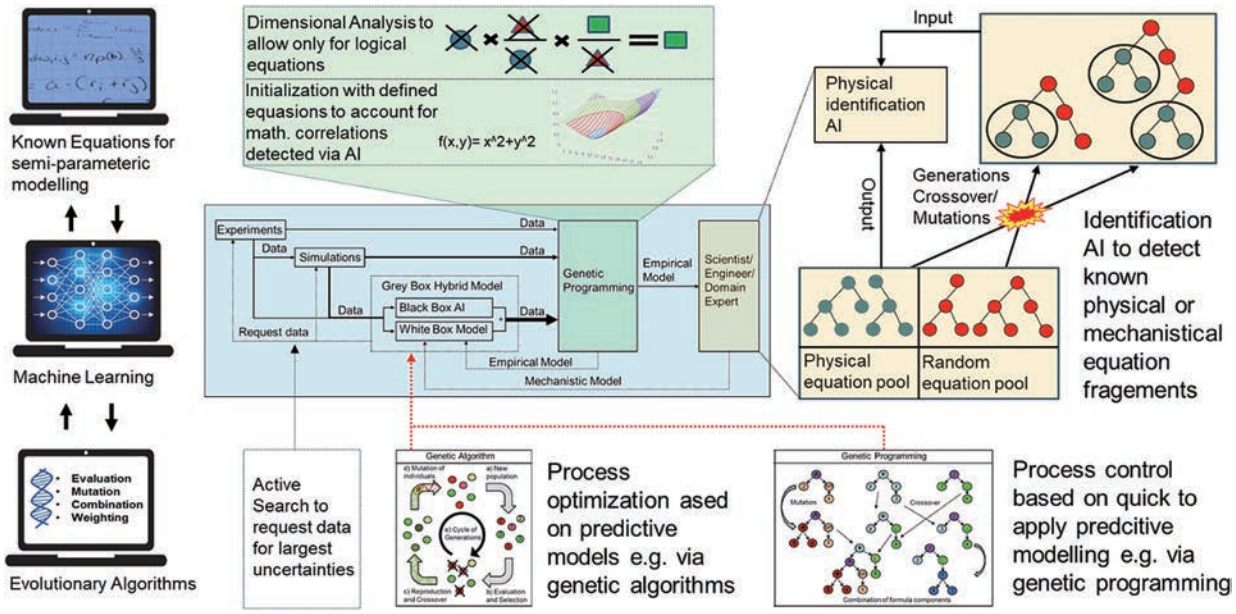


Fig. 14 Outlook for a comprehensive modeling system combining classical AI techniques such as neural nets with evolutionary approaches such as genetic algorithms and programming in conjunction with hybrid modeling. Integrated optimization and the establishment of control decision trees can be generated based on underlying hybrid models acting as digital twins. Furthermore, dimensionality analysis, equations, and physics recognition can be added to improve the underlying modeling capabilities and improve transparency and physical reasonability. The middle blue box is a reprint from Thon et al. (2021), as are the lower boxes for genetic algorithms and programming (Thon et al., 2022b), both under the terms of the CC-BY 4.0 license. Copyright: (2021) The Authors, published by Wiley.

defined by the transparent and established white-box model. Successive GPs can be performed to break down the black-box model component into more transparent representations to iteratively extend the white-box model. Depending on whether human intervention will be involved, the extensions can be empirical or mechanistic. Based on this as an outlook, several additional extensions are proposed, which are currently being developed.

2) Genetic reinforcement learning: One shortcoming of AI models is usually their large training data requirements. The GRL training technique has already addressed this shortcoming. Despite GRL's advantages, unknown regions in the parameter space in terms of the available training data can still compromise the generalizing capabilities of the model.

3) Active search and request: e.g., the comparison of the systematic predictions of independently trained AIs, can reveal parameter combinations of uncertainty in order to close these gaps with a minimum amount of additional data acquisition (via targeted simulations or experiments).

In regard to hybrid modeling and the iterative extension of white-box components, additional approaches can increase physical significance.

4) Dimensionality analysis: As shown in green, GP can be augmented through dimensionality analysis to ensure the mathematical and physical consistency of units.

5) AI-driven regression: Furthermore, initialization with suitable equations, derived from AI detection based on the (*n*-dimensional) shape of the data, can facilitate the process.

6) AI-driven physics recognition: Furthermore, empirical models can be transferred to mechanistic models in a semi-automated manner by generating a large pool of equations containing known physical or mechanistic equations. Resulting from generations of crossover and mutations, and involving tree structures from this equation pool, recognition AIs can be trained to later be applied to the identification of white-box equations or respective fragments in data from real use cases.

7) Digital twins for optimization and control: Based on the trained models (black, gray, or white box), subsequent techniques such as GA, GP, or AL, etc. can be performed and considered to be safe to interact with and quick-to-apply virtual process representations (AI-based digital twins) for optimization and control.

8) Online Learning: Further development opportunities and the application of data-driven methods in process, formulation, and material modeling are manifold, such as online learning in which AI is constantly running in parallel to processes or data banks to update its internal modeling and dynamically adapt to changing circumstances (e.g., anomalies such as the blocking of particles in a grinding process or changes in the product formulation). Similar to GAs, ALs allow for the optimization of defined goals.

9) Autonomous AI modularization: Via un- or self-supervised learning, the use of modular neural nets or dropout, automated identification and the decomposition of process and production engineering issues into

sub-processes and sub-mechanisms for better (hybrid) modeling and control of the entire process chain can be achieved. For instance, a complex production plant with various sensors and actuators can be autonomously broken down into closed unit systems, which can then be interconnected to represent the entire plant, simplifying the modeling effort while increasing the transparency of the model.

10) An Expert Management System for AI: As different AI tools (neural nets, evolutionary algorithms, Hierarchical Hidden Markov models, etc.) provide varying advantages and disadvantages, the best results can usually be achieved via the intelligent combination of methods either in the form of joint applications or the fusion of methods (ensemble methods). In the future, based on a comprehensive toolbox of methods, a self-supervised expert-management system can be established for the optimal allocation and interconnection of ML methods.

Since there exist real-world examples in particle technology of almost all unit operations in terms of predictive modeling and, increasingly, optimization and control via AI, the mostly untapped design, scale-up, modeling, optimization, control, and monitoring of large, highly connected systems such as entire plants or decentralized production facilities are likely to be the next steps in adoption.

11) AI-driven unit and geometry design: Furthermore, the design of individual components such as stirrer geometries can be facilitated. That is, the geometry design itself can be performed numerically, e.g., via AL or the use of GAs along predefined constraints, as can be the optimization of process parameters.

12) Surrogate models: Through the use of surrogate models, quick iteration and prototyping are possible. For process control, AI models can be used as quick-to-apply digital twins (predictive/surrogate models) that run faster than real time and have the potential to improve automation and the autonomous development of sophisticated control schemes.

13) Brain-derived AI: Finally, current AI is still loosely inspired by biological nerve systems. Recent developments in neuroscience and the successive adoption of AI, specifically in regard to neuroscientific theory about the mammalian neocortex, as found in Hawkins et al. (Hole and Ahmad, 2021; Hawkins and Ahmad, 2016; Hawkins et al., 2017, 2018; Lewis et al., 2019), can allow for more general levels of intelligence compared to the currently narrow AI. These advancements harbor the potential to allow for desired features currently investigated in the context of classical AI such as online learning (permanent model update), distributed voting AIs (robustness, generalizing capabilities), or reference frames (Hinton, 2022). This can allow for more general AI systems, which can apply and detect learned patterns, strategies, and solutions in the context of novel or other types of unit operations via analogies. Applied to particle technology, being a wide field involved in many industries, the autonomous transfer and detection of common patterns and solutions can allow for the identification of non-obvious solutions, e.g., the use of Michaelis–Menten kinetics for the dispersion of nanoparticles (Schilde et al., 2010).

Acknowledgments

We would like to thank the company ESSS (Florianópolis, Brasil) as the developer of Rocky DEM for the close research cooperation and provision of the research license. We especially thank Jan-Phillipp Fürstenau of CADFEM GmbH (Hanover, Germany) for the technical support. The authors want to thank the Deutsche Forschungsgemeinschaft (DFG) in the context of the Heisenberg Program SCHI 1265/19-1 “Digital methods for complex systems in process and production engineering” and the SPP 2364 “Autonomous Processes in Particle Technology”.

Nomenclature

AI	Artificial intelligence
ANFIS	Adaptive neuro-fuzzy inference system
ANN	Artificial neural network
ASIC	Application-specific integrated circuit
BP	Backpropagation
BPNN	Back propagation neural network
CFD	Computer fluid dynamic
CNN	Convolutional neural network
DEM	Discrete elements method
DL	Deep learning
DNN	Deep neural network
FA	Firefly algorithm
FEM	Finite elements method
FIS	Fuzzy inference system
GA	Genetic (or evolutionary) algorithm
GAM	Generalized additive model
GAN	Generative adversarial network
GP	Genetic programming
GRL	Genetic reinforcement learning
IoT	Internet of things
LIME	Local interpretable model agnostic explorations
LMR	Linear multiple regression
LSTM	Long short-term memory
MIMO	Multiple inputs and multiple outputs
ML	Machine learning
ODML	On-demand machine learning
PB	Population balance
PID	Proportional integral derivative (controller)
PLS	Partial least-squares regression
PSD	Particle size distributions
RVLFN	Random vector functional-link network
SEM	Scanning electron microscope

TBNN	Tensor basis neural networks
XAI	Explainable AI
YOLO	You only look once (object detection)

References

Ashraf C., Joshi N., Beck D.A.C., Pfaendtner J., Data science in chemical engineering: applications to molecular science, Annual Review of Chemical and Biomolecular Engineering, 12 (2021) 15–37. DOI: 10.1146/annurev-chembioeng-101220-102232

Astray G., Mejuto J.C., Approach of different properties of alkylammonium surfactants using artificial intelligence and response surface methodology, Tenside Surfactants Detergents, 54 (2017) 132–140. DOI: 10.3139/113.110483

Bajimaya S.M., Park S., Wang G.-N., Predicting extrusion process parameters using neural networks, International Journal of Mechanical and Mechatronics Engineering, 1 (2007) 644–648. DOI: 10.5281/zenodo.1061615

Beinert S., Fragnière G., Schilde C., Kwade A., Multiscale simulation of fine grinding and dispersing processes: stressing probability, stressing energy and resultant breakage rate, Advanced Powder Technology, 29 (2018) 573–583. DOI: 10.1016/j.apt.2017.11.034

Böttcher A.-C., Thon C., Fragnière G., Chagas A., Schilde C., Kwade A., Rigidly-mounted roll mill as breakage tester for characterizing fine particle breakage, Powder Technology, 383 (2021) 554–563. DOI: 10.1016/j.powtec.2021.01.055

Bowler A.L., Bakalis S., Watson N.J., Monitoring mixing processes using ultrasonic sensors and machine learning, Sensors, 20 (2020) 1813. DOI: 10.3390/s20071813

Calzolari G., Liu W., Deep learning to replace, improve, or aid CFD analysis in built environment applications: a review, Building and Environment, 206 (2021) 108315. DOI: 10.1016/j.buildenv.2021.108315

Chen M., Dixon D.A., Machine-learning approach for the development of structure–energy relationships of ZnO nanoparticles, The Journal of Physical Chemistry C, 122 (2018) 18621–18639. DOI: 10.1021/acs.jpcc.8b01667

Chen W., Fuge M., Synthesizing designs with interpart dependencies using hierarchical generative adversarial networks, Journal of Mechanical Design, 141 (2019) 111403. DOI: 10.1115/1.4044076

Dai W., Liu Q., Chai T., Particle size estimate of grinding processes using random vector functional link networks with improved robustness, Neurocomputing, 169 (2015) 361–372. DOI: 10.1016/j.neucom.2014.08.098

Demir-Kavuk O., Kamada M., Akutsu T., Knapp E.-W., Prediction using step-wise L1, L2 regularization and feature selection for small data sets with large number of features, BMC Bioinformatics, 12 (2011) 412. DOI: 10.1186/1471-2105-12-412

Deshpande S., Purwar A., Computational creativity via assisted variational synthesis of mechanisms using deep generative models, Journal of Mechanical Design, 141 (2019) 121402. DOI: 10.1115/1.4044396

El-Emam M.A., Shi W., Zhou L., CFD-DEM simulation and optimization of gas-cyclone performance with realistic macroscopic particulate matter, Advanced Powder Technology, 30 (2019) 2686–2702. DOI: 10.1016/j.apt.2019.08.015

Evans B.P., Xue B., Zhang M., What's inside the black-box?: a genetic programming method for interpreting complex machine learning models, Proceedings of the Genetic and Evolutionary Computation Conference, (2019) 1012–1020. DOI: 10.1145/3321707.3321726

Faghihi S., Keykhosravi A., Shahbazi K., Modeling of kinetic adsorption of natural surfactants on sandstone minerals: spotlight on accurate prediction and data evaluation, Colloid and Interface Science Communications, 33 (2019) 100208. DOI: 10.1016/j.colcom.2019.100208

Finke B., Sangrós Giménez C., Kwade A., Schilde C., Viscosity model for nanoparticulate suspensions based on surface interactions, Materials (Basel, Switzerland), 14 (2021) 2752. DOI: 10.3390/ma14112752

Furat O., Finegan D.P., Yang Z., Kirstein T., Smith K., Schmidt V., Super-resolving microscopy images of Li-ion electrodes for fine-feature quantification using generative adversarial networks, NPJ Computational Materials, 8 (2022) 68. DOI: 10.1038/s41524-022-00749-z

Gonçalves V.D., De Almeida L.F., Mathias M.H., Wear particle classifier system based on an artificial neural network, Strojniški vestnik–Journal of Mechanical Engineering, 56 (2010) 277–281.

Hawkins D.M., The problem of overfitting, Journal of Chemical Information and Computer Sciences, 44 (2004) 1–12. DOI: 10.1021/ci0342472

Hawkins J., Ahmad S., Why neurons have thousands of synapses, a theory of sequence memory in neocortex, Frontiers in Neural Circuits, 10 (2016) 23. DOI: 10.3389/fncir.2016.00023

Hawkins J., Ahmad S., Cui Y., A theory of how columns in the neocortex enable learning the structure of the world, Frontiers in Neural Circuits, 11 (2017) 81. DOI: 10.3389/fncir.2017.00081

Hawkins J., Lewis M., Klukas M., Purdy S., Ahmad S., A framework for intelligence and cortical function based on grid cells in the neocortex, Frontiers in Neural Circuits, 12 (2018) 121. DOI: 10.3389/fncir.2018.00121

Hinton G., How to represent part-whole hierarchies in a neural network, Neural Computation, (2022) 1–40. DOI: 10.1162/neco_a_01557

Hole K.J., Ahmad S., A thousand brains: toward biologically constrained AI, SN Applied Sciences, 3 (2021) 743. DOI: 10.1007/s42452-021-04715-0

Hoseinian F.S., Rezai B., Kowsari E., Safari M., A hybrid neural network/genetic algorithm to predict Zn(II) removal by ion flotation, Separation Science and Technology, 55 (2020) 1197–1206. DOI: 10.1080/01496395.2019.1582543

Hosokawa Alpine (Hosokawa Alpine AG), 2019, ISA von Hosokawa Alpine steigert effizienz in der produktion <https://www.hosokawa-alpine.de/unternehmen/news/detail/isa-steigert-anlageneffizienz/> accessed 04.11.2022.

Ittiphalin M., Arnonkijpanich B., Pathumnakul S., An artificial intelligence model to estimate the fat addition ratio for the mixing process in the animal feed industry, Journal of Intelligent Manufacturing, 28 (2017) 219–228. DOI: 10.1007/s10845-014-0972-x

Jatti V.S., Sekhar R., Patil R.K., Study of ball nose end milling of LM6 al alloy: surface roughness optimisation using genetic algorithm, International Journal of Engineering and Technology (IJET), 5 (2013) 2859–2865.

Jose N.A., Kovalev M., Bradford E., Schweidtmann A.M., Chun Zeng H., Lapkin A.A., Pushing nanomaterials up to the kilogram scale – An accelerated approach for synthesizing antimicrobial ZnO with high shear reactors, machine learning and high-throughput analysis, Chemical Engineering Journal, 426 (2021) 131345. DOI: 10.1016/j.cej.2021.131345

Kasie F.M., Bright G., Walker A., Decision support systems in manufacturing: a survey and future trends, Journal of Modelling in Management, 12 (2017) 432–454. DOI: 10.1108/JM2-02-2016-0015

Kattentidt H.U.R., Jong T.P.R. de, Dalmijn W.L., Multi-sensor identification and sorting of bulk solids, Control Engineering Practice, 11 (2003) 41–47. DOI: 10.1016/S0967-0661(02)00140-5

Khan S., Gunpinar E., Moriguchi M., Suzuki H., Evolving a psychophysical distance metric for generative design exploration of diverse shapes, Journal of Mechanical Design, 141 (2019) 111101. DOI: 10.1115/1.4043678

Khaydarov V., Heinze S., Graube M., Knüpfer A., Knespel M., Merkelbach S., Urbas L., From stirring to mixing: artificial intelligence in the process industry, 2020 25th IEEE International Conference on Emerging Technologies and Factory Automation (ETFA), (2020). DOI: 10.1109/ETFA46521.2020.9212018

Knoll D., Prüglmeier M., Reinhart G., Predicting future inbound logistics processes using machine learning, Procedia CIRP, 52 (2016) 145–150. DOI: 10.1016/j.procir.2016.07.078

Krishna C.V., Rohit H.R., Mohana, A review of artificial intelligence methods for data science and data analytics: applications and research challenges, 2018 2nd International Conference on I-SMAC (IoT in Social, Mobile, Analytics and Cloud) (I-SMAC). (2018) 591–594. DOI: 10.1109/I-SMAC.2018.8653670

Kundu P., Paul V., Kumar V., Mishra I.M., An adaptive modeling of petroleum emulsion formation and stability by a heuristic multiobjective artificial neural network-genetic algorithm, Petroleum Science and Technology, 34 (2016) 350–358. DOI: 10.1080/10916466.2015.1135169

Kwon O., Im G.P., Lee K.C., MACE-SCM: a multi-agent and case-based reasoning collaboration mechanism for supply chain management under supply and demand uncertainties, Expert Systems with Applications, 33 (2007) 690–705. DOI: 10.1016/j.eswa.2006.06.015

Leal A.M.M., Kyas S., Kulik D.A., Saar M.O., Accelerating reactive transport modeling: on-demand machine learning algorithm for chemical equilibrium calculations, Transport in Porous Media, 133 (2020) 161–204. DOI: 10.1007/s11242-020-01412-1

LeCun Y., Bengio Y., Hinton G., Deep learning, Nature, 521 (2015) 436–444. DOI: 10.1038/nature14539

Lee E.A., Cyber physical systems: design challenges, 2008 11th IEEE International Symposium on Object and Component-Oriented Real-Time Distributed Computing (ISORC), (2008) 363–369. DOI: 10.1109/ISORC.2008.25

Lee J.H., Shin J., Realff M.J., Machine learning: overview of the recent progresses and implications for the process systems engineering field, Computers & Chemical Engineering, 114 (2018) 111–121. DOI: 10.1016/j.compchemeng.2017.10.008

Lee X.Y., Balu A., Stoecklein D., Ganapathysubramanian B., Sarkar S., A case study of deep reinforcement learning for engineering design: application to microfluidic devices for flow sculpting, Journal of Mechanical Design, 141 (2019) 111401. DOI: 10.1115/1.4044397

Lewis M., Purdy S., Ahmad S., Hawkins J., Locations in the neocortex: a theory of sensorimotor object recognition using cortical grid cells, Frontiers in Neural Circuits, 13 (2019) 22. DOI: 10.3389/fncir.2019.00022

Li J., Chen T., Lim K., Chen L., Khan S.A., Xie J., Wang X., Deep learning accelerated gold nanocluster synthesis, Advanced Intelligent Systems, 1 (2019) 1900029. DOI: 10.1002/aisy.201900029

Li J., Tao J., CFD-DEM Two-way coupled numerical simulation of bridge local scour behavior under clear-water conditions, Transportation Research Record, 2672 (2018) 107–117. DOI: 10.1177/0361198118783170

Li L., Zhai Y., Jin Y., Wang J., Wang H., Ma M., Stability, thermal performance and artificial neural network modeling of viscosity and thermal conductivity of Al_2O_3-ethylene glycol nanofluids, Powder Technology, 363 (2020) 360–368. DOI: 10.1016/j.powtec.2020.01.006

Linkens D.A., AI in control systems engineering, The Knowledge Engineering Review, 5 (1990) 181–214. DOI: 10.1017/S0269888900005403

Liu X., Li K., McAfee M., Nguyen B.K., McNally G.M., Dynamic gray-box modeling for on-line monitoring of polymer extrusion viscosity, Polymer Engineering & Science, 52 (2012) 1332–1341. DOI: 10.1002/pen.23080

Marcos A.G., Pernía Espinoza A.V., Elías F.A., Forcada A.G., A neural network-based approach for optimising rubber extrusion lines, International Journal of Computer Integrated Manufacturing, 20 (2007) 828–837. DOI: 10.1080/09511920601108808

Martínez-de-Pisón F.J., Pernía A.V., Blanco J., González A., Lostado R., Control model for an elastomer extrusion process obtained via a comparative analysis of data mining and artificial intelligence techniques, Polymer-Plastics Technology and Engineering, 49 (2010) 779–790. DOI: 10.1080/03602551003749585

Massarelli C., Campanale C., Uricchio V.F., A handy open-source application based on computer vision and machine learning algorithms to count and classify microplastics, Water, 13 (2021) 2104. DOI: 10.3390/w13152104

Mavrovouniotis M., Artificial Intelligence in process engineering, Academic Press Inc, 2012, ISBN: 9780124315129.

McKay B., Lennox B., Willis M., Barton G.W., Montague G., Extruder modelling: a comparison of two paradigms, UKACC International Conference on Control '96 (Conf Publ No 427), (1996). DOI: 10.1049/cp:19960643

Mojtahedi S.F.F., Ebtehaj I., Hasanipanah M., Bonakdari H., Amnieh H.B., Proposing a novel hybrid intelligent model for the simulation of particle size distribution resulting from blasting, Engineering with Computers, 35 (2019) 47–56. DOI: 10.1007/s00366-018-0582-x

Nielsen R.F., Nazemzadeh N., Sillesen L.W., Andersson M.P., Gernaey K.V., Mansouri S.S., Hybrid machine learning assisted modelling framework for particle processes, Computers & Chemical Engineering, 140 (2020) 106916. DOI: 10.1016/j.compchemeng.2020.106916

Nirschl H., Winkler M., Sinn T., Menesklou P., Autonomous processes in particle technology, Chemie Ingenieur Technik, 94 (2022) 230–239. DOI: 10.1002/cite.202100059

Nobari A.H., Chen W., Ahmed F., Range-constrained generative adversarial network: design synthesis under constraints using conditional generative adversarial networks, Journal of Mechanical Design, 144 (2021) 021708. DOI: 10.1115/1.4052442

Oh S., Jung Y., Kim S., Lee I., Kang N., Deep generative design: integration of topology optimization and generative models, Journal of Mechanical Design, 141 (2019) 111405. DOI: 10.1115/1.4044229

Ongsulee P., Artificial intelligence, machine learning and deep learning, 2017 15th International Conference on ICT and Knowledge Engineering (ICT&KE), (2017). DOI: 10.1109/ICTKE.2017.8259629

Patel A.R., Ramaiya K.K., Bhatia C.V., Shah H.N., Bhavsar S.N., Artificial intelligence: prospect in mechanical engineering field—a review, Data Science and Intelligent Applications, (2021) 267–282. DOI: 10.1007/978-981-15-4474-3_31

Pellegrino F., Isopescu R., Pellutiè L., Sordello F., Rossi A.M., Ortel E., Martra G., Hodoroaba V.-D., Maurino V., Machine learning approach for elucidating and predicting the role of synthesis parameters on the shape and size of TiO_2 nanoparticles, Scientific Reports, 10 (2020) 18910. DOI: 10.1038/s41598-020-75967-w

Peršak T., Viltužnik B., Hernavs J., Klančnik S., Vision-based sorting systems for transparent plastic granulate, Applied Sciences, 10 (2020) 4269. DOI: 10.3390/app10124269

Pham D.T., Pham P.T.N., Artificial intelligence in engineering, International Journal of Machine Tools and Manufacture, 39 (1999) 937–949. DOI: 10.1016/S0890-6955(98)00076-5

Pilania G., Machine learning in materials science: from explainable predictions to autonomous design, Computational Materials Science, 193 (2021) 110360. DOI: 10.1016/j.commatsci.2021.110360

Psichogios D.C., Ungar L.H., A hybrid neural network-first principles approach to process modeling, AIChE Journal, 38 (1992) 1499–1511. DOI: 10.1002/aic.690381003

Qu X.Y., Zeng P., Xu C.C., Fu D.D., RNN-based method for fault diagnosis of grinding system, 2017 IEEE 7th Annual International Conference on CYBER Technology in Automation, Control, and Intelligent Systems (CYBER), (2017). 673–678. DOI: 10.1109/CYBER.2017.8446348

Rahmani A.M., Azhir E., Ali S., Mohammadi M., Ahmed O.H., Yassin Ghafour M., Hasan Ahmed S., Hosseinzadeh M., Artificial intelligence approaches and mechanisms for big data analytics: a systematic study, PeerJ Computer Science, 7 (2021) e488. DOI: 10.7717/peerj-cs.488

Raina A., Cagan J., McComb C., Transferring design strategies from

human to computer and across design problems, Journal of Mechanical Design, 141 (2019) 114501. DOI: 10.1115/1.4044258

Raschka S., Patterson J., Nolet C., Machine learning in python: main developments and technology trends in data science, Machine Learning, and Artificial Intelligence, Information, 11 (2020) 193. DOI: 10.3390/info11040193

RatnaRaju L., NandiT.K., Design optimization of perforated plate heat exchangers using genetic algorithm, International Journal of Advanced Materials Manufacturing and Characterization, 3 (2013) 89–93. DOI: 10.11127/ijammc.2013.02.016

Rupali M., Amit P., A review paper on general concepts of "artificial intelligence and machine learning", International Advanced Research Journal in Science, Engineering and Technology, 4 (2017) 79–82. DOI: 10.17148/iarjset/nciarcse.2017.22

Sakunthala S., Kiranmayi R., Mandadi P.N., A review on artificial intelligence techniques in electrical drives: neural networks, fuzzy logic, and genetic algorithm, 2017 International Conference on Smart Technologies for Smart Nation (SmartTechCon), (2017). DOI: 10.1109/SmartTechCon.2017.8358335

Sarkar S., Mondal S., Joly M., Lynch M.E., Bopardikar S.D., Acharya R., Perdikaris P., Multifidelity and multiscale Bayesian framework for high-dimensional engineering design and calibration, Journal of Mechanical Design, 141 (2019) 121001. DOI: 10.1115/1.4044598

Schaffer C., Selecting a classification method by cross-validation, Machine Learning, 13 (1993) 135–143. DOI: 10.1007/BF00993106

Schilde C., Kampen I., Kwade A., Dispersion kinetics of nano-sized particles for different dispersing machines, Chemical Engineering Science, 65 (2010) 3518–3527. DOI: 10.1016/j.ces.2010.02.043

Schrader M., Pommerehne K., Wolf S., Finke B., Schilde C., Kampen I., Lichtenegger T., Krull R., Kwade A., Design of a CFD-DEM-based method for mechanical stress calculation and its application to glass bead-enhanced cultivations of filamentous Lentzea aerocolonigenes, Biochemical Engineering Journal, 148 (2019) 116–130. DOI: 10.1016/j.bej.2019.04.014

Schweidtmann A.M., Esche E., Fischer A., Kloft M., Repke J.-U., Sager S., Mitsos A., Machine learning in chemical engineering: a perspective, Chemie Ingenieur Technik, 93 (2021) 2029–2039. DOI: 10.1002/cite.202100083

Srivastava N., Hinton G., Krizhevsky A., Sutskever I., Salakhutdinov R., Dropout: a simple way to prevent neural networks from overfitting, The Journal of Machine Learning Research, 15 (2014) 1929–1958.

Stosch M. von, Oliveira R., Peres J., Feyo de Azevedo S., Hybrid semi-parametric modeling in process systems engineering: past, present and future, Computers & Chemical Engineering, 60 (2014) 86–101. DOI: 10.1016/j.compchemeng.2013.08.008

Sun B., Fernandez M., Barnard A.S., Machine learning for silver nanoparticle electron transfer property prediction, Journal of Chemical Information and Modeling, 57 (2017) 2413–2423. DOI: 10.1021/acs.jcim.7b00272

Tao F., Sui F., Liu A., Qi Q., Zhang M., Song B., Guo Z., Lu S.C.-Y., Nee A.Y.C., Digital twin-driven product design framework, International Journal of Production Research, 57 (2019) 3935–3953. DOI: 10.1080/00207543.2018.1443229

Tao H., Wu T., Aldeghi M., Wu T.C., Aspuru-Guzik A., Kumacheva E., Nanoparticle synthesis assisted by machine learning, Nature Reviews Materials, 6 (2021) 701–716. DOI: 10.1038/s41578-021-00337-5

Taur J.S., Tao C.W., Tsai C.C., Temperature control of a plastic extrusion barrel using PID fuzzy controllers, Proceedings IEEE Conference on Industrial Automation and Control Emerging Technology Applications, (1995) 370–375. DOI: 10.1109/IACET.1995.527590

Thon C., Böttcher A.-C., Möhlen F., Yu M., Kwade A., Schilde C., Multi-modal framework to model wet milling through numerical simulations and artificial intelligence (part 1), Chemical Engineering Journal, 449 (2022a) 137794. DOI: 10.1016/j.cej.2022.137794

Thon C., Böttcher A.-C., Möhlen F., Yu M., Kwade A., Schilde C., Multi-modal framework to model wet milling through numerical simulations and artificial intelligence (part 2), Chemical Engineering Journal, 450 (2022b) 137947. DOI: 10.1016/j.cej.2022.137947

Thon C., Finke B., Kwade A., Schilde C., Artificial Intelligence in Process Engineering, Advanced Intelligent Systems, 3 (2021) 2000261. DOI: 10.1002/aisy.202000261

Tie M., Yue H., Chai T., A hybrid intelligent soft-sensor model for dynamic particle size estimation in grinding circuits, International Symposium on Neural Networks, Advances in Neural Networks – ISNN 2005, 3498 (2005) 871–876. DOI: 10.1007/11427469_138

Toorajipour R., Sohrabpour V., Nazarpour A., Oghazi P., Fischl M., Artificial intelligence in supply chain management: a systematic literature review, Journal of Business Research, 122 (2021) 502–517. DOI: 10.1016/j.jbusres.2020.09.009

Tsai C.C., Lu C.H., Fuzzy supervisory predictive PID control of a plastics extruder barrel, Journal of the Chinese Institute of Engineers, 21 (1998) 619–624. DOI: 10.1080/02533839.1998.9670423

Udrescu S.-M., Tan A., Feng J., Neto O., Wu T., Tegmark M., AI Feynman 2.0: pareto-optimal symbolic regression exploiting graph modularity, Advances in Neural Information Processing Systems, 33 (2020) 12pp.

Uhlemann J., Diedam H., Hoheisel W., Schikarski T., Peukert W., Modeling and simulation of process technology for nanoparticulate drug formulations—a particle technology perspective, Pharmaceutics, 13 (2021) 22. DOI: 10.3390/pharmaceutics13010022

Venkatasubramanian V., The promise of artificial intelligence in chemical engineering: is it here, finally?, AIChE Journal, 65 (2019) 466–478. DOI: 10.1002/aic.16489

Wahl C.B., Aykol M., Swisher J.H., Montoya J.H., Suram S.K., Mirkin C.A., Machine learning-accelerated design and synthesis of polyelemental heterostructures, Science Advances, 7 (2021) eabj5505. DOI: 10.1126/sciadv.abj5505

Wang T., Ramik D.M., Sabourin C., Madani K., Intelligent systems for industrial robotics: application in logistic field, Industrial Robot: An International Journal, 39 (2012) 251–259. DOI: 10.1108/01439911211217071

Wilts H., Garcia B.R., Garlito R.G., Gómez L.S., Prieto E.G., Artificial intelligence in the sorting of municipal waste as an enabler of the circular economy, Resources, 10 (2021) 28. DOI: 10.3390/resources10040028

Wisniewski J., Optimal design of reinforcing fibres in multilayer composites using genetic algorithms, Fibres And Textiles In Eastern Europe, 12 (2004) 58–63.

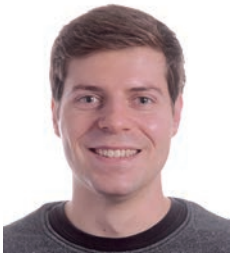
Ying X., An overview of overfitting and its solutions, Journal of Physics: Conference Series, 1168 (2019) 022022. DOI: 10.1088/1742-6596/1168/2/022022

Zhang S., Wang F., He D., Jia R., Batch-to-batch control of particle size distribution in cobalt oxalate synthesis process based on hybrid model, Powder Technology, 224 (2012) 253–259. DOI: 10.1016/j.powtec.2012.03.001

Zhang X., Chan F.T.S., Adamatzky A., Mahadevan S., Yang H., Zhang Z., Deng Y., An intelligent physarum solver for supply chain network design under profit maximization and oligopolistic competition, International Journal of Production Research, 55 (2017) 244–263. DOI: 10.1080/00207543.2016.1203075

Zhu M., Chen X., Zhou C.-s., Xu J.-s., Musa O., Numerical study of micron-scale aluminum particle combustion in an afterburner using two-way coupling CFD–DEM approach, Flow, Turbulence and Combustion, 105 (2020) 191–212. DOI: 10.1007/s10494-019-00104-1

Authors' Short Biographies



Christoph Thon

Christoph Thon studied bio- and chemical engineering at the Technische Universität Braunschweig and the Ostfalia University of Applied Sciences from 2011 to 2017 and finished with his master's thesis, "Investigation of the stress distribution through laminar flows by using CFD for scale transfer of kneading processes". His doctoral research, under the supervision of Prof. Dr.-Ing. Carsten Schilde at the Institute for Particle Technology (iPAT), focuses on the investigation of grinding processes in mills through computer simulations and the application of artificial intelligence.



Marvin Röhl

Marvin Röhl studied mechanical engineering at the Technische Universität Braunschweig from 2013 to 2020 and graduated with his master's thesis, "Modeling of a drying and structure formation process via coupling of DEM simulation and methods of artificial intelligence". His doctoral thesis, under the supervision of Prof. Dr.-Ing. Carsten Schilde at the Institute for Particle Technology (iPAT) deals with the development of an intelligent controlling approach to an electrode coating process using machine learning methods.



Somayeh Hosseinhashemi

Somayeh Hosseinhashemi studied computational science and engineering at the University of Rostock from 2017 to 2020 and graduated with her master's thesis, "Numerical investigation of pressure ripple in a rotary vane pump to determine optimization potentials with the software StarCCM+" at Robert Bosch Automotive Steering Company. Her doctoral thesis, under the supervision of Prof. Dr.-Ing. Carsten Schilde at the Institute for Particle Technology (iPAT), addresses the development of an intelligent and autonomous paste manufacturing process using machine learning approaches.



Arno Kwade

Prof. Dr.-Ing. Arno Kwade studied mechanical engineering at TU Braunschweig and University of Waterloo, finishing his PhD in 1996, receiving the Heinrich-Büssing-Price. He is head of the Institute for Particle Technology, Scientific Director of the Battery Lab Factory, spokesman of the Center of Pharmaceutical Engineering at TU Braunschweig, division head of the Fraunhofer Project Center for Energy Storage and Systems, member of the National Academy of Science and Engineering, chairman of the ProcessNet and EFCE working parties "Comminution and classification", vice chairman of the Advisory Board Battery Research Germany, and chair of the PARTEC 2024, with 300+ publications, a Google Scholar H Index of 40, and over 6000 citations.



Carsten Schilde

Prof. Dr-Ing. Carsten Schilde studied bioengineering at the Technische Universität Braunschweig and completed his PhD thesis on "Structure, Mechanics and Fracture of Nanoparticulate Aggregates" under Prof. Dr.-Ing. Arno Kwade. Later, he worked at the Institute for Particle Technology as a research associate and was appointed Assistant Professor for "Particle Simulation & Functional Structures" in 2017. In 2019, he received the Friedrich-Löffler award. His research focuses on the investigation of particulate systems and structures using computer simulation and artificial intelligence. His main application fields are pharmaceuticals and composite materials. With over 60 publications, he has a Google Scholar H Index of 18 and over 1000 citations.

KONA Powder and Particle Journal

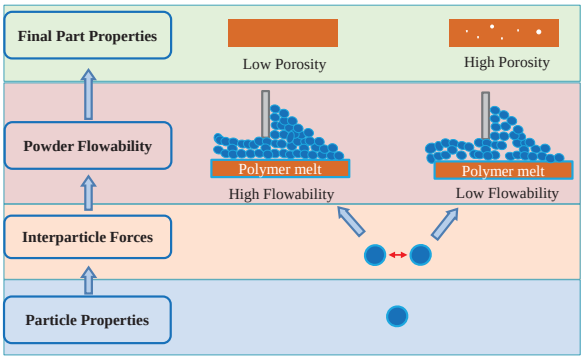
KONA Powder and Particle Journal No. 41 (2024) 26–41/https://doi.org/10.14356/kona.2024012 Review Paper

Role of Powder Properties and Flowability in Polymer Selective Laser Sintering—A Review†

Xi Guo and Brij M. Moudgil*

Department of Materials Science and Engineering, Center for Particulate and Surfactant Systems (CPaSS), University of Florida, USA

Polymer selective laser sintering (SLS) is an additive manufacturing technology that involves the melting of a selected area of particles on the powder bed. A 3D component is then printed using layer-by-layer sintering of the powder bed. SLS is considered one of the most promising technologies applicable to a variety of applications, particularly for manufacturing customized design products with high geometric complexity, such as patient-specific designed implants, surgical tools. Currently, only a small number of polymers are available that are suitable for SLS due to the complex multiple physical phenomena involved. Therefore, it is critical to develop new materials in order to fully realize the potential of SLS technology for manufacturing value-added customized products. For a given material, the quality of powder spreading in SLS plays a key role in printing performance and is a precondition for new material development. The aim of this review is to (1) present flowability characterization methods suitable for SLS, (2) examine the influence of powder properties and flowability on laser–material interaction and the quality of the final part, and (3) discuss the methods adopted in the literature to improve the quality of powder spreading.



Keywords: polymer selective laser sintering, powder property, flowability, powder packing

1. Introduction

Additive manufacturing (AM) is a group of solid freeform fabrication methods used to build 3D objects layer by layer based on computer-aided design files. The layer-by-layer building process, which is the opposite of traditional subtractive manufacturing, enables additive manufacturing to create highly complex structures. AM was introduced in the late 1980s (Ligon et al., 2017), primarily for building complex structure prototypes. With the development of technology, AM nowadays is capable of building products with various materials (polymers, metals, ceramics), processing desired properties and shapes.

The fundamental principle of AM process is to form parts by joining materials together. In polymer additive manufacturing, this is achieved through thermal reaction or chemical reaction, or both. Current processes in polymer AM include material extrusion, material jetting, powder bed fusion, binder jetting, vat photopolymerization, and sheet lamination (ISO/ASTM, 2021). In selective laser sintering (SLS), a laser is used to selectively melt or fuse particles in the powder bed, layer by layer. SLS is one of the most widely used AM technologies due to its high level of accuracy, high productivity in manufacturing complex structures, and good mechanical properties (Kruth et al., 1998; Lupone et al., 2022).

To address the unmet needs in various industries, researchers have investigated the processability of several polymers including Polyamides (PA) (Beitz et al., 2019; Benedetti et al., 2019; Berretta et al., 2014; Drummer et al., 2010; Soe, 2012; Starr et al., 2011; Vasquez et al., 2011, 2014), Polypropylene (Ituarte et al., 2018; Kleijnen et al., 2016, 2017; Tan et al., 2021; Wegner, 2016; Zhu et al., 2016), Polyetheretherketone (PEEK) (Benedetti et al., 2019; Berretta et al., 2014, 2016), Polyethylene (Drummer et al., 2010), Polyoxymethylene (Drummer et al., 2010), Poly-butylene terephthalate (Schmidt et al., 2016), Poly-ε-caprolactone (Williams et al., 2005), Polystyrene (Yan et al., 2011), Thermoplastic polyurethanes (Dadbakhsh et al., 2016; Vasquez et al., 2014; Verbelen et al., 2017; Yuan et al., 2017), Thermoplastic elastomers (Vasquez et al., 2014), etc. However, it is worth noting that the SLS process currently has a limited number of commercially available polymers. PA-related materials account for over 95 % of the market (Goodridge and Ziegelmeier, 2017; Stansbury and Idacavage, 2016). Semi-crystalline polymers such as Polyamide 12 (PA12) are the material of choice in SLS for the following reasons, (1) sharp melting peak to ensure homogeneous melting, (2) large melting temperature (T_m)

† Received 25 July 2022; Accepted 22 September 2022
J-STAGE Advance published online 29 July 2023
* Corresponding author: Brij M. Moudgil;
Add: Gainesville, FL 32611, USA
E-mail: bmoudgil@perc.ufl.edu
TEL: +1-352-846-1194 Fax: +1-352-846-1196

Copyright © 2024 The Authors. Published by Hosokawa Powder Technology Foundation. This is an open access article under the CC BY license (https://creativecommons.org/licenses/by/4.0/).

to degradation temperature (T_d) window to enable full melting, (3) a rapid viscosity drop once the crystalline region disappears enabling rapid particle coalescence (Drummer et al., 2010). The limited material option is a result of the high powder production cost, lower final part mechanical properties, and dimensional accuracy compared to the traditional manufacturing processes.

The physical phenomena involved in SLS include particle spreading and deposition, laser material interaction, polymer melting and coalescence, and polymer crystallization. Each phenomenon spans different time scales and has a significant impact on the final product properties (Bierwisch et al., 2021; Lupone et al., 2022). An in-depth understanding of these phenomena is the key to improving the final part properties and expanding the suitability of commercial powders for SLS applications.

A SLS process schematic and a process temperature profile are depicted in **Fig. 1**. The process temperature profile is embedded in a semi-crystalline polymer differential scanning calorimetry (DSC) graph to provide a better understanding of polymer heating and cooling behavior during SLS.

The SLS process initiates with a preheating step. An inert gas is continuously purged into the printing chamber from this step and throughout the entire printing process. As shown in **Fig. 1** diagram **A**, the polymer powder on the powder bed is preheated to a temperature below the polymer's T_m. This temperature is defined as the printing temperature. The preheating step holds significant importance for several reasons: (1) it stabilizes the temperature of the entire instrument, (2) it minimizes the energy required for melting the polymer in the target area, (3) it reduces the temperature gradient between the melt area and the chamber air to prevent curling (Soe, 2012). It should be noted that during the preheating stage, since the bed temperature is close to the onset of melting temperature, the unmelted powder may undergo physical and chemical changes after printing (Goodridge et al., 2010; Kuehnlein et al., 2010) and could reduce its reusability. The thermal properties and flowability of the polymer play essential roles in the preheating phase (Berretta et al., 2014; Drummer et al., 2010; Tan et al., 2021; Verbelen et al., 2017).

The second phase is laser scanning (**B** in **Fig. 1**). Laser scanning of the target area starts once the preheating temperature is stabilized. CO_2 laser (10600 nm wavelength) is the most common laser used in polymer SLS systems because of its high absorptance and low penetration depth in the polymer (Jones, 2013). When the polymer molecular structure interacts with the laser beam, which typically has a size of 500 μm for a CO_2 laser, heat is generated due to the vibration of the polymer's molecular structure. The generated heat raises the temperature above the melting point, but below the T_d, as illustrated by point 2 in **Fig. 1**. Upon heating, the polymer particles melt, resulting in viscous flow and coalescence. After laser scanning, the molten area rapidly cools down to the printing temperature (point 3 in **Fig. 1**) (Greiner et al., 2019). Once the layer scanning is completed, the printing bed will move down one layer and a new layer of powder is deposited on the printing bed by a blade or roller. The laser scanning step is repeated until the designed part is fully printed (**C** in **Fig. 1**). During the preheating phase as well as the later phases where there is no polymer melting involved, powder deposition is primarily governed by powder–powder interactions (**A1** in **Fig. 1**). During the scanning phase, where there is polymer melt on the top layer, powder deposition is mainly governed by powder–polymer melt interactions (**B1** in **Fig. 1**). Polymer flowability, optical properties, thermal properties, and rheology are the main factors that impact the laser scanning phase (Kruth et al., 2007; Laumer et al., 2016a;

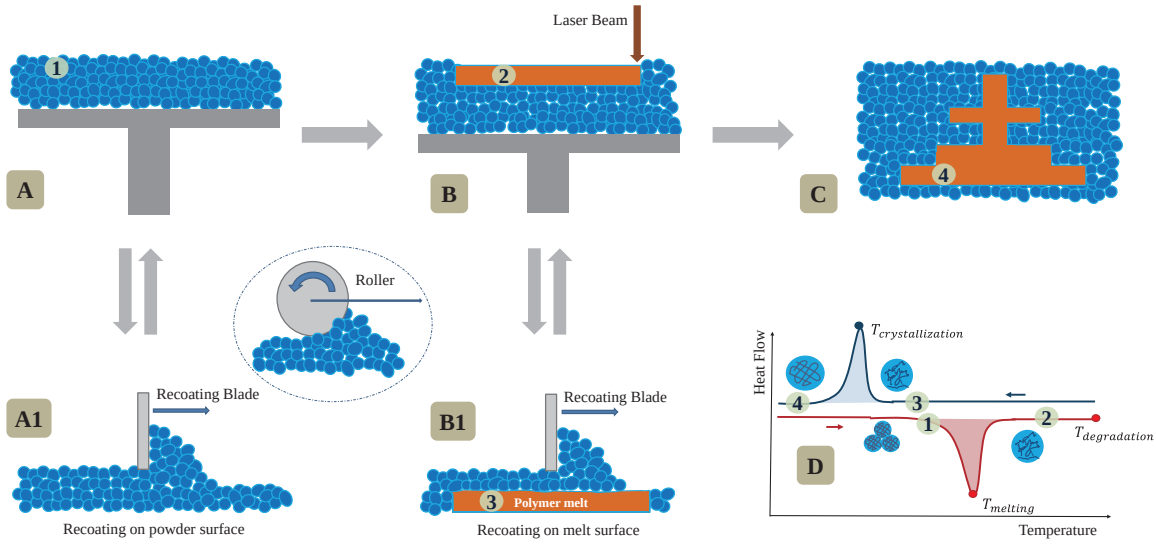


Fig. 1 Polymer SLS process schematic.

Verbelen et al., 2016, 2017; Vock et al., 2019a; Wudy et al., 2015).

After the completion of a printing job, the entire machine, including the printed parts, undergoes a gradual cooling process until it reaches room temperature. The slow cooling process allows the polymer chains to form a crystalline structure (point 4 in **Fig. 1**). Polymer crystallization plays an essential role in this step (Drummer et al., 2019; Goodridge and Ziegelmeier, 2017; Verbelen et al., 2016).

Fig. 2 illustrates the interplay between operational parameters of the SLS process, particle properties and material properties. Powder properties such as size, shape, size distribution, and surface roughness, not only determine its flowability but also affect the thermal and optical properties of the powder bed (Bierwisch et al., 2021; Myers et al., 2015).

An in-depth understanding of powder flowability is essential for designing a successful SLS material and product development scheme. However, due to the specific spreading mechanism involved in SLS, it is challenging to directly apply existing knowledge from traditional particle science research to SLS systems. The present review aims to provide an overview of the role of powder properties, particle deposition, and flowability characteristics in designing a successful SLS system. Experimental analysis, characterization methods, and computational modeling are reviewed to provide the current state of polymer powder research. Although it is challenging to establish comprehensive quantitative correlations between powder properties, powder deposition, process parameters, and final part properties, the review strives to enhance the understanding of the factors that influence the SLS powder deposition process and ultimately establish the science-based guidelines for new material development rather than the trial-and-error approaches currently practiced.

2. Flowability overview

In SLS, the powder bed packing density is directly linked to the achievable part density (Schmid et al., 2015). Despite some applications where porous parts are desired (Yan et al., 2017), the main objective of powder deposition in SLS is to transfer the powder from a feed container to the printing bed to form a homogenous and densely packed layer. Therefore, a good flowing powder is a necessary condition to constitute a suitable SLS material. Powder flow properties and flowability are commonly used to evaluate the suitability of a powder for SLS. Additionally, the newly deposited powder layer should exhibit uniform thickness. According to Prescott et al. (2000), powder flow properties are specific bulk characteristics and can be measured. Powder flow properties depend on the particle size distribution, particle shape, surface morphology, density, electrostatic charge, and environmental factors such as temperature and humidity. Powder flowability, on the other hand, refers to the ability of a powder to flow in a desired manner in a specific piece of equipment (Prescott and Barnum, 2000), and depends on powder flow properties, underlying surface layer morphology and spreading (recoating) mechanism. During recoating on top of the polymer melt scenario, the melt viscosity and surface tension of the molten layer also impact the powder flowability.

From the force perspective, the flowability of SLS powder is influenced by inter-particle forces and external forces

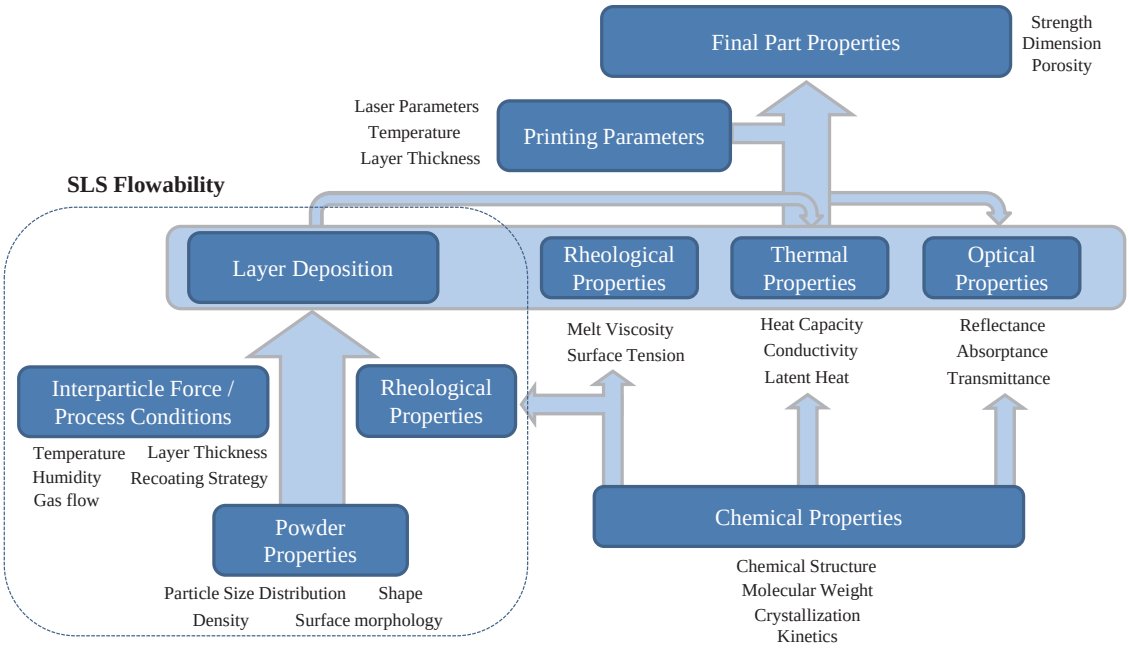


Fig. 2 Graphical representation of the relationships between material properties, printing parameters and final part properties.

due to mechanical interlocking and layer recoating. Van der Waals force, electrostatic force, liquid bridge formation (capillary force), and gravity are the main inter-particle forces between spherical particles (Suzuki, 2019). The van der Waals forces are based on electric dipoles of atoms and molecules. Their magnitude depends on particle size, distance and surface characteristics/morphology (Schulze et al., 2008). Liquid bridge force is formed by the surface tension of the liquid between particles. Considering that the printing temperature of the majority of SLS semi-crystalline polymers is above 100 °C and inert gas is commonly used, the liquid bridge force can be neglected. Electrostatic forces are generated by different electric potentials of particle surfaces (Schulze et al., 2008). Triboelectric charging of polymer powder occurs when the polymer particles come into contact with materials of different dielectric constants (e.g., a metal component) (Tanoue et al., 1999). Due to their low conductivity, it is common practice to allow polymer powder to remain undisturbed for at least 12 hours before printing to reduce/dissipate any electrostatic charge generated during powder preparation. However, triboelectric charging during powder deposition is inevitable. Although the charge build-up between particles improves powder spreading by reducing the attractive van der Waals force and liquid bridge forces, it leads to low packing density (Hesse et al., 2019). Understanding the relationships between these different forces is critical to explaining some of the flowability issues encountered in SLS.

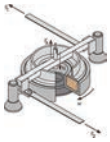
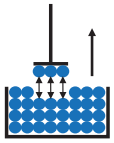
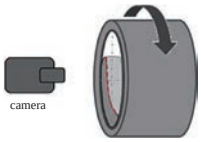
2.1 Flowability characterization

During the material development stage, powder flowability needs to be characterized and optimized before printing. Although the flowability characterization may not represent the powder flow conditions in the SLS process because of the different force and flow mechanisms employed, it can still provide a good indication of the powder flow behavior. **Table 1** gives an overview of the flowability characterization methods that have been used in polymer SLS research.

2.2 Flowability measurement techniques

The two most used methods are the angle of repose and Hausner ratio measurement techniques. Although different setups can be used to measure the angle of repose (Schwedes, 2003), the static angle of repose is widely used in SLS (Berretta et al., 2014; Montón Zarazaga et al., 2022; Tan et al., 2017). In the static angle of repose measurements, powder freely flows through a funnel onto a plate. The angle between the developed pile and the plate is defined as angle of repose (Spierings et al., 2016). A small angle of repose represents good flowability. The Hausner ratio is defined as the ratio between the tapped and loose bulk density of the powder. It describes powder compressibility and flowability. Geldart et al. (2006) found a linear relationship between angle of repose and Hausner ratio. Although being widely used in SLS (Arai et al., 2017, 2019; Chatham et al., 2019; Schmid et al., 2013; Wegner, 2021; Ziegelmeier et al., 2015), the Hausner ratio was found to be inaccurate in predicting the flowability of high-density polyethylene composite and polypropylene

Table 1 list of powder flowability characterization methods in polymer SLS.

Methods	Angle of repose (ASTM D6393)	Hausner ratio (ASTM D7481-09) / Carr index (ASTM D6393)	Shear cell (ASTM D6773)	Tensile tester	Powder rheometer (ASTM D7891)	Revolution powder analyzer	Modified film applicator
							
Parameters	▪Angle of repose	▪ Hausner ratio ▪ Carr index (C) - loose bulk density - tapped bulk density	▪ Shear force ▪ Yield loci	▪ Adhesion force	▪ Basic flowability energy ▪ Specific energy ▪ Conditioned bulk density	▪ Avalanche angle ▪ Surface fractal volume ▪ Expansion ratio	▪ Degree of coverage ▪ Packing density ▪ Packing ratio
References	(Berretta et al., 2014; Montón Zarazaga et al., 2022; Tan et al., 2017)	(Arai et al., 2017, 2019; Chatham et al., 2019; Schmid et al., 2013, 2019; Wegner, 2021; Ziegelmeier et al., 2015)	(Ruggi et al., 2020a, 2020b)	(Schmidt et al., 2014)	(Ziegelmeier et al., 2013, 2015)	(Amado et al., 2011; Amado Becker, 2016; Chatham et al., 2019; Sassaman et al., 2022)	(Laumer et al., 2016b; Van den Eynde et al., 2015; Van den Eynde et al., 2017; Verbelen et al., 2016)

composite materials (Laumer et al., 2016b). Another method that is similar to Hausner ratio but less common in SLS is the Carr index(*C*) (Schmid et al., 2019), which is the Carr Compressibility as referenced in ASTM D6393 (2021) and can be expressed as,

$$\text{Carr Compressibility} = \frac{\text{Tapped Bulk Density} - \text{Loose Bulk Density}}{\text{Tapped Bulk Density}} \times 100 \quad (1)$$

In addition to the Carr Compressibility, the measurement of Carr Angle of Repose is also described in the ASTM D6393 (2021) to test the flowability and floodability of bulk solids using Carr Indices method.

Tensile strength can also be used to measure SLS powder flowability (Schmidt et al., 2014). This method requires a tensile tester and a smooth loose powder bed. The tensile testing head is coated with jelly. The test starts with the testing head in contact with the powder surface, the first layer of the powder in the container adheres to the jelly-coated testing head. When the powder container moves downward, the force between the stamped powder layer and the remaining powder is measured. The measured force is a combination of gravity and adhesion force between the powder particles. This method provides a good insight into the fundamental interparticle force relationship. However, it is limited in indicating a suitable powder flow behavior.

Shear testers are commonly used to evaluate the powder flowability under well-defined shear conditions. Powder rheological properties like cohesive strength and wall friction under shear can be measured in a shear tester to represent flowability. Ruggi et al. (2020a, 2020b) characterized SLS polymers with a modified high-temperature ring shear tester. Among different types of shear testers, ring shear testers not only provide homogeneous shear displacement (Schulze et al., 2008), but they also have the capability of low normal stress measurements (Vock et al., 2019b). Although the force conditions in ring shear testers are closer to SLS printing conditions compared to other shear testers, the flow mechanism of the shear tester is different from that encountered in SLS (Schmidt et al., 2019). Another characterization method involving shear stress is the powder rheometer. It measures the resistance of a powder to flow against an upward or downward rotating helix under different consolidation conditions. Under specific consolidation and shear conditions, the powder rheometer and shear cell data correlate well with each other (Freeman, 2007).

More recently, the rotational revolution powder analyzer has become more popular (Amado et al., 2011; Amado Becker, 2016; Chatham et al., 2019; Sassaman et al., 2022). It consists of a transparent rotating drum and a camera that records the powder flow conditions in the drum. The Avalanche angle, which is the maximum angle of the powder surface before an avalanche occurs, is considered one of the most important indices of the rotating powder. The flow of powder in this method is considered closer to SLS process conditions than the other techniques (Spierings et al., 2016). The high temperature measurement capability of this method can provide more insights into powder flow behaviors under SLS temperature conditions (Amado Becker, 2016).

To provide a direct assessment of the powder flowability, some researchers modified a film applicator into a powder spreader with a similar powder spreading mechanism as in SLS (Laumer et al., 2016b; Verbelen et al., 2016; Van den Eynde et al., 2015). A basic powder spreader enables visual observation of the spreading condition. Van den Eynde et al. (2015) set up a powder bed plate on a balance so that layer weight and packing density could be measured in situ to assess powder flowability. Furthermore, a powder spreader with high-temperature capability (up to 140 °C) was developed (Van den Eynde et al., 2017). This modification not only facilitated the characterization of powder for recoating purposes but also allowed for the evaluation of melt surface recoating for low melting temperature polymers.

2.3 Comparative features of various techniques

With the availability of various characterization methods, it is important to understand their relationships, advantages, disadvantages, and differences. Ziegelmeier et al. (2013) compared cohesion, flowability and packing efficiency of polymer powders with different characterization methods—rotational revolution powder analyzer, powder rheometer and the Hausner Ratio technique. Different particle size distributions of a cryogenically ground polyurethane powder and standard PA12 were used to study the effect of both particle size distributions and particle shape. The revolution powder analyzer showed the best reproducible and reliable results under all experimental conditions examined.

Krantz et al. (2009) investigated the relationship between different characterization techniques using two different formulations of powders with particle sizes ranging between 22 to 31 μm. Characterization methods included angle of repose, powder rheometer and revolution powder analyzer. A linear relationship between angle of repose and avalanche angle was discovered regardless of powder formulation. This is because both techniques involve similar force conditions. Additionally, a linear relationship was discovered between angle of repose and cohesion (powder rheometer characterization index) for individual powder types. However, the trend line for different powders did not overlap because of the different forces encountered in the two techniques. The authors concluded that matching the measured and process force conditions is critical for reliable flowability characterization. Furthermore, they emphasized that utilizing multiple characterization techniques

provides a more comprehensive understanding of powder flowability compared to relying on a single technique alone.

The above discussion highlights that each flowability characterization technique focuses on examining powder flowability from a specific perspective related to a particular flow mechanism. The modified film applicator simulates the SLS flow behavior; however, the setup is not easily accessible. Therefore, it is important to obtain a better understanding of powder flowability by applying multiple flowability characterization techniques during the new material development.

3. Role of powder properties

3.1 Particle size distribution (PSD)

To achieve high surface quality and printing accuracy, smaller particle sizes are theoretically preferred. However, for fine powders, van der Waals forces are significantly greater than gravity which causes powder agglomeration issues leading to nonuniformity of layer thickness, and particle packing inhomogeneity during flow (Krantz et al., 2009). While polydisperse powders can benefit particle packing in free flow conditions (McGEARY, 1961), it is often limited by polymer powder production methods. From the laser material interactions perspective, a narrow PSD is preferred to obtain homogeneous melting (Berretta et al., 2014; Wegner, 2021). With the above considerations, a particle size range of 45 to 90 μm is usually preferred (Goodridge and Ziegelmeier, 2017), although some authors have reported this range to be from 20 to 80 μm (Schmid et al., 2015; Vock et al., 2019b).

Beitz et al. (2019) sieved PA12 into three grades: PA12 Coarse (D_{50} = 56.80 μm), PA12 Original (D_{50} = 51.14 μm) and PA12 Fine (D_{50} = 46.03 μm). All grades had an identical level of PSD span, which is defined as $(D_{90} - D_{10})/D_{50}$. The powders were characterized by Hausner ratio and used for laser printing under the same conditions. The three grades of PA12 showed no difference in either flowability or surface roughness of the printed parts. However, it is important to note that this conclusion should be considered valid only within the particle size range examined in this study. A larger difference in D_{50} could lead to different results.

As part of a flowability study by Van den Eynde et al. (2015), standard PA12 powder with a mass-median diameter of 59 μm was compared with a smaller average particle size PA12 (around 42 μm). The PSD span of standard PA12 (0.84) was higher than the smaller PA12 (0.58). A customized powder spreader setup that simulated the SLS spreading process was used to characterize flowability. The smaller PA12 showed lower packing density. Compared to the results from Beitz et al., it is inferred that the span of PSD plays a vital role in flowability; with a similar PA12 particle size in both studies, a smaller span could result in lower packing density.

It is noteworthy that the effect of PSD span has also been reported in a review primarily focusing on ceramic and metal powders (Vock et al., 2019b). With increasing PSD span, the printed part density and surface quality increased, but the mechanical properties decreased. This indicates that a higher PSD span improves particle packing and part density, however, it can lead to inhomogeneous melting and reduced mechanical properties. However, in a comparison between two commercially available PA12 powders, Schmid et al. (2017) suggested that powder with a smaller span exhibits better flowability and high packing density. Even though the different inter-particle forces could lead to opposite results, more systematic studies are needed to improve the understanding of the flow mechanism during the polymer SLS process.

Multiple studies have been conducted to identify a suitable PSD for SLS. Ziegelmeier et al. (2015) compared the flowability and printability of thermoplastic polyurethane (TPU) and thermoplastic elastomer Duraform Flex (DF). Except for the original particle size fraction, two additional fractions were obtained by sieving out particles below 25 μm or 45 μm. The overall packing density, flowability, printed part surface roughness, ultimate tensile strength and the elongation at break were found to be higher with a decreasing number of fine particles. It was concluded that the gravitational forces increase with particle size, resulting in reduced cohesiveness and improved flowability. Similarly, Schmid et al. (2015) compared two powders with similar volume distribution but different number distribution. The powder with a significant number of small particles (below 20 μm) failed the processability testing due to a higher ratio of cohesion to gravity forces.

On the contrary, other researchers reported the benefits of small particles for powder flow. Verbelen et al. (2016) compared PA6, PA11 and PA12 from different manufacturers with PA11 consisting of rough particles with sharp edges and a large fraction of smaller particles (D_{10} = 20.6 μm). Surprisingly, the rough PA11 had a higher packing density. One of the reasons the authors concluded was that the large fraction of smaller particles allowed more efficient packing at the given layer thickness. Although no quantified values were reported, this study along with the previous two studies emphasized that a smaller number of fine particles in the distribution promotes powder flow possibly due to the ball bearing effect, while an excess number of fine particles hinders flow due to agglomeration.

It should be noted that the PSD directly impacts the SLS printing results by changing the powder bed packing density. Indirectly, PSD changes the thermal and optical properties of the powder bed. The powder thermal conductivity is significantly lower than the bulk because of the high porosity of powder beds (Gong et al., 2013). Sillani et al.

reported a positive linear relationship between packing density and thermal conductivity for several SLS polymer powders (Sillani et al., 2021). The porosity also changes powder optical properties which in turn affects the amount of heat energy generated by laser–material interaction. In an infrared spectroscopy study, quantitative infrared directional–hemispherical reflectance spectra were obtained using a commercial integrating sphere (Myers et al., 2015). The results suggested that the optical reflectivity drops with increased particle size for most wavelengths. With a higher optical reflectivity, higher laser energy is needed to compensate for the energy loss. Overall, the change of powder optical reflectivity and thermal conductivity resulting from the PSD should be considered when selecting the laser power and laser scanning rate for a given material.

3.2 The impact of Particle morphology

In free-flowing particle packing, particles with high roundness and low roughness exhibit reduced mechanical interlocking and increased packing density (German, 1989; Hettiarachchi and Mampearachchi, 2020). Thus, particle morphology is important for the SLS process as well (Schmid et al., 2014; Van den Eynde et al., 2015; Verbelen et al., 2016).

In the spreading study conducted by Van den Eynde et al. (2015), medium roundness standard PA12, medium roundness PA12 with smoother edges, high roundness monodisperse Polystyrene (PS) and low roundness TPU were compared with a customized powder spreader. The high roundness PS exhibited the highest packing density and layer smoothness. Smoother edge PA12 had a higher packing density than the standard PA12. The low roundness TPU had the lowest packing density and resulted in incomplete layers. Accordingly, the high roundness and low roughness were emphasized as the optimal particle morphology conditions for SLS.

However, the high roundness and low roughness particles are not always available for SLS due to the limitation of polymer powder production methods. The current commercially available SLS powder is produced by three main methods: co-extrusion of two non-compatible polymers, precipitation of polymer solutions and cryogenic milling of large polymer granules. Co-extrusion methods produce spherical and smoother particles. However, only limited polymers can be produced by this method, one example is Polypropylene from IRPD AG. The most popular potato shape PA12 powders, such as PA2200 from EOS GmbH, is produced by the precipitation method. Cryogenic milling can process a wide range of polymers by milling below glass transition temperatures. However, milled particles result in irregular shapes and rough surfaces due to the random mechanical force application during the size reduction process. Cryogenic milling also generates a large amount of fine particles which reduces the powder flowability (Schmid et al., 2014). Some typical SLS powder particle shapes are shown in **Fig. 3**.

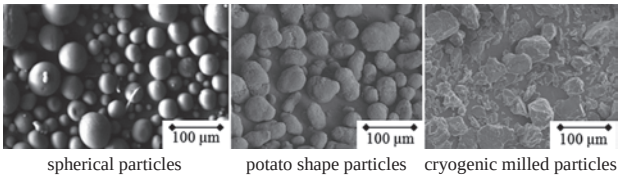


Fig. 3 Typical SLS powder particle shapes (Reprinted with permission from AIP Conference Proceedings “open access”, Schmid et al., 2015).

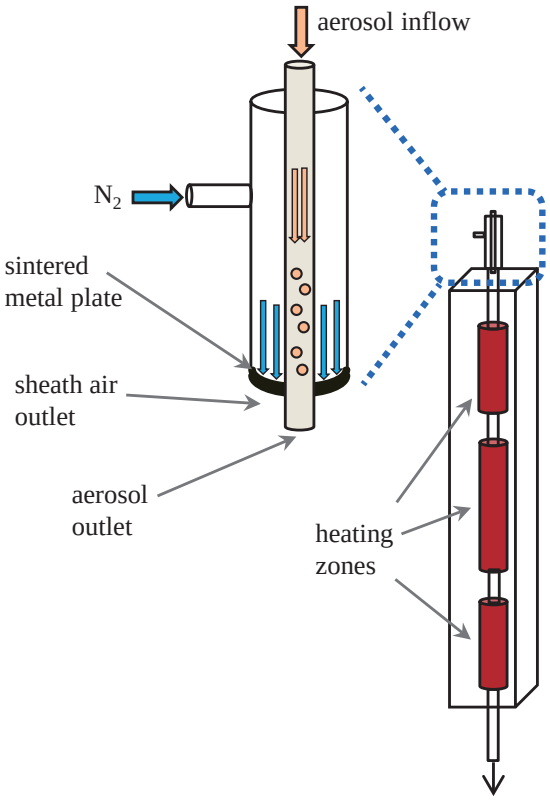


Fig. 4 Schematic drawing of downer reactor (Reprinted with permission from Procedia Engineering “open access”, Sachs et al., 2015).

In addition to the commercially available methods, multiple techniques have been developed in the literature to improve flowability by generating high-roundness particles.

Berretta et al. (2014) found that virgin PEEK particles did not yield a smooth powder bed during powder deposition. The powder was annealed at a temperature above its glass transition temperature for 24 hours in an air-ventilated oven, left to cool down naturally and sieved. The thermal treatment improved particle roundness and flowability significantly, ultimately enabling a smooth spreading within the printing system.

Downer reactor as shown in **Fig. 4**, which utilizes the effect of the surface tension of the molten polymer, is commonly used to smooth irregular polymer particles (Sachs et al., 2015). Schmidt et al. (2014; 2016) demonstrated the

rounding process of polystyrene (PS) and polybutylene terephthalate (PBT) powder and introduced a procedure to generate spherical particles for SLS. The polymer microparticles were produced by wet grinding first. Then the particle roundness was improved by passing them in a heated downer reactor. Finally, hydrophobic fumed silica was mixed with the polymer powder to further improve the flowability by reducing the interparticle van der Waals forces.

4. The impact of processing conditions

During layer deposition, factors such as layer thickness, spreading speed, spreading tool, and temperature are some of the important operational parameters that affect SLS process performance. The impact of these process conditions has also been reported in the literature.

4.1 Layer thickness

For given powder flow characteristics, the desired printing layer thickness depends on different product requirements. A smaller layer thickness is desired to improve printing resolution, but it is limited by the particle size discussed in the previous section. On the other hand, a larger layer thickness reduces printing time. The decreased printing time improves manufacturing efficiency and reduces overall cost. In general, the layer thickness in polymer SLS ranges from 80 to 150 μm. During the deposition of the subsequent layer, melting of the previous layer causes shrinkage in the bed thickness. New powder needs to form a smooth layer on top of the sintered bed. Static and dynamic wall effects are the other main mechanisms of voids formation during the sintering process (Chen et al., 2019). The static wall voids in SLS occur among particles, printing bed and spreading tool due to the round shape of the particles. On the other hand, dynamic wall voids are caused by the arches formed between particles during the spreading motion. In the scenario where particle size and shape cannot be modified to improve packing, increasing the layer thickness can improve the packing density by reducing both the static and dynamic wall effects. Dechet et al. (2020) utilized a layer thickness of 1.5 times the D_{90}, corresponding to around 300 μm, in PLLA development. Although this significantly thicker layer provided promising flowability, it compromised the printing resolution.

4.2 Spreading blade/roller

Blade and roller (counter-rotating with respect to the advancement direction) are the most common powder-spreading tools in SLS systems. The design and movement of the spreading tool also affect the powder packing condition.

Beitz et al. (2019) compared three blade geometries in PA12 printing, including flat, round and sharp bottom. The flat bottom blade shape resulted in the most uniform and dense powder bed due to the larger horizontal contact zone between the blade and the powder bed.

Haeri et al. (2017) simulated the spreading tool and its speed using discrete element simulation and validated the predicted values with experimental results. The use of a roller produced better bed quality compared to the flat bottom blade because of the adequate contact of a roller, which prevented particle dragging. It was also found that the lower roller translational speed produced better powder bed quality compared to a higher speed. It should be noted that non-spherical (rod-shaped) particles were used in this work which might not represent the spreading conditions of spherical or potato shape particles.

Drummer et al. (2015) investigated the effect of spreading speed with both blade and roller systems. The reproducibility of three spreading speeds (125 mm/s, 250 mm/s, 500 mm/s) was analyzed. An optimal spreading speed of 250 mm/s was found independent of spreading tools. The optimal speed was based on the curling phenomenon due to the temperature gradient after laser scanning as shown in **Fig. 5**. With a low speed, the long roller and molten area interaction time led to significant cooling of the molten area. Consequently, curling got worse and the warped layer became stuck to the roller and failed to print. With high speed, the varying compression force could shift the slightly curled section and fail the print.

Niino and Sato (2009) proposed a powder compaction method by using a two-steps roller spreading technique as shown in **Fig. 6**. Compaction was carried out by using a roller of whose rotation speed was controlled independent of its traversing speed. After a traditional roller spreading and layer formation, the powder bed moved up and an additional roller spreading step using the same roller was applied to compact the powder bed. This additional process improved the packing density of the powder bed by a factor of 20 % and reduced residual porosity by 30 %.

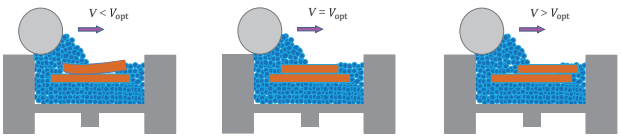


Fig. 5 The effect of powder recoating speed on molten areas.

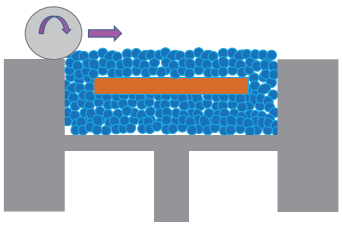


Fig. 6 Powder bed compacting step.

4.3 Other in-process factors

In addition to the powder properties and layer spreading mechanisms, there are other factors in the printing process that also affect powder flowability. One of the most crucial factors is the elevated temperature during the SLS process. The effect of elevated temperature on the flowability is threefold. (1) The polymer particles become softer thereby introducing additional forces by changing contact area and friction between particles during powder flow. (2) Humidity induces cohesive forces between the particles and strongly affects the flow of powders (Rescaglio et al., 2017). For the polymer with a melting temperature above 100 °C, the moisture in the powder evaporates during printing and liquid bridge force gets minimized. Both changes under the elevated temperature cannot be captured with the most powder flowability measurements. (3) The extended long time under elevated temperatures causes changes in the properties of unused powder, which affects its flowability during recycling.

Van den Eynde et al. (2017) examined PA12 flowability under elevated temperatures with a customized powder spreader. A slight increase in the packing condition was observed above the glass transition temperature, indicating that the softening of the polymer increased the powder compressibility. Similarly, Amado et al. (2014) compared PA12 and a co-polypropylene using a modified revolution powder analyzer. The results showed PA12 has reduced surface fractal and improved flowability when process temperatures were above its glass transition temperature.

Ruggi et al. (2020a; 2020b) evaluated PA12 flowability with a high-temperature annular shear cell. The followability was characterized using the "free-flowing range" method (ASTM D6773). The results showed that the flowability improved from 25 °C to 100 °C, then reduced from 100 °C to 160 °C. The liquid bridges present at 25 °C were proposed as the main limitation of the free flow. The flowability increased with reduced moisture from 25 °C to 100 °C. From 100 °C to 160 °C, powder became cohesive towards close to melting temperature because the softened polymer induced more contact points and contact area which reduced the flowability.

In the earlier discussion of morphology, it was mentioned that PEEK flowability can be optimized by high-temperature annealing. However, high-temperature annealing is not always desired. In a SLS print, most of the powder is not melted. It is important to recycle the unmelted powder to reduce the production cost (Dotchev and Yusoff, 2009). The recycling process involves sieving and storing the unmelted powder, which is then mixed with fresh powder for the next cycle of use. The purpose of powder mixing is to neutralize the changes in the properties of used powder that occur as a result of prolonged exposure to elevated temperatures. The mixing rate depends on the extent of property change in the used powder, and not all the polymers can be recycled (Dadbakhsh et al., 2017; Mwania et al., 2021). The change in the chemical structure, thermal properties and rheology properties of the used polymer have been well researched in the literature, especially for PA12 (Dooher et al., 2021; Kuehnlein et al., 2010; Wudy et al., 2014). Mielicki et al. (2015) reported a higher PA12 particle shape deviation for particle size bigger than 100 μm and longer aging times. Dadbakhsh et al. (2017) observed an increased cracking in used PA12 from scanning electron microscope images. The cracks might be caused by the evaporation of remaining alcohol and absorbed moisture and/or the subsequent expansion/shrinkage steps of the process cycles. From the powder flowability perspective, Wegner et al. (2014) reported reduced flowability of used polypropylene (PP) based on the Hausner-ratio method. On the contrary, Yang et al. (2021) reported an improved flowability of used PA12 based on the powder rheometer measurement. The discrepancy in flowability results could be attributed to the different measurement methods employed, where the simulated forced flow in a powder rheometer may yield different outcomes compared to free flow and tapped-based Hausner ratio methods.

In our study, both new and used PA12 were evaluated with the Hausner-ratio method. As shown in **Table 2**, new PA12 exhibits a lower Hausner-ratio compared to used PA12, which suggested a reduced flowability of used PA12. The used PA12, on the other hand, has a higher tapped density. Comparing this with the higher flowability in the previously mentioned PA12 powder rheometer measurement results, there could be a similarity between the tapped force during tapped density measurement and the simulated forced flow in the powder rheometer measurement.

Systematic studies of the triboelectric phenomena in polymer SLS are rare. Recently, Hesse et al. (2019) investigated the triboelectric charge of fresh and used PA12. A powder spreading setup with the electrostatic voltmeter was used to compare both fresh and aged PA12. The electrostatic charge build-up of used PA12 was found to be significantly higher than the fresh PA12. The degradation of an antistatic agent in the powder, or the electrical properties change due to the post-condensation were the reasons cited for the observation according to the author. This

Table 2 Hausner ratio of new and used PA12. The raw data on the Hausner ratio is available publicly at https://doi.org/10.50931/data.kona.23741511

Material	Loose bulk density (g/cm^3)	Tapped bulk density (g/cm^3)	Hausner ratio
New PA12	0.44	0.51	1.15 ± 0.01
Used PA12	0.42	0.52	1.23 ± 0.02

finding is important for the analysis of powder flowability and the development of powder recycling strategies.

5. Additives

Another approach to improve or modify material flow properties is combining additives with established SLS materials (Arai et al., 2018; Gulotty et al., 2013; Mousah, 2011; Sivadas et al., 2021; Tolochko et al., 2000; Yan et al., 2009; Yuan et al., 2019). Additives, especially hydrophobic fumed silica, have been widely used as flow aids to improve powder flowability (Berretta et al., 2014; Laumer et al., 2013; Schmidt et al., 2014, 2016; Verbelen et al., 2016). The presence of the flow aids reduces the interparticle van der Waals forces (Schmidt et al., 2014) and the effects of electrostatic charges (Lexow and Drummer, 2016).

Considering the significantly small particle size of flow aids, they have a large surface-to-volume ratio, and only a small percentage needs to be added to the polymer matrix. The optimal amount of flow aids is of great interest. Laumer et al. (2016b) investigated the effect of flow aids content in high-density polyethylene (PE-HD, D_{50} = 57 µm) and polypropylene (PP, D_{50} = 100 µm). Weight concentrations of 0.0 %, 0.1 %. 0.25 % and 1.0 % of nano-scaled fumed silica were mixed with the polymer by dry mixing. The Hausner ratio and degree of coverage were measured to evaluate flowability. The degree of coverage measurement was done by a customized powder spreader. The results showed that the addition of fumed silica improved overall flowability. However, the concertation effect differed between the two characterizations. The Hausner ratio increased with increasing concentration, with 0.1 % as the optimal concentration. On the other hand, in PE-HD degree of coverage testing, saturation was observed at 0.25 % and degree of coverage decreased above this concentration. The proposed explanation was that the increased amount of fumed silica after saturation caused the separation of fumed silica and polymer particles, and/or the fumed silica agglomeration reduced flowability. On the contrary, no saturation was found in the PP system. The degree of coverage continuously increased with the increase in fumed silica amount, which could be attributed to the different particle sizes and inter-particle forces between the two polymers.

Similarly, Kleijnen et al. (2019) reported the effect of fume silica concentration ranging from 0.005 % to 0.5 % in a PBT (D_{50} = 41.5 µm) powder system. Hausner ratio and a revolution powder analyzer were used to characterize the flowability. The results showed that the flowability did not change below 0.01 wt%, increased from 0.01 wt% to 0.1 wt%, then reached a plateau. Additionally, SEM images revealed that at 0.5 wt% of additive, the polymer surfaces were fully covered and aggregates were formed, which could justify the flowability plateau.

6. White spot

Besides the lack of a comprehensive understanding of powder flow mechanisms discussed in the previous sections, there are two other major areas that require further investigation.

Most of the existing powder flowability studies were conducted to improve particle packing. However, there are situations where a low packing density can be advantageous, such as when reducing printing time or achieving a porous product is desired. According to Beer-Lambert law, the laser intensity along with the powder depth as it transmits into a media decays exponentially (Osmanlic et al., 2018; Xin et al., 2017). A low particle packing density allows for a slow decay of the laser, which leads to deeper melting depth compared to a high powder packing density bed as shown in **Fig. 7**. A larger layer thickness can be employed in this condition which reduces the overall printing time. However, there are two potential penalties for printing with a low packing density. First, the high laser scattering caused by low packing density could lead to issues with printed part dimension, such as over-sintering. Second, extremely high melting depth could result in high surface temperatures, potentially leading to polymer

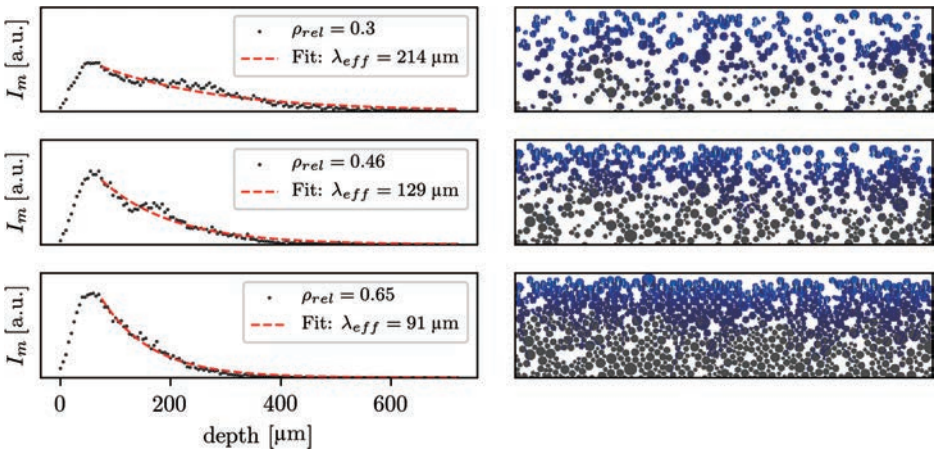


Fig. 7 Laser–powder interaction under different packing densities (Reprinted with permission from Polymers "open access", Osmanlic et al., 2018).

Table 3 The effect of powder properties and process conditions on SLS–other polymers.

Factors		Optimal range	SLS process			SLS printed part (Caused by flowability change)	Research needs
			Flowability	Layer smoothness	Packing density		
Powder property - PSD	+ Span	45 to 90 μm (Goodridge and Ziegelmeier, 2017). 20 to 80 μm (Schmid et al., 2015; Vock et al., 2019b) (General guild line, No experimental data support)			+ (PA12) (Van den Eynde et al., 2015) − (PA12) (Schmid et al., 2017)	− Homogeneous melting [49]	1. Detailed design of experiment to find out the optimal PSD 2. Improved polymer powder production methods
	+ D_{50}		0 (PA12) (Beitz et al., 2019)		+ (PA12) (Van den Eynde et al., 2015)	0 Surface roughness (PA12) (Beitz et al., 2019)	
	+ Fine particles		− (TPU, TPE) (Ziegelmeier et al., 2015) − (Schmid et al., 2015)		− (TPU, TPE) (Ziegelmeier et al., 2015) + (PA11, PA12) (Verbelen et al., 2016)	− Tensile strength (TPU, TPE) (Ziegelmeier et al., 2015) − Surface roughness (TPU, TPE) (Ziegelmeier et al., 2015) 0 Shore hardness (TPU, TPE) (Ziegelmeier et al., 2015)	
Powder property - Morphology	+ Roundness	High roundness (Berretta et al., 2014; Haeri et al., 2017; Van den Eynde et al., 2015)	+ (PEEK) (Berretta et al., 2014) + (Haeri et al., 2017)	+ (PA12) (Van den Eynde et al., 2015)	+ (Haeri et al., 2017) + (PA12) (Van den Eynde et al., 2015)		
	+ Roughness	Low roughness (Van den Eynde et al., 2015)			− (PA12) (Van den Eynde et al., 2015)		
Recoating	+ Layer thickness		+ (PLLA) (Dechet et al., 2020) + (HDPE, PP) (Laumer et al., 2016b)				3. Low packing density and large layer thickness scenario 4. Powder–polymer melt recoating scenario
	+ Blade flatness	Flat (Beitz et al., 2019)		+ (PA12) (Beitz et al., 2019)	+ (PA12) (Beitz et al., 2019)		
	+ Roller instead of blade	Roller (Haeri et al., 2017)		+ (Haeri et al., 2017)			
	+ Recoating speed	250 mm/s (Drummer et al., 2015)		− (Simulation) (Haeri et al., 2017) +− (PA12) (Drummer et al., 2015)			
Process conditions	+ Temperature		+ (PA12) (Amado et al., 2014) +− (PA12) (Ruggi et al., 2020a, 2020b)	+ (PA12) (Van den Eynde et al., 2017)			
	+ Reuse	Fresh Powder (Wegner and Ünlü, 2016)	− (PP) (Wegner and Ünlü, 2016) + (PA12) (Yang et al., 2021)				5. Aging effect on powder property change in different polymer systems
Particle additives	+ Concentration	0.25 wt% Fumed silica in HDPE, 1 wt.% Fumed silica in PP (Laumer et al., 2016b) 0.1 wt% Fumed silica in PBT (Kleijnen et al., 2019)		+− (Fumed silica in HDPE, PP) (Laumer et al., 2016b) (Fumed silica in PBT) (Kleijnen et al., 2019)			

"+" denotes a positive effect with an increased factor, "–" a negative effect with an increased factor, "0" for no effect. "+–" denotes a positive, then a negative effect with an increased factor. "()" denoted the polymer used in the cited work.

degradation. The detailed impact of packing density, layer thickness and laser parameters on polymer coalescence is not yet well understood and requires further systematic investigations.

Although studies have been conducted on the relationship between powder flow conditions and printed part properties, there remains a significant knowledge gap regarding powder–polymer melt recoating, as shown in **Fig. 1** diagram **B1**. This fundamentally differs from the widely investigated powder flow behavior on flat powder surfaces, which is a significantly different environment than the relatively uneven polymer melt surfaces in real systems. From a powder flowability perspective, most researchers have analyzed the flowability based on a designated single-layer thickness. However, the layer thickness would be different after melting. The powder packing density is about 40–50 % (Van den Eynde et al., 2015). During melting, the powder layer sinks due to the filling of gaps between particles. This phenomenon leads to powder layer height changes for the next powder deposition. In the case of metal SLS, this powder layer height is 4–5 times the designed layer thickness (Wischeropp et al., 2019). The dramatic increase in the layer thickness could change powder flow behavior. Furthermore, Mielicki et al. (2015) discovered that the temperature of the polymer melt, 10 seconds after laser exposure, is close to the printing temperature, indicating that the polymer is in a viscous flow undercooling stage during the next layer powder deposition. Powder deposition on a surface under viscous flow conditions encounters different force conditions compared to deposition on a cooled solid surface. From a polymer rheology perspective, most of the research has focused on the polymer melt coalescence (Haworth et al., 2013; Mielicki et al., 2012), except for a study by Wudy et al. (2015) who investigated the effect of different polymer melt surface tension conditions on the powder bed formation. The opposite scenario, where powder flows on the polymer melt, remains unexplored.

7. Conclusion and future perspectives

Polymer selective laser sintering is a powder-based additive manufacturing technology. In this paper, we have presented a review focusing on one of the most important aspects of SLS: powder flowability. The powder flowability determines layer packing and the final printed part properties. Besides a brief discussion of the powder flowability characterization methods used in polymer SLS, the primary objective of the review was to provide a better understanding of the powder flow mechanism during the printing process. The powder properties such as PSD and particle morphology play important roles in flowability.

The effect of powder properties and process conditions on SLS process performance, based on the literature cited in this review, is summarized in **Table 3**. Some factors exhibit contradictory effects when viewed from different perspectives., e.g., PSD span improves packing but results in inhomogeneous melting. There is also a delta between the findings for polymer and metal/ceramic regarding the effect of PSD as discussed in the previous section. The current research on polymer SLS is constrained by the limited variety of powder properties options i.e., availability of spherical, and smooth particles with controllable particle sizes. It is essential to improve existing polymer powder production methods and develop new methods so that the desired powder properties criteria for optimal printing conditions can be developed.

As discussed in the above sections, all material properties contribute to a successful SLS print. Regarding the powder properties and flowability:

- A smooth powder layer formation is the precondition of the layer-by-layer process. It is influenced by powder flowability, morphology and process conditions. The use of an optimal PSD (45–90 μm or 20–80 μm), high roundness particles or an appropriate concentration of flow aids often leads to an acceptable layer formation.
- The powder packing density is influenced by the same factors as powder flowability and can be improved by utilizing an appropriate PSD, high roundness particles and an optimal concentration of flow aids. The packing density affects the thermal and optical properties of the powder bed, which cause a direct impact on the laser–material interaction as shown in **Fig. 7**. By tuning laser parameters, process conditions and adding absorption intensifiers (Laumer et al., 2013), successful print properties can be achieved even with powder beds that have low packing densities.

In addition to experimental studies, simulations and modeling efforts are needed to provide further insights to develop meaningful guidelines for achieving optimal powder properties and successful process performance.

Considering that PA and its composites account for 95 % of the SLS polymer commercial market, there is a need to develop other polymers to meet diverse product property requirements and expand the range of SLS applications. The current understanding of polymer processing phenomena, including flowability, is primarily based on PA12. As a common approach, investigating the printing mechanism of PA12 and using it as a basis for developing guidelines for new materials is often employed. Without the development of universally quantified criteria for powder/material properties, the trial-and-error method will continue to be the most common approach for new material development in the industry. It is also critical to expand the investigation of other polymers, from feasibility tests to fundamental failure mode analysis, to gain a deeper understanding of the SLS process.

Data Availability Statement

The raw data on Polyamide 12 Hausner ratio is available publicly in J-STAGE Data (https://doi.org/10.50931/data.kona.23741511).

Acknowledgments

The authors acknowledge the financial support of the National Science Foundation Center of Particulate and Surfactant Science (CPaSS) and the industry members (NSF Award #1362060). Any opinions, findings, and conclusions or recommendations expressed in this material are those of the authors and do not necessarily reflect the views of the National Science Foundation or the CPaSS industry members.

References

Amado A., Schmid M., Levy G., Wegener K., Advances in SLS powder characterization, 22nd Annual International Solid Freeform Fabrication Symposium, (2011) 438–452. DOI: 10.26153/tsw/15306

Amado A., Schmid M., Wegener K., Flowability of SLS powders at elevated temperature, Swiss Institute of Technology, ETH Zürich, 2014. DOI: 10.3929/ethz-a-010057815

Amado Becker A.F., Characterization and prediction of SLS processability of polymer powders with respect to powder flow and part warpage, Doctoral Thesis, ETH-Zürich, 2016. DOI: 10.3929/ethz-a-010657585

Arai S., Tsunoda S., Kawamura R., Kuboyama K., Ougizawa T., Comparison of crystallization characteristics and mechanical properties of poly(butylene terephthalate) processed by laser sintering and injection molding, Materials & Design, 113 (2017) 214–222. DOI: 10.1016/j.matdes.2016.10.028

Arai S., Tsunoda S., Yamaguchi A., Ougizawa T., Effects of short-glass-fiber content on material and part properties of poly(butylene terephthalate) processed by selective laser sintering, Additive Manufacturing, 21 (2018) 683–693. DOI: 10.1016/j.addma.2018.04.019

Arai S., Tsunoda S., Yamaguchi A., Ougizawa T., Characterization of flame-retardant poly(butylene terephthalate) processed by laser sintering, Optics & Laser Technology, 117 (2019) 94–104. DOI: 10.1016/j.optlastec.2019.04.006

ASTM D6393, Standard Test Method for Bulk Solids Characterization by Carr Indices, ASTM International, 2021. DOI: 10.1520/d6393_d6393m-21

Beitz S., Uerlich R., Bokelmann T., Diener A., Vietor T., Kwade A., Influence of powder deposition on powder bed and specimen properties, Materials, 12 (2019) 297. DOI: 10.3390/ma12020297

Benedetti L., Brulé B., Decreamer N., Evans K.E., Ghita O., Shrinkage behaviour of semi-crystalline polymers in laser sintering: PEKK and PA12, Materials & Design, 181 (2019) 107906. DOI: 10.1016/j.matdes.2019.107906

Berretta S., Evans K.E., Ghita O.R., Predicting processing parameters in high temperature laser sintering (HT-LS) from powder properties, Materials and Design, 105 (2016) 301–314. DOI: 10.1016/j.matdes.2016.04.097

Berretta S., Ghita O., Evans K.E., Morphology of polymeric powders in Laser Sintering (LS): from Polyamide to new PEEK powders, European Polymer Journal, 59 (2014) 218–229. DOI: 10.1016/j.eurpolymj.2014.08.004

Bierwisch C., Mohseni-Mofidi S., Dietemann B., Grünewald M., Rudloff J., Lang M., Universal process diagrams for laser sintering of polymers, Materials & Design, 199 (2021) 109432. DOI: 10.1016/j.matdes.2020.109432

Chatham C.A., Long T.E., Williams C.B., Powder bed fusion of poly (phenylene sulfide) at bed temperatures significantly below melting, Additive Manufacturing, 28 (2019) 506–516. DOI: 10.1016/j.addma.2019.05.025

Chen H., Wei Q., Zhang Y., Chen F., Shi Y., Yan W., Powder-spreading mechanisms in powder-bed-based additive manufacturing: experiments and computational modeling, Acta Materialia, 179 (2019) 158–171. DOI: 10.1016/j.actamat.2019.08.030

Dadbakhsh S., Verbelen L., Vandeputte T., Strobbe D., Van Puyvelde P., Kruth J.P., Effect of powder size and shape on the SLS processability and mechanical properties of a TPU elastomer, Physics Procedia, 83 (2016) 971–980. DOI: 10.1016/j.phpro.2016.08.102

Dadbakhsh S., Verbelen L., Verkinderen O., Strobbe D., Effect of PA12 powder reuse on coalescence behaviour and microstructure of SLS parts, European Polymer Journal, 92 (2017) 250–262. DOI: 10.1016/j.eurpolymj.2017.05.014

Dechet M.A., Demina A., Römling L., Gómez Bonilla J.S., Lanyi F.J., Schubert D.W., Bück A., Peukert W., Schmidt J., Development of poly(L-lactide) (PLLA) microspheres precipitated from triacetin for application in powder bed fusion of polymers, Additive Manufacturing, 32 (2020) 100966. DOI: 10.1016/j.addma.2019.100966

Dooher T., Archer E., Walls T., McIlhagger A., Dixon D., Ageing of laser sintered glass-filled Polyamide 12 (PA12) parts at elevated temperature and humidity, Polymers and Polymer Composites, 12 (2021) 1–11. DOI: 10.1177/09673911211027127

Dotchev K., Yusoff W., Recycling of polyamide 12 based powders in the laser sintering process, Rapid Prototyping Journal, 15 (2009) 192–203. DOI: 10.1108/13552540910960299

Drummer D., Drexler M., Wudy K., Density of laser molten polymer parts as function of powder coating process during additive manufacturing, Procedia Engineering, 102 (2015) 1908–1917. DOI: 10.1016/j.proeng.2015.01.331

Drummer D., Greiner S., Zhao M., Wudy K., A novel approach for understanding laser sintering of polymers, Additive Manufacturing, 27 (2019) 379–388. DOI: 10.1016/j.addma.2019.03.012

Drummer D., Rietzel D., Kühnlein F., Development of a characterization approach for the sintering behavior of new thermoplastics for selective laser sintering, Physics Procedia, 5 (2010) 533–542. DOI: 10.1016/j.phpro.2010.08.081

Freeman R., Measuring the flow properties of consolidated, conditioned and aerated powders—a comparative study using a powder rheometer and a rotational shear cell, Powder Technology, 174 (2007) 25–33. DOI: 10.1016/j.powtec.2006.10.016

Geldart D., Abdullah E.C., Hassanpour A., Nwoke L.C., Wouters I., Characterization of powder flowability using measurement of angle of repose, China Particuology, 4 (2006) 104–107. DOI: 10.1016/s1672-2515(07)60247-4

German R.M., Particle Packing Characteristics, Metal Powder Industry, 1989, ISBN: 9780918404831. DOI: 10.1016/0032-5910(90)80071-6

Gong X., Cheng B., Price S., Chou K., Powder-bed electron-beam-melting additive manufacturing: powder characterization, process simulation and metrology, ASME District Early Career Technical Conference, ASME Early Career Technical Journal, (2013) 59–66.

Goodridge R., Ziegelmeier S., Powder bed fusion of polymers, Laser Additive Manufacturing: Materials, Design, Technologies, and Applications, (2017) 181–204. DOI: 10.1016/B978-0-08-100433-3.00007-5

Goodridge R.D., Hague R.J.M., Tuck C.J., Effect of long-term ageing on the tensile properties of a polyamide 12 laser sintering material, Polymer Testing, 29 (2010) 483–493. DOI: 10.1016/j.polymertesting.2010.02.009

Greiner S., Wudy K., Wörz A., Drummer D., Thermographic investigation of laser-induced temperature fields in selective laser beam melting of polymers, Optics and Laser Technology, 109 (2019) 569–576. DOI: 10.1016/j.optlastec.2018.08.010

Gulotty R., Castellino M., Jagdale P., Tagliaferro A., Balandin A.A., Effects of functionalization on thermal properties of single-wall and multi-wall carbon nanotube-polymer nanocomposites, ACS Nano, 7 (2013) 5114–5121. DOI: 10.1021/nn400726g

Haeri S., Wang Y., Ghita O., Sun J., Discrete element simulation and experimental study of powder spreading process in additive manufacturing, Powder Technology, 306 (2017) 45–54. DOI: 10.1016/j.powtec.2016.11.002

Haworth B., Hopkinson N., Hitt D., Zhong X., Shear viscosity measurements on Polyamide-12 polymers for laser sintering, Rapid Prototyping Journal, 19 (2013) 28–36. DOI: 10.1108/13552541311292709

Hesse N., Dechet M.A., Bonilla J.S.G., Lübbert C., Roth S., Bück A., Schmidt J., Peukert W., Analysis of tribo-charging during powder spreading in selective laser sintering: assessment of polyamide 12 powder ageing effects on charging behavior, Polymers, 11 (2019) 609. DOI: 10.3390/polym11040609

Hettiarachchi C., Mampearachchi W.K., Effect of surface texture, size ratio and large particle volume fraction on packing density of binary spherical mixtures, Granular Matter, 22 (2020) 1–13. DOI: 10.1007/s10035-019-0978-3

ISO/ASTM 52900:2021, Additive manufacturing—General principles—Fundamentals and vocabulary, 2021. <https://www.iso.org/standard/74514.html> accessed 20042023

Ituarte I.F., Wiikinkoski O., Jansson A., Additive manufacturing of polypropylene: a screening design of experiment using laser-based powder bed fusion, Polymers, 10 (2018) 1293. DOI: 10.3390/polym10121293

Jones I., Laser welding of plastics, in: Katayama S. (Ed.) Handbook of Laser Welding Technologies, Woodhead Publishing, 2013, pp. 280-301e, ISBN: 9780857092649. DOI: 10.1533/9780857098771.2.280

Kleijnen R.G., Schmid M., Wegener K., Nucleation and impact modification of polypropylene laser sintered parts, AIP Conference Proceedings, 1779 (2016) 100004-1–5. DOI: 10.1063/1.4965572

Kleijnen R.G., Schmid M., Wegener K., Impact of flow aid on the flowability and coalescence of polymer laser sintering powder, 2019 International Solid Freeform Fabrication Symposium, (2019) 806–817. DOI: 10.26153/tsw/17317

Kleijnen R.G., Sesseg J.P.W., Schmid M., Wegener K., Insights into the development of a short-fiber reinforced polypropylene for laser sintering, AIP Conference Proceedings, 1914 (2017) 190002. DOI: 10.1063/1.5016791

Krantz M., Zhang H., Zhu J., Characterization of powder flow: static and dynamic testing, Powder Technology, 194 (2009) 239–245. DOI: 10.1016/j.powtec.2009.05.001

Kruth J.P., Leu M.C., Nakagawa T., Progress in additive manufacturing and rapid prototyping, CIRP Annals—Manufacturing Technology, 47 (1998) 525–540. DOI: 10.1016/s0007-8506(07)63240-5

Kruth J.P., Levy G., Klocke F., Childs T.H.C., Consolidation phenomena in laser and powder-bed based layered manufacturing, CIRP Annals—Manufacturing Technology, 56 (2007) 730–759. DOI: 10.1016/j.cirp.2007.10.004

Kuehnlein F., Drummer D., Rietzel D., Seefried A., Degradation behavior and material properties of PA12-plastic powders processed by powder based additive manufacturing technologies, Annals of DAAAM and Proceedings of the International DAAAM Symposium, 21 (2010) 1547–1548. ISBN 9783901509735.

Laumer T., Stichel T., Nagulin K., Schmidt M., Optical analysis of polymer powder materials for Selective Laser Sintering, Polymer Testing, 56 (2016a) 207–213. DOI: 10.1016/j.polymertesting.2016.10.010

Laumer T., Stichel T., Raths M., Schmidt M., Analysis of the influence of different flowability on part characteristics regarding the simultaneous laser beam melting of polymers, Physics Procedia, 83 (2016b) 937–946. DOI: 10.1016/j.phpro.2016.08.098

Laumer T., Stichel T., Sachs M., Amend P., Schmidt M., Qualification and modification of new polymer powders for laser beam melting using Ulbricht spheres, in: High Value Manufacturing: Advanced Research in Virtual and Rapid Prototyping, 1st ed., CRC Press, 2013, pp. 255–260. ISBN: 9781138001374. DOI: 10.1201/b15961

Lexow M.M., Drummer D., New materials for SLS: the use of antistatic and flow agents, Journal of Powder Technology, 2016 (2016) 4101089. DOI: 10.1155/2016/4101089

Ligon S.C., Liska R., Stampfl J., Gurr M., Mülhaupt R., Polymers for 3D printing and customized additive manufacturing, Chemical Reviews, 117 (2017) 10212–10290. DOI: 10.1021/acs.chemrev.7b00074

Lupone F., Padovano E., Casamento F., Badini C., Process phenomena and material properties in selective laser sintering of polymers: a review, Materials 2022, 15 (2021) 183. DOI: 10.3390/ma15010183

McGeary R.K., Mechanical packing of spherical particles, Journal of the American Ceramic Society, 44 (1961) 513–522. DOI: 10.1111/j.1151-2916.1961.tb13716.x

Mielicki C., Gronhoff B., Wortberg J., Effects of laser sintering processing time and temperature on changes in polyamide 12 powder particle size, shape and distribution, AIP Conference Proceedings, 1593 (2015) 728–731. DOI: 10.1063/1.4873880

Mielicki C., Wegner a, Gronhoff B., Wortberg J., Witt G., Prediction of PA12 melt viscosity in laser sintering by a time and temperature dependent rheological model, RTeJournal, 32 (2012). <https://rtejournal.de/document/2012_11> accessed 20012023.

Montón Zarazaga A., Abdelmoula M., Küçüktürk G., Maury F., Ferrato M., Grossin D., Process parameters investigation for direct powder bed selective laser processing of silicon carbide parts, Progress in Additive Manufacturing, 7 (2022) 1307–1322. DOI: 10.1007/s40964-022-00305-7

Mousah A., Effects of filler content and coupling agents on the mechanical properties and geometrical accuracy of selective laser sintered parts in glass bead-filled polyamide 12 composites, Thesis (Ph.D.), Cardiff University, 2011, pp. 227–231. https://orca.cardiff.ac.uk/id/eprint/11094

Mwania F.M., Maringa M., Van Der Walt J.G., A review of the techniques used to characterize laser sintering of polymeric powders for use and re-use in additive manufacturing, Manufacturing Review, 8 (2021) 1–17. DOI: 10.1051/mfreview/2021012

Myers T.L., Brauer C.S., Su Y.-F., Blake T.A., Tonkyn R.G., Ertel A.B., Johnson T.J., Richardson R.L., Quantitative reflectance spectra of solid powders as a function of particle size, Applied Optics, 54 (2015) 4863. DOI: 10.1364/ao.54.004863

Niino T., Sato K., Effect of powder compaction in plastic laser sintering fabrication, 2009 International Solid Freeform Fabrication Symposium, (2009) 193–205. DOI: 10.26153/tsw/15100

Osmanlic F., Wudy K., Laumer T., Schmidt M., Drummer D., Körner C., Modeling of laser beam absorption in a polymer powder bed, Polymers, 10 (2018) 1–11. DOI: 10.3390/polym10070784

Prescott J., Barnum R.A., On powder flowability, Pharmaceutical Technology, 24(10) (2000) 60–84.

Rescaglio A., Schockmel J., Vandewalle N., Lumay G., Combined effect of moisture and electrostatic charges on powder flow, EPJ Web of Conferences, 140 (2017) 13009. DOI: 10.1051/epjconf/201714013009

Ruggi D., Barrès C., Charmeau J.Y., Fulchiron R., Barletta D., Poletto M., A quantitative approach to assess high temperature flow properties of a PA 12 powder for laser sintering, Additive Manufacturing, 33 (2020a) 101143. DOI: 10.1016/j.addma.2020.101143

Ruggi D., Lupo M., Sofia D., Barrès C., Barletta D., Poletto M., Flow properties of polymeric powders for selective laser sintering, Powder Technology, 370 (2020b) 288–297. DOI: 10.1016/j.powtec.2020.05.069

Sachs M., Schmidt J., Toni F., Blümel C., Winzer B., Peukert W., Wirth K.E., Rounding of irregular polymer particles in a downer reactor, Procedia Engineering, 102 (2015) 542–549. DOI: 10.1016/j.proeng.2015.01.119

Sassaman D., Phillips T., Milroy C., Ide M., Beaman J., A method for predicting powder flowability for selective laser sintering, JOM, 74 (2022) 1102–1110. DOI: 10.1007/s11837-021-05050-w

Schmid M., Amado F., Levy G., Wegener K., Flowability of powders for selective laser sintering (SLS) investigated by round robin test, in: High Value Manufacturing: Advanced Research in Virtual and Rapid Prototyping, 1st ed., CRC Press, 2013, pp. 95–99, ISBN: 9781138001374. DOI: 10.3929/ethz-a-010057806

Schmid M., Amado A., Wegener K., Materials perspective of polymers for additive manufacturing with selective laser sintering, Journal of Materials Research, 29 (2014) 1824–1832. DOI: 10.1557/jmr.2014.138

Schmid M., Amado A., Wegener K., Polymer powders for selective laser sintering (SLS), AIP Conference Proceedings, 1664 (2015) 160009-1–5. DOI: 10.1063/1.4918516

Schmid M., Kleijnen R., Vetterli M., Wegener K., Influence of the origin of polyamide 12 powder on the laser sintering process and laser sintered parts, Applied Sciences (Switzerland), 7 (2017) 462. DOI: 10.3390/app7050462

Schmidt J., Dechet M.A., Gómez Bonilla J.S., Hesse N., Bück A., Peukert W., Characterization of polymer powders for selective laser sintering, 2019 International Solid Freeform Fabrication Symposium, (2019) 779–789. DOI: 10.26153/tsw/17314

Schmidt J., Sachs M., Blümel C., Winzer B., Toni F., Wirth K.E., Peukert W., A novel process route for the production of spherical LBM polymer powders with small size and good flowability, Powder Technology, 261 (2014) 78–86. DOI: 10.1016/j.powtec.2014.04.003

Schmidt J., Sachs M., Fanselow S., Zhao M., Romeis S., Drummer D., Wirth K.E., Peukert W., Optimized polybutylene terephthalate powders for selective laser beam melting, Chemical Engineering Science, 156 (2016) 1–10. DOI: 10.1016/j.ces.2016.09.009

Schulze D., Powders and Bulk Solids: Behavior, Characterization, Storage and Flow, 1st ed., Springer Berlin, Heidelberg, 2008, ISSN: 9783540737674. DOI: 10.1007/978-3-540-73768-1

Schwedes J., Review on testers for measuring flow properties of bulk solids, Granular Matter, 5 (2003) 1–43. DOI: 10.1007/s10035-002-0124-4

Sillani F., de Gasparo F., Schmid M., Wegener K., Influence of packing density and fillers on thermal conductivity of polymer powders for additive manufacturing, International Journal of Advanced Manufacturing Technology, 117 (2021) 2049–2058. DOI: 10.1007/s00170-021-07117-z

Sivadas B.O., Ashcroft I., Khlobystov A.N., Goodridge R.D., Laser sintering of polymer nanocomposites, Advanced Industrial and Engineering Polymer Research, 4 (2021) 277–300. DOI: 10.1016/j.aiepr.2021.07.003

Soe S.P., Quantitative analysis on SLS part curling using EOS P700 machine, Journal of Materials Processing Technology, 212 (2012) 2433–2442. DOI: 10.1016/j.jmatprotec.2012.06.012

Spierings A.B., Voegtlin M., Bauer T., Wegener K., Powder flowability characterisation methodology for powder-bed-based metal additive manufacturing, Progress in Additive Manufacturing, 1 (2016) 9–20. DOI: 10.1007/s40964-015-0001-4

Stansbury J.W., Idacavage M.J., 3D printing with polymers: challenges among expanding options and opportunities, Dental Materials, 32 (2016) 54–64. DOI: 10.1016/j.dental.2015.09.018

Starr T.L., Gornet T.J., Usher J.S., The effect of process conditions on mechanical properties of laser-sintered nylon, Rapid Prototyping Journal, 17 (2011) 418–423. DOI: 10.1108/13552541111184143

Suzuki M., Chapter 3.5: Packing properties, in: Higashitani K., Makino, H., and Matsusaka, S. (Eds.), Powder Technology Handbook, 4th ed., CRC Press, 2019, pp.203–209, ISBN: 9781315184258. DOI: 10.1201/b22268

Tan L.J., Zhu W., Sagar K., Zhou K., Comparative study on the selective laser sintering of polypropylene homopolymer and copolymer: processability, crystallization kinetics, crystal phases and mechanical properties, Additive Manufacturing, 37 (2021) 101610. DOI: 10.1016/j.addma.2020.101610

Tan Y.-Q., Zheng J.-H., Gao W., Jiang S.-Q., Feng Yuntian, Zheng J., Gao Á.W., Jiang Á.S., Feng Y, The effect of powder flowability in the selective laser sintering process, Proceedings of the 7th International Conference on Discrete Element Methods, 188 (2017) 629–636. DOI: 10.1007/978-981-10-1926-5_65

Tanoue K.I., Ema A., Masuda H., Effect of material transfer and work hardening of metal surface on the current generated by impact of particles, Journal of Chemical Engineering of Japan, 32 (1999) 544–548. DOI: 10.1252/jcej.32.544

Tolochko N.K., Laoui T., Khlopkov Y.V., Mozzharov S.E., Titov V.I., Ignatiev M.B., Absorptance of powder materials suitable for laser sintering, Rapid Prototyping Journal, 6 (2000) 155–160. DOI: 10.1108/13552540010337029

Van den Eynde M., Verbelen L., Van Puyvelde P., Assessing polymer powder flow for the application of laser sintering, Powder Technology, 286 (2015) 151–155. DOI: 10.1016/j.powtec.2015.08.004

Van den Eynde M., Verbelen L., Van Puyvelde P., Influence of temperature on the flowability of polymer powders in laser sintering, AIP Conference Proceedings, 1914 (2017) 190007-1–5. DOI: 10.1063/1.5016796

Vasquez G.M., Majewski C.E., Haworth B., Hopkinson N., A targeted material selection process for polymers in laser sintering, Additive Manufacturing, 1 (2014) 127–138. DOI: 10.1016/j.addma.2014.09.003

Vasquez M., Haworth B., Hopkinson N., Optimum sintering region for laser sintered Nylon-12, Proceedings of the Institution of Mechanical Engineers, Part B: Journal of Engineering Manufacture, 225 (2011) 2240–2248. DOI: 10.1177/0954405411414994

Verbelen L., Dadbakhsh S., Van den Eynde M., Kruth J.P., Goderis B., Van Puyvelde P., Characterization of polyamide powders for determination of laser sintering processability, European Polymer Journal, 75 (2016) 163–174. DOI: 10.1016/j.eurpolymj.2015.12.014

Verbelen L., Dadbakhsh S., Van den Eynde M., Strobbe D., Kruth J.P., Goderis B., Van Puyvelde P., Analysis of the material properties involved in laser sintering of thermoplastic polyurethane, Additive Manufacturing, 15 (2017) 12–19. DOI: 10.1016/j.addma.2017.03.001

Vock S., Klöden B., Kirchner A., Weißgärber T., Kieback B., Powders for powder bed fusion: a review, Progress in Additive Manufacturing, 4 (2019a) 383–397. DOI: 10.1007/s40964-019-00078-6

Vock S., Klöden B., Kirchner A., Weißgärber T., Kieback B., Powders for powder bed fusion: a review, Progress in Additive Manufacturing, 4 (2019b) 383–397. DOI: 10.1007/s40964-019-00078-6

Wegner A., New polymer materials for the laser sintering process: polypropylene and others, Physics Procedia, 83 (2016) 1003–1012. DOI: 10.1016/j.phpro.2016.08.105

Wegner A., Introduction to powder bed fusion of polymers, Additive Manufacturing, (2021) 33–75. DOI: 10.1016/B978-0-12-818411-0.00011-2

Wegner A., Mielicki C., Grimm T., Gronhoff B., Witt G., Wortberg J., Determination of robust material qualities and processing conditions for laser sintering of polyamide 12, Polymer Engineering and Science, 54 (2014) 1540–1554. DOI: 10.1002/pen.23696

Wegner A., Ünlü T., Powder life cycle analyses for a new polypropylene laser sintering material, 2016 International Solid Freeform Fabrication Symposium, (2016) 834–846. https://hdl.handle.net/2152/89636

Williams J.M., Adewunmi A., Schek R.M., Flanagan C.L., Krebsbach P.H., Feinberg S.E., Hollister S.J., Das S., Bone tissue engineering using polycaprolactone scaffolds fabricated via selective laser sintering, Biomaterials, 26 (2005) 4817–4827. DOI: 10.1016/j.biomaterials.2004.11.057

Wischeropp T.M., Emmelmann C., Brandt M., Pateras A., Measurement of actual powder layer height and packing density in a single layer in

selective laser melting, Additive Manufacturing, 28 (2019) 176–183. DOI: 10.1016/j.addma.2019.04.019

Wudy K., Drummer D., Drexler M., Characterization of polymer materials and powders for selective laser melting, AIP Conference Proceedings, 1593 (2015) 702–707. DOI: 10.1063/1.4873875

Wudy K., Drummer D., Kühnlein F., Drexler M., Influence of degradation behavior of polyamide 12 powders in laser sintering process on produced parts, AIP Conference Proceedings, 1593 (2014) 691–695. DOI: 10.1063/1.4873873

Xin L., Boutaous M., Xin S., Siginer D.A., Multiphysical modeling of the heating phase in the polymer powder bed fusion process, Additive Manufacturing, 18 (2017) 121–135. DOI: 10.1016/j.addma.2017.10.006

Yan C., Shi Y., Hao L., Investigation into the differences in the selective laser sintering between amorphous and semi-crystalline polymers, International Polymer Processing, 26 (2011) 416–423. DOI: 10.3139/217.2452

Yan C.Z., Shi Y.S., Yang J.S., Xu L., Preparation and selective laser sintering of nylon-12-coated aluminum powders, Journal of Composite Materials, 43 (2009) 1835–1851. DOI: 10.1177/0021998309340932

Yan M., Tian X., Peng G., Cao Y., Li D., Hierarchically porous materials prepared by selective laser sintering, Materials and Design, 135 (2017) 62–68. DOI: 10.1016/j.matdes.2017.09.015

Yang F., Schnuerch A., Chen X., Quantitative influences of successive reuse on thermal decomposition, molecular evolution, and elemental composition of polyamide 12 residues in selective laser sintering, International Journal of Advanced Manufacturing Technology, 115 (2021) 3121–3138. DOI: 10.1007/S00170-021-07368-W/TABLES/7

Yuan S., Shen F., Bai J., Chua C.K., Wei J., Zhou K., 3D soft auxetic lattice structures fabricated by selective laser sintering: TPU powder evaluation and process optimization, Materials & Design, 120 (2017) 317–327. DOI: 10.1016/J.MATDES.2017.01.098

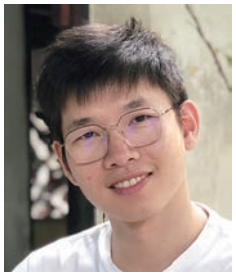
Yuan S., Shen F., Chua C.K., Zhou K., Polymeric composites for powder-based additive manufacturing: materials and applications, Progress in Polymer Science, 91 (2019) 141–168. DOI: 10.1016/j.progpolymsci.2018.11.001

Zhu W., Yan C., Shi Yunsong, Wen S., Han C., Cai C., Liu J., Shi Yusheng, Study on the selective laser sintering of a low-isotacticity polypropylene powder, Rapid Prototyping Journal, 22 (2016) 621–629. DOI: 10.1108/RPJ-02-2015-0014

Ziegelmeier S., Christou P., Wöllecke F., Tuck C., Goodridge R., Hague R., Krampe E., Wintermantel E., An experimental study into the effects of bulk and flow behaviour of laser sintering polymer powders on resulting part properties, Journal of Materials Processing Technology, 215 (2015) 239–250. DOI: 10.1016/j.jmatprotec.2014.07.029

Ziegelmeier S., Wollecke F., Tuck C., Goodridge R., Hague R., Characterizing the bulk & flow behaviour of ls polymer powders, Solid Freeform Fabrication Symposium, (2013) 354–367. DOI: 10.26153/tsw/15437

Authors' Short Biographies



Xi Guo

Xi Guo received his bachelor's degree in process equipment and control engineering from the Beijing University of Chemical Technology in 2014. He went to graduate school at the University of Florida and received his master's degree in mechanical engineering in 2016. Afterward, he worked for Johnson and Johnson as a materials engineer. In 2022, he completed his doctoral degree under the advisement of Dr. Brij M. Moudgil, Department of Materials Science and Engineering, University of Florida. His current research focus is on polymer selective laser sintering.



Brij M. Moudgil

Dr. Brij M. Moudgil is a Distinguished Professor of Materials Science and Engineering at the University of Florida. He received his B.E from the Indian Institute of Science, Bangalore, India, and his M.S. and Eng.Sc.D. degrees from Columbia University, New York. His current research interests are in surfactant and polymer adsorption, dispersion and aggregation of fine particles, adhesion, and removal of microbes from surfaces, synthesis of functionalized nanoparticles, antiscaling and surfactant mediated corrosion inhibitors, photocatalytic degradation of hazardous microbes, and nanotoxicity. He has published more than 400 technical papers and has been awarded over 25 patents. He is a member of the U.S National Academy of Engineering.

KONA Powder and Particle Journal

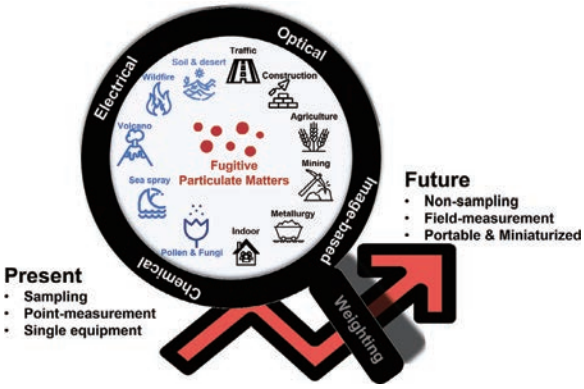
KONA Powder and Particle Journal No. 41 (2024) 42–57/https://doi.org/10.14356/kona.2024008 Review Paper

Measurement of Fugitive Particulate Matter Emission: Current State and Trends†

Tianyi Cai and Wu Zhou*

Institute of Particle and Two-phase Flow Measurement, Shanghai Key Laboratory of Multiphase Flow and Heat Transfer in Power Engineering, University of Shanghai for Science and Technology, China

Fugitive particulate matter (FPM) refers to a mixture of solid particles and liquid droplets that are released into the air without passing through confined flow equipment. These emissions of FPM can originate from natural processes and anthropogenic activities. FPM emissions are an important source of $PM_{2.5}$. Precisely measuring the size, concentration, and other properties of such particulate matter is crucial for effectively controlling emission sources and improving air quality. However, compared with particulate matter emission from stationary sources, it is difficult to monitor the FPM effectively owing to its dispersive and irregular emissions. Traditional measuring methods for FPM are based on sampling, which is a point monitoring approach and can be time-consuming. In recent years, several new techniques based on optical principles, image-based processes and low-cost sensors have been developed and applied for FPM measurement, with the advantages of spatial and time resolutions. The current state and future development of FPM measurements are reviewed in this paper.



Keywords: fugitive particulate matter, air quality, light scattering, image-based measurement, low-cost sensor, real-time

1. Introductions

Particulate matter (PM) has drawn massive attention owing to its great impact on human health and wealth (Amoushahi et al., 2022; Chen et al., 2019; Hassan et al., 2022), environment, and global climate (Hassan et al., 2020; Mutlu, 2020; Yang et al., 2021). Fugitive particulate matter (FPM), which refers to a mixture of solid particles or liquid droplets that are not discharged into the atmosphere through confined flow equipment (e.g., stack, chimney, pipe, vent, or duct), contributes a great portion to the total outdoor PM emission. Unlike particulate matter emitted from definable and stationary point sources, FPM is generally discharged from everywhere, such as anthropogenic land use, urban traffic, industrial activities, wind erosion, vegetation growth, and other natural processes. The emission intensity of FPM is different from site to site, and it often fluctuates temporally and spatially. Accordingly, it is challenging to develop the time- and space-resolved measurement for FPM emission but beneficial to understand its generation, track its migration, evaluate its effects and damage on human beings and the environment, and consequently figure out reliable mitigation measures to reduce FPM.

The objective of this review is to provide an overview of the current state and trends in measuring fugitive particulate matter. We will first introduce the main sources and key properties of FPM, analyze its effects and the current measurement standards on it. Then, we will provide a critical overview of the conventional methods and discuss the new trends for FPM measurement. Finally, we will propose a brief outlook on the future of FPM measurement.

1.1 Sources of FPMs

Typically, sources of FPMs can be separated into two categories: natural processes and anthropogenic activities. Common natural sources include soil & desert dust (Hassan et al., 2016; Vos et al., 2021), wildfire smoke (Sedlacek et al., 2018), volcanic ash (Sasaki et al., 2021), sea spray aerosol (February et al., 2021), and pollen & fungi grains (de Weger et al., 2020). The geomorphologic and geologic conditions mainly contribute to the compositions and distribution of the natural FPMs. For instance, arid regions are plagued by wind-blown soil, and coastal areas are familiar with sea salt-based or biogenic-enriched aerosols. Comparing with natural processes, human activities create more FPMs, mainly derived from traffic & transportation (Kuhns et al., 2010; Pervez et al., 2018; Wang H. et al., 2023), heavy constructions (Noh et al., 2018), agriculture &

† Received 25 July 2022; Accepted 19 October 2022
J-STAGE Advance published online 17 June 2023
* Corresponding author: Wu Zhou;
Add: 516 Jungong Rd., Shanghai 200093, China
E-mail: zhouwu@usst.edu.cn
TEL: +86-021-5527-7764 FAX: +86-021-5527-6854

Copyright © 2024 The Authors. Published by Hosokawa Powder Technology Foundation. This is an open access article under the CC BY license (https://creativecommons.org/licenses/by/4.0/).

Table 1 Fugitive particulate matter sources and activities.

Source	Activity
From natural processes	
soil & desert dust	windy weather / sandstorm
wildfire smoke	forest fire / prairie fire / hill fire
volcanic ash	volcanic eruption
sea spray aerosol	air bubbles bursting at the air-sea interface
pollen & fungi grains	pollination / spore dispersal
From anthropogenic activities	
traffic & transportation	roads / automotive exhaust / loading and offloading
heavy constructions	industrial & commercial building / road, bridge and other public constructions
agriculture & livestock operations	straw burning / grain harvest / storage and distribution / pasture mowing / animal feed
mining & quarrying	blasting / crushing / conveying and storage / heavy equipment operations
metal processing	sintering / blasting / casting / plating
residential combustion	cook / heating / cigarettes / incense

livestock operations (Gladding et al., 2020; Liu Y. et al., 2022), mining & quarries (Chang et al., 2010; Froyd et al., 2019), the metal industry (Zhang et al., 2022), and residential combustion (Nugraha et al., 2021). The main sources and activities that contribute to the FPM emissions are listed in **Table 1**.

1.2 Main properties of FPMs

1.2.1 Critical dimension and size distribution

Particle size has a great impact on the suspension, transport and distribution of FPM in the atmosphere. The residence time of submicron particles is on the order of 10^2–10^3 h, assuming the absence of precipitation. Particles with diameters between 1 μm and 10 μm can exist in the air for several days (Esmen and Corn, 1971). The typical residence time for 10 nm particles is about 15 minutes owing to their primarily coagulation with larger particles (Kim et al., 2021). The potential drift distance of particles is also related to particle size as well as the initial injection height of the particle and the intensity of atmospheric turbulence. Fugitive dust larger than about 100 μm is likely to settle out near the source under a typical wind speed of 16 km/h. Particles in the range of 30 μm to 100 μm are likely to undergo impeded settling without extra wind uplift. Smaller particles with much slower gravitational settling velocities are much easier to travel following atmospheric turbulence. Particles propelled higher from the source also travel further. For instance, volcanic ash can have an intercontinental diffusion (Ansmann et al., 2011).

Table 2 Description of common particle size bases.

Name	Description
TSP	Total Suspended Particulate, as measured by the standard high-volume air sampler, has a relatively coarse size range. It was the basis for the previous primary National Ambient Air Quality Standards of the U.S. (NAAQS) for PM and is still the basis of the secondary standard.
SP	Suspended Particulate, which is often used as a surrogate for TSP, is defined as PM with an aerodynamic diameter no greater than 30 μm.
IP	Inhalable Particulate, which is defined as PM with an aerodynamic diameter no greater than 15 μm, can get into the human body by breath.
PM_{10}	PM with an aerodynamic diameter no greater than 10 μm. It is the current primary NAAQS for particulate matter, representing the particle size range of the greatest regulatory interest. It is also known as Thoracic particles since it may reach the upper part of the airways and lungs.
$PM_{10–2.5}$	PM with diameters generally larger than 2.5 μm and smaller than or equal to 10 μm. It is also known as Coarse particles and is primarily generated from mechanical operations.
$PM_{2.5}$	PM with an aerodynamic diameter no greater than 2.5 μm. It is also known as alveolar particles, indicating that it can penetrate more deeply into the lungs and may reach the alveoli. It is called Fine Particulate (FP) as well.
UFP	Ultra Fine Particulate, which is defined as PM with an aerodynamic diameter no greater than 0.1 μm, can penetrate tissues and enter the bloodstream.

Particle size also has a major influence on the transport of particulate in the human respiratory system since the deposition efficiency of particles in the respiratory tract depends upon their size. Large particles can be hindered by the nasal hair (rhinothrix), medium particles can reach the upper respiratory tract, and small particles can deposit on alveoli or even invade the blood-circulatory system.

PM_{10} (particulate matter with a diameter of 10 μm or less in size) and $PM_{2.5}$ (particulate matter with a diameter of 2.5 μm or less in size) are currently common size bases for particulate matter. However, some other particle size bases, listed in **Table 2**, are used in research as well.

Different sources contribute to various size distributions of FPM. It is generally a narrow size distribution and small mean size for biomass-burning smoke, which is dominated by submicron particles (Wang F. et al., 2019). However, the size of smoke particles varies along different combustion phases (Ordou and Agranovski, 2019). Particles generated by mechanical force are normally widely distributed in size

(Zhang et al., 2022). Sea spray aerosols can range from a few tens of nanometers to tens of micrometers (February et al., 2021). Moreover, the size distribution of some FPMs may show bimodal or multimodal patterns (Chang et al., 2010; Chen et al., 2019).

1.2.2 Mass concentration, emission rate and emission factors

PM_{10} and $PM_{2.5}$ mass concentrations (γ_m) are the most commonly used criteria to evaluate air quality. The criteria can further be separated into 24-hour average values and annual mean values. Most countries and many international organizations have issued their standards or recommend thresholds for PM_{10} and $PM_{2.5}$ mass concentrations, as listed in **Table 3**. However, no current standards are set up for FPM.

Before determining the mass emission rate ($\dot{m}$), the volume flow rate of the flue ($\dot{V}$) should be measured. Then, the mass emission rate can be calculated by multiplying the mass concentration of the measured pollutant by its volume flow rate, as shown in **Eqn. (1)**:

$$\dot{m} = \gamma_m \dot{V} \tag{1}$$

The mass emission factor ($\dot{F}$) is a representative value indicating the emission intensity of a pollutant generated from a specific activity. It can be calculated following **Eqn. (2)**:

$$\dot{F} = \frac{\dot{m}}{a} \tag{2}$$

where a represents the activity rate.

The mass emission factor is usually expressed as the weight of the pollutant divided by the unit weight (g kg^{-1}), volume (g m^{-3}), distance (g km^{-1}), or duration of the activity that emits the pollutant (g h^{-1}).

1.2.3 Chemical components

Although the composition of FPM highly depends on its source, it can be roughly classified into five categories: minerals, metallic particles, soot, inorganic salts and biogenic substances. Wind-blown dust from dried land is mainly dominated by minerals, especially quartz. Volcanic ash contains more metallic minerals, such as Al_2O_3, Fe_2O_3 and MgO. Construction, mining and quarrying, which utilize stones and ores, contribute to the mineral dust emission. Metal processing generates both metal-rich and mineral particles. Hence, mineral dust is the major PM component at a global scale (Minguillón et al., 2013). Sea spray aerosols are little droplets containing inorganic salts (e.g. NaCl) or biogenic substances. Animal- and vegetation-related particles belong to biogenic ones. Soot is mainly generated from biomass or fuel combustion, including wildfire, residential combustion, and working engines. Non-exhausted PM from traffic, originating from tire wear, brake use and road dust resuspension, mainly consists of mineral particles. Since the reduction of exhaust emissions is performed worldwide, non-exhausted PM emissions will dominate traffic-related emissions in the near future.

Table 3 Criteria for PM_{10} and $PM_{2.5}$.

Criteria	PM_{10}		$PM_{2.5}$	
	Annual (μg m^{-3})	Daily (μg m^{-3})	Annual (μg m^{-3})	Daily (μg m^{-3})
WHO	15	45	5	15
USA	—	150	12	35
China	70	150	35	75
EU	40	50	25	—
Japan	—	—	15	35
Korea	50	100	15	35

1.2.4 Shape and morphology

Mineral dust typically has complex irregular shapes derived from its intrinsic crystal orientation and the force loading from crushing and abrasion (Kalashnikova and Sokolik, 2004; Nousiainen, 2009). Metallic particles, which are discharged from high-temperature processes like burning and metal cutting, are usually spherical (Sanderson et al., 2014). Soot is always amorphous and forms chain-like aggregates during its aging period (Adachi et al., 2010). Pollen and other biogenic particulates are often nonspherical (Amina et al., 2020), although it is commonly assumed that pollen grains are spherical (Theilade et al., 1993). Inorganic salts, including NaCl, sulfates and nitrates, are basically hydrophilic. Therefore, inorganic aerosols contain moisture at relatively high humidity levels, resulting in a spherical shape. Otherwise, the shape may be irregular (Ueda, 2021).

1.2.5 Optical properties

Complex refractive index (m) is the fundamental parameter to describe FPM, expressed in **Eqn. (3)**.

$$m = n - i\eta \tag{3}$$

where the real part, n is the refractive index indicating the degree of light dispersion through the media, and the imaginary part, η is the absorption coefficient, donating the light attenuation when it propagates through the media. If a particle can absorb light, its η is positive.

Among all the common FPMs, black carbon (BC) is the most light-absorbing component with an imaginary part ranging from 0.4 to 0.8 (Kelesidis and Pratsinis, 2019). Organic carbon (OC), also known as brown carbon (BrC), absorbs light as well (Zhang et al., 2017). Mineral and metallic particles both slightly absorb light (Ebert et al., 2002; Kandler et al., 2007).

The extinction coefficient (b_{ext}) of FPM includes the scattering coefficient and absorption coefficient (as detailed in **Section 2.3**), and it can be converted to visibility (*Vis*) by adapting the Koschmieder equation (Cao et al., 2012; ten Brink et al., 2018; Xiao et al., 2014):

$$Vis = \frac{k}{b_{ext}} \tag{4}$$

where k is a constant assumed to be 3.912.

Single scatter albedo (SSA) is defined as the ratio of particle-scattering efficiency to the total extinction efficiency. It is a key parameter in radiative transport models for estimating aerosol direct radiative forcing (Jeong et al., 2020).

1.3 Effects and damage from FPMs

1.3.1 Human health

Short-term and long-term exposure to particles increases the risk of developing cardiovascular and respiratory diseases, as well as lung cancer (Brook et al., 2010). Outdoor $PM_{2.5}$ is the fifth-largest risk factor for premature mortality worldwide (Feigin et al., 2016). Infants, the elderly, and outdoor workers are the most likely to be affected. The health effects of FPMs depend considerably on their size. Coarse PM reaches the upper part of the airways and lungs, while fine PM can penetrate more deeply into the lungs and may reach the alveoli. UFP can even directly translocate into the bloodstream and cells (Martinelli et al., 2013). Chemical composition issues in the health effects as well. Exposure to metal or metal-containing dust increases the risk of cardiovascular dysfunction (Ain and Qamar., 2021). Black carbon, as a universal carrier of various toxic constituents, has a strong association with premature mortality (Wang Y. et al., 2021). Inhalation of sand and concrete dust can lead to silicosis, an irreparable form of lung damage (Hoy and Chambers, 2020). Additionally, inhalation of pollen and other biogenic aerosols can induce allergy and respiratory problems (D'Amato et al., 2020).

1.3.2 Wealth and safely

FPMs impair visibility. Due to the prominent ability of light extinction, fine PM contributes more than gas pollutants to visibility degradation (Yu et al., 2016). On roads, visibility reduction increases the risk of accidents and escalates the costs associated with vehicle cleaning and equipment maintenance. FPM emissions also result in the cancellations of flights and avoidance of outdoor activities (Guo et al., 2021). For example, sudden volcanic ash discharges directly affect aircraft engines, causing them to stall and posing a threat to human and cargo safety (Prata, 2008). Heavy wind erosion of soils and dust storms diminish land values. Excessive emissions can also damage vegetation and reduce crop production. Burning smoke and flammable fine powders can cause fire or blast damage if ignited.

1.3.3 Environment and global climate

Various FPMs contribute differently to climate forcing owing to their distinct optical properties. For instance, black carbon aerosols strongly absorb solar radiation, leading to a warming effect (Bond et al., 2013). In contrast, mineral dust cools the atmosphere due to its ability to increase radiation reflection into space (Choobari et al., 2014). Besides, FPMs also have an indirect effect on the climate by modifying the properties of clouds given that particles act as cloud condensation nuclei (Williamson et al., 2019). For instance, soot is an efficient ice-nucleating particle that influences cirrus formation at the tropopause. Although the relatively short residence time and highly variable spatial distribution in the atmosphere further complicate the estimation of net effects of FPMs on the global climate, scientists are trying to include FPM emissions into global atmospheric models (Philip et al., 2017).

1.4 Current standards on FPM emissions

The most widely used method for PM measurements is based on sampling, and mass concentration, emission rate and emission factors are the highly concerned parameters. The International Organization for Standardization (ISO) has released the measurement standards for PM in the atmosphere and from the stationary source (ISO 11771-2010 / ISO 10155-1995 / ISO 9096-2017), and many countries have all set domestic standards. Since there are no specific standards for FPM, the above-mentioned ones are used for FPM measurements. In addition, some monitoring methods are recommended for FPM emissions by some institutions. The US Environmental Protection Agency (EPA) Method 22 "Visual Determination of Fugitive Emissions" was proposed. Through this method, viewers position themselves to have an unobstructed view of potential emissions. If visible emissions are observed, the viewer measures the duration of time that the visible emissions were present during the observation period. Method 22 is often used in the regulation of fugitive emissions from toxic materials that escape during material transfer (i.e. asbestos removal), escape from buildings housing material processing or handling equipment (i.e. asbestos presence in building demolitions), and/or are not captured by an exhaust hood or are emitted directly from process equipment. Method 9, known as the "Visible Determination of Opacity of Emissions from Stationary Sources," involves the recording of readings as a percentage of opacity in terms of black and white particulate plumes or dense clouds of matter. While Method 9 is used extensively to sight and control visible emissions from stationary and non-stationary industrial processes, it is also used to measure visible emissions from unconfined places such as roads and bulk material storage areas.

2. Conventional methods for FPM measurement

As mentioned in **Section 1.4**, sampling methods universally accepted for PM measurements are equally applicable to FPM measurements. However, due to the temporary and unsteady-in-position of FPM emissions, it is essential to implement well-performed sampling strategies and consider the use of multiple measurements to gather comprehensive information about FPM emissions.

2.1 Sampling strategies and conditions

2.1.1 Upwind-downwind method

Upwind-downwind sampling requires a high density of vertical and/or horizontal measurements to determine the PM emission rate. Measurements of FPM emission rates are usually performed using this method, which has been described in detail in the previous study (Cowherd et al., 1974). For instance, particulate emission rates from gravel processing sites and traffic-busy roads were calculated on the basis of a mass balance approach using the upwind/downwind technique, respectively (Chang et al., 2010; Etyemezian et al., 2004).

2.1.2 Wind tunnel method

The wind tunnel method is suitable for measuring fugitive dust emissions from dried land. To conduct this method, a wind tunnel with a working section of several tens of meters in length, several meters in width, and height is required. A blower works at the tunnel entrance and PM monitors sample the wind-blown dust along the tunnel to evaluate the dust emission properties. This method has been successfully applied to measure fugitive emissions from soil surfaces (Fitz et al., 2021; Gao et al., 2020; Roney and White, 2006).

2.1.3 Isokinetic sampling method

The isokinetic sampling method, which means the sampling velocity is the same as the FPM/airflow, is employed to prevent incorrect lower or higher particle concentrations owing to anisokinetic effects from particle bypassing or swarming, respectively.

2.1.4 Size-selective inlet and cascade impactor

A size-selective inlet removes larger particulates and allows the particulate smaller than the designed size to pass. By applying a size-selective inlet, PM_{10}, $PM_{2.5}$ or UFP can be separated from the pollutant flow (Su et al., 2020). Cascade impactors operate on the principle of curvilinear motion of particles in the aerosol stream, and as a result, particles of various sizes are divided and collected on different plates. In this way, the size distribution of the sampling FPM is obtained (Manojkumar and Srimuruganandam, 2022).

2.2 Filter-based techniques

2.2.1Direct gravimetric analysis

In direct gravimetric analysis, a filter is weighted by an electronic microbalance before and after sampling under constant temperature and humidity conditions. The mass change is used to calculate the degree of PM contamination (Lei et al., 2020). The collected filter can be used for offline chemical component analysis (Guo et al., 2021).

However, despite providing accurate and reliable data, the direct gravimetric method is time-consuming and inapplicable to FPM measurement.

2.2.2 Tapered element oscillating microbalances (TEOM)

Unlike the direct gravimetric method, the TEOM method uses a hollow glass tube as a microbalance for real-time mass loading measurement. Particles continuously deposit on the glass tube, increasing its inertia and consequently tuning its oscillation frequency. This frequency change is converted to an electrical signal, which is amplified for detection.

The TEOM method offers the advantage of high time resolution (2 seconds) (Sullivan et al., 2017), but it should be noted that this method is sensitive to temperature and moisture. Therefore, the incoming sample flow is heated and kept constant. Depending on these measuring conditions, it is difficult to precisely measure the semi-volatile particles. A filter dynamic measurement system (FDMS) is specially designed to overcome this drawback. TEOM instruments equipped with FDMS are operated alternately between a measuring cycle and a reference cycle. The mass loss of the glass tube in the reference cycle is used to correct the output in the measuring cycle, thereby increasing the accuracy of the TEOM results (Grover, 2005).

2.2.3 Beta attenuation monitoring (BAM)

The main principle of BAM is based on Lambert–Beer's law. When airflow passes through the filter tape, particles are left on it. The beta radiation is attenuated by the attached particles before reaching the detector on the other side of the filter tape. The attenuation is an exponential function of the deposit amount and it is roughly not affected by particle composition or other properties. Hence, the mass concentration of particles can be examined. However, the moisture in the air may cause an error, so a heater is necessarily equipped at the sample inlet. Typically, the BAM method can be used for continuous online measurement, providing the mass concentration data hourly (Mueller et al., 2013). Moreover, offline chemical analysis can carry out on the used filter tape (Raja et al., 2017).

2.2.4 Offline characterization

Filter-based offline characterization has low time resolutions and fails to reflect the dynamic nature of the fugitive

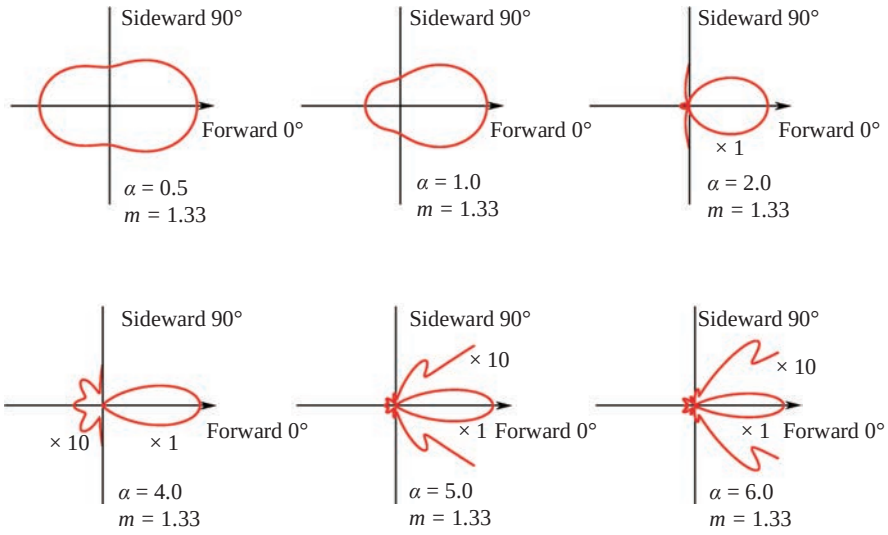


Fig. 1 Diagram of scattered light intensities of different size. $\alpha = \pi D/\lambda$, is a dimensionless particle size, where D is the mean particle diameter, m is particle refractive index.

pollution sources, nevertheless, it gives more information about the particulate.

Electron microscopy (EM) techniques are valuable to detect and quantify the shape and size of particles (Gelencsér et al., 2011; Omidvarborna et al., 2018).

Ion chromatography (IC) is performed to examine the concentrations of the water-soluble ions in the particulate (Guo et al., 2021; Hu et al., 2019; Tian et al., 2020; Xiao et al., 2014; Zou et al., 2018).

Elements and trace metals, including Ca, Sc, Ti, V, Fe, Co, Zn, and Mo, were analyzed by X-ray fluorescence (XRF) spectrometry (Gao et al., 2015; Tian et al., 2020; Xiao et al., 2014) or Inductively Coupled Plasma-Mass Spectrometry (ICP-MS) (Hu et al., 2019; Philip et al., 2017).

The concentrations of OC and element carbon (EC) are analyzed by a thermal/optical carbon analyzer (Guo et al., 2021; Hu et al., 2019; Lei et al., 2020; Tian et al., 2020; Xiao et al., 2014; Zou et al., 2018).

In general, filter-based techniques are the most technically mature. However, the sampling conditions should be tightly controlled to reduce the effect of sampling conditions on accuracy (Le and Tsai, 2021).

2.3 Optical-based techniques

2.3.1 Basics of light scattering, absorption and extinction

The scattering pattern of a particle refers to its scattering efficiency as a function of the angle. It depends on the particle size, shape, refractive index, and the wavelength (λ) of the excitation light. The distribution of the scattering light as a function of a dimensionless particle size parameter, α, assuming the refractive index equals 1.33, is demonstrated in **Fig. 1**.

It is shown that the smaller the particle is (compared to the excitation wavelength), the more spherical the scattering pattern is. For large particles (e.g. $\alpha \geq 4.0$ in **Fig. 1**), most of the scattered intensity deviates with smaller angles, and side lobes appear as the diameter increases. Besides, the polarization of scattering light is also influenced by the particle properties, which are not shown in **Fig. 1**. Therefore, the particle size, shape, component, and concentration can be predicted using the information from the scattering signature theoretically. Mie theory (Hergert and Wriedt, 2012) is the most common description of light scattering. Despite its simple hypothesis that a uniform sphere is illuminated by a monochromatic plane wave, this theory has proved to be quite robust and applicable in particle size and concentration prediction.

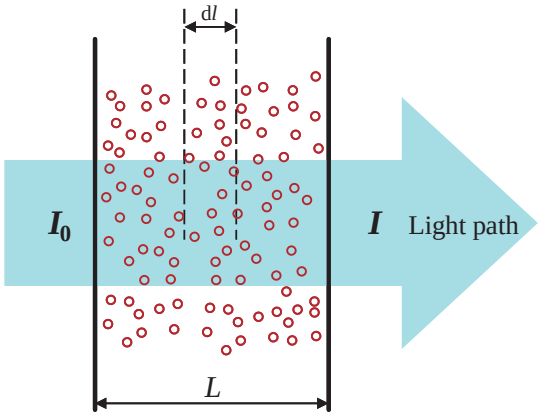


Fig. 2 Diagram of light extinction.

When light passes through a cloud of particles, its intensity (I_0) is attenuated because of the scattering and absorption effects of the particles, as seen in **Fig. 2**.

Assuming the particles disperse uniformly in the illuminated area, and then the transmitted light intensity (I) can be described with **Eqn. (5)**.

$$I = I_0 \, e^{-b_{ext}L} \quad (5)$$

where L is the path length of the light beam through the particles.

The extinction coefficient (b_{ext}) can be further divided into two parts, the scattering coefficient (b_{sca}) and the absorption coefficient (b_{abs}).

b_{ext}, as a function of the particle number, diameter D, wavelength of the incident light λ, and the complex refractive index m, can be computed by Mie theory.

2.3.2 Nephelometer

A nephelometer is the most commonly used optical equipment for PM measurement. The pollutant air is sampled into the measuring chamber of the nephelometer, illuminated by a light beam. The scattering light is detected by a light detector set to one side of the light source. Despite the intensity is also related to the refractive index, shape, and size distribution of the measured particles, nephelometers are calibrated to a known particulate, then use an environmental-related factor to compensate for the error accordingly. After calibrating to a known particulate, the PM mass concentration can be evaluated from the scattered light intensity.

The DustTrak™ (TSI Co., Ltd.) is a classical nephelometer-type tool to determine the mass concentration in real time. The DustTrak aerosol monitors (model 8520, TSI Co., Ltd.) were run in the kitchens and living rooms of the selected sites to measure fine particulate matter (Sidra et al., 2015).

Portable In Situ Wind Erosion Laboratory (PI-SWERL) is a portable wind tunnel surrogate, equipped with DustTrak (Etyemezian et al., 2007). It is contained in an open-bottomed, cylindrical chamber operated by a direct-current motor and set parallel to the soil surface. By adjusting the rotation speed, the desired high winds with known wind shear are created and the soil and dust particles are lifted. With the application of PI-SWERL, the behavior of FPM emissions from unpaved roads, farmlands, and deserts were studied without the deployment of flux tower systems (Kuhns et al., 2010; Sweeney et al., 2021; Vos et al., 2021).

Thanks to the calibration method, the measurement accuracy depends on the assumption that the properties of FPM are constant, except for the concentration. However, FPM emissions are complicated and diverse. Single- angle scattering measurement can result in unreliable results. To solve this problem, SHARP-5030i (Thermo Scientific Co., Ltd.) measures $PM_{2.5}$ mass concentrations based on the principles of particle light scattering (nephelometer) and beta attenuation (Su et al., 2020). The beta attenuation data can be used to calibrate the nephelometer.

2.3.3 Particulate counter

Optical particle counter (OPC) and condensed particle counter (CPC) are both used to measure particle number concentration and size distribution. OPC is based on sideward light scattering. The aerosols pass through the light-illuminated measuring spot particle by particle and the induced light scattering signal is detected by the light detector simultaneously. The particle size is a function of the scattering light intensity and the particle number is counted during the measuring period. Consequently, the particle number size concentration is achieved. CPC introduces condensation equipment before OPC, inducing the particle size growth by absorbing liquid, and therefore it can measure smaller aerosols with diameters of a few nanometers.

2.4 Electrical methods

2.4.1 Electrical low-pressure impactor (ELPI)

The ELPI (Dekati Ltd.) operates at 30 LPM and ambient particles are charged when the air sample passes through a unipolar charger. The charged particles are size-classified by aerodynamic diameter following the same principle as the cascade impactor mentioned in **Section 2.1**. The electrical currents arising from particle deposition are measured simultaneously from 12 stages with a multichannel electrometer in real time. Therefore, the ELPI is capable of measuring the particle number concentration over a wide size range (7 nm–10 μm) with 1–2 s resolution (Holmén et al., 2007).

2.4.2 Differential mobility analyzer (DMA)

The intake particles are electrically charged first and separated by deflection since the particles with different sizes have different electrical mobility. If it is combined with the CPC technique, known as scanning mobility particle sizer (SMPS), the lower limit of detection (several nanometers) is reached. Fast mobility particle sizer (FMPS) is another derived technique from DMA. It combines DMA with an electrometer to improve the time resolution to one second.

2.5 Real-time chemical characterization

The mass spectrometry techniques are quickly developed for the real-time chemical characterizations of ambient particulates, including aerosol mass spectrometer (AMS), high-resolution time-of-flight AMS, aerosol chemical speciation monitor, single-particle mass spectrometers, and aerosol time-of-flight mass spectrometer. The comparison between these techniques is well illustrated in Ref. (Wang F. et al., 2021).

However, continuous measurements at high time resolution remain impractical, and like most offline methods, volatile or reactive aerosol species can change before analysis.

3. New trends for FPM measurement

Conventional methods for FPM measurement all belong to point measurement techniques since they require a sampling process, which means that the space resolutions of these techniques are poor. Rigorous sampling strategies and multi-measuring equipment should be arranged to reveal the spatial distribution and movement of FPM. However, it is impractical to perform this arrangement considering the equipment is cumbersome and expensive. To achieve the high space- and time-resolved investigation of FPM, some cheap, portable, and remote sensing techniques are being developed.

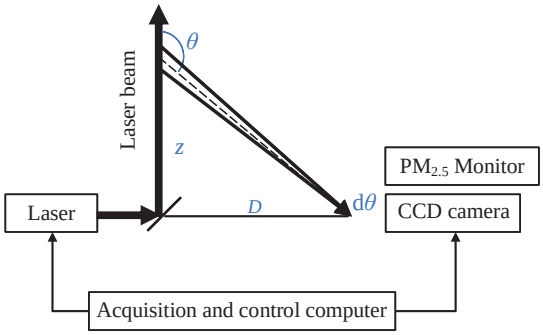


Fig. 3 Schematic of CLidar system. Reproduced from Ref. (Tao et al., 2016) with permission from Copernicus Gesellschaft mbH.

3.1 Open-path optical techniques

3.1.1 Light detection and ranging (Lidar)

Lidar is an active light scattering detection method, based on the analysis of the radiation backscattered from a target. This technique is often used in climate research to measure altitude-dependent aerosol extinction. For instance, the distribution and movement of volcanic ash were observed with the ground-based lidar systems of the European Aerosol Research Lidar Network (EARLINET) (Ansmann et al., 2011). The strong and long-lasting stratospheric aerosol perturbation was also monitored all over Europe with EARLINET (Baars et al., 2019).

Lidar remote sensing has been introduced to measure the FPM near the ground. A scanning lidar system was applied to measure FPM emissions from different industrial sources simultaneously, determining the potential of lidar for tracking and differentiating plumes from various sites (Pal et al., 1998). The reliable detection of early fire was accomplished using lidars operating at 355 nm, 532 nm, 1064 nm, and 1540 nm, and the maximum detection distance relied on the wavelength (Lavrov et al., 2003). A three-wavelength scanning lidar system was built to simultaneously monitor FPM emissions from agricultural operations and road traffic. The mass concentration and size distribution were inversed assuming a bimodal lognormal size distribution and calibrated by standard facilities, including optical particle counter, PM_{10} and $PM_{2.5}$ samplers, multistage impactors, and an AMS (Zavyalov et al., 2006).

Traditional lidars are monostatic, requiring expensive electronics to measure the time of flight of the backscattered light and its corresponding distance. The overlap effects between the backscattered signal and receiver field of view near ground levels may impact the detection reliability for the nearby pollution. To avoid these disadvantages, a bistatic lidar, named CLidar, was established. In the CLidar, a laser source and a camera fitted with a wide-angle lens were separated several hundred meters away from each other. The laser transmits light vertically into the atmosphere, and the scattering light was imaged by the camera, as shown in **Fig. 3**. Owing to this setup, the altitude resolution is excellent near ground level, providing an efficient detector of pollution at low altitudes. The aerosol extinction coefficient along the altitude was inverted from the intensities of pixels. A grilling activity was successfully monitored since the aerosol extinction increased from 0.03 km^{-1} with no grilling to 0.085 km^{-1} (Kabir A. et al., 2018).

Moreover, the CCD-based scattering Lidar system (including sideward scattering and backward scattering) is verified to be useful to measure particle mass concentration and size distribution of cooking fumes and open smoldering as well (Wang W. et al., 2019; Zhou W. et al., 2020).

3.1.2 Hybrid optical remote sensing (h-ORS)

The h-ORS was mainly developed by the University of Illinois to measure FPM emissions from military-related activities, including back blasts from firing artillery, open burning and detonation, tracked and wheeled vehicle operation, and helicopter landing (Du et al., 2011; Varma et al., 2008; Yuen et al., 2013, 2015, 2017). It combines micro pulse Lidar (MPL), open-path Fourier Transform Infrared spectroscopy/Laser transmissometer (OP-FTIR/OP-LT), and/or filter-based sampling techniques (DustTrak or TEOM). The measurement system is schematically demonstrated in **Fig. 4**.

2-D PM mass concentration profile and mass emission factors can be calculated using the h-ORS system. First, the 2-D MPL data obtained using scanning mode were converted to the 2-D light extinction profiles with the LIDAR inversion algorithm. Second, the 2-D PM mass concentration profiles were determined from the 2-D light extinction profiles by multiplying a factor. This factor refers to the mass concentration at the reference point (as the blue point shown in **Fig. 4**) divided by the local light extinction obtained in the first step. The mass concentration at the reference point can be derived from the light extinction calculation performed by OP-FTIR/OP-LT or the result from DustTrak and TEOM, respectively. Last, the mass emission factors can be easily calculated if the wind speed and direction are recorded.

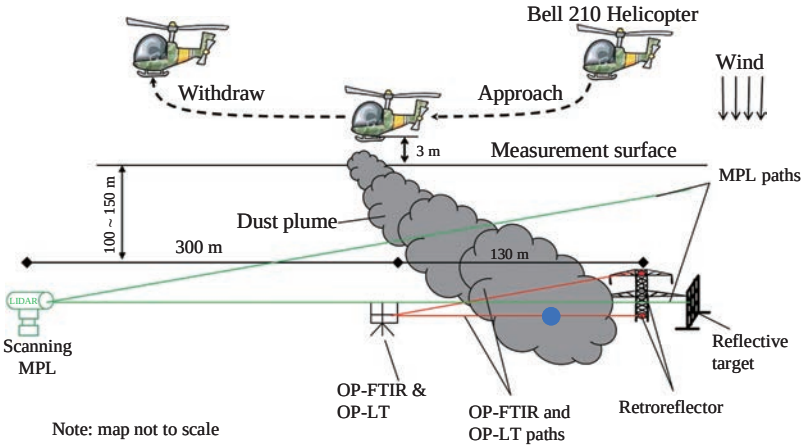


Fig. 4 Schematic of h-ORS system. The blue point represents the site for DustTraks or TEOM equipment. Reproduced from Ref. (Du et al., 2011) with permission from the American Chemical Society.

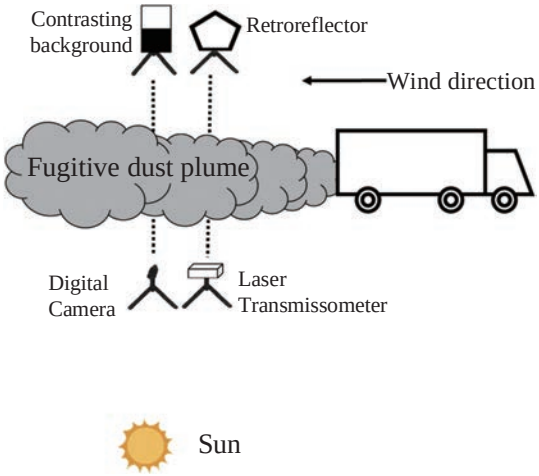


Fig. 5 Schematic of the camera-based light extinction system. Reproduced from Ref. (Du et al., 2013) with permission from Elsevier Ltd.

3.2 Image-based optical techniques

3.2.1 Camera-based detection

Biomass burning, especially wildfire, should be monitored and detected as soon as possible to avoid the expansion of combustion. As mentioned in **Section 3.1**, Lidar is useful to detect fire smoke in its early stage. It is demonstrated here that video monitoring is also effective for this smoke early sensing (Jakovčević et al., 2013). The camera-recorded video was segregated into a photographic sequence, then region segmentation and categorization, motion detection, and chromatic and shape analysis were performed on these photos to finally discriminate fire smoke from fog, clouds, and other stuff.

Besides, the road dust from busy traffic can be monitored by measuring the opacity of fugitive plume emissions. A camera-based light extinction method was described for quantifying the opacities of FPM (Du et al., 2013). This method was validated by performing simultaneous measurements using a co-located laser transmissometer, as shown in **Fig. 5**. Moreover, the values of the R, G, and B channels, and the grey value were all consistent with the opacities from the OP-LT measurement.

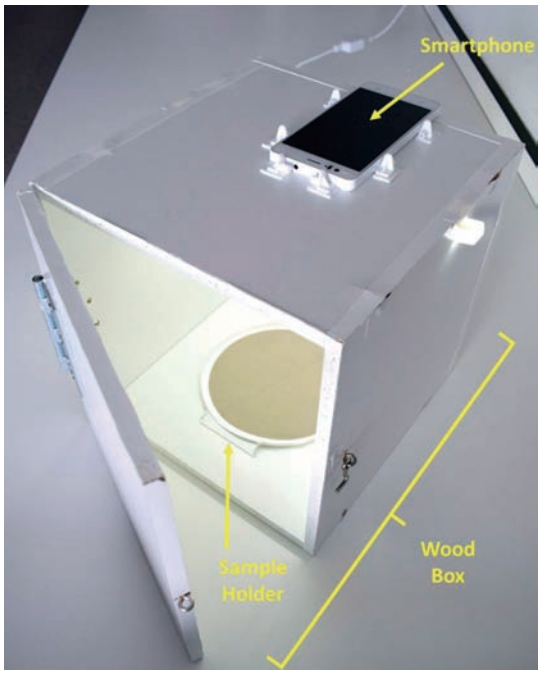


Fig. 6 The prototype of picture-based filter system. Reproduced from Ref. (Carretero-Pena et al., 2019) with permission from MDPI.

3.2.2 Photographic filter analysis

The direct gravimetric analysis of the filter is time-consuming and strict to the operating procedure. Picture-based filter analysis takes pictures of the filter before and after use and evaluates the mass of particles deposited on the filter depending on the difference of pictures accordingly. A smartphone is both easy to be attained and easy to operate and therefore it is a good option to perform the analysis. A prototype of such a system was proposed recently (Carretero-Pena et al., 2019), as displayed in **Fig. 6**. A testing box was designed to provide stable lighting

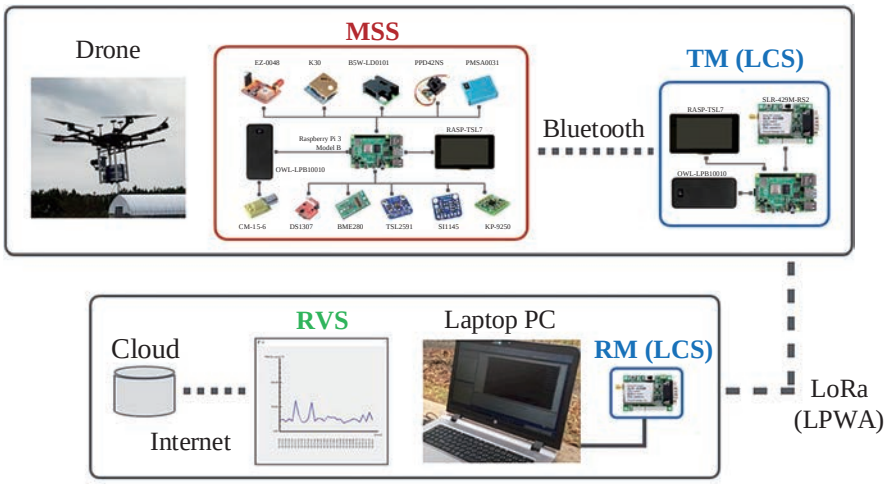


Fig. 7 Schematic of the integrated system for in-situ measurements. Reproduced from Ref. (Madokoro et al., 2021) with permission from MDPI.

conditions, in which a stable LED strip was equipped. The saturation parameter of the picture was proved to be able to estimate the mass concentration of dust deposited on the filter.

3.3 Low-cost, compact, mobile and connectable sensor system

Low-cost PM measurement techniques most commonly rely on the light-scattering-based (nephelometer or OPC) principle, which is available for below 50 USD (Kuula et al., 2019; Yi et al., 2018). PMS7003 (Plantower Co., Ltd.) and SDS011 (Nova Fitness Co., Ltd.) sensors, based on OPC and nephelometry, respectively, were confirmed precision and were linearly correlated with TEOM data (Kaźmierczak et al., 2018). However, these two sensors both had a bias concerning $PM_{2.5}$ concentrations obtained from TEOM, indicating the importance of calibration of low-cost devices before use. PMS7003 was capable of measuring PM_{10} and $PM_{2.5}$ with a measurement range from 0 to 500 μg m^{-3}, signal response of less than 1 s, and resolution of 1–2.5 μm and 2.5–10 μm, respectively (Camarillo-Escobedo et al., 2022). SDS011 was successfully applied in residential biomass combustion monitoring (Nugraha et al., 2021). The data obtained from SDS011 sensors were reliable, but it may cause errors since high RH (over 80 %) negatively affected the sensor response (Liu et al., 2019). Usually, there is a trade-off between the accuracy of measurement and the cost of the sensor, which are both vital to the wide and proper use of low-cost sensors (Castell et al., 2017).

3.3.1 Drone-based measurement and sensors networks

Mobile measurements used to be carried out on airplanes (Froyd et al., 2019; Hobbs et al., 2003; Taubman, 2004; Zhang et al., 2017). The drone is small and exquisite. It can quickly fly to the place where FPM emission happens, facilitating the monitoring of FPM. The fugitive dust at the quarry sites was measured using a Sniffer4D module-equipped drone, providing measurements at 1 s intervals through a light scattering method (Kim et al., 2021). The volcanic ash was detected remotely by drone-based sensors (Sasaki et al., 2021). Small, lightweight, and cheap sensors were integrated for multiple measurements of atmospheric phenomena and related environmental information. For in situ local area measurements, a long-range wireless communication module with real-time monitoring and visualizing software applications was integrated as established in **Fig. 7** (Madokoro et al., 2021).

3.4 Real-time laser-induced breakdown spectroscopy

Laser-induced breakdown spectroscopy (LIBS) has been proven to perform elemental microanalysis of PM on filters with high sensitivity (ppm-level) (Marina-Montes et al., 2021). The technique indicates the possibility of automated chemical analysis collaborating with conventional filter-based measurements in quasi-real time.

Moreover, online LIBS in open space detection has also been demonstrated in several field measurements, showing great potential for rapid monitoring and control of particulate emissions generated in public areas, such as toxic dust in a hostile environment of the steel industry (Girón et al., 2018), cigarette smoke in houses (Zhang et al., 2020), and incense smoke near around temples (Qu et al., 2021).

LIBS is a useful and promising tool to determine the elemental composition of FPM in situ. However, this technique is not sufficient for obtaining information on specific particulate sizes because of the breakdown of all particulates.

4. Summary and outlook

FPM has contributed a great portion to the total outdoor PM emissions, and it will account for more than PM

emissions from stationary point sources, given that serious regulations and effective control measures are applied to the latter. However, the FPM emissions are irregular, highly dispersive, and intensity-fluctuated. The precise measurement of FPM is challenging but worthy, yet there is currently no uniform regulation or standard measurement procedure in place. In this work, we first introduced the sources of FPMs both natural and artificial, including soil & desert dust, wildfire smoke, volcanic ash, sea spray aerosols, pollen and fungi grains, traffic and transportation activities, heavy constructions, agriculture and livestock operations, mining and quarrying, metal processing, and residential combustion. Although the sources are diverse, the FPM can be sorted into five main categories: minerals, metallic particles, soot, inorganic salts, and biogenic substances. Each category possesses distinctive properties, resulting in varying effects on human health and the environment. Next, we provided an overview of conventional PM measurement methods. Sampling is necessary for these methods, with the upwind–downwind technique widely adopted. Filter-based methods are accurate, but the time resolution is generally poor (except for TEOM). Additionally, the filter can be used for offline chemical analysis. We also discussed two conventional optical methods, namely the nephelometer and particle counter, and demonstrated the basics of light scattering. Furthermore, we briefly explained electrical methods and real-time chemical characterization techniques. Conventional PM measurement belongs to point measurement which can provide scarce information about the spatial distribution of FPM. In response, open-path and image-based technologies have been developed. Lidar technology, for example, is an easy-performed method to detect FPM. The light extinction coefficient can be derived from the Lidar data to evaluate the degree of pollution. A camera-based bistatic Lidar has been proposed to avoid expensive time-of-flight electronics in monostatic Lidar. Additionally, several hybrid remote sensing strategies combing Lidar with sampling gravimetric analysis have been illustrated. Image-based optical methods have also been used to detect FPM, especially fire smoke. Low-cost sensors show great promise for widespread FPM monitoring because they are light and small, and can be equipped on drones for dynamic measurement. Moreover, real-time LIBS holds great potential for in-situ chemical analysis.

By far, the mass concentration is the most concerned parameter in FPM measurement. Other factors such as size distribution, shape, and complex refractive index are less mentioned. Light-scattering-based methods have the potential to reveal more information about particles by performing multi-angle, multi-wavelength, and polarization/depolarization measurements. However, these measurement systems are much more complicated, and may not be feasible for field measurements. The image-based optical methods are promising for particle measurement since the spatial and temporal light signals (often scattering light) can be recorded simultaneously. Besides, machine learning/deep learning algorithms can be applied to decouple the relationship between light patterns and particle clouds. It is feasible to build an FPM monitoring network using low-cost, compact, mobile, and connectable sensors. Individuals equipped with portable sensors can contribute to the data collection process, and drone-based sensor systems can effectively monitor dangerous or hard-to-reached places, enhancing the overall effectiveness of the monitoring network.

Acknowledgments

Financial support from the National Key Research and Development Project of China (2017YFC0211500) and the Shanghai Sailing Program (22YF1429600) is gratefully acknowledged.

Nomenclature

AMS	Aerosol mass spectrometer
BAM	Beta attenuation monitoring
BC	Black carbon
BrC	Brown carbon
CPC	Condensed particle counter
DMA	Differential mobility analyzer
EARLINET	European Aerosol Research Lidar Network
EC	Element carbon
ELPI	Electrical low-pressure impactor
EM	Electron microscopy
EPA	U.S. Environmental Protection Agency
FDMS	Filter dynamic measurement system
FMPS	Fast mobility particle sizer
FP	Fine particulate
FPM	Fugitive particulate matter
h-ORS	Hybrid optical remote sensing
IC	Ion chromatography
ICP-MS	Inductively coupled plasma-mass spectrometry
IP	Inhalable particulate
ISO	International Organization for Standardization
LIBS	Laser-induced breakdown spectroscopy
Lidar	Light detection and ranging
LPM	Liter per minute
MPL	Micro pulse Lidar
NAAQS	National Ambient Air Quality Standards of the U.S.
OC	Organic carbon
OPC	Optical particle counter
OP-FTIR	Open-path Fourier transform infrared spectroscopy

OP-LT	Open-path laser transmissometer
PI-SWERL	Portable in-situ wind erosion laboratory
PM	Particulate matter
$PM_{2.5}$	Particulate matter with a diameter of 2.5 μm or less in size
$PM_{10–2.5}$	PM with diameters generally larger than 2.5 μm and smaller than or equal to 10 μm
PM_{10}	Particulate matter with a diameter of 10 μm or less in size
SMPS	Scanning mobility particle sizer
SP	Suspended particulate
SSA	Single scatter albedo
TEOM	Tapered element oscillating microbalances
TSP	Total suspended particulate
UFP	Ultra fine particulate
WHO	World Health Organization
XRF	X-ray fluorescence
a	polluting activity rates
b_{ext}	extinction coefficient (Mm^{-1})
b_{sca}	scattering coefficient (Mm^{-1})
b_{abs}	absorption coefficient (Mm^{-1})
D	particle diameter (μm)
$\dot{F}$	mass emission factor
I	transmitted light intensity (J)
I_0	initial light intensity (J)
k	Koschmieder constant (-)
L	path length of the light (m)
$\dot{m}$	mass emission rate (μg h^{-1})
m	complex refractive index (-)
n	refractive index (-)
$\dot{V}$	volume flow rate of flue (m^3 h^{-1})
γ_m	mass concentration (μg m^{-3})
Vis	visibility (km)
α	dimensionless particle size parameter (-)
λ	wavelength of extinction light (nm)
η	absorption coefficient (-)

References

Adachi K., Chung S.H., Buseck P.R., Shapes of soot aerosol particles and implications for their effects on climate, Journal of Geophysical Research, 115 (2010) D15206. DOI: 10.1029/2009jd012868

Ain N.U., Qamar S.U.R., Particulate matter-induced cardiovascular dysfunction: a mechanistic insight, Cardiovascular Toxicology, 21 (2021) 505–516. DOI: 10.1007/s12012-021-09652-3

Amina H., Ahmad M., Bhatti G.R., Zafar M., Sultana S., Butt M.A., Bahadur S., Haq I.-U., Ghufran M.A., Lubna, Ahmad S., Ashfaq S., Microscopic investigation of pollen morphology of Brassicaceae from Central Punjab-Pakistan, Microscopy Research and Technique, 83 (2020) 446–454. DOI: 10.1002/jemt.23432

Amoushahi S., Bayat R., Sanaei A., Szyszkowicz M., Faridi S., Hassanvand M.S., Health and economic impacts of ambient fine particulate matter in Isfahan, Iran, Urban Climate, 41 (2022) 101048. DOI: 10.1016/j.uclim.2021.101048

Ansmann A., Tesche M., Seifert P., Groß S., Freudenthaler V., Apituley A., Wilson K.M., Serikov I., Linné H., Heinold B., Hiebsch A., Schnell F., Schmidt J., Mattis I., Wandinger U., et al., Ash and fine-mode particle mass profiles from EARLINET-AERONET observations over central Europe after the eruptions of the Eyjafjallajökull volcano in 2010, Journal of Geophysical Research, 116 (2011) D00U02. DOI: 10.1029/2010jd015567

Baars H., Ansmann A., Ohneiser K., Haarig M., Engelmann R., Althausen D., Hanssen I., Gausa M., Pietruczuk A., Szkop A., Stachlewska I.S., Wang D., Reichardt J., Skupin A., Mattis I., et al., The unprecedented 2017–2018 stratospheric smoke event: decay phase and aerosol properties observed with the EARLINET, Atmospheric Chemistry and Physics, 19 (2019) 15183–15198. DOI: 10.5194/acp-19-15183-2019

Bond T.C., Doherty S.J., Fahey D.W., Forster P.M., Berntsen T., DeAngelo B.J., Flanner M.G., Ghan S., Kärcher B., Koch D., Kinne S., Kondo Y., Quinn P.K., Sarofim M.C., Schultz M.G., et al., Bounding the role of black carbon in the climate system: A scientific assessment, Journal of Geophysical Research: Atmospheres, 118 (2013) 5380–5552. DOI: 10.1002/jgrd.50171

Brook R.D., Rajagopalan S., Pope C.A., Brook J.R., Bhatnagar A., Diez-Roux A.V., Holguin F., Hong Y., Luepker R.V., Mittleman M.A., Peters A., Siscovick D., Smith S.C., Whitsel L., Kaufman J.D., et al., Particulate matter air pollution and cardiovascular disease, Circulation, 121 (2010) 2331–2378. DOI: 10.1161/CIR.0b013e3181dbece1

Camarillo-Escobedo R., Flores J.L., Marin-Montoya P., García-Torales G., Camarillo-Escobedo J.M., Smart multi-sensor system for remote air quality monitoring using unmanned aerial vehicle and LoRaWAN, Sensors, 22 (2022) 1706. DOI: 10.3390/s22051706

Cao J.-j., Wang Q.-y., Chow J.C., Watson J.G., Tie X.-x., Shen Z.-x., Wang P., An Z.-s., Impacts of aerosol compositions on visibility impairment in Xi'an, China, Atmospheric Environment, 59 (2012) 559–566. DOI: 10.1016/j.atmosenv.2012.05.036

Carretero-Pena S., Calvo Blazquez L., Pinilla-Gil E., Estimation of PM_{10} levels and sources in air quality networks by digital analysis of smartphone camera images taken from samples deposited on filters, Sensors, 19 (2019) 4791. DOI: 10.3390/s19214791

Castell N., Dauge F.R., Schneider P., Vogt M., Lerner U., Fishbain B., Broday D., Bartonova A., Can commercial low-cost sensor platforms contribute to air quality monitoring and exposure estimates?, Environment International, 99 (2017) 293–302. DOI: 10.1016/j.envint.2016.12.007

Chang C.T., Chang Y.M., Lin W.Y., Wu M.C., Fugitive dust emission source profiles and assessment of selected control strategies for particulate matter at gravel processing sites in Taiwan, Journal of the Air & Waste Management Association, 60 (2010) 1262–1268. DOI: 10.3155/1047-3289.60.10.1262

Chen S., Zhang X., Lin J., Huang J., Zhao D., Yuan T., Huang K., Luo Y., Jia Z., Zang Z., Qiu Y.A., Xie L., Fugitive road dust $PM_{2.5}$ emissions and their potential health impacts, Environmental Science & Technology, 53 (2019) 8455–8465. DOI: 10.1021/acs.est.9b00666

Choobari O.A., Zawar-Reza P., Sturman A., The global distribution of mineral dust and its impacts on the climate system: a review, Atmospheric Research, 138 (2014) 152–165. DOI: 10.1016/j.atmosres.2013.11.007

Cowherd C.Jr., Axetell K. Jr., Guenther C.M., Jutze G.A., Development of emission factors for fugitive dust sources, U.S. Environmental Protection Agency, NC, 1974.

Minguillón M.C., Viana M., Querol X., Particulate Matter: Environmental Monitoring and Mitigation, Future Science Book Series, Future Science Ltd, 2013, ISBN: 9781909453135. DOI: 10.4155/9781909453135

D'Amato G., Chong-Neto H.J., Monge Ortega O.P., Vitale C., Ansotegui

I., Rosario N., Haahtela T., Galan C., Pawankar R., Murrieta-Aguttes M., Cecchi L., Bergmann C., Ridolo E., Ramon G., Gonzalez Diaz S., et al., The effects of climate change on respiratory allergy and asthma induced by pollen and mold allergens, Allergy, 75 (2020) 2219–2228. DOI: 10.1111/all.14476

de Weger L.A., Molster F., de Raat K., den Haan J., Romein J., van Leeuwen W., de Groot H., Mostert M., Hiemstra P.S., A new portable sampler to monitor pollen at street level in the environment of patients, Science of The Total Environment, 741 (2020) 140404. DOI: 10.1016/j.scitotenv.2020.140404

Du K., Rood M.J., Welton E.J., Varma R.M., Hashmonay R.A., Kim B.J., Kemme M.R., Optical remote sensing to quantify fugitive particulate mass emissions from stationary short-term and mobile continuous sources: part i. method and examples, Environmental Science & Technology, 45 (2011) 658–665. DOI: 10.1021/es101904q

Du K., Shi P., Rood M.J., Wang K., Wang Y., Varma R.M., Digital Optical Method to quantify the visual opacity of fugitive plumes, Atmospheric Environment, 77 (2013) 983–989. DOI: 10.1016/j.atmosenv.2013.06.017

Ebert M., Weinbruch S., Rausch A., Gorzawski G., Helas G., Hoffmann P., Wex H., Complex refractive index of aerosols during LACE 98#x2010; as derived from the analysis of individual particles, Journal of Geophysical Research: Atmospheres, 107 (2002) 8121. DOI: 10.1029/2000JD000195

Esmen N.A., Corn M., Residence time of particles in urban air, Atmospheric Environment (1967), 5 (1971) 571–578. DOI: 10.1016/0004-6981(71)90113-2

Etyemezian V., Ahonen S., Nikolic D., Gillies J., Kuhns H., Gillette D., Veranth J., Deposition and removal of fugitive dust in the arid southwestern United States: measurements and model results, Journal of the Air & Waste Management Association, 54 (2004) 1099–1111. DOI: 10.1080/10473289.2004.10470977

Etyemezian V., Nikolich G., Ahonen S., Pitchford M., Sweeney M., Purcell R., Gillies J., Kuhns H., The portable in situ wind erosion laboratory (PI-SWERL): a new method to measure PM10 windblown dust properties and potential for emissions, Atmospheric Environment, 41 (2007) 3789–3796. DOI: 10.1016/j.atmosenv.2007.01.018

February F.J., Piazzola J., Altieri K.E., Van Eijk A.M.J., Contribution of sea spray to aerosol size distributions measured in a South African coastal zone, Atmospheric Research, 262 (2021) 105790. DOI: 10.1016/j.atmosres.2021.105790

Feigin V.L., Roth G.A., Naghavi M., Parmar P., Krishnamurthi R., Chugh S., Mensah G.A., Norrving B., Shiue I., Ng M., Estep K., Cercy K., Murray C.J.L., Forouzanfar M.H., Global burden of stroke and risk factors in 188 countries, during 1990–2013: a systematic analysis for the Global Burden of Disease Study 2013, The Lancet Neurology, 15 (2016) 913–924. DOI: 10.1016/s1474-4422(16)30073-4

Fitz D., Pankratz D., Pederson S., Bristow J., A semi-portable enclosure to measure emission rates from small fugitive sources: leaf blower dust example, Aerosol and Air Quality Research, 21 (2021) 200566. DOI: 10.4209/aaqr.200566

Froyd K.D., Murphy D.M., Brock C.A., Campuzano-Jost P., Dibb J.E., Jimenez J.L., Kupc A., Middlebrook A.M., Schill G.P., Thornhill K.L., Williamson C.J., Wilson J.C., Ziemba L.D., A new method to quantify mineral dust and other aerosol species from aircraft platforms using single-particle mass spectrometry, Atmospheric Measurement Techniques, 12 (2019) 6209–6239. DOI: 10.5194/amt-12-6209-2019

Gao S., Wang Y., Shan M., Teng Y., Hong N., Sun Y., Mao J., Ma Z., Xiao J., Azzi M., Chen L., Zhang H., Wind-tunnel and modelled PM_{10} emissions and dust concentrations from agriculture soils in Tianjin, northern China, Aeolian Research, 42 (2020) 100562. DOI: 10.1016/j.aeolia.2019.100562

Gao Y., Lai S., Lee S.C., Yau P.S., Huang Y., Cheng Y., Wang T., Xu Z., Yuan C., Zhang Y., Optical properties of size-resolved particles at a Hong Kong urban site during winter, Atmospheric Research, 155 (2015) 1–12. DOI: 10.1016/j.atmosres.2014.10.020

Gelencsér A., Kováts N., Turóczi B., Rostási Á., Hoffer A., Imre K., Nyirő-Kósa I., Csákberényi-Malasics D., Tóth Á., Czitrovszky A., Nagy A., Nagy S., Ács A., Kovács A., Ferincz Á., et al., The red mud accident in Ajka (Hungary): characterization and potential health effects of fugitive dust, Environmental Science & Technology, 45 (2011) 1608–1615. DOI: 10.1021/es104005r

Girón D., Delgado T., Ruiz J., Cabalín L.M., Laserna J.J., In-situ monitoring and characterization of airborne solid particles in the hostile environment of a steel industry using stand-off LIBS, Measurement, 115 (2018) 1–10. DOI: 10.1016/j.measurement.2017.09.046

Gladding T.L., Rolph C.A., Gwyther C.L., Kinnersley R., Walsh K., Tyrrel S., Concentration and composition of bioaerosol emissions from intensive farms: pig and poultry livestock, Journal of Environmental Management, 272 (2020) 111052. DOI: 10.1016/j.jenvman.2020.111052

Grover B.D., Measurement of total $PM_{2.5}$ mass (nonvolatile plus semivolatile) with the Filter Dynamic Measurement System tapered element oscillating microbalance monitor, Journal of Geophysical Research, 110 (2005) D07S03. DOI: 10.1029/2004jd004995

Guo L., Cui Y., He Q., Gao W., Pei K., Zhu L., Li H., Wang X., Contributions of aerosol chemical composition and sources to light extinction during haze and non-haze days in Taiyuan, China, Atmospheric Pollution Research, 12 (2021) 101140. DOI: 10.1016/j.apr.2021.101140

Hassan H., Kumar P., Kakosimos K.E., The impact of local fugitive particulate matter and emission inventories on air quality and health in dry and arid areas, Science of The Total Environment, 824 (2022) 153799. DOI: 10.1016/j.scitotenv.2022.153799

Hassan H., Saraga D., Kumar P., Kakosimos K.E., Vehicle-induced fugitive particulate matter emissions in a city of arid desert climate, Atmospheric Environment, 229 (2020) 117450. DOI: 10.1016/j.atmosenv.2020.117450

Hassan H.A., Kumar P., Kakosimos K.E., Flux estimation of fugitive particulate matter emissions from loose Calcisols at construction sites, Atmospheric Environment, 141 (2016) 96–105. DOI: 10.1016/j.atmosenv.2016.06.054

Hergert W., Wriedt T., The Mie Theory: Basics and Applications, Springer, 2012, ISBN: 978-3-642-43614-7. DOI: 10.1007/978-3-642-28738-1

Hobbs P.V., Sinha P., Yokelson R.J., Christian T.J., Blake D.R., Gao S., Kirchstetter T.W., Novakov T., Pilewskie P., Evolution of gases and particles from a savanna fire in South Africa, Journal of Geophysical Research: Atmospheres, 108 (2003) 8485. DOI: 10.1029/2002JD002352

Holmén B., Miller D., Hiscox A., Yang W., Wang J., Sammis T., Bottoms R., Near-source particulate emissions and plume dynamics from agricultural field operations, Journal of Atmospheric Chemistry, 59 (2007) 117–134. DOI: 10.1007/s10874-007-9086-6

Hoy R.F., Chambers D.C., Silica-related diseases in the modern world, Allergy, 75 (2020) 2805–2817. DOI: 10.1111/all.14202

Hu J., Wang H., Zhang J., Zhang M., Zhang H., Wang S., Chai F., $PM_{2.5}$ pollution in Xingtai, China: chemical characteristics, source apportionment, and emission control measures, Atmosphere, 10 (2019) 121. DOI: 10.3390/atmos10030121

Jakovčević T., Stipaničev D., Krstinić D., Visual spatial-context based wildfire smoke sensor, Machine Vision and Applications, 24 (2013) 707–719. DOI: 10.1007/s00138-012-0481-x

Jeong J.I., Jo D.S., Park R.J., Lee H.-M., Curci G., Kim S.-W., Parametric analysis for global single scattering albedo calculations, Atmospheric Environment, 234 (2020) 117616. DOI: 10.1016/j.atmosenv.2020.117616

Kabir A.S., Sharma N.C., Barnes J.E., Butt J., Bridgewater M., Using a

bistatic camera lidar to profile aerosols influenced by a local source of pollution, SPIE, 10636 (2018) 126–132. DOI: 10.1117/12.2303544

Kalashnikova O.V., Sokolik I.N., Modeling the radiative properties of nonspherical soil-derived mineral aerosols, Journal of Quantitative Spectroscopy and Radiative Transfer, 87 (2004) 137–166. DOI: 10.1016/j.jqsrt.2003.12.026

Kandler K., Benker N., Bundke U., Cuevas E., Ebert M., Knippertz P., Rodríguez S., Schütz L., Weinbruch S., Chemical composition and complex refractive index of Saharan Mineral Dust at Izaña, Tenerife (Spain) derived by electron microscopy, Atmospheric Environment, 41 (2007) 8058–8074. DOI: 10.1016/j.atmosenv.2007.06.047

Kaźmierczak B., Badura M., Batog P., Drzeniecka-Osiadacz A., Modzel P., Kutyłowska M., Piekarska K., Jadwiszczak P., Optical particulate matter sensors in $PM_{2.5}$ measurements in atmospheric air, E3S Web of Conferences, 44 (2018) 00006. DOI: 10.1051/e3sconf/20184400006

Kelesidis G.A., Pratsinis S.E., Soot light absorption and refractive index during agglomeration and surface growth, Proceedings of the Combustion Institute, 37 (2019) 1177–1184. DOI: 10.1016/j.proci.2018.08.025

Kim M.K., Jang Y., Heo J., Park D., A UAV-based air quality evaluation method for determining fugitive emissions from a quarry during the railroad life cycle, Sensors, 21 (2021) 3206. DOI: 10.3390/s21093206

Kuhns H., Gillies J., Etyemezian V., Nikolich G., King J., Zhu D., Uppapalli S., Engelbrecht J., Kohl S., Effect of soil type and momentum on unpaved road particulate matter emissions from wheeled and tracked vehicles, Aerosol Science and Technology, 44 (2010) 187–196. DOI: 10.1080/02786820903516844

Kuula J., Kuuluvainen H., Rönkkö T., Niemi J.V., Saukko E., Portin H., Aurela M., Saarikoski S., Rostedt A., Hillamo R., Timonen H., Applicability of optical and diffusion charging-based particulate matter sensors to urban air quality measurements, Aerosol and Air Quality Research, 19 (2019) 1024–1039. DOI: 10.4209/aaqr.2018.04.0143

Lavrov A., Utkin A.B., Vilar R., Fernandes A., Application of lidar in ultraviolet, visible and infrared ranges for early forest fire detection, Applied Physics B: Lasers and Optics, 76 (2003) 87–95. DOI: 10.1007/s00340-002-1053-y

Le T.-C., Tsai C.-J., Inertial impaction technique for the classification of particulate matters and nanoparticles: a review, KONA Powder and Particle Journal, 38 (2021) 42–63. DOI: 10.14356/kona.2021004

Lei Y., Shen Z., Tang Z., Zhang Q., Sun J., Ma Y., Wu X., Qin Y., Xu H., Zhang R., Aerosols chemical composition, light extinction, and source apportionment near a desert margin city, Yulin, China, PeerJ, 8 (2020) e8447. DOI: 10.7717/peerj.8447

Liu H.-Y., Schneider P., Haugen R., Vogt M., Performance assessment of a low-cost $PM_{2.5}$ sensor for a near four-month period in Oslo, Norway, Atmosphere, 10 (2019) 41. DOI: 10.3390/atmos10020041

Liu Y., Shao L., Wang W., Chen J., Zhang H., Yang Y., Hu B., Study on fugitive dust control technologies of agricultural harvesting machinery, Agriculture, 12 (2022) 1038. DOI: 10.3390/agriculture12071038

Madokoro H., Kiguchi O., Nagayoshi T., Chiba T., Inoue M., Chiyonobu S., Nix S., Woo H., Sato K., Development of drone-mounted multiple sensing system with advanced mobility for in situ atmospheric measurement: a case study focusing on $PM_{2.5}$ local distribution, Sensors, 21 (2021) 4881. DOI: 10.3390/s21144881

Manojkumar N., Srimuruganandam B., Size-segregated particulate matter characteristics in indoor and outdoor environments of urban traffic and residential sites, Urban Climate, 44 (2022) 101232. DOI: 10.1016/j.uclim.2022.101232

Marina-Montes C., Motto-Ros V., Pérez-Arribas L.V., Anzano J., Millán-Martínez M., Cáceres J.O., Aerosol analysis by micro laser-induced breakdown spectroscopy: a new protocol for particulate matter characterization in filters, Analytica Chimica Acta, 1181 (2021) 338947. DOI: 10.1016/j.aca.2021.338947

Martinelli N., Olivieri O., Girelli D., Air particulate matter and cardiovascular disease: a narrative review, European Journal of Internal Medicine, 24 (2013) 295–302. DOI: 10.1016/j.ejim.2013.04.001

Mueller S.F., Mallard J.W., Mao Q., Shaw S.L., Fugitive particulate emission factors for dry fly ash disposal, Journal of the Air & Waste Management Association, 63 (2013) 806818. DOI: 10.1080/10962247.2013.795201

Mutlu A., Air quality impact of particulate matter (PM10) releases from an industrial source, Environmental Monitoring and Assessment, 192 (2020) 547. DOI: 10.1007/s10661-020-08508-7

Noh H.-j., Lee S.-k., Yu J.-h., Identifying effective fugitive dust control measures for construction projects in Korea, Sustainability, 10 (2018) 1206. DOI: 10.3390/su10041206

Nousiainen T., Optical modeling of mineral dust particles: a review, Journal of Quantitative Spectroscopy and Radiative Transfer, 110 (2009) 1261–1279. DOI: 10.1016/j.jqsrt.2009.03.002

Nugraha M.G., Saptoadi H., Hidayat M., Andersson B., Andersson R., Particulate matter reduction in residual biomass combustion, Energies, 14 (2021) 3341. DOI: 10.3390/en14113341

Omidvarborna H., Baawain M., Al-Mamun A., Al-Muhtaseb A.H., Dispersion and deposition estimation of fugitive iron particles from an iron industry on nearby communities via AERMOD, Environmental Monitoring and Assessment, 190 (2018) 655. DOI: 10.1007/s10661-018-7009-4

Ordou N., Agranovski I.E., Contribution of fine particles to air emission at different phases of biomass burning, Atmosphere, 10 (2019) 278. DOI: 10.3390/atmos10050278

Pal S.R., Hlaing D., Carswell A.I., Roy G., Bastille C., Scanning LIDAR application for pollutant sources in an industrial complex, SPIE, 3504 (1998) 76–86. DOI: 10.1117/12.319574

Pervez S., Bano S., Watson J.G., Chow J.C., Matawle J.L., Shrivastava A., Tiwari S., Pervez Y.F., Source profiles for $PM_{10\text{-}2.5}$ resuspended dust and vehicle exhaust emissions in central India, Aerosol and Air Quality Research, 18 (2018) 1660–1672. DOI: 10.4209/aaqr.2017.08.0259

Philip S., Martin R.V., Snider G., Weagle C.L., van Donkelaar A., Brauer M., Henze D.K., Klimont Z., Venkataraman C., Guttikunda S.K., Zhang Q., Anthropogenic fugitive, combustion and industrial dust is a significant, underrepresented fine particulate matter source in global atmospheric models, Environmental Research Letters, 12 (2017) 044018. DOI: 10.1088/1748-9326/aa65a4

Prata A.J., Satellite detection of hazardous volcanic clouds and the risk to global air traffic, Natural Hazards, 51 (2008) 303–324. DOI: 10.1007/s11069-008-9273-z

Qu Y., Ji H., Oudray F., Yan Y., Liu Y., Online composition detection and cluster analysis of Tibetan incense, Optik, 241 (2021) 166999. DOI: 10.1016/j.ijleo.2021.166999

Raja S., Chandrasekaran S.R., Lin L., Xia X., Hopke P.K., Valsaraj K.T., Analysis of beta attenuation monitor filter rolls for particulate matter speciation, Aerosol and Air Quality Research, 17 (2017) 14–23. DOI: 10.4209/aaqr.2016.03.0122

Roney J.A., White B.R., Estimating fugitive dust emission rates using an environmental boundary layer wind tunnel, Atmospheric Environment, 40 (2006) 7668–7685. DOI: 10.1016/j.atmosenv.2006.08.015

Sanderson P., Delgado-Saborit J.M., Harrison R.M., A review of chemical and physical characterisation of atmospheric metallic nanoparticles, Atmospheric Environment, 94 (2014) 353–365. DOI: 10.1016/j.atmosenv.2014.05.023

Sasaki K., Inoue M., Shimura T., Iguchi M., In Situ, rotor-based drone measurement of wind vector and aerosol concentration in volcanic areas, Atmosphere, 12 (2021) 376. DOI: 10.3390/atmos12030376

Sedlacek Iii A.J., Buseck P.R., Adachi K., Onasch T.B., Springston S.R., Kleinman L., Formation and evolution of tar balls from northwestern US wildfires, Atmospheric Chemistry and Physics, 18 (2018)

11289–11301. DOI: 10.5194/acp-18-11289-2018

Sidra S., Ali Z., Sultan S., Ahmed S., Colbeck I., Nasir Z.A., Assessment of airborne microflora in the indoor micro-environments of residential houses of Lahore, Pakistan, Aerosol and Air Quality Research, 15 (2015) 2385–2396. DOI: 10.4209/aaqr.2014.12.0338

Su C.P., Peng X., Huang X.F., Zeng L.W., Cao L.M., Tang M.X., Chen Y., Zhu B., Wang Y., He L.Y., Development and application of a mass closure $PM_{2.5}$ composition online monitoring system, Atmospheric Measurement Techniques, 13 (2020) 5407–5422. DOI: 10.5194/amt-13-5407-2020

Sullivan B., Allawatt G., Emery A., Means P., Kramlich J., Posner J., Time-resolved particulate emissions monitoring of cookstove biomass combustion using a tapered element oscillating microbalance, Combustion Science and Technology, 189 (2017) 923–936. DOI: 10.1080/00102202.2016.1253564

Sweeney M.R., Forman S.L., McDonald E.V., Contemporary and future dust sources and emission fluxes from gypsum- and quartz-dominated eolian systems, New Mexico and Texas, USA, Geology, 50 (2021) 356–360. DOI: 10.1130/g49488.1

Tao Z., Wang Z., Yang S., Shan H., Ma X., Zhang H., Zhao S., Liu D., Xie C., Wang Y., Profiling the $PM_{2.5}$ mass concentration vertical distribution in the boundary layer, Atmospheric Measurement Techniques, 9 (2016) 1369–1376. DOI: 10.5194/amt-9-1369-2016

Taubman B.F., Smoke over haze: aircraft observations of chemical and optical properties and the effects on heating rates and stability, Journal of Geophysical Research, 109 (2004) D02206. DOI: 10.1029/2003jd003898

ten Brink H., Henzing B., Otjes R., Weijers E., Visibility in the Netherlands during New Year's fireworks: the role of soot and salty aerosol products, Atmospheric Environment, 173 (2018) 289–294. DOI: 10.1016/j.atmosenv.2017.11.020

Theilade I., Mærsk-Møller M.L., Theilade J., Larsen K., Pollen morphology and structure of Zingiber (Zingiberaceae), Grana, 32 (1993) 338–342. DOI: 10.1080/00173139309428961

Tian J., Wang Q., Han Y., Ye J., Wang P., Pongpiachan S., Ni H., Zhou Y., Wang M., Zhao Y., Cao J., Contributions of aerosol composition and sources to particulate optical properties in a southern coastal city of China, Atmospheric Research, 235 (2020) 104744. DOI: 10.1016/j.atmosres.2019.104744

Ueda S., Morphological change of solid ammonium sulfate particles below the deliquescence relative humidity: experimental reproduction of atmospheric sulfate particle shapes, Aerosol Science and Technology, 55 (2021) 423–437. DOI: 10.1080/02786826.2020.1864277

Varma R.M., Hashmonay R.A., Du K., Rood M.J., Kim B.J., Kemme M.R., A novel method to quantify fugitive dust emissions using optical remote sensing, in: Kim Y.J., Platt U. (Eds.), Advanced Environmental Monitoring, Springer Netherlands, Dordrecht, 2008, pp.143–154, ISBN: 978-1-4020-6364-0. DOI: 10.1007/978-1-4020-6364-0_11

Vos H.C., Fister W., von Holdt J.R., Eckardt F.D., Palmer A.R., Kuhn N.J., Assessing the PM_{10} emission potential of sandy, dryland soils in South Africa using the PI-SWERL, Aeolian Research, 53 (2021) 100747. DOI: 10.1016/j.aeolia.2021.100747

Wang F., Yu H., Wang Z., Liang W., Shi G., Gao J., Li M., Feng Y., Review of online source apportionment research based on observation for ambient particulate matter, Science of The Total Environment, 762 (2021) 144095. DOI: 10.1016/j.scitotenv.2020.144095

Wang F., Zhang Q., Xu X., Zhao W., Zhang Y., Zhang W., Thermo-optical and particle number size distribution characteristics of smoldering smoke from biomass burning, Applied Sciences, 9 (2019) 5259. DOI: 10.3390/app9235259

Wang H., Han L., Li T., Qu S., Zhao Y., Fan S., Chen T., Cui H., Liu J., Temporal-spatial distributions of road silt loadings and fugitive road dust emissions in Beijing from 2019 to 2020, Journal of Environmental Sciences, 132 (2023) 56–70. DOI: 10.1016/j.jes.2022.07.007

Wang W., Zhou W., Cai X., Qin J., Huang Y., A.. S., Remote measurement method for mass concentration of fugitive-dust-emission particulate based on backward light scattering (in Chinese), Acta Optica Sinica, 39 (2019) 1201001. DOI: 10.3788/aos201939.1201001

Wang Y., Li X., Shi Z., Huang L., Li J., Zhang H., Ying Q., Wang M., Ding D., Zhang X., Hu J., Premature mortality associated with exposure to outdoor black carbon and its source contributions in China, Resources, Conservation and Recycling, 170 (2021) 105620. DOI: 10.1016/j.resconrec.2021.105620

Williamson C.J., Kupc A., Axisa D., Bilsback K.R., Bui T., Campuzano-Jost P., Dollner M., Froyd K.D., Hodshire A.L., Jimenez J.L., Kodros J.K., Luo G., Murphy D.M., Nault B.A., Ray E.A., et al., A large source of cloud condensation nuclei from new particle formation in the tropics, Nature, 574 (2019) 399–403. DOI: 10.1038/s41586-019-1638-9

Xiao S., Wang Q.Y., Cao J.J., Huang R.J., Chen W.D., Han Y.M., Xu H.M., Liu S.X., Zhou Y.Q., Wang P., Zhang J.Q., Zhan C.L., Long-term trends in visibility and impacts of aerosol composition on visibility impairment in Baoji, China, Atmospheric Research, 149 (2014) 88–95. DOI: 10.1016/j.atmosres.2014.06.006

Yang D., Zhang H., Wang Z., Zhao S., Li J., Changes in anthropogenic particulate matters and resulting global climate effects since the Industrial Revolution, International Journal of Climatology, 42 (2021) 315–330. DOI: 10.1002/joc.7245

Yi E.E.P.N., Nway N.C., Aung W.Y., Thant Z., Wai T.H., Hlaing K.K., Maung C., Yagishita M., Ishigaki Y., Win-Shwe T.-T., Nakajima D., Mar O., Preliminary monitoring of concentration of particulate matter ($PM_{2.5}$) in seven townships of Yangon City, Myanmar, Environmental Health and Preventive Medicine, 23 (2018) 53. DOI: 10.1186/s12199-018-0741-0

Yu X., Ma J., An J., Yuan L., Zhu B., Liu D., Wang J., Yang Y., Cui H., Impacts of meteorological condition and aerosol chemical compositions on visibility impairment in Nanjing, China, Journal of Cleaner Production, 131 (2016) 112–120. DOI: 10.1016/j.jclepro.2016.05.067

Yuen W., Du K., Koloutsou-Vakakis S., Rood M.J., Kim B.J., Kemme M.R., Hashmonay R.A., Meister C., Fugitive particulate matter emissions to the atmosphere from tracked and wheeled vehicles in a desert region by hybrid-optical remote sensing, Aerosol and Air Quality Research, 15 (2015) 1613–1626. DOI: 10.4209/aaqr.2014.12.0310

Yuen W., Johnsen D.L., Koloutsou-Vakakis S., Rood M.J., Kim B.J., Kemme M.R., Open burning and open detonation PM_{10} mass emission factor measurements with optical remote sensing, Journal of the Air & Waste Management Association, 64 (2013) 227–234. DOI: 10.1080/10962247.2013.851045

Yuen W., Ma Q., Koloutsou-Vakakis S., Du K., Rood M.J., Lidar equation inversion methods and uncertainties in measuring fugitive particulate matter emission factors, Applied Optics, 56 (2017) 7691–7701. DOI: 10.1364/AO.56.007691

Zavyalov V.V., Marchant C., Bingham G.E., Wilkerson T.D., Swasey J., Rogers C., Ahlstrom D., Timothy P., Retrieval of physical properties of particulate emission from animal feeding operations using three-wavelength elastic lidar measurements, SPIE, 2006. DOI: 10.1117/12.680967

Zhang H., Sun W., Li W., Wang Y., Physical and chemical characterization of fugitive particulate matter emissions of the iron and steel industry, Atmospheric Pollution Research, 13 (2022) 101272. DOI: 10.1016/j.apr.2021.101272

Zhang Q., Liu Y., Yin W., Yan Y., Li L., Xing G., The in situ detection of smoking in public area by laser-induced breakdown spectroscopy, Chemosphere, 242 (2020) 125184. DOI: 10.1016/j.chemosphere.2019.125184

Zhang Y., Forrister H., Liu J., Dibb J., Anderson B., Schwarz J.P., Perring

A.E., Jimenez J.L., Campuzano-Jost P., Wang Y., Nenes A., Weber R.J., Top-of-atmosphere radiative forcing affected by brown carbon in the upper troposphere, Nature Geoscience, 10 (2017) 486–489. DOI: 10.1038/ngeo2960

Zhou W., Mei C., Qin J., Cai X., Wang T., He W., Shi A., A side-scattering imaging method for the in-line monitoring of particulate matter emissions from cooking fumes, Measurement Science and Technology, 32 (2020) 034006. DOI: 10.1088/1361-6501/abbd58

Zou J., Liu Z., Hu B., Huang X., Wen T., Ji D., Liu J., Yang Y., Yao Q., Wang Y., Aerosol chemical compositions in the North China Plain and the impact on the visibility in Beijing and Tianjin, Atmospheric Research, 201 (2018) 235–246. DOI: 10.1016/j.atmosres.2017.09.014

Authors' Short Biographies



Tianyi Cai

Tianyi Cai received his bachelor's degree and a Ph.D.in Engineering from Southeast University in 2014 and 2020, respectively. He is now a lecturer in the School of Energy and Power Engineering at the University of Shanghai for Science and Technology. His research interests include particles and two-phase flow measurement, heterogeneous reaction flow measurement. He also researches on theoretical modeling of the heterogeneous reactions related to various carbon capture and utilization processes.



Wu Zhou

Prof. Wu Zhou received her degree from Nanjing University of Science and Technology in 2006 and a Ph.D.in Engineering from Southeast University in 2011.She is now an professor in the School of Energy and Power Engineering at the University of Shanghai for Science and Technology. Her research interests include particles and two-phase flow measurement, combustion measurement, mainly by image-based methods. She is also interested in mathematical modelling of the above processes. She is a member of Youth Council of the Chinese Society of Particuology.

KONA Powder and Particle Journal

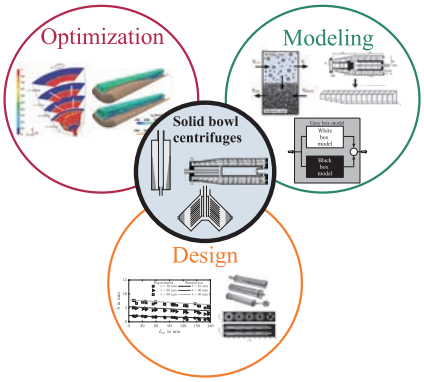
KONA Powder and Particle Journal No. 41 (2024) 58–77/https://doi.org/10.14356/kona.2024010 Review Paper

About Modeling and Optimization of Solid Bowl Centrifuges†

Marco Gleiss* and Hermann Nirschl

Institute of Mechanical Process Engineering and Mechanics, Karlsruhe Institute of Technology (KIT), Germany

Many processes involve solid bowl centrifuges as a solid–liquid separation step, typically used for clarification, thickening, classification, degritting, mechanical dewatering, and screening. In order to operate solid bowl centrifuges safely, with minimum resource consumption and reduced setup times, modeling and optimization are necessary steps. This is a challenge due to the complex process behavior, which can be overcome by developing advanced physical models and process analysis. This review provides an overview of solid bowl centrifuge applications, their modeling, and addresses future optimization potentials through digital tools. The impact of dispersed phase properties such as particle size, shape, surface roughness, structure, composition, and continuous liquid phase is the reason for the lack of generally applicable models. Laboratory-scale batch sedimentation centrifuges are used to predict material behavior and develop material functions describing separation-related properties such as sedimentation, sediment build-up and sediment transport. The combination of material functions and modeling allows accurate simulation of solid bowl centrifuges from laboratory to industrial scale. Since models usually do not cover all influencing variables, there are often deviations between predictions and the real process behavior. Gray-box modeling and on-line or in-situ process analytics are tools to improve centrifuge operation.



Keywords: solid bowl centrifuges, material characterization, multiphase flow, process modeling, gray-box modeling, process analytics

1. Introduction

The separation of fine particles from liquids plays an important role in daily products such as chemicals, pharmaceuticals, healthcare products, ingredients, beverages, proteins, food or consumer goods, see **Table 1** (Anlauf, 2007). Solid–liquid separation is an essential step in the processing and handling of products that are often obtained by precipitation, crystallization, or comminution.

The two main principles of solid–liquid separation are filtration and centrifugation. Filtration requires a filter medium that retains particles, while centrifugation relies on a rotating bowl.

Solid bowl centrifuges are sedimentation centrifuges and use the physical principle of sedimentation, based on a density difference between the solid and liquid phases. In the industry, there are several types of centrifuges that allow the separation of colloids or particles with several millimeters in size. Typical machines are solid bowl peeler centrifuges, tubular bowl centrifuges, disk stack centrifuges, or decanter centrifuges.

Fig. 1 shows the categorization of different centrifuge types in terms of cut size, which is the particle size that has an equal chance of being in the underflow or overflow. The influencing variables are numerous, and the cut size depends not only on the process conditions and the centrifuge geometry, but also on the properties of the dispersed and continuous phases. Furthermore, the limits can be arbitrarily shifted by suspension pre-treatment such as coagulation or flocculation.

For a spherical particle, in a creeping flow and infinitely diluted Newtonian fluid, the Stokes' settling velocity is valid (Stokes, 1850):

$$v_s = \frac{(\rho_s - \rho_l) C g x^2}{18 \mu_l} \tag{1}$$

Here, ρ_s is the density of solid phase, ρ_l is the density of liquid, g is gravity, x is the particle diameter, and μ_l is the dynamic viscosity. The Stokes' settling velocity can be derived from an equilibrium of forces consisting of buoyancy, centrifugal, and drag force, neglecting the influence of inertia and assuming small particle Reynolds number $Re < 0.1$.

For semi-batch or continuous solid bowl centrifuges, modeling requires the linkage between process conditions, geometric dimensions and material properties (Ambler, 1952). One approach to scale-up of solid bowl centrifuges is Sigma theory, which requires a significant amount of pilot testing, making the design process time-consuming and costly.

Increasing computational power and improvements in sensor technology have led to the development of more comprehensive and detailed models and measurement techniques in recent years (Gleiss et al., 2020; Hammerich

† Received 14 May 2022; Accepted 8 September 2022
J-STAGE Advance published online 30 June 2023
* Corresponding author: Marco Gleiss;
Add: Straße am Forum 8, 76131 Karlsruhe, Germany
E-mail: marco.gleiss@kit.edu
TEL: +49-721-608-42426 FAX: +49-721-608-40405

Copyright © 2024 The Authors. Published by Hosokawa Powder Technology Foundation. This is an open access article under the CC BY license (https://creativecommons.org/licenses/by/4.0/).

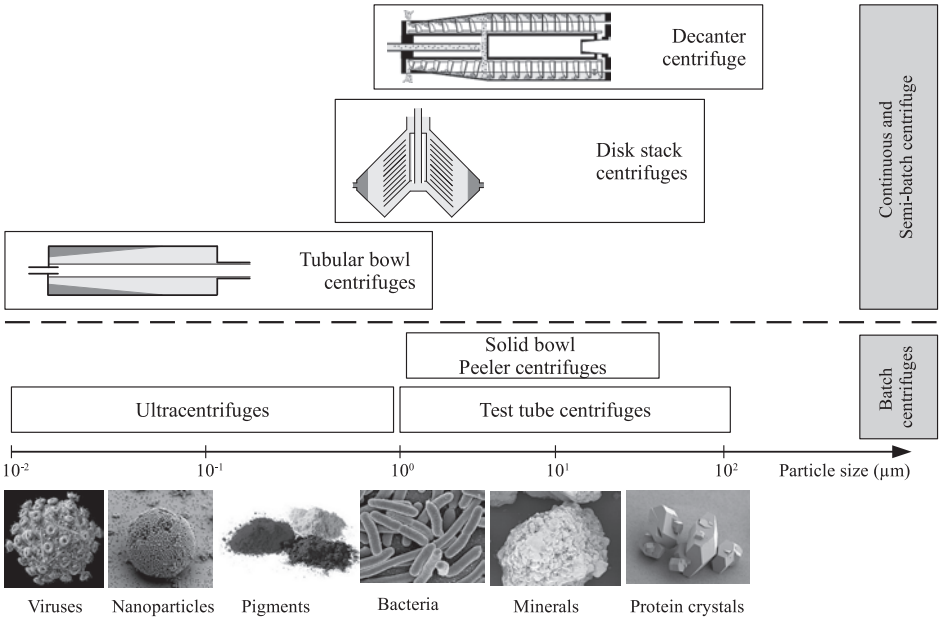


Fig. 1 Classification of different centrifuge types depending on the operation mode and applicable particle size range. Adapted from Ref. (Spelter et al., 2010) with permission from Elsevier, Copyright 2010.

Table 1 Overview of different applications of solid bowl centrifuges.

Centrifuge type	Field of application
Tubular bowl centrifuge	Biotechnology [a, b]
	Nanotechnology [c, d, e]
	Battery materials [f, g]
Disc stack centrifuge	Protein separation [h]
	Bio fuels [i, j]
	Pharmaceuticals [k, l]
	Oil industry [m]
Decanter centrifuge	Food industry [n, o]
	Biotechnology [p]
	Wastewater treatment [q, r]
	Protein separation [s, t]
	Minerals processing [u, v]

[a](Spelter et al., 2010), [b](Rathore et al., 2015), [c](Kohsakowski et al., 2019), [d](Flegler et al., 2016), [e](Flegler et al., 2018), [f](Sinn et al., 2020), [g](Wolf et al., 2021), [h](Byrne et al., 2002), [i](Najjar and Abu-Shamleh, 2020), [j](Arcigni et al., 2019), [k](Kempken et al., 1995), [l](Jungbauer, 2013), [m](Khatib et al., 1995), [n](Caponio et al., 2014), [o](Schubert et al., 2018), [p](Lopes et al., 2013), [q](Wakeman, 2007), [r](Ginisty et al., 2021), [s](Haller et al., 2021), [t](Haller and Kulozik, 2019), [u](W.F. Leung, 2004), [v](Merkl et al., 2012)

et al., 2018). The aim of this review is to provide an overview of the current developments in the field of modeling and optimization of solid bowl centrifuges.

First, the process behavior of solid bowl centrifuges is explained in more detail. This is followed by a description of the separation properties and their characterization based on laboratory centrifuges. Finally, different modeling strategies are discussed.

In this context, process modeling enables the simulation of the process behavior and provides a better understanding of the separation-related behavior of solid bowl centrifuges. Furthermore, this review highlights the capabilities of dynamic and gray-box modeling. Gray-box modeling combines physical and data-driven modeling. Direct coupling here means the integration of process analytics to measure particle properties on-line or in-situ, since dynamic modeling usually cannot capture all physical effects with sufficient accuracy.

2. Process behavior of solid bowl centrifuges

The process behavior of solid bowl centrifuges varies considerably depending on the type of centrifuge and affects the operation. The reasons for this are manifold. The most important influencing variables can be divided into three groups: centrifuge geometry, material properties and process conditions.

2.1 Batch and semi-batch centrifuges

Analytical and ultracentrifuges have a high degree of flexibility due to batch operation. The process time can be adjusted according to the sedimentation behavior, but is limited to small volumes and laboratory scale.

Compared to batch sedimentation centrifuges, semi-batch centrifuges have an overflow weir that forms a liquid pond. This allows continuous clarification of the liquid phase. Centrifugal acceleration is the driving force for particle separation. As a result, the accumulated solids form a liquid-saturated sediment on the rotor wall. The sediment

build-up influences the flow behavior by shortening the residence time.

For example, tubular bowl centrifuges are semi-batch operating machines and have a slim rotor. Conventional bearing systems provide high relative centrifugal numbers of $C = 70{,}000$ with special magnetic bearing technology of $C = 120{,}000$ (Konrath et al., 2016). The relative centrifugal number is an important value indicating the ratio of centrifugal acceleration to gravity. Due to the high relative centrifugal force, tubular bowl centrifuges are typically used for separation and classification of colloidal particles, bacteria, or human blood. Disk stack centrifuges operate either in semi-batch or continuous mode. Manual removal of sediment from the rotor is required for semi-batch operation, which is commonly used for dilute suspensions.

2.2 Continuous centrifuges

Decanter and disk stack centrifuges are continuously operating machines that have a discharge mechanism for both the clarified liquid (overflow weir and peeling disk) and the sediment.

Disk stack centrifuges consist of a conical rotor and conically inclined disks, forming a number of small flow channel which significantly shortens the settling distance. As a result, biological particles such as microorganisms, yeast, mammalian cells or algae can be separated. It is crucial that these substances have only a small density difference to the liquid phase. This fact makes it necessary to have a high centrifugal force. Discharge can be either intermittent, pressure controlled or through nozzles. The choice of discharge mechanism depends on the material properties and operating conditions. Typically, discharge of materials in disk stack centrifuges requires a flowable sediment.

The main components of a decanter centrifuge are a feed tube, a cylindrical conical bowl, and a screw conveyor. The screw conveyor transports the collected solids to the sediment discharge located in the conical section of the machine. The material behavior of the sediment has a significant influence on the performance of the centrifuge. Incompressible sediments exhibit a constant pressure gradient resulting in a constant sediment porosity. The centrifugal force leads to undersaturation of the sediment after it leaves the liquid pond.

In contrast to the aforementioned behavior, interparticle forces, which are dominant for finely dispersed particles influence the sediment formation process in a different way. Here, the sediment is compressible and high capillary pressures occur within the sediment resulting in saturation of $S = 1$. The compressive forces in the sediment lead to a nonlinear porosity gradient. Insufficiently compacted compressible sediments tend to flow easily and interfere with sediment transport.

To overcome this issue, a plain disk is welded at the conveyor hub between the feed zone and the conical part (Records and Sutherland, 2001). The cake baffle disk has a smaller diameter than the centrifuge bowl and creates a gap which serves for the pre-compaction of the material. This ensures a highly compacted non-flowable sediment during the operation.

Another important function of the cake baffle is to improve separation by preventing turbulence and resuspension of previously separated particles. Furthermore, it is possible to increase the pond level, which has a positive effect on the separation efficiency, especially for fine particles with low settling velocity.

2.3 Flow conditions

The flow conditions in solid bowl centrifuges are crucial for achieving the desired separation efficiency. In semi-batch and continuous solid bowl centrifuges, the liquid pond moves almost like a rigid-body. In practice, however, the tangential velocity is smaller than rigid-body motion due to friction losses or insufficient pre-acceleration of the feed. One way of describing the real tangential velocity analytically is a power law that relates the theoretical and actual values as a function of radial position (Gösele, 1968; Reuter, 1967). When deviations from the rigid-body motion are present, internals such as the screw conveyor, disks, internals or deflectors improve the pre-acceleration (Romani Fernández et al., 2010).

The axial velocity in solid bowl centrifuges occurs due to mass conservation between the feed and centrate. In the literature, two limiting cases are distinguished: a plug flow and a boundary layer flow. A uniform flow profile across the entire liquid pond characterizes the plug flow (Ambler, 1959; Stahl and Langeloh, 1983). In comparison, the boundary layer flow consists of two different zones: a fast-flowing layer near the gas-liquid interface and a stagnant layer below (Leung, 1998). For a particle entering the stagnant layer, the influence of axial velocity is negligible.

Both flow profiles do not accurately represent the real flow behavior. This has been demonstrated by recent experimental and numerical studies based on Laser Doppler Anemometry (LDA) and Computational Fluid Dynamics (CFD) (Spelter et al., 2011). The advantage of both methods is the ability to study the flow behavior in a solid bowl centrifuge in space and time (Romani Fernández et al., 2009).

Fig. 2 (I) illustrates the simulation of a mixture of water (blue) and air (red), its distribution in a vertical solid bowl centrifuge type STA at a constant flow rate of 150 L/min and a rotational speed of 2550 rpm. The method investigated here was the Volume-of-Fluid (VOF) method which considers the physical behavior of immiscible liquids where surface tension acts on both phases and forms a clear phase boundary between gas and liquid. Coriolis and centrifugal forces were included in the conservation of momentum in the form of volumetric forces (Hirt et al.,

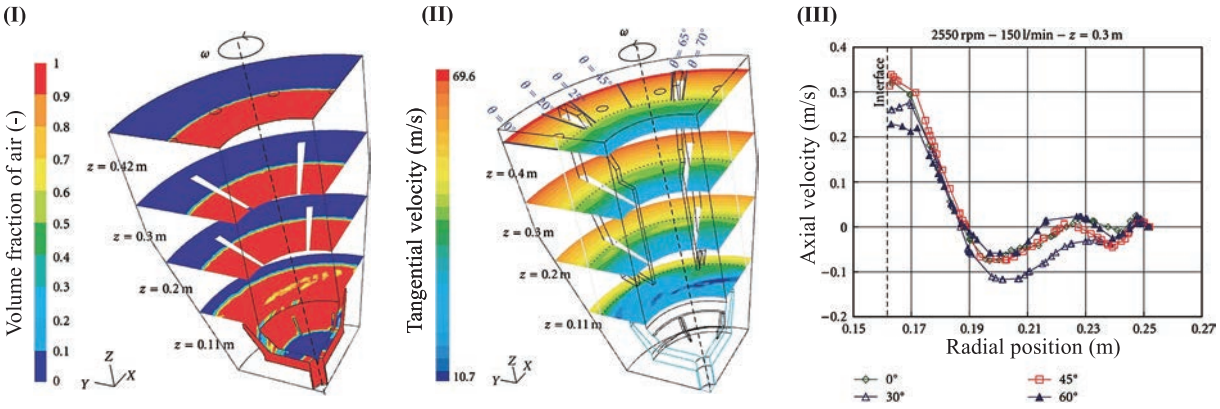


Fig. 2 Left: **(I)** Contours of volume fraction for air (red) and water (blue) **(II)** Contours of tangential velocity at 2550 rpm and 140 L/min inlet flow. **(III)** Axial velocity of water versus radius for different angular positions (0°, 30°, 45°, 60°) at the height of $z = 0.3$ m. Operation conditions are 150 L/min and 2550 rpm. Adapted with permission from Ref. (Romani Fernández et al., 2010) under the terms of the CC-BY 4.0 license. Copyright (2010) the Authors, published by Hindawi.

1981). The simulation indicates a sharp gas-liquid interface and the formation of a liquid pond. Furthermore, the liquid splits into smaller droplets due the pre-acceleration (Romani Fernández et al., 2010).

A closer look at **Fig. 2 (II)** depicts a contour plot of the tangential velocity. The increase of tangential velocity occurs due to the previously mentioned rigid-body motion of the rotor.

The resulting axial flow profile for the investigated vertical solid bowl centrifuge at different angles is shown in **Fig. 2 (III)**. A detailed analysis of the axial velocity suggests that neither plug flow nor boundary layer flow is present. This is due to the absence of slip on the inner wall of the rotor and reduced friction at the gas-liquid interface.

Decanter and disk stack centrifuges have a different flow behavior compared to vertical solid bowl centrifuges. The screw conveyor and the disk stack counteract a pure axial flow. Here, a complex flow behavior is present, which not only depends on the centrifuge geometry, but also on the flow rate and centrifugal acceleration. In the case of a decanter centrifuge, the screw conveyor and the overflow weir form a liquid pond. The main flow occurs along the formed helical channel. The mentioned flow direction was investigated by color tracer experiments in a transparent decanter centrifuge (Faust, 1985). The tracer observation indicates insufficiently pre-accelerated liquid in the feed zone, where the liquid is deflected towards the conical part, reverses and flows in the direction of the overflow weir.

In disk stack centrifuges, friction between the disks dominates which results in hydrodynamic instabilities (Janoske et al., 1999). The flow through the disks is usually based on a superposition of tangential, radial, and axial velocities. This causes the particle to settle on a three-dimensional trajectory along the formed disk channel toward the centrate (König et al., 2021). Disk spacing with axial stands between two disks minimizes the effect of centripetal force on the particle movement and has a positive effect on the separation efficiency.

Predicting local and temporal changes in flow behavior is very difficult, and so far, there is no CFD model that can simulate the flow conditions of an entire disk stack centrifuge. The reasons for this are the operating conditions, the difficult centrifuge geometry, the high pressure and velocity gradients, and the momentum exchange between the solid and liquid phases.

2.4 Residence time behavior

Another promising technique to evaluate the flow behavior of solid bowl centrifuges, is the indirect measurement of the residence time distribution. This method allows to investigate the residence time of fluids or particles in any kind of semi-batch or continuous apparatus. **Fig. 3** illustrates three methods for characterizing the residence time behavior of a machine. The tracer experiment (**Fig. 3 (I)**) is the simplest method with small experimental effort and low cost for the measurement equipment.

Saturated sodium chloride solution is a tracer that increases the conductivity of the continuous liquid phase after injection, and a sensor at the centrate tracks the change in conductivity until no change occurs. To avoid phase separation during conductivity measurement, the operator must ensure that the density of the sodium chloride solution is close to the density of the continuous phase.

The method has been successfully applied to vertical solid bowl, tubular bowl and decanter centrifuges. Residence time measurements for vertical and tubular bowl centrifuges show a broad distribution. This distribution differs significantly from the behavior calculated by plug or boundary layer flow (Konrath et al., 2015; Romani Fernández, 2012). In the case of a decanter centrifuge, the volume flow and the solids content have a significant influence on the residence time distribution (Frost, 2000).

Another method of indirectly measuring flow behavior is to experimentally characterize system behavior (**Fig. 3 (II)**)

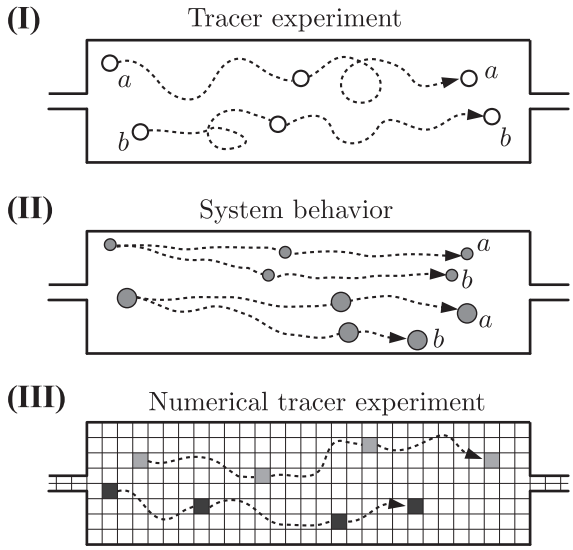


Fig. 3 Schematic representation of three methods to determine residence time behavior. **(I)** Tracer experiment, **(II)** Characterization of system behavior, **(III)** Numerical simulation. Reprinted with permission from Ref. (Gleiß, 2018) under the terms of the CC-BY 4.0 license. Copyright: 2018, the Authors, published by KIT scientific publishing.

by examining a step response following a sudden change in volumetric flow rate or solids volume fraction during feeding. Compared to tracer experiments, step response measurements require considerably more equipment. An experimental setup consists of two storage tanks for two feed suspensions with different solids volume fractions and a three-way valve to cause a sudden change in the feed composition. Time-dependent analysis of the step response can be performed by time sampling of the centrate flow and gravimetric measurement of the solids volume fraction (Gleiss et al., 2017). A more automated method of measuring step response is to integrate a turbidity sensor on the centrate for on-line prediction of solids content (Konrath et al., 2014).

The third promising approach to characterize the residence time behavior is CFD simulation (**Fig. 3 (III)**), which requires a model to evaluate the flow behavior in solid bowl centrifuges (Gleiß, 2018). Numerical simulations are usually not possible without calibration with experimental data, as CFD relies on many assumptions, such as turbulence models.

3. Separation behavior

The selection and operation of solid bowl centrifuges depends not only on the flow conditions, but also on the material properties, which are influenced by the particle and liquid phase properties. Particle size, particle shape, particle interactions, solids content, densities, and liquid viscosity play an important role. Moreover, a distinction must be made between the properties of individual particles, agglomerates and bulk materials (Hammerich et al., 2019a). When evaluating the separation process in batch or semi-batch centrifuges, the sedimentation behavior and sediment build-up are important parameters. For continuous centrifuges, sediment transport and discharge must also be taken into account (Karolis et al., 1986). It is not possible to draw general theoretical conclusions about the separation process in solid bowl centrifuges because the influencing variables at the particle level are manifold.

Table 2 Comparison of hindered settling functions to describe the settling behavior of a concentrated slurry with uniform settling velocity.

Author	Hindered settling function
Richardson et al. [a]	$v = v_{St}(1-\phi)^{n_{RZ}}$
Michaels et al. [b]	$v = v_{St}\left(1-\frac{\phi}{\phi_{max}}\right)^{n}$
Ekdawi et al. [c]	$v = v_{St}(1-\phi)\left(1-\frac{\phi}{\phi_{max}}\right)^{\mu_1\phi_{max}}$

[a](Richardson et al., 1954), [b](Michaels et al., 1962), [c](Ekdawi et al., 1985)

3.1 Settling behavior

Sedimentation is the settling of particles in a surrounding liquid phase. Typically, sedimentation can be divided into four areas: free settling, cluster formation, cluster breaking, and hindered settling (Bhatty, 1986). Free settling means that the particles do not interfere with each other and settle under Stokes' conditions. Moderate increases in solids content lead to clustering and faster settling. At a critical level, the clusters are destroyed by the upward flow, reducing the settling rate. Further increase in solids content leads to slower settling due to increased momentum exchange. Theoretical prediction of the described behavior as a function of particle properties is time-consuming and requires resolved simulations at the particle level (Romaní Fernández et al., 2013).

Experimental investigation of the influence of particle and continuous phase properties is therefore more effective. In practice, empirical material functions are commonly used to describe the influence of the solids content on the settling velocity. A large number of researchers have studied the settling behavior of monodisperse (Richardson et al., 1954) and polydisperse particles (Al-Naafá et al., 1989; Beiser et al., 2004; Ettmayr et al., 2001; Ha et al., 2002). This is summarized in **Table 2**. One approach to describe hindered settling is based on (Richardson et al., 1954) and is valid for monodisperse suspensions, where the exponent n_{RZ} depends on the particle Reynolds number. The approach by Michaels et al. (1962) treats flocculated systems and considers two correction factors (n, ϕ_{max}) for hindered settling. The approach by Ekdawi et al. (1985) takes into account the influence of maximum packing and liquid viscosity.

Table 3 Comparison of different empirical and semi-empirical equations describing compressive yield stress as a function of solids volume fraction.

Author	Compressive yield stress
Auzerais et al. [a]	$p_s = a\frac{\phi^n}{\phi_{max} - \phi}$
Buscall et al. [b]	$p_s = a(\phi - \phi_{gel})^m$
Green et al. [c]	$p_s = p_1\left[\left(\frac{\phi}{\phi_{gel}}\right)^{p_2} - 1\right]$
Landman et al. [d]	$p_s = p_1\left(\frac{\phi}{\phi_{gel}} - 1\right)^{p_2}$
Usher et al. [e]	$p_s = \left[\frac{a(\phi_{max} - \phi)(b + \phi - \phi_{gel})}{\phi - \phi_{gel}}\right]^{-k}$

[a](Auzerais et al., 1988), [b](Buscall et al., 1988), [c](Green et al., 1996), [d](Landman et al., 1995), [e](Usher et al., 2013)

For dilute suspensions and polydisperse particles, the settling velocity is not uniform. Rather, a settling velocity distribution can be observed in the experimental characterization (Balbierer et al., 2019). This makes the development of material functions much more complex, as the influence of different particle fractions or species on the sedimentation behavior must be taken into account.

3.2 Sediment formation process

Particles accumulate on the rotor wall after sedimentation and form a liquid-saturated sediment, which allows the transfer of normal and shear forces due to permanent particle contacts. A saturated sediment behaves either incompressible or compressible while forming.

Incompressible sediments consist mostly of coarser particles $x > 10$ µm. In this size range, inertial forces dominate, whereas in compressible sediments the influence of interparticle forces increases. If the particles are uniformly distributed in the sediment, incompressible materials have a constant porosity. In contrast, a compressible sediment exhibits a porosity gradient based on compressive forces in the sediment. Compressibility modeling combines compressive yield stress and solids volume fraction, where compressive yield stress is defined as the integral strength of a particle network.

Table 3 compares different material functions to model compressive yield stress depending on solids volume fraction. All presented models are empirical or semi-empirical equations which use fit parameters (a, b, k, m, n, p_1, and p_2) and characteristic value such as gel point ϕ_{gel} or maximum packing density ϕ_{max}. The gel point determines the transition from a suspension to a sediment (Skinner et al., 2016). Here, the material behavior changes abruptly, since forces are transferable in the sediment due to permanent particle contacts. The common practice is to fit the material functions to experimental data which are based on batch centrifugation test on a laboratory scale.

4. Material characterization

Laboratory and pilot scale trials are essential for the design and optimization of solid bowl centrifuges. However, due to the amount of material and time required, it is advisable to keep the experimental effort of pilot tests to a minimum. For this purpose, a variety of laboratory centrifuges are available to measure material-related properties such as particle size distribution, sedimentation behavior and sediment compressibility. These are described in more detail in the following sections.

4.1 Particle size distribution

The particle size is an imperative parameter for the evaluation and design of solid bowl centrifuges. Since the particles are not uniformly distributed, it is helpful to measure a particle size distribution (PSD).

Since most particles are non-spherical, the concept of equivalent diameter is applied to calculate particle size. The equivalent diameter is a reference value to the real particle diameter and depends on the measurement technique. Examples are the Sauter', the Feret', and the Stokes' diameter. For solid bowl centrifuges, it is desirable to use sedimentation-based methods for particle size analysis. All sedimentation methods have in common that the determination of the equivalent diameter is based on the Stokes' velocity.

Typically, sedimentation methods are divided into incremental or cumulative methods. For the incremental method, three main principles are conceivable: the pipette, the photo-, and the X-ray sedimentation method (Hayakawa et al., 1998). The cumulative method also differentiates three measuring principles: the manometer centrifuge, the sedimentation balance, and the imbalance centrifuge (Yoshida et al., 2001).

Two analytical centrifuges based on the incremental method are CPS disk centrifuge and LUMiSizer® analytical centrifuge (Detloff et al., 2007; Neumann et al., 2013).

The CPS disk centrifuge uses the well known principle of differential centrifugal sedimentation (DCS). The particle size is analyzed by applying a density gradient in the rotating disk. After injection of a small amount of suspension, the particles migrate in radial direction depending on their individual settling velocity. Particles are counted by a CCD sensor which measures the signal of a monochromatic laser beam.

In contrast to the DCS, the measuring principle of the LUMiSizer analytical centrifuge is the spatial and temporal measurement of absorbance in a rectangular cuvette (Detloff et al., 2007). Both methods use Stokes' settling velocity to calculate the equivalent particle diameter. This

supposes additional physical parameters such as the solid density, liquid density, liquid viscosity, and the refractive index of both phases.

There are other physical principles to measure particle size or shape distributions, such as laser diffraction, ultrasonic spectroscopy, X-ray scattering or dynamic light scattering. Details on the measuring principles can be found in (Frank et al., 2022).

4.2 Settling behavior measurement

The use of measuring cylinders in the Earth's gravitational field is one way to measure the sedimentation rate. For concentrated suspensions, experiments usually show a clear phase boundary between the clarified liquid and the sedimenting solids, indicating hindered settling (Lester et al., 2005). Modern instruments measure the settling velocity automatically (Horozov et al., 2004). To reduce measuring time, the settling behavior of finely dispersed particles can be determined using analytical centrifuges (Detloff et al., 2007). According to the measuring principle of particle size measurement, the temporal and spatial variation of absorbance along the radial position of a cuvette in the LUMiSizer is used to calculate the settling velocity distribution from experimental data.

4.3 Sediment characterization

Batch sedimenting centrifuges are also suitable for the experimental characterization of sediment formation. There are several methods that differ in the amount of measurement required and the complexity of data post-processing. The simplest method is to centrifuge a sample at constant speed and measure the solids volume fraction gravimetrically. The volume-averaged compressive yield stress can be derived from the analysis of the sediment at different speeds. However, information about the porosity gradient in the sediment is lost by this method. Alternatively, two different measurement setups in combination with batch sedimenting centrifuges allow to measure the local solids volume fraction as a function of sediment height.

The centrifuged sediment can be divided into a defined number of layers after centrifuging. The solid volume fraction of each layer is then measured gravimetrically. A disadvantage of this method is the destruction of the sediment.

Non-invasive X-ray measurements are another promising technique for the analysis of local sediment structures. Examples for measuring cake structures with X-rays are the LUMiReader X-Ray or micro-computed tomography (μCT) (Peth, 2010). Both measurement principles are limited to the Earth's gravitational field, which requires a two-step measurement procedure based on centrifugation and subsequent X-ray measurement (Sobisch et al., 2016).

Fig. 4 illustrates the experimental result of the mentioned two-step procedure for solids volume fraction depending on sediment height. The suspension studied was a mixture of limestone and water, which was first centrifuged and then measured in the LUMiReader X-Ray.

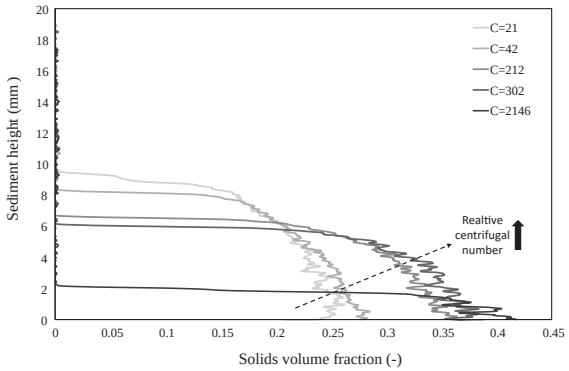


Fig. 4 Spatial distribution of solids volume fraction in a limestone sediment as a function of centrifugal acceleration. The measurement requires a two-step measuring procedure. First, suspension is centrifuged with the LUMiSizer analytical centrifuge at a speed. Subsequently, the sediment structure is investigated with X-Ray measurement with the LUMiReader X-Ray.

Closer examination of the measured data serves to study the influence of the relative centrifugal number on the compressibility of the formed sediment. Two effects are observable. First, the solids volume fraction increases toward the bottom of the cell. Second, the solids volume fraction of the sediment shifts to a higher value with increasing centrifugal acceleration.

However, this method is only applicable to sediments that exhibit plastic behavior. This means that the sediment does not tend to elastic recovery after reducing the centrifugal force (Hammerich et al., 2019b). Typically, biological systems tend to behave elastically due to the existing cell structure (Usher et al., 2013).

Additionally, the sediment transport in decanter centrifuges leads to a superposition of shear yield and normal stress (Erk et al., 2004). Shear stress moves and rearranges the particles in the sediment, resulting in denser packing (Hammerich et al., 2020; Radel et al., 2022).

To study the influence of shear yield stress on the sediment compressibility, several measurement principles can be found in the literature. One method is to measure the effect of shear in a vane-under-compressional-loading rheometer (Höfgen et al., 2020). Here, a cylinder at the top of the rheometer produces a normal stress on the sediment, while at the same time a vane rotates at a constant angular velocity and introduces a shear yield stress. Furthermore, modified ring shear cells are suitable to analyze sediments with a saturation of $S = 1$. This involves the modification of the ring shear cell by incorporating semi-permeable membranes at the top and bottom to allow the liquid to escape during the experiment (Erk et al., 2004; Hammerich et al., 2020).

5. Modeling of solid bowl centrifuges

During process development, accurate estimation of centrifuge type and size with the lowest possible product and resource consumption is essential. It is also important to optimize existing solid bowl centrifuges to increase productivity and minimize energy consumption and maintenance.

The following section provides an overview of different methods for predicting centrifuge size and process behavior. A variety of approaches can be found in the literature. This review focuses on the scale-up using analytical equations such as sigma theory, process modeling for real-time simulation, CFD simulations of solid bowl centrifuges, and the extension of process modeling to gray-box models to improve the predictive accuracy of process models (Menesklou et al., 2021a).

5.1 Steady-state models

The first published theory to describe clarification in solid bowl centrifuges is the Sigma theory (Ambler, 1952). Sigma theory is based on several assumptions. These include spherical particles in a creeping flow, uniform flow, and Stokes settling. Also, the approach neglects insufficient pre-acceleration or turbulences, resulting in the assumption of uniform distribution of the solid at the feed. Furthermore, hydrodynamic interactions between solid and liquid which are present for high solids content and the sediment build-up are also not considered (Leung, 1998).

The basis of the original Sigma theory is a shallow pond with ($r_w/r_b \geq 0.75$). Here, r_w is the weir radius and r_b is the bowl radius. Extensions are available for deep pond solid bowl centrifuges ($r_w/r_b \leq 0.65$) (Records and Sutherland, 2001). To predict the clarification, the theory assumes that a solid bowl centrifuge removes the cut size with a probability of 50 %. With the above assumption, the flow rate of a solid bowl centrifuge can be calculated by the product of settling velocity in the earth's gravity field and the Σ-value which is defined as an equivalent clarification area:

$$Q_f = 2\,\Sigma\,v_g \tag{2}$$

Looking more closely at **Table 4**, the Σ-value considers the influence of the centrifuge geometry by integrating the weir radius, the bowl radius, and the centrifuge length. Additionally, the Σ-value takes the angular velocity into account. At this point it should be noted, that there are further modifications of the Sigma theory, which can be found in the literature (Ambler, 1952; 1959). Due to the previously mentioned assumptions underlying the Sigma theory, it is not reasonable to use this approach for designing the capacity of a solid bowl centrifuge. Instead, Sigma theory is applied to transfer for a geometrically similar machine to a larger scale with known experimental pilot scale data. For tubular bowl and decanter centrifuges, the radial dimension is defined by the bowl radius and the weir radius. For disc stack centrifuges the radial dimension is defined by r_{do}, r_{di} and θ, which are the outer radius, inner radius and inclination angle of the disc channel.

Table 4 Overview of Σ-value for different types of solid bowl centrifuges. According to Ref. (Ambler, 1961).

Centrifuge type	Sigma value
Batch sedimenting centrifuges	$\Sigma = \dfrac{\omega^2 V}{4.6 \log\left(\dfrac{2r^2}{r_w + r_b}\right)}$
Tubular bowl or decanter centrifuges (shallow pond)	$\Sigma = \dfrac{\pi l \omega^2}{g} \dfrac{(r_b^2 - r_w^2)}{\ln\left(\dfrac{2r_b^2}{r_b^2 - r_w^2}\right)}$
Tubular bowl or decanter centrifuges (deep pond)	$\Sigma = \dfrac{\pi l \omega^2}{2g} \dfrac{(r_b^2 - r_w^2)}{\ln\left(\dfrac{r_b^2}{r_w^2}\right)}$
Disc stack centrifuges	$\Sigma = \dfrac{2\pi n \omega^2}{3g}(r_{do}^3 - r_{di}^3)\cot\theta$

In terms of practice, this means that pilot tests are essential for the selection and scale-up of solid bowl centrifuges. For the description of two geometrically similar machines the following equation is valid:

$$\frac{Q_{f2}}{Q_{f1}} = \frac{\Sigma_2}{\Sigma_1} \tag{3}$$

The integration of correction factors ξ_1 and ξ_2 allows to transfer for non-geometrically similar machines:

$$\frac{Q_{f2}}{Q_{f1}} = \frac{\xi_2}{\xi_1}\frac{\Sigma_2}{\Sigma_1} \tag{4}$$

Another mathematical model for the scale-up of decanter centrifuges is the g-volume, which is a modified form of the sigma theory. Similar to the Sigma theory, the g-volume also allows the comparison of geometrically different decanter centrifuges. The g-volume is the ability of a decanter to clarify a suspension, but is not a measure of the available surface area as in the Sigma theory, but of the available centrifuge volume.

Therefore, the g-volume approach considers the influence of sediment build-up on the clarification process (Stahl, 2004). The dimensionless Leung number has been developed for spin tube, disk, tubular bowl, and decanter centrifuges. Leung number depends on the properties of suspended particles, liquid and design parameters (Leung, 2004).

5.2 CFD simulation

CFD is based on the conservation of mass and momentum, also known as the Navier-Stokes equations. The Navier-Stokes equations can only be solved using numerical methods such as the finite volume method. This

requires a computational grid. The advantage of CFD is the ability to simulate temporal and spatial changes in velocity and pressure. The optimization of solid bowl centrifuges is an interesting task in terms of process behavior and energy consumption. However, due to the presence of several phases (gas, liquid and solid), the simulation of the material behavior is very challenging. In addition, high pressure and velocity gradients lead to very small time steps.

When simulating multiphase flows, CFD distinguishes between the Euler-Euler and Euler-Lagrange methods. The Euler-Euler method treats the continuous and disperse phases as interacting continua. A volume-averaged drag force, allows to model the momentum exchange between several phases. In contrast, the Euler-Lagrange method uses a Euler model to estimate the behavior of the continuous phase. The dispersed phase is modeled by Newton's equation of motion. The implementation of a drag force is essential to calculate the momentum exchange between discrete particles and the liquid phase.

One problem with the computational time of the Euler-Lagrange method is that sediments in solid bowl centrifuges consist of billions of particles. Simulating this large number of particles is not possible with today's computing power.

One promising method to solve this issue is to reduce the domain size. For solid bowl centrifuges, this means that only specific parts of the machine such as the infeed wheel or discharge zone are simulated (Bell et al., 2016; Törnblom, 2018).

A suitable method for simulating the velocity and pressure field of gas-liquid flows without taking into account the influence of particles is the Volume-of-Fluid (VOF) method (Hirt et al., 1981). VOF is mostly used to simulate gas-liquid interfaces by incorporating the surface tension as volume force into conservation of momentum (Romani Fernández et al., 2009). The VOF approach is well suited for the optimization process of solid bowl centrifuges with the target of minimized friction loss of the rotating liquid pond to ensure rigid-body motion (Romani Fernández et al., 2010). Furthermore, the coupling of CFD with the discrete element method (DEM) is also used to study the temporal change of sediment build-up (Romani Fernández et al., 2013). DEM uses additional forces for particle and particle–wall interactions by considering nonlinear contact models.

Another method to study the process of sediment build-up in solid bowl centrifuges is based on an extended mixture model, as this involves significantly lower computational costs compared to Euler-Euler or Euler-Lagrange models (Hammerich et al., 2018).

The extended mixture model does not solve the mass and momentum conservation for each phase separately, but considers the suspension as a mixed phase. The algorithm is based on different rheological models for the suspension and the sediment. Power laws are suitable to consider the influence of solids volume fraction on suspension viscosity (Quemada, 1977). Whereas sediments in many cases have a yield point which depends for compressible materials on the solid volume fraction (Erk et al., 2004).

Fig. 5 (I) shows the simulation of the sediment formation process for a constant time step in a tubular bowl centrifuge for two scenarios: a cohesive non-flowable (1.) and a pasty flowable material (2.) (Hammerich et al., 2019a). The rheological behavior of the sediment has a significant influence on the sediment distribution. For easily flowable materials, shear forces at the sediment surface result in a sediment transport and a uniform distribution of the accumulated solids. For cohesive materials, the friction

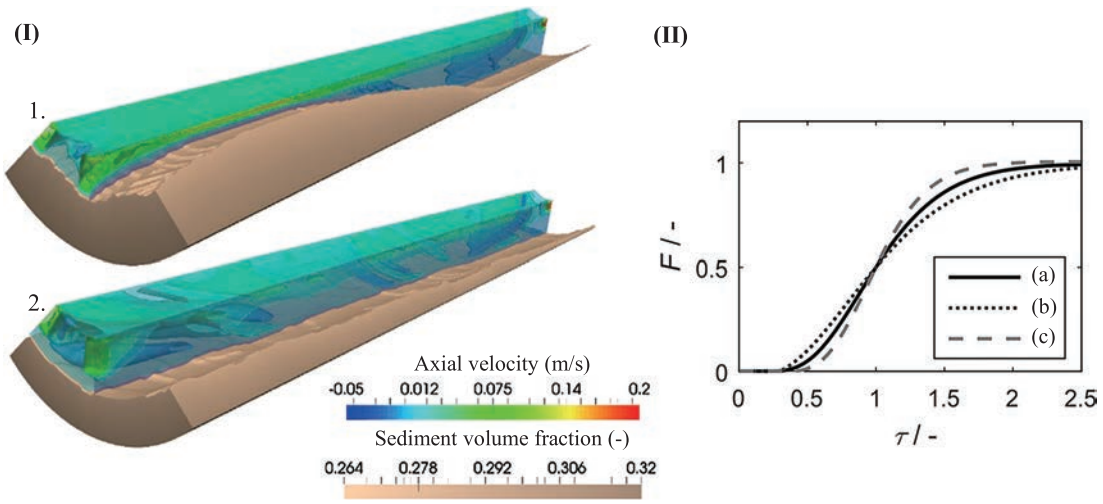


Fig. 5 **(I)** Contour plot of axial velocity and sediment solids volume fraction in a tubular bowl centrifuge type Z11 for two materials with different rheological behavior. 1. Cohesive non-flowable sediment. 2. Pasty, flowable sediment. **(II)** Residence time distribution F as a function of flow number τ for three cases: empty machine (a), sediment formation process of a cohesive sediment (b) and a pasty sediment (c). Adapted with permission from Ref. (Hammerich et al., 2019a). Copyright 2019, Wiley.

within the sediment is high and a slope angle has formed, leading to higher axial dispersion and back-mixing in the flow domain.

Additionally, **Fig. 5 (II)** compares the residence time distribution F depending on the flow number τ for three different scenarios. The flow number is the ratio of elapsed time to mean residence time and allows to compare the residence time distribution of different centrifuges and operating conditions.

Further investigations are devoted to the flow field in disk stack centrifuges. For biological systems, the shear stress in the feed and discharge zone is crucial to keep the stress on microorganisms low and the vitality high, such as in mammalian cell cultures (Shekhawat et al., 2018). To predict the separation behavior of a disk stack centrifuge, detailed information about the flow and particle trajectories within two disks is necessary. A suitable simulation method is direct numerical simulation (DNS) which can be used to predict flow instabilities that significantly affect particle trajectories (Janoske et al., 1999b). Furthermore, CFD is a promising method to compare different centrifuge types such as disk stack and tubular bowl centrifuges (Esmaeilnejad-Ahranjani et al., 2022).

The complex geometry of a decanter centrifuge with the rotating screw conveyor and the cylindrical-conical bowl makes it difficult to study the process behavior. Few studies have focused on olive oil and polymer production (Zhu et al., 2013; 2020). Current studies assume stationary rotation and apply a multi reference frame (MRF) (Zhu et al., 2020). MRF is a stationary approach to treat rotation of a system and does not consider the transient nature of the relative motion between the screw conveyor and the centrifuge bowl.

In summary, some numerical studies are available. However, some simplifications have been made here in the area of turbulence modeling and momentum exchange between solid and liquid.

5.3 Process modeling

In contrast to CFD, the goal of process modeling is to have a simplified model that can predict the dynamic behavior with minimal computational effort. Ideally, process models should be faster than real-time simulation to enable further applications such as advanced process control (Sinn et al., 2020).

5.3.1 Batch sedimenting centrifuges

A widely used approach to simulate the sedimentation-consolidation process for batch sedimenting centrifuges is based on a 1D advection-diffusion equation (Bürger et al., 2001; Garrido et al., 2003). These 1D models assume highly concentrated suspensions where hindered settling is present to neglect the influence of segregation (Kynch, 1952).

Essential material properties are the flux density function, the effective solid stress, the density of solid and liquid phase, and the liquid viscosity (Garrido et al., 2000). A major limitation of 1D models is that they are not suitable for capturing the physical behavior caused by internal disks in disk stack centrifuges, sediment transport in decanter centrifuges, and particle classification for low concentrated suspensions in tubular bowl centrifuges. Models that consider the geometry and the influence of the particle size distribution are necessary to describe the above process behavior.

5.3.2 Tubular bowl centrifuges

The modeling of the technical separation in tubular bowl centrifuges is complex, since the flow conditions and material properties have a significant influence on the process behavior. One promising strategy to simulate the process behavior of tubular bowl centrifuges is a pseudo-2D compartment approach. The idea of compartmentalization is to distribute the particles along the axial length of the rotor based on the calculated sedimentation path, see **Fig. 6 (II)** (Spelter et al., 2013). Compared to steady-state models such as the Sigma theory, the pseudo-2D compartment model predicts the temporal change of sediment build-up and the degree of filling. The degree of filling is the ratio of sediment to centrifuge volume and provides information about the current filling status. One limitation of the pseudo-2D compartment model is the modeling of the particle motion which is based on the assumption of a plug flow neglecting the influence of the turbulences and back-mixing (Spelter et al., 2013).

The extension of pseudo-2D to 2D compartment modeling addresses the previously discussed limitation by accounting for nonideal flow behavior by interconnecting a defined number of compartments to approximate the residence time behavior of tubular bowl centrifuges (Gleiss et al., 2020). **Fig. 6** illustrates the differences between the two presented algorithms. The 2D compartment model divides the tubular bowl centrifuge into two zones: the sedimentation and sediment zone. Both zones consider different material streams and material functions to capture the physical behavior of the suspension and sediment. The upper zone is the sedimentation zone. Compartments of the sedimentation zone consist of one incoming and two outgoing streams. The feature of the algorithm is to calculate the particle classification along the rotor for a predefined number of particle classes. A more detailed description of the algorithm can be found in (Gleiss et al., 2020).

The sediment zone is located below the sedimentation zone to calculate the sediment build-up for incompressible and compressible materials. A compartment of the sediment zone consists of one ingoing stream which represents the separated solids from the sedimentation zone. The relationship between compressive yield stress and solids

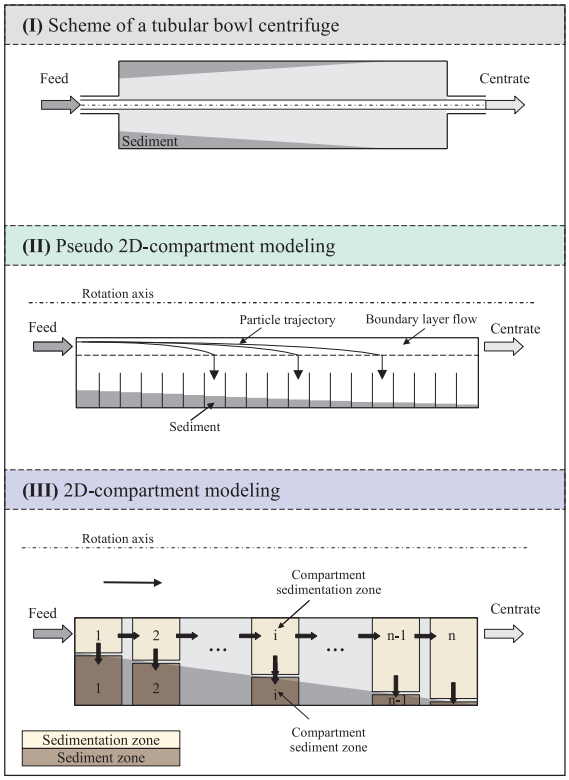


Fig. 6 **(I)** Schematic representation of a tubular bowl centrifuge. **(II)** Pseudo 2D-compartment modeling according to Ref. (Spelter et al., 2013) with the discretized sediment zone. **(III)** 2D-compartment modeling of a tubular bowl centrifuge based on the interconnection of compartments which are based on the sedimentation and sediment zone (Gleiss et al., 2020).

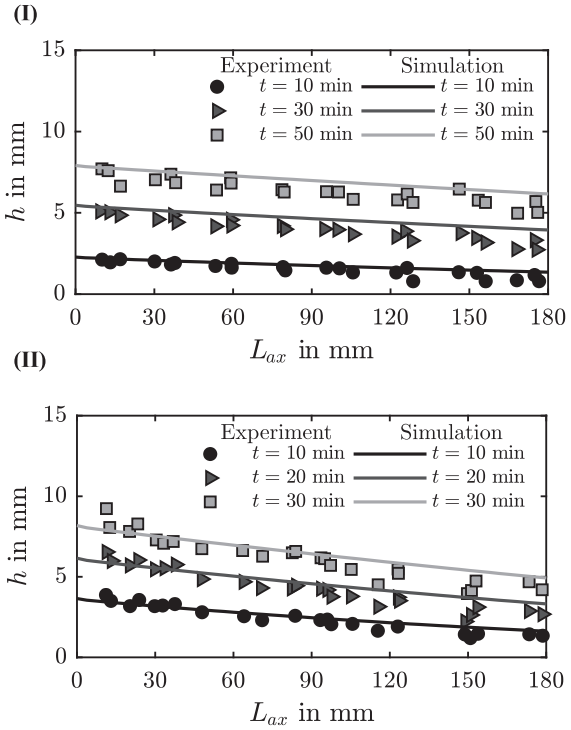


Fig. 7 Comparison between simulation and experiment for sediment distribution along the axial length L_{ax} of the rotor for colloidal silica particles at a constant flow rate of 0.2 L/min. **(I)** C = 19,200, **(II)** C = 38500.

volume fraction is used to compute sediment compressibility which can be measured in batch sedimenting centrifuges as mentioned earlier in **Section 4.3**.

It should be noted that the sediment influences the separation process, as the available free flow cross-section is reduced and results in a shorter residence time.

Fig. 7 depicts the comparison between simulation and experiment for the sediment distribution of colloidal silica particles at a flow rate of 0.2 L/min and two different centrifugal numbers of C = 19,200 **(I)** and C = 38,500 **(II)** for a tubular bowl centrifuge type Z11 from CEPA. The flow direction is from left to right. As already mentioned, particles accumulate at the inner wall of the rotor. Due to the polydispersity of the particle system and different settling velocities, the sediment accumulation is not uniform, but has a constant slope along the axial length of the tubular bowl centrifuge. A closer look at the relative centrifugal numbers C = 19,200 and C = 38,500 shows different time intervals for the filling process. For C = 38,500, the rotor fills faster compared to C = 19,200, because the centrifugal force leads to faster settling rates and therefore faster solids accumulation. Analytical equations such as the Sigma theory (see **Section 5.1**) do not allow to estimate temporal changes in solid bowl centrifuges. However, this is necessary to achieve a constant separation performance, especially for tubular bowl centrifuges.

5.3.3. Decanter centrifuges

The modeling of decanter centrifuges requires the consideration of sediment transport as one of the most important influencing variables during operation. As mentioned earlier, the material properties of the sediment are critical, and a distinction must be made between incompressible and compressible sediments. For incompressible materials, friction between the material, the screw conveyor and the centrifuge bowl is dominant. Friction in the conical part of the machine has the highest impact on the screw torque (Bell et al., 2014; Reif and Stahl, 1989). After the material leaves the liquid pond, undersaturation occurs which increases the frictional forces. The required power consumption can be determined from four components: feed acceleration, product transport, windage and power transmission losses (Bell et al., 2014).

In contrast, compressible sediments have a totally different transport behavior. The pasty consistency leads to considerable difficulties during sediment transport when applying unfavorable operating conditions. This can lead to total failure of the machine. However, so far only simplified material functions and models can be found which represent the rheological behavior of compressible sediments with good accuracy (Karolis et al., 1986). As

previously described, the material has a yield point depending on solids volume fraction (Erk et al., 2004; Mladenchev, 2007).

For decanter centrifuges, the concept of 2D compartment modeling is also a suitable approach to calculate the process behavior (Gleiss et al., 2017). However, the approach needs to be extended to the process behavior of decanter centrifuges. **Fig. 8 (I)** shows the structure of a 2D compartment model for countercurrent decanter centrifuges. In contrast to tubular bowl centrifuges, the simulation domain is an unrolled screw channel which is formed by the screw conveyor and the overflow weir. Furthermore, **Fig. 8 (II)** illustrates the detailed structure of a single compartment with the inlet and outlet flows (Menesklou et al., 2020). The 2D compartment model for decanter centrifuges considers two additional material streams in the sediment zone to model the sediment transport by screw conveyor system (Menesklou et al., 2020). The applicability of the 2D compartment approach for scale-up purposes was tested using different decanter centrifuges. **Fig. 9 (I)** depicts the comparison between simulation and experiment for the solids mass fraction in the centrate for three countercurrent decanter centrifuges of different sizes, which are not geometrically similar. With increasing speed, a higher centrifugal force occurs and the solids mass fraction of the centrate decreases. Another application of 2D compartment modeling is to simulate the solids mass fraction of the sediment, see **Fig. 9 (II)** (Menesklou et al., 2021b). The material functions were determined at laboratory scale and integrated into the 2D compartment model. The successful simulation of different machine sizes is a first step away from many pilot tests towards a predictive design and scale-up starting from laboratory tests to significantly reduce the number of pilot tests.

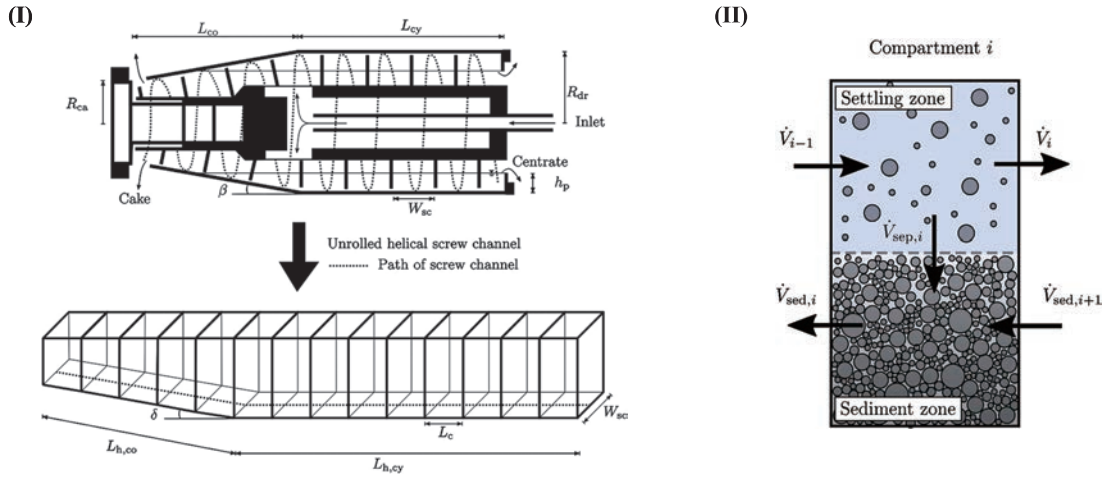


Fig. 8 **(I)** Schematic representation of a countercurrent decanter centrifuge and unrolled helical screw channel which is the basis of the 2D-compartment model. **(II)** Ingoing and outgoing streams for the sedimentation and sediment zone of one compartment in the 2D compartment approach. Adapted from Ref. (Menesklou et al., 2020) with permission from Elsevier, Copyright 2020.

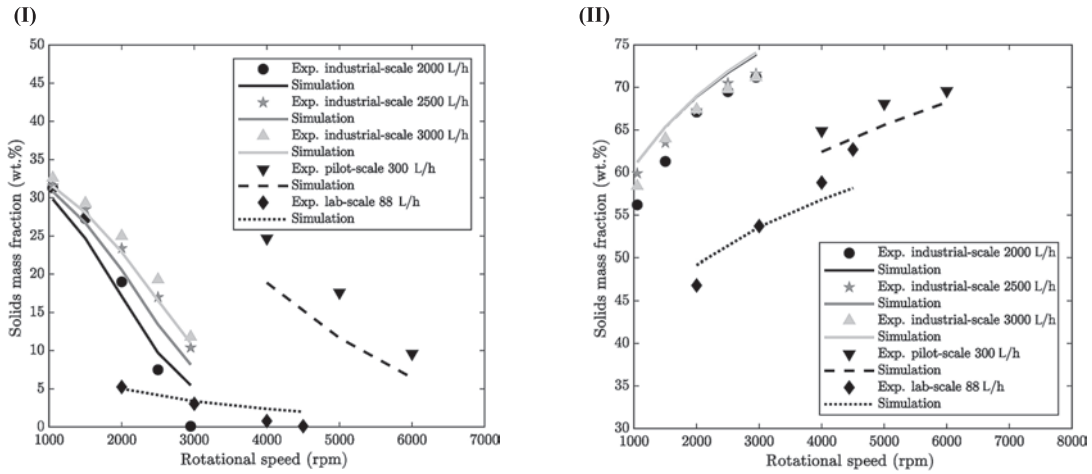


Fig. 9 **(I)** Comparison between simulation and experiment for solids mass fraction of the centrate for three countercurrent decanter centrifuges of different size which are not geometric similar. **(II)** Comparison between simulation and experiment for the mean solids mass fraction of the concentrate for three countercurrent decanter centrifuges of different size which are not geometric similar. The investigated product was finely dispersed limestone. Reprinted from Ref. (Menesklou et al., 2021b) under the terms of the CC-BY 4.0 license. Copyright: (2021) The Authors, published by MDPI.

A further application of a decanter centrifuge is the particle classification, where the local flow behavior is crucial for accurately predicting the particle size distribution in the centrate. While the 2D compartment model assumes a uniform flow profile and ideal back-mixing, extensions of the approach take into account the local flow profile and the influence of screw conveyor motion on the flow (Bai et al., 2021a).

5.3.4 Disk stack centrifuges

The process modeling of disc stack centrifuges is currently limited to the use of analytical equations and does not consider process dynamics. Existing models are steady-state and divide disk stack centrifuges into different zones: the pre-acceleration zone, the disk stack zone and the resuspension zone (König et al., 2020). However, it is also conceivable to apply the 2D-compartment model also to disk stack centrifuges. This would have the advantage of a uniform modeling strategy for different solid bowl centrifuges which would improve comparability and thus the selection of the optimal centrifuge type especially for industries where no centrifuge experts are not available.

5.4 Gray-box modeling

The idea of gray-box modeling is to combine white-box and black-box models. White-box models represent the physical laws, i.e. conservation of mass, momentum, and energy. An example of a white-box model is the 2D compartment model introduced in **Section 5.3**. Black-box models are mostly data-driven algorithms (e.g. support vector machines, linear, nonlinear regression, or neural networks) that are trained and validated with experimental data (Xiong et al., 2002). Data acquisition can be accomplished by integrating off-line, on-line, or in-situ measurement techniques to determine particle properties at the process. On-line and in-situ measurement has tremendous potential for the safe and cost-effective operation of solid bowl centrifuges and is necessary to collect data for gray-box models. Gray-box models are suitable for applications where white-box models are not accurate enough. For solid bowl centrifuges in particular, there is a complex relationship between centrifuge geometry, material properties and process conditions that has not been adequately captured by white-box models. At the same time, data-driven algorithms require a huge amount of experimental data which is often not available due to the costs of measurement equipment. Furthermore, black-box models are not extrapolatable and are difficult to adapt to new conditions without enough new experimental data.

Two basic structures of a gray-box model are the parallel and serial structures which are compared in **Fig. 10**. The advantage of the parallel structure is that the white-box and black-box models can be easily combined into a gray-box model. If the white-box model has a poor accuracy the black-box model takes over to simulate the process. A disadvantage of the parallel structure is that both models do not work simultaneously. Depending on the accuracy of the prediction, either the white-box or the black-box model is used for the calculation (Menesklou et al., 2021a). In the case of a white-box model with a poor accuracy, the gray-box model will be a pure black-box model, which needs a huge amount of data.

An improvement to the aforementioned drawback is the serial structure which uses the black-box model to be able to improve the uncertainties of the white-box model (Nazemzadeh et al., 2021). For example, it is conceivable to use the black-box model to predict the influence of flow conditions in a serial gray-box model structure or to correct separation-related properties, such as the hindered settling function, through on-line learning algorithms. However, this is challenging task and currently part of the research in the field of particle technology.

Fig. 11 shows experimental results of the solids mass fraction in the centrate of a pilot scale decanter centrifuge and simulation data based on a developed gray-box model based on a parallel structure. In this study, the white box model is the previously discussed 2D compartment model and the black box model corresponds to a neural network

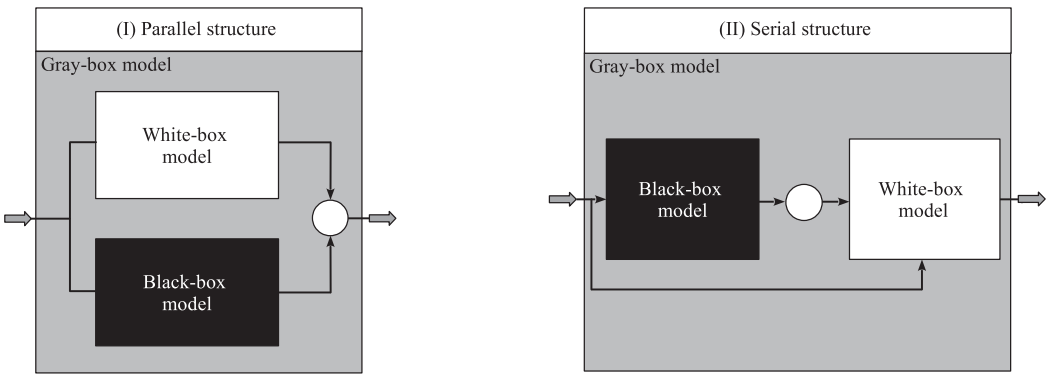


Fig. 10 Comparison between the two main structures of a gray-box model which is typically based on a deterministic and data-driven model. **(I)** Parallel structure **(II)** Serial structure.

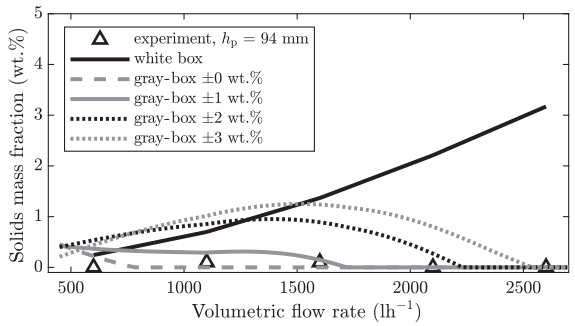


Fig. 11 Comparison between white-box and gray-box modeling for the investigated centrate mass fraction of a pilot-scale decanter centrifuge as a function of flow rate and confidence interval at constant speed. The model system is a limestone-water suspension. Reprinted from Ref. (Menesklou et al., 2021a) under the terms of the CC-BY 4.0 license. Copyright 2021, the Authors, published by MDPI.

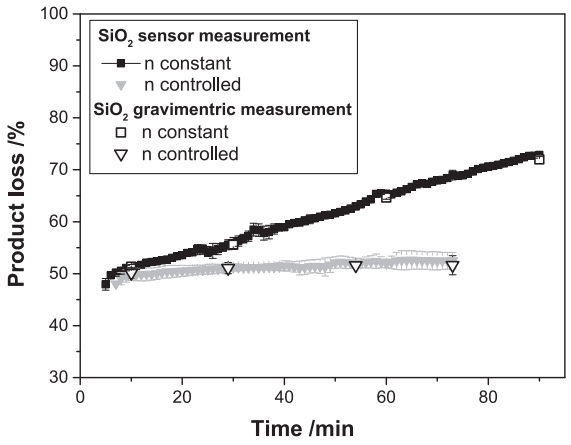


Fig. 12 Comparison of sensor data and gravimetric measurement for the product loss as a function of time for colloidal silica for the non-controlled case (*n* constant) and the controlled case (*n* controlled). For a tubular bowl centrifuge type Z11. Reprinted from Ref. (Konrath et al., 2014) with permission from Elsevier. Copyright 2014.

with one input, hidden and output layer. The training procedure of the neural network consists of a training and a test phase. The training data includes pilot test data for material properties measured at the feed, centrate and concentrate and the relevant process conditions.

Another important point for the application of a gray-box model with parallel structure is the confidence interval necessary to allow the intervention of the black-box model when the white-box model has a poor accuracy. For the case presented in **Fig. 11**, there is a deviation of the white-box model at higher speeds. The smaller the confidence interval is set, the earlier the correction of the white-box model prediction by the black-box model occurs. As mentioned earlier, this allows the prediction of process behavior for decanter centrifuges to be improved by integrating experimental data.

6. Process analytics

Process monitoring is playing an increasingly important role in optimizing the operation of solid bowl centrifuges to achieve a higher product quality and shorter setup times. To avoid reject rates or exceeding tolerance limits, quality control is moving from off-line to on-line, or in-situ applications. On-line measurements typically use a bypass to guide the material into the measurement system. In contrast to off-line measurements, on-line detection requires both a sampling system and often a dilution station to measure particle properties with high accuracy. The following section summarizes several measurement methods for on-line and in-situ characterization of particle and bulk properties that have been applied to solid bowl centrifuges.

6.1 On-line measurement of particle properties

In tubular bowl centrifuges, the flow conditions change over time due to the accumulated solids. To maintain consistent product characteristics, the rotor speed or flow rate must be adjusted during the centrifugation process. However, in order to change the rotor speed, it is essential to monitor the particle properties at the centrate. For dilute suspensions, light scattering sensors are suitable to determine the solids volume fraction on-line (Konrath et al., 2014). To integrate such a system into the process, calibration with the initial suspension is required. Typically, a dilution series is necessary, which can be characterized by off-line measurements.

Fig. 12 illustrates the comparison of the product loss for the controlled (*n* controlled) and the non-controlled (*n* constant) scenario for a tubular bowl centrifuge type Z11. The controller design is based on the step response after changing solids volume fraction at the feed. A closer look at **Fig. 12** reveals a fundamentally different process behavior for the non-controlled and the controlled case.

While the product loss increases with time for *n* = constant, since the machine fills continuously, the product loss remains constant for *n* = controlled. In this case, the decreasing residence time is compensated by increasing the rotational speed. Light scattering sensors can also be used to detect turbidity in the centrate of decanter and disk stack centrifuges to monitor centrate clarification and control the process to maintain product quality (Leung, 2007).

Another measurement system for on-line analysis of total suspended solids is UV-Vis spectroscopy. Unlike light scattering sensors, UV-Vis spectroscopy does not operate at a constant wavelength, but uses the full range of ultraviolet and visible light to produce an absorption spectrum. UV-Vis spectroscopy also requires extensive calibration based on a dilution series for the measured suspension. A promising technique to correlate the measured UV-Vis data with the solids volume fraction is the use of multivariate regression which is typically based on generalized ordinary least squares (Winkler et al., 2020). Another application of on-line UV-Vis spectroscopy is to detect the composition of

binary mixtures (Winkler et al., 2021). One example is the on-line measurement of polymethyl methacrylate (PMMA) and zinc oxide (ZnO) in an aqueous system. Both particle systems consist of submicron particles. For composition prediction, both components must scatter a UV-Vis signal at different wavelengths. By directly coupling UV-Vis data with product-related properties such as the product loss, the UV-Vis sensor acts as a soft sensor that directly outputs the quality of a classification, or fractionation process (Winkler et al., 2021).

Fig. 13(a) shows the comparison between off-line and on-line measurement of the temporal change of the product loss for the fractionation of PMMA and ZnO. The results indicate a good agreement between reference values and the prediction also for the variation of the centrifugal number. Additionally, **Fig. 13(b)** illustrates the prediction of the temporal change of the product loss during the classification of a suspension consisting of PMMA and water.

Another method of recording the change in solids volume fraction in the centrate over time is to use a measuring cell with a light source and a camera system. The measured data can be evaluated using a convolutional neural network (CNN). Prediction requires a pre-trained CNN that has been trained with experimental data (Bai et al., 2021b). The presented deep learning algorithm is a hybrid neural network based on a CNN and a short-term memory network (LSTM). The LSTM helps to ensure that previous data is not forgotten, when searching for the correct gradients during the new training period (Bai et al., 2021b). The measuring system can be applied to a low concentrated suspension with a solids mass fraction of up to 0.5 wt %, which allows to detect the clarification in the centrate. On-line measurement of particle size distribution is challenging, but there are several methods such as laser diffraction, ultrasonic extinction, and X-ray. The practicality of an instrument depends on the particle properties, the solids volume fraction, and the process itself. If the measurement time is less than the residence time, the instrument can be used directly for process control after successful calibration. However, if the measurement time is longer than the residence time, the direct coupling of process control and measurement is challenging due to the different time scales. Furthermore, most particle size measurement techniques are only suitable for a defined particle size range, making experiments irreplaceable.

6.2 In-situ measurement of slurry properties

The in-situ measurement of particle properties in solid bowl centrifuges is very challenging due to the high centrifugal acceleration and requires costly sensors, but provides detailed information about the local physical behavior. Several aspects are necessary for the application of in-situ sensors in solid bowl centrifuges. First, gaps are needed inside the rotor to install the sensors. Therefore, it is necessary to calculate the influence of the gaps on the mechanical strength of the rotor. Second, signal transmission requires a transmitter, e.g., Wi-Fi, to transmit the measured signal to the receiver.

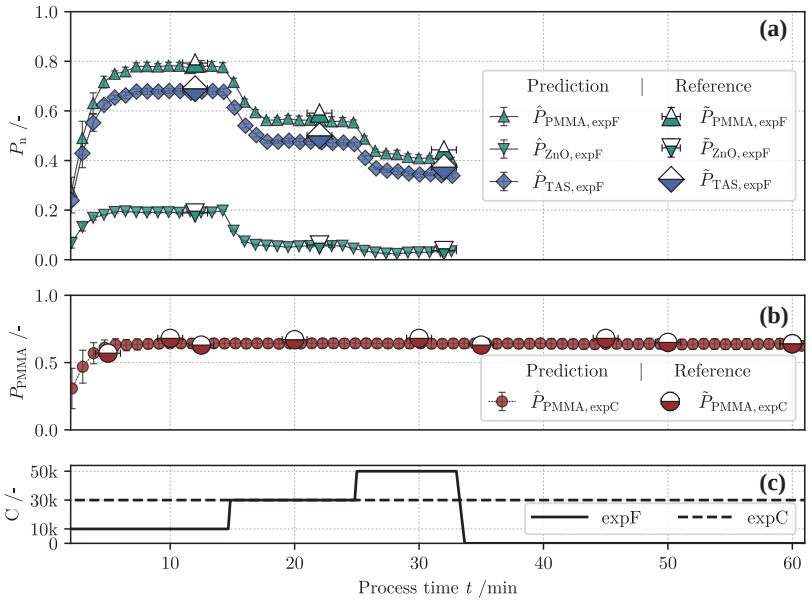


Fig. 13 **(a)** Comparison between soft-sensor prediction and reference for the temporal change of product loss for a binary mixture of polydisperse PMMA and ZnO particles for a tubular bowl centrifuge type Z11. **(b)** Comparison between soft-sensor prediction and reference for the temporal change of product loss P_{PMMA} for a polydisperse PMMA suspension at a constant relative centrifugal number C **(c)** Temporal change of relative centrifugal number for the two illustrated experiments **(a)** and **(b)**. Here, the solid line (expF) represents the centrifugal number for the case of a binary mixture **(a)** and the dashed line (expC) the PMMA system **(b)**. Reprinted from Ref. (Winkler et al., 2021) under the terms of the CC-BY 4.0 license. Copyright 2021, the Authors, published by MDPI.

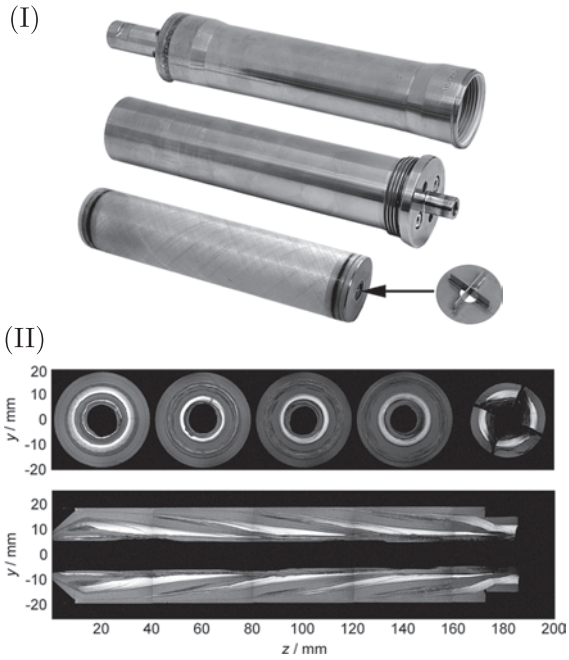


Fig. 14 **(I)** glass fiber reinforced plastic (GBP) tube and original rotor of tubular bowl centrifuge GLE from CEPA GmbH. **(II)** MRI analysis of rotor with longitudinal and lateral cross section. Flow direction from right to left. Adapted with permission from Ref. (Stahl et al., 2008). Copyright 2008, Wiley.

Wireless electrical resistance (WERD) is a technique to investigate sediment thickness at high relative centrifugal number (Prayitno et al., 2020). The measurement system records the change in electrical conductivity of the liquid phase in-situ by integrating multiple pairs of electrodes along the cylindrical conical bowl. The measured data can be used to indirectly calculate the solids volume fraction in the sediment.

An extension of this method is the Periodic Segmentation Technique in Wireless Electrical Resistance Detector (psWERD), which enables in-situ prediction of material functions such as the hindered settling function for decanter centrifuges. The periodic segmentation technique is necessary due to the influence of relative motion between the screw conveyor and the centrifuge bowl. The screw conveyor disturbs the measurement signal, due to the different material and is filtered by the periodic segmentation technique (Prayitno et al., 2022).

Another promising non-invasive and in-situ analysis of the sediment distribution is the Magnetic Resonance Imaging (MRI), which is an imaging technique based on the physical principle of nuclear magnetic resonance (Hardy, 2011). This is done by placing the rotor of the centrifuge in the tube of the tomograph.

In contrast to WERD or psWERD, the size of the tomography limits the application of MRI to small solid bowl centrifuges. An example of MRI is the study of sediment distribution in tubular bowl centrifuges (Spelter et al., 2013; Stahl et al., 2008). **Fig. 14 (I)** presents an adapted rotor of a tubular bowl centrifuge type GLE from CEPA. The rotor consists of a glass fiber reinforced plastic (GRP). The adapted rotor is necessary for the undisturbed MRI measurements of sediment distribution. The analysis of sediment involves a contrast agent such as carbon black (CB). CB generates a white contrast during MRI measurement, see **Fig. 14 (II)**. A closer look at **Fig. 14 (II)** depicts that the temporal filling process starts from the right (inflow) to the left (centrate). The axial flow and the simultaneous classification of the particles along the rotor explain the non-uniform sediment build-up according to the previously mentioned CFD results and process simulation.

In summary, in-situ measurement methods provide very accurate insight into the physical behavior of solid bowl centrifuges, but experiments are time-consuming and equipment costs are high, limiting their use to research.

7. Conclusions

This work presented an overview of research in the field of modeling and optimization of solid bowl centrifuges. Modeling on different time and length scales helps to better understand the physical behavior of solid bowl centrifuges and optimize their operation. One of the major challenges in the selection and development of suitable models arises from the influence of distributed particle properties.

Conventional steady-state methods for the design of solid bowl centrifuges are based on several assumptions and are not predictive without several pilot scale experiments. The transfer from pilot to industrial scale is usually only possible for geometrically similar machines in combination with decades of experience of the manufacturers. A counter idea to conventional methods is to apply process modeling and to consider material functions for separation-related properties such as sedimentation, sediment build-up, and sediment transport. The measurement of the material properties is not carried out on the pilot but on a smaller laboratory scale, with well-established laboratory centrifuges. Furthermore, CFD helps to gain a better understanding of the usually inaccessible parts of a solid bowl centrifuge. At the same time, CFD can be used to optimize different centrifuge geometries, such as the feed accelerator or other parts of the machine.

However, since any form of modeling is based on assumptions and therefore does not completely reproduce the physics, there will always be deviations. This is where gray-box models have great potential to successively improve the modeling of solid bowl centrifuges. Data-driven methods such as supervised learning and neural networks allow an intensive analysis of process data.

Nevertheless, this requires the measurement of particle properties on-line or in-situ by integrating process analytics. Various measurement techniques such as turbidity or UV-Vis sensors, camera systems, laser diffraction, ultrasonic extinction and X-ray are available. However, due to the

high cost of measuring equipment, individual testing of the particle system is necessary.

In summary, useful tools for the modeling and optimization of solid bowl centrifuges are available and their application has already been demonstrated in research. The task now is to further improve the algorithms and measurement methods. With further developments and the interconnection of gray-box models, process analytics, and advanced process control, the overriding goal of autonomous centrifugation will be possible in the future.

Acknowledgments

The authors gratefully acknowledge the funding by German Research Foundation (DFG) in the priority program SPP 1679 “Dynamic simulation of interconnected solids processes” and the Federal Ministry of Economic Affairs and Climate Action in the program IGF—Industrial Collective Research.

References

Al-Naafá M.A., Selim M.S., Sedimentation of polydisperse concentrated suspensions, The Canadian Journal of Chemical Engineering, 67 (1989) 253–264. DOI: 10.1002/cjce.5450670212

Ambler C.M., The evaluation of centrifuge performance, Chemical Engineering Progress, 48 (1952) 150–158.

Ambler C.M., The theory of scaling up laboratory data for the sedimentation type centrifuge, Journal of Microbial and Biochemical Technology, 1 (1959) 185–205. DOI: 10.1002/jbmte.390010206

Ambler C.M., The fundamentals of separation, including Sharples Sigma value for predicting equipment performance, Industrial and Engineering Chemistry Research, 48 (1961) 430–433.

Anlauf H., Recent developments in centrifuge technology, Separation and Purification Technology, 58 (2007) 242–246. DOI: 10.1016/j.seppur.2007.05.012

Arcigni F., Friso R., Collu M., Venturini M., Harmonized and systematic assessment of microalgae energy potential for biodiesel production, Renewable and Sustainable Energy Reviews, 101 (2019) 614–624. DOI: 10.1016/j.rser.2018.11.024

Auzerais F.M., Jackson R., Russel W.B., The resolution of shocks and the effects of compressible sediments in transient settling, Journal of Fluid Mechanics, 195 (1988) 437–462. DOI: 10.1017/S0022112088002472

Bai C., Park H., Wang L., Modelling solid-liquid separation and particle size classification in decanter centrifuges, Separation and Purification Technology, 263 (2021a) 118408. DOI: 10.1016/j.seppur.2021.118408

Bai C., Park H., Wang L., Measurement of solids concentration in aqueous slurries for monitoring the solids recovery in solid bowl centrifugation, Minerals Engineering, 170 (2021b) 107068. DOI: 10.1016/j.mineng.2021.107068

Balbierer R., Gordon R., Schuhmann S., Willenbacher N., Nirschl H., Guthausen G., Sedimentation of lithium–iron–phosphate and carbon black particles in opaque suspensions used for lithium-ion-battery electrodes, Journal of Materials Science, 54 (2019) 5682–5694. DOI: 10.1007/s10853-018-03253-2

Beiser M., Bickert G., Scharfer P., Comparison of sedimentation behavior and structure analysis with regard to destabilization processes in suspensions, Chemical Engineering and Technology, 27 (2004) 1084–1088. DOI: 10.1002/ceat.200403252

Bell G.R.A., Pearse J.R., Experimental and computational analysis of the feed accelerator for a decanter centrifuge, Proceedings of the Institution of Mechanical Engineers, Part E: Journal of Process Mechanical Engineering, 230 (2016) 97–110. DOI: 10.1177/0954408914539940

Bell G.R.A., Symons D.D., Pearse J.R., Mathematical model for solids transport power in a decanter centrifuge, Chemical Engineering Science, 107 (2014) 114–122. DOI: 10.1016/j.ces.2013.12.007

Bhatty J.I., Clusters formation during sedimentation of dilute suspensions, Separation Science and Technology, 21 (1986) 953–967. DOI: 10.1080/01496398608058389

Bürger R., Concha F., Settling velocities of particulate systems: 12. Batch centrifugation of flocculated suspensions, International Journal of Mineral Processing, 63 (2001) 115–145. DOI: 10.1016/S0301-7516(01)00038-2

Buscall R., Mills P.D.A., Goodwin J.W., Lawson D.W., Scaling behaviour of the rheology of aggregate networks formed from colloidal particles, Journal of the Chemical Society, Faraday Transactions 1: Physical Chemistry in Condensed Phases, 84 (1988) 4249–4260. DOI: 10.1039/F19888404249

Byrne E.P., Fitzpatrick J.J., Pampel L.W., Titchener-Hooker N.J., Influence of shear on particle size and fractal dimension of whey protein precipitates: Implications for scale-up and centrifugal clarification efficiency, Chemical Engineering Science, 57 (2002) 3767–3779. DOI: 10.1016/S0009-2509(02)00315-9

Caponio F., Summo C., Paradiso V.M., Pasqualone A., Influence of decanter working parameters on the extra virgin olive oil quality, European Journal of Lipid Science and Technology, 116 (2014) 1626–1633. DOI: 10.1002/ejlt.201400068

Detloff T., Sobisch T., Lerche D., Particle size distribution by space or time dependent extinction profiles obtained by analytical centrifugation, Powder Technology, 174 (2007) 50–55. DOI: 10.1016/j.powtec.2006.10.021

Ekdawi N., Hunter R.J., Sedimentation of disperse and coagulated suspensions at high particle concentrations, Colloids and Surfaces, 15 (1985) 147–159. DOI: 10.1016/0166-6622(85)80062-7

Erk A., Anlauf H., Stahl W., Fließeigenschaften feinstdisperser, gesättigter Haufwerke während ihrer Kompression im Zentrifugalfeld, Chemie-Ingenieur-Technik, 76 (2004) 1494–1499. DOI: 10.1002/cite.200407025

Erk A., Luda B., Influencing sludge compression in solid-bowl centrifuges, Chemical Engineering and Technology, 27 (2004) 1089–1093. DOI: 10.1002/ceat.200403260

Esmaeilnejad-Ahranjani P., Hajimoradi M., Optimization of industrial-scale centrifugal separation of biological products: comparing the performance of tubular and disc stack centrifuges, Biochemical Engineering Journal, 178 (2022) 108281. DOI: 10.1016/j.bej.2021.108281

Ettmayr A., Bickert G., Stahl W., Zur Konzentrationsabhängigkeit des Sedimentationsvorgangs von Feinstpartikelsuspensionen in Zentrifugen, F+S Filtrieren u. Separieren, 15 (2001) 58–65.

Faust T., Gösele W., Untersuchungen zur klärwirkung von dekantierzentrifugen, Chemie Ingenieur Technik, 57 (1985) 698–699. DOI: 10.1002/cite.330570814

Flegler A., Schneider M., Prieschl J., Stevens R., Vinnay T., Mandel K., Continuous flow synthesis and cleaning of nano layered double hydroxides and the potential of the route to adjust round or platelet nanoparticle morphology, RSC Advances, 6 (2016) 57236–57244. DOI: 10.1039/c6ra09553d

Flegler A., Wintzheimer S., Schneider M., Gellermann C., Mandel K., Tailored nanoparticles by wet chemical particle technology: from lab to pilot scale, in: Handbook of Nanomaterials for Industrial Applications, Elsevier, 2018, pp. 137–150.

Frost S., Neue Einblicke in die Abscheidung feiner Feststoffe in Dekantierzentrifugen, VDI-Verlag, 2000.

Garrido P., Bürger R., Concha F., Settling velocities of particulate systems: 11. comparison of the phenomenological sedimentation-

consolidation model with published experimental results, International Journal of Mineral Processing, 60 (2000) 213–227. DOI: 10.1016/S0301-7516(00)00014-4

Garrido P., Concha F., Bürger R., Settling velocities of particulate systems: 14. unified model of sedimentation, centrifugation and filtration of flocculated suspensions, International Journal of Mineral Processing, 72 (2003) 57–74. DOI: 10.1016/S0301-7516(03)00087-5

Ginisty P., Mailler R., Rocher V., Sludge conditioning, thickening and dewatering optimization in a screw centrifuge decanter: which means for which result?, Journal of Environmental Management, 280 (2021) 111745. DOI: 10.1016/j.jenvman.2020.111745

Gleiß M., Dynamische Simulation der Mechanischen Flüssigkeitsabtrennung in Vollmantelzentrifugen, KIT Scientific Publishing, Karlsruhe, 2018.

Gleiss M., Hammerich S., Kespe M., Nirschl H., Application of the dynamic flow sheet simulation concept to the solid-liquid separation: separation of stabilized slurries in continuous centrifuges, Chemical Engineering Science, 163 (2017) 167–178. DOI: 10.1016/j.ces.2017.01.046

Gleiss M., Nirschl H., Dynamic simulation of mechanical fluid separation in solid bowl centrifuges, in: Dynamic Flowsheet Simulation of Solids Processes, 2020, pp. 237–268. DOI: 10.1007/978-3-030-45168-4_7

Gösele W., Schichtströmung in röhrenzentrifugen, Chemie Ingenieur Technik, 40 (1968) 657–659. DOI: 10.1002/cite.330401307

Green M.D., Eberl M., Landman K.A., Compressive yield stress of flocculated suspensions: determination via experiment, AIChE Journal, 42 (1996) 2308–2318. DOI: 10.1002/aic.690420820

Ha Z., Liu S., Settling velocities of polydisperse concentrated suspensions, Canadian Journal of Chemical Engineering, 80 (2002) 783–790. DOI: 10.1002/cjce.5450800501

Haller N., Greßlinger A.S., Kulozik U., Separation of aggregated β-lactoglobulin with optimised yield in a decanter centrifuge, International Dairy Journal, 114 (2021) 104918. DOI: 10.1016/j.idairyj.2020.104918

Haller N., Kulozik U., Separation of whey protein aggregates by means of continuous centrifugation, Food and Bioprocess Technology, 12 (2019) 1052–1067. DOI: 10.1007/s11947-019-02275-1

Hammerich S., Gleiß M., Kespe M., Nirschl H., An efficient numerical approach for transient simulation of multiphase flow behavior in centrifuges, Chemical Engineering & Technology, 41 (2018) 44–50. DOI: 10.1002/ceat.201700104

Hammerich S., Gleiß M., Nirschl H., Modeling and simulation of solid-bowl centrifuges as an aspect of the advancing digitization in solid-liquid separation, ChemBioEng Reviews, 6 (2019a) 108–118. DOI: 10.1002/cben.201900011

Hammerich S., Gleiss M., Stickland A.D., Nirschl H., A computationally-efficient method for modelling the transient consolidation behavior of saturated compressive particulate networks, Separation and Purification Technology, 220 (2019b) 222–230. DOI: 10.1016/j.seppur.2019.03.060

Hammerich S., Stickland A.D., Radel B., Gleiss M., Nirschl H., Modified shear cell for characterization of the rheological behavior of particulate networks under compression, Particuology, 51 (2020) 1–9. DOI: 10.1016/j.partic.2019.10.005

Hardy E.H., NMR Methods for the Investigation of Structure and Transport, Springer Science & Business Media, 2011.

Hayakawa O., Nakahira K., Naito M., Tsubaki J.I., Experimental analysis of sample preparation conditions for particle size measurement, Powder Technology, 100 (1998) 61–68. DOI: 10.1016/S0032-5910(98)00053-9

Hirt C.W., Nichols B.D., Volume of fluid (VOF) method for the dynamics of free boundaries, Journal of Computational Physics, 39 (1981) 201–225. DOI: 10.1016/0021-9991(81)90145-5

Höfgen E., Teo H.E., Scales P.J., Stickland A.D., Vane-in-a-Filter and Vane-under-Compressional-Loading: novel methods for the characterisation of combined shear and compression, Rheologica Acta, 59 (2020) 349–363. DOI: 10.1007/s00397-020-01193-w

Horozov T.S., Binks B.P., Stability of suspensions, emulsions, and foams studied by a novel automated analyzer, Langmuir, 20 (2004) 9007–9013. DOI: 10.1021/la0489155

Janoske U., Piesche M., Numerische Simulation der Strömungsvorgänge und des Trennverhaltens von Suspensionen im freien Einzelspalt eines Tellerseparators, Chemie Ingenieur Technik, 71 (1999a) 249–253. DOI: 10.1002/cite.330710315

Janoske U., Piesche M., Numerical simulation of the fluid flow and the separation behavior in a single gap of a disk stack centrifuge, Chemical Engineering and Technology, 22 (1999b) 213–216. DOI: 10.1002/(SICI)1521-4125(199903)22:3<213::AID-CEAT213>3.0.CO;2-C

Jungbauer A., Continuous downstream processing of biopharmaceuticals, Trends in Biotechnology, 31 (2013) 479–492. DOI: 10.1016/j.tibtech.2013.05.011

Karolis A., Stahl W., An expanded mathematical model describing the conveying of pasty material in decanter centrifuges, in: 4th World Filtration Congress, 1986, pp. 9.9–9.16.

Kempken R., Preissmann A., Berthold W., Assessment of a disc stack centrifuge for use in mammalian cell separation, Biotechnology and Bioengineering, 46 (1995) 132–138. DOI: 10.1002/bit.260460206

Khatib Z.I., Faucher M.S., Sellman E.L., Field evaluation of disc-stack centrifuges for separating oil/water emulsions on offshore platforms, in: SPE Annual Technical Conference and Exhibition, 1995.

Kohsakowski S., Seiser F., Wiederrecht J.-P. pdfilip., Reichenberger S., Vinnay T., Barcikowski S., Marzun G., Effective size separation of laser-generated, surfactant-free nanoparticles by continuous centrifugation, Nanotechnology, 31 (2019) 95603. DOI: 10.1088/1361-6528/ab55bd

König J., Janssen N., Janoske U., Visualization of the deposition mechanisms in disk stack centrifuges with an acrylic glass bowl top and high-speed image processing, Separation Science and Technology, 56 (2021) 640–652. DOI: 10.1080/01496395.2020.1728326

König J., Ueding J., Janoske U., Analytical model to characterize the efficiency of disk stack separators, Chemie-Ingenieur-Technik, 92 (2020) 701–710. DOI: 10.1002/cite.201900177

Konrath M., Brenner A.-K., Dillner E., Nirschl H., Centrifugal classification of ultrafine particles: Influence of suspension properties and operating parameters on classification sharpness, Separation and Purification Technology, 156 (2015) 61–70. DOI: 10.1016/j.seppur.2015.06.015

Konrath M., Gorenflo J., Hübner N., Nirschl H., Application of magnetic bearing technology in high-speed centrifugation, Chemical Engineering Science, 147 (2016) 65–73. DOI: 10.1016/j.ces.2016.03.025

Konrath M., Hackbarth M., Nirschl H., Process monitoring and control for constant separation conditions in centrifugal classification of fine particles, Advanced Powder Technology, 25 (2014) 991–998. DOI: 10.1016/j.apt.2014.01.022

Kynch G.J., A theory of sedimentation, Transactions of the Faraday Society, 48 (1952) 166–176. DOI: 10.1039/tf9524800166

Landman K.A., White L.R., Eberl M., Pressure filtration of flocculated suspensions, AIChE Journal, 41 (1995) 1687–1700. DOI: 10.1002/aic.690410709

Lester D.R., Usher S.P., Scales P.J., Estimation of the Hindered Settling Function from Batch-Settling Tests, 51 (2005) 1158–1168. DOI: 10.1002/aic.10333

Leung W.F., New decanter centrifuge technology for improved separation and high throughput, Fluid-Particle Separations Journal, 16 (2004) 37–51.

Leung W.W.-F., Industrial Centrifugation Technology, McGraw-Hill, New York, 1998, ISBN: 9780070371910.

Leung W.W.F., Separation of dispersed suspension in rotating test tube,

Separation and Purification Technology, 38 (2004) 99–119. DOI: 10.1016/j.seppur.2003.10.003

Leung W.W.F., Centrifugal Separations in Biotechnology, Elsevier Science, 2007, ISBN: 978-1-85617-477-0. DOI: 10.1016/B978-1-85617-477-0.X5000-9

Lopes A.G., Keshavarz-Moore E., Ultra scale-down device to predict dewatering levels of solids recovered in a continuous scroll decanter centrifuge, Biotechnology Progress, 29 (2013) 1494–1502. DOI: 10.1002/btpr.1814

Menesklou P., Nirschl H., Gleiss M., Dewatering of finely dispersed calcium carbonate-water slurries in decanter centrifuges: about modelling of a dynamic simulation tool, Separation and Purification Technology, 251 (2020) 117287. DOI: 10.1016/j.seppur.2020.117287

Menesklou P., Sinn T., Nirschl H., Gleiss M., Grey box modelling of decanter centrifuges by coupling a numerical process model with a neural network, Minerals, 11 (2021a) 755. DOI: 10.3390/min11070755

Menesklou P., Sinn T., Nirschl H., Gleiss M., Scale-up of decanter centrifuges for the particle separation and mechanical dewatering in the minerals processing industry by means of a numerical process model, Minerals, 11 (2021b) 1–18. DOI: 10.3390/min11020229

Merkl R., Steiger W., Properties of decanter centrifuges in the mining industry, Minerals and Metallurgical Processing, 29 (2012) 6–12. DOI: 10.1007/bf03402327

Michaels A., Bolger J., Settling rates and sediment volumes of flocculated kaolin suspensions, Industrial & Engineering Chemistry Fundamentals, 1 (1962) 24–33. DOI: 10.1021/i160001a004

Mladenchev T., Modellierung des Filtrations- und Fließverhaltens von ultrafeinen, kompressiblen, flüssigkeitsgesättigten Partikelpackungen, Otto-von-Guericke-Universität Magdeburg, 2007.

Najjar Y.S.H., Abu-Shamleh A., Harvesting of microalgae by centrifugation for biodiesel production: a review, Algal Research, 51 (2020) 102046. DOI: 10.1016/j.algal.2020.102046

Nazemzadeh N., Malanca A.A., Nielsen R.F., Gernaey K. V, Andersson M.P., Mansouri S.S., Integration of first-principle models and machine learning in a modeling framework: an application to flocculation, Chemical Engineering Science, 245 (2021) 116864. DOI: 10.1016/j.ces.2021.116864

Neumann A., Hoyer W., Wolff M.W., Reichl U., Pfitzner A., Roth B., New method for density determination of nanoparticles using a CPS disc centrifuge™, Colloids and Surfaces B: Biointerfaces, 104 (2013) 27–31. DOI: 10.1016/j.colsurfb.2012.11.014

Peth S., Applications of microtomography in soils and sediments, in: Developments in Soil Science, Elsevier, 2010, pp. 73–101. DOI: 10.1016/S0166-2481(10)34003-7

Peukert W., Frank U., Uttinger M.J., Wawra S.E., Lübbert C., Progress in multidimensional particle characterization, KONA Powder and Particle Journal, 39 (2022) 3–28. DOI: 10.14356/kona.2022005

Prayitno Y.A.K., Sejati P.A., Zhao T., Iso Y., Kawashima D., Takei M., In situ measurement of hindered settling function in decanter centrifuge by periodic segmentation technique in wireless electrical resistance detector (psWERD), Advanced Powder Technology, 33 (2022) 103370. DOI: 10.1016/j.apt.2021.11.022

Prayitno Y.A.K., Zhao T., Iso Y., Takei M., In situ measurement of sludge thickness in high-centrifugal force by optimized particle resistance normalization for wireless electrical resistance detector (WERD), Measurement Science and Technology, 32 (2020) 034001. DOI: 10.1088/1361-6501/abc108

Quemada D., Rheology of concentrated disperse systems and minimum energy dissipation principle, Rheologica Acta, 16 (1977) 82–94. DOI: 10.1007/BF01516932

Radel B., Gleiß M., Nirschl H., Crystal breakage due to combined normal and shear loading, Crystals, 12 (2022) Article no: 644. DOI: 10.3390/cryst12050644

Rathore A.S., Agarwal H., Sharma A.K., Pathak M., Muthukumar S., Continuous processing for production of biopharmaceuticals, Preparative Biochemistry and Biotechnology, 45 (2015) 836–849. DOI: 10.1080/10826068.2014.985834

Records A., Sutherland K., Decanter Centrifuge Handbook, Elsevier Science, 2001, ISBN:9781856173698.

Reif F.R., Stahl W., Transportation of moist solids in decanter centrifuges, Chemical Engineering Progress, 85 (1989) 57–67.

Reuter H., Sedimentation in der Überlaufzentrifuge, Chemie Ingenieur Technik, 39 (1967) 548–553. DOI: 10.1002/cite.330390910

Richardson J.F., Zaki W.N., The sedimentation of a suspension of uniform spheres under conditions of viscous flow, Chemical Engineering Science, 3 (1954) 65–73. DOI: 10.1016/0009-2509(54)85015-9

Richardson J.F., Zaki W.N., Sedimentation and fluidisation: part I, Chemical Engineering Research and Design, 75 (1997) S82–S100. DOI: 10.1016/S0263-8762(97)80006-8

Romani Fernández X., Prediction of multiphase flow and separation efficiency of industrial centrifuges by means of numerical simulation, Karlsruher Institut für Technologie (KIT), 2012, ISBN: 9783954041527.

Romaní Fernández X., Nirschl H., A numerical study of the impact of radial baffles in solid bowl centrifuges using computational fluid dynamics, Physical Separation in Science and Engineering, (2010) 510570. DOI: 10.1155/2010/510570

Romaní Fernández X., Nirschl H., Multiphase CFD simulation of a solid bowl centrifuge, Chemical Engineering & Technology, 32 (2009) 719–725. DOI: 10.1002/ceat.200800531

Romaní Fernández X., Nirschl H., Fernández X.R., Nirschl H., Simulation of particles and sediment behaviour in centrifugal field by coupling CFD and DEM, Chemical Engineering Science, 94 (2013) 7–19. DOI: 10.1016/j.ces.2013.02.039

Schubert T., Meric A., Boom R., Hinrichs J., Atamer Z., Application of a decanter centrifuge for casein fractionation on pilot scale: effect of operational parameters on total solid, purity and yield in solid discharge, International Dairy Journal, 84 (2018) 6–14. DOI: 10.1016/j.idairyj.2018.04.002

Shekhawat L.K., Sarkar J., Gupta R., Hadope S., Application of CFD in bioprocessing: separation of mammalian cells using disc stack centrifuge during production of biotherapeutics, Journal of Biotechnology, 267 (2018) 1–11. DOI:10.1016/j.jbiotec.2017.12.016

Sinn T., Flegler A., Wolf A., Stübinger T., Witt W., Nirschl H., Gleiß M., Investigation of centrifugal fractionation with time-dependent process parameters as a new approach contributing to the direct recycling of lithium-ion battery components, Metals, 10 (2020) 1–18. DOI: 10.3390/met10121617

Skinner S.J., Stickland A.D., White L.R., Lester D.R., Shane P., Analysis of centrifugal settling of strongly flocculated suspensions, in: 12th World Filtration Congress, 2016.

Sobisch T., Kavianpour D., Lerche D., Characterization of solid-liquid separation of flocculated mineral slurries by NIR-transmission and X-ray concentration profiling, Proceedings Filtech Köln, Germany, 2016. https://papers.ssrn.com/sol3/papers.cfm?abstract_id=2977872

Spelter L.E., Nirschl H., Stickland A.D., Scales P.J., Pseudo two-dimensional modeling of sediment build-up in centrifuges: a compartment approach using compressional rheology, AIChE Journal, 59 (2013) 3843–3855. DOI: 10.1002/aic.14115

Spelter L.E., Schirner J., Nirschl H., A novel approach for determining the flow patterns in centrifuges by means of laser-doppler-anemometry, Chemical Engineering Science, 66 (2011) 4020–4028. DOI: 10.1016/j.ces.2011.05.022

Spelter L.E., Steiwand A., Nirschl H., Processing of dispersions containing fine particles or biological products in tubular bowl centrifuges, Chemical Engineering Science, 65 (2010) 4173–4181. DOI: 10.1016/j.ces.2010.04.028

Stahl S., Spelter L.E., Nirschl H., Investigations on the separation efficiency of tubular bowl centrifuges, Chemical Engineering & Tech-

nology, 31 (2008) 1577–1583. DOI: 10.1002/ceat.200800300
Stahl W., Langeloh T., Improvement of clarification in decanting centrifuges, German Chemical Engineering, 55 (1983) 324–325. DOI: 10.1002/cite.330550423
Stahl W.H., Fest-Flüssig-Trennung Band II: Industrie-Zentrifugen, Maschinen- Und Verfahenstechnik, DRM Press, CH-Männedorf, 2004, ISBN:9783952279403.
Stokes G.G., On the effect of the internal friction of fluids on the motion of pendulums, Transactions of the Cambridge Philosophical Society, 9 (1850).
Törnblom O., Turbulent shear and breakup of flocculated biomaterial in centrifuge inlets, Chemical Engineering & Technology, 41 (2018) 2366–2374. DOI: 10.1002/ceat.201800297
Usher S.P., Studer L.J., Wall R.C., Scales P.J., Characterisation of dewaterability from equilibrium and transient centrifugation test data, Chemical Engineering Science, 93 (2013) 277–291. DOI: 10.1016/j.ces.2013.02.026
Wakeman R.J., Separation technologies for sludge dewatering, Journal of Hazardous Materials, 144 (2007) 614–619. DOI: 10.1016/j.jhazmat.2007.01.084
Winkler M., Gleiss M., Nirschl H., Soft sensor development for real-time process monitoring of multidimensional fractionation in tubular centrifuges, Nanomaterials, 11 (2021). DOI: 10.3390/nano11051114
Winkler M., Sonner H., Gleiss M., Nirschl H., Fractionation of ultrafine particles: Evaluation of separation efficiency by UV–vis spectroscopy, Chemical Engineering Science, 213 (2020) 115374. DOI: 10.1016/j.ces.2019.115374
Wolf A., Flegler A., Prieschl J., Stuebinger T., Witt W., Seiser F., Vinnay T., Sinn T., Gleiß M., Nirschl H., others, Centrifugation based separation of lithium iron phosphate (LFP) and carbon black for lithium-ion battery recycling, Chemical Engineering and Processing-Process Intensification, 160 (2021) 108310. DOI: 10.1016/j.cep.2021.108310
Xiong Q., Jutan A., Grey-box modelling and control of chemical processes, Chemical Engineering Science, 57 (2002) 1027–1039. DOI: 10.1016/s0009-2509(01)00439-0
Yoshida H., Masuda H., Fukui K., Tokunaga Y., Particle size measurement with an improved sedimentation balance method and microscopic method together with computer simulation of necessary sample size, Advanced Powder Technology, 12 (2001) 79–94. DOI: 10.1163/156855201744976
Zhu G., Tan W., Yu Y., Liu L., Experimental and numerical study of the solid concentration distribution in a horizontal screw decanter centrifuge, Industrial & Engineering Chemistry Research, 52 (2013) 17249–17256. DOI: 10.1021/ie401902m
Zhu M., Hu D., Xu Y., Zhao S., Design and computational fluid dynamics analysis of a three-phase decanter centrifuge for oil-water-solid separation, Chemical Engineering and Technology, 43 (2020) 1005–1015. DOI: 10.1002/ceat.201900245

Authors' Short Biographies



Marco Gleiss

Marco Gleiss has studied Chemical Engineering at the Karlsruhe Institute of Technology (KIT) and subsequently became a doctoral student at the Institute of Mechanical Process Engineering and Mechanics (KIT), where he got his Ph.D in Chemical Engineering and became Senior scientist. His research interest is in the field of solid–liquid separation, on the digitization of filtration and centrifugation, the development of digital twins, and autonomous processes.



Hermann Nirschl

Hermann Nirschl received his Ph.D. in fluid mechanics from the Technical University in Munich in 1994. In the years between 1997 and 2003 he was responsible for process engineering developments for the 3M company. From 2003 on he is Professor for Mechanical Process Engineering at the KIT. The focus of the research is on particle technology with a special emphasis on separation processes, numerical simulation and the development of particle characterization technologies.

KONA Powder and Particle Journal

KONA Powder and Particle Journal No. 41 (2024) 78–107/https://doi.org/10.14356/kona.2024017 Review Paper

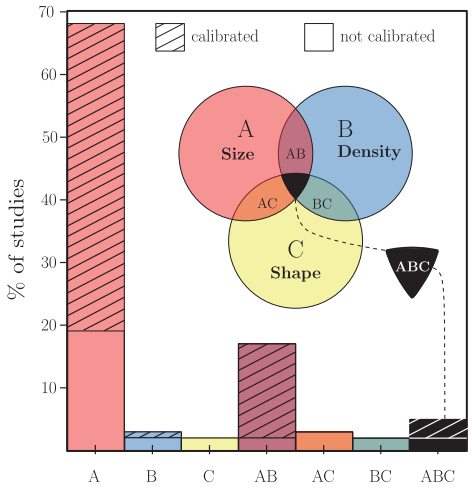
DEM Modelling of Segregation in Granular Materials: A Review†

Ahmed Hadi‡, Raïsa Roeplal‡, Yusong Pang and Dingena L. Schott*

Department of Maritime and Transport Technology, Faculty of Mechanical Engineering, Delft University of Technology, The Netherlands

Segregation control is a challenging yet crucial aspect of bulk material handling processes. The discrete element method (DEM) can offer useful insights into segregation phenomena, provided that reliable models are developed. The main challenge in this regard is finding a good balance between including particle-level details and managing the computational load. This is especially true for industrial applications, where multi-component flows consisting of particles with various irregular shapes and wide size distributions are encountered in huge amounts. In this work, we review the state of the art in DEM modelling of segregation in industrial applications involving the gravity-driven flow of dry, cohesionless granular materials. We start by introducing a novel scientific notation to distinguish between different types of mixtures. Next, we review how parameters for mixture models are determined in the current literature, and how segregation is affected by material, geometric and operational parameters based on these models. Finally, we review existing segregation indices and their applicability to multi-component segregation. We conclude that systematic calibration procedures for segregation models are currently missing in the literature, and realistic models representing multi-component mixtures have not yet been developed. Filling these gaps will pave the way for optimising industrial processes dealing with segregation.

Keywords: segregation, granular materials, discrete element method, granular flow, DEM calibration



1. Introduction

Particulate materials are ubiquitous on Earth and are the second-most common materials handled in the industry (Richard et al., 2005). Nowadays, almost all commodities are composed of, and/or derived from granular materials through agriculture, mining, chemical, and/or mechanical processing (Coulson, 2012). Particulate materials being handled in the real world exhibit complex behaviour arising from the fact that almost all of them are either mixtures of different sizes, shapes, densities, or combinations thereof. Taking into account the market-driven demand for increasing production, lowering costs and the development of new sustainable products and systems, it is important to study and unravel the complex behaviour of granular materials, as well as to advance the technologies related to producing, processing, and transporting them (Rosato and Windows-Yule, 2020).

Segregation, also referred to as reverse mixing or de-mixing, is a phenomenon happening in moving granular materials in which particles with similar properties, e.g., size, density and shape, tend to collect in certain parts of a mixture. Except for a few specific applications in mining and agricultural engineering (Zhang et al., 2004), segregation is generally considered an undesirable occurrence affecting product homogeneity in a negative way. A well-known example is the blast furnace, where segregation adversely influences the distribution of materials at the burden surface, which has a detrimental effect on the bed permeability (Yu and Saxén, 2010). This negative effect on permeability introduces an inconsistency in the pressure drop which leads to the inefficient use of reductant gas and resulting in both economic and environmental consequences (Bhattacharya and McCarthy, 2014). This example, along with several cases of other industries (e.g., food processing and pharmaceuticals industries) highlights the importance of increasing knowledge about the underlying roots of segregation, as well as investigating how segregation is influenced by various factors.

According to de Silva et al. (2000), there are thirteen segregation mechanisms in general. However, some of these mechanisms are either rare or special cases of others. Therefore, past researchers attempted to condense these segregation roots in different ways (Carson et al., 1986; Tang and Puri, 2004; Williams, 1991). Based on the size, Williams mentioned the four main mechanisms as

† Received 5 April 2023; Accepted 6 June 2023
J-STAGE Advance published online 15 September 2023
‡ Authors with equal contribution
* Corresponding author: Dingena L. Schott;
Add: Delft 2628 CD, The Netherlands
E-mail: d.l.schott@tudelft.nl
TEL: +31152783130

Copyright © 2024 The Authors. Published by Hosokawa Powder Technology Foundation. This is an open access article under the CC BY license (https://creativecommons.org/licenses/by/4.0/).

trajectory, percolation, the rise of coarse particles due to vibration (or Brazil-nut effect) and elutriation (Rhodes, 2008; Williams, 1991). In addition to these size-based mechanisms, the buoyancy mechanism in which the difference in density drives segregation should be considered for multi-component mixtures (Ottino and Khakhar, 2000). Having said that, multiple mechanisms might take place simultaneously, making the prediction of the segregation pattern extremely challenging. For instance, in the case of the mixture of small light and large heavy particles, percolation and buoyancy mechanisms oppose each other and the overall segregation behaviour of such a mixture is not known a priori (Jain et al., 2005). Furthermore, since segregation only occurs for particles that are in motion—due to either shearing, by means of moving walls (such as in a shear cell or bladed mixer) or as a result of gravitational force (as is the case in hoppers) or vibration—it can be deduced that the formation of segregation patterns depends not only on the properties of the components relative to each other, but also on the system configuration and the degree and type of agitation imposed on the material. Although having knowledge of the mentioned mechanisms can shed light on the segregation behaviour of particulate mixtures, it is necessary to investigate each case independently to determine the dominant segregation mechanism(s).

Researchers have attempted to experimentally observe segregation phenomena in common applications since the early ’70s in order to first understand why and how granular mixture components tend to separate spatially during different types of agitation (Gray, 2018) and subsequently developed models capable of capturing the observed phenomena. Given the complexity of the segregation problem, the general approach was to scrutinize the effects of different material properties separately by considering material mixtures differing only in either size (Duffy and Puri, 2002) or density (Shlnohara and Mlyata, 1984) and, ultimately, the combined effect of size and density (Jain et al., 2005). This allowed researchers to systematically observe and incorporate the effect of each material property in mathematical models. However, there are several limitations associated with the experimental investigation of segregation. First, despite the recent advances in measurement techniques (Asachi et al., 2018; Bowler et al., 2020), extracting data on the composition of a granular mixture is still not a trivial task. Second, it is nearly impossible to obtain all the information on a particle scale which can shed light on the macro-scale granular behaviour. Finally, it is expensive and time-consuming to systematically study the effect of various factors on segregation in experiments.

As computational models gained popularity, the Discrete Element Method (DEM) initially introduced by Cundall and Strack (1979) became a widely used tool for simulating granular phenomena. The main advantage of DEM is that any mixture of materials—whether they have different sizes, densities, shapes, or combinations thereof—can be modelled to provide detailed, particle-level insight on segregation patterns, which is both difficult and expensive to achieve experimentally and is not yet possible with mathematical models for segregation. This is highly relevant since most materials encountered in industry are of this complex nature. Hence, DEM has expedited researchers’ ability to predict segregation in multi-component mixtures, irrespective of the application, and can therefore be considered a practical tool for modelling and optimising industrial processes. However, until now it is unclear to what extent the existing DEM models of segregation are representative of the complex multi-component mixtures often encountered in real-world applications. Moreover, a DEM model can accurately represent granular material behaviour only if its parameters are reliably chosen, i.e., the model is calibrated and validated.

The objective of this paper is to provide an overview of the state of the art in modelling the segregation behaviour of complex multi-component mixtures using DEM. Specifically, this review assesses to what extent the existing DEM studies of segregation in cohesionless materials represent actual mixtures encountered in industry. Furthermore, the reliability of these existing studies in terms of their approach to calibration and validation is evaluated. The paper is structured as follows. For the sake of consistency, a novel way of defining and using consistent terminology for the description of mixtures is proposed in **Section 2**. Then in **Section 3**, we first evaluate different ways of analysing segregation employed by past studies including their applicability to multi-component mixtures. Next, the approach of past DEM studies on segregation for determining DEM parameters is critically reviewed. Thereafter, an overview of the methods used for the validation of DEM models of segregation is presented and evaluated. Finally, the results of past DEM studies on the effect of several factors on segregation in different systems are reviewed in **Section 4**. **Section 5** concludes the review and provides recommendations for future work.

The scope of this paper is limited to DEM-based studies of gravity-driven segregation of dry and cohesionless granular materials. Cohesionless (or free-flowing) granular materials are of interest because they are more susceptible to segregation compared to cohesive particles (Schulze et al., 2008). Studies on fluidised segregation are excluded since investigating such a phenomenon is conducted using the coupled CFD-DEM approach, which does not fit in this review. Also, applications such as rotating drums and various types of mixers in which gravity is not the only source of energy causing segregation are beyond the scope of this review.

2. Terminology

For consistency and to make a clear distinction between various terminologies used in this paper regarding mixtures, **Fig. 1** is presented. In this figure, a component is defined as a material with constant particle density. In case a mixture is composed of more than one component, it is generically referred to as a multi-component or more specifically, as two-component, three-component, etc. by mentioning the exact number of components. Moreover, the particles constituting each component can be mono- to poly-sized and/or mono- to multi-shaped. In this regard, referring to complex mixtures composed of several components is not yet straightforward. To overcome this issue, we present in **Eqn. (1)** a novel way to define multi-component mixtures:

$$nC\left[\sum_{k=1}^{n}(i_k S / j_k Sh)\right] \quad (1)$$

where n is the number of components and the composition of each component is specified in the corresponding parenthesis. That is, i_k is the number of sizes in kth component which could be 1, 2, 3, M or P representing a mono-, binary-, ternary-, multi- or poly-sized component. Similarly representing the shape, j_k might take the value of 1, 2, 3 or M denoting a mono-, binary-, ternary- or multi-shaped component. For instance, $2C[(2S/1Sh + (MS/1Sh)]$ represents a two-component ($2C$) mixture composed of a binary-sized ($2S$) mono-shaped ($1Sh$) component mixed with a multi-sized (MS) mono-shaped ($1Sh$) one. This formula will be consistently used in this review to refer to different types of mixtures in a concise way.

3. Discrete element method (DEM) for segregation

3.1 Overview of DEM

A DEM model calculates the forces and moments of inertia acting on all particles and subsequently uses Newton's second law to compute their positions at each time step through numerical integration. The interaction forces between particles and their surroundings are determined using contact models such as the Linear spring-dashpot (Luding, 2008) and Hertz-Mindlin model (Zhu et al., 2007), which are the most widely used for cohesionless granular materials. The model inputs can generally be divided into three categories: (i) morphological parameters such as particle size and shape distributions; (ii) material parameters such as particle density (ρ), shear modulus (G) and Poisson ratio (ϑ); and (iii) interaction parameters such as sliding and rolling friction coefficients (μ_s and μ_r, respectively) and the restitution coefficient (CoR).

The first step in developing a DEM model is generally measuring morphological parameters, and determining how they will be included in the model. In industrial applications, millions of particles with many irregular shapes and wide size distributions are typically handled. From a computational standpoint, modelling the true size and shape distributions for such applications can be very challenging for several reasons (Marigo and Stitt, 2015; Roessler and Katterfeld, 2018; Sakai, 2016). First of all, tracking a large number of particles and their mutual interactions demands huge amounts of computational power, even for simulating a few seconds of a simple process. Secondly, modelling the actual size distribution can prolong simulation times significantly since the numerical time step is determined by the smallest particle in the flow. Finally, realistic (non-spherical) particle shapes can be

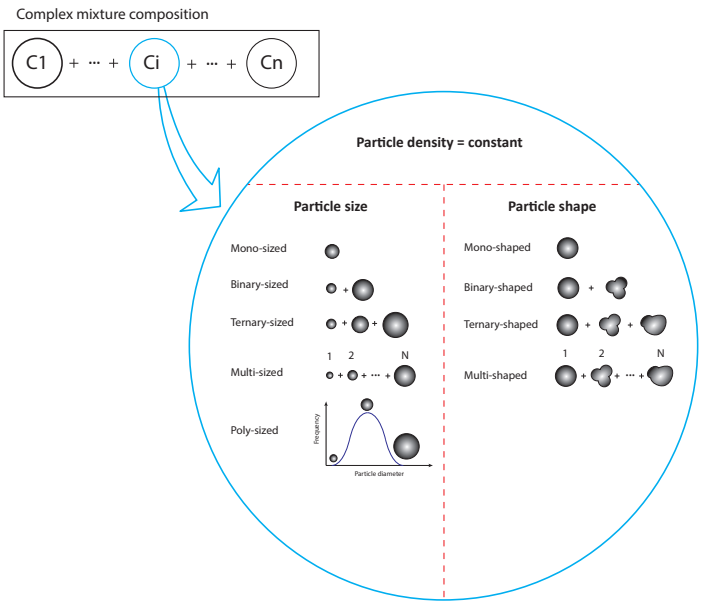


Fig. 1 Terminology to describe various types of mixtures.

modelled using multi-spheres or superquadrics which require computationally expensive algorithms (Soltanbeigi et al., 2018). Several solutions have been proposed to reduce computational effort such as downscaling the full three-dimensional system to a 2D representation or simulating a portion using periodic boundaries (Yang et al., 2014; 2015) using larger, so-called "coarse-grained" or "upscaled" particles (Coetzee, 2019; Lommen et al., 2019; Roessler and Katterfeld, 2018), ignoring small sizes of the full particle size distribution (PSD—also referred to as "scalping" or "cut-off" (Cleary and Sawley, 2002)—and reducing the shear modulus (G), although the latter should be carried out with caution as it might cause serious errors (Lommen et al., 2014). Besides all these techniques, DEM code development in conjunction with parallel computing techniques using high-performance clusters (HPC) look promising to overcome the high computational time in due course (Marigo and Stitt, 2015).

The next step is determining the remaining model parameters such that the simulated flow behaviour matches the real behaviour to an acceptable degree (Marigo and Stitt, 2015). When it comes to modelling segregation, the parameters should be determined in a way that not only the global behaviour (e.g., angle of repose, mass flow rate, etc.) but also the local behaviour, i.e., spatial concentration of components, are captured. The reliability of DEM predictions depends on the proper selection of a contact model for a specific application and the values assigned to the model parameters, given the simplifications which have been made for computational reasons. Model validation is therefore an important final step for both verifying and demonstrating the model's credibility.

We encountered 63 papers on the segregation of the gravity-driven flow of cohesionless granular materials in the literature. These studies are mostly focused on segregation during hopper filling and discharge, chute flow and heap formation and are summarised in **Table 1**. These studies have been categorised into four groups based on their approach to obtaining DEM parameters. In the remainder of this section, we will review the studies from **Table 1** with respect to the methods used to quantify segregation (**Section 3.2**) and model development practices (**Sections 3.3 and 3.4**).

3.2 Methods for assessing segregation

Since DEM allows tracking the position of each

Table 1 Overview of DEM studies for segregation (LSD = Linear spring dashpot, HM = Hertz-Mindlin, n.s. = not specified, N/A = not applicable, *for the definition and notation of the mixture type see **Eqn. (1)** in **Section 2**). (continued on next page)

Group	Source	Software	Contact model	Mixture type*	Material (in experiments)	Particle shape
I. Parametric sensitivity studies	(Tripathi and Khakhar, 2011; 2013)	n.s.	LSD	1*C*[(2*S*/1*Sh*)] 2*C*[(1*S*/1*Sh*) + (1*S*/1*Sh*)]	N/A	Sphere
	(Ketterhagen et al., 2008)	n.s.	LSD	1*C*[(2*S*/1*Sh*)] 2*C*[(1*S*/1*Sh*) + (1*S*/1*Sh*)]		Sphere
	(Pereira and Cleary, 2013)	n.s.	LSD	2*C*[(1*S*/1*Sh*) + (1*S*/1*Sh*)]		Sphere
	(Panda and Tan, 2020a; 2020b)	LIGGGHTS	HM	1*C*[(2*S*/1*Sh*)] 2*C*[(1*S*/1*Sh*) + (1*S*/1*Sh*)]		Sphere
	(Huang et al., 2022)	n.s.	n.s.	1*C*[(2*S*/1*Sh*)]		Sphere
	(Yu and Saxén, 2014)	EDEM	HM	1*C*[(3*S*/1*Sh*)]		Sphere
	(Xu et al., 2019)	n.s.	HM	3*C*[(*MS*/1*Sh*) + (*MS*/1*Sh*) + (*MS*/1*Sh*)]		Sphere
	(Li et al., 2022)	n.s.	HM	2*C*[(2*S*/1*Sh*) + (2*S*/1*Sh*)]		Sphere
	(Vuilloz et al., 2021)	LMGC90	n.s.	1*C*[(2*S*/1*Sh*)]		Sphere
	(Zhao et al., 2022)	PFC3D	LSD	1*C*[(3*S*/1*Sh*)]		Sphere
II. Parameter assumption	(Tao et al., 2013)	n.s.	n.s.	1*C*[(2*S*/2*Sh*)]	Soybean	Ellipsoidal, corn-shaped, cylinder, spherical
	(Shirsath et al., 2015)	n.s.	LSD	2*C*[(1*S*/1*Sh*) + (1*S*/1*Sh*)]	Glass beads	Sphere
	(Xu et al., 2017)	n.s.	n.s.	1*C*[(2*S*/1*Sh*)]	Alumina spheres	Sphere
	(Zhang et al., 2018)	n.s.	HM	1*C*[(2*S*/1*Sh*)]	Plastic pellets, rape seeds	Sphere
	(Mantravadi and Tan, 2020)	LIGGGHTS	HM	1*C*[(2*S*/1*Sh*)]	Glass beads	Sphere
	(Mio et al., 2020)	n.s.	Voigt	1*C*[(*MS*/1*Sh*)]	Sintered ore, coke	Sphere
	(Zhang et al., 2014)	n.s.	HM	1*C*[(*MS*/1*Sh*)]	Coke, iron ore	Sphere
	(Zhao et al., 2018)	LIGGGHTS	HM	1*C*[(*PS*/1*Sh*)]	Glass beads	Sphere
	(Zhao and Chew, 2020b)	LIGGGHTS	HM	1*C*[(*PS*/1*Sh*)]	Glass particles	Sphere, ellipsoid, cylinder, cuboid
	(Kumar et al., 2020)	LIGGGHTS	HM	1*C*[(*PS*/1*Sh*)]	Glass beads	Sphere

Table 1 Overview of DEM studies for segregation (LSD = Linear spring dashpot, HM = Hertz-Mindlin, n.s. = not specified, N/A = not applicable, *for the definition and notation of the mixture type see **Eqn. (1)** in **Section 2**). (continued from previous page)

Group	Source	Software	Contact model	Mixture type*	Material (in experiments)	Particle shape
III. Parameters from literature	(Ketterhagen et al., 2007; 2009)	n.s.	LSD	1*C*[(2*S*/1*Sh*)] 2*C*[(1*S*/1*Sh*) + (1*S*/1*Sh*)]	Glass beads, cast steel shot	Sphere
	(Ketterhagen and Hancock, 2010)	n.s.	LSD	1*C*[(2*S*/1*Sh*)]	Glass beads	Sphere
	(Kou et al., 2015; 2018)	n.s.	HM	4*C*[(1*S*/1*Sh*) + (1*S*/1*Sh*) + (1*S*/1*Sh*) + (1*S*/1*Sh*)]	Pellet, ore, coke, flux	Sphere
	(Cliff et al., 2021)	MFiX	LSD	1*C*[(2*S*/1*Sh*)]	Mustard seed	Sphere
	(Yu and Saxén, 2013)	EDEM	HM	1*C*[(2*S*/1*Sh*)]	Pellet	Sphere
	(Liao et al., 2023)	n.s.	n.s.	2*C*[(1*S*/1*Sh*) + (1*S*/1*Sh*)]	Lump ore, pellet	Sphere, clumped spheres
	(Asachi et al., 2021)	EDEM	HM	3*C*[(1*S*/1*Sh*) + (1*S*/1*Sh*) + (1*S*/1*Sh*)]	TAED, BP, EPG (detergent powder)	Sphere, clumped spheres
	(Tian et al., 2022)	n.s.	HM	1*C*[(3*S*/1*Sh*)]	Coke	Sphere, clumped spheres
	(Yu et al., 2018)	EDEM	HM	1*C*[(2*S*/1*Sh*)]	Pellet	Sphere
	(Xu et al., 2018b)	n.s.	HM	1*C*[(2*S*/1*Sh*)]	Mung bean	Sphere
	(Mandal and Khakhar, 2019)	n.s.	LSD	1*C*[(2*S*/1*Sh*)]	N/A	Spheres, dumbbells
	(Zhao and Chew, 2020a)	LIGGGHTS	HM	1*C*[(1*S*/2*Sh*)]	N/A	Ellipsoids, cylinders, cuboids
	(Zhang et al., 2021)	n.s.	HM	1*C*[(2*S*/1*Sh*)]	Coke	Sphere
	(Yu and Saxén, 2010)	EDEM	HM	1*C*[(3*S*/1*Sh*)]	Pellets	Sphere
	(Yu and Saxén, 2012)	EDEM	HM	1*C*[(3*S*/1*Sh*)]	Pellets, coke, steel ball	Sphere, clumped spheres
	(Kou et al., 2013)	n.s.	Voigt	1*C*[(3*S*/1*Sh*)]	Coke	Sphere
	(Wu et al., 2013)	n.s.	HM	1*C*[(3*S*/1*Sh*)]	Sinter	Sphere
	(You et al., 2016)	n.s.	HM	1*C*[(3*S*/1*Sh*)]	Coal	Sphere
	(Xu et al., 2021)	n.s.	n.s.	1*C*[(*MS*/1*Sh*)]	Coke	Sphere
	(Kou et al., 2019)	n.s.	HM	3*C*[(1*S*/1*Sh*) + (1*S*/1*Sh*) + (1*S*/1*Sh*)]	Sinter, pellet, lump ore	Sphere
	(Chibwe et al., 2020)	LIGGGHTS	HM	2*C*[(*MS*/1*Sh*) + (1*S*/1*Sh*)]	Sinter, pellet	Sphere
	(Hong et al., 2021)	n.s.	HM	3*C*[(1*S*/1*Sh*) + (1*S*/1*Sh*) + (1*S*/1*Sh*)]	Sinter, pellet, ore	Sphere
IV. Parameter calibration/ measurement	(Z. Zhang et al., 2020)	EDEM	HM	1*C*[(2*S*/1*Sh*)]	Acrylic spheres	Sphere
	(Izard et al., 2021)	EDEM	HM	1*C*[(2*S*/1*Sh*)]	Sinter	Clumped spheres
	(Alizadeh et al., 2017)	EDEM	HM	2*C*[(1*S*/1*Sh*) + (1*S*/1*Sh*)]	TAED, BP (detergent powder)	Clumped spheres
	(Kim et al., 2020)	EDEM	HM	2*C*[(3*S*/1*Sh*) + (3*S*/1*Sh*)]	Sinter, briquette	Sphere, clumped sphere
	(Qiu and Pabst, 2022)	PFC3D	LSD	1*C*[(*MS*/1*Sh*)]	Waste rock	Sphere
	(Wang et al., 2023)	LIGGGHTS	HM	2*C*[(1*S*/1*Sh*) + (1*S*/1*Sh*)]	Steel and aluminium spheres	Sphere
	(Barik et al., 2023)	LIGGGHTS	HM	1*C*[(3*S*/1*Sh*)]	Microcrystalline cellulose (MCC)	Sphere
	(Mio et al., 2008a; 2009; 2010; 2012)	n.s.	Voigt	1*C*[(3*S*/1*Sh*)]	Sintered ore	Sphere
	(Nakano et al., 2012)	n.s.	Voigt	1*C*[(3*S*/1*Sh*)]	Sinter	Sphere
	(Bhattacharya and McCarthy, 2014)	n.s.	HM	1*C*[(3*S*/1*Sh*)]	Polystyrene spheres	Sphere
	(Li et al., 2017)	n.s.	HM	1*C*[(*MS*/1*Sh*)]	Iron ore	Sphere
	(Li et al., 2019)	LIGGGHTS	HM	1*C*[(*MS*/1*Sh*)]	Iron ore	Sphere
	(Shimosaka et al., 2013)	n.s.	LSD	1*C*[(*MS*/1*Sh*)]	Glass bead, sand, alumina	Sphere
	(Combarros et al., 2014)	LIGGGHTS	HM	1*C*[(2*S*/1*Sh*)] 2*C*[(1*S*/1*Sh*) + (1*S*/1*Sh*)]	Aluminium oxide	Sphere, cylinders
	(Combarros et al., 2016)	LIGGGHTS	HM	1*C*[(2*S*/1*Sh*)]	Sand	Sphere
	(Terui et al., 2017)	n.s.	Voigt	2*C*[(1*S*/1*Sh*) + (1*S*/1*Sh*)]	Coke, sinter	Sphere

individual particle, it becomes relatively simple to assess the degree of segregation within a system. This can be done in different ways. One approach is to divide the system into subdomains and subsequently determine how different mixture components are distributed in the subdomains by means of plots. Gradient plots are useful for visualising the distribution of a single mixture component in a system. For example, a gradient plot as in **Fig. 2(a)** has been used to visualise how small particles within a binary mixture were distributed after filling a hopper (Xu et al., 2017). Since they were dealing with a binary mixture, showing the distribution of one component was sufficient to demonstrate how well the material was mixed in the hopper. When dealing with multi-component mixtures, monitoring only one component's distribution is no longer sufficient, and other types of plots can be used. **Fig. 2(b)** shows an example of line plots for monitoring the radial distribution of four different particle sizes in a blast furnace. The method of plots is beneficial as it provides two important insights: (1) whether or not different mixture components are evenly distributed and (2) where the different components are concentrated in the case of uneven distribution.

Another method is to use an index which reflects the degree of segregation based on its value. There are generally two types of segregation indices: grid-dependent and grid-independent (Bhalode and Ierapetritou, 2020). In the first type, the system is divided into subdomains, similar to the method of plots. The distribution of one mixture component (referred to as the tracer) is evaluated, and the segregation index is then determined through statistical analysis of the tracer distribution. If the tracer is distributed evenly, then the material is considered to be well-mixed, and this is reflected by the value of the segregation index. In the second type, the value of the segregation index is determined by considering how the tracer particle is distributed within the system as a whole, rather than in subdomains. The tracer's distribution is generally evaluated on a distance or contact basis, as described by Bhalode and Ierapetritou (2020). The index value reflects how spread out the tracer particles are in the whole system.

The benefit of using an index is that it allows for a quantitative comparison of segregation for different scenarios by means of a single value. This might be more difficult to do with the method of plots, which provides a more qualitative comparison. However, it is generally known that grid-dependent indices depend on the chosen size of the subdomains (Cho et al., 2017; Jin et al., 2022; Rosato and Windows-Yule, 2020), which makes it difficult to judge the degree of segregation based on the index value. For this reason, researchers often investigate how sensitive their segregation predictions are to the grid size. While the grid-independent indices do not have this shortcoming, they are often computationally intensive, especially for industrial applications where millions of particles are involved.

The majority of literature from **Table 1** used the plot method to quantify segregation, with only a few used segregation indices. These indices are presented in **Table 2** and are grouped by the calculation method (grid dependent/independent). The equations for calculating the indices are

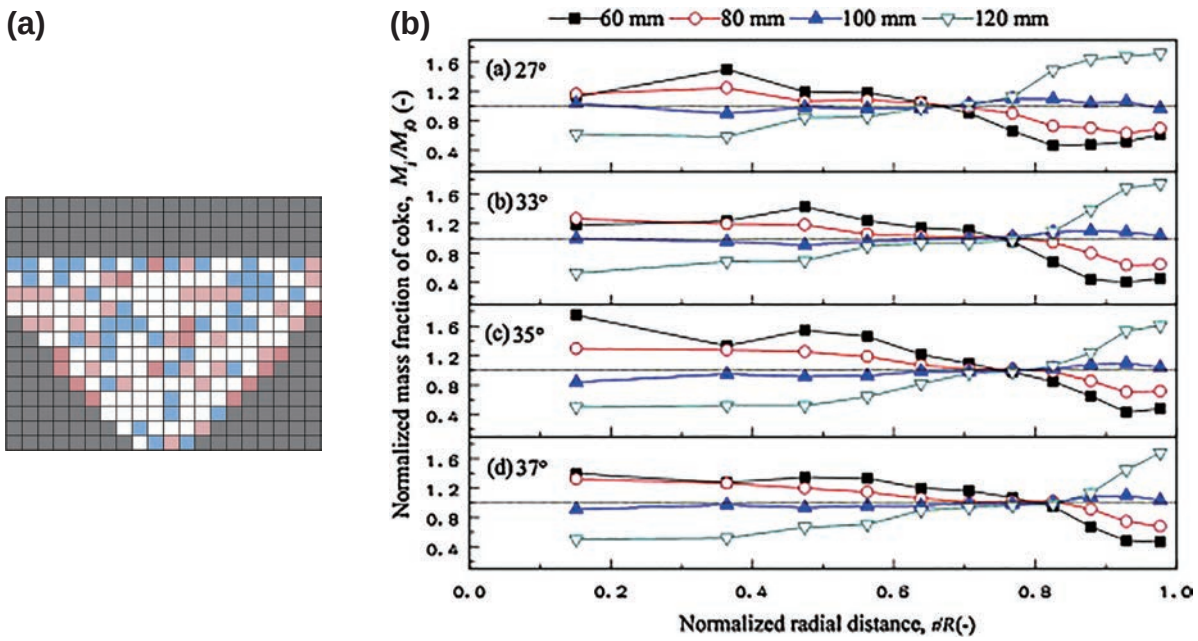


Fig. 2 **(a)** Gradient plot for demonstrating how a single component is spatially distributed inside a system, where white colour represents a well-mixed status and red and blue colours denote segregated areas. Reproduced with permission from Ref. (Xu et al., 2017). Copyright 2017, Elsevier. and **(b)** line plots for different coke sizes, showing how they are distributed inside a blast furnace after being charged using various chute angles Reproduced with permission from Ref. (Zhang et al., 2014). Copyright 2014, Elsevier.

Table 2 Common segregation indices used in DEM studies of **Table 1**. Legend: refer to the **Appendix** for symbol definitions. Subscripts: "t" refers to "tracer" when a single tracer is used; t_i refers to the *i*-th tracer when multiple tracers are used(*).

No.	Source	Segregation index	Values (mixed–segregated)	Classification
Grid-dependent				
1	(Panda and Tan, 2020a; 2020b)	$SI = \sqrt{\frac{\sum_{j=1}^{m}\left(c_t^j - c_t\right)^2}{m}}$	0–(**)	Variance-based / single tracer
2	(Li et al., 2022)	$SI = \frac{\sum_{j=1}^{m}\left[\frac{N^j}{N}\left(y_t^j - y_t\right)^2\right]}{y_t\left(1-y_t\right)}$	0–1	Variance-based / single tracer
3	(Mantravadi and Tan, 2020)	$SI = \sqrt{\frac{\sum_{j=1}^{m}\left[\frac{x_t^j}{x_t} - \left(\frac{x_t^j}{x_t}\right)_{avg.}\right]^2}{m-1}}$	0–(**)	Variance-based / single tracer
4	(Mantravadi and Tan, 2020)	$SI = \frac{\sigma_0^2 - \sigma^2}{\sigma_0^2 - \sigma_r^2}$	1–0(***)	Variance-based / single tracer
5	(Zhang et al., 2014), (Ketterhagen and Hancock, 2010)	$SI = \sqrt{\frac{\sum_{j=1}^{m}\left[\frac{x_t^j}{x_t} - \left(\frac{x_t^j}{x_t}\right)_{avg.}\right]^2}{m}}$	0–(**)	Variance-based / single tracer
6	(Zhao et al., 2018)	$SI = \frac{\frac{\sum_{j=1}^{m}\left[x_{t_1}^j \cdot h_j\right]}{\sum_{j=1}^{m}\left[x_{t_2}^j \cdot h_j\right]} - 1}{\frac{2x_{t_2} + x_{t_1}}{x_{t_1}} - 1}$	0–1	Distance-based / two tracers
7	(Combarros et al., 2014)	$SI = \sqrt{\frac{\log\sigma_0^2 - \log\sigma^2}{\log\sigma_0^2 - \log\sigma_r^2}}$	1–0	Variance-based / single tracer
Grid-independent				
8	(Zhang et al., 2018)	$SI = \frac{\sigma_0^2 - \sigma^2}{\sigma_0^2 - \sigma_r^2}$ (*)	1–0	Contact-based
9	(Mandal and Khakhar, 2019)	$SI = \frac{COM_{final} - COM_{initial}}{\delta}$	0–0.5	Distance-based / single tracer
10	(Chibwe et al., 2020)	$SI = \frac{\bar{l} - l_{min}}{l_{ud} - l_{min}}$	1–0	Distance-based / single tracer

(*) The readers are referred to **Table A1** in the **Appendix** for detailed equations on calculating component concentrations of indices 1–8.
(**) For these indices, the maximum value of *SI* depends on the mixture composition, as the equations contain the variables c_t, y_t and x_t which represent the concentration of the tracer in the entire mixture.
(***) In these equations, σ^2, σ_0^2 and σ_r^2 are calculated by
$\sigma^2 = \sum_{i=1}^{n}\frac{\left(y_t^i - y_t\right)^2}{n-1}$, $\sigma_0^2 = y_t\left(1-y_t\right)$, $\sigma_r^2 = \frac{y_t\left(1-y_t\right)}{N^i}$

given along with the range of values that can be assigned to each index. Additionally, the type of segregation index based on the classification according to Bhalode and Ierapetritou (2020) is indicated. It is important to note that, similar to the method of plots, the single-tracer approach is only useful when considering a binary mixture. We have therefore also indicated whether the segregation indices are based on the distribution of a single tracer. The common symbols used in index no. 1–8 from **Table 2** are defined in the **Appendix**, and for index no. 9–10, the reader is referred to the respective references.

We conclude that all grid-dependent indices in **Table 2** are based on a statistical analysis of a single tracer, which is not surprising since they were applied to studies of binary mixtures. In studies of three or more particle types (Bhalode and Ierapetritou, 2020), the plot method was used to visualize the degree of segregation. For indices which can be applied to multi-component segregation, the reader

is referred to the work of Cho et al. (2017), who studied segregation in a mixer.

3.3 Determination of DEM parameters for segregation

The literature mentioned in **Table 1** has been categorized based on the way in which the authors dealt with model parameters. We identified the following four categories:

I. ***Parametric sensitivity studies.*** This group of studies carried out parametric sensitivity studies to identify the critical factors (i.e., model, material, geometric and operational parameters) affecting the segregation behaviour of mixtures in different systems. Hence, parameter values in these studies are systematically varied. Since they are not aimed at modelling a specific material, calibration and validation are not performed in these studies.

II. ***Parameter assumption.*** The second group contains studies in which the authors assumed parameters without any justification or referring to related resources (for instance chosen by experience). Although these studies attempted to justify the parameter values by comparing the DEM results with physical tests, this is insufficient because more than one parameter set can yield the same bulk behaviour (Roessler et al., 2019). Furthermore, major errors were reported in some cases (Tao et al., 2013), which could be the consequence of not calibrating the parameters.

III. ***Parameters from literature.*** Many DEM studies on segregation have taken either all or merely a selection of the parameters from the literature (Asachi et al., 2021; Chibwe et al., 2020; Cliff et al., 2021; Hong et al., 2021; Ketterhagen et al., 2007, 2009; Ketterhagen and Hancock, 2010; Kou et al., 2013, 2015, 2018, 2019; Liao et al., 2023; Mandal and Khakhar, 2019; Tian et al., 2022; Wu et al., 2013; Xu et al., 2018b, 2021; You et al., 2016; Yu et al., 2018; Yu and Saxén, 2010, 2012, 2013; Zhang et al., 2021; Zhao and Chew, 2020a). This approach has the same shortcoming as the previous group, since the parameters are obtained from resources that have not conducted calibration. Furthermore, it is unclear if the material under study is similar or exactly the same as in the literature (Zhang et al., 2021).

IV. ***Parameter calibration/ measurement.*** Several past studies have established DEM parameters through either direct measurements or bulk calibration (Alizadeh et al., 2017; Barik et al., 2023; Bhattacharya and McCarthy, 2014; Combarros et al., 2014; Combarros Garcia et al., 2016; Izard et al., 2021; Kim et al., 2020; Li et al., 2019, 2017; Mio et al., 2010, 2009, 2008a, 2012; Nakano et al., 2012; Qiu and Pabst, 2022; Shimosaka et al., 2013; Terui et al., 2017; Wang et al., 2023; Z. Zhang et al., 2020). Each of these approaches comes with a set of advantages and disadvantages as summarized in **Table 3**. The calibration approaches of the studies in this group are summarized in **Table 4**. All calibration tests presented in this table capture only the global behaviour of granular materials (e.g., angle of repose) and none of them has calibrated the DEM model for local behaviour using a segregation test.

Calibration of DEM models against experimental data ensures that the model captures the material behaviour and therefore provides credibility (Coetzee, 2017). However, calibration can be very time-consuming. This is especially true for multi-component mixtures since the number of model parameters increases with the number of components in the mixture. Sensitivity studies enable us to explore the importance of the model parameters for inclusion in the calibration step. **Table 5** presents a summary of the results of the existing DEM sensitivity studies on segregation. As can be seen, the significance of DEM parameters depends on the system and the granular flow regime being studied.

Fig. 3 visually presents deeper insight into studies listed in **Table 1** to highlight the percentage of studies with respect to the approach for determining DEM parameters, reproducibility and the types of the mixtures being studied.

According to **Table 1**, not all past DEM studies have determined the parameters in a proper way. To highlight this with respect to segregation, **Fig. 3(a)** shows the percentage of studies in groups II to IV, where only studies in group IV include calibration. It should be noted that group I is excluded since calibration is not necessary for parametric sensitivity analysis. As can be seen, 66 % of the existing studies have omitted the calibration of the DEM model. This is relevant since calibrated DEM models are required if they are intended to be used as predictive tools that yield

Table 3 Pros and cons of two main approaches to determining DEM parameters (Coetzee, 2017; Marigo and Stitt, 2015; Wang et al., 2022).

	Advantage	Disadvantage
Direct measurement	+ Independent of the contact model + Independent of the DEM code + Maintaining physical meaning	– Mostly limited to mm-sized particles – Not practical for irregular particles – Not practical for all parameters – Not considering the stochastic nature of the parameters
Bulk Calibration	+ Compensating for the inaccuracy of the parameters + Obtaining values for all parameters	– Probability of losing physical meaning on particle level – DEM code dependency – Probability of not resulting in a unique parameter set – Challenging in the case of a high number of parameters

Table 4 Detailed calibration approach of studies in group IV of **Table 1**.

Source	Direct measurement	Bulk calibration test
(Z. Zhang et al., 2020)	$\mu_{s,pp}$, $\mu_{s,pw}$, CoR	—
(Izard et al., 2021)	$\mu_{s,pw}$, ρ_s	$\mu_{s,pp}$ (angle of repose)
(Alizadeh et al., 2017)	CoR, $\mu_{s,pw}$, particle shape	The number of spheres in clumped approach, μ_r (angle of repose), $\mu_{s,pp}$ (sliding process),
(Kim et al., 2020)	PSD, ρ_s, CoR, μ_s, E	μ_r (angle of repose)
(Qiu and Pabst, 2022)	PSD	μ_s, μ_r (angle of repose, both at lab and field scales)
(Wang et al., 2023)	ρ_s, CoR	—
(Barik et al., 2023)	—	μ_s (silo discharging)
(Mio et al., 2008a; 2009; 2010; 2012)	PSD, ρ_s	μ_s (shear test), μ_r (particle rolling test)
(Nakano et al., 2012)	—	μ_r (angle of movement)
(Bhattacharya and McCarthy, 2014)	PSD, ρ_s	Tuning the contact model
(Li et al., 2017)	PSD, ρ_s, G	μ_s, μ_r (angle of repose)
(Li et al., 2019)	PSD, ρ_s, G, μ_s, μ_r	—
(Shimosaka et al., 2013)	—	μ_r (inclined plate test)
(Combarros et al., 2014)	PSD, ρ_s	μ_s, μ_r (sensitivity analysis + dynamic and static angle of repose)
(Combarros Garcia et al., 2016)	ρ_s, D_{50}	μ_s, CoR (sensitivity analysis + shear test, angle of repose and drop fall test)
(Terui et al., 2017)	—	μ_s (stationary bed angle), μ_r (angle of repose)

Table 5 A summary of the results of DEM sensitivity studies on the significance of model parameters for segregation.

DEM parameter	Range (source)	System	Significance
Particle-particle sliding friction ($\mu_{s,p\text{-}p}$)	(0.0–0.5) (Ketterhagen et al., 2008)	Hopper discharge	High
	(0.01–0.9) (Yu and Saxén, 2010)		Low
	(0.15–0.95) (Z. Zhang et al., 2020)		High
	(0.1–1.0) (Zhang et al., 2018)	Hopper filling	High
	(0.3–0.9) (Li et al., 2022)	Blast furnace throat	Low
Particle-wall sliding friction ($\mu_{s,p\text{-}w}$)	(0.0–0.5) (Ketterhagen et al., 2008)	Hopper discharge	High
	(0.01–0.9) (Yu and Saxén, 2010)		High
	(0.05–0.85) (Z. Zhang et al., 2020)		High
Particle-particle rolling friction ($\mu_{r,p\text{-}p}$)	(0.0–0.045d_c) (Ketterhagen et al., 2008)	Hopper discharge	Low
	(0.05–0.9) (Yu and Saxén, 2010)		Low
	(0.001d_p–0.2d_p) (Zhang et al., 2018)	Hopper filling	High
Particle-wall rolling friction ($\mu_{r,p\text{-}w}$)	(0.0–0.045d_c) (Ketterhagen et al., 2008)	Hopper discharge	Low
	(0.01–0.9) (Yu and Saxén, 2010)		High
Particle-particle coefficient of restitution ($e_{p\text{-}p}$)	(0.2–0.94) (Ketterhagen et al., 2008)	Hopper filling	High
Particle-wall coefficient of restitution ($e_{p\text{-}w}$)	(0.2–0.9) (Ketterhagen et al., 2008)	Hopper filling	High
Local damp	(0.2–0.8) (Qiu and Pabst, 2022)	Pile formation	Low

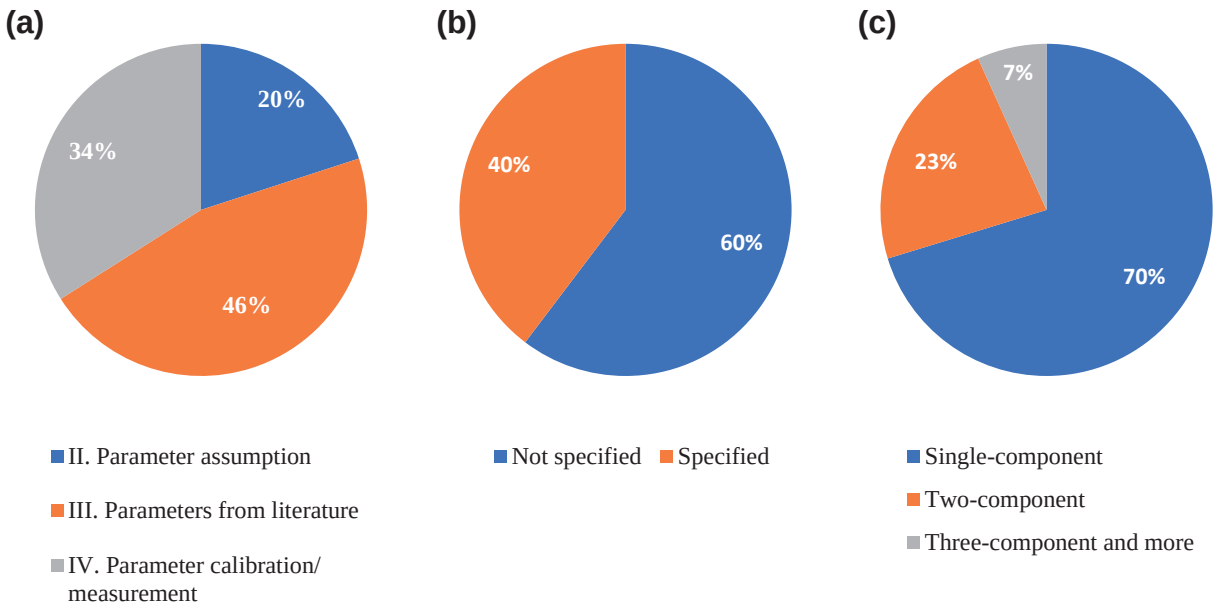


Fig. 3 Distribution of past DEM-based studies of segregation by **(a)** approach of calibration, **(b)** DEM software and **(c)** types of mixtures.

reliable results (Coetzee, 2017). Even though the studies in group IV have applied calibration to some extent, not all of them have carried it out in a systematic way (cf. **Table 4**). In several studies, only a portion of the parameters has been calibrated (Nakano et al., 2012; Shimosaka et al., 2013). Also, in several cases, a single experiment is used to determine the values of more than one parameter (Izard et al., 2021; Li et al., 2017). As shown by Wensrich and Katterfeld (2012), this approach leads to ambiguity since an infinite combination of parameter values might lead to the same bulk behaviour.

There are good examples of systematic calibration of DEM models with respect to bulk material behaviour for various operational conditions in the literature (Coetzee, 2016; Do et al., 2018; El Kassem et al., 2021; Marigo and Stitt, 2015; Mohajeri et al., 2020; Roessler et al., 2019). When it comes to the calibration of models for segregation, several authors have shown that bulk calibration also ensures that the local material behaviour is accurately captured. For example, Li et al. (2017) calibrated the friction coefficients of iron ore pellets using a repose angle test and verified that the calibrated model could reproduce the experimentally observed size segregation in simulations. Similarly, Izard et al. (2021) modelled the size segregation of sinter particles after determining the model parameters through bulk calibration. However, it has not yet been addressed to what extent the DEM parameters obtained through bulk calibration (e.g., dynamic and static angle of repose) can be employed to accurately replicate the segregation of multi-component mixtures, which is essentially a local occurrence. Furthermore, the systematic calibration of mixture models has received little attention. One of the few studies where mixture calibration was performed is the work of Alizadeh et al. (2017). The authors modelled the segregation of a detergent mixture during heap formation and found that the segregation behaviour was not accurately captured by their model, which was calibrated using a combination of direct measurement and bulk calibration. They attributed the model's inaccuracy to the fact that spheres were used to model the particle shape. When using clumped spheres to approximate the actual particle shape, the predicted segregation behaviour was in good agreement with the experiments. Other researchers have also modelled the segregation of mixtures, but the interaction parameters between mixture components were not mentioned (Combarros et al., 2014; Terui et al., 2017).

Fig. 3(b) illustrates the various DEM software that has been used by past researchers to investigate segregation. It is notable that 60 % of the studies have not specified the DEM software they employed. This is highly important because not only the same DEM parameters might be defined in different ways in various software, but also models may be differently implemented, making the parameters code-dependent (Coetzee, 2017; González-Montellano et al., 2012). It means that the calibrated parameters of these studies cannot be reliably and directly used by others to reproduce the work or to model the same material. Therefore, it is essential to specify in detail the DEM code or software used in future studies.

The different types of mixtures that have been modelled and studied are shown in **Fig. 3(c)**. A vast majority of past studies (i.e. 70 %) have been dedicated to single-component mixtures i.e., with the general form of $1C[(iS/jSh)]$ (see **Section 2**), most of which have modelled simple binary- or ternary-sized mixtures with spherical particles (i.e., $1C[(2S/1Sh)]$ or $1C[(3S/1Sh)]$). In addition, a few

studies considered two or three components (Chibwe et al., 2020; Combarros et al., 2014; Hong et al., 2021; Ketterhagen et al., 2007; Kou et al., 2019; Li et al., 2022; Panda and Tan, 2020a; Pereira and Cleary, 2013; Shirsath et al., 2015; Terui et al., 2017; Xu et al., 2019), but they also simplified the mixtures by modelling mono-sized and mono-shaped components. In conclusion, although past DEM studies have attempted to shed light on segregation in granular materials, they have failed to represent the real-world complex mixtures which are mostly multi-component with each component having a size distribution and different particle shapes (Gao et al., 2021).

As can be seen in **Table 1** (columns *Mixture type* and *Particle shape*), the particle shape and size distribution have often been simplified, mainly to prevent high computational time. The effect of particle shape on segregation is not crystal clear yet as can be illustrated by seemingly contradictory results in the literature. For instance, Yu and Saxén (2014) asserted that particle shape has an insignificant effect on the size segregation during charging and discharging from a hopper since spherical particles yielded the best agreement with the experimental results of Standish (1985). It is notable that they used the same DEM parameters for both spherical and non-spherical particles, which can lead to misinterpretation. In another study, Alizadeh et al. (2017) concluded that modelling non-spherical particles as spherical with rolling friction underestimates the segregation extent during heap formation. Despite this conflict, Lu et al. (2015) and Combarros Garcia et al. (2016) concluded that particle shape has to be modelled as accurately as possible to ensure that the DEM model is accurate and predictive. Similarly, particle size distribution has usually been approximated either by using a limited number of sizes or scalping (cf. **Section 3.1**). However, since particle size is the most crucial parameter affecting segregation (Williams, 1976), size distribution should be modelled as precisely as possible. As stated by Coetzee (2017), particle shape along with the particle size distribution should be explicitly included in the calibration process and they have to be determined prior to other parameters.

3.4 Validation of DEM models for segregation

The parameters obtained through calibration must be independent of the application (Coetzee, 2016). Therefore, once the model is calibrated, it should be capable of accurately reproducing other experiments. In order to prove this, the results of the DEM simulation have to be compared with either experimental tests, analytical or "well-established" numerical results related to segregation which are available in the literature. If a "good agreement" is observed, the model is validated. Regardless of the above-mentioned approaches being adopted for determining the DEM parameters, the studies in groups II, III and IV of **Table 1** (except for parametric studies in group I) attempted to validate their DEM model for segregation. The validation techniques found in the literature overview of **Table 1** can be classified into two main categories as illustrated in **Table 6**: (1) using other research results as the benchmark and (2) using first-hand experimental results.

3.4.1 Validation using other work's results

In this approach, existing experimental, mathematical or numerical (i.e., DEM) results on segregation are used to validate the DEM model. Although adopting this approach facilitates the process of developing a DEM model, it suffers from several drawbacks. Firstly, some of these references have not particularly investigated the local behaviour (i.e., segregation) of granular materials and as a result, even in the case of an acceptable agreement, one cannot make sure the DEM model is valid for segregation. Secondly, in some cases, the size distribution of the DEM model differs from the source study against which the model has been validated. For example, Zhao et al. (2018) compared the results of the model for mono-sized particles and used the same model for modelling the segregation behaviour of granular materials with log-normal size distribution. However, according to Coetzee (2017), if particle size in the model changes, the model parameters must be re-calibrated, i.e., the previous parameters' values are not valid anymore. Thirdly, some studies employed a different setup in DEM than the experiment in the benchmark, which might significantly affect the simulation results. For instance, Wu et al. (2013) simulated a virtual factory instead of a conveyor belt in the original study (Kajiwara et al., 1988). While simplifying real-life scenarios is a common practice among researchers, it's crucial to ensure that the velocity field is accurately mimicked, as it has a significant impact on segregation.

All in all, the approach of using other work's results to validate the DEM model can have serious shortcomings. In other words, the model can be validated in this way only if all the details are accurately documented. This is often challenging since some data may have been omitted due to confidentiality. In addition, this approach is limited to specific materials (e.g., glass beads, iron ores), because there is a shortage of experimental data on the segregation of various kinds of granular materials in the literature.

3.4.2 Validation by conducting experiments

Unlike the above-mentioned category which relied on existing data in the literature, other studies have conducted experiments themselves and used first-hand experimental data to validate the DEM model. Two types of experiments have been carried out (cf. **Table 6**): the flow-related measurements of the granular materials, i.e., global/bulk behaviour, or segregation-related measurements, i.e., local behaviour.

Examples of the first type of experiment in which

Table 6 Validation approaches of past DEM studies on segregation (cf. **Table 1** for the type of mixture in each study).

Approach for validation				Source
Other work's results	Experimental			(Liao et al., 2023; Wu et al., 2013; T.F. Zhang et al., 2020; Zhang et al., 2018; Zhao et al., 2018; Zhao and Chew, 2020b)
	DEM			(Kumar et al., 2020; Mandal and Khakhar, 2019; Mantravadi and Tan, 2020)
	Mathematical			(Ketterhagen et al., 2008; Ketterhagen and Hancock, 2010; Yu and Saxén, 2013; Zhao and Chew, 2020a)
First-hand experimental results	Flow-related (bulk behaviour)	The mass fraction of the whole particles discharged from the hopper		(Tao et al., 2013)
		The velocity profile of particles using particle tracking velocimetry (PTV)		(Shirsath et al., 2015)
		Angle of repose measured in practice		(Kou et al., 2015; Tian et al., 2022)
		The discharge time of the particles from the hopper		(Xu et al., 2017; 2018b)
		Burden profile		(Kou et al., 2013; Yu and Saxén, 2013)
		Mass distribution of "all" particles in the radial direction in furnace throat		(Kou et al., 2013)
		Laser grid (Gao et al., 2010) measurement of burden falling trajectories		(Zhang et al., 2014)
		Bed height		(Li et al., 2019)
	Segregation (local behaviour)	Invasive	Sampling spaces composed of 24 cuboid-shaped cells inside the hopper	(Combarros Garcia et al., 2016)
			The discontinuous start-stop sampling method (Standish and Kilic, 1985) has been mostly adopted	(Ketterhagen et al., 2007; Yu and Saxén, 2010; Z. Zhang et al., 2020)
			Including a number of sampling boxes at the bottom to capture the trajectory segregation of materials	(Bhattacharya and McCarthy, 2014; Mio et al., 2008b, 2009, 2010, 2012; Yu and Saxén, 2012)
			Heaps are divided into a number of sub-regions in the horizontal and/ or vertical direction	(Li et al., 2017; Mio et al., 2020; Qiu and Pabst, 2022; Terui et al., 2017; You et al., 2016)
			Using rotating sampling table with pie slicing configuration	(Cliff et al., 2021)
			Measuring mass flow rate of fine particles using Copley flowability tester BEP2 model	(Barik et al., 2023)
			Sampling in the horizontal and vertical direction of the sinter cooler	(Izard et al., 2021)
			Sampling box in QPM segregation tester	(Combarros et al., 2014)
		Non-invasive	Taking pictures and counting the number of different components	(Yu et al., 2018)
			Colouring equal-sized components and using image analysis to analyse segregation	(Combarros et al., 2014)
			Taking pictures and using image processing to measure the fraction of components	(Alizadeh et al., 2017; Wang et al., 2018)

physical measurements related to global behaviour have been carried out are listed in **Table 6**. With respect to segregation, this approach fails to provide detailed spatial and temporal or "local" information about segregation such as the fraction of different components. Although this approach can be adequately adopted to validate DEM models

for "flow behaviour" on the bulk level, it cannot necessarily prove the validity of the model for segregation. In other words, to validate the models for segregation, component fractions are required to obtain local information and assess segregation.

The second type of the studies relied on segregation-related measurements. As can be seen in **Table 6**, there are two main ways of measuring segregation, namely invasive and non-invasive methods (Huang and Kuo, 2014). Invasive methods for evaluating segregation simply involve taking a number of samples, separating the components in each sample and weighting each component to obtain its mass fraction. Several sampling methods have been adopted by researchers for different systems as listed in **Table 6**. Although all the mentioned invasive methods are relatively simple and can provide valuable information about the local composition of granular mixtures, they have a number of disadvantages. First and foremost, invasive methods disturb the original structure of the mixture which affects the accuracy of the measurement. Moreover, particles from locations other than the target points might be collected during sampling (Muzzio et al., 1997). And, as mentioned above, components in each sample must be separated to further calculate their fractions. This can be straightforward for components differing in size, however for multi-component mixtures with overlapping particle sizes, this can be challenging and time-consuming. Terui et al. (2017) successfully employed the gravity separation method to separate sinter and coke particles based on the density difference. However, besides being time-consuming, this method is not applicable to all types of materials.

The mentioned drawbacks of invasive methods pushed the search for non-invasive techniques as an alternative. Because they do not disturb the granular structure, these techniques have been increasingly employed in recent years, especially in the powder blending industry (Nadeem and Heindel, 2018). There are several comprehensive review papers in the literature explaining the pros and cons as well as the applications and limitations of these methods in detail (Asachi et al., 2018; Bowler et al., 2020; Huang and Kuo, 2014; Nadeem and Heindel, 2018). Because of the inherent limitation of those techniques, not all of them are applicable to the segregation analysis of any granular mixture. For instance, the electrical conductivity method, electrical capacitance tomography (ECT), positron emission particle tracking (PEPT) and magnetic resonance imaging tomography (MRI) cannot be readily utilised to analyse the mixing and segregation of all multi-component mixtures (Asachi et al., 2018). This is because the electrical conductivity method and ECT work based on the noticeable difference in electrical conductivity and permittivity, respectively, which is not the case in all multi-component mixtures (Asachi et al., 2018; Shenoy et al., 2015). Also, a limited number of tracers is tracked in PEPT, which is not suitable to measure segregation, and in MRI, the component should be coated with oil to be detectable, which might significantly affect its flow behaviour (Stannarius, 2017). Other techniques such as Raman spectroscopy, near-infrared spectroscopy (NIR) and acoustic emissions which are feasible for multi-components, are conducted on very small samples (Bowler et al., 2020), which makes them unsuitable for coarser particles. Image analysis is another existing non-invasive method which has been widely used due to its simplicity and low cost. The main advantage of image analysis over other techniques is that it is applicable to multi-component mixtures. However, this method is limited to surface analysis, it requires a transparent vessel and the components must differ in colour (Asachi et al., 2018). This method has been successfully employed by a number of studies to provide experimental results for the calibration and validation of DEM models of segregation. Yu et al. (2018) took photos of the heap, divided the heap into sub-regions radially and counted the number of small and coarse particles in each region to analyse segregation. Adopting a more robust approach, Wang et al. (2018) and Alizadeh et al. (2017) employed image processing techniques to measure local concentrations of mixture components at the surface of the heap. To be fully consistent, they used the same approach in DEM by taking snapshots of the granular system and applying image processing (see **Fig. 4**).

In conclusion, all the methods being adopted to validate DEM models come with a set of advantages and disadvantages. Although the use of existing results in the literature facilitates the validation, it is often difficult to precisely replicate the experimental setup and sometimes, the other study has not itself been validated. Additionally, utilising existing results is confined to a few materials which have

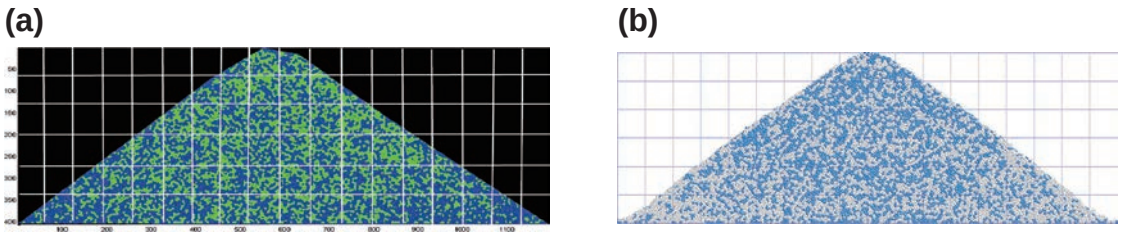


Fig. 4 An example of using image analysis to measure segregation in **(a)** experiments and **(b)** DEM. Reproduced with permission from Ref. (Alizadeh et al., 2017). Copyright 2017, Elsevier.

already been investigated. To overcome these obstacles, carrying out experiments and using first-hand results would be beneficial. However, it should be noted that the experimental measurements should provide detailed spatial information for segregation on a local level supplemented by global level or bulk behaviour such as mass flow rate. The segregation-related measurements can be performed using either invasive or non-invasive methods. Image analysis as a non-invasive method is considered superior to invasive techniques since it not only maintains the structure of the granular materials but also is applicable to multi-component mixtures, provided that the components differ in colour.

4. Results of DEM-based studies on segregation

The work we presented in **Table 1** in the previous section will be elaborated in detail here. We gather and analyse the findings of those studies on how segregation is affected by adjusting material properties, system configurations and operational parameters.

4.1 Material properties

Generally, any difference between the particles of a particulate system can cause segregation. For free-flowing granular materials, it has been proven that particle size, density and shape affect segregation more than other factors such as surface roughness and elasticity (Tang and Puri, 2004). The studies listed in **Table 1** are analysed and the effect of these factors are presented in the following paragraphs. To systematically discuss the results in the literature, we present **Fig. 5** which illustrates the possible combinations of different particle properties and **Table 7** which shows the relevant subsection addressing the corresponding type of mixture.

4.1.1 Particle size

Particle size is unequivocally the most influential property contributing to segregation among the other particle properties (Williams, 1976). This is why numerous research studies have been dedicated to gaining a full understanding of the effect of particle size and especially particle size distribution (PSD) on segregation.

In the case of binary-sized mixtures, i.e., mixtures in the form of $1C[(2S/1Sh)]$, the effect of size distribution can be investigated by varying either the size ratio or the mass fraction of the components. It is generally accepted that a larger size ratio leads to more pronounced segregation (Bridgwater, 1994). **Fig. 6** shows the investigated ranges of size ratio in the DEM-based studies of binary-sized free-flowing mixtures in various systems. For hoppers and in one of the earliest attempts to study segregation using DEM, Ketterhagen et al. (2007) concluded that the extent of segregation significantly increases for size ratios greater than 1.9. Using the velocity difference between small and large particles as an indicator of percolation, T.F. Zhang et al. (2020) investigated the segregation during conical hopper discharging and found that in their case, percolation was not dominant for size ratios smaller than 6.0 (i.e., corresponding to the velocity difference of 0.07 mm/s). Z. Zhang et al. (2020) observed that the percolation which occurred during the discharge of a wedge-shaped hopper near the wall and the bottom of the hopper was eliminated

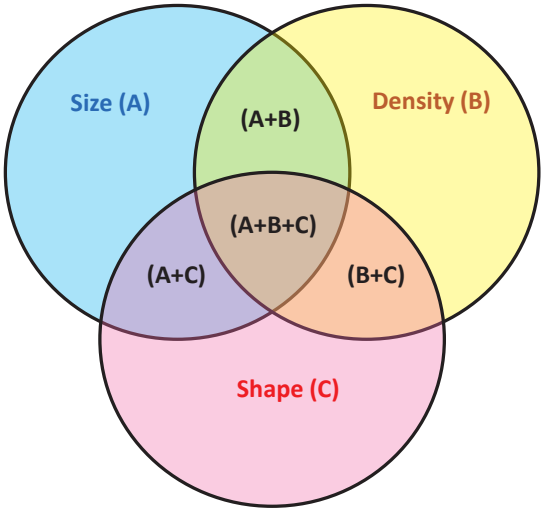


Fig. 5 Different possible combinations of particle properties.

Table 7 Corresponding subsection for different types of mixtures.

Section	Type of mixture		
	Symbol	Notation	
4.1.1 Particle size	A	$1C[(iS/1Sh)]$	$i = 2, 3, \ldots, M, P$
4.1.2 Particle density	B	$nC[(1S/1Sh) + \cdots + (1S/1Sh)]$	$n = 2, 3$, etc.
4.1.3 Particle shape	C	$1C[(1S/jSh)]$	$j = 2, 3$, etc.
4.1.4 Combinations of particle size, density and shape	(A+B)	$nC[(i_1S/1Sh) + \cdots + (i_nS/1Sh)]$	$n = 2, 3$, etc. & $i = 2, 3, \ldots, M, P$
	(A+C)	$1C[(iS/jSh)]$	$i = 2, 3, \ldots, M, P$ & $j = 2, 3$, etc.
	(B+C)	$nC[(1S/j_1Sh) + \cdots + (1S/j_nSh)]$	$n = 2, 3$, etc. & $j = 2, 3$, etc.
	(A+B+C)	$nC[(i_1S/j_1Sh + \cdots + (i_nS/j_nSh)]$	$n = 2, 3$, etc. & $j = 2, 3$, etc.

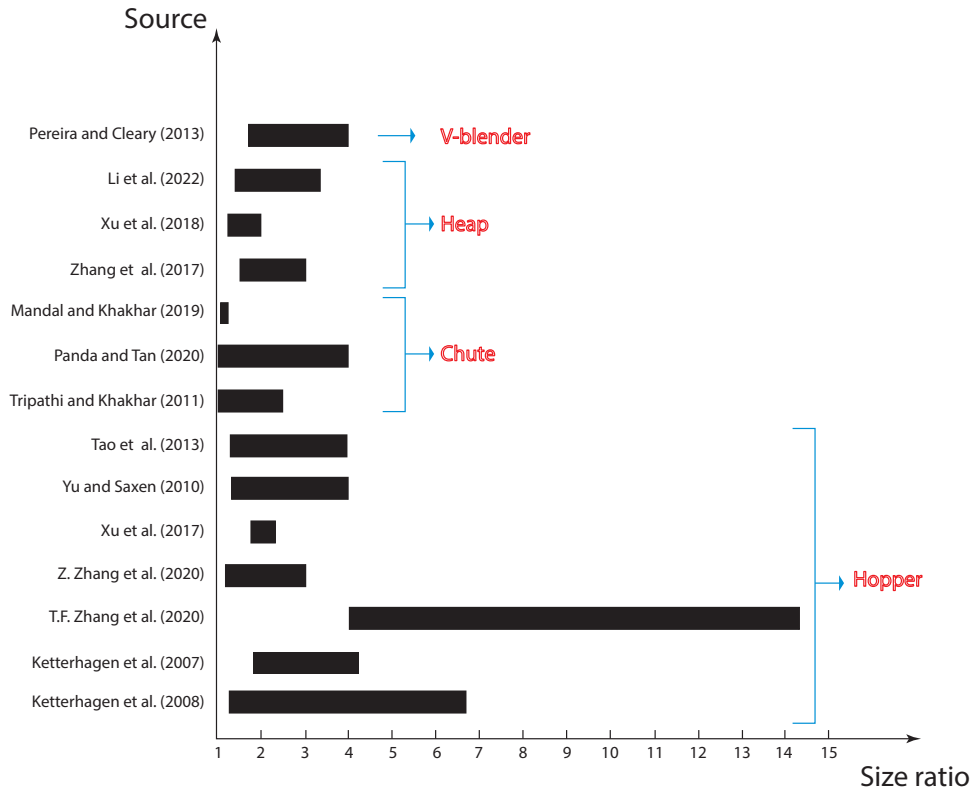


Fig. 6 Size ratio ranges in the past DEM studies on segregation.

for a size ratio lower than 1.2. Varying size ratios from 1.3 to 4.0, Yu and Saxén (2010) observed significant segregation even for the minimum ratio of 1.3. Unlike these studies, Ketterhagen et al. (2008) found that in the case of the hopper bottom wall angle of 15° (as opposed to 90°), no considerable segregation was observed for all size ratios tested.

In addition to hoppers, several studies have examined the effect of size ratio on segregation in other systems such as inclined planes, chutes, the throat of the blast furnace and V-blender. In their work on the segregation of binary mixtures down an inclined plane, Tripathi and Khakhar (2011) found that varying size ratio does not affect the extent of segregation. In the case of a chute, Panda and Tan (2020a) observed that although the stream-wise, cross-stream and vertical velocities all increase with increasing size ratio, the degree of segregation did not increase significantly in the stream-wise direction. Li et al. (2022) studied the particle segregation in the throat of the blast furnace. For this, they charged a layer of binary-sized cokes followed by a layer of binary-sized ore particles. Varying the size ratio equally for coke and ore particles, they observed that larger size ratios result in a more segregated state, which was more evident for the coke mixture. In their study on the de-mixing of binary-sized mixtures during discharge from a V-blender, Pereira and Cleary (2013) observed that the segregation extent becomes significant for large size ratios, i.e., 3 and 4.

Apart from the particle size ratio, the mass fraction of fine particles has been proven to have a significant impact on segregation (Tang and Puri, 2004). Artega and Tüzün (1990) proposed a model for binary-sized mixtures to determine the fine mass fraction (x_f) for which segregation via percolation becomes feasible during hopper discharge. They claimed that percolation no longer occurs when the surface area of the large spheres is completely covered by small spheres, implying that percolation only occurs if the mass fraction of finer particles is lower than the limiting value defined as $x_{L,crit} = [4/(4 + Ø_R)]$, where $Ø_R$ is the size ratio. This model is applicable to free-flowing materials of approximately spherical shape and is independent of the hopper geometry. While the findings of Ketterhagen et al. (2008) and Z. Zhang et al. (2020) are in accordance with Artega and Tüzün's model, Xu et al. (2017) observed segregation for mass fractions higher than the above-mentioned $x_{L,crit}$. Nevertheless, all of these studies agree that increasing the fine mass fraction decreases segregation (Barik et al., 2023; Ketterhagen et al., 2008; Tian et al., 2022; Xu et al., 2017; Zhang et al., 2018; Z. Zhang et al., 2020).

While in most of the DEM studies a limited number of particle sizes has been used, Zhao et al. (2018) and Kumar et al. (2020) used a continuous distribution of particle size, i.e. poly-sized mixtures with the general form of $1C[(PS/1Sh)]$. Zhao et al. (2018) studied the discharge of mixtures with a log-normal size distribution from a conical

hopper. As shown in **Fig. 7**, they examined the effect of the width of size distribution, defined as the ratio of standard deviation to mean diameter (σ/μ) on segregation and concluded that the higher the width, the greater the size segregation will be. This agrees with observations on the impact of size ratio on the segregation of binary-sized mixtures, as the size ratio in binary-sized mixtures is essentially the same as the width of size distribution in poly-sized mixtures.

In another study, Kumar et al. (2020) studied the discharge from a hopper of mixtures with the Rosin-Rammler size distribution as follows:

$$R = 1 - \exp\left[-\left(\frac{x}{x'}\right)^{n}\right] \tag{2}$$

with size distribution's width (n) and location parameters (x'). It was found that the width has more impact on the segregation than location parameters. Moreover, they conducted a comparative analysis between the log-normal and Rosin-Rammler particle size distribution (PSD) with the same width and observed that the latter showed a higher segregation extent. They also reported that the extent of segregation is increased with more fine particles which contradicts the observations in past studies on the segregation of binary-sized mixtures (Ketterhagen et al., 2008; Xu et al., 2017; Zhang et al., 2018; Z. Zhang et al., 2020). This conflict may lie in the fact that comparing a continuous size distribution with a binary-sized mixture requires selection of the right cut-off size between fine and coarse particles, which is not always a trivial task.

To date, a large number of segregation-related studies focused on the effect of particle size and mass fraction in binary-sized mixtures. Generally, it has been found that reducing the size ratio as well as increasing the mass fraction of fine particles lessen segregation. With respect to the size ratio, however, there is no unanimous agreement either on the critical size ratio which promotes segregation or on the effect of increasing the size ratio on segregation in general. Overall, there is no single limiting size ratio above which segregation happens. Also, there is no unanimous agreement on the effect of increasing the size ratio on segregation. The reason behind this is twofold. Firstly, apart from size ratio, other factors such as material properties (e.g., mass fraction), geometric, and operational parameters also play a crucial role in segregation phenomena. Secondly, percolation rate measurements in shear cells have shown that segregation can occur for all size ratios, and larger size ratios only serve to accelerate its occurrence (Bridgwater, 1994; Bridgwater et al., 1978; Tang and Puri, 2005). Similar to the size ratio, the effect of the mass ratio of fine particles on segregation is not consistent, leading to the conclusion that the results of one study cannot be applied to all cases since other factors (e.g., geometrical and operational parameters) play a key role as well.

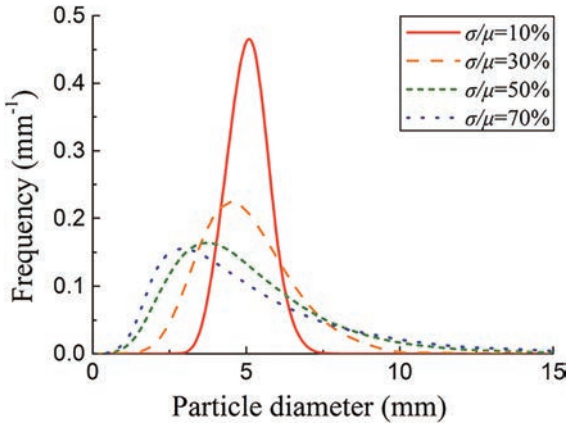


Fig. 7 Different log-normal size distributions. Reproduced with permission from Ref. (Zhao et al., 2018). Copyright 2017, John Wiley and Sons.

4.1.2 Particle density

The difference in particle density is another known factor to cause segregation. As mentioned in **Section 2**, the density of particles in a single material is assumed to be constant. Therefore, the difference in particle density is equivalent to having different materials. For instance, what is referred to as a "binary-density" mixture is basically a two-component mixture with the notation of $2C[(1S/1Sh) + (1S/1Sh)]$.

While a number of earliest experimental studies on the mixing and segregation of granular materials argued that particle density does not affect segregation considerably (Vallance and Savage, 2000; Williams, 1976), some others suggested that the difference in density should be taken into account in segregation analysis (Bridgwater et al., 1978; Drahun and Bridgwater, 1983; Khakhar et al., 1999). There has been, however, little systematic analysis of density-driven segregation in free-flowing granular materials using DEM. Seil et al. (2012) investigated the segregation of mixtures discharging from two hoppers. They observed that the heavier particles tend to gather in the centre areas and that the extent of segregation is linear to the density ratio. In another study on an inclined plane, Tripathi and Khakhar (2013) observed that heavy particles sink to near the base, and light particles form a layer close to the free surface with a mixed region in between, which was confirmed in other studies (Panda and Tan, 2020a; Wang et al., 2018, 2023). Furthermore, they showed that higher density ratios result in stronger segregation.

In conclusion, particle density has been shown to affect segregation to some extent. However, the significance of its effect compared to other factors such as the difference in particle size is unclear as yet. More effort on density-induced segregation in various systems is required to pave the way for developing DEM models for multi-component segregation.

4.1.3 Particle shape

Only a few of the studies found focused on modelling the effect of particle shape on the extent of segregation. These studies can be classified into two groups. The first group includes studies in which the mixtures are composed of two particle shapes to investigate shape-induced segregation. Using the multi-sphere approach, Mandal and Khakhar (2019) studied the flow of mixtures of spherical and non-spherical particles of the same volume down a rough inclined plane (cf. **Fig. 8**). They found that the geometric mean diameter (i.e., $d_g = \lambda^{1/3}d$, where λ is the aspect ratio and d is the diameter of the constituent spheres) is a good representative of the effective size for irregularly shaped particles, and the extent of segregation of two species depends on the ratio of the geometric mean diameter of particles. Moreover, it was observed that at the steady state, the particles with a larger geometric mean diameter accumulate near the free surface.

Zhao and Chew (2020a) studied the flow behaviour of binary-shaped mixtures during discharge from a hopper. They modelled seven different particle shapes (a sphere, two ellipsoids, two cylinders, and two cuboids (as shown in **Fig. 9**), all with an aspect ratio between 0 and 2 and the same volume. Considering various combinations of these particle shapes, they observed that mixtures of cylinders and cuboids exhibited the least segregation and the ellipsoids mixed with cylinders were the most segregated mixtures.

Second, studies in which the segregation behaviour of different mixtures, each component composed of a particular shape, is analysed. Zhao and Chew (2020b) compared the discharging behaviour of mixtures with log-normal PSD composed of ellipsoids, cylinders or cuboids and observed that ellipsoids show a very similar segregation behaviour to spheres. The cuboids and ellipsoids exhibit the lowest and the highest segregation extent, respectively.

Concluding, very little attention has been paid to shape-induced segregation in DEM-based studies. Past studies have demonstrated that the difference in particle shape itself can induce segregation (Mandal and Khakhar, 2019; Zhao and Chew, 2020a). However, it is unclear how particle shape induces segregation and specifically, which shape characteristics are more significant for segregation. Therefore, further work needs to be done to shed light on shape-induced segregation. Challenging herein are the computational expense of irregularly shaped particles and the fact that particle shape is not independent of particle size. This is very important since if only the segregation induced by particle shape is of interest, the "effective" particle size should be the same to avoid misinterpretation (Shekhar et al., 2023). Therefore, we second that attempts should be made to establish the criteria for finding the "effective" size of non-spherical particles for segregation (Yu et al., 2020).

4.1.4 Combinations of particle size, density and shape

While the preceding subsections were focused on studies examining variations in a single particle property (such as size, density, or shape), a limited number of research works investigated mixtures with multiple properties that vary simultaneously. To systematically discuss them, these studies are grouped below using the symbols in **Fig. 5** and **Table 7**:

(A+B). Most of the studies varied the particle size and density at the same time. Two different scenarios can be distinguished: 1. a mixture of (small/heavy) and (large/light) particles, in which the percolation and buoyancy mechanisms work together, or, 2. a mixture composed of small/light and large/heavy particles where percolation and buoyancy mechanisms oppose each other. **Fig. 10** illustrates these two scenarios. As can be seen in **Fig. 10(a)**, in the first scenario, both percolation and buoyancy mechanisms act together and (small/heavy) particles sink into the mixture. However, in the second scenario as in **Fig. 10(b)**, the dominant segregation mechanism is not known a priori and should be studied case by case. Past studies indicated that in the first scenario, reducing the size ratio and/or density ratio leads to less segregation and could be used as a way to suppress segregation (Terui et al., 2017; Xu et al., 2017, 2018a). For the second scenario, Ketterhagen et al.

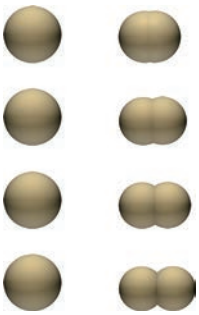


Fig. 8 Different combinations of spherical and non-spherical particles. Reproduced with permission from Ref. (Mandal and Khakhar, 2019). Copyright 2019, AIP Publishing.

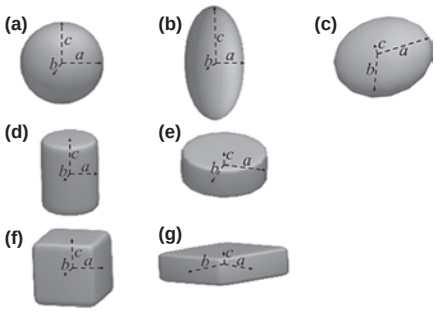


Fig. 9 Different particle shapes modelled. Reproduced with permission from Ref. (Zhao and Chew, 2020a). Copyright 2020, John Wiley and Sons.

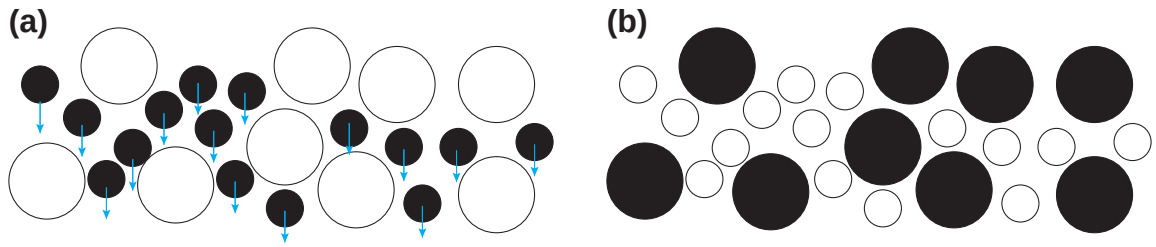


Fig. 10 Two scenarios for particles differing in both size and density (solid black colour indicates heavier particles), **(a)** first scenario; a mixture of (small/heavy) and (large/light) particles, and **(b)** second scenario; a mixture of (small/light) and (large/heavy) particles.

(2008) varied the density ratio from 0.33 to 3.0 for a size ratio of 4.3, and no significant segregation was detected during discharge from a wedge-shaped hopper. Similarly, Tao et al. (2013) increased the density ratio from 0.5 to 2.0 for a mixture with a size ratio of 4.0 and observed that segregation was negligible.

(A+C). In attempts to explore the simultaneous effect of particle size and shape on segregation, several studies varied the particle shape of binary-sized mixtures, i.e. mixtures in the form of 1*C*[(2*S*/2*Sh*)]. Mandal and Khakhar (2019) studied the flow of mixtures of non-spherical particles where the two particle types differ in both volume (i.e., size) and shape, and observed that the segregation extent increases for larger geometric mean diameter ratios. Tao et al. (2013) simulated binary-sized mixtures with different particle shapes including spherical, corn-shaped, cylindrical and ellipsoidal particles. It was observed that particle shape has a significant effect on the segregation extent with the most segregated system for ellipsoidal and the least for spherical particles.

(A+B+C). A few studies examined the segregation in mixtures differing in particle size, density and shape. Liao et al. (2023) investigated the segregation behaviour of lump ore and pellets that differed in size and density. To examine the impact of particle shape on segregation, they simulated three different shapes of lump ore particles, namely spheres, cylinders, and schistous particles and concluded that particle shape has a significant effect on segregation, with spheres showing the least amount of segregation. In the mixture of sinter and briquette, Kim et al. (2020) changed both the shape and mass ratio of the briquette and observed that while the shape had little effect on segregation, a mass ratio higher than 20 % led to significant segregation.

Despite previous efforts to investigate the influence of various material properties on segregation, there remains a significant knowledge gap. While the majority of natural and industrial mixtures are multi-component, i.e. **(A+B+C)** in **Table 7**, most studies have concentrated on binary or ternary-sized mixtures consisting of spheres. Therefore, a more comprehensive and rigorous approach towards material properties that takes various combinations of size, density and shape into account is required to accurately predict segregation patterns and occurrences.

4.2 System configurations

In addition to the material properties, system parameters play a key role in the segregation phenomena occurring in particulate systems because they influence the motion of the particles. In gravity-driven handling processes, two main pieces of equipment can be distinguished: hopper/silo and chute/inclined surfaces. A review of these systems in the context of segregation is presented in the following paragraphs.

4.2.1 Hopper

Segregation during hopper discharge has been studied since the early ’80s when most studies were experimental. Ketterhagen et al. (2007) were one of the first to model segregation during cylindrical hopper discharge using DEM in 2007. Since then, a number of DEM studies have investigated the influence of geometric properties on the extent of segregation by varying the outlet width, the slope of the bottom wall and the smoothness of the walls.

Two main flow regimes are distinguished during hopper discharge: mass flow, where the entire body of mass inside the hopper is in motion during discharge, and funnel flow (Jenike, 1967; Saleh et al., 2018; Schulze et al., 2008); funnel flow is less desirable as it imposes asymmetric pressure distribution and causes significant segregation which can be harmful to both hopper structural stability and particulate homogeneity (Saleh et al., 2018). The flow mode is mainly dependent on the bottom wall angle (θ_c) and wall friction angle (ϕ_x). Smoother and steeper walls (i.e., low θ_c) most likely induce a mass flow regime and are less likely to induce segregation. This was also confirmed in several DEM studies (Ketterhagen et al., 2009, 2008; Saleh et al., 2018; Yu and Saxén, 2010).

Several studies used DEM to gain a deeper insight into segregation during hopper discharge. T.F. Zhang et al. (2020) varied the angle of the hopper wall from 15° to 90° and observed that larger angles (i.e., flatter walls) lead to faster percolation of small particles, increasing their tendency to gather at side walls (cf. **Fig. 11(a)**). Similarly, Z. Zhang et al. (2020) showed that the increase in the hopper angle promotes segregation in the bottom regions (red

regions in **Fig. 11(b)**). However, they found that with larger angles, the percolation near the wall region decreases. This disagreement might be because of the different size ratio, wall condition (i.e. boundary walls in T.F. Zhang et al. (2020)), or a different method of assessing segregation (cf. **Section 3.2**). Also, it is remarkable that in T.F. Zhang et al. (2020), the hopper outlet size of $3d_l$ (where d_l is the diameter of the large particles) is used, which does not satisfy fundamental hopper design principles (Schulze et al., 2008) and can affect the segregation results.

Stating that the bottom angle of the hopper is a decisive factor in the flow mode, Huang et al. (2022) proposed an optimised design which increases the mass flow zone and as a result, achieves less size segregation (cf. **Fig. 12**).

In addition to the hopper wall angle, the outlet size can also affect segregation during hopper discharge. Ketterhagen et al. (2008) found that the increase in outlet width reduces the segregation of mixtures discharging from wedge-shaped hoppers. Although Z. Zhang et al. (2020) confirmed that the percolation in the bottom part of the hopper reduces in the case of a bigger outlet, a higher segregation degree near hopper walls was observed which can be related to wall effects. Taking the effect of both the hopper outlet and wall angle into account, Ketterhagen et al. (2008) claimed that segregation conditions remain the same for hoppers with the same aspect ratio of hopper height to hopper width.

To investigate the effect of flow-correcting inserts, Cliff et al. (2021) compared the segregation behaviour of binary-sized mixtures during discharge from a hopper with

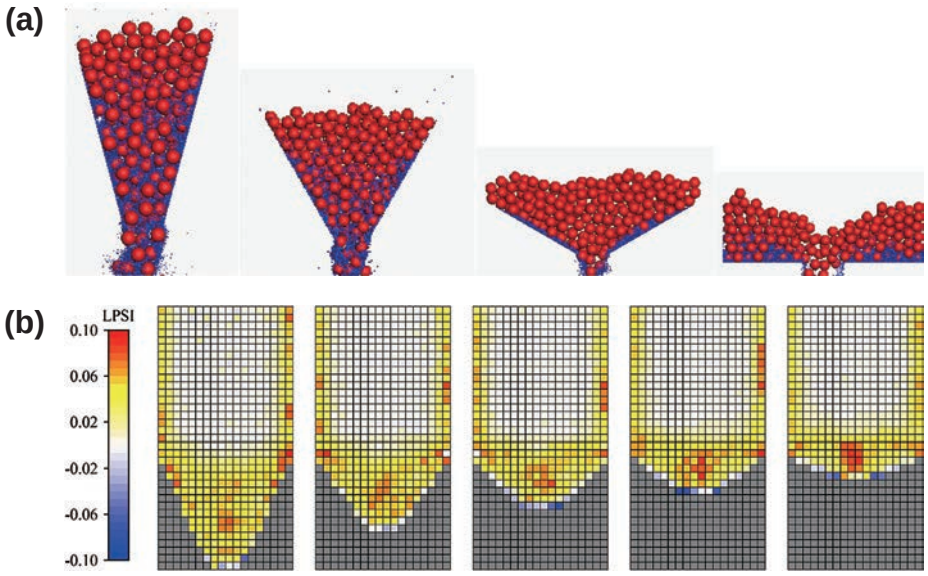


Fig. 11 The effect of hopper wall angle on size segregation in two studies: **(a)** Reproduced with permission from Ref. (T.F. Zhang et al., 2020). Copyright 2020, Elsevier. and **(b)** Reproduced from Ref. Z. Zhang et al. (2020), used under Creative Commons CC-BY-NC-ND License.

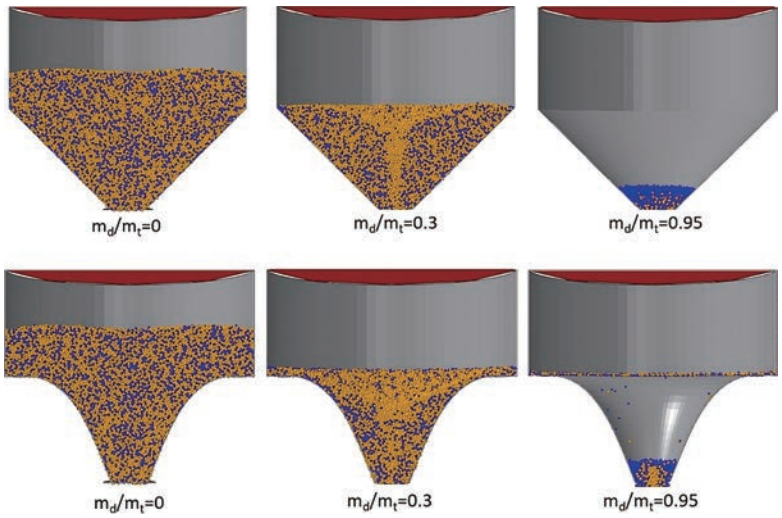


Fig. 12 The effect of different hopper design on segregation during hopper discharge at different discharging fractions (m_d/m_t). Reproduced with permission from Ref. (Huang et al., 2022). Copyright 2022, Elsevier.

and without an insert (cf. **Fig. 13(a)**). They stated that in the case of a hopper with an insert, lower velocity gradients at the free surface lead to less segregation (cf. **Fig. 13(b)**).

While most of the works mentioned above studied concentric hoppers, Ketterhagen and Hancock (2010) compared the segregation of binary-sized mixtures in eccentric and concentric hoppers (cf. **Fig. 14(a)**). They found that while the eccentric hopper had slightly less segregation, the segregation profiles around the outlet were completely different (cf. **Fig. 14(b)**). Additionally, they modified the design of the eccentric hopper, resulting in improved segregation.

In conclusion, designing for mass flow is beneficial to avoid size segregation during hopper discharge. This can be achieved by steeper and smoother walls. However, several studies observed insignificant effects of these factors on segregation. The reason for the conflict between these studies is that besides geometric parameters, material properties and operational parameters can influence particle velocities and segregation. This makes it challenging to compare the findings of different studies and arrive at a definitive conclusion. Therefore, a more robust approach is needed to investigate the simultaneous effect of different geometric factors on segregation and its dependence on material properties. Moreover, the work found evaluated only single-component mixtures, and the effect of geometric design parameters in the case of multi-component segregation is missing.

4.2.2 Chutes

Chutes are often used to transfer materials from one piece of equipment to another. They can have different cross-sectional shapes (e.g., semicircular, rectangular), lengths, curvatures and wall roughness. While the chute angle may be regarded as a system configuration parameter in certain cases, e.g., transfer chutes, it is considered an operational parameter in dynamic systems such as blast furnaces. Therefore, we will be discussing the chute angle later in **Section 4.3.2** of this paper.

Segregation can occur simultaneously in three directions: in the direction of the flow (longitudinal/stream-wise segregation), from the chute to the free surface (vertical/normal segregation) and from one side wall to the other (horizontal/cross-stream-wise segregation). During chute

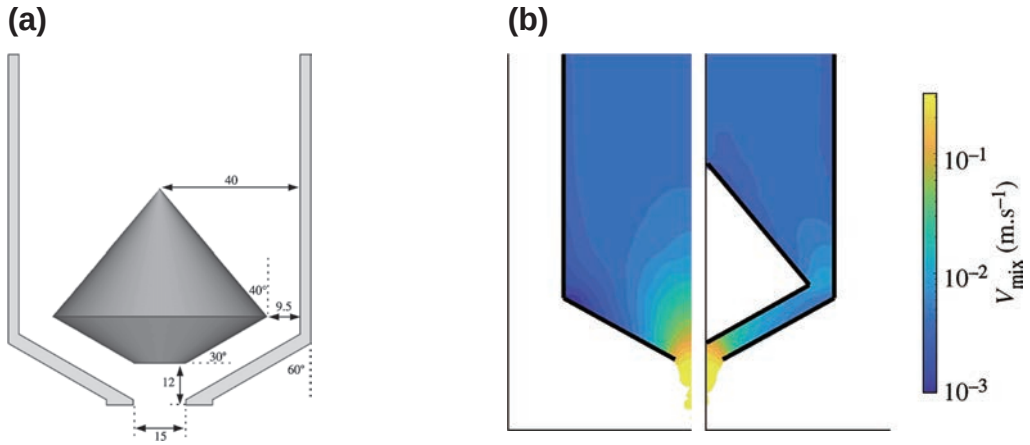


Fig. 13 **(a)** The cross-sectional view of the hopper with insert, **(b)** Difference in the velocity gradient between the hopper with (right) and without (left) insert. Reproduced with permission from Ref. (Cliff et al., 2021). Copyright 2021, The Royal Society.

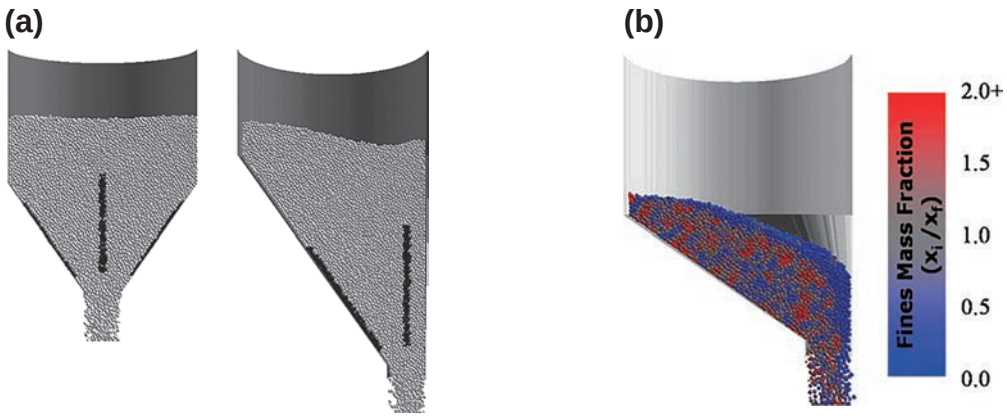


Fig. 14 **(a)** Concentric and eccentric hopper, and **(b)** Segregation profile in the eccentric hopper. Reproduced with permission from Ref. (Ketterhagen and Hancock, 2010). Copyright 2010, Elsevier.

flow, segregation can happen in two stages. Firstly when the material is inside the chute, gravitational forces, centrifugal and Coriolis forces, inter-particle friction and particle-wall friction forces act on the particles (Zhang et al., 2014). Mio et al. (2008b) found that particles segregate inside the chute with smaller particles at the bottom wall of the chute and larger ones on top. In the second stage, the material leaves the chute and trajectory segregation causes larger particles to travel further (Mio et al., 2008b). The effect of chute-related geometric parameters on segregation was researched by employing either a simple inclined plane (Zhao et al., 2022) (to minimise the effect of side walls) or a real 3D chute (Panda and Tan, 2020a).

With respect to the effect of the cross-sectional shape of the chute, Kou et al. (2019) investigated the effect of three different shapes, namely semi-circular, trapezoid, and rectangular on the segregation of ferrous burden (i.e., pellet, sinter and lump ore) forming a heap in the blast furnace throat. They found that the chute cross-sectional shape significantly affects the radial size distribution of materials and the effect is intensified with larger chute angles and higher rotating speeds. Moreover, unlike trapezoid and rectangular chutes, the semi-circular chute was reported to maintain a uniform radial size distribution regardless of the chute angle and rotating speed. Panda and Tan (2020a; 2020b) focused on the segregation inside the chute and compared the segregation between rectangular and semi-circular chutes. It was observed that the rectangular channel resulted in slightly higher segregation in the stream-wise direction, while there were barely any differences in cross-stream and vertical directions.

In terms of the impact of chute length, the observations revealed that since segregation occurs within the chute, an increase in the chute length leads to a greater extent of segregation (Bhattacharya and McCarthy, 2014; Kou et al., 2013; Yu and Saxén, 2012; Zhang et al., 2014). Bhattacharya and McCarthy (2014) determined the critical chute length for trajectory segregation of ternary-sized mixtures discharging from a hopper on to the chute, using both theoretical equations and simulations which yielded 4.0 and 5.4 m, respectively. They claimed that with other parameters fixed, there is significant segregation in the sampling boxes located under the chute for the chute longer than the critical length. For the radial segregation of multi-component mixtures of sinter, pellet and ore, Hong et al. (2021) observed that the effect of chute length is negligible.

Mantravadi and Tan (2020) examined the effect of bend angle (i.e. curvature) in periodic flow inversions (see **Fig. 15**)—an idea initially introduced by Shi et al. (2007)—on reducing the size segregation of binary-sized mixtures and observed that a bend angle between 120 and 150 degrees leads to the minimum extent of segregation.

Zhou et al. (2016) varied the wall roughness by using the wall friction coefficient and found that a higher base roughness significantly accelerates segregation. However, in the case that base friction was larger than inter-particle friction, no effect on the flow regime and segregation was observed. Shirsath et al. (2015) studied the effect of chute wall roughness on the segregation of binary-density mixtures, i.e., $2C[(1S/1Sh) + (1S/1Sh)]$. They implemented the roughness artificially by modelling a number of particles at chute walls, attributing the ratio of the diameter between surface particles and flowing particles (ranging from 0.5 to 2.0) to the degree of roughness. They reported that wall roughness has a considerable effect on segregation as it is negligible for the smooth (but frictional) chute wall. While it was observed that the degree of segregation increases with wall roughness, this increase plateaus when the diameter of wall particles exceeds the flowing particle size. However, it is unclear to what extent the method of modelling wall roughness in this work is representative for roughness at micro scale.

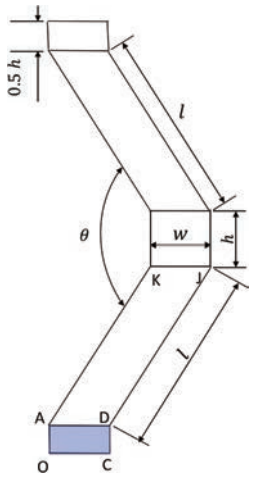


Fig. 15 The periodic flow inversion with a bend angle of θ. Reproduced with permission from Ref. (Mantravadi and Tan, 2020). Copyright 2020, Elsevier.

Concluding, the geometric aspects of chutes including cross-section shape, length, curvature and wall roughness can significantly influence segregation. Generally, it has been found that longer chutes with rougher walls promote segregation.

4.3 Operational parameters

Besides the material properties and system configurations discussed above, operational parameters are also among the influencing factors on segregation. In order to gain a deeper insight, related studies are reviewed in the following subsections under different categories based on the system type, namely hopper, chute and other systems.

4.3.1 Hopper filling operations

Various hopper-related operational parameters, including filling method, filling angle, and filling position have been studied in the past. Several studies investigated the

influence of various hopper filling methods, i.e., different components/sizes being charged in separate layers or in a pre-mixed state, on the segregation after hopper discharge (Chibwe et al., 2020; Ketterhagen et al., 2008, 2007; Mio et al., 2010; Yu and Saxén, 2010). Although Ketterhagen et al. (2008), Yu and Saxén (2010) and Chibwe et al. (2020) used slightly different setups and filling patterns, their conclusion was that the initial filling method significantly affects the segregation.

Apart from the filling method, the filling position was found to significantly influence segregation. Wu et al. (2013) investigated the effect of burden apex (i.e., the highest point on the hill formed when materials are charged into the hopper) on the segregation during hopper charging and discharging. It was found that the burden apex mostly influences the particle size distribution during charging but has little effect during discharging. In the case of a Paul-Wurth hopper, Zhang et al. (2021) also observed that the filling position has a significant effect on the segregation and there was strong segregation in the case of the right and left filling positions (cf. **Fig. 16(a)**). Moreover, they observed that a filling angle closer to the vertical position (cf. **Fig. 16(b)**) and a larger charging outlet (cf. **Fig. 16(c)**) reduced the extent of segregation.

Cliff et al. (2021) showed that a continuous filling operation, as opposed to batch processing, significantly reduces the amount of segregation because segregation mostly occurs in the last 25 % of hopper discharge.

Concluding, the filling method, filling position and filling angle significantly affect segregation downstream (i.e., during hopper discharge). This means that all the handling steps should be accurately modelled in order to achieve a reliable assessment of segregation.

4.3.2 Chute operations

With respect to chute-related operational parameters, several studies have investigated the effect of chute angle (θ) (Jing et al., 2015; Kou et al., 2019, 2018, 2013; Mio et al., 2009; Nakano et al., 2012; Tripathi and Khakhar, 2011; Xu et al., 2018b; You et al., 2016; Zhang et al., 2014), tilting direction (Terui et al., 2017), rotating speed (ω) (Kou et al., 2019, 2013; You et al., 2016), fill level (Izard et al., 2021; Panda and Tan, 2020a), the number of chute rotations (Mio et al., 2012) and installation of a damper (Mio et al.,

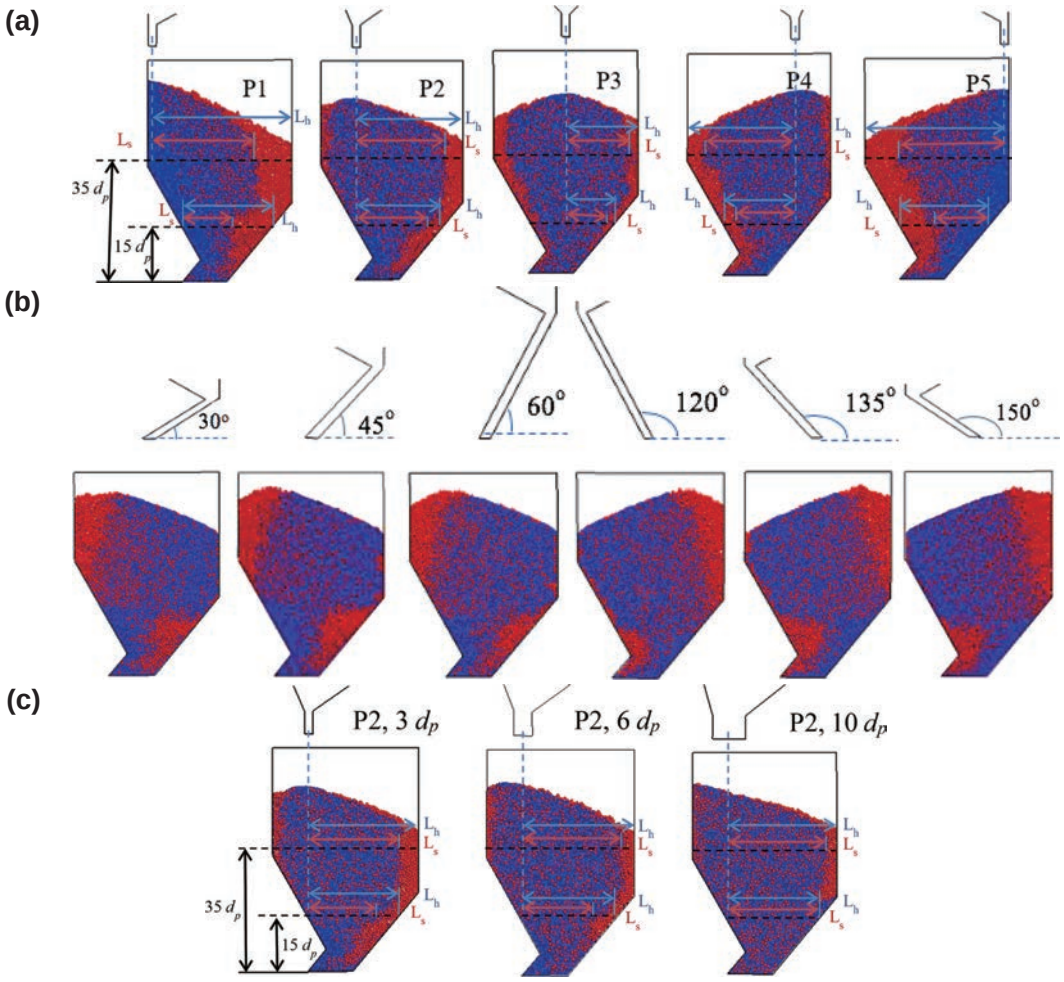


Fig. 16 The effect of **(a)** filling position, **(b)** filling angle and **(c)** hopper outlet on segregation during hopper charging. Reproduced with permission from Ref. (Zhang et al., 2021). Copyright 2021, Elsevier.

2008b). Some of the parameters are schematically illustrated in **Fig. 17**.

It should be noted that in a rotating chute, particles are subjected not only to gravitational forces but also to Coriolis and centrifugal forces (Shirsath et al., 2015). The relative impact of inertial and Coriolis forces is quantified by the Rossby number (**Eqn. (3)**):

$$Ro = \frac{v_a}{2\omega L \cos\theta} \tag{3}$$

where v_a, ω, L, and θ denote the flow velocity, chute rotation rate, chute length and chute angle, respectively. In the case of $Ro \gg 1$, the effect of the rotation rate can be neglected. For instance, Shirsath et al. (2015) varied the chute rotation rate from 4 to 16 rpm and observed Ro larger than 1, concluding that the flow was gravity driven. Also, the Froude number (**Eqn. (4)**) can be used to quantify the relative significance of the centrifugal force compared to the gravitational force (Shirsath et al., 2015):

$$Fr = \frac{\omega^2 L \cos\theta}{g} \tag{4}$$

In the case of $Fr \ll 1$, the gravitational force is dominant, preventing the particles from escaping out of the chute.

The chute angle is an important flow control parameter as it is used to increase or decrease the flow velocity. Past DEM studies have investigated the effect of chute angle on the segregation occurring either inside the chute or when particles flow out and form a heap. Regarding the segregation happening inside the chute, Tripathi and Khakhar (2011) observed that the shear rate and extent of segregation in a vertical direction increased with a lower angle. Similarly, Jing et al. (2015) found that segregation occurs faster as the angle decreases, which was expected since the rate of acceleration increases as the chute is steeper. However, the final (converged) segregation degree was similar for different chute angles and, surprisingly, the converged state was reached at approximately the same time for different angles.

For segregation occurring after discharging from chutes, several studies have found that reducing the chute angle intensifies the segregation in different systems, namely blast furnace throat (Kou et al., 2019; Mio et al., 2009; Xu et al., 2018b; Zhang et al., 2014), feed bed of sintering machine (Nakano et al., 2012), COREX melter gasifier (Kou et al., 2015, 2013; You et al., 2016). However, Zhang et al. (2014) varied the chute angle from 21° to 37° and observed that the radial segregation index (RSI) would not necessarily decrease (cf. **Fig. 18**). Also, Kou et al. (2013) observed that increasing the chute angle from 10° to 30° first leads to a decrease of segregation of large particles and then to an increase.

In modern blast furnaces equipped with the Paul-Wurth Bell-Less Top® charging system, as well as in the COREX process, a rotating chute is used to distribute materials in the circumferential directions of the furnace throat (Cameron et al., 2019; Kou et al., 2013). In addition to the previously discussed chute angle, other operational parameters such as the rotating speed, tilting direction (i.e. changing the angle from low to high or vice versa as shown in **Fig. 17**), and the number of rotations have been studied with respect to segregation. Terui et al. (2017) modelled a mixture of coke and sinter and two types of tilting directions, namely conventional tilting (i.e., from wall to centre direction) and reverse tilting (i.e., from centre to the wall direction). They found that with reverse tilting, coke particles are less segregated as shown in **Fig. 19**. The rotating speed of the chute was found to have a negligible effect on segregation compared to the chute angle (Kou et al., 2019, 2013; You et al., 2016). Mio et al. (2012) observed that an increase in the number of chute rotations intensifies segregation, leading to a larger mean particle size near the

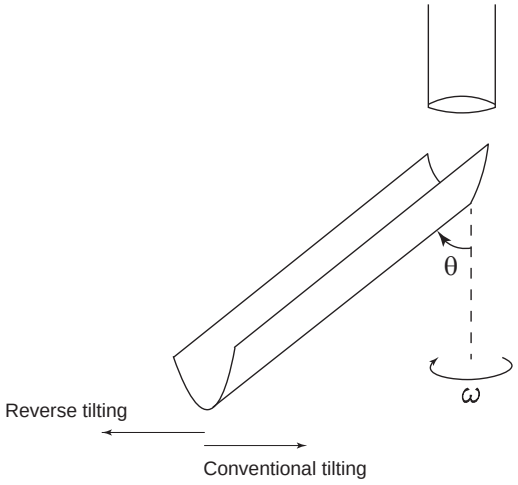


Fig. 17 Schematic view of a rotating chute and related operational parameters: chute angle (θ), rotating speed (ω).

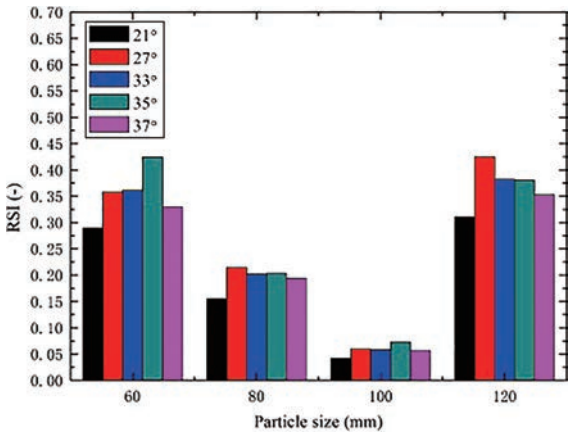


Fig. 18 Change in radial segregation index (RSI) with different chute angle. Reproduced with permission from Ref. (Zhang et al., 2014). Copyright 2014, Elsevier.

centre of the blast furnace.

The volume (or mass) flow rate through a chute is another operational parameter which is generally varied on an on-demand basis. For a given chute design, increasing/decreasing the flow rate results in a higher/lower fill level of the chute. Panda and Tan (2020a) found that the increase in the fill level causes the small and large particles to move together, i.e., decreases the velocity difference, resulting in lower segregation in the cross-stream and vertical directions of the chute. Although it was observed that the fill level does not affect velocities in a stream-wise direction, segregation was decreased because of less available space for percolation due to denser packing. In a study on sinter cooler charging systems, Izard et al. (2021) investigated the effect of the fill level of the chute (i.e. 20 %, 50 % and 90 %) on the segregation pattern in the trolleys and found that while a filling ratio smaller than 50 % imposes an increasing size heterogeneity in the trolley, no change in the segregation pattern was observed for a filling ratio larger than 50 %.

In conclusion, the operational parameters for operating moving chutes including chute angle, tilting direction, rotating speed and fill level, affect the segregation to some extent. Based on the studies reviewed here, it appears that chute angle and fill level may be more significant than the other parameters. However, further research is needed to confirm this hypothesis and to fully understand the complex nature of segregation in granular mixtures discharging from moving chutes. Nevertheless, all the parameters have the potential to be adjusted with the purpose of reducing or controlling segregation.

4.3.3 Other systems

In addition to hoppers and chutes, other operation-related factors have been investigated in the context of the gravity-driven segregation of cohesionless materials. This includes the falling height in the stockpile (Kou et al., 2013; Zhang et al., 2017), the method of "discharge" from a v-blender (which is essentially a gravity-driven flow) (Pereira and Cleary, 2013), the bottom base shape of the COREX furnace (cf. **Fig. 20**) (Kou et al., 2018) and feed rate as well as rill plate angle in an iron ore sinter strand (Li et al., 2019). Hence, in every industrial system, there are several operational parameters that can affect segregation. Detecting these parameters and studying their effect utilising DEM can pave the way to optimise the industrial processes with respect to segregation. This is highly advantageous because, in industrial applications, it is not always possible to control segregation by modifying material properties and system configurations.

5. Conclusion

This review paper presents an overview of the state of the art in the DEM modelling of the segregation behaviour of complex multi-component mixtures in applications involving the gravity-driven flow of dry, cohesionless granular materials. First of all, a novel scientific notation has been introduced to ensure consistency and accurately describe different types of mixtures. The main findings of this review can be summarised as follows:

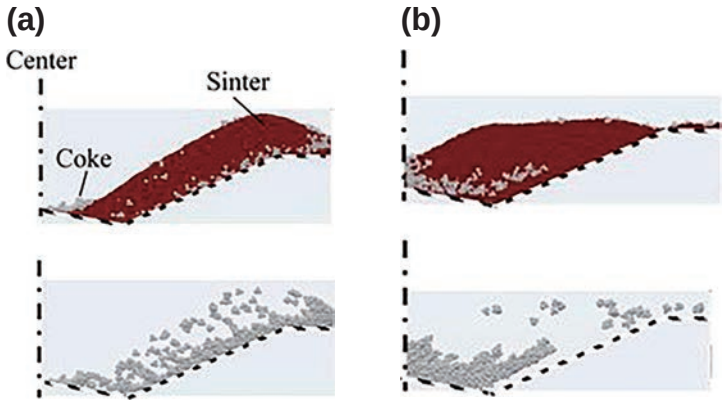


Fig. 19 Cross-sectional view of the radial distribution of a coke-sinter mixture for **(a)** reverse tilting and **(b)** conventional tilting. Reproduced with permission from Ref. (Terui et al., 2017), used under Creative Commons CC-BY-NC-ND License.

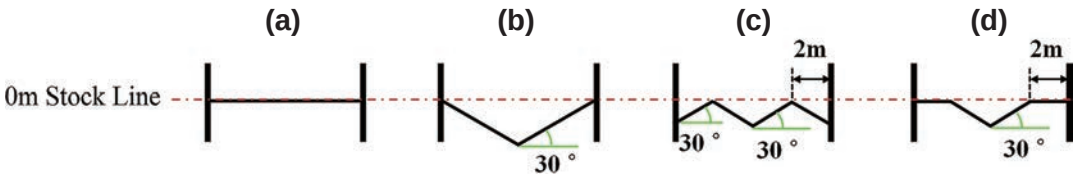


Fig. 20 Different bottom base shape of the COREX furnace. Reproduced with permission from Ref. (Kou et al., 2018). Copyright 2018, Elsevier.

- Although most mixtures existing in nature and industrial settings are considered multi-component (i.e., they contain particles differing simultaneously in size, density and shape), relatively few studies have investigated the segregation behaviour of such mixtures.
- Despite the fact that calibration is an essential part of developing a reliable DEM model, most of the past studies have omitted it. This is especially true when it comes to models of multi-component mixtures. For instance, the effect of interaction parameters between components has not yet been studied in detail. Furthermore, it is not clear whether calibrated parameter values obtained for a certain mixture composition are applicable to other compositions as well.
- The effect of size distribution and particle shape on segregation has not yet been fully understood. Considering the fact that including small particles and irregular particle shapes in the model increases computational time considerably, the effect of approximating real-world mixtures with a finite number of particle sizes and spherical particles should be comprehensively studied.
- When quantifying segregation experimentally, non-invasive techniques such as image analysis are generally more suitable than conventional invasive methods (i.e., sampling and weighing), since non-invasive techniques do not disturb the mixture structure and are applicable to mixtures differing in both size and density.
- Results of past DEM studies on segregation show that the effects of different parameters influencing segregation, i.e., material properties, system configurations and operational parameters, should be considered together since they are highly intertwined.
- Compared to material properties and system configurations, operational parameters are relatively easier to change. Hence, to reduce and control segregation in industrial applications, operational parameters are preferential.

Acknowledgements

This research was carried out under project number T18019 in the framework of the Research Program of the Materials innovation institute (M2i) (www.m2i.nl) supported by the Dutch government. Also, this work was carried out as part of the “Industrial Dense Granular Flows” project, which received funding from the Dutch Research Council (NWO) in the framework of the ENW PPP Fund for the top sectors and from the Ministry of Economic Affairs in the framework of the “PPS-Toeslagregeling”.

The authors would like to extend their acknowledgements to dr.ir. Jan van der Stel and dr.ir. Allert Adema from Tata Steel IJmuiden for their invaluable contributions to this review paper.

References

Alizadeh M., Hassanpour A., Pasha M., Ghadiri M., Bayly A., The effect of particle shape on predicted segregation in binary powder mixtures, Powder Technology, 319 (2017) 313–322. DOI: 10.1016/j.powtec.2017.06.059

Artega P., Tüzün U., Flow of binary mixtures of equal-density granules in hoppers-size segregation, flowing density and discharge rates, Chemical Engineering Science, 45 (1990) 205–223. DOI: 10.1016/0009-2509(90)87093-8

Asachi M., Behjani M.A., Nourafkan E., Hassanpour A., Tailoring particle shape for enhancing the homogeneity of powder mixtures: experimental study and DEM modelling, Particuology, 54 (2021) 58–68. DOI: 10.1016/j.partic.2020.03.006

Asachi M., Nourafkan E., Hassanpour A., A review of current techniques for the evaluation of powder mixing, Advanced Powder Technology, 29 (2018) 1525–1549. DOI: 10.1016/j.apt.2018.03.031

Barik S.K., Lad V.N., Sreedhar I., Patel C.M., Investigation of mass discharge rate, velocity, and segregation behaviour of microcrystalline cellulose powder from a Copley flow tester, Powder Technology, 417 (2023) 118234. DOI: 10.1016/j.powtec.2023.118234

Bhalode P., Ierapetritou M., A review of existing mixing indices in solid-based continuous blending operations, Powder Technology, 373 (2020) 195–209. DOI: 10.1016/j.powtec.2020.06.043

Bhattacharya T., McCarthy J.J., Chute flow as a means of segregation characterization, Powder Technology, 256 (2014) 126–139. DOI: 10.1016/j.powtec.2014.01.092

Bowler A.L., Bakalis S., Watson N.J., A review of in-line and on-line measurement techniques to monitor industrial mixing processes, Chemical Engineering Research and Design, 153 (2020) 463–495. DOI: 10.1016/j.cherd.2019.10.045

Bridgwater J., Mixing and segregation mechanisms in particle flow, in: Mehta A. (Ed.) Granular Matter: An Interdisciplinary Approach, Springer New York, New York, NY, 1994, pp. 161-193, ISBN: 978-1-4612-4290-1.

Bridgwater J., Cooke M.H., Scott A.M., Interparticle percolation: equipment development and mean percolation velocities, Transactions of the Institution of Chemical Engineers, 56 (1978) 157–167.

Cameron I., Sukhram M., Lefebvre K., Davenport W., Blast Furnace Ironmaking: Analysis, Control, and Optimization, Elsevier Inc., 2019, ISBN: 978-0-12-814227-1. DOI: 10.1016/C2017-0-00007-1

Carson J.W., Royal T.A., Goodwill D.J., Understanding and eliminating particle segregation problems, Bulk Solids Handling, 6 (1986) 139–144.

Chibwe D.K., Evans G.M., Doroodchi E., Monaghan B.J., Pinson D.J., Chew S.J., Charge material distribution behaviour in blast furnace charging system, Powder Technology, 366 (2020) 22–35. DOI: 10.1016/j.powtec.2020.02.048

Cho M., Dutta P., Shim J., A non-sampling mixing index for multicomponent mixtures, Powder Technology, 319 (2017) 434–444. DOI: 10.1016/j.powtec.2017.07.011

Cleary P.W., Sawley M.L., DEM modelling of industrial granular flows: 3D case studies and the effect of particle shape on hopper discharge, Applied Mathematical Modelling, 26 (2002) 89–111. DOI: 10.1016/S0307-904X(01)00050-6

Cliff A., Fullard L.A., Breard E.C.P., Dufek J., Davies C.E., Granular size segregation in silos with and without inserts, Proceedings of the Royal Society A: Mathematical, Physical and Engineering Sciences, 477 (2021). 20200242. DOI: 10.1098/rspa.2020.0242

Coetzee C.J., Calibration of the discrete element method and the effect of particle shape, Powder Technology, 297 (2016) 50–70. DOI: 10.1016/j.powtec.2016.04.003

Coetzee C.J., Review: calibration of the discrete element method, Powder Technology, 310 (2017) 104–142. DOI: 10.1016/j.powtec.2017.01.015

Coetzee C.J., Particle upscaling: calibration and validation of the discrete

element method, Powder Technology, 344 (2019) 487–503. DOI: 10.1016/j.powtec.2018.12.022

Combarros M., Feise H.J., Zetzener H., Kwade A., Segregation of particulate solids: experiments and DEM simulations, Particuology, 12 (2014) 25–32. DOI: 10.1016/j.partic.2013.04.005

Combarros Garcia M., Feise H.J., Strege S., Kwade A., Segregation in heaps and silos: comparison between experiment, simulation and continuum model, Powder Technology, 293 (2016) 26–36. DOI: 10.1016/j.powtec.2015.09.036

Coulson M., The History of Mining: The Events, Technology and People Involved in the Industry That Forged the Modern World, Harriman House Limited, 2012, ISBN: 9781897597903.

Cundall P.A., Strack O.D.L., A discrete numerical model for granular assemblies, Geotechnique, 29 (1979) 47–65. DOI: 10.1680/geot.1979.29.1.47

de Silva S.R., Dyrøy A., Enstad G.G., Segregation mechanisms and their quantification using segregation testers, in: Rosato A.D., Blackmore D.L. (Eds), IUTAM Symposium on Segregation in Granular Flows, Dordrecht, Springer Netherlands, 2000, pp. 11–29. DOI: 10.1007/978-94-015-9498-1_2

Do H.Q., Aragón A.M., Schott D.L., A calibration framework for discrete element model parameters using genetic algorithms, Advanced Powder Technology, 29 (2018) 1393–1403. DOI: 10.1016/j.apt.2018.03.001

Drahun J.A., Bridgwater J., The mechanisms of free surface segregation, Powder Technology, 36 (1983) 39–53. DOI: 10.1016/0032-5910(83)80007-2

Duffy S.P., Puri V.M., Primary segregation shear cell for size-segregation analysis of binary mixtures, KONA Powder and Particle Journal, 20 (2002) 196–207. DOI: 10.14356/kona.2002022

El Kassem B., Salloum N., Brinz T., Heider Y., Markert B., A semi-automated dem parameter calibration technique of powders based on different bulk responses extracted from auger dosing experiments, KONA Powder and Particle Journal, 38 (2021) 235–250. DOI: 10.14356/kona.2021010

Gao S., Ottino J.M., Umbanhowar P.B., Lueptow R.M., Modeling granular segregation for overlapping species distributions, Chemical Engineering Science, 231 (2021) 116259. DOI: 10.1016/j.ces.2020.116259

Gao Z., Liu J., Gao T., Advanced inside-furnace monitoring techniques implemented on the new large blast furnace of Shagang, in: AISTech—Iron and Steel Technology Conference Proceedings, 2010, pp. 565–571.

González-Montellano C., Fuentes J.M., Ayuga-Téllez E., Ayuga F., Determination of the mechanical properties of maize grains and olives required for use in DEM simulations, Journal of Food Engineering, 111 (2012) 553–562. DOI: 10.1016/j.jfoodeng.2012.03.017

Gray J.M.N.T., Particle segregation in dense granular flows, Annual Review of Fluid Mechanics, 50 (2018) 407–433. DOI: 10.1146/annurev-fluid-122316-045201

Hong Z., Zhou H., Wu J., Zhan L., Fan Y., Zhang Z., Wu S., Xu H., Wang L.P., Kou M., Effects of operational parameters on particle movement and distribution at the top of a bell-less blast furnace based on discrete element method, Steel Research International, 92 (2021) 2000262. DOI: 10.1002/srin.202000262

Huang A.N., Kuo H.P., Developments in the tools for the investigation of mixing in particulate systems—A review, Advanced Powder Technology, 25 (2014) 163–173. DOI: 10.1016/j.apt.2013.10.007

Huang X., Zheng Q., Liu D., Yu A., Yan W., A design method of hopper shape optimization with improved mass flow pattern and reduced particle segregation, Chemical Engineering Science, 253 (2022) 117579. DOI: 10.1016/j.ces.2022.117579

Izard E., Moreau M., Ravier P., Discrete element method simulation of segregation pattern in a sinter cooler charging chute system, Particuology, 59 (2021) 34–42. DOI: 10.1016/j.partic.2020.08.004

Jain N., Ottino J.M., Lueptow R.M., Regimes of segregation and mixing in combined size and density granular systems: an experimental study, Granular Matter, 7 (2005) 69–81. DOI: 10.1007/s10035-005-0198-x

Jenike A.W., Quantitative design of mass-flow bins, Powder Technology, 1 (1967) 237–244. DOI: 10.1016/0032-5910(67)80042-1

Jin X., Chandratilleke G.R., Wang S., Shen Y., DEM investigation of mixing indices in a ribbon mixer, Particuology, 60 (2022) 37–47. DOI: 10.1016/j.partic.2021.03.005

Jing L., Kwok F.C.Y., Leung A.Y.F., Discrete element modelling of grain size segregation in bi-disperse granular flows down chute, The 4th International Conference on Particle-based Methods, Fundamentals and Applications (PARTICLES 2015), (2015) 474–484. http://hdl.handle.net/10722/213642

Kajiwara Y., Aminaga Y., Inada T., Tanaka T., Sato K. ichi, Size segregation of sinter in the top bunker of a bell-less type blast furnace, Tetsu-To-Hagane/Journal of the Iron and Steel Institute of Japan, 74 (1988) 978–984. DOI: 10.2355/tetsutohagane1955.74.6_978

Ketterhagen W.R., Curtis J.S., Wassgren C.R., Hancock B.C., Modeling granular segregation in flow from quasi-three-dimensional, wedge-shaped hoppers, Powder Technology, 179 (2008) 126–143. DOI: 10.1016/j.powtec.2007.06.023

Ketterhagen W.R., Curtis J.S., Wassgren C.R., Hancock B.C., Predicting the flow mode from hoppers using the discrete element method, Powder Technology, 195 (2009) 1–10. DOI: 10.1016/j.powtec.2009.05.002

Ketterhagen W.R., Curtis J.S., Wassgren C.R., Kong A., Narayan P.J., Hancock B.C., Granular segregation in discharging cylindrical hoppers: A discrete element and experimental study, Chemical Engineering Science, 62 (2007) 6423–6439. DOI: 10.1016/j.ces.2007.07.052

Ketterhagen W.R., Hancock B.C., Optimizing the design of eccentric feed hoppers for tablet presses using DEM, Computers and Chemical Engineering, 34 (2010) 1072–1081. DOI: 10.1016/j.compchemeng.2010.04.016

Khakhar D.V., McCarthy J.J., Ottino J.M., Mixing and segregation of granular materials in chute flows, Chaos, 9 (1999) 594–610. DOI: 10.1063/1.166433

Kim K.M., Bae J.H., Park J.I., Han J.W., Segregation charging behavior of ultra-fine iron ore briquette in sinter feed bed: DEM analysis, Metals and Materials International, 26 (2020) 1218–1225. DOI: 10.1007/s12540-019-00415-y

Kou M., Wu S., Du K., Shen W., Sun J., Zhang Z., DEM simulation of burden distribution in the upper part of COREX shaft furnace, ISIJ International, 53 (2013) 1002–1009. DOI: 10.2355/isijinternational.53.1002

Kou M., Wu S., Wang G., Zhao B., Cai Q., Numerical simulation of burden and gas distributions inside COREX shaft furnace, Steel Research International, 86 (2015) 686–694. DOI: 10.1002/srin.201400311

Kou M., Xu J., Wu S., Zhou H., Gu K., Yao S., Wen B., Effect of cross-section shape of rotating chute on particle movement and distribution at the throat of a bell-less top blast furnace, Particuology, 44 (2019) 194–206. DOI: 10.1016/j.partic.2018.07.010

Kou M., Xu J., Zhou H., Wen B., Gu K., Yao S., Wu S., Effects of bottom base shapes on burden profiles and burden size distributions in the upper part of a COREX shaft furnace based on DEM, Advanced Powder Technology, 29 (2018) 1014–1024. DOI: 10.1016/j.apt.2018.01.020

Kumar R., Gopireddy S.R., Jana A.K., Patel C.M., Study of the discharge behavior of Rosin-Rammler particle-size distributions from hopper by discrete element method: a systematic analysis of mass flow rate, segregation and velocity profiles, Powder Technology, 360 (2020) 818–834. DOI: 10.1016/j.powtec.2019.09.044

Li C., Honeyands T., O'Dea D., Moreno-Atanasio R., The angle of repose and size segregation of iron ore granules: DEM analysis and experi-

mental investigation, Powder Technology, 320 (2017) 257–272. DOI: 10.1016/j.powtec.2017.07.045

Li C., Honeyands T., O'Dea D., Moreno-Atanasio R., DEM study on size segregation and voidage distribution in green bed formed on iron ore sinter strand, Powder Technology, 356 (2019) 778–789. DOI: 10.1016/j.powtec.2019.09.014

Li C.X., Dong K.J., Liu S.D., Chandratilleke G.R., Zhou Z.Y., Shen Y.S., DEM study of particle segregation in the throat region of a blast furnace, Powder Technology, 407 (2022) 117660. DOI: 10.1016/j.powtec.2022.117660

Liao H., Zong Y., Li K., Bu Y., Bi Z., Jiang C., Liu Z., Zhang J., Influence of lump ore ratio and shapes on the particle flow behavior inside the direct reduction shaft furnace by discrete element modeling model, Steel Research International, 94 (2023) 2200531. DOI: 10.1002/srin.202200531

Lommen S., Mohajeri M., Lodewijks G., Schott D., DEM particle upscaling for large-scale bulk handling equipment and material interaction, Powder Technology, 352 (2019) 273–282. DOI: 10.1016/j.powtec.2019.04.034

Lommen S., Schott D., Lodewijks G., DEM speedup: Stiffness effects on behavior of bulk material, Particuology, 12 (2014) 107–112. DOI: 10.1016/j.partic.2013.03.006

Lu G., Third J.R., Müller C.R., Discrete element models for non-spherical particle systems: from theoretical developments to applications, Chemical Engineering Science, 127 (2015) 425–465. DOI: 10.1016/j.ces.2014.11.050

Luding S., Introduction to discrete element methods: basic of contact force models and how to perform the micro-macro transition to continuum theory, European Journal of Environmental and Civil Engineering, 12 (2008) 785–826. DOI: 10.1080/19648189.2008.9693050

Mandal S., Khakhar D.V., Dense granular flow of mixtures of spheres and dumbbells down a rough inclined plane: segregation and rheology, Physics of Fluids, 31 (2019) 23304. DOI: 10.1063/1.5082355

Mantravadi B., Tan D.S., Effect of bend angle on granular size segregation in the chute flow under periodic flow inversion, Powder Technology, 360 (2020) 177–192. DOI: 10.1016/j.powtec.2019.10.005

Marigo M., Stitt E.H., Discrete element method (DEM) for industrial applications: comments on calibration and validation for the modelling of cylindrical pellets, KONA Powder and Particle Journal, 32 (2015) 236–252. DOI: 10.14356/kona.2015016

Mio H., Kadowaki M., Matsuzaki S., Kunitomo K., Development of particle flow simulator in charging process of blast furnace by discrete element method, Minerals Engineering, 33 (2012) 27–33. DOI: 10.1016/j.mineng.2012.01.002

Mio H., Komatsuki S., Akashi M., Shimosaka A., Shirakawa Y., Hidaka J., Kadowaki M., Matsuzaki S., Kunitomo K., Validation of particle size segregation of sintered ore during flowing through laboratory-scale chute by discrete element method, ISIJ International, 48 (2008a) 1696–1703. DOI: 10.2355/isijinternational.48.1696

Mio H., Komatsuki S., Akashi M., Shimosaka A., Shirakawa Y., Hidaka J., Kadowaki M., Matsuzaki S., Kunitomo K., Validation of particle size segregation of sintered ore during flowing through laboratory-scale chute by discrete element method, ISIJ International, 48 (2008b) 1696–1703. DOI: 10.2355/isijinternational.48.1696

Mio H., Komatsuki S., Akashi M., Shimosaka A., Shirakawa Y., Hidaka J., Kadowaki M., Matsuzaki S., Kunitomo K., Effect of chute angle on charging behavior of sintered ore particles at bell-less type charging system of blast furnace by discrete element method, ISIJ International, 49 (2009) 479–486. DOI: 10.2355/isijinternational.49.479

Mio H., Komatsuki S., Akashi M., Shimosaka A., Shirakawa Y., Hidaka J., Kadowaki M., Yokoyama H., Matsuzaki S., Kunitomo K., Analysis of traveling behavior of nut coke particles in bell-type charging process of blast furnace by using discrete element method, ISIJ International, 50 (2010) 1000–1009. DOI: 10.2355/isijinternational.50.1000

Mio H., Narita Y., Nakano K., Nomura S., Validation of the burden distribution of the 1/3-scale of a blast furnace simulated by the discrete element method, Processes, 8 (2020) 6. DOI: 10.3390/pr8010006

Mohajeri M.J., Do H.Q., Schott D.L., DEM calibration of cohesive material in the ring shear test by applying a genetic algorithm framework, Advanced Powder Technology, 31 (2020) 1838–1850. DOI: 10.1016/j.apt.2020.02.019

Muzzio F.J., Robinson P., Wightman C., Dean Brone, Sampling practices in powder blending, International Journal of Pharmaceutics, 155 (1997) 153–178. DOI: 10.1016/S0378-5173(97)04865-5

Nadeem H., Heindel T.J., Review of noninvasive methods to characterize granular mixing, Powder Technology, 332 (2018) 331–350. DOI: 10.1016/j.powtec.2018.03.035

Nakano M., Abe T., Kano J., Kunitomo K., DEM analysis on size segregation in feed bed of sintering machine, ISIJ International, 52 (2012) 1559–1564. DOI: 10.2355/isijinternational.52.1559

Ottino J.M., Khakhar D.V., Mixing and segregation of granular materials, Annual Review of Fluid Mechanics, 32 (2000) 55–91. DOI: 10.1146/annurev.fluid.32.1.55

Panda S., Tan D.S., Effect of external factors on segregation of different granular mixtures, Advanced Powder Technology, 31 (2020a) 571–594. DOI: 10.1016/j.apt.2019.11.013

Panda S., Tan D.S., Study of external factors to minimize segregation of granular particles, International Journal of Modern Physics C, 31 (2020b) 2050147. DOI: 10.1142/S0129183120501478

Pereira G.G., Cleary P.W., De-mixing of binary particle mixtures during unloading of a V-blender, Chemical Engineering Science, 94 (2013) 93–107. DOI: 10.1016/j.ces.2013.02.051

Qiu P., Pabst T., Waste rock segregation during disposal: calibration and upscaling of discrete element simulations, Powder Technology, 412 (2022) 117981. DOI: 10.1016/j.powtec.2022.117981

Rhodes M., Introduction to Particle Technology, 2nd edition, John Wiley & Sons, 2008, ISBN: 9780470014271. DOI: 10.1002/9780470727102

Richard P., Nicodemi M., Delannay R., Ribière P., Bideau D., Slow relaxation and compaction of granular systems, Nature Materials. 4 (2005) 121–128. DOI: 10.1038/nmat1300

Roessler T., Katterfeld A., Scaling of the angle of repose test and its influence on the calibration of DEM parameters using upscaled particles, Powder Technology, 330 (2018) 58–66. DOI: 10.1016/j.powtec.2018.01.044

Roessler T., Richter C., Katterfeld A., Will F., Development of a standard calibration procedure for the DEM parameters of cohesionless bulk materials – part I: Solving the problem of ambiguous parameter combinations, Powder Technology, 343 (2019) 803–812. DOI: 10.1016/j.powtec.2018.11.034

Rosato A., Windows-Yule C., Segregation in Vibrated Granular Systems, Elsevier Inc., 2020, ISBN: 9780128141991. DOI: 10.1016/C2017-0-00407-X

Sakai M., How should the discrete element method be applied in industrial systems?: a review, KONA Powder and Particle Journal, 33 (2016) 169–178. DOI: 10.14356/kona.2016023

Saleh K., Golshan S., Zarghami R., A review on gravity flow of free-flowing granular solids in silos – Basics and practical aspects, Chemical Engineering Science, 192 (2018) 1011–1035. DOI: 10.1016/j.ces.2018.08.028

Schulze D., Powders and Bulk Solids: Behavior, Characterization, Storage and Flow, Springer Berlin, 2008, ISBN: 978-3-540-73767-4. DOI: 10.1007/978-3-540-73768-1

Seil P., Gómez J.O., Pirker S., Kloss C., Numerical and experimental studies on segregation patterns in granular flow from two hoppers, in: ECCOMAS 2012—European Congress on Computational Methods in Applied Sciences and Engineering, E-Book Full Papers, 2012, pp. 5389–5402.

Shekhar S., Pereira G.G., Hapgood K.P., Morton D.A.V., Cleary P.W., Simulation study on the influence of particle properties on radial and axial segregation in a Freeman rheometer, Chemical Engineering

Science, 265 (2023) 118210. DOI: 10.1016/j.ces.2022.118210
Shenoy P., Innings F., Tammel K., Fitzpatrick J., Ahrné L., Evaluation of a digital colour imaging system for assessing the mixture quality of spice powder mixes by comparison with a salt conductivity method, Powder Technology, 286 (2015) 48–54. DOI: 10.1016/j.powtec.2015.07.034
Shi D., Abatan A.A., Vargas W.L., McCarthy J.J., Eliminating segregation in free-surface flows of particles, Physical Review Letters, 99 (2007) 148001. DOI: 10.1103/PhysRevLett.99.148001
Shimosaka A., Shirakawa Y., Hidaka J., Effects of particle shape and size distribution on size segregation of particles, Journal of Chemical Engineering of Japan, 46 (2013) 187–195. DOI: 10.1252/jcej.12we179
Shirsath S.S., Padding J.T., Kuipers J.A.M., Clercx H.J.H., Simulation study of the effect of wall roughness on the dynamics of granular flows in rotating semicylindrical chutes, AIChE Journal, 61 (2015) 2117–2135. DOI: 10.1002/aic.14828
Shlnohara K., Mlyata S.I., Mechanism of density segregation of particles in filling vessels, Industrial and Engineering Chemistry Process Design and Development, 23 (1984) 423–428. DOI: 10.1021/i200026a003
Soltanbeigi B., Podlozhnyuk A., Papanicolopulos S.A., Kloss C., Pirker S., Ooi J.Y., DEM study of mechanical characteristics of multi-spherical and superquadric particles at micro and macro scales, Powder Technology, 329 (2018) 288–303. DOI: 10.1016/j.powtec.2018.01.082
Standish N., Studies of size segregation in filling and emptying a hopper, Powder Technology, 45 (1985) 43–56. DOI: 10.1016/0032-5910(85)85059-2
Standish N., Kilic A., Comparison of stop-start and continuous sampling methods of studying segregation of materials discharging from a hopper, Chemical Engineering Science, 40 (1985) 2152–2153. DOI: 10.1016/0009-2509(85)87036-6
Stannarius R., Magnetic resonance imaging of granular materials, The Review of scientific instruments, 88 (2017) 51806. DOI: 10.1063/1.4983135
Tang P., Puri V.M., Methods for minimizing segregation: a review, Particulate Science and Technology, 22 (2004) 321–337. DOI: 10.1080/02726350490501420
Tang P., Puri V.M., An innovative device for quantification of percolation and sieving segregation patterns—Single component and multiple size fractions, Particulate Science and Technology, 23 (2005) 335–350. DOI: 10.1080/02726350500212871
Tao H., Zhong W., Jin B., Ren B., DEM simulation of non-spherical granular segregation in hopper, AIP Conference Proceedings, American Institute of Physics, 1547 (2013) 720–726. DOI: 10.1063/1.4816925
Terui K., Kashihara Y., Hirosawa T., Nouchi T., Optimization of coke mixed charging based on discrete element method, ISIJ International, 57 (2017) 1804–1810. DOI: 10.2355/isijinternational.ISIJINT-2017-204
Tian X., Zhou H., Huang J., Wu S., Wang G., Kou M., DEM study on discharge behavior of ternary cylindrical activated coke particles, Powder Technology, 409 (2022) 117785. DOI: 10.1016/j.powtec.2022.117785
Tripathi A., Khakhar D. V, Rheology of binary granular mixtures in the dense flow regime, Physics of Fluids, 23 (2011) 113302. DOI: 10.1063/1.3653276
Tripathi A., Khakhar D. V, Density difference-driven segregation in a dense granular flow, Journal of Fluid Mechanics, 717 (2013) 643–669. DOI: 10.1017/jfm.2012.603
Vallance J.W., Savage S.B., Particle segregation in granular flows down chutes, in: Rosato A.D., Blackmore D.L. (Eds), IUTAM Symposium on Segregation in Granular Flows, Dordrecht, Springer Netherlands, 2000, pp. 31–51. DOI: 10.1007/978-94-015-9498-1_3
Vuilloz T., Cantor D., Ovalle C., DEM modeling of segregation and stratification in pouring heaps of bidispersed mixtures of rounded particles, EPJ Web of Conferences, 249 (2021) 3049. DOI: 10.1051/epjconf/202124903049
Wang C., Deng A., Taheri A., Digital image processing on segregation of rubber sand mixture, International Journal of Geomechanics, 18 (2018) 4018138. DOI: 10.1061/(asce)gm.1943-5622.0001269
Wang M., Liang L.-x., Guan S.-h., Ma G., Lai Z.-q., Niu X.-q., Zhang S.-f., Tian W.-x., Zhou W., Experimental and numerical investigation of the collapse of binary mixture of particles with different densities, Powder Technology, 415 (2023) 118167. DOI: 10.1016/j.powtec.2022.118167
Wang X., Ma H., Li B., Li T., Xia R., Bao Q., Review on the research of contact parameters calibration of particle system, Journal of Mechanical Science and Technology, 36 (2022) 1363–1378. DOI: 10.1007/s12206-022-0225-4
Wensrich C.M., Katterfeld A., Rolling friction as a technique for modelling particle shape in DEM, Powder Technology, 217 (2012) 409–417. DOI: 10.1016/j.powtec.2011.10.057
Williams J., Mixing and segregation in powders, in: M.J. Rhodes(ed.), Principles of Powder Technology, John Wiley & Sons, 1991, pp. 71–90, ISBN: 978-0-471-92422-7
Williams J.C., The segregation of particulate materials. A review, Powder Technology, 15 (1976) 245–251. DOI: 10.1016/0032-5910(76)80053-8
Wu S., Kou M., Xu J., Guo X., Du K., Shen W., Sun J., DEM simulation of particle size segregation behavior during charging into and discharging from a Paul-Wurth type hopper, Chemical Engineering Science, 99 (2013) 314–323. DOI: 10.1016/j.ces.2013.06.018
Xu J., Hu Z., Xu Y., Wang D., Wen L., Bai C., Transient local segregation grids of binary size particles discharged from a wedge-shaped hopper, Powder Technology, 308 (2017) 273–289. DOI: 10.1016/j.powtec.2016.12.013
Xu W., Cheng S., Li C., Experimental study of the segregation of burden distribution during the Charging Process of Bell-less Top Blast Furnace with Two Parallel Hoppers, in: Journal of Physics: Conference Series, Taylor & Francis, 2021, pp. 337–343. DOI: 10.1088/1742-6596/2044/1/012129
Xu W., Cheng S., Niu Q., Hu W., Bang J., Investigation on the uneven distribution of different types of ores in the hopper and stock surface during the charging process of blast furnace based on discrete element method, Metallurgical Research and Technology, 116 (2019) 314. DOI: 10.1051/metal/2018099
Xu Y., Ma K., Sun C., Liao Z., Xu J., Wen L., Bai C., Effect of density difference on particle segregation behaviors at bell-less top blast furnace with parallel-type hopper, in: Minerals, Metals and Materials Series, Springer, 2018a, pp. 391–399. DOI: 10.1007/978-3-319-72138-5_39
Xu Y., Xu J., Sun C., Ma K., Shan C., Wen L., Zhang S., Bai C., Quantitative comparison of binary particle mass and size segregation between serial and parallel type hoppers of blast furnace bell-less top charging system, Powder Technology, 328 (2018b) 245–255. DOI: 10.1016/j.powtec.2018.01.020
Yang W., Zhou Z., Pinson D., Yu A., Periodic boundary conditions for discrete element method simulation of particle flow in cylindrical vessels, Industrial and Engineering Chemistry Research, 53 (2014) 8245–8256. DOI: 10.1021/ie404158e
Yang W.J., Zhou Z.Y., Yu A.B., Discrete particle simulation of solid flow in a three-dimensional blast furnace sector model, Chemical Engineering Journal, 278 (2015) 339–352. DOI: 10.1016/j.cej.2014.11.144
You Y., Hou Q.F., Luo Z.G., Li H.F., Zhou H., Chen R., Zou Z.S., Three-dimensional DEM study of coal distribution in the melter gasifier of COREX, Steel Research International, 87 (2016) 1543–1551. DOI: 10.1002/srin.201500481

Yu F., Zhang Y., Zheng Y., Han M., Chen G., Yao Z., Comparison of different effective diameter calculating methods for sphero-cylinders by geometrically exact DEM simulations, Powder Technology, 360 (2020) 1092–1101. DOI: 10.1016/j.powtec.2019.10.097

Yu Y., Saxén H., Experimental and DEM study of segregation of ternary size particles in a blast furnace top bunker model, Chemical Engineering Science, 65 (2010) 5237–5250. DOI: 10.1016/j.ces.2010.06.025

Yu Y., Saxén H., Flow of pellet and coke particles in and from a fixed chute, Industrial and Engineering Chemistry Research, 51 (2012) 7383–7397. DOI: 10.1021/ie201362n

Yu Y., Saxén H., Particle flow and behavior at bell-less charging of the blast furnace, Steel Research International, 84 (2013) 1018–1033. DOI: 10.1002/srin.201300028

Yu Y., Saxén H., Segregation behavior of particles in a top hopper of a blast furnace, Powder Technology, 262 (2014) 233–241. DOI: 10.1016/j.powtec.2014.04.010

Yu Y., Zhang J., Zhang J., Saxén H., DEM and experimental studies on pellet segregation in stockpile build-up, Ironmaking and Steelmaking, 45 (2018) 264–271. DOI: 10.1080/03019233.2016.1261244

Zhang D., Zhou Z., Pinson D., DEM simulation of particle stratification and segregation in stockpile formation, EPJ Web of Conferences, 140 (2017) 15018. DOI: 10.1051/epjconf/201714015018

Zhang J., Hu Z., Ge W., Zhang Y., Li T., Li J., Application of the discrete approach to the simulation of size segregation in granular chute flow, Industrial and Engineering Chemistry Research, 43 (2004) 5521–5528. DOI: 10.1021/ie034254f

Zhang J., Qiu J., Guo H., Ren S., Sun H., Wang G., Gao Z., Simulation of particle flow in a bell-less type charging system of a blast furnace using the discrete element method, Particuology, 16 (2014) 167–177. DOI: 10.1016/j.partic.2014.01.003

Zhang T.F., Gan J.Q., Pinson D., Zhou Z.Y., Size-induced segregation of granular materials during filling a conical hopper, Powder Technology, 340 (2018) 331–343. DOI: 10.1016/j.powtec.2018.09.031

Zhang T.F., Gan J.Q., Yu A.B., Pinson D., Zhou Z.Y., Segregation of granular binary mixtures with large particle size ratios during hopper discharging process, Powder Technology, 361 (2020) 435–445. DOI: 10.1016/j.powtec.2019.07.010

Zhang T.F., Gan J.Q., Yu A.B., Pinson D., Zhou Z.Y., Size segregation of granular materials during Paul-Wurth hopper charging and discharging process, Powder Technology, 378 (2021) 497–509. DOI: 10.1016/j.powtec.2020.10.025

Zhang Z., Liu Y., Zheng B., Sun P., Li R., Local percolation of a binary particle mixture in a rectangular hopper with inclined bottom during discharging, ACS Omega, 5 (2020) 20773–20783. DOI: 10.1021/acsomega.0c01514

Zhao Y., Chew J.W., Discrete element method study on hopper discharge behaviors of binary mixtures of nonspherical particles, AIChE Journal, 66 (2020a) e16254. DOI: 10.1002/aic.16254

Zhao Y., Chew J.W., Effect of lognormal particle size distributions of non-spherical particles on hopper discharge characteristics, Chemical Engineering Research and Design, 163 (2020b) 230–240. DOI: 10.1016/j.cherd.2020.09.001

Zhao Y., Luo Y., Wang W., Liu S., Zhan Z., Effect of base roughness on flow behaviour and size segregation in dry granular flows, Geotechnique Letters, 12 (2022) 258–264. DOI: 10.1680/jgele.22.00044

Zhao Y., Yang S., Zhang L., Chew J.W., DEM study on the discharge characteristics of lognormal particle size distributions from a conical hopper, AIChE Journal, 64 (2018) 1174–1190. DOI: 10.1002/aic.16026

Zhu H.P., Zhou Z.Y., Yang R.Y., Yu A.B., Discrete particle simulation of particulate systems: theoretical developments, Chemical Engineering Science, 62 (2007) 3378–3396. DOI: 10.1016/j.ces.2006.12.089

Appendix

In **Table 2**, we summarized the segregation indices used in the literature. These indices quantify to which degree the tracer particle is homogeneously distributed within the mixture. For indices no. 1–8, the concentration of tracer particles is determined in each sub-domain, which can be expressed in terms of the number, mass or volume fraction, as indicated in **Table A1**.

Table A1 Equations for calculating the concentration of different types of particles (type-A or type-B) on number, mass and volume basis. Legend: N = number of particles, m = mass of particles, V = volume of particles.

	Number-based	Mass-based	Volume-based
Fraction of particle type-A	$(\phi_N)_A = \frac{N_A}{N}$ where $N = N_A + N_B$	$(\phi_m)_A = \frac{m_A}{m}$ where $m = m_A + m_B$	$(\phi_V)_A = \frac{V_A}{V}$ where $V = V_A + V_B$
Fraction of particle type-B	$(\phi_N)_B = \frac{N_B}{N}$	$(\phi_m)_B = \frac{m_B}{m}$	$(\phi_V)_B = \frac{V_B}{V}$
Total (number/mass/volume) fraction	$\phi_N = (\phi_N)_A + (\phi_N)_B = 1$	$\phi_m = (\phi_m)_A + (\phi_m)_B = 1$	$\phi_V = (\phi_V)_A + (\phi_V)_B = 1$
Relative fraction of tracer particle in bin i	$y_t^i = \frac{(\phi_N)_t^i}{\phi_N} = (\phi_N)_t^i$ where t = A or B	$x_t^i = \frac{(\phi_m)_t^i}{\phi_m} = (\phi_m)_t^i$ where t = A or B	$c_t^i = \frac{(\phi_V)_t^i}{\phi_V}$ where t = A or B
Relative fraction of tracer particle in the entire system	$y_t = \frac{(\phi_N)_t}{\phi_N} = (\phi_N)_t$ where t = A or B	$x_t = \frac{(\phi_m)_t}{\phi_m} = (\phi_m)_t$ where t = A or B	$c_t = \frac{(\phi_V)_t}{\phi_V}$ where t = A or B

Authors' Short Biographies



Ahmed Hadi

Ahmed Hadi earned a BSc in Civil Engineering from Isfahan University of Technology in 2015. He then pursued an MSc in Geotechnical Engineering at the University of Tehran, graduating in 2018. During his master's degree, he specialised in the DEM modelling of shear banding in granular soils. Currently, Ahmed Hadi is a PhD candidate at the GranChaMlab@TUDelft. His current research project focuses on the DEM modelling of multi-component segregation in the blast furnace charging system.



Raïsa Roeplal

Raïsa Roeplal pursued a master's degree in Mechanical Engineering at the University of Twente in 2016. During that time, she studied the mixing of cohesive particles in paddle mixers and became fascinated with the segregation behaviour of granular materials. She joined the GranChaMlab@TUDelft at Delft University of Technology in 2020, in pursuit of her PhD degree. She is currently developing a DEM model to study the flow and packing behaviour of blast furnace mixtures during furnace charging. Her main focus areas in this regard are: high-velocity dense granular flows, industrial granular flow modelling, multi-component segregation and mixture calibration.



Yusong Pang

Yusong Pang received his MSc degree in Electrical Engineering in 1996. In 2000 he started working at Practic B.V. and Seaview B.V., the Netherlands, for industrial production life cycle management. After his PhD research of intelligent belt conveyor monitoring and control in 2007, he was employed by the Advisory Group Industrial Installations of Royal Haskoning, the Netherlands, as an expert in material handling. In 2010 he was appointed Assistant Professor in the section of Transport Engineering and Logistics, Delft University of Technology, the Netherlands. His research focuses on the intelligent control for large-scale material handling systems and logistics processes.



Dingena Schott

Dingena Schott is a Full Professor at TU Delft on Machine Cargo Interaction Engineering. She obtained her PhD in 2004 from TU Delft on the homogenisation of bulk materials in mammoth silos. In 2007 she started the GranChaMlab@TUDelft to characterise, model, calibrate and validate granular materials for enabling the simulation-supported design of cargo handling equipment on an industrial scale. Since then, she has worked on developing calibration frameworks and modelling particle-based systems in various design contexts; including terminal designs for particulate materials, as well as an award-winning new grab design. Her main research interests include: machine-cargo interfaces, simulation-supported design, biomass materials and energy-transition-driven handling and logistics.

KONA Powder and Particle Journal

KONA Powder and Particle Journal No. 41 (2024) 108–122/https://doi.org/10.14356/kona.2024013 Review Paper

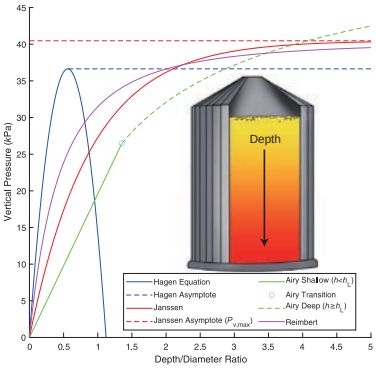
A Review of Analytical Methods for Calculating Static Pressures in Bulk Solids Storage Structures†

George Dyck[1], Adam Rogers[2] and Jitendra Paliwal[1]*

[1] *Department of Biosystems Engineering, University of Manitoba, Canada*
[2] *AGCO Corporation, Canada*

The Janssen equation is a widely used method for calculating pressures in bulk storage structures. This review explores the historical legacy of Janssen's equation and its applications in both planar and three-dimensional structures. Our focus is on the limitations of the original formulation of Janssen, extensions made to avoid these deficiencies, and alternative models that have been developed. The motivation behind these modifications is to improve the representation of shear stress within a grain bin in both the horizontal and vertical directions. Modifications to Janssen's basic assumptions include the vertical-to-horizontal stress ratio (k), the coefficient of friction between the wall and the stored bulk material (μ), internal angle of friction (ϕ), and bulk density (ρ). We also discuss recent developments in pressure theories, which have provided new insights into pressure fields in bulk storage bins. These modern approaches include the continuum elastic theory and microscopic theory. Finally, we discuss recent developments in pressure theories which provide new insights into the storage of bulk solids. Overall, this review provides a comprehensive overview of the Janssen equation and its historical development, limitations, and extensions, as well as recent advancements in pressure theory that offer a more accurate representation of pressure fields in bulk storage structures.

Keywords: powder, particle, bulk solids, Janssen effect, stress distribution, granular matter



1. Introduction

A bulk solid is an aggregate material consisting of solid particles and fluids (gases/air). Considered as a whole, the material has properties common to both fluids and solids, i.e., it can change its shape to fill volumes like a liquid but responds to internal shear stresses like a solid (Walker, 1966). Bulk solids occupy an intermediate position on the spectrum between liquids and solids. These materials exhibit many novel, counter-intuitive properties, for example the stress (pressure) distribution within the material when it is stored in bins. This behavior is associated with "the Janssen effect", as pressure is commonly described by H.A. Janssen's equation. The Janssen effect predicted that the bottom of a bin did not experience the full force of the weight of the commodity stored below some critical height. This phenomenon resulted from the friction between the sidewall and the stored material: the walls carried some of the material weight. Knowledge of internal and wall friction is essential to Janssen's theory. Coulomb's work on friction and failure of soils due to shearing led to the first understanding of the relationship between internal stress and the orientation of failure planes within a material. Rankine synthesized Coulomb's work and Mohr's description of failure planes and provided an analysis of material failure. This paper will first discuss the historical developments leading up to pressure models before discussing Janssen's work, and then investigate important refinements and critiques of the model over the past century. There are three modern works with a similar historical perspective on the topic of pressures in bulk storage structures. The first was the translation of Janssen's entire original paper into English, 111 years after its original publication and a century's worth of citations (Sperl, 2006). This paper contains original data and figures as well as a short commentary that speaks to the legacy of the original publication. The second and third publications were conference papers by A.W. Roberts presented during the PARTEC Congress held in Nuremberg, Germany, 21–23 March 1995. He provided a detailed description of Janssen's work, and a review of the past 100 years of bulk solids research (1895–1995; Roberts, 1995). The work was formally rewritten and later published (Roberts, 1998). The historical section is indebted to Milo Ketchum's "The Design of Bins, Walls and Grain Elevators" (Ketchum, 1911). While this paper provided a novel interpretation of Janssen's equation, the alternative models have not been as resilient to time as Janssen's solution. Furthermore, the paper was written in 1998, and advancements in computational technologies have allowed for new

† Received 31 May 2022; Accepted 22 March 2023
J-STAGE Advance published online 29 July 2023
* Corresponding author: Jitendra Paliwal;
Add: Winnipeg, Manitoba, MB R3T 2N2, Canada
E-mail: j.paliwal@umanitoba.ca
TEL: +1-204-474-6700

Copyright © 2024 The Authors. Published by Hosokawa Powder Technology Foundation. This is an open access article under the CC BY license (https://creativecommons.org/licenses/by/4.0/).

approaches to modeling bulk solids, which were before "insoluble problems" as noted by Jenike (1961). There will be a brief overview of the experiments covered in this literature review for historical context. Information about the pressures in a bin can also provide insight into a wide range of physical phenomena. The pressure field affects bulk solid's packing, flowability, porosity, and tortuosity, to name a few. For example, Janssen along with empirical packing equations has been used to predict the density change within a bin (Thompson et al., 1991; Bhadra et al., 2015, 2018; Turner et al., 2016; Cheng et al., 2017).

2. Historical Pressure Theories

This section focuses on a review of pressure models for grain storage bins. Historically, the "Janssen Effect" was known before Janssen's mathematical description, noted anonymously by Gotthilf Heinrich Ludwig Hagen. Hagen's account is the oldest published theory of pressure in bulk materials, 40 years before Janssen in 1852 (Hagen, 1852). Hagen attempted to predict saturation pressure with respect to height (sand). The paper was translated into English by Tighe et al., which provided a detailed view of this seminal work (Tighe and Sperl, 2007). Hagen suggested that the friction on the side of the wall acted in the upward direction, opposing to the gravitational force. The pressure felt by a "disk which is easily movable but seals tightly" was given by the expression,

$$\sigma_{\text{disc}} = r^2\pi\rho g y - 2r\rho g \mu y^2 \tag{1}$$

where r is the radius of the disc (bin), ρ the bulk density, y the height of bulk material, and μ the friction coefficient. This equation reached a maximum at a characteristic height—related to the diameter of the bin, height, and friction coefficient—and began to decrease afterwards, a mathematical prediction but physically incorrect; Hagen stated that the pressure followed this curve until this maximum was reached. After, the bin pressure remained constant at this maximum, which was a similar behavior to the "Janssen Effect". The difference from Janssen's formulation was that Hagen used a quadratic to explain the change in pressure, whereas Janssen's approach solved a differential equation whose solution was an exponential function, which allowed for an asymptotic approach to the maximum pressure. A noteworthy reference found in Hagen's work regarded an observation Huber-Bernand published in 1829, likely the first published research on the so-called "Janssen Effect," which was highlighted in both Hagen and Janssen's publications. Huber-Bernand noticed that when he filled a container with eggs, added sand in the voids between the eggs extending several inches above the eggs, as well as a 25 kg weight on top, the eggs placed at the bottom of the container remained unbroken, even though all this weight should crush them. He concluded that only a portion of the pressure was transmitted to the bottom of the container, indicating some kind of saturation depth (Sperl, 2006), (Tighe and Sperl, 2007). A Welsh engineer Isaac Roberts published a crucial pre-Janssen study that observed an asymptotic trend in bulk solid bin pressures. He claimed that the pressures at the bottom of bins stopped increasing at the height of two diameters, which was an empirical demonstration of the Janssen effect (Roberts, 1883). He conducted two experiments on this topic. The first was prone to measurement errors due to the mechanical nature of the scales used, an issue other researchers (e.g. Prante) would struggle with and overcome; the second experiment produced reliable results that were widely referenced (Ketchum, 1911). Ten years later, H.A. Janssen formulated his seminal equation analytically modeling Roberts's work, although the work was not cited. Both Hagen and Roberts worked on mathematical descriptions of stresses of earth pressure systems and experimental data from agricultural commodities. H.A. Janssen would be the first to formulate a simple way to calculate pressures in deep bins, the standard reference for well over a century on the topic. This equation's influence was enormous and has been used in almost all design codes and standards in the world, such as the European bulk storage building codes (European Standard EN 1991-4, 2006). The expression was also used in the calculation of apparent weight for bin capacities by the ASABE (American Society of Agricultural and Biological Engineers; ASABE, 2005). Janssen's work has been used by a vast community of researchers and industry because it explained the complicated phenomenon of bin pressures via a straightforward expression (**Eqn. (7)**). Janssen was an engineer from Germany; not much is known about the individual and his work outside of this one publication, a seminal paper for the science of bulk solids. Roberts postulates that it was likely his work and records were destroyed during the Second World War (Roberts, 1995). The life and work of Janssen is accessed through his 1895 paper, "Experiments on Corn Pressure in Silo Cells." One year after its publication, an English translation of Janssen's abstract was published in the Proceedings of the Institution of Civil Engineers, the work often cited as Janssen (1896). Soon, the equation was added to the building practices outline in the "Des Ingenieurs Taschenbuch or The Hütte - Das Ingenieurwissen", a book of references for practicing engineers, initially written in German and now translated into many languages (Ketchum, 1911). During this time, many aspects of the work were validated, critiqued, and modified, which is discussed later in this review. It should also be noted that M. Koenen worked on a similar theory of pressure but published it a year after Janssen. Koenen's work is challenging to find because it was never translated from German to English, and the conclusions were passed down by secondary literature. His most significant contribution suggested the lateral to vertical pressure ratio could be calculated using established equations, such as Rankine's

active pressure state (**Eqn. (14)**), while Janssen experimentally determined its value (Reimbert M. and Reimbert A., 1976; Schulze, 2008; Koenen, 1896). Koenen explicitly connected Janssen's work to the Mohr-Coloulmb failure criterion by relating it to the principal stresses acting on a mass. It is an interesting historical point that Janssen referenced two other works incorrectly, which Sperl addressed in the translation of Janssen's original document (Sperl, 2006). The first was a fellow German researcher, C. Arndt, and was used to discuss the then-new developments in grain storage in North America. The paper's title is "The Silos of Galati and Braila", which are Romanian cities that hold the oldest concrete grain bins. These were built in the late 1880s, designed by an engineer Anghel Saligny, and were two of the earliest examples of reinforced concrete bins. Janssen described these bins as "...iron-strengthened brickwork, and in six-fold profiles like honeycombs. The grain was introduced through the upper end of the cell through a hatch. For discharge, stock transfer, or embarkation, the bottoms of the cells provided close-able openings" (Sperl, 2006). This sounds similar to modern grain storage bin design; Janssen saw these as the future of bin design and wanted to provide mathematical models for predicting pressures. The second citation was Hagen, who has been discussed thoroughly above (Sperl, 2006). Ketchum discussed the design of concrete bins in Chapter XVIII of his text "The Design of Bins, Walls and Grain Elevators". Unfortunately, he did not mention Saligny and only discussed the concrete bins of North America.

2.1 Quantitative description of the Janssen effect

Janssen began with a force-balance equation of a thin horizontal layer of bulk material in a deep bin. Note two things: first, Janssen was investigating deep bins but the theory can be applied to shallow bins (Xu and Liang, 2022). Second, the following is not directly Janssen's formulation but a modernization of the derivation for clarity that was made popular by Ketchum, but is essentially the same (Ketchum, 1911). The first difference lies in incorporating a hydraulic radius R_H, which generalized the container geometry from Cartesian (rectangles) to arbitrary shapes. Secondly, in Janssen's work, he expressed $K = \mu k$ and solved for K experimentally. The lateral pressure ratio, k, is defined as the ratio of the horizontal stress to the vertical effective stress. Within a filled container (bin), the force balance on an infinitesimal thin disk element of granular material in the vertical direction is given as:

$$A\sigma_y + g\rho A\,\mathrm{d}\,y = A\left(\sigma_y + \mathrm{d}\,\sigma_y\right) + \tau_w C\,\mathrm{d}\,y \tag{2}$$

where A is the cross-sectional area and C the circumference of the bin, ρ the bulk density of the material, g the gravitational acceleration, σ_x and σ_y the horizontal and vertical stresses, respectively, and τ_w the shear stress acting on the material at the wall, which opposes the gravitational force. Here, x and y are the horizontal and vertical coordinates, respectively. It should be noted that the depth of the stored material is given by y, increasing in the downward direction. The shear stress is related to the normal stress in the horizontal direction through the wall friction coefficient μ as follows:

$$\tau_w = \sigma_x \mu = \sigma_x \tan\phi_w \tag{3}$$

with $\mu = \tan\phi_w$ given by the wall friction angle ϕ_w. Finally, the ratio of horizontal (σ_x) to vertical stress (σ_y) is assumed to be constant,

$$k = \frac{\sigma_x}{\sigma_y} \tag{4}$$

Defining the hydraulic radius

$$\frac{A}{C} = R_H \tag{5}$$

substituting **Eqns. (3)** and **(4)** into **Eqn. (2)** yields the Janssen differential equation,

$$\frac{\mathrm{d}\,\sigma_y}{\mathrm{d}\,y} + \frac{\mu k}{R_H}\sigma_y = g\rho \tag{6}$$

Solving for vertical pressure gives

$$\sigma_y = \frac{\rho g R_H}{\mu k}\left(1 - \mathrm{e}^{-\frac{\mu y k}{R_H}}\right) \tag{7}$$

Janssen's equation may also be derived from the fundamental (standard) static equilibrium equations for an infinitesimal element of material in 2*D* Cartesian or cylindrical coordinates. For a 2*D* Cartesian coordinate system, the equilibrium equations on an infinitesimal element of material in the vertical and horizontal directions are given as:

$$\begin{aligned} \frac{\partial \sigma_y}{\partial y} + \frac{\partial \tau_{xy}}{\partial x} &= g\rho \\ \frac{\partial \sigma_x}{\partial x} + \frac{\partial \tau_{xy}}{\partial y} &= 0 \end{aligned} \tag{8}$$

For the axisymmetric conditions where a cylindrical coordinate system (r,θ,z) is used, the following equilibrium equations are used:

$$\begin{aligned} \frac{\partial \sigma_z}{\partial z} + \frac{\tau_{rz}}{r} + \frac{\partial \tau_{rz}}{\partial r} &= g\rho \\ \frac{\partial \sigma_r}{\partial r} + \frac{\partial \tau_{rz}}{\partial z} &= 0 \end{aligned} \tag{9}$$

These formulae were used by Rahmoun et al. (2008) and Schillinger & Malla (2008) among others to derive pressure equations. The equilibrium approach is well-established in the field of continuum mechanics (Negi and Ogilvie, 1977), and Janssen's results can be obtained from these expressions, with certain assumptions. For example, assuming the shear stress is related to the normal stress by

equation $\tau_{rz} = \mu\sigma_r$ and using the ratio of principal stresses, $\sigma_r/\sigma_z = k$, we obtain

$$\tau_{rz}(z) = \mu k \sigma_z(z) \tag{10}$$

Combining **Eqns. (9)** and **(10)** with the definition of the hydraulic radius $R_H = b/2$ reproduces the Janssen's differential **Eqn. (6)**.

2.2 Lateral pressure ratio *k*

In addition to producing the equation that bears his name, Janssen also gathered experimental data to validate his model for calculating pressures in bulk storage structures (**Eqn. (7)**). With novel instruments and measuring techniques, Janssen measured μ, the pressure exerted on the bottom of the bin (σ_y) and had planned to measure the horizontal force on the wall (σ_x) but failed to succeed due to the arching effects of the material and the construction of the apparatus. He suggested an improvement that was adapted by Jamieson in 1906. To solve **Eqn. (6)**, Janssen assumed that k was a constant, an assumption that many would question (Ketchum, 1911). Typically, the vertical-to-horizontal stress ratio k is assumed—unrealistically—to be constant throughout a bin, in the range 0 for rigid solids and 1 for liquids. For granular materials, the Rankine coefficient is often used which gives the stress ratio in terms of the internal angle of friction ϕ,

$$k = \frac{1-\sin\phi}{1+\sin\phi} \tag{11}$$

In fact, even with the assumption of constant k there is still a wide variety of values cited throughout the literature. This lack of consensus exists because k is not a fundamental, innate physical property of bulk solids; it is an emergent result of equilibrium, arising from the "fluid" nature of bulk materials. The value of k is not realistically expected to be constant within a storage structure at all. The simplifying assumption is made because Janssen's equation works well within a narrow column of material, but the variation of k through a large volume of bulk material has not been well-studied experimentally. It has been difficult to include a varying k analytically. Coulomb, Rankine and Janssen all made the simplifying assumption of constant $0 < k < 1$. Coulomb's approach produced a stress ratio which related lateral and vertical pressure of soil, and was determined by using the Moore-Coulomb failure criterion (Labuz and Zang, 2012) as follows:

$$k_a = \frac{\cos^2(\phi-\omega)}{\cos^2(\omega)\sin(\phi_w+\beta)\left(1+\sqrt{\frac{\sin(\phi_w+\phi)\sin(\phi-\beta)}{\cos(\phi_w+\omega)\cos(\omega-\beta)}}\right)^2} \tag{12}$$

$$k_p = \frac{\cos^2(\phi+\omega)}{\cos^2(\omega)\sin(\phi_w-\omega)\left(1-\sqrt{\frac{\sin(\phi_w+\phi)\sin(\phi+\beta)}{\cos(\phi_w-\omega)\cos(\beta-\omega)}}\right)^2} \tag{13}$$

where k_a is the active pressure ratio (the bulk solid exerts pressure on the wall), k_p the passive pressure ratio (the wall exerts pressure on the bulk solid), ϕ_w the friction angle of wall, ω the slope of the wall, ϕ the internal angle of friction, and β the angle of the backfill surface. Rankine provided a simplification of the above equations by assuming a frictionless and non-adhesive interface between the vertical wall and the bulk solid. Under such conditions the following stress ratios can be formulated (Rankine, 1856),

$$k_a = \tan^2\left(\frac{\pi}{4}-\frac{\phi}{2}\right) \tag{14}$$

$$k_p = \tan^2\left(\frac{\pi}{4}+\frac{\phi}{2}\right) \tag{15}$$

Note that k_a, shown in **Eqn. (14)**, is mathematically identical to **Eqn. (11)**. Rankine's formulation of k was one of the first theories of pressure for shallow bins, because the pressure distributions within these structures behave analogously to retaining walls. The assumptions fail when the bin height is increased, as the pressure exerted on the bottom and sides of the bin no longer fit the observations because the bin walls were assumed to be frictionless (Xu and Liang, 2022). This phenomenon is a property of bulk solids, but not considered until Janssen. Pleissner convincingly established the variation of k at the beginning of the 20th century. Many different numerical methods have adopted simplified versions of the Rankine formulation (14). For example, the Eurocode (European Standard EN 1991-4, 2006) used

$$k = 1.10\times(1-\sin\phi) \tag{16}$$

A mathematical model to account for vertical and radial changes in stresses and k is discussed in detail later through the work of Zhang et al. (1998a). They provided a literature review on the topic in the context of agricultural commodities, up to the publication date, and reported that there was no consistent agreement on how pressure, and the resulting k, varied radially. Rusinek investigated the variation in pressure of rape seeds using a hydraulic pressure transducer to determine the mean normal stress and mean shear stress on the wall, as well as the vertical pressure distribution, and found that k was significantly lower in the middle of the bin than the wall, and when wall friction increased, so did k (Rusinek, 2003). Horabik et al. discussed the behavior of k within bins (Horabik and Rusinek, 2002), and reported that the pressure ratio was mostly dependent on the internal angle of friction but also the shape of the seed (particles), and inversely related to moisture content; the experimental uniaxial compression test produced similar

values to theoretical predictions given by **Eqn. (16)**. Qadir et al. (2010) showed experimentally that k increased with the ratio of the individual grain and diameter of the bin. Sun et al. presented four independent approaches to k and applied them to deep and shallow bins. The results were compared with experimental data and three national standards (Sun et al., 2018). They also compared different failure criteria to the typical Mohr-Coulomb criterion and recommended the Lade-Duncan (L-D) criterion to be used to calculate wall pressure. Uniaxial compression tests showed, for cereal grains, k decreased with increased moisture content (Horabik and Rusinek, 2002), whereas for calcareous sand, using a similar procedure, increased water content initially increased k, which reached a maximum and eventually declined again (Wang et al., 2020). Numerical studies that used discrete element methods suggested that k did not change with polydispersity (Wiącek and Molenda, 2014). Zhang et al. applied a two-parameter failure criterion that was typically used for soils to determine failure points (Zhang et al., 1994). When both parameters were nonzero, the lateral to vertical stress ratio increased with the vertical stress. At the same time, in other configurations, it was observed to be roughly equal to that determined from the Mohr-Coulomb failure criterion. Xu & Liang considered the elastic deformation of the bin walls in both static and dynamic states and demonstrated that the Rankine formulation of k would underestimate lateral forces (Xu and Liang, 2022). Back et al. studied the effect of friction on the pressure ratio k. Specifically, they focused on particle-particle friction, which the lateral pressure ratio was associated with through analytical arguments (Back, 2011). They established that k increased with particle–particle friction and packing.

2.3 After Janssen

The reaction to Janssen's work was immediate, and many people rushed to both validate and critique his analysis in the decades after the paper was published.

2.3.1 Wilfrid Airy: 1898

Airy noted at the beginning of his paper both the works of Isaac Roberts and Janssen, although he admitted he was not able to find any, "Tables of coefficients of friction of grain, wither on grain, or wood, iron, or brickwork..." (Airy, 1898). Moreover, the reference to Janssen was to the English translation of the abstract (Janssen, 1896), which was the reason why Airy did not have access to the friction coefficients. The translation only included the dimensions of the test cell, the equation describing the vertical pressure of grain, empirical data on corn depth and the resulting side pressure. Regardless, he noted these were reasonable investigations on the pressure of wheat (Janssen investigated corn) on the bottom of small bins. In the conclusion, Airy commented on the geometry of Roberts and Janssen's work and the limitation of "small bins", precisely how it would adjust the coefficient of friction on the rupture plane. Unfortunately, this topic was addressed by Janssen only in the original German publication. Moreover, Airy cited a textbook by Weisbach to describe "semi-fluids" for which, "the pressure on the side of a bin was the maximum pressure due to a wedge-shaped mass of the grain which might be supposed to separate from the general mass, and the angle of slope of the wedge-shaped mass which exerted the maximum pressure had to be determined" (Airy, 1898; Weisbach, 1849). The Mohr-Coulomb failure criterion was used as the basis for the pressure ratio. A slightly different approach was the specific application to "fluid–solids", which are known in the modern literature as "bulk solids". Airy was a contemporary of Janssen and took a different approach to modeling pressure, applicable to both shallow and deep bins. Airy defined the critical height h_L in terms of the coefficient of friction on the rupture plane $\mu' = \tan\phi$ as well as the coefficient of friction between the grain and the bin wall μ such that

$$h_L = D\left[\mu' + \sqrt{\mu'\frac{1+(\mu')^2}{\mu+\mu'}}\right] \tag{17}$$

Airy then defined two regimes for shallow and deep bins.
Case 1: Shallow Bin, $h < h_L$

$$\sigma_x = \rho y\left[\frac{1}{\sqrt{\mu'(\mu'+\mu)}+\sqrt{1+(\mu')^2}}\right]^2 \tag{18}$$

Case 2: Deep Bin, $h \geq h_L$

$$\sigma_x = \frac{\rho D}{\mu'\mu}\left[1-\frac{\sqrt{1+(\mu')^2}}{\sqrt{\frac{2h}{D}(\mu'+\mu)+1-\mu\mu'}}\right] \tag{19}$$

where h was the height of grain bulk solid pile, D the diameter of the bin and y the depth of grain measured from the surface of the pile. Airy started with the Mohr-Coulomb failure criterion, which was used to calculate the static condition of the wedge shape above the failure plane. The proof and resulting equations were complicated, and although the deep bin equation produces similar results to Janssen's. Airy's approach was not widely used due to the difficult calculation (Ketchum, 1911).

2.3.2 Milo Ketchum: 1907 and others

Milo Ketchum wrote a book "The Design of Bins, Walls and Grain Elevators", which exhaustively covered how to build all aspects of a modern elevator for the early part of the 20th century. It is an interesting text for a historical picture of the turn of the century in bin design and still provides a relevant pedagogical explanation of practices and equations. In chapter XVI, Ketchum discussed both

Janssen and Airy's proposed solutions to grain bin pressure (Ketchum, 1911). It is from this text that we find the formulation of **Eqn. (7)**. In Janssen's original text, the formulation was different, but only superficially. However, Ketchum's form is dominant because its derivation was clearly articulated in his text. Ketchum's work was important because it formalized Janssen's theory in a text discussing proper engineering practices and organized data that engaged with Janssen's theory. Ultimately, he concluded that Airy's equations were too complicated for practical use and recommended a graphical method for obtaining solutions. Ketchum provided summaries of many researchers who responded directly to Janssen's work, including Roberts, Prante, Toltz, Jamieson, Luft, Pleissner, Bovey, Lufft, and Pleissner. A.W. Roberts provided citations to all the original works discussed by Ketchum (Roberts, 1995; Roberts, 1998). This was the primary channel for understanding the development following Janssen's efforts.

As for the development after Janssen's efforts, a few are mentioned below to establish issues with Janssen's conclusions. A.W. Roberts provided a good summary of the work, which extended much beyond Ketchum's analysis (Roberts, 1995; 1998). Prante (1896) observed that the flow of bulk solids increased pressure as much as four times static values. Still, the results might have been unreliable due to the experimental apparatus, although the general trend was correct. These experiments established that grain removal should be symmetrical, otherwise this pressure increase on one side of the bin could bring about bin failure. Toltz (1903) utilized Prante's work while designing a grain elevator to account for fluid pressure within the facility. Toltz repeated Prante's experiment but changed the technique used to measure the deflection of steel plates and calculated the resulting pressure during filling and emptying. These results were considered reliable and confirmed that static and dynamic pressures were different, with dynamic pressures being significantly higher. Jamieson (1903) validated Janssen's model and calculations of lateral pressure ratio and also showed pressure changes in static and dynamic states with symmetric and asymmetric outlets. Furthermore, Jamieson's measurement device was complex, and allowed for both vertical and lateral pressures to be measured; his work added robustness to Janssen's theory. Pleissner (1906) conducted many experiments throughout 1902–1905 that showed k was not a constant in a bin and changed for different commodities. This was one of Janssen's assumptions, which most researchers adopted. Other experiments conducted by Bovey (1904) and Lufft (1902–1904) showed variability in k but less comprehensively than Pleissner. Finally, it should also be noted that outside of the enormous project of writing "The Design of Bins, Walls and Grain Elevators," Ketchum conducted experiments, which showed that the flow of bulk solids was independent of the grain height (the height of a bulk solid pile). This phenomenon is commonly known through Beverloo's model, published in 1961 but is also found in the second half of Hagen's work and is commonly called the Hagen-Beverloo Equation (Beverloo et al., 1961).

2.3.3 Andrew W. Jenike: 1961

Jenike was the first to mathematically describe the flow of bulk materials, which culminated in his book "Gravity Flow of Bulk Solids" (Jenike, 1961). While the topic of this paper is static pressure, Jenike developed essential descriptions of flow that determined what future state a system would take and is thus relevant to this review. Jenike's work drew heavily on his contemporaries as well as investigations into mathematical descriptions of plasticity. In addition to new analytical theories and methods, the advent of computers would make it possible to carry out otherwise "insoluble" mathematical problems. This comment hinted at the future of bulk solid research and where one finds the forefront of research today, introduced through the work of P.A. Cundall and O.D.L. Strack, who developed the discrete element method (Cundall and Strack, 1979). The work "Gravity Flow of Bulk Solids" was outlined into six parts: 1) the nature of the yield function; 2) differential equations that described steady-state flow and produce pressure, density, and velocity fields; 3) the initiation of flow, which was called incipient failure; 4) necessary criteria for the bulk solid to flow; 5) apparatuses to test flow properties of bulk solids; and 6) experiments and applications of this flow theory. Jenike categorized different types of bulk solid flows and how the bin/hopper geometry and other properties could influence flow types. Jenike noted that there existed no perfect bin; each bin had its own unique advantages and disadvantages. In part VI, Jenike mentioned both Janssen and Ketchum's work as being the most important contributions to the knowledge of bulk solids at the turn of the century. Jenike also produced several other important publications. One was written with J.R. Johanson and J.W. Carson that described bin design, mass flow, and funnel flow in a four-part series (Jenike et al., 1973a; 1973b; 1973c). Moreover, Jenike summarized bin loads under different flow states: static, during flow, and steady flow (Jenike and Johanson, 1969). These later publications were often cited in both research and engineering practices because they included design formulas and examples of calculations.

2.3.4 Walker: 1966

Walker investigated pressure and arching in hoppers, using Janssen's model and calculating a k value in both static and flow states. His work also was an attempt to determine whether a specific hopper would experience blockage through arching of powder across the outlet. In addition, he investigated the role cohesion played in the gravity flow in a hopper (Walker, 1966).

2.3.5 Marcel Reimbert and André Reimbert: 1976

Marcel and André Reimbert wrote a book titled "Silos-Theory and Practice", which presented a new model for bin pressures (Reimbert M. and Reimbert A., 1976). The book was written with the same spirit as Milo Ketchum's "The Design of Bins, Walls and Grain Elevators". It was ultimately interested in the construction of grain elevators but diverged by presenting a new theory of bulk solid phenomenon to inform calculations instead of aggregating established theories. The book also offered critiques on the traditional Koenen-Janssen approach and noted that the Janssen method needed to assume a constant *k*. Additionally, Ketchum suggested *k* as a function of bin geometry and material depth. The model proposed in the book produced similar results to Janssen's. However, a significant difference between the two was that Reimbert et al. used an empirical equation (hyperbola) to describe the change in pressure as a function of depth. The equation was developed for cylindrical silos and can also be used for n-sided polygons. Furthermore, while the authors argued that *k* changed throughout a bin, they still assumed it to be constant in calculation, and the value they took ("the characteristic abscissae") was calculated at the maximum vertical pressure, which resulted in

$$A = \frac{D}{4\tan\phi'\tan^2\left(\frac{\pi}{4}-\frac{\phi'}{2}\right)} - \frac{h}{3} \tag{20}$$

where *D* the diameter of the bin. The maximum stress was given by

$$\sigma_{\max} = \frac{\rho g D}{4\tan\phi'} \tag{21}$$

with the horizontal stress,

$$\sigma_x = \sigma_{\max}\left[1-\left(\frac{y}{A}+1\right)^{-2}\right] \tag{22}$$

where *y* was the depth of the material.

3. Comparison

Many models have been proposed in the past 100 years and the immediate differences between these models are not intuitive. A quantitative comparison was conducted to compare the results between Hagen, Janssen, Airy, and Reimbert. Each model uses the same properties as shown in **Table 1**.

Hagen's work attempted to recreate the "Janssen effect" using a parabolic increase in pressure until a maximum was reached, after which it remained constant. This piece-wise approach used a quadratic equation to describe the increase in pressure, and constant once the maximum was reached, represented by the dashed line in **Fig. 1**. Hagen's model is the crudest of the historical methods but provided an essential first step; subsequent models predicted very similar behavior giving a more gradual increase than Hagen. Janssen's model predicted an exponential change in pressure with the material depth that approached an asymptote. Airy's model used a complicated geometric approach and applied the knowledge developed by Coulomb and others in earth pressure theory to bulk solids in bins. Both Airy and Hagen's models are separated by a transition point in which the pressure changes discontinuously. Reimbert's equation found the maximum pressure at the bottom of the bin and modeled the change in pressure using a hyperbolic approach. Reimbert attempted to create a new variable for *k* that could account for more factors than the other methods. For example, Janssen assumes a lateral pressure ratio to remain constant within a particular bin, but we would expect *k* to vary from bin to bin as a function of geometry.

Our analysis of these models at different depth/diameter ratios revealed that the differences in pressure predictions between the models can be divided into three main regions: low (0–1.5), intermediate (1.5–3), and high (3–5). At the low *h*/*d* ratio region, the equations exhibited the most variation between each other. The following percentage differences were observed: Hagen vs Reimbert, 16.0 %; Hagen vs Janssen, 31.3 %; Hagen vs Airy, 64.6 %; Reimbert vs

Table 1 Model variables and values used to generate **Fig. 1**, with the bin diameter *d*, grain height *h* or *y*, mass density ρ, stress ratio *k*, coefficient of friction μ and the internal angle of friction ϕ.

Parameter	Value	Unit
d	6	m
h or y	30	m
ρ	770	kg/m^3
k	0.4	N/A
μ	0.7	N/A
ϕ	30	deg

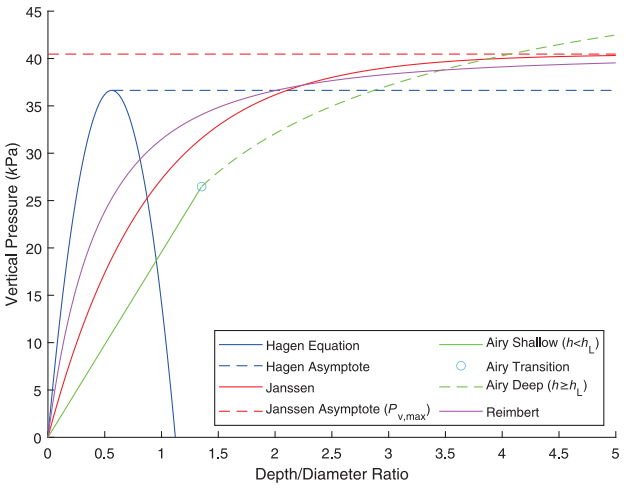


Fig. 1 Comparing historical bin pressure models. (The data are available publicly at https://doi.org/10.50931/data.kona.23741598)

Janssen, 15.6 %; Reimbert vs Airy, 50.0 %; and Janssen vs Airy, 35.1 %. In the intermediate region, Reimbert and Janssen closely approached the Hagen asymptote, with Airy's equation being 10.0 % lower during this intersection. At the extreme end of the high h/d ratio region, Reimbert and Janssen were very close, within 2.0 % of each other, while Airy and Hagen's asymptote were 5.1 % above and 7.6 % below them, respectively. It is important to note that there is a 9.9 % difference between the Hagen and Janssen asymptote, with Janssen predicting greater pressure.

4. New developments in static pressure theories

While the Janssen equation produces satisfactory results for static conditions if the "right" parameters are selected, it does not represent the full pressure field present within a bin. Many new models and approaches to the pressure field within a bin have provided new insights. Such modern approaches include elastic theory (Bräuer, 2006; Ovarlez and Clément, 2005; Schillinger and Malla, 2008), ordinary stress linearity (OSL) and incipient failure everywhere (IFE) models (Vanel et al., 2000), microscopic theory (Xu et al., 1996), the principal stress cap approach (Matchett, 2006), as well as a plethora of numerical methods (Chen, et al., 1999).

4.1 Investigations and modifications of Janssen's model

Rigorous validation of Janssen's model occurred within the first decade of its publication (Ketchum, 1911; Roberts, 1995). Many modern studies have attempted to validate or modify Janssen's model. Di Felice et al. (Di Felice and Scapinello, 2010) highlighted several works in the past decade and identified a literature gap that questioned important parameters in the Janssen model: μ and k. Their work showed that while many studies determined the numerical values of these parameters, their physical interpretation was not as clear. Moreover, empirically their study showed some discrepancies when measuring these parameters. While De Felice et al. highlighted the need to investigate Janssen's assumptions, others have taken up this task. Janssen assumed bins to be a static and closed environment, where no forces are transferred from outside the system besides the self weight of stored materials. This is not the case for most bins, which experience external forces from their environments, such as vibrations caused by machinery (Körzendörfer, 2022), earthquakes (Silvestri et al., 2012), intentional flow-inducing inertia forces (Pascot et al., 2020) and bin honking (Buick et al., 2004). Bertho et al. looked at the applicability of Janssen's model in dynamic environments, provided an overview of the current research, and considered the effect of wall movement on packing (Bertho et al., 2003). They found the classical Janssen model was valid for bin walls that experienced several centimeters per second movement. Moreover, Windows-Yule et al. investigated horizontal wall movement and found that the Janssen model was also valid for a wide range of dynamic movement (Windows-Yule et al., 2019). It is worth noting that this topic was often investigated by numerical methods, an important tool for understanding bulk solids but a topic outside the scope of this paper.

Janssen's model is a macroscopic model, which treats the material as a continuum instead of a collection of particles. Bratberg et al. examined the threshold where microscopic behaviors turn into macroscopic behaviors through narrow granular columns (Bratberg et al., 2005). They found that Janssen's model could not account for small container diameters. Similarly, for shallow granular pile heights, an interesting result was discovered by Mahajan et al. (Mahajan et al., 2020)—a "reverse Janssen effect". Specifically, the wall frictional forces could become compressive, effectively reversing the usual Janssen effect. Under this condition, the walls increase the effective mass of the bulk material at the bottom, which requires modification to Janssen's equation to predict the changes in effective mass as a function of height. This reverse effect was only observable when the height of a bulk solid pile was relatively small, i.e., $h \leq 30d_G$ with d_G the diameter of a single particle. Thus, we do not generally expect to see this effect on large scales such as within bins. The continuum approach is typically used in analytical models, whereas numerical models can be applied to both continuum and particulate materials (Chen et al., 1999; Schulze, 2008).

Many works focused on addressing the inadequacies of Janssen's assumptions. Some examples include variable bulk density due to particle packing (Vanel and Clément, 1999; Haque, 2013; Landry et al., 2004), variable angle of repose (Pont et al., 2003), horizontal bins (Tang et al., 2021), pressures in the hopper section (Walker, 1966), obstacles in bins (Endo et al., 2017), elastic deformation of bin walls (Xu and Liang, 2022), moisture content (Zhang et al., 1998b; Chen, et al., 2020), temperature (Lapko et al., 2003), shallow bins (Ooi and Rotter, 1990; Xu and Liang, 2022), as well as loading and unloading stresses (Walters, 1973), among others (Ayuga, 2008). These modifications are relevant because they point toward higher fidelity models that can better describe physical systems. Such modifications are potentially important for future industrial applications as well as advancing development of state-of-the-art models. While it is not realistic to review the studies that address all the factors listed above, this paper has selected one significant topic to discuss, namely variable stress fields.

4.2 Variable stress fields

The most fundamental and controversial assumption in

Janssen's theory is the constant lateral to vertical pressure ratio, k (discussed at length in **Section 2.2**). This ratio is fundamentally dictated by the stress field in the bulk solid mass. Many experiments have shown that this ratio is a function of material properties and location in a bin (Chen, et al., 2020; Liu et al., 2021). In this section, the stress field is investigated analytically in a 2D Cartesian coordinate system (x,y), where the y direction points "downward," with $y = 0$ representing the top of the bulk solid surface. Deriving Janssen's equation in the Cartesian case requires the use of a "slip-state" condition throughout the bin such that $\tau_{xy} = \mu\sigma_x(y)$ at the wall. In terms of vertical stress, we have

$$\tau_{xy}(y) = \mu\sigma_x(y) = \mu k\sigma_y(y) \tag{23}$$

The equilibrium in the vertical direction can be expressed as:

$$\frac{\partial\sigma_y}{\partial y} + \frac{\partial\tau_{xy}}{\partial x} = g\rho \tag{24}$$

If the stresses are assumed not to vary in the horizontal direction, as in Janssen's theory, or $\tau_{xy} = \tau_{xy}(y)$, the partial derivative of shear stress with respect to x vanishes,

$$\frac{\partial\tau_{xy}}{\partial x} = 0 \tag{25}$$

This means the equilibrium equation in the vertical direction is simplified as

$$\frac{\partial\sigma_y}{\partial y} = g\rho \tag{26}$$

which has the solution of

$$\sigma_y = g\rho y \tag{27}$$

This indicates that the bulk solids behave like a fluid if the shear stress varies only in the vertical direction. Here, the stress changes with depth, just as a fluid does. In this case the wall friction has no effect on the vertical stress in the material. Mathematically, this vanishing of the partial derivative of the shear stress can be observed due to the relationships presented in **Eqn. (25)**. Let's now consider a variable stress field in the horizontal direction. Specifically, we postulate a shear stress which varies linearly in the horizontal direction,

$$\tau_{xy}(x,y) = \frac{x}{b}\mu\sigma_x(y) \tag{28}$$

where b is the radius of the bin. Now the partial derivative term is expressed as

$$\frac{\partial\tau_{xy}}{\partial x} = \frac{\mu}{b}\sigma_x(y) \tag{29}$$

and the equilibrium equation has the form of

$$\frac{\mathrm{d}\sigma_y}{\mathrm{d}y} + \frac{\mu k}{b}\sigma_y = g\rho \tag{30}$$

This equation form is similar to that of Janssen's differential equation. This means that in order to account for the Janssen effect, the shear stress in 2D must include radial dependence. It should be noted that exchanging b to R_H in **Eqn. (28)** would identically result in the Janssen equation. The difference between the granular and liquid-like behaviors occurs because the effect of wall friction is not included in the problem when the derivative term drops out. Deriving the Janssen equation requires a specific choice of shear stress that links the friction coefficient and the vertical stress through the horizontal to vertical stress ratio $\sigma_x(y) = k\sigma_y(y)$. Geometrically, this term naturally arises in cylindrical coordinates (r, θ, z) due to the radially dependent volume of infinitesimal cylindrical elements $\mathrm{d}V = r\mathrm{d}r\mathrm{d}\theta\mathrm{d}z$. However, this geometrical effect does not occur in Cartesian coordinates (x, y, z), in which the volume of all infinitesimal elements are independent of the radial coordinate.

Radial variation of the shear stress can be traced back to 1948 (Jaky, 1948). In relation to flow problems this term shows up in the work of McInnes (1968) and Savage (1967). Later, it was used by Zhang et al. (1998a) and Milleteet al. (2006) to develop a theory of radial stress behavior in a 2D Cartesian coordinate system and later to expand to 3D cylindrical coordinates (Rahmoun et al., 2008).

We compare the results of Zhang et al. (1998a) with the usual Janssen approach for a hypothetical bin of 5 m in diameter (**Fig. 2**). Zhang et al.'s model accounted for the non-uniformity of stresses in the horizontal and vertical directions, whereas Janssen's work only considered change in the vertical direction. Additionally, in the Zhang model k varies throughout the bin, whereas variation in k is neglected by Janssen. Zhang's model suggests that higher stresses occur at the center of a bin. This may have design implications for airflow in aeration and drying.

To quantify the differences between the Zhang and Janssen models, we calculated the percentage differences between their stress values at various depths and distances from the bin center. The analysis revealed a range of percentage differences between the two models in both horizontal and vertical stress distributions. The vertical stress distribution exhibited more variation than the horizontal, so we focused on this set of data. At the most distant point from the center of the bin, Zhang's model predicted less pressure than Janssen, ranging from 40.0 % to 24.0 %, with the maximum discrepancy occurring at the 1 m depth and decreasing afterward without a clear trend. In contrast, Zhang's model predicted higher pressure at the center of the bin, with differences ranging from 22.5 % to 7.6 %; the maximum discrepancy occurred at the 1 m depth and decreased with depth. At all depths, Zhang's pressure crossed

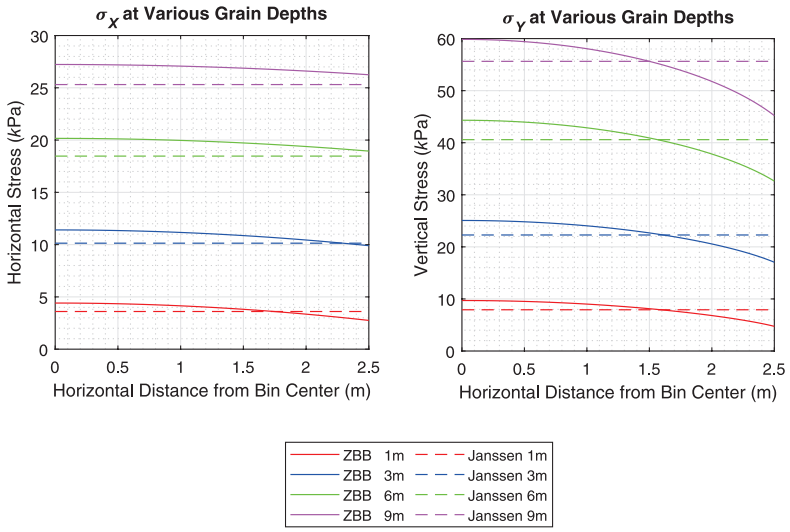


Fig. 2 Differences between the linear stress variation used by Zhang, Bu and Britton (Zhang et al., 1998a) and the planar Janssen result using the Rankine coefficient (**Eqs. 30** and **11**) assuming a bin radius of $b = 2.5$ m, uncompacted mass density $\rho = 834$ kg m^{-3}, coefficient of static friction $\mu = 0.36$ and internal angle of friction $\phi = 22°$ using $h = 1$ m. Bin depth is given in the legend. Change in the radial dependence is introduced by the linear modification to Janssen's equation. (The data are available publicly at https://doi.org/10.50931/data.kona.23741598)

over Janssen's between 1.5 and 1.6 meters from the bin center, and generally, as depth increased, this crossover occurred closer to the center of the bin. This indicated that the Zhang model's predictions could significantly deviate from those of the Janssen model, depending on the depth and distance from the bin center. A consistent trend observed across various depths and distances was that Zhang's model predicted lower pressure and greater discrepancy on the outside, while the center experienced higher pressure and relatively less discrepancy compared to Janssen's model. This finding further emphasized the importance of considering non-uniform stress distributions in grain bin design for optimal aeration and drying performance.

The work of Rahmoun, Millet and de Saxcé (Millet et al., 2006; Rahmoun et al., 2008) included significant expansions over the original Janssen model, specifically applicable to cohesive powder materials. The analysis in Millet et al. (2006) for a planar bin with the 2D Cartesian equilibrium equations (**Eqn. (8)**) resulted in a differential equation for the angle between the horizontal axis and the principal stress direction. The differential equation was solved analytically. The model was numerically compared to Janssen's equation for low cohesion ~ 10^{-6} Pa and the results were found to agree for the passive and active states. A similar approach was taken in Rahmoun et al. (2008) in which the cylindrical equilibrium equations (**Eqn. (9)**) were used to produce a more general 3D result. The resulted model could be solved analytically for cohesionless materials, but a numerical approach was required when finite cohesion was included.

An important model used to complement the Mohr-Coulomb criterion is known as the incipient failure everywhere (IFE), or the rigid-plastic model (Nedderman, 1992; Wittmer et al., 1996, 1997). The IFE model assumes that the material is on the edge of failure throughout the entire bin. This means that through each point there is some plane over which the shear force is linearly related to the normal force. The variable vertical to horizontal stress ratio given by the IFE model has the form of Wittmer et al. (1996)

$$\alpha(\beta) = \frac{(1+\sin^2\phi) \pm 2\sin\phi\sqrt{1-\left(\frac{\cot\phi\tau_{xy}}{\sigma_x}\right)^2}}{\cos^2\phi} \tag{31}$$

where α is the vertical to horizontal stress ratio (k^{-1}) and β is the shear stress to horizontal stress ratio,

$$\sigma_y = \alpha\sigma_x \tag{32}$$
$$\tau_{xy} = \beta\sigma_x \tag{33}$$

Substituting **Eqns. (32)** and **(33)** into **Eqn. (31)** yields

$$\alpha(\beta) = \frac{(1+\sin^2\phi) \pm 2\sin\phi\sqrt{1-\frac{\beta^2}{\tan^2\phi}}}{\cos^2\phi} \tag{34}$$

The $\alpha(\beta)$ has real solutions if $\beta \le \tan\phi$. This condition is upheld because the stress ratio β is a maximum at the bin wall $\beta|_{r=b} = \mu$, so we have generally $\beta \le \mu \le \tan\phi$. Moreover, under static conditions the vertical stress should exceed the horizontal stress, so we expect $\alpha > 1$, which selects the + sign in the quadratic solution. In this case, the variation in α accounts for the change in stress across the bin radius. Similar to the approach outlined above, Millet et al. (2006) considered the variation in radial stresses for cohesive materials.

After Jenike outlined proper designs to avoid arching and funnel flow, hoppers became a common addition to bins. The stress field in a hopper is variable and Janssen's equation is not applicable to hoppers. Walker (1966) and Takami (1975) both used force-balance conditions on a conical slice to describe the stress distribution within a conical hopper and showed vertical and horizontal variations in stresses using Rankine's formulation of k. This work, similar to Janssen's theory, considered forces on a planar differential slice, which was assumed axisymmetric, which is a reasonable assumption for most cases, but not all. Some bins have eccentric hoppers, which produce a non-axisymmetric distribution of material and stresses. While there have been many studies into eccentric discharge of bins in terms of improper flow, there have been far fewer on structural loads (stresses), but this has changed in the past two decades (Wojcik et al., 2003; Vidal et al., 2006, 2008). A detailed study was reported by Ramírez et al. (2010), which provided a thorough discussion of the benefits of eccentric hoppers, experimental work, and several numerical models. This work inspired Matchett's analytical model based on the "principal stress cap" approach, which was capable of accounting for eccentricities in bin loads, as well as symmetrical loads (Matchett, 2006; Matchett, 2020; Matchett and Close, 2021). This research provided a fundamental start to designing safe eccentric hoppers.

4.3 Variable density

Janssen's equation assumed the density of a bulk solid to be constant throughout the entirety of a bin. There have been substantial attempts at numerically incorporating packing into pressure models and considering the effect of particle impact forces on spatial arrangements of particles (Volfson et al., 2003; Landry et al., 2004; Umbanhowar and Goldman, 2010; Petingco et al., 2022). There are some direct modifications to Janssen's model to account for density variations, with varying complexity. Vanel reported that packing could affect k and these effects could be quite significant when the porosity changed from 0.43 to 0.39 (Vanel and Clément, 1999). They proposed a modification to Janssen's model by introducing a fit parameter to account for inhomogeneous density. Cheng et al. directly modified Janssen's equation to account for changes in density and investigated bins with hopper sections (Cheng et al., 2017). They related the degree of packing to the principal stress through a quadratic equation and addressed gaps and ambiguous understandings of pressures in the literature. They concluded that bulk density increased rapidly with the material depth in the upper cylindrical part of the bin but decreased slowly in the hopper. Haque utilized hoop stress and hoop pressure, which represent the circumferential stress and force exerted by stored material in a cylindrical structure, to analytically describe packing within a bin (Haque, 2013). Developing a modified Janssen's equation, Haque's model accounted for variations in bulk density when calculating vertical and horizontal pressures within a bin, offering a more comprehensive understanding of the forces involved in grain storage.

4.4 Non-continuum approaches

4.4.1 Microscopic theory

Bulk solids are discontinuous in nature and microscopic theory may provide a better alternative to the continuum approach such as Janssen's, but with greater complexity. Bratberg et al. investigated the failure of Janssen's theory as the bin and material scale transitioned from macroscopic to microscopic. A few researchers have investigated the bin pressure from the microscopic angle. Xu et al. developed a bin pressure model accounting for the discontinuous nature of bulk solids (Xu et al., 1996). Their model was based on a more general microscopic approach by Granik & Ferrari that used principles of thermodynamics to investigate a system of doublets (pairs of adjacent particles; Granik and Ferrari, 1993). The particles modeled by Xu et al. were idealized spheres in hexagonal packing and held within 2D frictionless walls. Under a pair of contact forces within a doublet, the two particles experienced microstrains due to deformation, rotation, and slipping. Microstress (elongation, compression, torsion, and shearing) were calculated from the contact forces, but torsion and shear microstresses were found to be negligible. Their model results showed that Janssen's results were a special case of their microscopic theory. Moreover, k was only a constant value when the model used frictionless walls and rigid particles. Xu had a deeper examination of the application of microscopic theories in his Ph.D. dissertation (Xu, 1966). Xu et al. demonstrated how this microscopic theory could be used to predict moisture induced stresses within the mass of hygroscopic bulk solids. Zhang et al. further developed this theory to explain discharge loads in bins (Zhang and Britton, 2003). Ferrari et al. compiled a review of doublet microscopic theory (Ferrari et al., 1997). The strength of this theory was the ability to analytically describe the discontinuous nature of particle assemblies, something that was beyond the scope of the continuum approach.

4.4.2 Granular elasticity

Jiang and Liu gave a brief overview of granular elastic theory (Jiang and Liu, 2007a), which covered the original work done by Jiang and Liu (2003). Granular elasticity was distinct due to its definition of strain, which has two parts. The first accounted for particle deformation (elastic). The second accounted for irreversible rolling and slippage (a process that also causes heat) of particles and was considered plastic. The irreversible plastic phenomenon was the main contributor to the overall deformations. The energy within the material under loading could be articulated as a

function of strains and static stresses. Elastic strains were used because particles are compressed and sheared, which stores energy reversibly. These models are based on a relationship between elastic energy, static stress and the deformation of particles. The stress distributions in a granular material could be determined the same way as in elastic media. Granular elasticity could account for a bulk solid's yield, volume dilatancy, and shear-induced anisotropy. Jiang & Liu discussed the applicability of this theory to bins and compared it to Janssen's method. They found that bins were a good fit for granular elastic theory because all six stress tensor elements could be calculated. Bräuer et al. validated granular elasticity for its application to bin stress (Bräuer, 2006). Their model showed a saturation pressure that matched Janssen's. The remaining components of the stress tensor were also computed, which Janssen's theory could not perform. They assumed a constant k and found little variation in vertical stress radially. Other interesting works on granular elasticity included a slow movement of deforming particles (Jiang and Liu, 2007b), which accounted for the infamous stress dip in granular piles (Krimer et al., 2006), showing good agreement with experimental data (Jiang and Liu, 2008). Sun et al. applied granular elasticity to the mesoscopic scale using numerical methods, which examined packing, pressure, and force network structures (Sun et al., 2015). While the study was focused on mesoscopic objects, there was a possibility that this approach could be applied to many discontinuous systems.

5. Concluding remarks

New perspectives and viewpoints are often required to solve stubborn, longstanding problems. This was certainly the state of the field when Janssen's approach produced a revolution in describing and predicting the behavior of granular materials in bins. Even in the modern literature, Janssen's model forms the cornerstone of our understanding of pressures in bins. Modifications to Janssen's model have been sought to generalize it for describing the observed phenomena to higher accuracy, but the starting point is usually Janssen. Otherwise, it is the first validation case to test a new theory against. This ubiquity is a monument to Janssen's success. Just as a new perspective spurred the revolution that led to Janssen's insights, a survey of the literature reveals many new promising approaches.

Despite these successes, there are several limitations of Janssen's model. First, the vertical stress is assumed to be constant across a bin. This is not generally true as the pressure is expected to vary from the center to wall of a bin. Second, the horizontal stress is assumed to be proportional to the vertical stress through the factor k, which is constant throughout a bin. Finally, the density is considered constant throughout a bin. The first of these assumptions is incorrect. The second statement is ad hoc, and generally it should require some deeper theoretical justification. The third assumption is generally incorrect.

In recent years the computational power available to perform DEM simulations has significantly increased, and numerical methods used to simulate granular properties have been extensively studied. The discussion of material properties acquisition and standardization has made DEM a more viable approach for solving bulk solid problems (Xu et al., 2002; González-Montellano et al., 2011; González-Montellano et al., 2012; Horabik and Parafiniuk, 2016). Generally, DEM simulations need to limit the number of particles for computational purposes, and the particle shape sometimes needs to be crudely approximated. However, strategies have been developed to mitigate these limitations (Ramírez-Gómez, 2020). DEM provides the numerical revolution analogous to the analytical revolution provided by Janssen.

Data Availability Statement

The data from the pressure models are available publicly in J-STAGE Data (https://doi.org/10.50931/data.kona.23741598).

Acknowledgments

We acknowledge the effort of the anonymous referee, whose careful reading of our work helped to focus and refine our manuscript.

References

ASABE, Tower Silos: Unit Weight of Silage and Silo Capacities, ASABE Standard, 1982 (2005) D252.1. <https://elibrary.asabe.org/abstract.asp?aid=32005&t=2> accessed 01.11.2023.

Airy W., The pressure of grain, Minutes of Proceedings Institution of Civil Engineers, 131 (1898) 347–358. DOI: 10.1680/imotp.1898.19213

Ayuga F., Some unresolved problems in the design of steel cylindrical silos, In: Structures and Granular Solids. CRC Press, 2008, pp. 135–146. ISBN: 9780429207228. DOI: 10.1201/9780203884447.ch12

Back R., Frictional effects on mass measurements in a column of glass beads, Granular Matter, 13 (2011) 723–729. DOI: 10.1007/s10035-011-0285-0

Bertho Y., Giorgiutti-Dauphiné F., Hulin J.P., Dynamical Janssen Effect on granular packing with moving walls, Physical Review Letters, 90 (2003) 144301. DOI: 10.1103/PhysRevLett.90.144301

Beverloo W.A., Leniger H.A., van de Velde J., The flow of granular solids through orifices, Chemical Engineering Science, 15 (1961) 260–269. DOI: 10.1016/0009-2509(61)85030-6

Bhadra R., Casada M.E., Turner A.P., Montross M.D., Thompson S.A., McNeill S.G., Maghirang R.G., Boac J.M., Stored grain pack factor measurements for soybeans, grain sorghum, oats, barley, and wheat, Transactions of the ASABE, 61 (2018) 747–757. DOI: 10.13031/trans.12645

Bhadra R., Turner A.P., Casada M.E., Montross M.D., Thompson S.A., Boac J.M., McNeill S.G., Maghirang R.G., Pack factor measurements for corn in grain storage bins, Transactions of the ASABE, 58 (2015) 879–890. DOI: 10.13031/trans.58.11033

Bovey H.T., Experiments on grain pressure in deep bins and strength of wooden bins, Engineering News, 52 (1904) 32–34.

Bratberg I., Måløy K.J., Hansen A., Validity of the Janssen law in narrow granular columns, European Physical Journal E, 18 (2005) 245–252. DOI: 10.1140/epje/e2005-00030-1

Bräuer K., Pfitzner M., Krimer D.O., Mayer M., Y., Liu M., Granular elasticity: stress distributions in silos and under point loads, Physical Review E—Statistical, Nonlinear, and Soft Matter Physics, 74 (2006) 061311. DOI: 10.1103/PhysRevE.74.061311

Buick J.M., Pankaj, Ooi J.Y., Chavez-Sagarnaga J., Pearce A., Houghton G., Motion of granular particles on the wall of a model silo and the associated wall vibrations, Journal of Physics D: Applied Physics, 37 (2004) 2751–2760. DOI: 10.1088/0022-3727/37/19/022

Chen J.F., Rotter J.M., Ooi J.Y., A review of numerical prediction methods for silo wall pressures, Advances in Structural Engineering, 2 (1999) 119–135. DOI: 10.1177/136943329900200205

Chen Y., Liang C., Wang X., Guo X., Chen X., Liu D., Static pressure distribution characteristics of powders stored in silos, Chemical Engineering Research and Design, 154 (2020) 1–10. DOI: 10.1016/j.cherd.2019.10.050

Cheng X., Zhang Q., Shi C., Yan X., Model for the prediction of grain density and pressure distribution in hopper-bottom silos, Biosystems Engineering, 163 (2017) 159–166. DOI: 10.1016/j.biosystemseng.2017.09.006

Cundall P.A., Strack O.D.L., A discrete numerical model for granular assemblies, Géotechnique, 29 (1979) 47–65. DOI: 10.1680/geot.1979.29.1.47

Di Felice R., Scapinello C., On the interaction between a fixed bed of solid material and the confining column wall: the Janssen approach, Granular Matter, 12 (2010) 49–55. DOI: 10.1007/s10035-009-0157-z

Endo K., Reddy K.A., Katsuragi H., Obstacle-shape effect in a two-dimensional granular silo flow field, Physical Review Fluids, 2 (2017) 1–16. DOI: 10.1103/PhysRevFluids.2.094302

European Standard E.N., BS EN 1991-4: 2006, Eurocode 1—Actions on structures—Part 4: Silos and tanks, 2006, ISBN: 9780580839153.

Ferrari M., Granik V.T., Imam A., Nadeau J.C., Advances in Doublet Mechanics, Springer, Berlin, 1997, ISBN: 9783540496366. DOI: 10.1007/978-3-540-49636-6

González-Montellano C., Ayuga F., Ooi J.Y., Discrete element modelling of grain flow in a planar silo: influence of simulation parameters, Granular Matter, 13 (2011) 149–158. DOI: 10.1007/s10035-010-0204-9

González-Montellano C., Fuentes J.M., Ayuga-Téllez E., Ayuga F., Determination of the mechanical properties of maize grains and olives required for use in DEM simulations, Journal of Food Engineering, 111 (2012) 553–562. DOI: 10.1016/j.jfoodeng.2012.03.017

Granik V.T., Ferrari M., Microstructural mechanics of granular media, Mechanics of Materials, 15 (1993) 301–322. DOI: 10.1016/0167-6636(93)90005-C

Hagen G.H.L., Las uber den druck und die bewegung des trocken sandes, Bericht über die zur Bekanntmachung geeigneten Verhandlungen der Königlich Preussischen Akademie der Wissenschaften zu Berlin, (1852), pp. 35–42.

Haque E., Estimating bulk density of compacted grains in storage bins and modifications of Janssen's load equations as affected by bulk density, Food Science & Nutrition, 1 (2013) 150–156. DOI: 10.1002/fsn3.23

Horabik J., Parafiniuk P., Molenda M., Experiments and discrete element method simulations of distribution of static load of grain bedding at bottom of shallow model silo, Biosystems Engineering, 149 (2016) 60–71. DOI: 10.1016/j.biosystemseng.2016.06.012

Horabik J., Rusinek R., Pressure ratio of cereal grains determined in a uniaxial compression test, International agrophysics, (2002) 23–28. <https://agro.icm.edu.pl/agro/element/bwmeta1.element.agro-article-7c91baca-ee19-4dd8-9675-83281c7e73ae> accessed 01.11.2023.

Jaky J., Pressure in silos, Proceedings of the 2nd International Conference on Soil Mechanics and Foundation Engineering (Rotterdam), (1948) 103–107.

Jamieson J.A., Grain pressures in deep bins, Transactions of the Canadian Society for Civil Engineering, 17 (1903) 554–607.

Janssen H.A., On the pressure of gain in silo, Proceedings of the Institution of Civil Engineers, 124 (1896) 553–555.

Jenike A.W., Gravity Flow of Bulk Solids, Bulletin 108 of the Utah Engineering Experiment Station, University of Utah, (1961).

Jenike A.W., Johanson J.R., Carson J.W., Bin loads—part 2. concepts, Journal of Manufacturing Science and Engineering, 95 (1973a) 1–5. DOI: 10.1115/1.3438100

Jenike A.W., Johanson J.R., Carson J.W., Bin loads—part 3: mass-flow bins, Journal of Manufacturing Science and Engineering, 95 (1973b) 6–12. DOI: 10.1115/1.3438163

Jenike A.W., Johanson J.R., Carson J.W., Bin loads—part 4: funnel-flow bins, Journal of Manufacturing Science and Engineering, 95 (1973c) 13–16. DOI: 10.1115/1.3438089

Jenike A.W., Johanson J.R., On the theory of bin loads, The Journal of Manufacturing Science and Engineering, 91 (1969) 339–344. DOI: 10.1115/1.3591570

Jiang Y., Liu M., Granular elasticity without the coulomb condition, Physical Review Letters, 91 (2003) 1–4. DOI: 10.1103/PhysRevLett.91.144301

Jiang Y., Liu M., A brief review of "granular elasticity", The European Physical Journal E, 22 (2007a) 255–260. DOI: 10.1140/epje/e2007-00009-x

Jiang Y., Liu M., From elasticity to hypoplasticity: dynamics of granular solids, Physical Review Letters, 99 (2007b) 5–8. DOI: 10.1103/PhysRevLett.99.105501

Jiang Y., Liu M., Incremental stress-strain relation from granular elasticity: comparison to experiments, Physical Review E, 77 (2008) 1–9. DOI: 10.1103/PhysRevE.77.021306

Ketchum M.S., The Design of Walls, Bins and Grain Elevators, 2nd edition, The Engineering News Publishing Company, New York, 1911, ISBN: 9781236382566.

Koenen M., Berechnung des seiten- und bodendrucks in Silozellen, Central-blatt der Bauverwaltung, 16 (1896) 446–449.

Krimer D.O., Pfitzner M., Bräuer K., Jiang Y., Liu M., Granular elasticity: general considerations and the stress dip in sand piles, Physical Review E—Statistical, Nonlinear, and Soft Matter Physics, 74 (2006) 1–10. DOI: 10.1103/PhysRevE.74.061310

Körzendörfer A., Vibrations and ultrasound in food processing–sources of vibrations, adverse effects, and beneficial applications–an overview, Journal of Food Engineering, 324 (2022) 110875. DOI: 10.1016/j.jfoodeng.2021.110875

Labuz J.F., Zang A., Mohr–Coulomb failure criterion, Rock Mechanics and Rock Engineering, 45 (2012) 975–979. DOI: 10.1007/s00603-012-0281-7

Landry J.W., Grest G.S., Plimpton S.J., Discrete element simulations of stress distributions in silos: crossover from two to three dimensions, Powder Technology, 139 (2004) 233–239. DOI: 10.1016/j.powtec.2003.10.016

Lapko A., Gnatowski M., Prusiel J.A., Analysis of some effects caused by interaction between bulk solid and r.c. silo wall structure, Powder Technology, 133 (2003) 44–53. DOI: 10.1016/S0032-5910(03)00095-0

Liu Y.Y., Zhang D.L., Dai B.B., Su J., Li Y., Yeung A.T., Experimental study on vertical stress distribution underneath granular silos, Powder Technology, 381 (2021) 601–610. DOI: 10.1016/j.powtec.2020.11.066

Mahajan S., Tennenbaum M., Pathak S.N., Baxter D., Fan X., Padilla P., Anderson C., Fernandez-Nieves A., Pica Ciamarra M., Reverse Janssen effect in narrow granular columns, Physical Review Letters, 124 (2020) 128002. DOI: 10.1103/PhysRevLett.124.128002

Matchett A.J., Stresses in a bulk solid in a cylindrical silo, including an analysis of ratholes and an interpretation of rathole stability criteria, Chemical Engineering Science, 61 (2006) 2035–2047. DOI: 10.1016/j.ces.2005.10.049

Matchett A.J., Exponential stress in silos—an example from literature, Chemical Engineering Research and Design, 161 (2020) 125–129.

DOI: 10.1016/j.cherd.2020.06.030
Matchett A.J., Close R., A principal stress cap model for stresses in eccentric, circular hoppers, Powder Technology, 391 (2021) 403–424. DOI: 10.1016/j.powtec.2021.06.032
McInnes D.B., Stresses developed by granular material in cylindrical bins, Master of Engineering thesis, McGill University, Canada (Apr. 1968). <https://escholarship.mcgill.ca/concern/theses/m900nv97s> accessed 01.11.2023.
Millet O., Rahmoun J., De Saxcé G., Analytic calculation of the stresses in an ensiled granular medium, Comptes Rendus Mécanique, 334 (2006) 137–142. DOI: 10.1016/j.crme.2005.11.005
Nedderman R.M., Statics and Kinematics of Granular Materials, Cambridge University Press, (1992). ISBN: 9780521404358.
Negi S.C., Ogilvie J.R., Silage pressure in tower silos. part 1. theoretical and design considerations, Canadian Agricultural Engineering, 19 (1977) 92–97.
Ooi J.Y., Rotter J.M., Wall pressures in squat steel silos from simple finite element analysis, Computers and Structures, 37 (1990) 361–374. DOI: 10.1016/0045-7949(90)90026-X
Ovarlez G., Clément E., Elastic medium confined in a column versus the Janssen experiment, European Physical Journal E, 16 (2005) 421–438. DOI: 10.1140/epje/i2004-10098-8
Pascot A., Gaudel N., Antonyuk S., Bianchin J., Kiesgen De Richter S., Influence of mechanical vibrations on quasi-2D silo discharge of spherical particles, Chemical Engineering Science, 224 (2020) 115749. DOI: 10.1016/j.ces.2020.115749
Petingco M.C., Casada M.E., Maghirang R.G., Thompson S.A., Turner A.P., McNeill S.G., Montross M., Discrete element method simulation of wheat bulk density as affected by grain drop height and kernel size distribution, Journal of the ASABE, 65 (2022) 555–566. DOI: 10.13031/ja.14811
Pleissner J., Versuche zur Ermittlung der Boden und Seitenwanddrucke in Getreidesilos. Zeitschrift des Vereines deutscher Ingenieure, 50 (1906) 976–986.
Pont S.C.d., Gondret P., Perrin B., Rabaud M., Wall effects on granular heap stability, Europhysics Letters, 61 (2003) 492–498. DOI: 10.1209/epl/i2003-00156-5
Prante N.I. Messungen des getreidedruckes gegen silowandungen, Zeitschrift des Verein Deutscher Ingenieure (Germany), 40 (1896) 1122–1125.
Qadir A., Guo H., Liang X., Shi Q., Sun G., Effect of the ratios of diameter of silo to bead on the pressure screening in granular columns, European Physical Journal E, 31 (2010) 311–314. DOI: 10.1140/epje/i2010-10581-7
Rahmoun J., Millet O., De Saxcé G., A continuous media approach to modeling the stress saturation effect in granular silos, Journal of Statistical Mechanics: Theory and Experiment, 2008 (2008) P06011. DOI: 10.1088/1742-5468/2008/06/P06011
Ramírez A., Nielsen J., Ayuga F., Pressure measurements in steel silos with eccentric hoppers, Powder Technology, 201 (2010) 7–20. DOI: 10.1016/j.powtec.2010.02.027
Ramírez-Gómez Á., The discrete element method in silo/bin research. Recent advances and future trends, Particulate Science and Technology, 38 (2020) 210–227. DOI: 10.1080/02726351.2018.1536093
Reimbert M., Reimbert A., Silos: Theory and Practice: Vertical Silos, Horizontal Silos, Trans Tech Publications (1976), ISBN: 9782852063655.
Roberts A.W., 100 years of Janssen, 5th International Conference on Bulk Materials Storage, Handling and Transportation: Proceedings, (1995) 1–19.
Roberts A.W., Particle technology—reflections and horizons, Chemical Engineering Research and Design, 76 (1998) 775–796. DOI: 10.1205/026387698525522
Roberts I., Determination of the vertical and lateral pressures of granular substances, The Royal Society Publishing, 36 (1883) 225–240. DOI: 10.1098/rspl.1883.0106
Rusinek R., Experimental method for determination of the pressure distribution in granular solids, Research in Agricultural Engineering, 49 (2003) 61–64. DOI: 10.17221/4954-rae
Savage S.B., Some considerations of flow on cohesionless granular solids, Ph.D. thesis, McGill University, 1967. <https://escholarship.mcgill.ca/concern/theses/5t34sk27k> accessed 01.11.2023.
Schillinger D., Malla R.B., Analytical elastic solution based on Fourier series for a laterally confined granular column, Journal of Engineering Mechanics, 134 (2008) 937–951. DOI: 10.1061/(asce)0733-9399(2008)134:11(937)
Schulze D., Powders and Bulk Solids, Springer, Berlin Heidelberg New York, 2008, ISBN: 9783540737674. DOI: 10.1007/978-3-540-73768-1
Silvestri S., Gasparini G., Trombetti T., Foti D., On the evaluation of the horizontal forces produced by grain-like material inside silos during earthquakes, Bulletin of Earthquake Engineering, 10 (2012) 1535–1560. DOI: 10.1007/s10518-012-9370-y
Sperl M., Experiments on corn pressure in silo cells—Translation and comment of Janssen's paper from 1895, Granular Matter, 8 (2006) 59–65. DOI: 10.1007/s10035-005-0224-z
Sun Q., Jin F., Wang G., Song S., Zhang G., On granular elasticity, Scientific Reports, 5 (2015) 9652. DOI: 10.1038/srep09652
Sun S., Zhao J., Zhang C., Calculation of silo wall pressure considering the intermediate stress effect, Advances in Civil Engineering, 2018 (2018) 3673515. DOI: 10.1155/2018/3673515
Takami A., Mathematical analysis of pressure distribution in powder in equilibrium in a conical vessel, Power Technology, 14 (1975) 1–6. DOI: 10.1016/0032-5910(76)80001-0
Tang J., Lu H., Guo X., Liu H., Static wall pressure distribution characteristics in horizontal silos, Powder Technology, 393 (2021) 342–348. DOI: 10.1016/j.powtec.2021.07.084
Thompson S.A., Schwab C.V., Ross I.J., Calibration of a model for packing whole grains, Applied Engineering in Agriculture, 7 (1991) 450–456. DOI: 10.13031/2013.26244
Tighe B.P., Sperl M., Pressure and motion of dry sand: translation of Hagen's paper from 1852, Granular Matter, 9 (2007) 141–144. DOI: 10.1007/s10035-006-0027-x
Toltz M., Discussion on grain pressures in deep bins, Transactions of the Canadian Society for Civil Engineering, 17 (1903) 641.
Turner A.P., Montross M.D., McNeill S.G., Sama M.P., Casada M.E., Boac J.M., Bhadra R., Maghirang R.G., Thompson S.A., Modeling the compressibility behavior of hard red wheat varieties, Transactions of the ASABE, 59 (2016) 1029–1038. DOI: 10.13031/trans.59.11432
Umbanhowar P., Goldman D.I., Granular impact and the critical packing state, Physical Review E, 82 (2010) 010301. DOI: 10.1103/PhysRevE.82.010301
Vanel L., Claudin P., Bouchaud J.P., Cates M.E., Clément E., Wittmer J.P., Stresses in silos: comparison between theoretical models and new experiments, Physical Review Letters, 84 (2000) 1439–1442. DOI: 10.1103/PhysRevLett.84.1439
Vanel L., Clément E., Pressure screening and fluctuations at the bottom of a granular column, European Physical Journal B, 11 (1999) 525–533. DOI: 10.1007/s100510050965
Vidal P., Gallego E., Guaita M., Ayuga F., Simulation of the filling pressures of cylindrical steel silos with concentric and eccentric hoppers using 3-dimensional finite element models, Transactions of the ASABE, 49 (2006) 1881–1895. DOI: 10.13031/2013.22290
Vidal P., Gallego E., Guaita M., Ayuga F., Finite element analysis under different boundary conditions of the filling of cylindrical steel silos having an eccentric hopper, Journal of Constructional Steel Research, 64 (2008) 480–492. DOI: 10.1016/j.jcsr.2007.08.005
Volfson D., Tsimring L.S., Aranson I.S., Partially fluidized shear granular flows: continuum theory and molecular dynamics simulations, Physical Review E, 68 (2003) 021301. DOI: 10.1103/PhysRevE.68.021301

Walker D.M., An approximate theory for pressures and arching in hoppers, Chemical Engineering Science, 21 (1966) 975–997. DOI: 10.1016/0009-2509(66)85095-9

Walters J.K., A theoretical analysis of stresses in silos with vertical walls, Chemical Engineering Science, 28 (1973) 779–789. DOI: 10.1016/0009-2509(77)80012-2

Wang S., Yan Y., Ji S., Transition of granular flow patterns in a conical hopper based on superquadric DEM simulations, Granular Matter, 22 (2020) 79. DOI: 10.1007/s10035-020-01051-9

Weisbach J., The Mechanics of Machinery and Engineering—Applied Mechanics, Philadelphia: Lea and Blanchard, Vol. 2 (1849). <http://hdl.handle.net/2027/coo.31924021905652> accessed 01.11.2023.

Windows-Yule C.R.K., Mühlbauer S., Cisneros L.A.T., Nair P., Marzulli V., Pöschel T., Janssen effect in dynamic particulate systems, Physical Review E, 100 (2019) 022902. DOI: 10.1103/PhysRevE.100.022902

Wittmer J.P., Cates M.E., Claudin P., Stress propagation and Arching in Static Sandpiles, Journal de Physique I, 7 (1997) 39–80. DOI: 10.1051/jp1:1997126

Wittmer J.P., Claudin P., Cates M.E., Bouchaud J.P., An explanation for the central stress minimum in sand piles, Nature, 382 (1996) 336–338. DOI: 10.1038/382336a0

Wiącek J., Molenda M., Effect of particle size distribution on micro-and macromechanical response of granular packings under compression, International Journal of Solids and Structures, 51 (2014) 4189–4195. DOI: 10.1016/j.ijsolstr.2014.06.029

Wojcik M., Enstad G.G., Jecmenica M., Numerical calculations of wall pressures and stresses in steel cylindrical silos with concentric and eccentric hoppers, Particulate Science and Technology, 21 (2003) 247–258. DOI: 10.1080/02726350307486

Xu S., Predictions of loads in grain storage bins using microstructural mechanics and endochronic theories, Ph.D. thesis, University of Manitoba, 1996. <http://hdl.handle.net/1993/19371> accessed 01.11.2023.

Xu S., Zhang Q., Britton M.G., A microscopic theory for predicting loads in storage bins for granular materials, Journal of Agricultural and Engineering Research, 65 (1996) 253–259. DOI: 10.1006/jaer.1996.0098

Xu Y., Kafui K.D., Thornton C., Lian G., Effects of material properties on granular flow in a silo using dem simulation, Particulate Science and Technology, 20 (2002) 109–124. DOI: 10.1080/02726350215338

Xu Z., Liang P., Modified lateral pressure formula of shallow and circular silo considering the elasticities of silo wall and storage materials, Scientific Reports, (2022) 1–10. DOI: 10.1038/s41598-022-11305-6

Zhang Q., Britton M.G., A micromechanics model for predicting dynamic loads during discharge in bulk solids storage structures, Canadian Biosystems Engineering, 45 (2003) 5.21–5.27.

Zhang Q., Bu X., Britton M.G., An analytical model for predicting stresses in grain storage bins, Transactions of the ASAE, 41 (1998a) 1835–1841. DOI: 10.13031/2013.17337

Zhang Q., Puri V.M., Manbeck H.B., Applicability of a two-parameter failure criterion to wheat en masse, Transactions of the American Society of Agricultural Engineers, 37 (1994) 571–575. DOI: 10.13031/2013.28114

Zhang Q., Shan Y., Britton M.G., Measuring Moisture-induced Loads in a Model Grain Bin, Transactions of the ASABE, 41 (1998b) 813–817. DOI: 10.13031/2013.17219

Authors' Short Biographies



George Dyck

George Dyck is a Biosystems Engineering PhD student from the University of Manitoba, Winnipeg, Canada. His research focuses on the application of digital twin technology in bulk solids storage systems, with an emphasis on the development of comprehensive and efficient models for these systems. George's work is aimed at advancing sustainable and efficient bulk solids storage practices, making a significant contribution to the field of agricultural engineering.



Adam Rogers

Adam Rogers is a Research Scientist with a doctorate degree in Physics and Astronomy from the University of Manitoba in Winnipeg, Canada. He has worked with AGCO since 2020, where his focus has been on model development and mathematical analysis. His research interests broadly encompass the physics of granular materials.



Jitendra Paliwal

Dr. Jitendra Paliwal is a Professor of Biosystems Engineering whose expertise lies in the storage, handling, and quality monitoring of cereal grains, oilseeds, leguminous crops, and their derivatives. His research on developing hardware and software solutions is widely referred to by the designers of grain quality monitoring and assessment instruments. In 2018, he was part of a distinguished team of industry and academic researchers, who won the American Society of Agricultural and Biological Engineering's AE50 award for adapting a cancer detection imaging technique for remote monitoring grain bins.

KONA Powder and Particle Journal

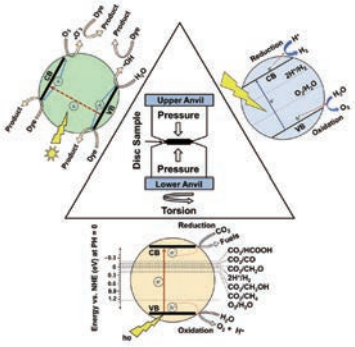
KONA Powder and Particle Journal No. 41 (2024) 123–139/https://doi.org/10.14356/kona.2034003 Review Paper

High-Pressure Torsion for Highly-Strained and High-Entropy Photocatalysts †

Saeid Akrami [1], Parisa Edalati [1], Masayoshi Fuji [1,2*] and Kaveh Edalati [3,4*]

[1] *Department of Life Science and Applied Chemistry, Nagoya Institute of Technology, Japan*
[2] *Advanced Ceramics Research Center, Nagoya Institute of Technology, Japan*
[3] *WPI International Institute for Carbon-Neutral Energy Research (WPI-I2CNER), Kyushu University, Japan*
[4] *Mitsui Chemicals, Inc.- Carbon Neutral Research Center (MCI-CNRC), Kyushu University, Japan*

Nowadays, the environmental crisis caused by using fossil fuels and CO_2 emissions has become a universal concern in people's life. Photocatalysis is a promising clean technology to produce hydrogen fuel, convert harmful components such as CO_2, and degrade pollutants like dyes in water. There are various strategies to improve the efficiency of photocatalysis so that it can be used instead of conventional methods, however, the low efficiency of the process has remained a big drawback. In recent years, high-pressure torsion (HPT), as a severe plastic deformation (SPD) method, has shown extremely high potential as an effective strategy to improve the activity of conventional photocatalysts and synthesize new and highly efficient photocatalysts. This method can successfully improve the activity by increasing the light absorbance, narrowing the bandgap, aligning the band structure, decreasing the electron-hole recombination, and accelerating the electron-hole separation by introducing large lattice strain, oxygen vacancies, nitrogen vacancies, high-pressure phases, heterojunctions, and high-entropy ceramics. This study reviews the recent findings on the improvement of the efficiency of photocatalysts by HPT processing and discusses the parameters that lead to these improvements.



Keywords: photocatalysis, water splitting, oxygen vacancy, nitrogen vacancy, heterojunctions, high-entropy alloys (HEAs), high-entropy ceramics

1. Introduction

Nowadays, serious environmental crises such as global warming and the formation of wastewater have forced humans to find alternatives like using clean fuels without carbon dioxide emissions such as hydrogen, reducing the pollutant gases such as carbon dioxide, and degrading the toxic pollutants in wastewater through clean strategies (Gaya and Abdullah, 2008). Using photocatalysts is an effective strategy to deal with these environmental crises using renewable sunlight energy (Ma et al., 2014). The function of photocatalysts is the acceleration of reduction and oxidation (redox) reactions under light irradiation. Reduction and oxidation reactions occur on the surface of a photocatalyst using the electrons and holes, respectively (Tong et al., 2012), to promote processes such as dye degradation (Akpan and Hameed, 2009), water splitting (Maeda, 2011), CO_2 conversion (Tu et al., 2014), etc.

In photocatalytic dye degradation, photoexcited electrons take part in the degradation reaction of dyes (e.g. rhodamine B, methylene orange, acid red B, etc.) which normally exist in wastewaters produced by factories, laboratories and different industries (Akpan and Hameed, 2009). Photocatalytic water splitting includes the reduction to hydrogen and oxidation to oxygen (Maeda, 2011). In photocatalytic CO_2 conversion, photoexcited electrons contribute to the conversion of CO_2 to reactive and useful components such as carbon monoxide (CO), formic acid (HCOOH), formaldehyde (HCHO), methanol (CH_3OH) and methane (CH_4) (Tu et al., 2014). The mechanism of photocatalytic dye degradation, water splitting and CO_2 conversion is shown in **Figs. 1(a)**, **1(b)** and **1(c)**, respectively.

A photocatalyst should have some features to support the photocatalytic reactions including a narrow bandgap, appropriate band positions to cover the desired reactions, appropriate light absorbance, potential to absorb and activate the reactants, easy electron transition, and low recombination rate of electrons and holes (Akpan and Hameed, 2009; Maeda, 2011; Tu et al., 2014). Furthermore, high specific surface area, low cost, low toxicity and high stability are the other required properties that should be considered to select a photocatalyst (Tong et al., 2012). Challenging in this field is finding a photocatalyst

† Received 9 September 2022; Accepted 19 December 2022
J-STAGE Advance published online 25 March 2023
* Corresponding author: Masayoshi Fuji and Kaveh Edalati;
[1,2] Add: 3-101-1 Hon-machi, Tajimi, Gifu 507-0033, Japan
[3,4] Add: 744 Motooka, Nishi-ku, Fukuoka 819-0395, Japan
E-mail: fuji@nitech.ac.jp (M.F.); kaveh.edalati@kyudai.jp (K.E.)
TEL: +81-572-27-6811 (M.F.); +81-92-802-6744 (K.E.)

Copyright © 2024 The Authors. Published by Hosokawa Powder Technology Foundation. This is an open access article under the CC BY license (https://creativecommons.org/licenses/by/4.0/).

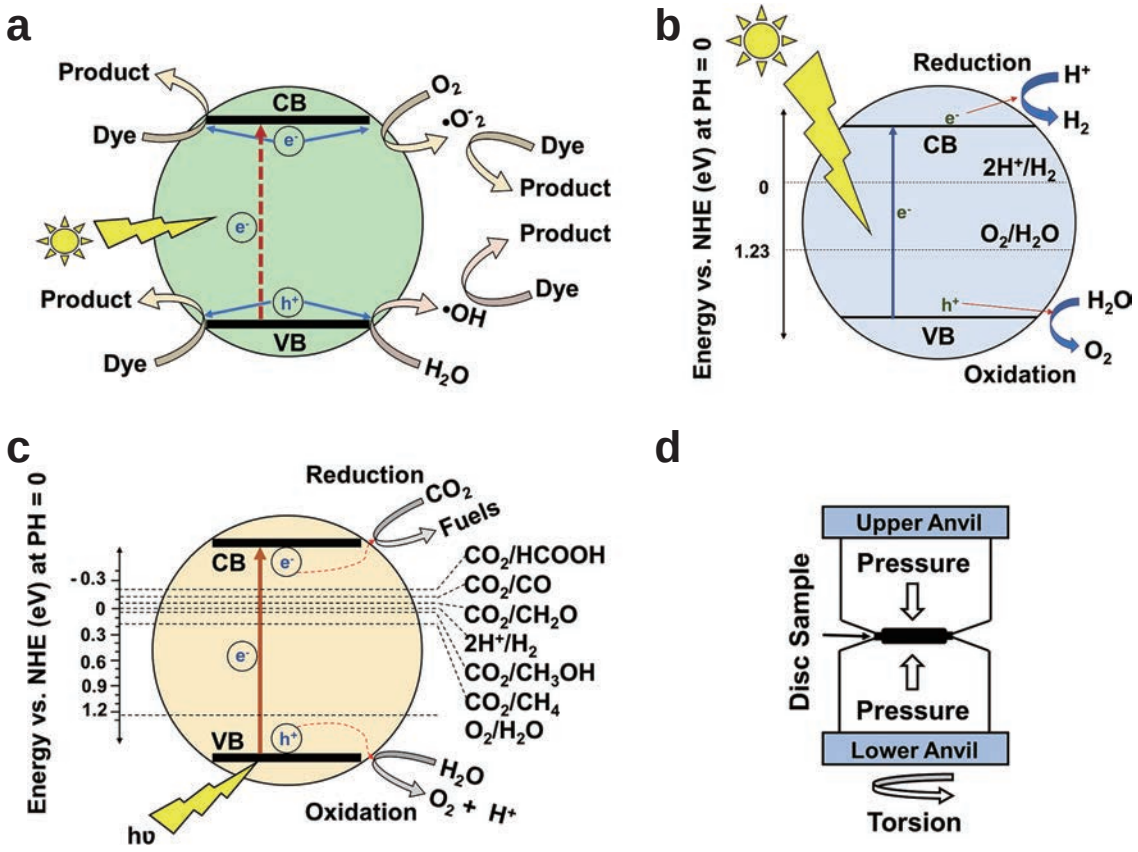


Fig. 1 Schematic illustration of **(a)** photocatalytic dye degradation, **(b)** photocatalytic water splitting, **(c)** photocatalytic CO_2 conversion, and **(d)** the HPT process.

with sufficient properties for considerable photocatalytic efficiency compared with the conventional catalytic processes. TiO_2 (Ajmal et al., 2014; Ni et al., 2007; Ola and Maroto-Valer, 2015), ZnO (Chakrabarti and Dutta, 2004; Lin et al., 2012; Zhao et al., 2019), g-C_3N_4 (Wen et al., 2017; Ye et al., 2015; Yuan et al., 2016), WO_3 (Liu Y. et al., 2010; Wang et al., 2012; Wang et al., 2019a), $SrTiO_3$ (Huang et al., 2014a; Iwashina and Kudo, 2011; Shan et al., 2017), GaN–ZnO (Hagiwara et al., 2017; Maeda et al., 2005; Ohno et al., 2012) and $BiVO_4$ (Gao et al., 2017; Sun et al., 2014; Zhou et al., 2010) are some of the most promising photocatalysts which have been utilized for photocatalytic dye degradation, water splitting and CO_2 conversion. The efficiencies of all these photocatalysts are still low for practical applications, and thus, various strategies were utilized to enhance the optical and structural properties and accordingly the photocatalytic activity of these materials.

Vacancy introduction (Huang et al., 2014b; Lei et al., 2014; Yu H. et al., 2019), strain engineering (Di J. et al., 2020; Feng et al., 2015; Sa et al., 2014), using mesoporous structures (Li Y. et al., 2010; Pauporté and Rathouský, 2007; Puangpetch et al., 2009), formation of heterojunctions (Cao et al., 2018; Moniz et al., 2015; Uddin et al., 2012), nanosheet production (Etman et al., 2018; Tu et al., 2012; Yu J. et al., 2010) and doping with impurities (Kuvarega et al., 2011; Lee et al., 2016; Liu B. et al., 2018) are some of the reported methods which have been effective to improve the photocatalytic activity. Doping with impurities is the most common method which is used to improve the activity by narrowing the bandgap, but it usually causes recombination effects (Kuvarega et al., 2011).

High-pressure torsion (HPT) as one of the severe plastic deformation (SPD) methods has been introduced as an effective process to improve the photocatalytic efficiency of various materials by introducing vacancies (oxygen vacancy and nitrogen vacancy), dislocations, nanocrystals, lattice strain, heterojunctions, high-pressure phases and high-entropy ceramics. The HPT method is effective in reducing the recombination rate of electrons and holes which are usually observed in doped photocatalysts. The HPT method decreases the optical bandgap and enhances the photocatalytic activity of various oxides and oxynitrides including TiO_2 (Razavi-Khosroshahi et al., 2016b), ZnO (Razavi-Khosroshahi et al., 2017b), Al_2O_3 (Edalati et al., 2019b), MgO (Fujita et al., 2020a), ZrO_2 (Wang et al., 2020b), SiO_2 (Wang et al., 2020a), $LiTaO_3$ (Edalati et al., 2020a), $CsTaO_3$ (Edalati et al., 2020a), $BiVO_4$ (Akrami et al., 2022c), Ga_6ZnON_6 (Edalati et al., 2020b) for dye degradation, hydrogen production and CO_2 conversion. Furthermore, HPT was successfully used to synthesize new high-entropy oxides such as $TiHfZrNbTaO_{11}$ (Edalati

et al., 2020c) and high-entropy oxynitrides such as $TiZrHfNbTaO_6N_3$ (Akrami et al., 2022a) for hydrogen production, oxygen evolution and CO_2 conversion. Moreover, it was also utilized to form heterojunctions in binary and high-entropy composites such as TiO_2–ZnO (Hidalgo-Jimenez et al., 2020) and $TiZrNbTaWO_{12}$ (Edalati et al., 2022b) to improve the photocatalytic activity for hydrogen and oxygen production.

In this review paper, the influence of the HPT method on optical properties, electronic structure, electron-hole separation, migration and recombination rates and photocatalytic efficiency of various photocatalysts is discussed. The improvement of photocatalytic activity of these materials for dye degradation, hydrogen production, oxygen production and CO_2 conversion is discussed by considering the generation of oxygen vacancies, nitrogen-vacancy complexes, high-pressure phases, heterojunctions and high-entropy ceramics.

2. High-pressure torsion (HPT)

The SPD process is typically used to form ultrafine-grained (UFG) and nanostructured materials with enhanced mechanical and functional properties (Estrin and Vinogradov, 2013; Valiev, 2004). SPD has various methods including HPT, introduced by Bridgman in 1935 for the first time (Bridgman, 1935). In this method, torsional strain under high pressure is applied to induce large plastic strain in various ranges of materials. In the HPT process, a disc-shape sample (Bridgman, 1935) that has typically a 10 mm diameter or a ring sample (Edalati and Horita, 2009) is inserted between two anvils under high pressure and strained by rotation of anvils against each other. A schematic illustration of HPT is shown in **Fig. 1(d)**. The applied shear strain (γ) to the sample can be calculated by the following equation (Edalati and Horita, 2016).

$$\gamma = \frac{2\pi rN}{h} \quad (1)$$

where r, N and h are the distance from the center of the disc or ring, the number of turns and the sample height, respectively.

In addition to grain refinement, the HPT method is widely used for hardening of pure metals (Edalati and Horita, 2011; Starink et al., 2013), mechanical alloying of miscible and immiscible systems (Edalati et al., 2015b; Edalati, 2019a) and plastic deformation of hard-to-deform materials (Edalati et al., 2010a; Edalati et al., 2010b; Ikoma et al., 2012). Phase transformation, consolidation of powders, the introduction of defects such as oxygen vacancies and dislocations, narrowing of the bandgap and improvement of functionalities were frequently reported after HPT processing (Edalati, 2019d). The HPT method can be utilized for plastic deformation of oxides and ceramics which are hard and brittle materials at ambient temperature (Edalati et al., 2022a). The presence of covalent or ionic bonding in ceramics results in their lower grain size after HPT processing compared to metals. Moreover, such bonding features result in the formation of large densities of defects such as vacancies and dislocations which can improve the properties and functionality of ceramics.

Despite the high potential of ceramics for various applications, there are some limited publications on the effect of HPT on the structure, properties and functionality of ceramics. A list of ceramics treated by HPT for various properties and applications and their relevant publications are given in **Table 1**. **Table 1** indicates that these HPT-processed ceramics, including oxides, nitrides, oxynitrides and borides, have been investigated for photocatalysis, phase transformation, electrocatalysis, photocurrent generation, dielectric properties, bandgap narrowing, optical properties, mechanical properties, Li-ion batteries and microstructural features. Furthermore, the HPT method was also utilized to synthesize new ceramics for various applications. As can be seen in **Table 1**, ceramic photocatalysts processed or synthesized by HPT were used for water splitting ($CsTaO_3$, $LiTaO_3$, ZrO_2, GaN–ZnO, TiO_2–ZnO, TiO_2, $TiHfZrNbTaO_{11}$, $TiZrNbTaWO_{12}$ and $TiZrHfNbTaO_6N_3$), dye degradation (ZnO, MgO, γ-Al_2O_3 and SiO_2), CO_2 conversion (TiO_2, $BiVO_4$, $TiHfZrNbTaO_{11}$ and $TiZrHfNbTaO_6N_3$) and oxygen production ($TiZrNbTaWO_{12}$).

3. Fundamentals and mechanism of photocatalysis

In photocatalysis, which is also called artificial photosynthesis, electrons in the valence band absorb the light photons, separate from the holes and transfer to the conduction band of the photocatalyst to form the electron-hole charge carriers. The charge carriers then migrate to the surface of the photocatalyst and finally take part in various chemical reactions. In this process, both reduction and oxidation reactions occur on the surface of the photocatalyst, provided that the thermodynamic and kinetic conditions are satisfied. From the thermodynamic point of view, a photocatalytic process will perform when the reduction and oxidation reaction potentials are between the valence band and the conduction band of a photocatalyst (Tong et al., 2012). For the reduction reactions, potentials lower than the valence band top are desirable, while for the oxidation reactions, potentials higher than the conduction band bottom are desirable. From the kinetic point of view, the electron-hole separation should be fast, and their recombination should be slow. Here, the fundamentals of three main photocatalytic reactions are mentioned.

3.1 Photocatalytic dye degradation

In photocatalytic dye degradation, there are two direct and indirect pathways. In the direct pathway, the dye

Table 1 Summary of major publications about ceramics treated by HPT and their major applications or features.

Materials	Investigated properties and application	Reference
Photocatalysis		
$TiHfZrNbTaO_{11}$	Photocatalytic activity for CO_2 conversion	(Akrami et al., 2022b)
$TiZrHfNbTaO_6N_3$	Photocatalytic activity for CO_2 conversion	(Akrami et al., 2022a)
$BiVO_4$	Photocatalytic activity for CO_2 conversion	(Akrami et al., 2022c)
TiO_2-II	Photocatalytic activity for CO_2 conversion	(Akrami et al., 2021b)
MgO	Photocatalytic activity for dye degradation	(Fujita et al., 2020a)
SiO_2	Photocatalytic activity for dye degradation	(Wang et al., 2020a)
γ-Al_2O_3	Photocatalytic activity for dye degradation	(Edalati et al., 2019b)
ZnO	Photocatalytic activity for dye degradation	(Razavi-Khosroshahi et al., 2017b)
$TiZrHfNbTaO_6N_3$	Photocatalytic activity for hydrogen production	(Edalati et al., 2021)
ZrO_2	Photocatalytic activity for hydrogen production	(Wang et al., 2020b)
$CsTaO_3$, $LiTaO_3$	Photocatalytic activity for hydrogen production	(Edalati et al., 2020a)
GaN–ZnO	Photocatalytic activity for hydrogen production	(Edalati et al., 2020b)
$TiHfZrNbTaO_{11}$	Photocatalytic activity for hydrogen production	(Edalati et al., 2020c)
TiO_2–ZnO	Photocatalytic activity for hydrogen production	(Hidalgo-Jimenez et al., 2020)
TiO_2-II	Photocatalytic activity for hydrogen production	(Razavi-Khosroshahi et al., 2016b)
$TiZrNbTaWO_{12}$	Photocatalytic activity for oxygen production	(Edalati et al., 2022b)
Reviews		
Oxides	Review on HPT of oxides	(Edalati, 2019b)
	Review on HPT	(Edalati and Horita, 2016)
Phase transformation		
SiO_2, VO_2	Phase transformation	(Edalati et al., 2019a)
TiO_2	Grain coarsening and phase transformation	(Edalati et al., 2019c)
ZrO_2	Phase transformation by ball milling and HPT	(Delogu, 2012)
ZrO_2	Allotropic phase transformations	(Edalati et al., 2011)
TiO_2	Plastic strain and phase transformation	(Razavi-Khosroshahi et al., 2016a)
BN	FEM modeling of plastic flow and strain-induced phase transformation	(Feng et al., 2019)
BN	Coupled elastoplasticity and plastic strain-induced phase transformation	(Feng and Levitas, 2017)
Electrocatalysis		
TiO_2-II	Electrocatalysis for hydrogen generation	(Edalati et al., 2019c)
Photocurrent		
Bi_2O_3	Enhanced photocurrent generation	(Fujita et al., 2020b)
TiO_2-II	Visible light photocurrent generation	(Wang et al., 2020c)
Dielectric properties		
$BaTiO_3$	Optical and dielectric properties	(Edalati et al., 2015a)
CuO	Dielectric properties	(Makhnev et al., 2011)
Bandgap investigation		
ZnO	Bandgap narrowing	(Qi et al., 2021)
Optical properties		
Y_2O_3	Optical properties	(Razavi-Khosroshahi et al., 2017a)
CuO, $Y_3Fe_5O_{12}$, $FeBO_3$	Optical properties and electronic structure	(Gizhevskii et al., 2011)
Cu_2O, CuO	Middle infrared absorption and X-ray absorption	(Mostovshchikova et al., 2012)
CuO, $Y_3Fe_5O_{12}$, $FeBO_3$	Optical properties	(Telegin et al., 2012)
Mechanical properties		
α-Al_2O_3	Microstructure and mechanical properties	(Edalati and Horita, 2010)
$Fe_{53.3}Ni_{26.5}B_{20.2}$, $Co_{28.2}Fe_{38.9}Cr_{15.4}Si_{0.3}B_{17.2}$	Microstructure and mechanical properties	(Permyakova and Glezer, 2020)
Lithium-ion batteries		
Fe_3O_4	Lithium-ion batteries	(Qian et al., 2018)
Microstructural features		
ZnO	Plastic flow and microstructural instabilities	(Qi et al., 2018)
$YBa_2Cu_3O_y$	Microstructural investigation	(Kuznetsova et al., 2017)
$Fe_{71.2}Cr_{22.7}Mn_{1.3}N_{4.8}$	Microstructural features	(Shabashov et al., 2018)

degrades directly by the excited electrons and holes in the conduction band and the valence band, respectively, as shown in **Fig. 1(a)**. In the indirect pathway, which is more conventional than the direct pathway, the electrons in the conduction band react with the O_2 to produce the $O_2^{\bullet-}$ radicals. The $O_2^{\bullet-}$ radicals then react with the dye to form the reduction products (Li X. et al., 2018). In the valence band, holes react with H_2O to produce $^{\bullet}OH$, and the $^{\bullet}OH$ radicals react with the dye to produce the oxidation products as shown in **Fig. 1(a)**.

3.2 Photocatalytic water splitting

In photocatalytic water splitting, electrons in the conduction band take part in the reduction reaction to produce H_2, while holes in the valence band take part in the oxidation reaction to produce O_2 (Lu et al., 2021), as shown in **Fig. 1(b)**. In most photocatalysts, overall water splitting does not occur, and the process is limited to either reduction or oxidation reactions thus a sacrificial agent or scavenger is usually required to produce electrons or holes. Methanol and $AgNO_3$ are popular sacrificial agents for photocatalytic hydrogen and oxygen production, respectively.

3.3 Photocatalytic CO_2 conversion

In photocatalytic CO_2 conversion, electrons in the conduction band along with protons (H^+) produced from water oxidation in the valence band, take part in various reduction reactions leading to the formation of CO, CH_4 and some other hydrocarbons as shown in **Fig. 1(c)**. The first step in photocatalytic CO_2 conversion is the adsorption of CO_2 molecules on the surface of the photocatalyst which occurs in three modes including oxygen coordination, carbon coordination and mixed coordination (Lu et al., 2021), as shown in **Fig. 2**. These CO_2 adsorption modes determine the reaction pathway for photocatalytic CO_2 conversion. For instance, the oxygen coordination mode, with the bidentate bonding of oxygen atoms with the surface of the photocatalyst, leads to the fabrication of formate anions as an intermediate product and formic acid as the final product. In the carbon coordination mode, with the monodentate binding of carbon and photocatalyst surface, the reaction results in carboxyl radical production. After the adsorption step of CO_2 to the surface of the photocatalyst, the conversion reactions occur via different pathways.

It was reported that there are three main pathways for CO_2 photoreduction: (i) carbene pathway (ii) formaldehyde pathway and (iii) glyoxal pathway (Habisreutinger et al., 2013; Maeda and Domen, 2007; Wang et al., 2021). The reactions for these three pathways are presented in **Table 2**. In all these pathways, the $CO_2^{\bullet-}$ radical is the main intermediate product which is formed by the reaction of

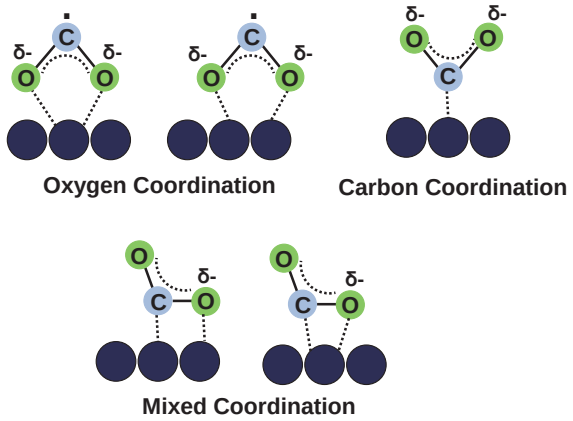


Fig. 2 CO_2 adsorption modes on the surface of photocatalysts.

Table 2 CO_2 photoreduction pathways (Habisreutinger et al., 2013).

Carbene Pathway	Formaldehyde Pathway	Glyoxal Pathway
(1) $CO_2 + e^- \rightarrow CO_2^{\bullet-}$	(1) $CO_2 + e^- \rightarrow CO_2^{\bullet-}$	(1) $CO_2 + e^- \rightarrow CO_2^{\bullet-}$
(2) $CO_2^{\bullet-} + e^- + H^+ \rightarrow CO + OH^-$	(2) $CO_2^{\bullet-} + H^+ \rightarrow {}^{\bullet}COOH$	(2) $CO_2^{\bullet-} + e^- + H^+ \rightarrow CHOO^-$
(3) $CO + e^- \rightarrow CO^{\bullet-}$	(3) $^{\bullet}COOH + e^- + H^+ \rightarrow HCOOH$	(3) $CHOO^- + H^+ \rightarrow HCOOH$
(4) $CO^{\bullet-} + e^- + H^+ \rightarrow C + OH^-$	(4) $HCOOH + e^- + H^+ \rightarrow H_3OOC^{\bullet}$	(4) $HCOOH + e^- \rightarrow HOC^{\bullet}$
(5) $C + e^- + H^+ \rightarrow CH^{\bullet}$	(5) $HCOOH_2^{\bullet} + e^- + H^+ \rightarrow HCOH + H_2O$	(5) $HOC^{\bullet} + OH^- \rightarrow C_2H_2O_2$
(6) $CH^{\bullet} + e^- + H^+ \rightarrow CH_2$	(6) $HCOH + e^- \rightarrow H_2C^{\bullet}O^-$	(6) $C_2H_2O_2 + e^- + H^+ \rightarrow H_3O_2C_2^{\bullet}$
(7) $CH_2 + e^- + H^+ \rightarrow CH_3^{\bullet}$	(7) $H_2C^{\bullet}O^- + H^+ \rightarrow H_2OHC^{\bullet}$	(7) $H_3O_2C_2^{\bullet} + e^- + H^+ \rightarrow C_2H_4O_2$
(8) $CH_3^{\bullet} + e^- + H^+ \rightarrow CH_4$	(8) $H_2OHC^{\bullet} + e^- + H^+ \rightarrow CH_3OH$	(8) $C_2H_4O_2 + e^- + H^+ \rightarrow H_3OC_2^{\bullet} + H_2O$
(9) $CH_3^{\bullet} + OH^- \rightarrow CH_3OH$	(9) $CH_3OH + e^- + H^+ \rightarrow {}^{\bullet}CH_3 + H_2O$	(9) $H_3OC_2^{\bullet} + e^- + H^+ \rightarrow C_2H_4O$
	(10) $^{\bullet}CH_3 + e^- + H^+ \rightarrow CH_4$	(10) $C_2H_4O + h^+ \rightarrow H_3OC_2^{\bullet} + H^+$
		(11) $H_3OC_2^{\bullet} \rightarrow CH_3^{\bullet} + CO$
		(12) $CH_3^{\bullet} + e^- + H^+ \rightarrow CH_4$

adsorbed CO_2 and an electron. In the carbene pathway, $CO_2^{\bullet-}$ converts to $CO^{\bullet}$ and leads to the production of CO, CH_2, CH_4 and CH_3OH. In this pathway, carbon coordination is the main binding mode. In the formaldehyde pathway, $CO_2^{\bullet-}$ converts to $^{\bullet}COOH$ to produce HCOOH, CH_3OH and CH_4. In this pathway, $CO_2^{\bullet-}$ attaches to the catalyst by monodentate or bidentate binding. In monodentate binding, either one oxygen atom in $CO_2^{\bullet-}$ or one carbon atom in $CO_2^{\bullet-}$ are bonded to the surface of the photocatalyst. In the bidentate mode, both oxygen atoms in $CO_2^{\bullet-}$ are bonded to the photocatalyst surface. In the glyoxal pathway, C_2 components are formed by some complicated reactions, though there are limitations to producing C_2 due to the low selectivity of the photocatalyst. In this pathway, $CO_2^{\bullet-}$ converts to the formyl radical $HOC^{\bullet}$ to form $C_2H_2O_2$, $C_2H_4O_2$, C_2H_4O, CO and CH_4. In all these pathways, CO_2 adsorption and activation are key parameters to adjust the selectivity of photocatalysts and this should be empowered by some strategies such as oxygen vacancy generation and strain engineering (Fu et al., 2020).

4. Impact of HPT on photocatalysis

As given in **Table 1**, numerous studies in recent years reported that the HPT method can be used to improve the photocatalytic activity of ceramics. Bandgap narrowing for the easier transition of photoexcited electrons from the valence band to the conduction band, increasing the light absorbance in the visible region of light, electronic band structure alignment, decreasing the recombination rate of electrons and holes and accelerating the electron-hole separation and migration are some phenomena responsible for the high activity of photocatalysts processed or synthesized by HPT. The occurrence of these phenomena was attributed to the formation of oxygen vacancies, nitrogen-vacancy complexes, high-pressure phases, heterojunctions and high-entropy phases which will be discussed in detail as follows.

4.1 Generation of oxygen vacancies

Oxygen vacancies on the surface have a significant effect on the photocatalytic activity of materials, since they can act as active sites to adsorb and activate the reactants and as trap sites for photoexcited electrons. In contrast, oxygen vacancies in the bulk of photocatalysts may act as recombination centers and lead to decreasing photocatalytic efficiency. Oxygen vacancies can also reduce the optical bandgap by changing the electronic structure of materials via the formation of defect states between the valence band and the conduction band. The formation of oxygen vacancies after HPT processing has been evidenced by several analysis methods such as electron paramagnetic resonance (EPR), X-ray photoelectron spectroscopy (XPS), Raman spectroscopy, differential scanning calorimetry (DSC), and X-ray diffraction (XRD) (Fujita et al., 2020a; Razavi-Khosroshahi et al., 2016b; Wang et al., 2020a). Furthermore, changing the color of catalysts to the darker ones, which are frequently observed after HPT processing, indicates the light absorbance in the visible region due to the formation of oxygen vacancies as color centers (Fujita et al., 2020b; Razavi-Khosroshahi et al., 2017b; Wang et al., 2020b). Among the photocatalysts treated by HPT, Al_2O_3 (Edalati et al., 2019b), MgO (Fujita et al., 2020a), ZrO_2 (Wang et al., 2020b), SiO_2 (Wang et al., 2020a), $LiTaO_3$ (Edalati et al., 2020a), $CsTaO_3$ (Edalati et al., 2020a) and $BiVO_4$ (Akrami et al., 2022c) are oxides which exhibited enhanced photocatalytic activity by oxygen vacancy formation.

Al_2O_3: Al_2O_3 is an insulator with a large bandgap (~9 eV) and does not show photocatalytic activity. First-principles calculations suggested that the formation of oxygen vacancies can reduce the optical bandgap of Al_2O_3 even to the visible light region (Edalati et al., 2019b). The application of HPT to Al_2O_3 resulted in the formation of oxygen vacancies, the reduction of optical bandgap and its photocatalytic activity. The formation of oxygen vacancies after HPT is shown in **Fig. 3(a)** using DSC analysis by the appearance of a peak at 530 K. After the HPT process, a narrow bandgap of 2.5 eV was achieved, in good agreement with the first-principles calculations, and the material showed photocatalytic activity for rhodamine B dye degradation under UV irradiation with an activity comparable to TiO_2 (**Fig. 3(b)**).

MgO: MgO, as another ceramic insulator, also exhibited high light absorbance and bandgap narrowing (from 7.8 eV to 3.9 eV) after HPT processing (Fujita et al., 2020a). The HPT-processed MgO showed photocatalytic activity for methylene blue dye degradation under UV irradiation (55 % decomposition after 3 h). The formation of oxygen vacancies in this material was evidenced by XPS analysis of Mg 2p, which showed a shift to lower energy, and such a shift became more significant by increasing the applied shear strain (i.e. by increasing the number of HPT turns).

ZrO_2: ZrO_2 is another ceramic that was processed by HPT to introduce a high concentration of oxygen vacancies (Wang et al., 2020b). The optical bandgap of this material decreased from 5.1 to 4.0 eV due to the formation of oxygen vacancies after HPT. The formation of oxygen vacancies after HPT processing at various temperatures is shown in **Fig. 3(c)** using the EPR analysis. The appearance of a pair peak with a g factor of ~2 indicates the formation of oxygen vacancies, while the formation of oxygen vacancies is enhanced by increasing the HPT processing temperature. Improvement of photocatalytic activity of ZrO_2 using HPT for hydrogen evolution is shown in **Fig. 3(d)**, indicating that the photocatalytic activity is improved by increasing the concentration of oxygen vacancies.

SiO_2: SiO_2 quartz sand also was examined for photocatalytic activity after processing using the HPT method

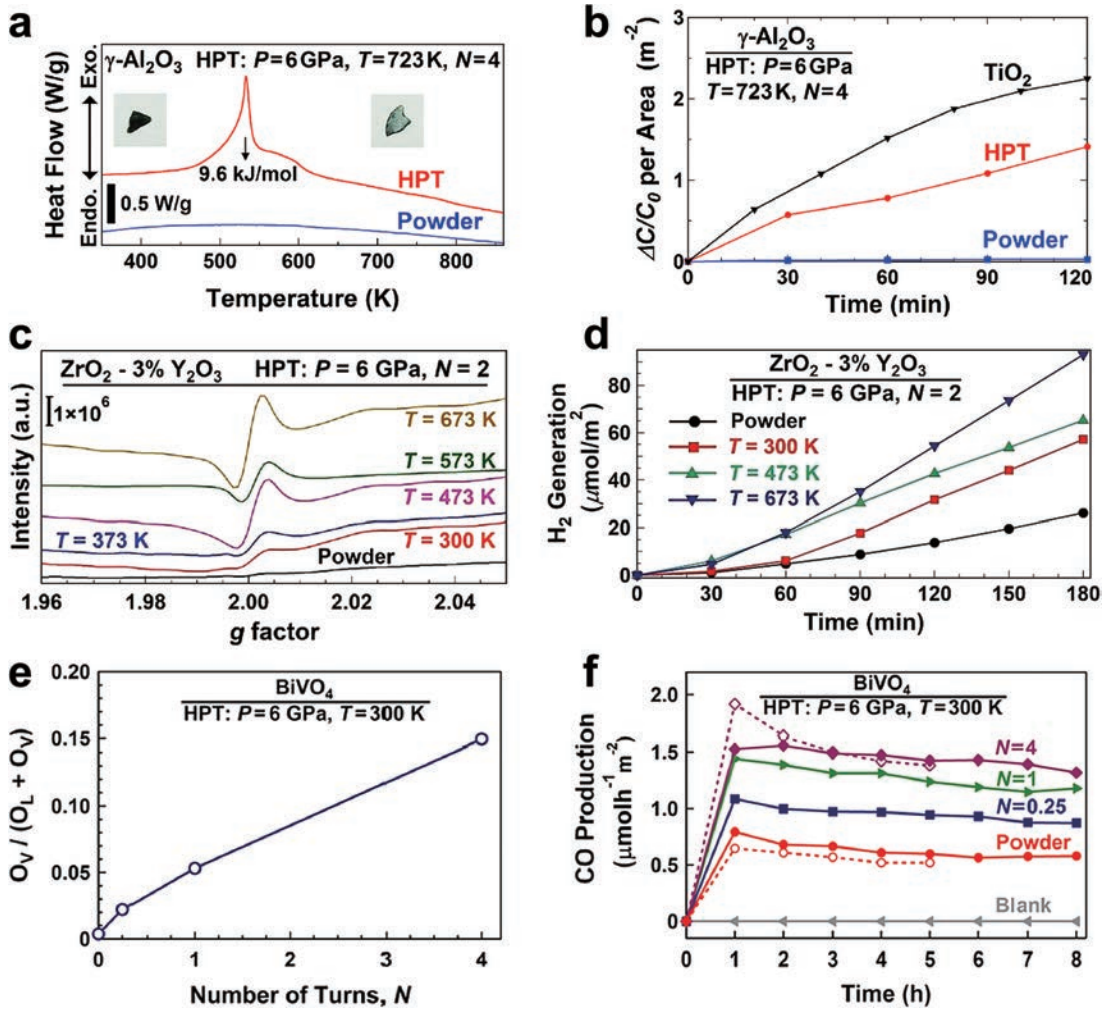


Fig. 3 Formation of oxygen vacancies achieved by HPT processing and improvement of photocatalytic activity. **(a)** DSC analysis and **(b)** photocatalytic rhodamine B degradation for γ-Al_2O_3 before and after HPT processing compared with TiO_2 (Edalati et al., 2019b). **(c)** EPR spectra and **(d)** corresponding photocatalytic hydrogen production for ZrO_2–3 wt% Y_2O_3 before and after HPT processing at 300, 437, 573 and 673 K (Wang et al., 2020b). **(e)** Oxygen vacancy concentration and **(f)** photocatalytic CO_2 to CO conversion for $BiVO_4$ before and after HPT processing for N = 0.25, 1 and 4 turns (Akrami et al., 2022c). Copyright: (2019) Elsevier, (2020) Royal Society of Chemistry, (2022) Elsevier.

(Wang et al., 2020a). This material with the initially reported bandgap of ~9 eV and negligible light absorbance exhibited a bandgap narrowing to 2.8 eV, with a small activity for rhodamine B dye degradation under UV light irradiation.

$LiTaO_3$ and $CsTaO_3$: $LiTaO_3$ and $CsTaO_3$ are two tantalate perovskites that show activity for photocatalytic hydrogen production. After oxygen vacancy generation by HPT processing, both materials exhibited bandgap narrowing (4.7 to 4.2 eV for $LiTaO_3$ and 4.7 to 3.6 eV for $CsTaO_3$) and enhanced photocatalytic activity for hydrogen generation (Edalati et al., 2020a).

$BiVO_4$: $BiVO_4$ is a popular photocatalyst for CO_2 conversion due to its low bandgap, but it suffers from a high recombination rate of electrons and holes and a low position of the conduction band. HPT could successfully solve these two problems by simultaneously introducing the oxygen vacancies and lattice strain (Akrami et al., 2022c). Increasing the oxygen vacancy concentration by increasing the number of HPT turns, calculated from XPS, is shown in Fig. 3(e). These structural modifications by HPT processing resulted in significant improvement of photocatalytic CO_2 conversion on $BiVO_4$, as shown in Fig. 3(f).

4.2 Generation of nitrogen-vacancy complexes

Oxynitrides are promising photocatalysts due to their low bandgap compared with oxide photocatalysts. It was reported that nitrogen vacancies, which are formed during the synthesis of these materials, can act as recombination centers, and reduce photocatalytic activity (Maeda and Domen, 2007). However, it was observed that HPT processing of Ga_6ZnON_6 led to the formation of nitrogen-based vacancies, decreasing the electron and hole recombination and enhancement of photocatalytic activity (Edalati et al., 2020b). Fig. 4(a) shows the EPR spectra of

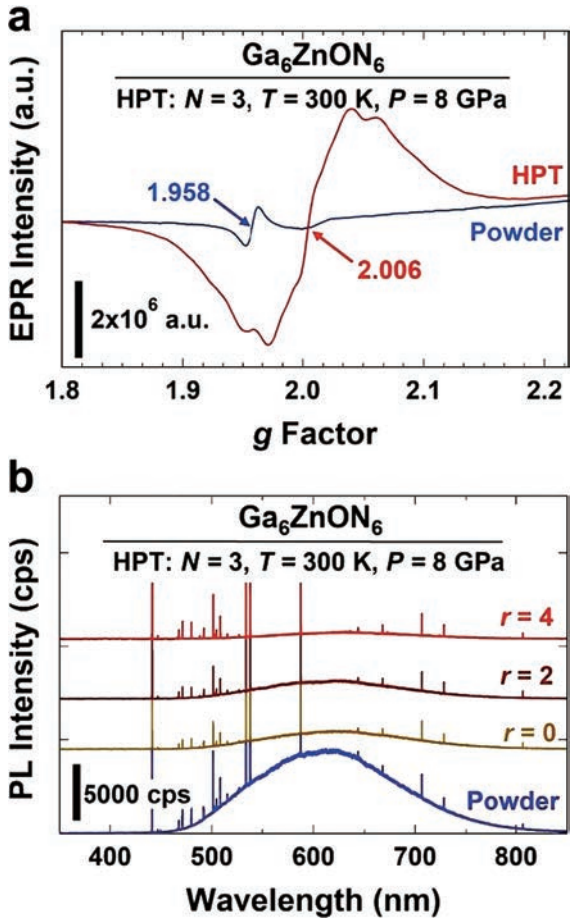


Fig. 4 Formation of nitrogen-based vacancy complexes and suppression of recombination in oxynitride processed by HPT. **(a)** EPR spectra and **(b)** photoluminescence spectra for Ga_6ZnON_6 before and after HPT processing (*r*: radial distance from center of HPT-processed disc) (Edalati et al., 2020b). Copyright: (2020) Elsevier.

Ga_6ZnON_6 before and after HPT processing. A *g* factor of 1.958 for powder is a piece of evidence for the formation of nitrogen monovacancies during the synthesis of oxynitrides, while a *g* factor of 2.006 indicates the presence of nitrogen-based vacancy complexes by HPT processing. Introducing the nitrogen-based vacancy complexes to this material by HPT, led to reducing the bandgap from 2.7 eV to 2.4 eV, enhancing the light absorbance and improvement of photocatalytic hydrogen production under UV irradiation. This study showed that in addition to the location of vacancies (surface or bulk), their arrangement (monovacancy or vacancy complex) can affect photocatalytic activity. These vacancy complexes can act as active sites for reactions rather than the recombination centers for electrons and holes. Decreasing the recombination of electrons and holes after HPT processing for this oxynitride is presented in **Fig. 4(b)**, in which the photoluminescence intensity is suppressed effectively after the HPT process.

4.3 Formation of high-pressure phases

Due to high pressure and high strain in HPT, the method can lead to the formation of metastable and high-pressure phases. These phases usually form with fast kinetics at lower pressures during HPT processing compared to the transition pressures under static conditions due to the presence of high concentrations of nanograin boundaries and defects. It was suggested that the formation of these defects and their interaction increase localized pressure and result in the formation and stability of high-pressure phases (Edalati, 2019b). $BaTiO_3$ (tetragonal to cubic) (Makhnev et al., 2011), TiO_2 (anatase-tetragonal to orthorhombic TiO_2-II) (Razavi-Khosroshahi et al., 2016b), Y_2O_3 (cubic to monoclinic) (Razavi-Khosroshahi et al., 2017a), ZnO (wurtzite-hexagonal to rocksalt-cubic) (Razavi-Khosroshahi et al., 2017b) and SiO_2 (quartz to coesite) (Wang et al., 2020a) are some oxides which showed transition to high-pressure phases after HPT processing. Among these materials, the formation of high-pressure phases in TiO_2 and ZnO was reported to lead to the improvement of photocatalytic activity for hydrogen production, CO_2 conversion and dye degradation. **Figs. 5(a)** and **5(b)** illustrate the pressure-temperature phase diagrams of TiO_2 and ZnO, respectively; **Figs. 5(c)** and **5(d)** show the formation of TiO_2-II and rocksalt-ZnO high-pressure phases after HPT processing, respectively; and **Figs. 5(c)** and **5(d)** show the influence of HPT processing on the enhancement of the photocatalytic activity of TiO_2 and ZnO, respectively. Since TiO_2 and ZnO are the most common photocatalysts, the reports on the application of HPT to these two photocatalysts are of significance as they suggested new solutions to enhance the activity by nanostructure and polymorphic control and without dopant or impurity addition (Razavi-Khosroshahi et al., 2016b; Razavi-Khosroshahi et al., 2017b).

TiO_2: TiO_2 light absorbance improved significantly after the formation of the high-pressure TiO_2-II (columbite) phase by HPT processing (Akrami et al., 2021b; Razavi-Khosroshahi et al., 2016b). The color of TiO_2 changed from white to gray or green and its bandgap decreased from 3.1 eV to 2.5 eV, which resulted in photocatalytic activity of the material under visible light. To solve the recombination issue due to the presence of bulk defects after HPT processing, the HPT-processed sample was processed by annealing which resulted in a further increase in the photocatalytic activity and photocurrent generation. It was shown that the formation of TiO_2-II results in photocatalytic activity for hydrogen production under visible light and CO_2 conversion under UV light (**Fig. 5(e)**), although the high activity is influenced by other factors such as the presence of oxygen vacancies and interphase boundaries.

ZnO: HPT processing of ZnO led to the formation of a high-pressure rocksalt phase and accordingly to the improvement of light absorbance in the visible region with a bandgap narrowing from 3.0 eV to 1.8 eV (Razavi-

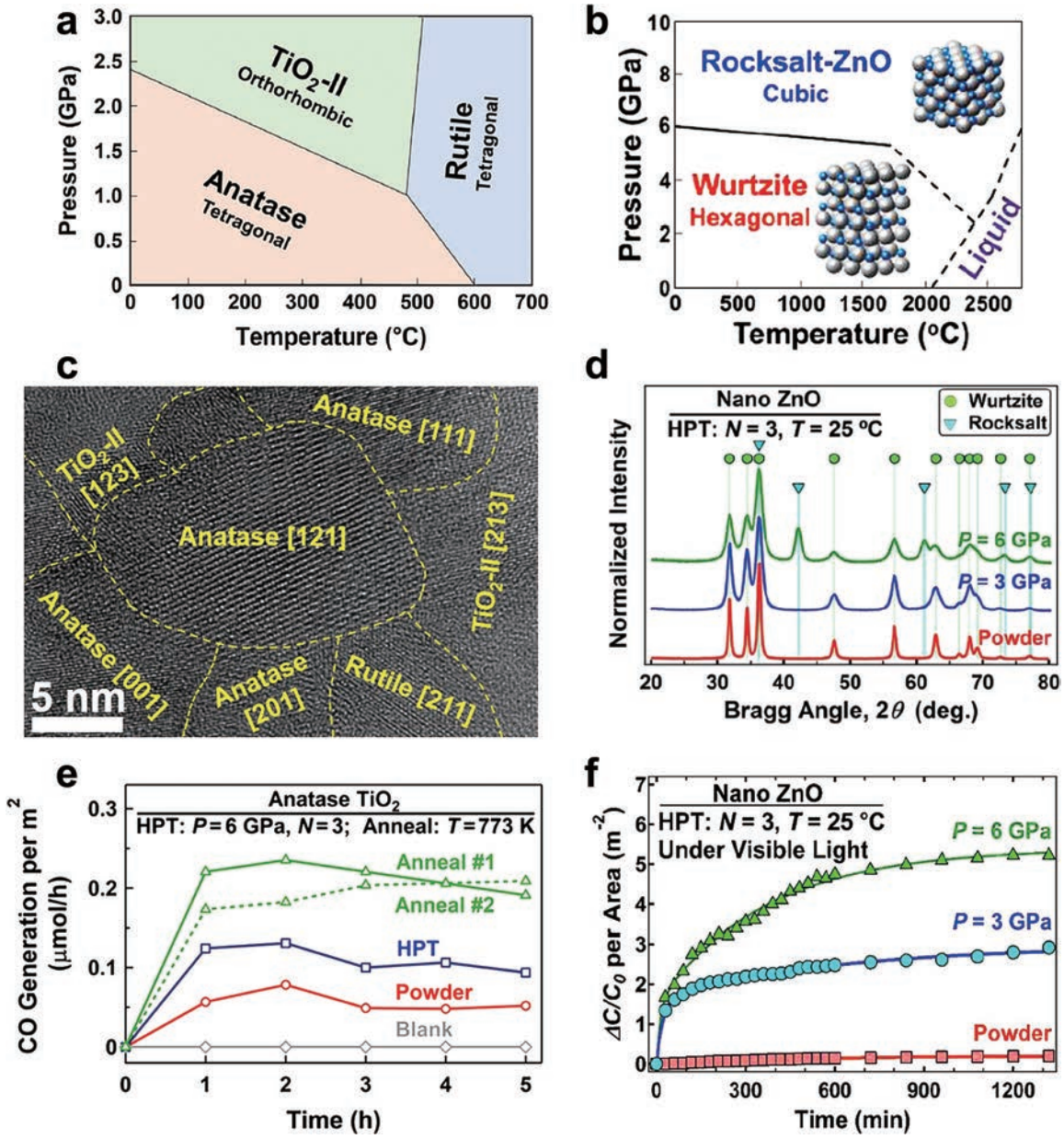


Fig. 5 Improved photocatalytic activity by introducing high-pressure phases. **(a)** Phase diagram of TiO_2 (Akrami et al., 2021b), **(b)** phase diagram of ZnO (Razavi-Khosroshahi et al., 2017b), **(c)** high-resolution lattice image of TiO_2 including TiO_2-II high-pressure phase (Akrami et al., 2021b), **(d)** XRD profile of ZnO including rocksalt high-pressure phase (Razavi-Khosroshahi et al., 2017b), **(e)** photocatalytic CO_2 conversion on TiO_2 before and after HPT processing and after annealing under UV light (Akrami et al., 2021b), and **(f)** photocatalytic rhodamine B dye degradation for ZnO before and after HPT processing under visible light (Razavi-Khosroshahi et al., 2017b). Copyright: (2021) Elsevier, (2017) Royal Society of Chemistry.

Khosroshahi et al., 2017b). This bandgap narrowing was also predicted by first-principles calculations. The HPT-processed ZnO, containing a high-pressure phase with a large fraction of oxygen vacancies and interphase boundaries, showed photocatalytic rhodamine B dye degradation under visible light, while its activity improved with increasing the processing pressure (**Fig. 5(f)**).

4.4 Formation of heterojunctions

Heterojunctions are the space-charge regions that are formed by the combination of two different phases or different semiconductors. Charge carriers can penetrate heterojunctions which results in the formation of an electronic field in this region (Moniz et al., 2015). Heterojunctions accelerate the electron and hole separation and improve their migration to the surface of the photocatalyst for the reactions. Furthermore, they significantly suppress recombination (Cao et al., 2018; Uddin et al., 2012). As mentioned earlier, among HPT-processed materials, some of them exhibit phase transformation resulting in the formation of heterojunctions between two or more phases such as cubic-rhombohedral phases in Al_2O_3 (Edalati et al., 2019b), monoclinic-tetragonal phases in ZrO_2 (Wang et al., 2020b) and coesite-quartz

phases in SiO_2. (Wang et al., 2020a). There is also an application of HPT to TiO_2–ZnO composite to generate heterojunctions for enhanced photocatalytic hydrogen production (Hidalgo-Jimenez et al., 2020). There is another attempt to generate 10 different heterojunctions in a high-entropy oxide $TiZrNbTaWO_{12}$ for visible-light-driven photocatalytic oxygen production (Edalati et al., 2022b). In all these cases, the interphase boundaries formed by HPT can act as sites to accelerate the electron-hole separation to effectively improve the photocatalytic activity, as will be discussed below for the TiO_2–ZnO composite.

TiO_2–ZnO: A recent study generated heterojunctions using HPT by making a composite of TiO_2 and ZnO as two typical catalysts for photocatalytic hydrogen production (Hidalgo-Jimenez et al., 2020). This work was performed to ease electron-hole separation as shown in **Fig. 6(a)**. In addition to TiO_2–ZnO heterojunctions, HPT processing led to the formation of high-pressure phases and formation of various kinds of heterojunctions. XRD profiles of TiO_2–ZnO composite show the presence of five different phases of TiO_2 and ZnO in **Fig. 6(b)**. After HPT processing, the light absorbance of the composite significantly increased in the visible light region and a bandgap narrowing was observed from 3.2 eV to 2.6 eV and 1.6 eV for $N = 3$ and 15 HPT turns, respectively. The recombination rate of electrons and holes was also suppressed effectively after HPT processing. Although electronic structure, light absorbance and recombination suppression improved by increasing the number of HPT turns to $N = 15$, photocatalytic hydrogen production for $N = 15$ was lower compared to the powder mixture and sample processed by $N = 3$ due to the formation of very small crystals and poor crystallinity (**Fig. 6(c)**). The composite processed with $N = 3$ had a hydrogen production amount of 2.5 time better than initial powders mixture under UV irradiation.

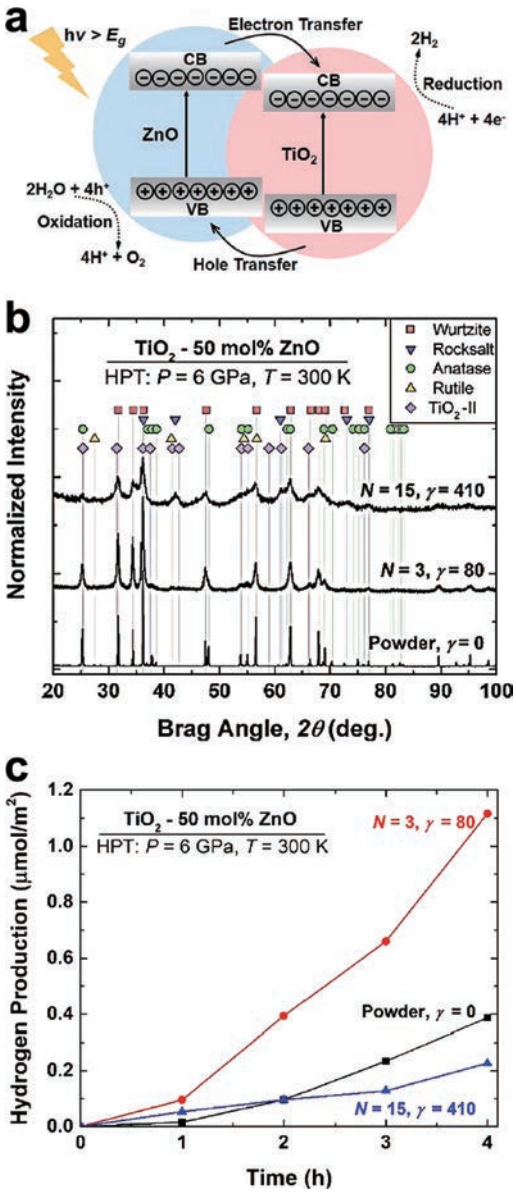


Fig. 6 Enhanced photocatalytic hydrogen production by heterojunction formation. **(a)** Schematic illustration of electronic band structure of TiO_2–ZnO composite including heterojunctions. **(b)** XRD profile and **(c)** photocatalytic hydrogen production on TiO_2–ZnO composite before and after HPT processing for $N = 3$ and 15 turns (Hidalgo-Jimenez et al., 2020). Copyright: (2020) Elsevier.

4.5 Production of high-entropy ceramics

High-entropy ceramics are materials with at least five principal cations and a mixing entropy higher than 1.5R (R: gas constant) (Akrami et al., 2021a; Oses et al., 2020). These materials have been employed for various applications due to their high stability, lattice strain, inherent defects and high entropy of mixing (Zhang and Reece, 2019; Xiang et al., 2021). They have potential to be used as Li-ion batteries (Lun et al., 2021; Nguyen et al., 2020; Wang et al., 2019b), catalysts (Albedwawi et al., 2021; Qiao et al., 2021; Xu et al., 2020), photocatalysts (Akrami et al., 2022a; Akrami et al., 2022b; Edalati et al., 2020c), supercapacitors (Jin et al., 2018; Liang et al., 2020; Talluri et al., 2021), dielectrics (Bérardan et al., 2016; Zhou et al., 2020; Zhou et al., 2022), thermal barrier coatings (Li F. et al., 2019; Ren et al., 2020; Zhang et al., 2022), etc. Utilizing the high-entropy ceramics as photocatalysts, which was performed for the first time by the authors of the current work, is a new functional aspect of these materials which is in its initial research stage. The high stability of high-entropy ceramics and the formation of defects and strain in these materials were the main motivations to use them as photocatalysts. As will be discussed below, the oxides $TiZrHfNbTaO_{11}$ and $TiZrNbTaWO_{12}$ and the oxynitride $TiZrHfNbTaO_6N_3$ are high-entropy ceramics synthesized by HPT and used for photocatalytic hydrogen production, CO_2 conversion and O_2 evolution. Since oxides and oxynitrides with d^0 and d^{10} electronic configurations show good photocatalytic activity, five d^0 cations were selected to design these photocatalysts.

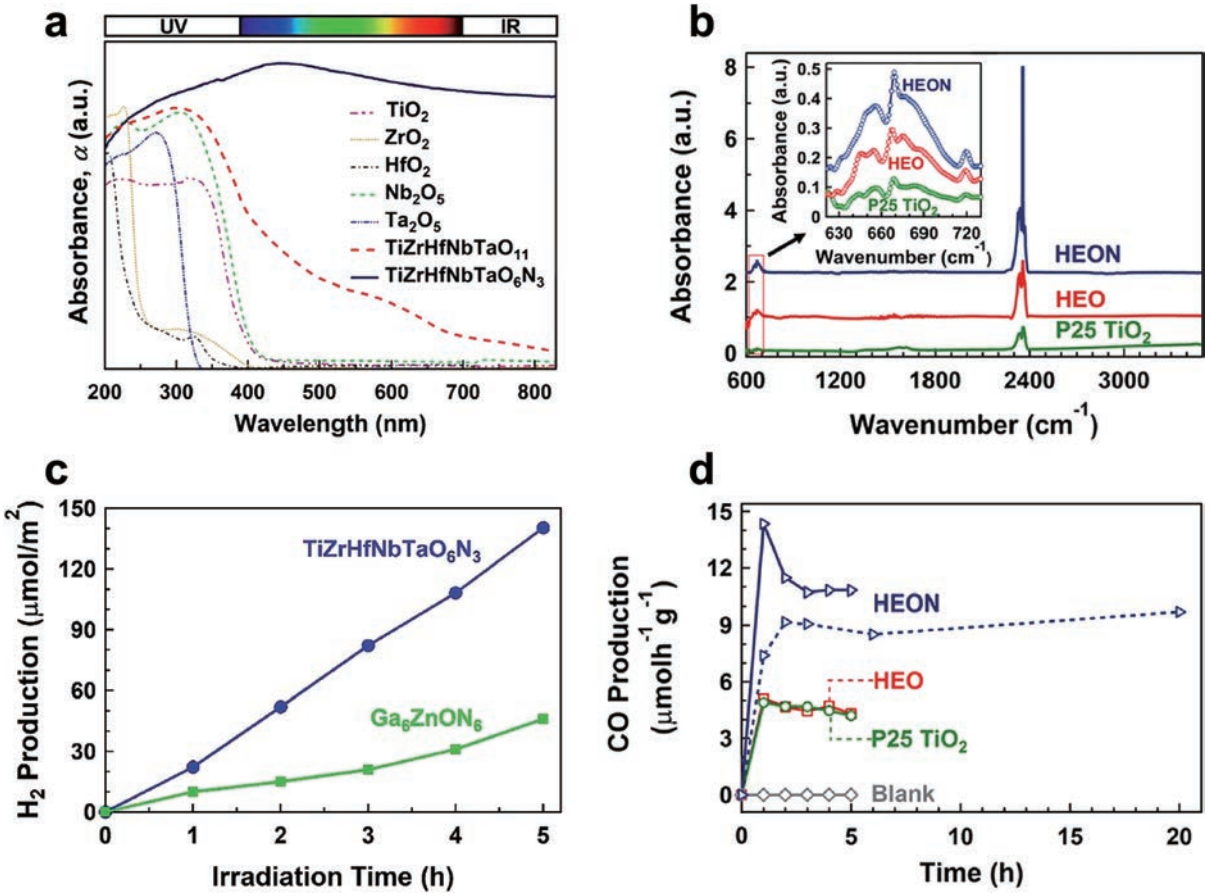


Fig. 7 High light absorbance and significant photocatalytic activity of high-entropy ceramics. **(a)** UV-vis spectra of $TiZrHfNbTaO_{11}$, $TiZrHfNbTaO_6N_3$ and relevant binary oxides including TiO_2, ZrO_2, HfO_2, Nb_2O_5 and Ta_2O_5 (Edalati et al., 2021), **(b)** diffuse reflectance infrared Fourier transform spectra for $TiZrHfNbTaO_{11}$ and $TiZrHfNbTaO_3N_6$ compared with P25 TiO_2 in which the peaks at 665 cm^{-1} and 2350 cm^{-1} represent chemisorption and physisorption of CO_2 on surface (Akrami et al., 2022a), **(c)** photocatalytic hydrogen production on $TiZrHfNbTaO_6N_3$ compared with Ga_6ZnON_6 (Edalati et al., 2021), and **(d)** photocatalytic CO_2 to CO conversion on $TiZrHfNbTaO_{11}$ and $TiZrHfNbTaO_6N_3$ compared with P25 TiO_2 (Akrami et al., 2022a). Copyright: (2021) Royal Society of Chemistry, (2022) Elsevier.

$TiZrHfNbTaO_{11}$: $TiZrHfNbTaO_{11}$ high-entropy oxide (HEO) with two monoclinic and orthorhombic phases which was synthesized by the HPT method and high-temperature oxidation, showed better light absorbance compared to relevant binary oxides including TiO_2, ZrO_2, HfO_2, Nb_2O_5 and Ta_2O_5 (**Fig. 7(a)**) (Edalati et al., 2020c). This material contained defects such as oxygen vacancies and dislocations as shown in **Fig. 8(a)**. Furthermore, it demonstrated lower photoluminescence intensity compared to anatase TiO_2 and $BiVO_4$ as two typical photocatalysts, indicating the low recombination rate of electrons and holes in this HEO (Akrami et al., 2022b). Moreover, this material showed the potential to generate photocurrent, produce hydrogen and convert CO_2 to CO under UV light. The rate of hydrogen and CO production for $TiZrHfNbTaO_{11}$ was higher than anatase TiO_2 and $BiVO_4$ and almost the same as P25 TiO_2 as a benchmark photocatalyst. This high photocatalytic activity was attributed to the formation of defects, interphases and high-entropy phases which led to the acceleration of electron-hole separation and diminishing their recombination.

$TiZrHfNbTaO_6N_3$: Low-bandgap high-entropy oxynitride (HEON) $TiZrHfNbTaO_6N_3$ was produced by HPT processing followed by oxidation and nitriding (Edalati et al., 2021). This HEON showed significantly higher light absorbance compared to corresponding high-entropy and binary oxides (**Fig. 7(a)**) with a narrow bandgap of 1.6 eV, which is lower than the bandgap of most reported oxynitride photocatalysts in the literature. This HOEN could successfully generate photocurrent with a significantly low recombination rate of electrons and holes compared to HEO and P25 TiO_2 as a benchmark photocatalyst (Akrami et al., 2022a). Furthermore, it showed a high potential to adsorb the CO_2 molecules on the surface as shown in **Fig. 7(b)**. This material produced hydrogen under UV irradiation with better activity than Ga_6ZnON_6 as one of the most popular oxynitride photocatalysts (**Fig. 7(c)**). It also showed a higher photocatalytic activity per surface area for CO_2 conversion compared to HEO and P25 TiO_2 (**Fig. 7(d)**) and all reported photocatalysts in the literature. Improved photocatalytic activity on this HEON was attributed to the high light absorbance

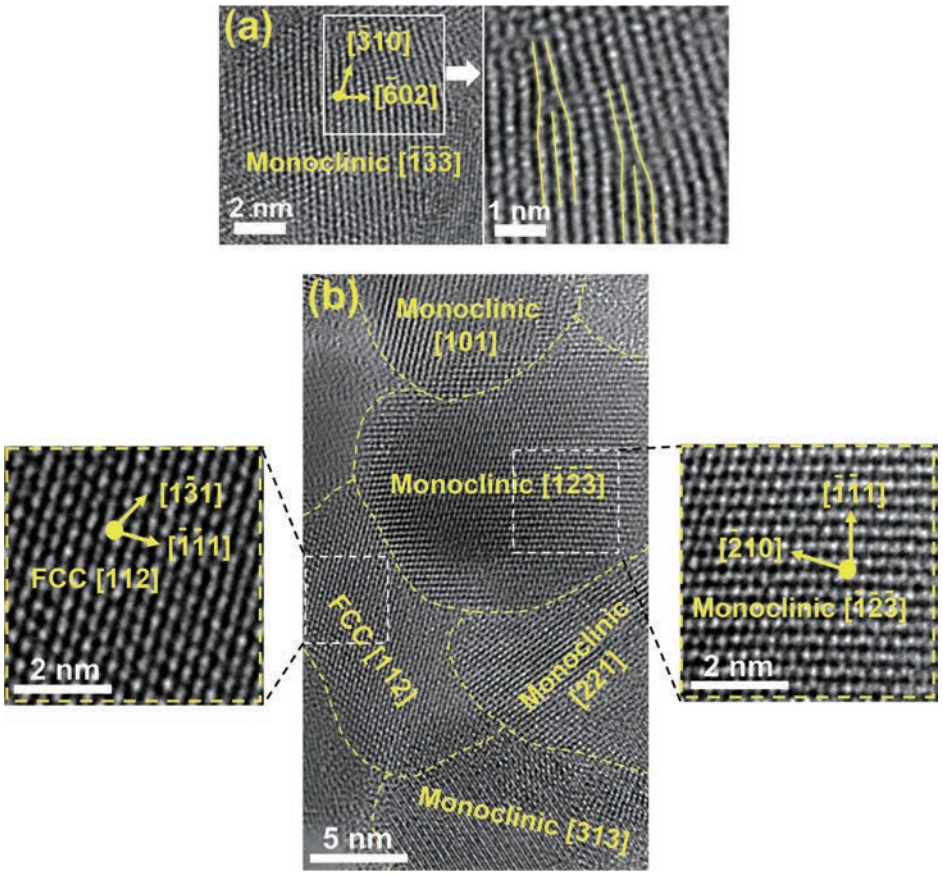


Fig. 8 Formation of nanograins, grain boundaries, interphases, and dislocation defects in high-entropy ceramics synthesized by HPT. High-resolution lattice images of **(a)** $TiZrHfNbTaO_{11}$ including dislocations (Akrami et al., 2022b) and **(b)** $TiZrHfNbTaO_6N_3$ including monoclinic and FCC phases and their heterojunctions (Edalati et al., 2021). Copyright: (2022) Elsevier, (2021) Royal Society of Chemistry.

and easy electron-hole separation, low recombination rate, and high surface activity for adsorption and conversion of water and CO_2. The presence of two phases in this HEON and the formation of interphases, as shown in **Fig. 8(b)**, was also believed to contribute to its high activity.

$TiZrNbTaWO_{12}$: The HEO, $TiZrNbTaWO_{12}$, was produced by HPT and consequent high-temperature oxidation (Edalati et al., 2022b). It had five different phases including one orthorhombic, two monoclinic and two tetragonal phases and ten heterojunctions. This material showed a low bandgap of 2.3–2.8 eV and a light absorbance higher than relevant binary oxides. Introducing the heterojunctions in this material resulted in successful photocatalytic oxygen production under viable light irradiation.

5. Concluding remark and outlook

Photocatalytic production of hydrogen from water, conversion of CO_2 to value-added compounds and degradation of toxic materials in wastewater under sunlight, are clean processes that have high potential to be used instead of conventional chemical methods. Photocatalysts used for these applications should have a narrow bandgap, appropriate band positions to support the reactions, low recombination rate of electrons and holes and high surface activity. In recent years, the high-pressure torsion (HPT) method was used to generate active photocatalysts for various applications. This method applies very high strain and pressure to material and subsequently introduces nanocrystals, lattice defects, lattice strain and heterojunctions. Furthermore, HPT can synthesize high-pressure and high-entropy phases. One main reason for the successful application of HPT to develop highly active photocatalysts is that the method can simultaneously introduce a few structural/microstructural features as effective strategies to enhance the activity. It was shown that the HPT method improves photocatalytic activity by increasing light absorbance, decreasing the optical bandgap, optimizing the electronic band structure, accelerating the electron-hole separation and migration and reducing the recombination rate of electrons and holes. The HPT method also contributed to the introduction of high-entropy photocatalysts which show high activity for hydrogen production, oxygen evolution and CO_2 conversion.

Despite the high activity of HPT-processed photocatalysts, the mechanism for their high efficiency needs to be investigated further by employing theoretical calculations.

Moreover, the catalysts produced by HPT have usually low surface area and new methods are expected to be developed to enhance the surface area of these catalysts. Although the HPT method has opened a new path to employing high-pressure and high-entropy phases as new photocatalysts, other synthesis methods should be used in the future for the large-scale production of these new catalysts. It is expected that HPT will continue its contribution to the field of photocatalysis, particularly due to the significance of establishing a carbon-neutral society in recent years.

Acknowledgments

The authors S.A. and P.E. thank Hosokawa Powder Technology Foundation, Japan for funding HPTF21511 and HPTF21512. The author K.E. was supported in part by the MEXT, Japan through Grants-in-Aid for Scientific Research (JP19H05176 & JP21H00150, JP22K18737).

References

Ajmal A., Majeed I., Malik R.N., Idriss H., Nadeem M.A., Principles and mechanisms of photocatalytic dye degradation on TiO_2 based photocatalysts: a comparative overview, RSC Advances, 4 (2014) 37003–37026. DOI: 10.1039/C4RA06658H

Akpan U.G., Hameed B.H., Parameters affecting the photocatalytic degradation of dyes using TiO_2-based photocatalysts: a review, Journal of Hazardous Materials, 170 (2009) 520–529. DOI: 10.1016/j.jhazmat.2009.05.039

Akrami S., Edalati P., Edalati K., Fuji M., High-entropy ceramics: review of principles, production and applications, Materials Science and Engineering: R: Reports, 146 (2021a) 100644. DOI: 10.1016/j.mser.2021.100644

Akrami S., Edalati P., Shundo Y., Watanabe M., Ishihara T., Fuji M., Edalati K., Significant CO_2 photoreduction on a high-entropy oxynitride, Chemical Engineering Journal, 449 (2022a) 137800. DOI: 10.1016/j.cej.2022.137800

Akrami S., Murakami Y., Watanabe M., Ishihara T., Arita M., Fuji M., Edalati K., Defective high-entropy oxide photocatalyst with high activity for CO_2 conversion, Applied Catalysis B: Environmental, 303 (2022b) 120896. DOI: 10.1016/j.apcatb.2021.120896

Akrami S., Murakami Y., Watanabe M., Ishihara T., Arita M., Guo Q., Fuji M., Edalati K., Enhanced CO_2 conversion on highly-strained and oxygen-deficient $BiVO_4$ photocatalyst, Chemical Engineering Journal, 442 (2022c) 136209. DOI: 10.1016/j.cej.2022.136209

Akrami S., Watanabe M., Ling T.H., Ishihara T., Arita M., Fuji M., Edalati K., High pressure TiO_2-II polymorph as an active photocatalyst for CO_2 to CO conversion, Applied Catalysis B: Environmental, 298 (2021b) 120566. DOI: 10.1016/j.apcatb.2021.120566

Albedwawi S.H., AlJaberi A., Haidemenopoulos G.N., Polychronopoulou K., High entropy oxides-exploring a paradigm of promising catalysts: a review, Materials & Design, 202 (2021) 109534. DOI: 10.1016/j.matdes.2021.109534

Bérardan D., Franger S., Dragoe D., Meena A.K., Dragoe N., Colossal dielectric constant in high entropy oxides, Physica Status Solidi (RRL)—Rapid Research Letters, 10 (2016) 328–333. DOI: 10.1002/pssr.201600043

Bridgman P.W., Effects of high shearing stress combined with high hydrostatic pressure. Physical Review, 48 (1935) 825–847. DOI: 10.1103/PhysRev.48.825

Cao S., Shen B., Tong T., Fu J., Yu J., 2D/2D heterojunction of ultrathin MXene/Bi_2WO_6 nanosheets for improved photocatalytic CO_2 reduction, Advanced Functional Materials, 28 (2018) 1800136. DOI: 10.1002/adfm.201800136

Chakrabarti S., Dutta B.K., Photocatalytic degradation of model textile dyes in wastewater using ZnO as semiconductor catalyst, Journal of Hazardous Materials, 112 (2004) 269–278. DOI: 10.1016/j.jhazmat.2004.05.013

Delogu F., Are processing conditions similar in ball milling and high-pressure torsion? The case of the tetragonal-to-monoclinic phase transition in ZrO_2 powders, Scripta Materialia, 67 (2012) 340–343. DOI: 10.1016/j.scriptamat.2012.05.031

Di J., Song P., Zhu C., Chen C., Xiong J., Duan M., Long R., Zhou W., Xu M., Kang L., Lin Bo, Liu D., Chen S., Liu C., Li H., Zhao Y., Li S., Yan Q., Song L., Liu Z., Strain-engineering of $Bi_{12}O_{17}Br_2$ nanotubes for boosting photocatalytic CO_2 reduction, ACS Materials Letter, 2 (2020) 1025–1032. DOI: 10.1021/acsmaterialslett.0c00306

Edalati K., Metallurgical alchemy by ultra-severe plastic deformation via high-pressure torsion process, Materials Transactions, 60 (2019a) 1221–1229. DOI: 10.2320/matertrans.MF201914

Edalati K., Review on recent advancements in severe plastic deformation of oxides by high-pressure torsion (HPT), Advanced Engineering Materials, 21 (2019b) 1800272. DOI: 10.1002/adem.201800272

Edalati K., Arimura M., Ikoma Y., Daio T., Miyata T., Smith D.J., Horita Z., Plastic deformation of $BaTiO_3$ ceramics by high-pressure torsion and changes in phase transformations, optical and dielectric properties, Materials Research Letters, 3 (2015a) 216–221. DOI: 10.1080/21663831.2015.1065454

Edalati K., Bachmaier A., Beloshenko V.A., Beygelzimer Y., Blank V.D., Botta W.J., Bryła K., Čížek J., Divinski S., Enikeev N.A., Estrin Y., Faraji G., Figueiredo R.B., Fuji M., Furuta T., et al., Nanomaterials by severe plastic deformation: review of historical developments and recent advances, Materials Research Letters, 10 (2022a) 163–256. DOI: 10.1080/21663831.2022.2029779

Edalati K., Emami H., Staykov A., Smith D.J., Akiba E., Horita Z., Formation of metastable phases in magnesium-titanium system by high-pressure torsion and their hydrogen storage performance, Acta Materialia, 99 (2015b) 150–156. DOI: 10.1016/j.actamat.2015.07.060

Edalati K., Fujita I., Sauvage X., Arita M., Horita Z., Microstructure and phase transformations of silica glass and vanadium oxide by severe plastic deformation via high-pressure torsion straining, Journal of Alloys and Compounds, 779 (2019a) 394–398. DOI: 10.1016/j.jallcom.2018.11.086

Edalati K., Fujita I., Takechi S., Nakashima Y., Kumano K., Razavi-Khosroshahi H., Arita M., Watanabe M., Sauvage X., Akbay T., Ishihara T., Fuji M., Horita Z., Photocatalytic activity of aluminum oxide by oxygen vacancy generation using high-pressure torsion straining, Scripta Materialia, 173 (2019b) 120–124. DOI: 10.1016/j.scriptamat.2019.08.011

Edalati K., Fujiwara K., Takechi S., Wang Q., Arita M., Watanabe M., Sauvage X., Ishihara T., Horita Z., Improved photocatalytic hydrogen evolution on tantalate perovskites $CsTaO_3$ and $LiTaO_3$ by strain-induced vacancies, ACS Applied Energy Materials, 3 (2020a) 1710–1718. DOI: 10.1021/acsaem.9b02197

Edalati K., Horita Z., Scaling-up of high-pressure torsion using ring shape, Materials Transactions, 50 (2009) 92–95. DOI: 10.2320/matertrans.MD200822

Edalati K., Horita Z., Application of high-pressure torsion for consolidation of ceramic Powders, Scripta Materialia, 63 (2010) 174–177. DOI: 10.1016/j.scriptamat.2010.03.048

Edalati K., Horita Z., Mine Y., High-pressure torsion of hafnium, Materials Science and Engineering: A, 527 (2010a) 2136–2141. DOI: 10.1016/j.msea.2009.11.060

Edalati K., Horita Z., High-pressure torsion of pure metals: Influence of atomic bond parameters and stacking fault energy on grain size and correlation with hardness, Acta Materialia, 59 (2011) 6831–6836. DOI: 10.1016/j.actamat.2011.07.046

Edalati K., Horita Z., A review on high-pressure torsion (HPT) from 1935 to 1988, Materials Science and Engineering: A, 652 (2016) 325–352. DOI: 10.1016/j.msea.2015.11.074

Edalati K., Toh S., Ikomaa Y., Horita Z., Plastic deformation and allotropic phase transformations in zirconia ceramics during high-pressure torsion, Scripta Materialia, 65 (2011) 974–977. DOI: 10.1016/J.SCRIPTAMAT.2011.08.024

Edalati K., Uehiro R., Takechi S., Wang Q., Arita M., Watanabe M., Ishihara T., Horita Z., Enhanced photocatalytic hydrogen production on GaN-ZnO oxynitride by introduction of strain-induced nitrogen vacancy complexes, Acta Materialia, 185 (2020b) 149–156. DOI: 10.1016/j.actamat.2019.12.007

Edalati K., Wang Q., Eguchi H., Razavi-Khosroshahi H., Emami H., Yamauchi M., Fuji M., Horita Z., Impact of TiO_2-II phase stabilized in anatase matrix by high-pressure torsion on electrocatalytic hydrogen production, Materials Research Letters, 7 (2019c) 334–339. DOI: 10.1080/21663831.2019.1609111

Edalati K., Wang Q., Razavi-Khosroshahi H., Emami H., Fuji M., Horita Z., Low-temperature anatase-to-rutile phase transformation and unusual grain coarsening in titanium oxide nanopowders by high-pressure torsion straining, Scripta Materialia, 162 (2019d) 341–344. DOI: 10.1016/j.scriptamat.2018.11.044

Edalati K., Yokoyama Y., Horita Z., High-pressure torsion of machining chips and bulk discs of amorphous $Zr_{50}Cu_{30}Al_{10}Ni_{10}$, Materials Transactions, 51 (2010b) 23–26. DOI: 10.2320/matertrans.MB200914

Edalati P., Itagoe Y., Ishihara H., Ishihara T., Emami H., Arita M., Fuji M., Edalati K., Visible-light photocatalytic oxygen production on a high-entropy oxide by multiple-heterojunction introduction, Journal of Photochemistry and Photobiology A: Chemistry, 433 (2022b) 114167. DOI: 10.1016/j.jphotochem.2022.114167

Edalati P., Shen X.F., Watanabe M., Ishihara T., Arita M., Fuji M., Edalati K., High-entropy oxynitride as a low-bandgap and stable photocatalyst for hydrogen production, Journal of Materials Chemistry A, 9 (2021) 15076–15086. DOI: 10.1039/D1TA03861C

Edalati P., Wang Q., Razavi-Khosroshahi H., Fuji M., Ishihara T., Edalati K., Photocatalytic hydrogen evolution on a high entropy oxide, Journal of Materials Chemistry A, 8 (2020c) 3814–3821. DOI: 10.1039/C9TA12846H

Estrin Y., Vinogradov A., Extreme grain refinement by severe plastic deformation: a wealth of challenging science, Acta Materialia, 61 (2013) 782–817. DOI: 10.1016/j.actamat.2012.10.038

Etman A.S., Abdelhamid H.N., Yuan Y., Wang L., Zou X., Sun J., Facile water-based strategy for synthesizing MoO_{3-x} nanosheets: efficient visible light photocatalysts for dye degradation, ACS Omega, 3 (2018) 2193–2201. DOI: 10.1021/acsomega.8b00012

Feng B., Levitas V.I., Coupled elastoplasticity and plastic strain-induced phase transformation under high pressure and large strains: formulation and application to BN sample compressed in a diamond anvil cell, International Journal of Plasticity, 96 (2017) 156–181. DOI: 10.1016/j.ijplas.2017.05.002

Feng B., Levitas V.I., Li W., FEM modeling of plastic flow and strain-induced phase transformation in BN under high pressure and large shear in a rotational diamond anvil cell, International Journal of Plasticity, 113 (2019) 236–254. DOI: 10.1016/j.ijplas.2018.10.004

Feng H., Xu Z., Wang L., Yu Y., Mitchell D., Cui D., Xu X., Shi J., Sannomiya T., Du Y., Hao W., Dou S.X., Modulation of photocatalytic properties by strain in 2D BiOBr nanosheets, ACS Applied Materials & Interfaces, 7 (2015) 27592–27596. DOI: 10.1021/acsami.5b08904

Fu J., Jiang K., Qiu X., Yu J., Liu M., Product selectivity of photocatalytic CO_2 reduction reactions, Materials Today, 32 (2020) 222–243. DOI: 10.1016/j.mattod.2019.06.009

Fujita I., Edalati K., Wang Q., Arita M., Watanabe M., Munetoh S., Ishihara T., Horita Z., High-pressure torsion to induce oxygen vacancies in nanocrystals of magnesium oxide: enhanced light absorbance, photocatalysis and significance in geology, Materialia, 11 (2020a) 100670. DOI: 10.1016/j.mtla.2020.100670

Fujita I., Edalati P., Wang Q., Watanabe M., Arita M., Munetoh S., Ishihara T., Edalati K., Novel black bismuth oxide (Bi_2O_3) with enhanced photocurrent generation, produced by high-pressure torsion straining, Scripta Materialia, 187 (2020b) 366–370. DOI: 10.1016/j.scriptamat.2020.06.052

Gao S., Gu B., Jiao X., Sun Y., Zu X., Yang F., Zhu W., Wang C., Feng Z., Ye B., Xie Y., Highly efficient and exceptionally durable CO_2 photoreduction to methanol over freestanding defective single-unit-cell bismuth vanadate layers, Journal of the American Chemical Society, 139 (2017) 3438–3445. DOI: 10.1021/jacs.6b11263

Gaya U.I., Abdullah A.H., Heterogeneous photocatalytic degradation of organic contaminants over titanium dioxide: a review of fundamentals, progress and problems, Journal of Photochemistry and Photobiology C: Photochemistry Reviews, 9 (2008) 1–12. DOI: 10.1016/j.jphotochemrev.2007.12.003

Gizhevskii B.A., Sukhorukov Y.P., Nomerovannaya L.V., Makhnev A.A., Ponosov Y.S., Telegin A.V., Mostovshchikov E.V., Features of optical properties and the electronic structure of nanostructured oxides of 3d-Metals, Solid State Phenomenon, 168-169 (2011) 317–320. DOI: 10.4028/www.scientific.net/SSP.168-169.317

Habisreutinger A.S.N., Schmidt-Mende L., Stolarczyk J.K., Photocatalytic reduction of CO_2 on TiO_2 and other semiconductors, Angewandte Chemie International Edition, 52 (2013) 7372–7408. DOI: 10.1002/anie.201207199

Hagiwara H., Kakigi R., Takechi S., Watanabe M., Hinokuma S., Ida S., Ishihara T., Effects of preparation condition on the photocatalytic activity of porphyrin-modified GaN:ZnO for water splitting, Surface and Coatings Technology, 324 (2017) 601–606. DOI: 10.1016/j.surfcoat.2016.10.054

Hidalgo-Jimenez J., Wang Q., Edalati K., Cubero-Sesín J.M., Razavi-Khosroshahi H., Ikoma Y., Gutiérrez-Fallas D., Dittel-Meza F.A., Rodríguez-Rufino J.C., Fuji M., Horita Z., Phase transformations, vacancy formation and variations of optical and photocatalytic properties in TiO_2-ZnO composites by high-pressure torsion, International Journal of Plasticity, 124 (2020) 170–185. DOI: 10.1016/j.ijplas.2019.08.010

Huang S.T., Lee W.W., Chang J.L., Huang W.S., Cho S.Y., Chen C.C., Hydrothermal synthesis of $SrTiO_3$ nanocubes: characterization, photocatalytic activities, and degradation pathway, Journal of the Taiwan Institute of Chemical Engineers, 45 (2014a) 1927–1936. DOI: 10.1016/j.jtice.2014.02.003

Huang Y., Li H., Balogun M.S., Liu W., Tong Y., Lu X., Ji H., Oxygen vacancy induced bismuth oxyiodide with remarkably increased visible-light absorption and superior photocatalytic performance, ACS Applied Materials & Interfaces, 6 (2014b) 22920–22927. DOI: 10.1021/am507641k

Ikoma Y., Hayano K., Edalati K., Saito K., Guo Q., Horita Z., Phase transformation and nanograin refinement of silicon by processing through high-pressure torsion, Applied Physics Letters, 101 (2012) 121908. DOI: 10.1063/1.4754574

Iwashina K., Kudo A., Rh-Doped $SrTiO_3$ photocatalyst electrode showing cathodic photocurrent for water splitting under visible-light irradiation, Journal of the American Chemical Society, 133 (2011) 13272–13275. DOI: 10.1021/ja2050315

Jin T., Sang X., Unocic R.R., Kinch R.T., Liu X., Hu J., Liu H., Dai S., Mechanochemical assisted synthesis of high-entropy metal nitride via a soft urea strategy, Advanced Materials, 30 (2018) 1707512. DOI: 10.1002/adma.201707512

Kuvarega A.T., Krause R.W.M., Mamba B.B., Nitrogen/palladium-codoped TiO_2 for efficient visible light photocatalytic dye degradation, The Journal of Physical Chemistry C, 115 (2011) 22110–22120. DOI: 10.1021/jp203754j

Kuznetsova E.I., Degtyarev M.V., Zyuzeva, I.B. Bobylev N.A., Pilyugin V.P., Microstructure of $YBa_2Cu_3O_y$ subjected to severe plastic deformation by high pressure torsion, Physics of Metals and Metallography, 118 (2017) 773–781. DOI: 10.1134/S0031918X17080099

Lee G.J., Anandan S., Masten S.J., Wu J.J., Photocatalytic hydrogen evolution from water splitting using Cu doped ZnS microspheres under visible light irradiation, Renewable Energy, 89 (2016) 18–26. DOI: 10.1016/j.renene.2015.11.083

Lei F., Sun Y., Liu K., Gao S., Liang L., Pan B., Xie Y., Oxygen vacancies confined in ultrathin indium oxide porous sheets for promoted visible-light water splitting, Journal of the American Chemical Society, 136 (2014) 6826–6829. DOI: 10.1021/ja501866r

Li F., Zhou L., Liu J.X., Liang Y., Zhang G.J., High-entropy pyrochlores with low thermal conductivity for thermal barrier coating materials, Journal of Advanced Ceramics, 8 (2019) 576–582. DOI: 10.1007/s40145-019-0342-4

Li X., Xie J., Jiang C., Yu J., Zhang P., Review on design and evaluation of environmental Photocatalysts, Frontiers of Environmental Science & Engineering, 12 (2018) 14. DOI: 10.1007/s11783-018-1076-1

Li Y., Wang W.N., Zhan Z., Woo M.H., Wu C.Y., Biswas P., Photocatalytic reduction of CO_2 with H_2O on mesoporous silica supported Cu/TiO_2 catalysts, Applied Catalysis B: Environmental, 100 (2010) 386–392. DOI: 10.1016/j.apcatb.2010.08.015

Liang B., Ai Y., Wang Y., Liu C., Ouyang S., Liu M., Spinel-type $(FeCoCrMnZn)_3O_4$ high-entropy oxide: facile preparation and supercapacitor performance, Materials, 13 (2020) 5798. DOI: 10.3390/ma13245798

Lin Y.G., Hsu Y.K., Chen Y.C., Chen L.C., Chen S.Y., Chen K.H., Visible-light-driven photocatalytic carbon-doped porous ZnO nanoarchitectures for solar water-splitting, Nanoscale, 4 (2012) 6515–6519. DOI: 10.1039/C2NR31800H

Liu B., Ye L., Wang R., Yang J., Zhang Y., Guan R., Tian L., Chen X., Phosphorus-doped graphitic carbon nitride nanotubes with amino-rich surface for efficient CO_2 capture, enhanced photocatalytic activity, and product selectivity, ACS Applied Materials & Interfaces, 10 (2018) 4001–4009. DOI: 10.1021/acsami.7b17503

Liu Y., Ohko Y., Zhang R., Yang Y., Zhang Z., Degradation of malachite green on Pd/WO_3 photocatalysts under simulated solar light, Journal of Hazardous Materials, 184 (2010) 386–391. DOI: 10.1016/j.jhazmat.2010.08.047

Lu H., Tournet J., Dastafkan K., Liu Y., Ng Y.H., Karuturi S.K., Zhao C., Yin Z., Noble-metal-free multicomponent nanointegration for sustainable energy conversion, Chemical Reviews, 121 (2021) 10271–10366. DOI: 10.1021/acs.chemrev.0c01328

Lun Z., Ouyang B., Kwon D.H., Ha Y., Foley E.E., Huang T.Y., Cai Z., Kim H., Balasubramanian M., Sun Y., Huang J., Tian Y., Kim H., McCloskey B.D., Yang W., Clément R.J., Ji H., Ceder G., Cation-disordered rocksalt-type high-entropy cathodes for Li-ion batteries, Nature Materials, 20 (2021) 214–221. DOI: 10.1038/s41563-020-00816-0

Ma Y., Wang X., Jia Y., Chen X., Han H., Li C., Titanium dioxide-based nanomaterials for photocatalytic fuel, Chemical Reviews, 114 (2014) 9987–10043. DOI: 10.1021/cr500008u.

Maeda K., Photocatalytic water splitting using semiconductor particles: history and recent developments, Journal of Photochemistry and Photobiology C: Photochemistry Reviews, 12 (2011) 237–268. DOI: 10.1016/j.jphotochemrev.2011.07.001

Maeda K., Domen K., New non-oxide photocatalysts designed for overall water splitting under visible light, The Journal of Physical Chemistry C, 111 (2007) 7851–7861. DOI: 10.1021/jp070911w

Maeda K., Takata T., Hara M., Saito N., Inoue Y., Kobayashi H., Domen K., GaN:ZnO Solid solution as a photocatalyst for visible-light-driven overall water splitting, Journal of the American Chemical Society, 127 (2005) 8286–8287. DOI: 10.1021/ja0518777

Makhnev A.A., Nomerovannaya L.V., Gizhevskii B.A., Naumov S.V., Kostromitin N.V., Effect of redistribution of the optical spectral weight in CuO nanostructured ceramics, Solid State Phenomenon, 168-169 (2011) 285–288. DOI: 10.4028/www.scientific.net/SSP.168-169.285

Moniz S.J.A., Shevlin S.A., Martin D.J., Guo Z.X., Tang J., Visible-light driven heterojunction photocatalysts for water splitting — a critical review, Energy & Environmental Science, 8 (2015) 731–759. DOI: 10.1039/C4EE03271C

Mostovshchikova E.V., Gizhevskii B.A., Loshkareva N.N., Galakhov V.R., Naumov S.V., Ponosov Y.S., Ovechkina N.A., Kostromitina N.V., Buling A., Neumann M., Infrared and X-ray absorption spectra of Cu_2O and CuO nanoceramics, Solid State Phenomenon, 190 (2012) 683–686. DOI: 10.4028/www.scientific.net/SSP.190.683

Nguyen T.X., Patra J., Chang J.K., Ting J.M., High entropy spinel oxide nanoparticles for superior lithiation–delithiation performance, Journal of Materials Chemistry A, 8 (2020) 18963–18973. DOI: 10.1039/D0TA04844E

Ni M., Leung M.K.H., Leung D.Y.C., Sumathy K., A review and recent developments in photocatalytic water-splitting using TiO_2 for hydrogen production, Renewable and Sustainable Energy Reviews, 11 (2007) 401–425. DOI: 10.1016/j.rser.2005.01.009

Ohno T., Bai L., Hisatomi T., Maeda K., Domen K., Photocatalytic water splitting using modified GaN:ZnO solid solution under visible light: long-time operation and regeneration of activity, Journal of the American Chemical Society, 134 (2012) 8254–8259. DOI: 10.1021/ja302479f

Ola O., Maroto-Valer M.M., Review of material design and reactor engineering on TiO_2 photocatalysis for CO_2 reduction, Journal of Photochemistry and Photobiology C: Photochemistry Reviews, 24 (2015) 16–42. DOI: 10.1016/j.jphotochemrev.2015.06.001

Oses C., Toher C., Curtarolo S., High-entropy ceramics, Nature Reviews Materials, 5 (2020) 295–309. DOI: 10.1038/s41578-019-0170-8

Pauporté T., Rathouský J., Electrodeposited mesoporous ZnO thin films as efficient photocatalysts for the degradation of dye pollutants, Journal of Physical Chemistry C, 111 (2007) 7639–7644. DOI: 10.1021/jp071465f

Permyakova I., Glezer A., Amorphous-nanocrystalline composites prepared by high-pressure torsion, Metals, 10 (2020) 511. DOI: 10.3390/met10040511

Puangpetch T., Sreethawong T., Yoshikawa S., Chavadej S., Hydrogen production from photocatalytic water splitting over mesoporous-assembled $SrTiO_3$ nanocrystal-based photocatalysts, Journal of Molecular Catalysis A: Chemical, 312 (2009) 97–106. DOI: 10.1016/j.molcata.2009.07.012

Qi Y., Kauffmann Y., Kosinova A., Kilmametov A.R., Straumal B.B., Rabkin E., Gradient bandgap narrowing in severely deformed ZnO nanoparticles, Materials Research Letters, 9 (2021) 58–64. DOI: 10.1080/21663831.2020.1821111

Qi Y., Kosinova A., Kilmametov A.R., Straumal B.B., Rabkin E., Plastic flow and microstructural instabilities during high-pressure torsion of Cu/ZnO composites, Materials Characterization, 145 (2018) 389–401. DOI: 10.1016/j.matchar.2018.09.001

Qian C., He Z., Liang C., Ji W., New in situ synthesis method for Fe_3O_4/flake graphite nanosheet composite structure and its application in anode materials of lithium-ion batteries, Journal of Nanomaterials, 2018 (2018) 2417949. DOI: 10.1155/2018/2417949

Qiao H., Wang X., Dong Q., Zheng H., Chen G., Hong M., Yang C.P., Wu M., He K., Hu L., A high-entropy phosphate catalyst for oxygen evolution reaction, Nano Energy, 86 (2021) 106029. DOI: 10.1016/j.nanoen.2021.106029

Razavi-Khosroshahi H., Edalati K., Arita M., Horita Z., Fuji M., Plastic strain and grain size effect on high-pressure phase transformations in nanostructured TiO_2 ceramics, Scripta Materialia. 124 (2016a) 59–62. DOI: 10.1016/j.scriptamat.2016.06.022

Razavi-Khosroshahi H., Edalati K., Emami H., Akiba E., Horita Z., Fuji

M., Optical properties of nanocrystalline monoclinic Y_2O_3 stabilized by grain size and plastic strain effects via high-pressure torsion, Inorganic Chemistry, 56 (2017a) 2576–2580. DOI: 10.1021/acs.inorgchem.6b02725

Razavi-Khosroshahi H., Edalati K., Hirayama M., Emami H., Arita M., Yamauchi M., Hagiwara H., Ida S., Ishihara T., Akiba E., Horita Z., Fuji M., Visible-light-driven photocatalytic hydrogen generation on nanosized TiO_2-II stabilized by high-pressure torsion, ACS Catalysis, 6 (2016b) 5103–5107. DOI: 10.1021/acscatal.6b01482

Razavi-Khosroshahi H., Edalati K., Wu J., Nakashima Y., Arita M., Ikoma Y., Sadakiyo M., Inagaki Y., Staykov A., Yamauchi M., Horita Z., Fuji M., High-pressure zinc oxide phase as visible-light-active photocatalyst with narrow band gap, Journal of Materials Chemistry A, 5 (2017b) 20298–20303. DOI: 10.1039/C7TA05262F

Ren K., Wang Q., Shao G., Zhao X., Wang Y., Multicomponent high-entropy zirconates with comprehensive properties for advanced thermal barrier coating, Scripta Materialia, 178 (2020) 382–386. DOI: 10.1016/j.scriptamat.2019.12.006

Sa B., Li Y.-L., Qi J., Ahuja R., Sun Z., Strain engineering for phosphorene: the potential application as a photocatalyst, The Journal of Physical Chemistry C, 118 (2014) 26560–26568. DOI: 10.1021/jp508618t

Shabashov V.A., Makarov A.V., Kozlov K.A., Sagaradze V.V., Zamatovskii A.E., Volkova E.G., Luchko S.N., Deformation-induced dissolution and precipitation of nitrides in austenite and ferrite of a high-nitrogen stainless steel, Physics of Metals and Metallography, 119 (2018) 180–190. DOI: 10.1134/S0031918X18020096

Shan J., Raziq F., Humayun M., Zhou W., Qu Y., Wang G., Li Y., Improved charge separation and surface activation via boron-doped layered polyhedron $SrTiO_3$ for co-catalyst free photocatalytic CO_2 conversion, Applied Catalysis B: Environmental, 219 (2017) 10–17. DOI: 10.1016/j.apcatb.2017.07.024

Starink M.J., Cheng X., Yang S., Hardening of pure metals by high-pressure torsion: A physically based model employing volume-averaged defect evolutions, Acta Materialia, 61 (2013) 183–192. DOI: 10.1016/j.actamat.2012.09.048

Sun S., Wang W., Li D., Zhang L., Jiang D., Solar light driven pure water splitting on quantum sized $BiVO_4$ without any cocatalyst, ACS Catalysis, 4 (2014) 3498–3503. DOI: 10.1021/cs501076a

Talluri B., Aparna M.L., Sreenivasulu N., Bhattacharya S.S., Thomas T., High entropy spinel metal oxide $(CoCrFeMnNi)_3O_4$ nanoparticles as a high-performance supercapacitor electrode material, Journal of Energy Storage, 42 (2021) 103004. DOI: 10.1016/j.est.2021.103004

Telegin A.V., Gizhevskii B.A., Nomerovannaya L.V., Makhnev A.A., The optical and magneto-optical properties of nanostructured oxides of 3d-metals, Journal of Superconductivity and Novel Magnetism, 25 (2012) 2683–2686. DOI: 10.1007/s10948-011-1242-1

Tong H., Ouyang S., Bi Y., Umezawa N., Oshikiri M., Ye J., Nano-photocatalytic materials: possibilities and challenges, Advanced Materials, 24 (2012) 229–251. DOI: 10.1002/adma.201102752

Tu W., Zhou Y., Liu Q., Tian Z., Gao J., Chen X., Zhang H., Liu J., Zou Z., Robust hollow spheres consisting of alternating titania nanosheets and graphene nanosheets with high photocatalytic activity for CO_2 conversion into renewable fuels, Advanced Functional Materials, 22 (2012) 1215–1221. DOI: 10.1002/adfm.201102566

Tu W., Zhou Y., Zou Z., Photocatalytic conversion of CO_2 into renewable hydrocarbon fuels: state-of-the-art accomplishment, challenges, and prospects, Advanced Materials, 26 (2014) 4607–4626. DOI: 10.1002/adma.201400087

Uddin M.T., Nicolas Y., Olivier C., Toupance T., Servant L., Müller M.M., Kleebe H.J., Ziegler J., Jaegermann W., Nanostructured SnO_2-ZnO heterojunction photocatalysts showing enhanced photocatalytic activity for the degradation of organic dyes, Inorganic Chemistry, 51 (2012) 7764–7773. DOI: 10.1021/ic300794j

Valiev R., Nanostructuring of metals by severe plastic deformation for advanced properties, Nature Materials, 3 (2004) 511–516. DOI: 10.1038/nmat1180

Wang F., Valentin C.D., Pacchioni G., Doping of WO_3 for photocatalytic water splitting: hints from density functional theory, The Journal of Physical Chemistry C, 116 (2012) 8901–8909. DOI: 10.1021/jp300867j

Wang H., Zhang L., Wang K., Sun X., Wang W., Enhanced photocatalytic CO_2 reduction to methane over $WO_3 \cdot 0.33H_2O$ via Mo doping, Applied Catalysis B: Environmental, 243 (2019a) 771–779. DOI: 10.1016/j.apcatb.2018.11.021

Wang K., Lu J., Lu Y., Lau C.H., Zheng Y., Fan X., Unravelling the C-C coupling in CO_2 photocatalytic reduction with H_2O on Au/TiO_{2-x}: combination of plasmonic excitation and oxygen vacancy, Applied Catalysis B: Environmental, 292 (2021) 120147. DOI: 10.1016/j.apcatb.2021.120147

Wang Q., Edalati K., Fujita I., Watanabe M., Ishihara T., Horita Z., High-pressure torsion of SiO_2 quartz sand: Phase transformation, optical properties, and significance in geology, Journal of the American Ceramic Society, 103 (2020a) 6594–6602. DOI: 10.1111/jace.17362

Wang Q., Edalati K., Koganemaru Y., Nakamura S., Watanabe M., Ishihara T., Horita Z., Photocatalytic hydrogen generation on low-band-gap black zirconia (ZrO_2) produced by high-pressure torsion, Journal of Materials Chemistry A, 8 (2020b) 3643–3650. DOI: 10.1039/C9TA11839J

Wang Q., Sarkar A., Wang D., Velasco L., Azmi R., Bhattacharya S.S., Bergfeldt T., Düvel A., Heitjans P., Brezesinski T., Hahn H., Breitung B., Multi-anionic and -cationic compounds: new high entropy materials for advanced Li-ion batteries, Energy & Environmental Science, 12 (2019b) 2433–2442. DOI: 10.1039/C9EE00368A

Wang Q., Watanabe M., Edalati K., Visible-light photocurrent in nanostructured high-pressure TiO_2-II (Columbite) Phase, The Journal of Physical Chemistry C, 124 (2020c) 13930–13935. DOI: 10.1021/acs.jpcc.0c03923

Wen J., Xie J., Chen X., Li X., A review on g-C_3N_4-based photocatalysts, Applied Surface Science, 391 (2017) 72–123. DOI: 10.1016/j.apsusc.2016.07.030

Xiang H., Xing Y., Dai F., Wang H., Su L., Miao L., Zhang G., Wang Y., Qi X., Yao L., Wang H., Zhao B., Li J., Zhou Y., High-entropy ceramics: present status, challenges, and a look forward, Journal of Advanced Ceramics, 10 (2021) 385–441. DOI: 10.1007/s40145-021-0477-y

Xu H., Zhang Z., Liu J., Do-Thanh C.L., Chen H., Xu S., Lin Q., Jiao Y., Wang J., Wang Y., Chen Y., Dai S., Entropy-stabilized single-atom Pd catalysts via high-entropy fluorite oxide supports, Nature Communications, 11 (2020) 3908. DOI: 10.1038/s41467-020-17738-9

Ye S., Wang R., Wu M.Z., Yuan Y.P., A review on g-C_3N_4 for photocatalytic water splitting and CO_2 reduction, Applied Surface Science, 358 (2015) 15–27. DOI: 10.1016/j.apsusc.2015.08.173

Yu H., Li J., Zhang Y., Yang S., Han K., Dong F., Ma T., Huang H., Three-in-one oxygen vacancies: whole visible-spectrum absorption, efficient charge separation, and surface site activation for robust CO_2 photoreduction, Angewandte Chemie International Edition, 58 (2019) 3880–3884. DOI: 10.1002/anie.201813967

Yu J., Qi L.,, Jaroniec M., Hydrogen production by photocatalytic water splitting over Pt/TiO_2 nanosheets with exposed (001) facets, The Journal of Physical Chemistry C, 114 (2010) 13118–13125. DOI: 10.1021/jp104488b

Yuan X., Zhou C., Jin Y., Jing Q., Yang Y., Shen X., Tang Q., Mu Y., Du A.K., Facile synthesis of 3D porous thermally exfoliated g-C_3N_4 nanosheet with enhanced photocatalytic degradation of organic dye, Journal of Colloid and Interface Science, 468 (2016) 211–219. DOI: 10.1016/j.jcis.2016.01.048

Zhang D., Yu Y., Feng X., Tian Z., Song R., Thermal barrier coatings with high-entropy oxide as a top coat, Ceramics International, 48 (2022) 1349–1359. DOI: 10.1016/j.ceramint.2021.09.219

Zhang R.Z., Reece M.J., Review of high entropy ceramics: design, synthesis, structure and properties, Journal of Materials Chemistry A, 7 (2019) 22148–22162. DOI: 10.1039/C9TA05698J

Zhao J., Liu B., Meng L., He S., Yuan R., Hou Y., Ding Z., Lin H., Zhang Z., Wang X., Long J., Plasmonic control of solar-driven CO_2 conversion at the metal/ZnO interfaces, Applied Catalysis B: Environmental, 256 (2019) 117823. DOI: 10.1016/j.apcatb.2019.117823

Zhou B., Zhao X., Liu H., Qu J., Huang C.P., Visible-light sensitive cobalt-doped $BiVO_4$ (Co-$BiVO_4$) photocatalytic composites for the degradation of methylene blue dye in dilute aqueous solutions, Applied Catalysis B: Environmental, 99 (2010) 214–221. DOI: 10.1016/j.apcatb.2010.06.022

Zhou S., Pu Y., Zhang Q., Shi R., Guo X., Wang W., Ji J., Wei T., Ouyang T., Microstructure and dielectric properties of high entropy Ba$(Zr_{0.2}Ti_{0.2}Sn_{0.2}Hf_{0.2}Me_{0.2})O_3$ perovskite oxides, Ceramics International, 46 (2020) 7430–7437. DOI: 10.1016/j.ceramint.2019.11.239

Zhou S., Pu Y., Zhao X., Ouyang T., Ji J., Zhang Q., Zhang C., Sun S., Sun R., Li J., Wang D., Dielectric temperature stability and energy storage performance of NBT-based ceramics by introducing high-entropy oxide, Journal of the American Ceramic Society, 105 (2022) 4796–4804. DOI: 10.1111/jace.18455

Authors' Short Biographies



Saeid Akrami

Saeid Akrami obtained a M.Sc. degree in Chemical Engineering, and he is currently a Ph.D. candidate in Applied Chemistry and Life Sciences at Nagoya Institute of Technology, Japan. His research interest is the development of highly-strained and high-entropy ceramics for CO_2 conversion and he is the author of several papers in this field.



Parisa Edalati

Parisa Edalati is currently a Ph.D. candidate in the Advanced Ceramics Research Center, Nagoya Institute of Technology, Japan. She was a visiting researcher at Kyushu University in 2019 before starting her Ph.D. study. She works on the design and synthesis of functional high-entropy alloys and ceramics for various applications including photocatalysis, biomedical application, hydrogen storage, and batteries.



Masayoshi Fuji

Masayoshi Fuji received his Dr. Eng. in 1999 and joined the Tokyo Metropolitan University, as a research associate in 1991. He was a visiting researcher at the University of Florida, USA, from 2000 to 2001. He joined the Nagoya Institute of Technology as an Associate Professor in 2002 and became a Professor in 2007. He is the editor-in-chief of Advanced Power Technology since 2019. His representative awards include the award from the Minister of Education, Culture, Sports, Science and Technology Japan in 2013, CerSJ award for academic achievements in ceramic science and technology in 2014, and the science award of the Society of Inorganic Materials, Japan in 2017.



Kaveh Edalati

Kaveh Edalati received his Ph.D. degree in Materials Physics and Chemistry from Kyushu University, Japan, in 2010. He currently serves as an Associate Professor at the International Institute for Carbon-Neutral Energy Research, Kyushu University, Fukuoka, Japan. His interests are the development of functional materials for carbon-neutral energy and hydrogen-related applications such as hydrogen storage and photocatalytic hydrogen generation and CO_2 conversion. He particularly utilizes the high-pressure torsion method to develop new functional materials. He is the author of over 150 journal papers and serves as the editor of several journals.

KONA Powder and Particle Journal

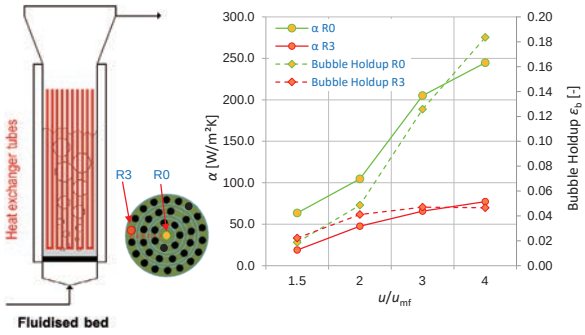
KONA Powder and Particle Journal No. 41 (2024) 140–150/https://doi.org/10.14356/kona.2024009 Review Paper

Applying Bubbling Fluidized-Bed Reactors for Strongly Exothermic Reactions: Focus on Methanation†

Philipp Riechmann and Tilman J. Schildhauer*

Paul Scherrer Institute (PSI), Switzerland

Strongly exothermic reactions inherently pose the risk of thermal reactor runaway, which may lead to very high increase in temperature, hot spots and potential catalyst deactivation. For such reaction systems, reactors with excellent heat removal performance are needed. In the case of methanation of CO/CO_2-rich gases, full conversion is not possible in a single adiabatic reactor due to the equilibrium limitation, and in large-scale plants, e.g. coal-to-synthetic natural gas (SNG) plants, series of four and more reactors with intercooling have been realized. To allow for complete conversion within one reactor, the potential of bubbling fluidized bed (BFB) reactors with immersed heat exchangers was investigated in the US and Germany from the 1960s to the 1980s. A Swiss consortium started to expand the concept to small- and medium-scale plants to allow the production of renewable methane from decentral renewable sources such as wood gasification and biogas. During their tests, it could be shown that the catalyst particle movement does not only allow for optimal heat removal—close to isothermal operation and thus little catalyst sintering—but that the catalyst particle movement over the height of the reactor with different concentration zones favors the chemical catalyst stability. This contribution will review the fluid-dynamic studies for BFB reactors with immersed heat exchangers in the last decades comprising studies with pressure fluctuation probes, optical probes, X-ray tomography studies, and particle attrition studies.



Keywords: Bubbling Fluidized Bed (BFB) reactors, methanation, immersed heat exchanger, chemical catalyst stability, heat transfer

1. Introduction

Many processes in the chemical industry and those converting chemical energy carriers are either strongly endo- or exothermic. Most hydrogen-producing reactions are endothermic e.g. steam reforming, gasification, reverse water gas shift, dehydrogenations, and methane dehydroaromatization to benzene. In consequence, many reactions that consume hydrogen are exothermic, e.g. hydrogenation of double bonds or aromatic systems, water–gas shift reaction, and important fuel syntheses such as methanation, Fischer–Tropsch and methanol synthesis.

While endothermic reactions lead to the formation of a cold spot where the further conversion of the reactant completely depends on further heat supply, strongly exothermic reactions inherently bring the risk of thermal reactor runaway with them leading to a significant increase in temperature, formation of hot spots, often low selectivity, and potential catalyst deactivation. For such reaction systems, either highly temperature-stable catalysts or reactors with exceptional heat removal performance are required.

The methanation reaction is a typical example of a highly exothermic and equilibrium-limited reaction. The equilibrium is generally favored by lower temperatures of about 100 °C, where the conversion rate is close to 100 % (Witte, 2018). However, due to the low activity of the typically used catalysts at temperatures below 200–300 °C, catalytic methanation reactors are usually operated above this temperature level, at temperatures between 200 °C and 500 °C (Götz et al., 2016; Mills and Steffgen, 1974). The typical pressure range is between 3 and 30 × 10^5 Pa with higher pressures leading to slightly increased methane yields (Götz et al., 2016). While ruthenium is the most active catalyst, it is seldom used due to its high cost. Nickel is highly active, very selective and relatively cheap. It is therefore the preeminent catalyst material for catalytic methanation processes (Mills and Steffgen, 1974; Ghaib et al., 2016).

2. Reactor types for methanation

Commonly used reactor types for the catalytic methanation process are series of adiabatic fixed-bed reactors, cooled fixed-bed reactors, fluidized-bed reactors, slurry reactors, and metal monolith reactors (Schildhauer and Biollaz, 2015; Schildhauer, 2016). Fig. 1 shows illustrations of some of these reactor types. The requirements for the reactor primarily depend on the composition and flow

† Received 21 May 2022; Accepted 6 September 2022
J-STAGE Advance published online 30 June 2023
* Corresponding author: Tilman J. Schildhauer;
Add: Forschungsstrasse 111, 5232 Villigen PSI, Switzerland
E-mail: tilman.schildhauer@psi.ch
TEL: +41-56-310-2706

Copyright © 2024 The Authors. Published by Hosokawa Powder Technology Foundation. This is an open access article under the CC BY license (https://creativecommons.org/licenses/by/4.0/).

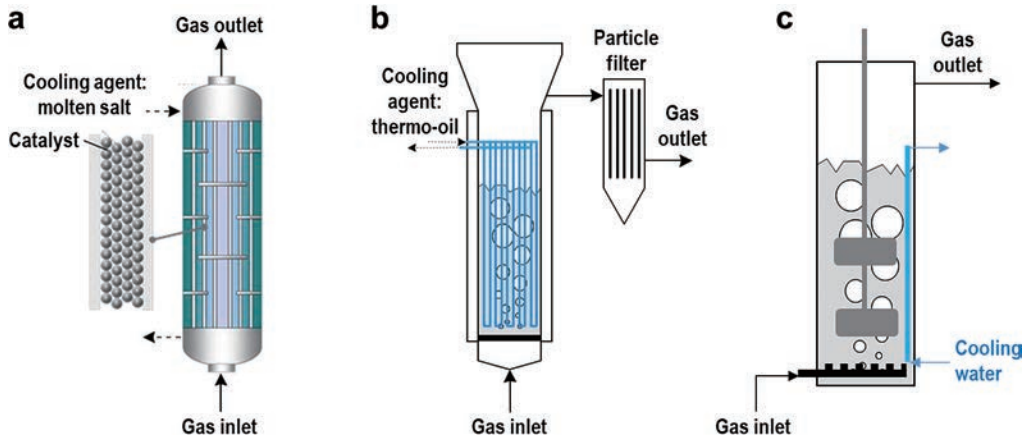


Fig. 1 Schematic representation of typical reactor types for methanation. **(a)**: Multi-tubular cooled fixed bed, **(b)**: Fluidized bed, **(c)**: Stirred slurry bubble column.

rates of the gas sources, as they determine the requirements for the removal of the reaction heat and the prevention of catalyst deactivation (Kopyscinski et al., 2010; Schildhauer, 2016; Schildhauer and Biollaz, 2015).

Using fixed-bed methanation reactors is an established method for gas cleaning in the ammonia synthesis process chain. In this application, relatively small concentrations of carbon oxides have to be eliminated from the hydrogen-rich feed streams to avoid catalyst deactivation. No additional cooling is required in this case due to the large ratio between the inert gas and reactant gas volumes and the resulting relatively large heat capacity of the gas stream. For the production of Synthetic Natural Gas (SNG), however, concentrations of inert gases are very low and cooling becomes necessary. This can be achieved through intermittent cooling of the gas stream between multiple fixed-bed reactor stages. Additionally, gas can be recirculated for cooling. Adiabatic reactors require robust catalyst materials that can withstand a broad temperature range without sintering or cracking (Bartholomew, 2001). For the production of SNG from coal gasification gas, this reactor type is well-established, and plants at the GW-scale have been realized (Schildhauer, 2016). It is also possible to directly cool the multi-tubular fixed-bed reactors by having cooling media flow around the catalyst-filled tubes.

Metal monolith reactors are designed to overcome some of the drawbacks of fixed-bed reactors. They are characterized by their high specific surface area, which allows relatively compact reactor designs. Their metal framework, usually based on aluminum or copper, increases the radial heat transfer, while the pressure drop is reduced significantly in comparison to fixed-bed reactors (Schildhauer, 2016; Schlereth et al., 2015). In this way, heat transfer coefficients of more than 1000 $W/m^2 K$ can be reached (Boger and Heibel, 2015; Schildhauer, 2016). However, the deposition of the catalyst material on the structured framework is technically complex, especially when the catalyst is deactivated and the reactor has to be coated again with the catalyst.

In three-phase reactors, also known as slurry bubble column reactors, the catalyst is suspended in an inert liquid by the reactant gas flow. On the one hand, the liquid phase is beneficial as it significantly facilitates the heat removal, leading to almost isothermal conditions within the reactor and allowing a dynamic plant operation, where the reactor temperature can be kept stable due to the thermal inertia of the liquid phase. On the other hand, the liquid phase induces an additional mass transfer resistance and needs to fulfill several specifications such as high thermal stability, chemical inertness, low evaporation rates, low viscosity, and surface tension (Götz et al., 2013; Schildhauer, 2016).

Gas-solid fluidized-bed reactors are characterized by nearly isothermal conditions resulting from intensive particle circulation. Bubbles play a crucial role in catalytic bubbling fluidized bed (BFB) reactors as they significantly influence key properties of the fluidized bed, such as the heat and mass transfer, the mixing of gas and solids as well as elutriation of bed material. Rising bubbles transport particles upwards in their wake, which causes an intensive particle motion resulting in a uniform temperature profile of the fluidized bed. Consequently, the heat transfer between the bed and heat exchanger surfaces is intensified through the steady replacement of the particles. Due to the even heat distribution throughout the reactor, the entire immersed heat exchanger surface can be used at the same time, which is the most important difference from fixed-bed reactors. In this way, local temperature peaks and any associated thermal runaway of reactions can be effectively avoided. Therefore, BFBs with heat exchangers are well suited for highly exothermic reactions such as catalytic methanation. The properties of the bubble phase, including intensity of particle circulation, are dependent on the ratio between the superficial gas velocity u and the minimum fluidization velocity u_{mf}, which is referred to as the

fluidization number. By setting the u/u_{mf}, the reactor performance can be adjusted according to the requirements. For instance, it is possible to recirculate part of the product gas stream or reduce the system pressure to increase the fluidization number and thus intensify the heat transfer if necessary.

A commonly stated disadvantage of fluidized-bed reactors is the attrition of the catalyst material resulting from the comparatively high mechanical stress exerted on the particles through elastic collisions with other particles or the reactor walls. Such attrition can lead to the deactivation and elutriation of the catalyst particles, which therefore would have to be replaced periodically.

Additionally, the formation of bubbles may lead to a bypass of reactants through the reactor within the bubbles and thus to an incomplete conversion of the CO or CO_2 in the feed stream. Other frequently mentioned disadvantages are the possible erosion of internals, such as heat exchanger tubes, varying solids residence time distributions, and the frequently complex hydrodynamics that make scaling-up difficult (Götz et al., 2016; Yang, 2013; Yatesand Lettieri, 2016). The choice of suitable bed materials and detailed knowledge of the fluid dynamics of BFBs allows overcoming these challenges during scale-up.

3. Fluidized-bed reactors for methanation

Fluidized-bed methanation was developed since the late 1950s to convert synthesis gas from coal gasification (Kopyscinski et al., 2010). The Bureau of Mines developed a relatively slender reactor with a 2.5 cm diameter, operated with Geldart A type catalyst particles at 20 bar and around 400 °C. Three feed injections were used to avoid the strong axial temperature gradients observed when fed only from the bottom. In 1963, the Bituminous Coal Research Inc. continued in the Bigas project with a 150 mm diameter reactor, about 2 m bed height and two injection points that were cooled with immersed heat exchanger tubes. At temperatures from 430 to 530 °C, pressures from 6.9 to 8.7 × 10^5 Pa, it was operated as a BFB for several 1000 hours (Kopyscinski et al., 2010).

Within the Comflux process, the technology was scaled up to the 20 MW scale in the early 1980s by Didier Engineering GmbH and Thyssengas GmbH, supported by the Technical University of Karlsruhe, and tested up to 2125 h (Friedrichs et al., 1985; Hedden et al., 1986). The aim was a conversion process from coal to SNG with significantly lower costs than the fixed-bed methanation concepts. As in the Bigas project, very high conversion was reached within one reactor which allowed for significantly lower equipment and capital costs (–30 %) than a series of adiabatic fixed beds. Because of the falling oil and gas prices, however, the development was stopped in the mid-1980s.

Since about the year 2000, the development of this technology has been pursued again, now for the implementation of wood gasification. Seemann et al. (2006) showed that an internal regeneration of catalysts with carbon depositions takes place in BFB methanation reactors operated with producer gas from wood gasification. Accordingly, the fluidized-bed reactor can be divided into different zones. At the inlet zone, the deposition of carbon takes place due to high concentrations of CO and unsaturated hydrocarbons (ethene, benzene). In the zone above, steam gasification and hydrogenation of the carbon deposits or their precursors are predominant. Ultimately, an equilibrium between carbon deposition and the regeneration of the catalyst can be reached in this way.

Both for the conversion of wood gasification gas and for the upgrading of biogas by methanation of the CO_2 content with added renewable hydrogen, extensive long-duration field studies (>1000 h) with a container-based TRL 4/5 plant were conducted showing the catalyst's resilience against coke formation (Schildhauer and Biollaz, 2016; Witte et al., 2019). As part of a long-term field test of over 1100 h regular operation, the particle elutriation rate of catalyst material was measured for a reactor with a diameter of 5.2 cm and an original catalyst mass of 800 g. This is illustrated in **Fig. 2**, which shows the elutriation rates and the concentration profiles over the duration of the field test. Throughout the campaign, only 70 g of the catalyst was elutriated from the reactor. The elutriation rate, measured by an in-line PCME sensor, spiked when fresh catalyst material was inserted, because fine particles are elutriated at much higher rates. It was therefore concluded that attrition rates are low and the catalyst material has to be replaced only once per year (Witte et al., 2019). These findings are supported by the results of the experimental campaigns for the Comflux process development, where the fluidized bed methanation of coal gasification gas was demonstrated up to 20 MW in the early 1980s (Friedrichs et al., 1985; Hedden et al., 1986). The concentration profiles were stable throughout the campaign and showed a high methane yield of 85–90 mol%. Further, optimizing the gas cleaning process step was identified in these tests to be of crucial importance for the extension of the catalyst lifetime, especially limiting the number of sulfur species (Calbry-Muzyka et al., 2019; Calbry-Muzyka and Schildhauer, 2020; Struis et al., 2009).

Other groups are now also investigating this technology, for example in the French GAYA project (Hervy et al., 2021), in Korea (Nam et al., 2021) or in China; there, however, for the conversion of coal to methane (Liu et al., 2016).

4. Hydrodynamics of fluidized-bed reactors with vertical internals

Understanding the hydrodynamics of BFB reactors is of great importance for the design, scale-up and optimization

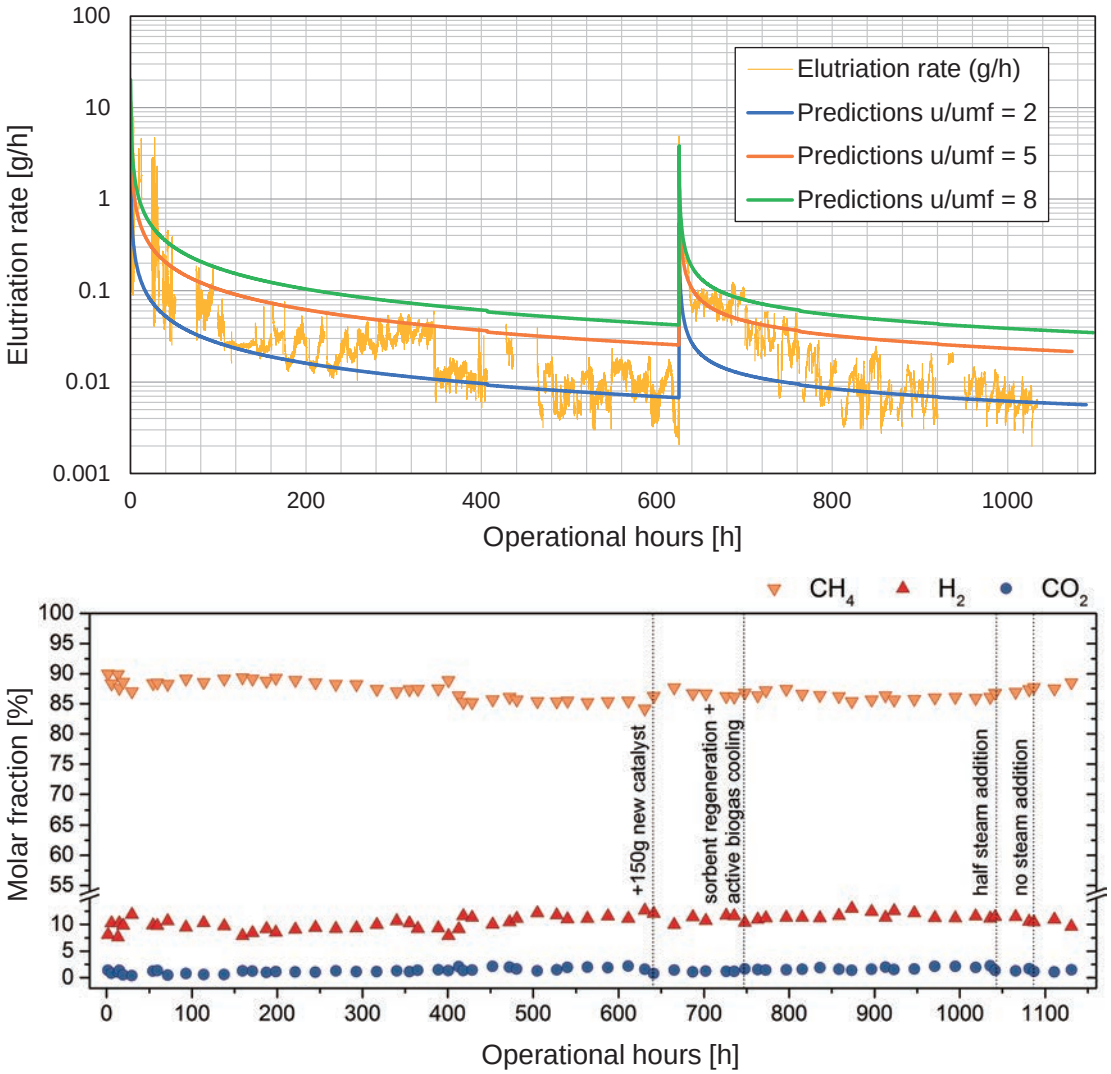


Fig. 2 Long-duration test at TRL 5 (10 kW) with real biogas from the biogas plant in Zürich Werdhölzli. Results of the particle elutriation measurement and (dry) gas composition downstream of the reactor, adapted from Ref. (Witte et al., 2019).

of the reactor, especially in the case of the highly exothermic methanation process, where efficient heat removal is essential. Rising bubbles and correlated hydrodynamic phenomena strongly influence key properties of catalytic BFB reactors, e.g. the heat transfer between the bed and heat exchanger surfaces, gas–solid contacting, mass transfer between bubbles and the bed, residence time distributions, bed expansion, solids segregation and mixing as well as catalyst lifetime, specifically the attrition and elutriation of catalyst particles (Glicksman, 1984; Grace, 2020; Schildhauer and Biollaz, 2016; Valenzuela and Glicksman, 1985; Werther, 2007).

The most relevant bubble properties are the diameter d_b, the rise velocity of the bubble u_{br}, the bubble hold-up ε_b and ultimately the shape of the bubble, which allow a good estimation of the above-mentioned phenomena. Extensive experimental studies have been conducted over several decades; however, the majority of the correlations to predict bubble properties are empirical or semi-empirical and often are only valid for a specific range of conditions.

Additionally, the increase of available computational power in recent years led to significant advancement in the field of computational fluid dynamics (CFD), which allows the investigation of fluidized bed hydrodynamics through numerical simulations. While certain properties such as the bubble hold-up ε_b, the average bed expansion or the minimum fluidization velocity u_{mf} can be predicted accurately through CFD simulations, it usually requires empirically determined tuning parameters to reach an agreement between simulated and experimentally measured bubble properties. While many aspects of fluidized beds without internals have been researched, there are far fewer publications on the influence of vertical heat exchanger tubes. Simulations with CFD software (Liu and Hinrichsen, 2014; Lv et al., 2020; Verma et al., 2016) were compared to experimental results and showed significant deviations between fluidized beds with and without vertical internals where the internals such as vertical sheets or heat

exchanger tubes reduce the increase of the bubble size and lead to more elongated bubbles.

4.1 Pressure fluctuation measurements

Measuring the pressure drop and the pressure fluctuations caused by bubble passing, coalescence and bubble eruptions is a simple, usually non-intrusive method that can be applied in experimental studies on cold-flow models, but also hot reactors (with some adaptations). It was found that vertical internals can decrease the pressure drop by up to 10 % (Taofeeq and Al-Dahhan, 2018a), shift the onset of slugging to higher gas flow rates (Coronella et al., 1994) and also have an influence on the transition to turbulent flow (Taofeeq and Al-Dahhanl, 2018b) in reactors with 10 cm and 14 cm inner diameter, respectively. For the measurements of the pressure fluctuations with fast piezo-electric probes, spectral decomposition was applied to retrieve the average bubble size (Rüdisüli et al., 2012a; b; c). It could be shown that the bubbles in fluidized beds with vertical tubes not only grow more slowly, but also have a smaller hydraulic diameter. Thus, a better mass transfer between bubbles and the dense phase can be expected (Rüdisüli, 2012). This was recently confirmed for a bed of densely packed, small-diameter tubes where the standard deviation of the pressure fluctuations was halved by the presence of the vertical tubes, while the diameter of the bubbles at the bed surface during eruptions went down by a factor of around four (Antonini, 2019).

Horizontal heat exchanger tubes with the necessary packing density, on the other hand, led to gas cushions and local defluidization, which means that relatively poor mass transfer can be expected (Rüdisüli et al., 2012d). In addition, the transversely installed pipes should limit the vertical transport of the particles, which counteracts the limitation of carbon deposits by internal regeneration.

4.2 Sector approach

Rüdisüli et al. (2012d) also presented a modified approach for the up-scaling of fluidized-bed reactors with vertical internals, which considers defined sectors of internals as autonomous regions. As was already assumed by Volk et al. (1962), it was shown that the vertical pipes, with a spacing of only a few centimeters, strongly structure the fluidized bed and thus minimize the influence of the reactor wall. Experiments with optical probes were conducted with variation of the cross-section of a fluidized bed cold-flow model while keeping tube diameter and pitch constant (i.e. by increasing the number of tubes in the same arrangement). From at least two complete rows of tubes around a measuring point, the measurement is largely representative for all other such “elementary cells” and can be used to design larger reactors with a correspondingly increased number of vertical tubes (with the square of the diameter ratio) (Maurer et al., 2014), see also **Fig. 3**. This significantly simplifies the construction of pilot plants and the resulting scale-up, as was confirmed by comparing the pressure fluctuations from a pilot scale (1 MW) plant in Güssing and a bench-scale cold-flow model (Rüdisüli et al., 2012d).

4.3 Optical probes incl. Monte Carlo

Optical probes are versatile tools to facilitate deeper insight into the hydrodynamics of fluidized beds. While the pressure fluctuation measurements only give information on the average size of the rising bubbles, a vertical arrangement of two optical probes can deliver the rise velocity of a bubble, which in combination with the signal duration can be translated into a pierced chord length. The challenge is, however, that the optical probes only allow local measurements, and thus many radially and axially resolved measurements as well as several statistical corrections are needed. Statistical analysis and a Monte Carlo study led Rüdisüli et al. (2012e) to the conclusion that the mean chord length measured with optical probes in freely bubbling beds is a good approximation for the mean bubble diameter. This is due to the increased pierce probability of larger bubbles (which lead to an increased average chord length), which is counterbalanced by the fact that the optical probes do not necessarily pierce the bubbles at their longest axial expansion. This was confirmed by Maurer et al. (2015a) who, however, found that these two counteracting effects are not valid for the measurement of the mean bubble rise velocity for which a different correction approach is required. Further measurements with optical probes in fluidized beds with vertical internals showed significantly different chord lengths and rise velocities (Taofeeq and Al-Dahhan, 2018c). It is therefore necessary to adjust the data evaluation appropriately.

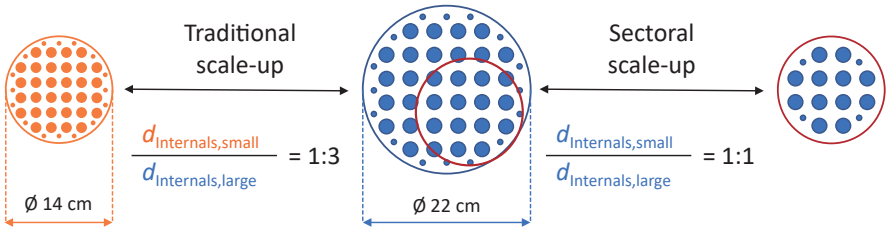


Fig. 3 Sectorial scaling approach for fluidized bed reactors with vertical internals.

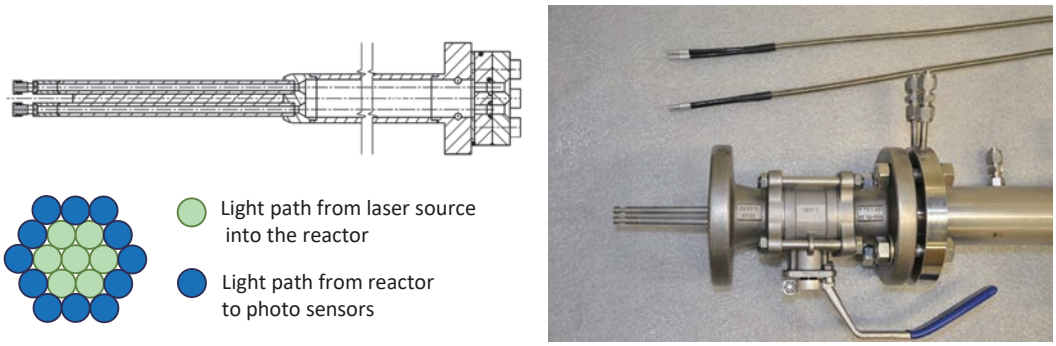


Fig. 4 Details of optical probe.

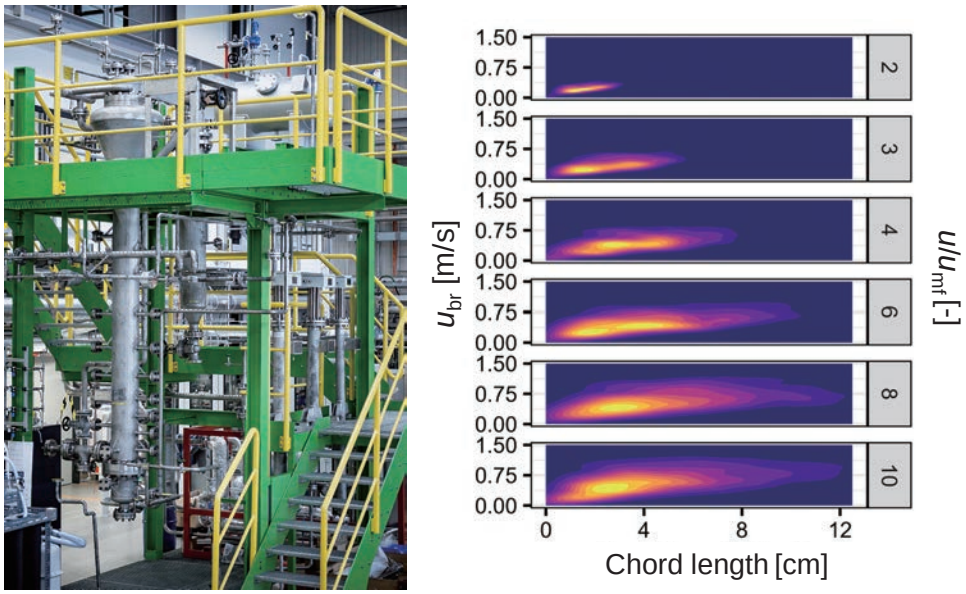


Fig. 5 Results **(right)** of optical probe measurements in a pressurized pilot scale plant **(left)** at a pressure of 6 bar and a measurement height of 32 cm.

While most cold-flow models reported in the literature are operated at ambient pressure, Maurer (2015) developed and tested a new optical probe sensor, which is able to measure under reactive conditions with pressures of up to 2.5×10^6 Pa and temperatures of up to 400 °C, see **Fig. 4**.

First cold-flow measurements in the pilot plant Gany-Meth (22.4 cm inner diameter, operation up to 1–11 × 10^5 Pa, see **Fig. 5**, left) with pressurized air and alumina particles at pressures of up to 5×10^5 Pa were conducted and proved the system (Schillinger, 2018).

Recently, a unique data set was measured with these radially movable optical probes at six heights and six radial positions for Geldart-A and Geldart-B-type bed material, pressures of 1–11 × 10^5 Pa and fluidization numbers u/u_{mf} of 2–10, see **Fig. 5** (right) (Riechmann, 2022). It becomes obvious that not a single value but rather distributions of bubble properties (chord length, rise velocity u_{br}) exist for each experimental setting. Meanwhile, data evaluation is ongoing to obtain correlations for the distributions of bubble properties to enable improved modelling/simulation of such reactors.

4.4 X-ray tomography

In cooperation with TU Delft, X-ray tomographic investigations were conducted and evaluated by an algorithm allowing the reconstruction of the bubbles in a fluidized bed of Geldart-B particles. This allowed determining their properties with regard to spatial distribution over the cross-section, bubble size and bubble velocity (Maurer et al., 2015b). As can be seen in **Fig. 6**, a square or concentric arrangement of heat exchanger tubes has very similar effects: there are more bubbles compared to the configuration without internals, and the bubbles deviate significantly from the round shape. Further, experiments with cold-flow models of two diameters (14 cm and 22 cm) confirmed once again the sectorial scaling approach: the differences between beds of different sizes are small if they are structured by vertical internals, while in fluidized beds without internals, the bubble size increases significantly with the reactor diameter.

Compared to measurements with local samples (e.g. optical sensors), the possibility of X-ray tomography to determine the bubble size and the bubble velocity of all rising bubbles over the entire cross-section is a great advantage,

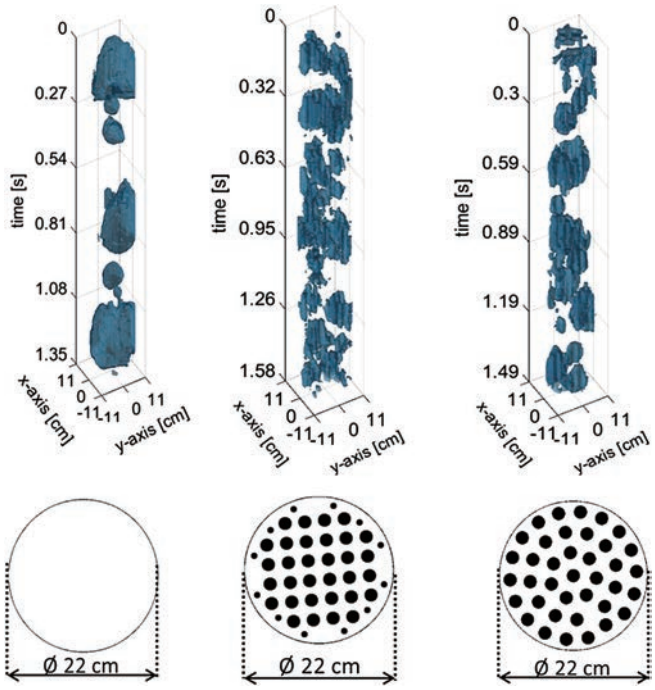


Fig. 6 Reconstructed passing of bubbles in the measurement height (chronological order, *z*-axis = time) for beds without **(left)** and with internals **(middle, right)** (Schillinger, 2018).

as such measurements are less subject to statistical effects. To derive conclusive bubble property distributions from the local measurement at a measurement height, measurements must be taken at several radial positions, assuming rotational symmetry. Bubbles with a larger cross-section in the direction of flow have a higher probability of hitting the sensor, but the bubbles are not always hit at the point of the longest expansion of the bubble in the direction of flow as already mentioned above.

X-ray tomography reconstructions were also used to simulate the measurements of an ideal virtual optical probe. The resulting chord lengths and rise velocities were then compared to the bubble properties derived from the X-ray tomography reconstructions. Statistical effects resulting from the assumed shape of the bubbles, such as chord length distributions and the reduced probability of the optical probe to pierce elongated bubbles in comparison to oblate bubbles, were identified and correction factors were proposed accordingly (Schillinger, 2018). This approach opens the door to improving the evaluation of local optical probe data in ongoing work that is additionally supported by projecting X-ray radiography. Neutron radiography (Ozawa et al., 2002) as well as recent X-ray radiography data (see **Fig. 7**) show not only bubble sizes and their rise velocities but also the interactions with optical probes. Further, the trajectories can be observed which show that bubbles rise vertically in between or if larger, along the vertical tubes, while in freely bubbling beds significantly more lateral movements and therefore increased coalescence is found (Ozawa et al., 2002).

4.5 Heat transfer

The importance of removing or supplying heat is the main motivation for introducing vertical heat exchanger tubes into fluidized beds, as they allow reaching more or less isothermal operation conditions. For the proper design of the reactors, quantitative data of heat transfer are needed. Already in 1996, Gunn and Hilal (1996) measured the total heat transfer from electrically heated tubes to the bed of glass beads (BALLOTINI) at ambient pressure. For Geldart-A-type material, total heat transfer coefficients from 350 W/m^{2}K (at $u/u_{mf} = 2$) to 550 W/m^{2}K (at $u/u_{mf} > 7$) were found, independent of the number of tubes and the gas distributor. For Geldart-B materials, the best results were reached with a porous-plate-type distributor, ranging from 250 W/m^{2}K (at $u/u_{mf} = 2$) to >350 W/m^{2}K (at $u/u_{mf} > 5$). Ozawa et al. (2002) measured total heat transfer coefficients from 250 W/m^{2}K (at $u/u_{mf} = 2$) to 400 W/m^{2}K (at $u/u_{mf} > 5$) for Geldart-B-type alumina particles at ambient pressure.

These results are confirmed by our own measurements of PSI at the pilot scale plant GanyMeth, heating up cold nitrogen at 4×10^5 Pa with thermo-oil of 250 °C in a bed of Geldart-B alumina particles. At a fluidization number of around 1.3, the axial temperature profile from the distributor to 1.5-m height ranged from 232 °C to 243 °C, proving the strong axial heat dispersion in these systems. The estimated total heat transfer coefficient (though not very precise due to the small temperature difference of 7 to 18 K) is 170 W/m^{2}K, which fits exactly to the results of (Gunn and Hilal, 1996) for Geldart-B materials and a porous plate

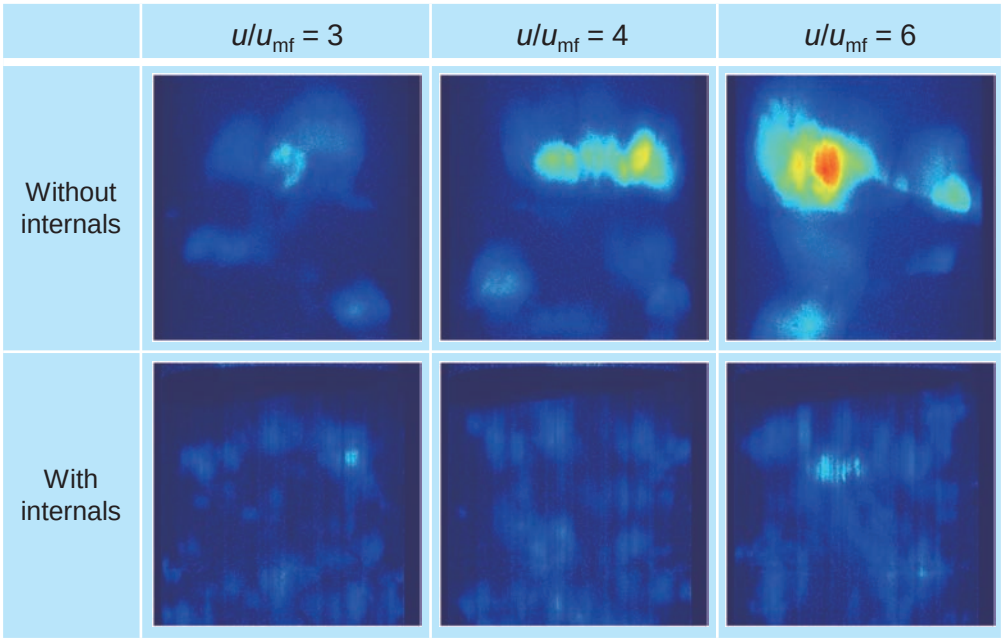


Fig. 7 Recent X-ray radiography data (PSI in collaboration with TU Delft) in a 22.4 cm column at ambient pressure with Geldart-B-type material (γ-alumina particles).

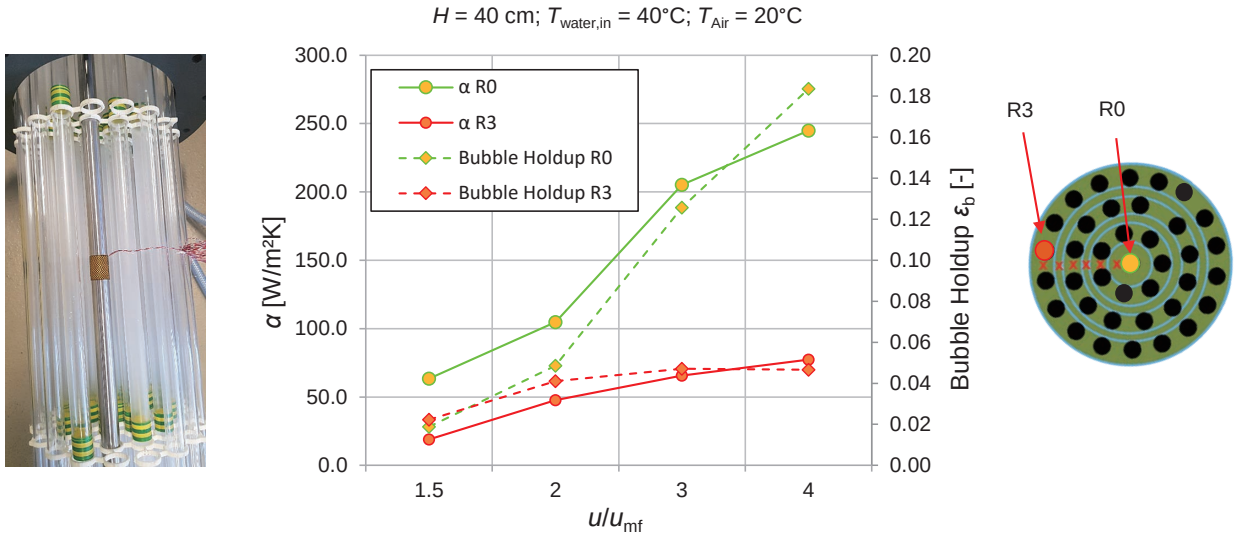


Fig. 8 Results of locally applied optical and heat transfer probes in a cold-flow model (diameter 22.4 cm) with Geldart-B-type alumina particles.

distributor at such low fluidization.

Taofeeq et al. introduced advanced non-invasive fast response heat transfer probes in the research field and used them for local measurements in a 14 cm column with Geldart-B-type glass particles for fluidization numbers from 1.4 to 2.5 (Taofeeq and Al-Dahhan, 2018a, b, c; Taofeeq et al., 2022). For fluidization numbers below 2, they found that the presence of vertical internals improved the local heat transfer by up to 20 % in regions closer to the wall, but not in the center of the column. Generally, local heat transfer coefficients from 270 W/m^{2}K (at u/u_{mf} = 1.4) to 320 W/m^{2}K (at u/u_{mf} = 2.5) were found for beds with an aspect ratio of >1.5.

Further, they found that the local heat transfer is enhanced by the presence of bubbles; our own measurements at PSI with a similar approach with locally applied optical and heat transfer probes (Geldart-B-type alumina particle in a cold-flow model) showed even a direct proportionality of bubble hold-up and local heat transfer, see **Fig. 8**.

5. Conclusions and outlook

Bubbling fluidized bed (BFB) reactors with immersed vertical heat exchanger tubes proved to be a suitable reactor type for strongly exothermic reactions such as the methanation of CO/CO$_2$-rich gases to form synthetic natural gas. They help to avoid hotspots and the risk of thermal

reactor runaway, potentially leading to catalyst deactivation. Many studies in literature and our own experiments were able to show that the catalyst particle movement does not only allow for optimal heat removal, close to isothermal operation and thus little catalyst sintering, but that the catalyst particle movement over the height of the reactor with different concentration zones favors the chemical catalyst stability. This contribution reviewed the fluid-dynamic studies for BFB reactors with immersed heat exchangers in the last decades comprising studies with pressure fluctuation probes, optical probes, X-ray tomography and studies on heat transfer.

With the results obtained so far, it can be concluded that immersed vertical heat exchanger tube banks improve the fluidization and have the potential to facilitate up-scaling. Further, important knowledge was collected to better describe and correlate the distribution of sizes and rise velocities of bubbles which improve heat transfer and particle movement but may limit the reactor performance in the case of too low mass transfer. With the obtained correlations, the reactor models can be significantly improved in terms of mass transport predictions. Planned measurements of temperature and concentration profiles during reactive operation in PSI's pilot plant will help to practically validate the methanation reactor model in the experimentally investigated pressure and temperature range. This together with the sector scaling model will allow upscaling to the different applications with significantly reduced risk.

Acknowledgments

The authors would like to thank Marion Ziegler, Roham Seif, Evert Wagner, Ruud van Ommen and the whole TCP team at PSI for support during experiments and for scientific discussions. Further, the financial support of the Energy Systems Integration platform at PSI is acknowledged.

References

Antonini T., Di Carlo A., Foscolo P.U., Gallucci K., Stendardo S., Fluidized bed reactor assisted by Oxygen Transport Membranes: numerical simulation and experimental hydrodynamic study, Chemical Engineering Journal, 377 (2019) 120323. DOI: 10.1016/j.cej.2018.11.021

Bartholomew C.H., Mechanisms of catalyst deactivation, Applied Catalysis A: General, 212 (2001) 17–60. DOI: 10.1016/s0926-860x(00)00843-7

Boger T., Heibel A.K., Heat transfer in conductive monolith structures, Chemical Engineering Science, 60 (2005) 1823–1835. DOI: 10.1016/j.ces.2004.11.031

Calbry-Muzyka A.S., Gantenbein A., Schneebeli J., Frei A., Knorpp A.J., Schildhauer T.J., Biollaz S.M.A., Deep removal of sulfur and trace organic compounds from biogas to protect a catalytic methanation reactor, Chemical Engineering Journal, 360 (2019) 577–590. DOI: 10.1016/j.cej.2018.12.012

Calbry-Muzyka A.S., Schildhauer T.J., Direct methanation of biogas—technical challenges and recent progress, Frontiers in Energy Research, 8 (2020) 570887. DOI: 10.3389/fenrg.2020.570887

Coronella C.J., Lee S.Y., Seader J.D., Minimum slugging velocity in fluidized beds containing vertical rods, Fuel, 73 (1994) 1537–1543. DOI: 10.1016/0016-2361(94)90076-0

De Groot P., Coulon M., Dransfeld K., $Ni(CO)_4$ formation on single Ni crystals: reaction kinetics and observation of surface facetting induced by the reaction, Surface Science, 94 (1980) 204–220. DOI: 10.1016/0039-6028(80)90164-8

Friedrichs G., Proplesch P., Wismann G., Lommerzheim W., Methanisierung von kohlenvergasungsgasen im wirbelbett pilot entwicklungsstufe, Technologische Forschung und Entwicklung—Nichtnukleare Energietechnik, Duisburg, 1985.

Ghaib K., Nitz K., Ben-Fares F.-Z., Chemical methanation of CO_2: a review, ChemBioEng Reviews, 3 (2016) 266–275. DOI: 10.1002/cben.201600022

Glicksman L.R., Scaling relationships for fluidized beds, Chemical Engineering Science, 39 (1984) 1373–1379. DOI: 10.1016/0009-2509(84)80070-6

Götz M., Lefebvre J., Mörs F., McDaniel Koch A., Graf F., Bajohr S., Reimert R., Kolb T., Renewable power-to-gas: a technological and economic review, Renewable Energy, 85 (2016) 1371–1390. DOI: 10.1016/j.renene.2015.07.066

Götz M., Ortloff F., Reimert R., Basha O., Morsi B.I., Kolb T., Evaluation of organic and ionic liquids for three-phase methanation and biogas purification processes, Energy and Fuels, 27 (2013) 4705–4716. DOI: 10.1021/ef400334p

Grace J.R., Hydrodynamics of bubbling fluidization, in: Grace J.R., Bi X., Ellis N. (Eds.), Essentials of Fluidization Technology, Wiley-VCH Verlag GmbH & Co. KGaA, 2020, pp. 131-152, ISBN: 9783527699483. DOI: 10.1002/9783527699483.ch7

Gunn D.J., Hilal N., Heat transfer from vertical inserts in gas-fluidized beds, International Journal of Heat and Mass Transfer, 39 (1996) 3357–3365. DOI: 10.1016/0017-9310(95)00410-6

Hedden K., Anderlohr A., Becker J., Zeeb H., Cheng Y., Forschungsbericht T 86-044: gleichzeitige konvertierung und methanisierung von CO-reichen gasen, Technologische Forschung und Entwicklung–Nichtnukleare Energietechnik, 1986.

Hervy M., Maistrello J., Brito L., Rizand M., Basset E., Kara Y., Maheut M., Power-to-gas: CO_2 methanation in a catalytic fluidized bed reactor at demonstration scale, experimental results and simulation, Journal of CO_2 Utilization, 50 (2021) 101610. DOI: 10.1016/j.jcou.2021.101610

Kopyscinski J., Schildhauer T.J., Biollaz S.M.A., Production of synthetic natural gas (SNG) from coal and dry biomass—a technology review from 1950 to 2009, Fuel, 89 (2010) 1763–1783. DOI: 10.1016/j.fuel.2010.01.027

Liu J., Cui D., Yao C., Yu J., Su F., Xu G., Syngas methanation in fluidized bed for an advanced two-stage process of SNG production, Fuel Processing Technology, 141 (2016) 130–137. DOI: 10.1016/j.fuproc.2015.03.016

Liu Y., Hinrichsen O., CFD simulation of hydrodynamics and methanation reactions in a fluidized-bed reactor for the production of synthetic natural gas, Industrial and Engineering Chemistry Research, 53 (2014) 9348–9356. DOI: 10.1021/ie500774s

Lv B., Deng X., Luo Z., Fu Y., Chen C., Xu X., Impact of vertical internals on the hydrodynamics and separation performance of a gas–solid separation fluidized bed, Powder Technology, 360 (2020) 577–587. DOI: 10.1016/j.powtec.2019.10.071

Maurer S., Hydrodynamic characterization and scale-up of bubbling fluidized beds for catalytic conversion, doctoral dissertation, ETH Zurich, 2015. DOI: 10.3929/ethz-a-010453120

Maurer S., Rüdisüli M., Teske S.L., Schildhauer T.J., van Ommen J.R., Biollaz S.M.A., Wokaun A., Transformation of local bubble rise velocity measurements to global results: shown by a Monte Carlo simulation of a fluidized bed, International Journal of Multiphase Flow, 70 (2015a) 89–95. DOI: 10.1016/j.ijmultiphaseflow.2014.11.008

Maurer S., Schildhauer T.J., Ruud van Ommen J., Biollaz S.M.A., Wokaun A., Scale-up of fluidized beds with vertical internals: studying the sectoral approach by means of optical probes, Chemical Engineering Journal, 252 (2014) 131–140. DOI: 10.1016/j.cej.2014.04.083

Maurer S., Wagner E.C., van Ommen J.R., Schildhauer T.J., Teske S.L., Biollaz S.M.A., Wokaun A., Mudde R.F., Influence of vertical internals on a bubbling fluidized bed characterized by X-ray tomography, International Journal of Multiphase Flow, 75 (2015b) 237–249. DOI: 10.1016/j.ijmultiphaseflow.2015.06.001

Mills G.A., Steffgen F.W., Catalytic methanation, Catalysis Reviews, 8 (1974) 159–210. DOI: 10.1080/01614947408071860

Nam H., Kim J.H., Kim H., Kim M.J., Jeon S.G., Jin G.T., Won Y., Hwang B.W., Lee S.Y., Baek J.I., Lee D., Seo M.W., Ryu H.J., CO_2 methanation in a bench-scale bubbling fluidized bed reactor using Ni-based catalyst and its exothermic heat transfer analysis, Energy, 214 (2021) 118895. DOI: 10.1016/j.energy.2020.118895

Ozawa M., Umekawa H., Furui S., Hayashi K., Takenaka N., Bubble behavior and void fraction fluctuation in vertical tube banks immersed in a gas–solid fluidized-bed model, Experimental Thermal and Fluid Science, 26 (2002) 643–652. DOI: 10.1016/S0894-1777(02)00178-4

Riechmann P.F., Cross verified independent measurements of correlated bubble property distributions as part of the scale-up of a catalytic bubbling fluidized bed reactor, EPFL Theses, 2022.

Rönsch S., Schneider J., Matthischke S., Schlüter M., Götz M., Lefebvre J., Prabhakaran P., Bajohr S., Review on methanation - from fundamentals to current projects, Fuel, 166 (2016) 276–296. DOI: 10.1016/j.fuel.2015.10.111

Rüdisüli M., Characterization of rising gas bubbles in fluidized beds by means of statistical tools, doctoral dissertation, ETH Zurich, (2012). DOI: 10.3929/ethz-a-007089625

Rüdisüli M., Schildhauer T.J., Biollaz S.M.A., Van Ommen J.R., Monte Carlo simulation of the bubble size distribution in a fluidized bed with intrusive probes, International Journal of Multiphase Flow, 44 (2012a) 1–14. DOI: 10.1016/j.ijmultiphaseflow.2012.03.009

Rüdisüli M., Schildhauer T.J., Biollaz S.M.A., van Ommen J.R., Evaluation of a sectoral scaling approach for bubbling fluidized beds with vertical internals, Chemical Engineering Journal, 197 (2012b) 435–439. DOI: 10.1016/j.cej.2012.04.097

Rüdisüli M., Schildhauer T.J., Biollaz S.M.A., Van Ommen J.R., Radial bubble distribution in a fluidized bed with vertical tubes, Industrial and Engineering Chemistry Research, 51 (2012c) 13815–13824. DOI: 10.1021/ie3004418

Rüdisüli M., Schildhauer T.J., Biollaz S.M.A., van Ommen J.R., Bubble characterization in a fluidized bed with vertical tubes, Industrial & Engineering Chemistry Research, 51 (2012d) 4748–4758. DOI: 10.1021/ie2022306

Rüdisüli M., Schildhauer T.J., Biollaz S.M.A., Wokaun A., Ruud van Ommen J., Comparison of bubble growth obtained from pressure fluctuation measurements to optical probing and literature correlations, Chemical Engineering Science, 74 (2012e) 266–275. DOI: 10.1016/J.CES.2012.01.045

Schildhauer T.J., Methanation for synthetic natural gas production – chemical reaction engineering aspects, in: Schildhauer T.J., Biollaz S.M.A. (Eds.), Synthetic Natural Gas from Coal, Dry Biomass, and Power-to-Gas Applications, John Wiley & Sons, 2016, pp.77–159. DOI: 10.1002/9781119191339.ch4

Schildhauer T.J., Biollaz S.M.A., Fluidized bed methanation for SNG production – process development at the Paul-Scherrer Institut, in: Schildhauer T.J., Biollaz S.M.A. (Eds.), Synthetic Natural Gas from Coal, Dry Biomass, and Power-to-Gas Applications, John Wiley & Sons, 2016, pp.221–230. DOI: 10.1002/9781119191339.ch8

Schildhauer T.J., Biollaz S.M.A., Reactors for catalytic methanation in the conversion of biomass to synthetic natural gas (SNG), Chimia, 69 (2015) 603–607. DOI: 10.2533/chimia.2015.603

Schillinger F., Systematic assessment and application of local optical and two-dimensional X-ray measurement techniques for hydrodynamic characterization of bubbling fluidized beds, doctoral dissertation, ETH Zurich, (2018). DOI: 10.3929/ethz-b-000306127

Schillinger F., Maurer S., Künstle M., Schildhauer T.J., Wokaun A., Hydrodynamic investigations by a local optical measurement technique designed for high-temperature applications – first measurements at a fluidized bed immersed by vertical internals at cold conditions, Powder Technology, 344 (2019) 849–863. DOI: 10.1016/j.powtec.2018.11.050

Schlereth D., Donaubauer P.J., Hinrichsen O., Metallic honeycombs as catalyst supports for methanation of carbon dioxide, Chemical Engineering & Technology, 38 (2015) 1845–1852. DOI: 10.1002/CEAT.201400717

Seemann M.C., Schildhauer T.J., Biollaz S.M.A., Stucki S., Wokaun A., The regenerative effect of catalyst fluidization under methanation conditions, Applied Catalysis A: General, 313 (2006) 14–21. DOI: 10.1016/J.APCATA.2006.06.048

Struis R.P.W.J., Schildhauer T.J., Czekaj I., Janousch M., Biollaz S.M.A., Ludwig C., Sulphur poisoning of Ni catalysts in the SNG production from biomass: a TPO/XPS/XAS study, Applied Catalysis A: General, 362 (2009) 121–128. DOI: 10.1016/J.APCATA.2009.04.030

Taofeeq H., Al-Dahhan M., The impact of vertical internals array on the key hydrodynamic parameters in a gas-solid fluidized bed using an advance optical fiber probe, Advanced Powder Technology, 29 (2018a) 2548–2567. DOI: 10.1016/J.APT.2018.07.008

Taofeeq H., Al-Dahhan M., Flow regimes in gas–solid fluidized bed with vertical internals, Chemical Engineering Research and Design, 138 (2018b) 87–104. DOI: 10.1016/J.CHERD.2018.07.019

Taofeeq H., Al-Dahhan M.H., Effect of vertical internals on the pressure drop in a gas-solid fluidized bed, The Canadian Journal of Chemical Engineering, 96 (2018c) 2185–2205. DOI: 10.1002/CJCE.23299

Taofeeq H., Uribe S., Al-Dahhan M., Flow regimes in gas-solid fluidized beds via micro-foil heat flux sensor, Chemical Engineering & Technology, 45 (2022) 220–229. DOI: 10.1002/ceat.202000559

Valenzuela J.A., Glicksman L.R., Gas flow distribution in a bubbling fluidized bed, Powder Technology, 44 (1985) 103–113. DOI: 10.1016/0032-5910(85)87016-9

Verma V., Li T., Dietiker J.F., Rogers W.A., Hydrodynamics of gas–solids flow in a bubbling fluidized bed with immersed vertical U-tube banks, Chemical Engineering Journal, 287 (2016) 727–743. DOI: 10.1016/J.CEJ.2015.11.049

Volk W., Johnson C.A., Stotler H.H, Effect of reactor internals on quality of fluidization, Chemical Engineering Progress, 58 (1962) 44–47.

Werther J., Fluidized-bed reactors, in: Ullmann's Encyclopedia of Industrial Chemistry (Ed.), Wiley, 2007, ISBN: 9783527303854. DOI: 10.1002/14356007.b04_239.pub2

Witte J., Experimental and techno-economic assessment of catalytic methanation of biogas for power-to-gas processes, doctoral dissertation, ETH Zurich, 2018. DOI: 10.3929/ethz-b-000304900

Witte J., Calbry-Muzyka A., Wieseler T., Hottinger P., Biollaz S.M.A., Schildhauer T.J., Demonstrating direct methanation of real biogas in a fluidised bed reactor, Applied Energy, 240 (2019) 359–371. DOI: 10.1016/J.APENERGY.2019.01.230

Yang W.-C., Handbook of Fluidization and Fluid-Particle Systems, 1st edition, CRC Press, Boca Raton, 2003, ISBN: 9780429223341. DOI: 10.1201/9780203912744

Yates J.G., Lettieri P., Catalytic processes, in: Yates J.G., Lettieri P. (Aus.), Fluidized-Bed Reactors: Processes and Operating Conditions, Particle Technology Series, vol 26, Springer, Cham, 2016, pp.23–65, ISBN: 9783319395937. DOI: 10.1007/978-3-319-39593-7_2

Authors' Short Biographies



Philipp Riechmann

Philipp Riechmann studied process and energy engineering at TU Berlin and is a scientist at the Paul Scherrer Institut with focus on the hydrodynamic aspects of fluidized beds. He recently defended his PhD thesis successfully.



Tilman Schildhauer

Tilman Schildhauer is Senior Scientist at Paul Scherrer Institut in Switzerland where he leads the research in methanation, gas cleaning and PtX processes. He studied chemical engineering in Dortmund, received a PhD from ETH Zurich and spent his postdoc time in the Reactor and Catalysis Engineering group at TU Delft.

KONA Powder and Particle Journal

KONA Powder and Particle Journal No. 41 (2024) 151–171/https://doi.org/10.14356/kona.2024015 Review Paper

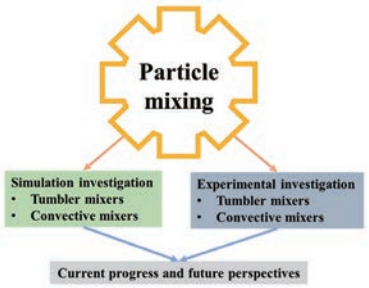
Current Progress of Experimental and Simulation Work of Mixing Processes in Particulate Systems†

Xin Jin and Yansong Shen*

School of Chemical Engineering, University of New South Wales, Australia

Particle mixing is a fundamental process used in various industries to handle powders, granules, and pellets. Understanding particle mixing is critical for optimizing industrial processes involving particulate systems, making it an important scientific and practical consideration. In this review, the current research progress of experimental and simulation works for widely used tumbler and convective mixers is reviewed, and research gaps are summarized for future investigations. Finally, some new development points of modern particle mixing technologies and topics are mentioned. This paper provides a comprehensive review of the research work of mixers in particulate systems and sheds light on future research in the field of particle mixing.

Keywords: particle mixing, mixture homogeneity, mixer, discrete element method



1. Introduction

Granular materials, powders, and bulk solids are ubiquitous in nature, including soil, sand, and grains as well as in various process industries, such as detergent, paint, plastics, chemical, mineral processing, metallurgical, pharmaceutical, biotechnology, and chemical industries (Duran, 2012; Forterre and Pouliquen, 2008). According to relevant statistical data, about half of industrial products and three-quarters of the raw materials exist in the chemical industry and are treated in the form of particle state (Lee and Henthorn 2012; Rhodes, 2008). Currently, the fundamental theory of motion equations of individual particles and the force analysis of their interaction with other particles are not enough to describe the bulk particles' behavior in a practical industrial process because a large number of particles makes it difficult to predict their complex interactions accurately. Meanwhile, particles naturally own different physical properties (such as size, density and shape) (Ghadiri et al., 2020), and the segregation phenomenon is frequently encountered while the bulk particles are treated during the industries, further hindering the deep understanding of the granular system. Unfortunately, due to the opaque nature of granular materials, there are few reliable measuring methods available to date. Furthermore, in practical industrial applications, granular systems are often incompletely fluidised, resulting in a complex system comprising multiple coexisting granular flow states. This complexity poses challenges to researchers studying granular systems. Therefore, the fundamental study of the granular system is still a great challenge for both industry and academia at the current stage.

For powder, granular, or pellet products in different industrial processes, particle mixing is an essential unit operation, such as the drying and storage of grains, the processing and packaging of pharmaceuticals, and the mining and processing of coal, etc. (Bridgwater, 2012; Ottino and Khakhar, 2000). Most of these industrial processes require a well-mixed degree of mixture for the final or middle products to confirm consistent product quality and high production efficiency. The development of effective techniques and technologies for controlling particle mixing and separation is of great importance, as it can lead to energy and cost savings in processing, as well as advancements in the field of particle mechanics. Achieving rapid and homogeneous mixing is a crucial objective. Therefore, it is of great significance to reveal the underlying fundamentals and promote the operating performance of particle mixing processes for modern industries.

In this review, the current research progress of experimental and simulation works for widely used tumbler and convective mixers is reviewed, and research gaps are summarized for future investigations. Finally, some new development points of modern particle mixing technologies and topics are mentioned (Jin, 2022).

2. Research progress summary of experimental work

Over the past few decades, numerous experiments have been conducted to examine the mixing behavior of various mixers. This section will present a concise summary of

† Received 27 March 2023; Accepted 9 May 2023
J-STAGE Advance published online 31 August 2023

* Corresponding author: Yansong Shen;
Add: Via Gate 2, High Street, UNSW Sydney, NSW 2052, Australia
E-mail: ys.shen@unsw.edu.au
TEL: +61-2-9385-4448

Copyright © 2024 The Authors. Published by Hosokawa Powder Technology Foundation. This is an open access article under the CC BY license (https://creativecommons.org/licenses/by/4.0/).

relevant experimental studies organised and reviewed based on the categorisation of mixers.

2.1 Experimental work of tumbler mixers

Rotating drums, as versatile equipment, are extensively employed in various industries, such as rotary kilns, dryers, mixers, reactors, and granulators for processing granular materials. The rotating drum is a widely used apparatus in laboratory studies of solid mixing phenomena due to its simplicity in geometry and ease of operation control compared to other mixing equipment. Moreover, the rotating drum can be designed to be transparent, closed, and relatively thin, making it suitable for observing particle motion and studying fundamental phenomena of solid mixing. For example, to investigate the movement of particles in a three-dimensional rotating drum at low to medium rotational speeds, Ding et al. (2001) employed a combination of experimental and theoretical methods. The researchers employed the non-invasive positron emission particle tracking (PEPT) technique to monitor the trajectories and velocities of particles. Additionally, they developed a mathematical model utilizing the thin-layer approximation to characterise the motion of solids within the active layer. The experimental results were compared with the model, and good agreement was found between the two. Santomaso et al. (2004) conducted a study on the mixing of non-ideal powders, specifically granular tetraacetylethylenediamine (TAED), in rotating batch cylinders that were operating in the rolling regime. They characterised and quantified the local mixture composition by utilizing a solidification technique in combination with computerised image analysis. Observations showed the formation of a temporarily poorly mixed core at low rotation speeds, and the role of convection in the mixing mechanism of non-ideal granular material was identified through the identification of convective fluxes resulting from the friction between the powder and end plates of the mixer. Zhang et al. (2018) conducted a study utilizing the Magnetic Particle Tracking (MPT) method to examine the particle motion in flighted rotating drums. This was the first investigation of its kind to utilise MPT. The study focused on the behavior of plastic balls and soybeans in a rotating drum with a 5 % filling degree at various drum rotating speeds ranging from 10 to 40 rpm. The study analysed the particle motion in a rotating drum by examining particle trajectories, distributions of translational and rotational velocity, falling time of the dilute phase, and instantaneous velocity of the dilute phase in the equatorial region. The analysis showed that the rotating speed of the drum had a significant impact on the particle motion, with only minor effects from particle size and shape within the studied range. The schematic of the experimental setup and the critical results can be seen in **Fig. 1**. Li R. et al. (2021) conducted experiments to investigate the velocity distribution of rice particles in a rotating drum. As illustrated in **Fig. 2**, the results revealed that the flow of rice particles often displayed multiple velocity peaks. At low rotation speeds of 1–3 rpm, the particle flow within the rotating drum transforms into an avalanche mode. This is due to the slope of the accumulation surface exceeding the angle of repose, causing particles to slide and cover the entire particle bed. As a widely used apparatus in solid mixing studies, rotating drum experiments have yielded important insights in the past three years, as summarized in **Table 1**.

In contrast to the rotating drum, there exists a relatively limited amount of experimental work on other types of tumbler mixers. The following section provides a review of some important experimental studies.

Brone and Muzzio (2000) performed a comparison of

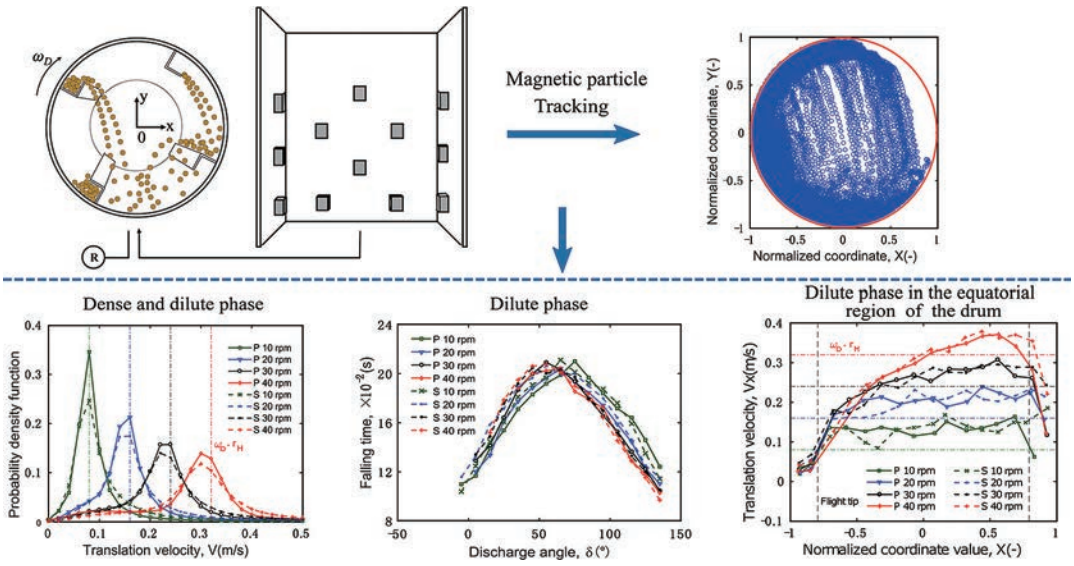


Fig. 1 Schematic of the experimental setup and critical experimental results, reprinted with permission from Ref. (Zhang et al., 2018). Copyright: (2018) Elsevier B.V.

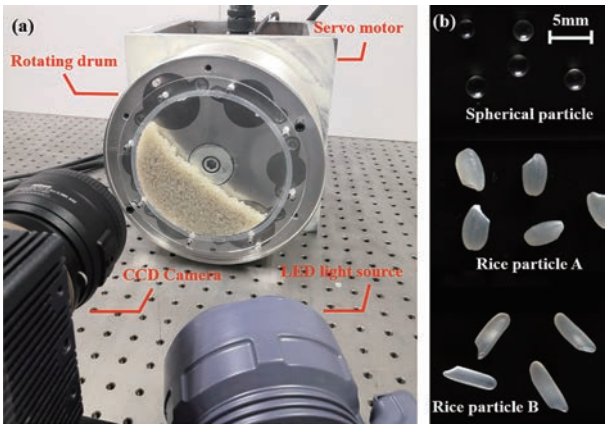


Fig. 2 System and particle setup: **(a)** the measuring system includes a LED light source and a CCD camera; **(b)** the drum is half filled with three types of particles, respectively: spherical particles, Rice particles A with AR = 2 and Rice particles B with AR = 3, reprinted with permission from Ref. (Li R. et al., 2021). Copyright: (2021) Elsevier B.V.

the mixing performance between a conventional double-cone blender and a modified version incorporating a stationary deflector plate. The latter was designed to enhance axial particle flow and was found to be highly effective in achieving improved mixing outcomes. The results showed that the incline of the deflector plate relative to the mixer plane resulted in the creation of a convective axial flow across the centre of the blender, leading to an increase in the mixing rate by a factor of 25. The images demonstrating the plate effect on mixing within the double cone can be found in **Fig. 3**. Volpato et al. (2018) examined the effects of the unloading process on mixture quality in three distinct types of tumbling mixers, namely symmetrical double cones, asymmetrical double cones, and conic mixers. The experiments utilised tetraacetylethylenediamine (TAED) powder that was available in different size ranges and differentiated by colour, either white or blue. The results showed that tumblers capable of unloading the material in the mass flow regime performed better than those operating in funnel flow. Specifically, the best mixing performance was obtained using an asymmetrical double-cone mixer. An intrusive investigation of mixing characteristics in a double-cone mixer utilizing discrete pocket samplers was conducted by Cho et al. (2012). Millimetre-sized glass beads were used in the study. The results indicated that axial mixing was improved by 70–90 % with the implementation of dual-axis rotation, compared to single-axis rotation. It was observed that particles of smaller size (art sand) exhibited faster mixing compared to larger particles (glass beads) due to the presence of mild cohesive effects. **Fig. 4** provides visual representations, obtained through experiments, of the mixing characteristics of glass beads of varying sizes during single-axis and dual-axis rotations.

Alexander et al. (2004) conducted experimental studies to examine the stable segregation patterns in V-blenders under varying vessel capacities, fill levels, and rotation speeds. The findings indicated that the magnitudes of particle velocities determined the pattern formation. However, the relationship between the formation of segregation patterns and the fill level of the blender could not be established due to the intricate flow patterns in the V-blender. The photographs related to this study are depicted in **Fig. 5**. Kuo et al. (2005) utilised the PEPT technique to investigate the movement of 3 mm glass beads within a V-mixer. The results of their experimentation exhibited a linear correlation between the axial dispersion coefficient of the particles and the rotational speed of the V-mixer, with an increase observed in the coefficient from 15 rpm to 60 rpm. Crouter and Briens (2015) conducted a study exploring the feasibility of utilizing passive acoustic emission monitoring as a tool for monitoring the mixing process in a V-blender. The acoustic emissions acquired during the tumbling of the V-shell were subjected to a wavelet filter to remove the associated vibrational noise. This enabled a concentration of information pertaining to particle movement and interactions within the V-shell. The study conducted by Crouter and Briens demonstrates that passive acoustic emissions can be employed as a monitoring method to gain insight into the movement and interactions of particles in a V-blender. By analysing the measured vibrations, valuable information about particle behavior can be obtained. As such, the study highlights the potential of this approach for monitoring V-blender operations.

2.2 Experimental work of convective mixers

In contrast to tumbler mixers, convective mixers incorporate rotating components to increase the mixing rate and improve mixing performance (Rahmanian N. et al., 2008). Some typical types of ribbon mixer can be found in our previous work, as shown in **Fig. 6**. MArczuk et al. (2017) conducted experimental studies on a horizontal ribbon mixer in a livestock farming mechanization laboratory, employing a personal computer, measurement and control devices, and instruments in accordance with GOST 15.101-98. The results indicated that the mixing time significantly affected the amount of mixing components, the uniformity coefficient of the mix, the capacity, and the specific energy consumption. Yeow et al. (2011) conducted an experimental investigation to examine the effects of various operating parameters and feed preparation characteristics on the homogeneity of mixing in a batch ribbon mixer. Lactose 100 M, Lactose 200 M, Ascorbic Acid, and Zinc Oxide powders were utilised as the testing materials for the study. The physical geometry of the batch ribbon mixer is depicted in **Fig. 6**. The findings indicated that improved mixing homogeneity could be achieved by increasing the rotational speed and duration of mixing, as well as through pre-blending and using smaller feed particle sizes, which enabled the attainment of the desired homogeneity in a

Table 1 Some essential experimental experiences for the mixing processes in the rotating drum in the last 3 years. (Continued on next page)

Reference	Structure	Solid properties	Operating condition	Measuring method	Reported results
(Nijssen et al., 2022)	D = 50 mm L = 50 mm Plexiglass	Cork particles 6.3 mm 152 kg/m^3	35 % and 45 % fill level 20, 40, 60 and 80 rpm	Magnetic particle tracking (MPT)	・The presence of water leads to significant alterations in the particle-wall and particle-particle interactions, resulting in significant changes in the behaviour of the bed.
(Miao et al., 2022)	D = 400 mm L = 400 mm Plexiglass	6 and 12 mm 2500 kg/m^3	10 % and 20 % fill level ±40 rpm	Multi-camera acquisition system	・The formation of alternating axial segregation bands can be observed in adjacent axial segments with similar velocity directions, while improved overall mixing is observed under conditions where the velocity direction is opposite.
(Kumar et al., 2022)	D = 290 mm L = 50 mm Plexiglass	Sphere, oblate, prolate and elongated-needle 1–6 mm 2500 kg/m^3	60 % fill level 5 rpm	Digital camera (NIKON D5300)	・The mixing behaviour is influenced by the shape of both coarse and fine particles. ・The extent of radial segregation for coarse particles demonstrates a decreasing trend: sphere>oblate>prolate>elongated-needle. For the fine particle, the trend follows as sphere>cube>prolate.
(Kato et al., 2022)	D = 122 mm L = 75 mm Plexiglass	Plastic particles 6 mm 1800 kg/m^3	2000 white 2000 black 30, 50 and 70 rpm	Digital camera	・A novel approach for determining the mixing curve of particles was established through the use of discrete element method (DEM) simulation, which involved the examination of particle behaviour over a limited time.
(Jadidi et al., 2022)	D = 220 mm L = 320 mm Plexiglass	Glass beads 5 mm 2500 kg/m^3	40 % 10, 40 and 70 rpm	Digital camera	・The mixing performance was significantly impacted by both the impeller speed and the initial loading pattern.
(Li R. et al., 2021)	D = 160 mm L = 10 mm Plexiglass	Glass beads 2 mm 2500 kg/m^3 Rice length = 4 mm aspect ratio 2 1020 kg/m^3	50 % fill level 3–5 rpm	PIV algorithm using the images	・The flow of rice particles frequently exhibits a distribution with multiple velocity peaks. ・When the rotating drum's speed is lowered to 1–3 rotations per minute, the flow of rice particles transforms into an avalanche mode.
(Jiang et al., 2021)	D_1 = 287 mm D_2 = 209 mm D_3 = 162 mm L = 100 m	Acrylonitrile butadiene styrene (ABS) 15, 10, 6, and 3 mm 1100 kg/m^3	30 % fill level 0–200 rpm	PhantomV10 high-speed camera	・The movement trajectories of individual and multiple particles in rotating drums were found to conform to the established similarity criteria.
(Huang et al., 2021)	D = 400 mm L = 400 mm Plexiglass	Glass beads 22 mm and 12 mm 2500 kg/m^3	20 %–50 % fill level 10 rpm	Image recognition method using stacked images	The segregation indices, radial for short drums and axial for long drums, can be utilised to quantify the overall level of segregation in rotating drums.

Table 1 Some essential experimental experiences for the mixing processes in the rotating drum in the last 3 years. (Continued from previous page)

Reference	Structure	Solid properties	Operating condition	Measuring method	Reported results
(Huang et al., 2021b)	D = 100 mm L = 400 mm Plexiglass	Glass beads 1.19 mm–1.41 mm 0.84 mm–1.00 mm 2500 kg/m^3	20 % fill level 20 rpm	Camera (1 fps, HDR XR-520, Sony, Japan)	・When the IS ring pair is positioned outside the end wall shearing zone, which is defined as an area with a radius of 10 particle diameters, it was observed to have an independent impact on local mixing through its ring shearing mechanism. ・In a drum with 40 % of the particles present, the critical width that must be present for an Inner-Shear (IS) ring pair to exist is roughly 30 particle diameters or 52 % of the transverse area of the bed.
(L and Huang, 2021)	D = 280 mm L = 20 mm Glass	Polyformaldehyde beads 3 mm and 4 mm	50 % fill level 2, 3 and 4 rpm	Image-processing method and particle-tracking technology	・The state of liquid distribution significantly impacts the behaviour of size-based granular segregation. ・In this study, an examination of the relationship between the granular temperature and segregation behaviour was conducted.
(Chung et al., 2021)	D = 280 mm L = 20 mm Glass	Polyformaldehyde Particles 3 mm and 4 mm 1410 kg/m^3 7 μm Al_2O_3 powders	50 % fill level 2, 3 and 4 rpm	Digital video motion recorder/ analyzer (SONY HDR-PJ820)	・The research has shown that the flow properties of granular mixtures can be enhanced by the lubricating effect generated by an optimal amount of fine powders. ・The degree of segregation, as measured by the segregation index, as well as the rate of segregation, exhibit a positive correlation with the fraction of fine powder and the rotational speed of the drum.
(Zhang et al., 2020)	D = 194 mm L = 150 mm Acrylic glass	Glass bead 6 mm 596 kg/m^3	10, 15, and 20 % fill level 10, 20, and 30 rpm	Particle tracking velocimetry (PTV)	・In relation to the rotating drum, an increase in the speed of rotation corresponds to an increase in the holdup ratio and the discharge range of materials from the flight. The cascading rate of a single flight is found to be more affected by the rotation speed during the initial and final discharging stages.
(Liao et al., 2020)	D = 280 mm L = 20 mm Glass	Polyformaldehyde 4 mm 1410 kg/m^3 7 μm Al_2O_3	50 % fill level 1, 2, 3, and 4 rpm	Image-processing technology and a particle-tracking method	・The inclusion of a minimal quantity of fine powder substantially impacts the dynamic characteristics and segregation behaviour as influenced by density. ・An increase in the fine powder content is found to result in a corresponding increase in both the average velocity and the average granular temperature. This phenomenon is attributed to the presence of a lubrication effect between the particles.
(Lia and Tsai, 2020)	D = 300 mm L = 15 mm Glass	Polyformaldehyde 3 mm 2480 kg/m^3 1410 kg/m^3 900 kg/m^3	50 % fill level 2, 3, and 4 rpm	Digital Video (DV) camcorder (SONY HDR-PJ820)	・In a binary granular mixture, the steady-state segregation index increases proportionally with the density ratio. ・The final steady-state segregation index for multi-density granular materials is lower than that of binary granular mixtures.
(Chen et al., 2020)	D = 140 mm L = 200 mm Plexiglass	Glass beads 4–6 mm 2500 kg/m^3	10 %–50 % fill level 0.3 rpm	Area CCD camera (IDT Y7-S1)	・The movement of particles resulting from an avalanche mode induces the rearrangement of particles at the upstream region of the granular bed. ・The magnitude of energy dissipation through particle rearrangement increases with the degree of particle filling.

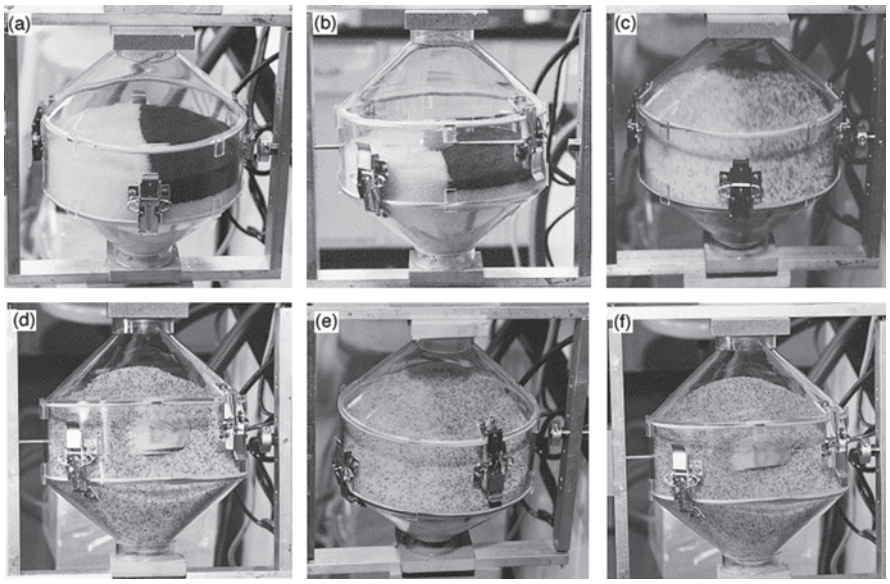


Fig. 3 Demonstration of the effect of the plate on mixing within the double cone. All experiments correspond to a filling level of 50 %. The standard double cone shown at **(a)** the initial condition, **(b)** after one min and **(c)** after 10 min (160 revolutions). The enhanced double cone shown at **(d)** the initial condition, **(e)** after 1 min and **(f)** after 10 min (160 revolutions), reprinted with permission from Ref. (Brone and Muzzio, 2000). Copyright: (2000) Elsevier B.V.

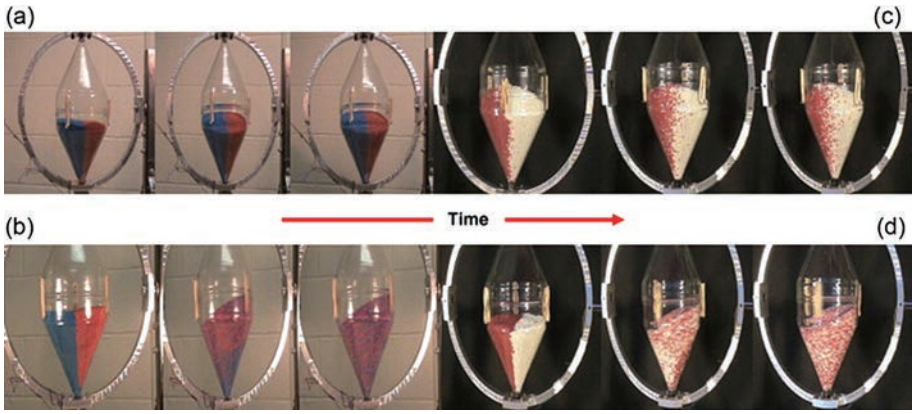


Fig. 4 Snapshots from the experiment with glass beads of different sizes for single and dual axes rotations. **(a)** 1 mm glass beads: corresponds to *X* rotational speed = 10 rpm; no rotation about the *Y* axis (i.e. 0 rpm); **(b)** 1 mm glass beads: corresponds to *X* rotational speed = 10 rpm; the *Y* rotational speed = 10 rpm; **(c)** 3 mm glass beads: corresponds to *X* rotational speed = 10 rpm; no rotation about the *Y* axis (i.e. 0 rpm); and **(d)** 3 mm glass beads: corresponds to *X* rotational speed = 10 rpm; the *Y* axis rotational speed = 30 rpm. Dual rotation enhances mixing. Reprinted with permission from Ref. (Cho et al., 2012). Copyright: (2012) Elsevier B.V.

shorter period at a lower rotational speed. Muzzio et al. (2008) conducted a study to evaluate the impact of processing and equipment parameters in a ribbon blender on the homogeneity of magnesium stearate. The study was carried out by analysing the properties of the blender using a core sampling technique, which involved collecting at least one hundred samples from throughout the blender and characterizing the entire bed. The investigation took into account several parameters, such as the loading technique for the lubricant, fill level, blade design, and blade speed, to evaluate their influence on the homogeneity of mixing in a batch ribbon mixer. The outcomes of this research can serve as a valuable reference for devising suitable blending processes and characterisation protocols for ribbon blenders, as presented in **Fig. 7**. Gijón-Arreortúa and Tecante (2015) conducted a study to evaluate the impact of helical double-ribbon impeller parameters on the mixing time and power consumption during the blending of normal corn starch and icing sugar. Results indicated that the optimal mixing performance was achieved with an impeller speed of 75 rpm and a load ratio of 0.33, resulting in the lowest mixing time and the highest coefficient of mixing rate.

By summering the previous experimental studies of ribbon mixers, it can be observed that the mixing behavior of ribbon mixers is influenced by various parameters, including the design and geometry of the mixer, rotational speed, fill level, feed preparation characteristics, and loading methods. The results of these studies suggest that an

optimal combination of these parameters can result in efficient mixing and homogenisation of the material. Moreover, various sampling and characterisation techniques, such as core sampling and PEPT, have allowed for a more comprehensive understanding of the mixing behavior in ribbon mixers. Despite the advancements in the understanding of mixing in ribbon mixers, there is still a need for further research to fully comprehend the mixing mechanisms in these mixers and optimise their design for specific industrial applications. This is especially important for the pharmaceutical and food industries, where strict standards are in place for homogeneity, particle size distribution and product quality. Furthermore, the limited number of studies conducted in this area highlights the need for future research to bridge the gap and provide a more comprehensive understanding of the fundamental aspects of ribbon mixer design, performance, and optimization.

The paddle mixer is a significant type of convective mixer that finds widespread application in industrial operations. Ebrahimi et al. (2018) conducted an experimental study to investigate the influence of impeller design on the mixing efficiency of mono-disperse, free-flowing spherical particles in a horizontal paddle mixer. **Fig. 8** displays the experimental setup. The study involved collecting 16 samples for each experiment, which can be utilised to verify simulation results. Sixteen samples were gathered during each experiment, which can be employed to verify the results of simulations. Shenoy et al. (2015) conducted a study that involved the examination of binary powder mixing in a 2 L prototype lab-scale paddle mixer using several types of food powders with varying particle sizes and poured

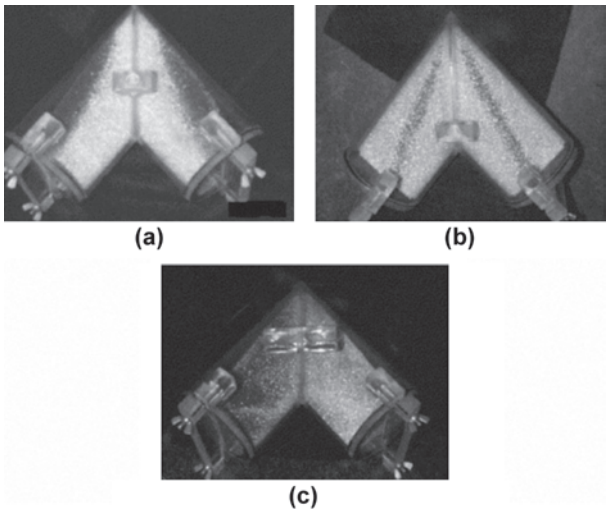


Fig. 5 The three segregation patterns found in the 1 quart V-blender when run at 50 % of capacity. **(a)** At low rotation rates (<7.5 rpm), the 'small-out' pattern forms; **(b)** intermediate speeds (7.9–19 rpm) produce 'stripes'; and **(c)** high rotation rates (>19.3 rpm) induce 'left–right' segregation, reprinted with permission from Ref. (Alexander et al., 2004). Copyright: (2004) Elsevier B.V.

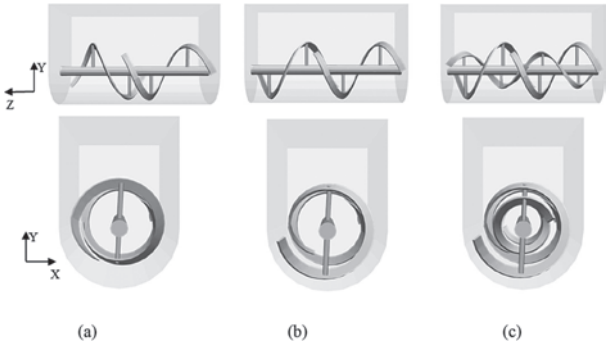


Fig. 6 The geometry of ribbon impellers: **(a)** 2-bladed impeller spiralling in the same direction (i.e., Design I); **(b)** 2-bladed impeller spiralling in the opposite direction (i.e., Design II); **(c)** 4-bladed impeller (i.e., Design III), reprinted with permission from Ref. (Jin et al., 2022). Copyright: (2022) Elsevier B.V.

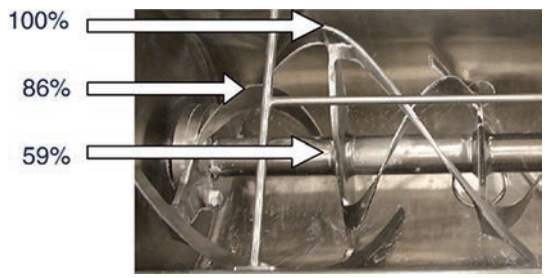


Fig. 7 Blender and fill level designations, reprinted with permission from Ref. (Muzzio et al., 2008). Copyright: (2008) Elsevier B.V.



Fig. 8 The experimental setup, reprinted with permission from Ref. (Ebrahimi et al., 2018). Copyright: (2018) Elsevier B.V.

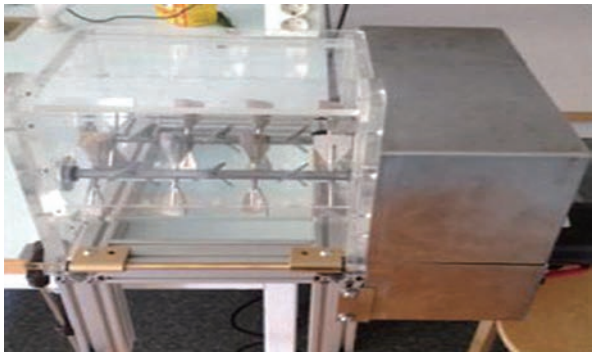


Fig. 9 Image of the 2 L paddle mixer, reprinted with permission from Ref. (Shenoy et al., 2015). Copyright: (2015) Elsevier B.V.

bulk densities (**Fig. 9**). The results of the study conducted by Shenoy et al. showed that a particle size ratio of up to 4.45 resulted in a well-mixed powder mixture. However, for higher ratios, there was a decrease in mixture quality without any visual observation of segregation. The study found that bulk density had a greater impact on mixture quality compared to particle size. When the bulk density ratios were elevated, complete segregation was noted, and its manifestation was primarily attributed to the irregular shapes of thyme and oregano powder particles. Berntsson et al. (2002) proposed a technique for quantifying the chemical composition of powder mixtures in situ using near-infrared spectroscopy (NIRS) and a fibre-optic diffuse reflection probe. The probe was inserted into the powder in a Nauta mixer. The application of NIRS and a fibre-optic diffuse reflection probe for in-situ quantitative measurement of the chemical composition of powder mixtures in a Nauta mixer was examined, and the results demonstrated its feasibility. The findings indicated that high-speed sampling is an effective method for evaluating both the mean composition and the distribution of the mixture composition during processing. The empirical content-over-time trajectories were found to be consistent with a theoretical simulation model of blending in Nauta mixers.

Despite some progress being made, the research and understanding of solid mixing processes remain relatively limited in scope. This highlights the need for further experimental studies to be conducted in this field in order to gain a more comprehensive understanding of the underlying principles and mechanisms involved in these processes. Most experimental studies in the field of solid mixing were limited to a paradigm where only a few samples were collected for characterisation. Recent experimental studies have investigated the impact of various parameters, such as fill level, blade speed, and the number of blades, on the mixing performance of mixers. Advanced measurement techniques, such as non-invasive near-infrared (NIR) spectroscopy, tomography, and PEPT, have been utilised in these investigations (Cullen et al., 2017; Page et al., 2015). However, the experimental analysis of mixers is impeded by the opaqueness of the equipment and the intricacy of the flow within the mixer. As a result, obtaining particle-scale details, such as particle velocity, inter-particle contact force, and particle dispersion, is challenging. The absence of such data limits the prospects for improving mixer performance. Furthermore, due to the high cost of experiments, the optimal design of mixers, which necessitates extensive experimentation, has not been fully explored.

3. Research progress summary of simulation work

The progression of computer technology and parallel computing has facilitated the utilisation of numerical simulation as a primary approach in the advancement of solid mixing technology. This approach can potentially reduce the cost of design, operating time, and technical risks and is increasingly being utilised to optimise mixer performance. Additionally, numerical simulation offers the advantage of observing the mixing process in a virtual environment, allowing for in-depth analysis and understanding of the mixing mechanisms. As a result, numerical simulation has become an indispensable tool in the field of solid mixing technology, providing valuable information and insights that are otherwise difficult to obtain through experimental methods.

The current simulation approaches used in the field of solid mixing can be classified into two main categories: the two-fluid model (TFM) and the discrete element method (DEM). TFM is a commonly used simulation method for the study of mixing processes in industry-scale simulations. In this approach, the gas and solid phases are treated as interpenetrating continua, and the computational load is manageable. As an Eulerian-Eulerian method, TFM employs the kinetic theory of granular flow (KTGF) to determine the solid pressure and viscosity, providing valuable mathematical insights into the particulate material's microscopic and macroscopic behavior (Brone et al., 1998). The method employs the kinetic theory of non-uniform dense phases to model particle-particle collisions. However, the model's accuracy is constrained as it relies on simplified and estimated empirical relationships for the physical properties of the solid particles, including their shape and size. Another approach is DEM approach. In DEM, individual particles are considered within the mixer, and the forces acting on each particle are calculated through the specification of contact with all other particles. This approach allows for the calculation of the resulting acceleration of each particle through the application of the equation of motion. The trajectory of each individual particle is determined by applying Newton's equation of motion, which is calculated by considering the forces acting on the particle and its acceleration. Nonetheless, it is worth noting that the Lagrangian approach for simulating solid mixing systems demands a vast amount of computational resources (CPU and memory). Due to the importance of particle-particle interaction details in solid mixing processes, DEM is widely utilised for investigating such processes. Therefore, this section will focus on a literature review of the DEM approach.

DEM has been utilised extensively to examine the processes of particle mixing and segregation within a variety of mixer configurations (Marigo M. and Stitt E.H., 2015; Sakai M., 2016; Sakai M. et al., 2020). This section will present a review of relevant DEM studies, which will be summarized based on the classification of mixers.

3.1 Simulation work of tumbler mixers

Considerable DEM simulations have been carried out to

examine the intricate particle mixing behaviors and the impact of different parameters on the mixing efficiency in the rotating drum. For example, (Yang et al., 2016) employed DEM to conduct a three-dimensional simulation of the motion of solid particles in a laboratory-scale rotating drum. The validity of the simulation results was confirmed through comparison with experimental data. Subsequently, the active-passive interface was identified, and particle-scale information was obtained for both of these regions, as shown in **Fig. 10**, utilizing DEM to perform a three-dimensional simulation of the solid motion in a laboratory-scale rotating drum. The active-passive interface was identified upon validation of the simulation results with available experimental data, and particle-scale information were obtained for both regions. The investigation explored the influence of fill level and rotating velocity on the solid motion. The study results revealed a higher concentration of particles in the passive region compared to the active region, with a more significant collision force observed in the active region, particularly in the *y*-direction, compared to the *x* and *z* directions. Yamamoto et al. (2016) investigated the mixing behavior of particles in a rotating drum mixer (RDM) by means of DEM simulation to examine the impact of particle density. DEM results of the study revealed the effects of fill level and rotating velocity on the mixing behavior of stainless steel and alumina particles within a rotating drum. The results indicated that the lower-density particles had greater mobility compared to higher-density particles, leading to segregation. However, the use of lifters was found to control the behavior of both high and low-density particles and improve the mixing of particles. The mixing degree of the alumina and stainless-steel particles was evaluated, and the results were in good agreement with the DEM simulation. Yazdani and Hashemabadi (2019) examined the effects of cohesive forces and rotating speed on the segregation and mixing of cohesive particles in a horizontal rotating drum. The simulation results indicated that both cohesion and rotation speed significantly impacted the behavior of highly cohesive particles in the drum, as illustrated in **Fig. 11**. Ma and Zhao (2017) conducted an investigation on the flow of granular materials comprising ellipsoidal particles in a horizontal rotating drum by using DEM. The study focused on examining the influence of the aspect ratio and rotation speed of the drum on transverse mixing, as shown in **Fig. 12**. The simulation demonstrated that cohesive particles' cohesion and rotation speed in a horizontal rotating drum significantly impact their behavior. The results showed that particles with lower sphericity had a higher consistency in their orientation and that better coating could be achieved at lower rotation speeds in the rolling/cascading regime.

Currently, numerous DEM investigations of the rotating drum have been conducted. Given a large number of rotating drum simulation studies, **Table 2** presents a summary of some representative recent DEM works regarding the mixing processes in the rotating drum.

A limited number of simulations can be found for other types of tumbler mixers. Hence, the following discussion

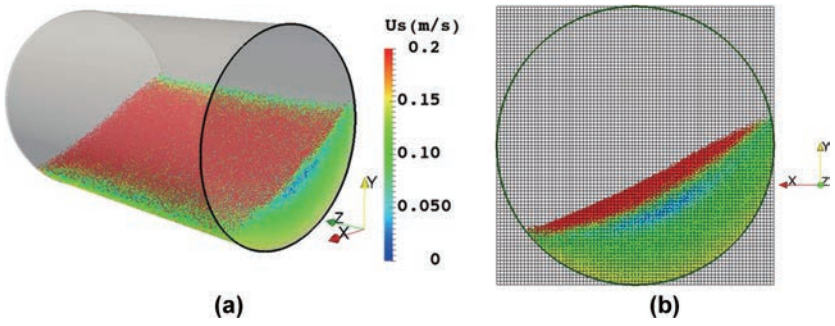


Fig. 10 Schematic representation of the apparatus showing the instantaneous velocity distribution of the solid phase in the rotating drum, reprinted with permission from Ref. (Yang et al., 2016). Copyright: (2016) Wiley Online Library.

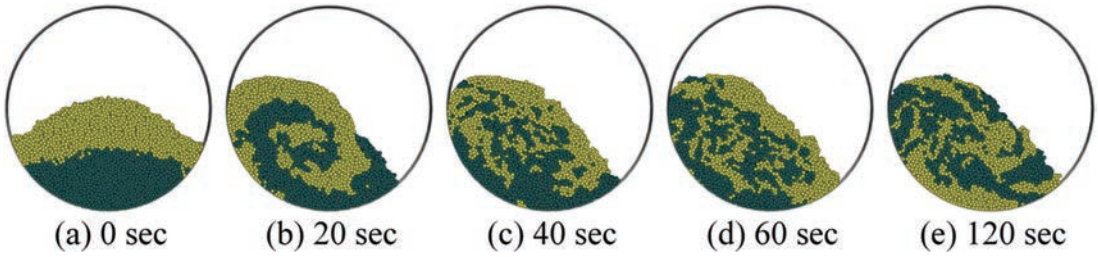


Fig. 11 Snapshots of mixing of binary cohesive mixture for segregated loading pattern in the rotating drum containing 6000 cohesive particles with k_{ii} and k_{jj} of 100 kJ/m^3 and without interparticle cohesion ($k_{ij} = k_{ji} = 0$), reprinted with permission from Ref. (Yazdani and Hashemabadi, 2019). Copyright: (2019) Elsevier B.V.

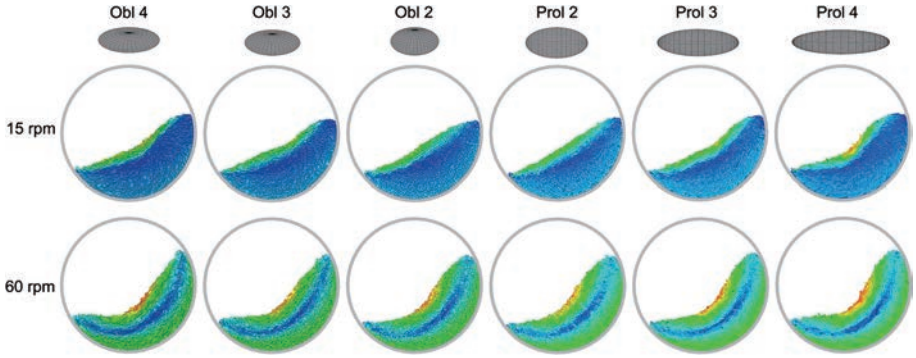


Fig. 12 Snapshots of the flow of particles coloured by their magnitude of the translational velocity (from blue (minimum) to red (maximum)), reprinted with permission from Ref. (Ma and Zhao, 2017). Copyright: (2017) Elsevier B.V.

presents a review of selected literature on other types of mixers to provide a representative sample. Arratia et al. (2006) utilised DEM to examine the flow dynamics of spherical particles within a tumbling cone blender. The simulation results showed that the radial convection rate was more significant than the axial dispersive transport, leading to decreased mixing performance within this geometry. The particle velocity profiles were analysed, revealing the presence of two distinct regions in the flow: a high-velocity layer cascading above and a region with a nearly solid body rotation, as depicted in **Fig. 13**. Ren et al. (2013) employed a GPU-based DEM software to investigate the mixing and flow dynamics of granular materials in a conical tote blender. A parametric study was performed to evaluate the impact of fill level and rotation rate on the mixing rate, productivity, and energy consumption. The study revealed that the optimal values for fill level and rotation rate could enhance mixing effectively. Moreover, the findings indicate that the conventional horizontal configuration of the blender leads to inadequate axial mixing. However, tilting the blender at a specific angle can considerably enhance the mixing efficiency. Tanabe et al. (2019) utilised DEM to assess the impact of an increase in particle size and a reduction in blender geometry on the uniformity of the blend. The study revealed that the variation in particle size among components resulted in the segregation of the three blends, as evidenced by the diverse standard deviation of active ingredient content. The research also identified two crucial factors that impact blending performance, namely, the ratio of the blender container to particle size and the total number of particles and samples in the blender. Furthermore, the study demonstrated the process of quantitative prediction of the sample BU probability density distribution using DEM simulation, which can be found in **Fig. 14**.

Tahvildarian et al. (2013) employed DEM to simulate the behavior of monodisperse, non-cohesive particles in a V-blender. The simulation accounted for both particle–particle and particle–boundary interactions, as depicted in **Fig. 15**. As the filling level increased from 20 % to 46 %, the circulation intensity decreased, and at a filling level of 34 %, it reached its minimum value for all rotational speeds. No significant change in circulation intensity was observed for filling levels greater than 34 %. The results also depict the particle velocity in the *Y*–*X* plane when the V-blender rotates from 0° to 360° at a fill level of 20 % and rotational speed of 30 rpm. Lemieux et al., (2008) employed DEM to predict the flow dynamics of multiple particles over extended periods, with a specific emphasis on the mixing phenomena that necessitate a considerable amount of time to develop in such systems. To this end, the researchers performed several extensive numerical simulations using the DEM approach, investigating the flow of monodisperse and bidisperse blends consisting of up to 225,000 particles for 120 seconds in a V-blender. Quantities such as particle velocity, granular temperature, mixing system torque, RSD curves, and mixing times are examples of variables commonly used to characterise and analyse the behavior of granular materials during mixing processes.

3.2 Simulation work of convective mixers

In contrast to the tumbler mixer, convective mixers employ stationary outer vessels with added moving components to improve solid mixing performance.

Sarkar and Wassgren (2015) conducted a study using DEM to examine the impact of modelled particle size on flow and mixing in a bladed granular mixer. The findings revealed that the macroscopic advective flow was considerably influenced by particle size, particularly in areas with sparse flow. Yaraghi et al., (2018) utilised DEM to investigate the flow patterns and mixing kinetics of non-cohesive, monodisperse, and spherical particles in a horizontal paddle blender. The authors found that the most significant factor affecting mixing quality was the rotational speed of the impeller, with the quadratic effect of the impeller rotational speed and the vessel fill level having a lesser impact. Furthermore, the empirical data obtained on granular temperature demonstrated that an increase in impeller rotational speed, from 10 to 70 rpm, resulted in a corresponding increase in the granular temperature values. In a study

Table 2 Summary of representative DEM work for the mixing processes in the rotating drum in recent years. (Continued on next page)

Reference	Solid properties	Operating condition	Research Descriptions	Reported results
(Yu et al., 2022)	Particle size: 3–6 mm Particle density 2500 kg/m^3 Particle number: 88379, 10105, 113630.	Fill level 30 %, 40 % 45 % Rotating speed 5.4, 8.5, 11.6 rpm	The flow behavior of polydisperse particles in a rolling mode rotating drum.	・Polydisperse particles are characterised by a composite structure where small particles serve as nuclei surrounded by larger particles. ・Monodisperse particles exhibit a relatively elevated velocity of the active layer, whereas polydisperse particles tend to exhibit greater radial segregation.
(Mori and Sakai, 2022)	Particle size: 5.0 × 2.5 × 2.5 mm 4.0 × 4.0 × 2.0 mm Particle density 1150 kg/m^3 Particle number:1000	Rotating speed 20, 60 rpm	The powder mixing of non-spherical particles in an industrial rotating drum mixer.	・The influence of a nonspherical shape on the progression of powder mixing in a ribbon mixer has been demonstrated to be negligible.
(Silveira et al., 2022)	Particle size: 1.09 mm Particle density 2445 kg/m^3 Particle number: 43,200, 54,000, and 63,837	Fill level 10.1 %, 12.7 %, and 15 %, Rotating speed 21.3 rpm	Identify the optimal configuration and layout of the vanes or blades to achieve maximum dispersion and distribution of the particles in the active zone.	・The experimental findings revealed that the flight configuration with a separation distance of 15° resulted in a 24.6 % increase in the occupied area by the particles in the active region, and a 38.5 % reduction in the heterogeneity of the solid dispersion compared to the configuration with aligned flights.
(Li M. et al., 2021)	Particle diameter: 4.9–10 mm Particle density 1200 kg/m^3 Aspect ratio: 1.0–6.0 Particle number: 25,027–31,764	Fill level 40.5 % Rotating speed 10–50 rpm	Investigate the flow behavior and mixing process of sphero-cylinders with varying shapes at a filling level of 40.5 % in a rotating drum.	・Sphero-cylinders with different Ars can reach well-mixed states under sufficient rotation conditions. ・Both the macro- and microscopic properties change with the rotation speed and AR; however, when AR > 3, its influence becomes less obvious.
(Zhang et al., 2021)	Particle diameter: 0.1–0.3 mm Particle density 596 kg/m^3 Particle number: 3474	Fill level 15 % Rotating speed 10–30 rpm	Influence of the number of flights on the dilute phase ratio in flighted rotating drums	・The number of flights varies depending on the holdup ratio and cascading rate of both single and active flights. ・The FRD exhibits a greater production of the dilute phase, which is more stable, when configured with either 8 or 12 flights.
(Huang et al., 2021a)	Particle diameter: 0.71 mm–0.84 mm 0.50 mm–0.59 mm Particle density 2492 kg/m^3	Fill level 20 % Rotating speed 20 rpm	Study size segregation of binary mixture in a rotating drum with inner diameter variations.	・When the CR value equals 0.9, the percolation mechanism is improved, and the contracting wall has a greater impact on smaller particles, leading to their migration towards regions with larger inner diameters, resulting in expanded dimensions. On the other hand, when the CR value is 0.5 or 0.3, the contracting wall imposes additional shear forces on the bed and impedes the migration of particles of both sizes.
(Deng et al., 2021)	Particle diameter: 1–10 mm Particle density 3100 kg/m^3 Particle number: 29623, 24241, 9846 9928	Fill level 30–33 % Rotating speed 10 rpm	The effect of slag size distributions on mixing and segregation	・Previous studies have highlighted the limitations of whole-process mixing criteria in fully capturing the intricate nuances of subprocesses. ・The use of subprocess criteria, which combine the index of entry order and the number of contacts, has been shown to be effective in accurately evaluating the duration of mixing in granular beds.

Table 2 Summary of representative DEM work for the mixing processes in the rotating drum in recent years. (Continued from previous page)

Reference	Solid properties	Operating condition	Research Descriptions	Reported results
(Wang et al., 2021)	Particle density 2500 kg/m^3 Aspect ratios 0.5 and 2.0	Rotating speed 7.5–130 rpm	The influences of particle shape, standard deviation of the mixture, and rotating speed on the segregation behaviors.	・The distribution of small and large particles in the drum was found to be concentrated in the centre and periphery, respectively, while medium-sized particles were evenly distributed throughout the system. ・As the granular system approaches a high-speed centrifugal state, the smallest particles exhibit the highest radial velocity and tend to be located near the drum wall.
(He et al., 2021)	Particle density 2500 kg/m^3 Aspect ratios 0.4–2.5 volume-equivalent diameter: 3 mm Particle number: 400000	Fill level 38 % Rotating speed 40 rpm	Report an interesting phenomenon that for ellipsoid-sphere mixtures.	・The severity of axial segregation attains a peak at aspect ratios of 0.67 and 2.0. ・In the outer region, the migration of both ellipsoids and spheres towards the central section of the transverse slice was observed, while in the inner region, particles showed a propensity to migrate towards the end walls.
(Li D. et al., 2021)	Particle diameter: 1.5 and 3 mm Particle density 2500 kg/m^3 Particle number: 2500 for 3 mm 20,000 for 1.5 mm	Fill level 20 % Rotating speed 40,150 and 200 rpm	Forecast the flow characteristics of two-sized particles, binary particle systems, in a horizontal rotating cylindrical drum and an ellipsoidal drum, a numerical simulation approach can be employed.	・At elevated rotational speeds, the degree of mixing of binary-sized particles in the RED can be augmented. ・The resulting contact forces exhibit a gradual increase with the increment of rotational speed and flattening.
(Brandao et al., 2020)	Particle diameter: 1.1 and 6.3 mm Particle density 2455 and 1160 kg/m^3 Particle number: 2500 for 3 mm 20,000 for 1.5 mm	Fill level 25 % and 50 % Rotating speed 0.59, 1.10 and 1.77 rad/s	Investigate the mixing/segregation behavior of particles in an unbaffled rotary drum	・The simulations, utilising experimentally determined input parameters obtained through the DEM, demonstrated the closest agreement with the experimental responses, such as the repose angle and radial mixture.
(Rong et al., 2020)	Particle diameter: 3 mm Particle density 2500 kg/m^3 Particle number: 2000	Fill level 35 % Rotating speed 40 rpm	Investigate the effects of particle contact parameters, sliding friction coefficient (SFC), rolling friction coefficient (RFC) and restitution coefficient (RC) in a rotating drum.	・The sliding friction coefficient was identified as a crucial element in determining both the mean power draw and mean collision energy. On the other hand, the restitution coefficient had the most pronounced impact on the frequency of collisions. ・The influence of the sliding friction coefficient and restitution coefficient on both the collision frequency and mean collision energy was observed to vary across different rotational speeds.
(Yazdani and Hashemabadi, 2019)	Particle diameter: 1.5 and 2 mm Particle density 1000 kg/m^3 Particle number: 14,222 for 1.5 mm 6000 for 2.0 mm	Fill level 25 % and 55 % Rotating speed 6, 12 and 18 rpm	Simulate the segregation and mixing of cohesive particles in a horizontal rotating drum	・When mixing cohesive and non-cohesive particles, the bed displayed a tendency towards segregation, with cohesive particles gravitating towards the outer layer of the rotating bed. Conversely, complete mixing was not attained without interparticle cohesion between two types of cohesive particles. ・The results indicated that the duration necessary to attain the final mixed state increased in the case of highly cohesive particles.

conducted by (Ebrahimi et al., 2018), the efficacy of mixing monodisperse spherical particles in a horizontal agitating paddle mixer was investigated using the DEM method. The study involved simulating five different impeller designs to determine their influence on mixing performance. The study evaluated five distinct impeller designs through simulation. The findings demonstrated that impeller design significantly affected both the mixing performance and the granular behavior of the materials, as demonstrated in **Fig. 16**. Additionally, the study analysed the effect of impeller configuration on the forces of contact between the impeller and particles, and between the particles themselves.

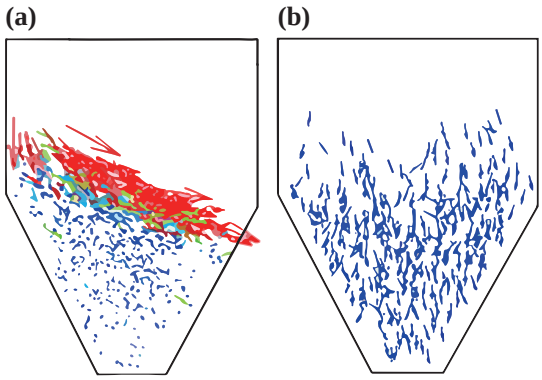


Fig. 13 Example of velocity fields of a mono-disperse system at 40 % fill level. **(a)** Side view at 3/4 of a revolution. **(b)** Top view at 3/4 of a revolution, reprinted with permission from Ref. (Arratia et al., 2006). Copyright: (2006) Elsevier B.V.

Ribbon mixers are deemed appropriate for blending dry powders and free-flowing granular materials. Literature suggests that a ribbon mixer can achieve improved uniformity in powder mixing due to the high shear stresses it generates and its ability to handle a mixture of particles of varying sizes. Hence, the utilisation of DEM in analysing the ribbon mixer offers valuable insights into its performance and potential optimization. Halidan et al. conducted a series of DEM studies investigating the mixing behaviors in ribbon mixers. A survey was conducted by the researcher to investigate the influence of impeller speed on the mixing behavior of cohesive and non-cohesive particle mixtures in a ribbon mixer, which is characterised by a horizontal cylindrical vessel (Halidan et al., 2016; Musha et al., 2013). The DEM simulations indicated that the mixing rate of both cohesive and non-cohesive mixtures in the ribbon mixer increased as the impeller speed increased up to a certain threshold, after which a decrease was observed. For non-cohesive particles, the mixture quality may deteriorate at higher impeller speeds, but this was not the case for cohesive particles. Halidan et al. (2018) employed DEM to examine the impact of impeller speed and fill level on the blending behaviors of particle mixtures with varying

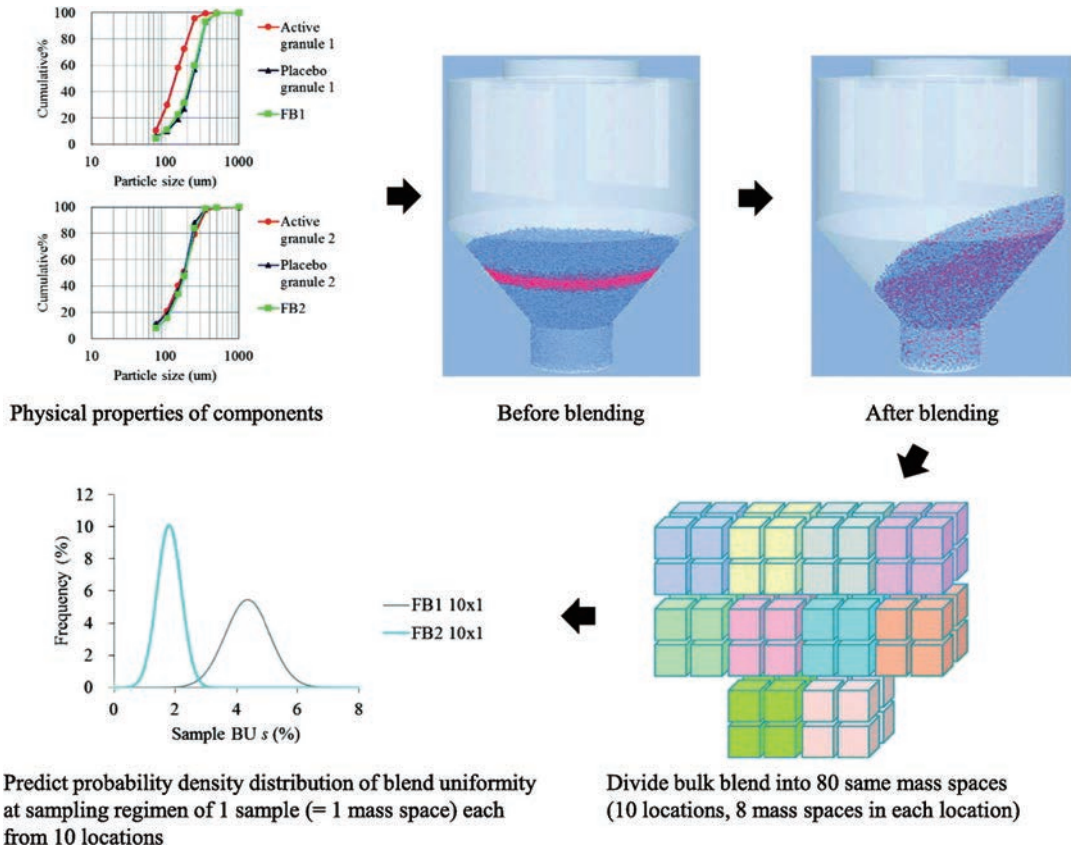


Fig. 14 Quantitative prediction of the sample BU probability density distribution in reality using the DEM simulation, reprinted with permission from Ref. (Tanabe et al., 2019). Copyright: (2019) Elsevier B.V.

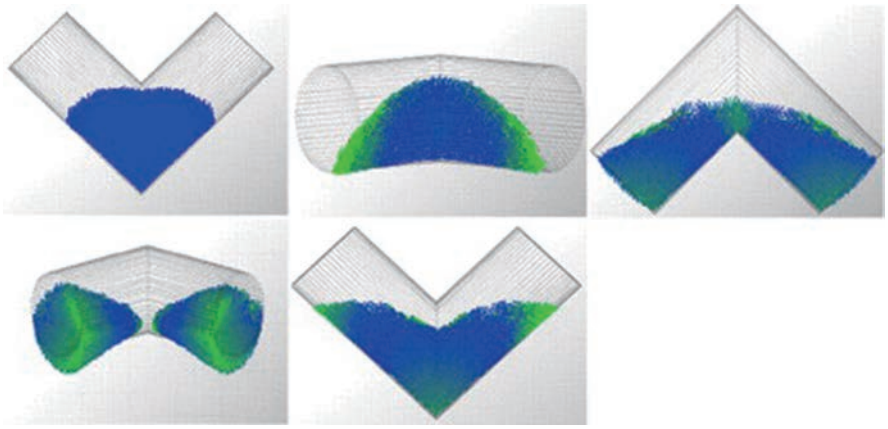


Fig. 15 Particle velocity in the *Y-X* plane when the V-blender rotated from 0° to 360° at 20 % fill level and 30 rpm, reprinted with permission from Ref. (Tahvildarian et al., 2013). Copyright: (2013) Elsevier B.V.

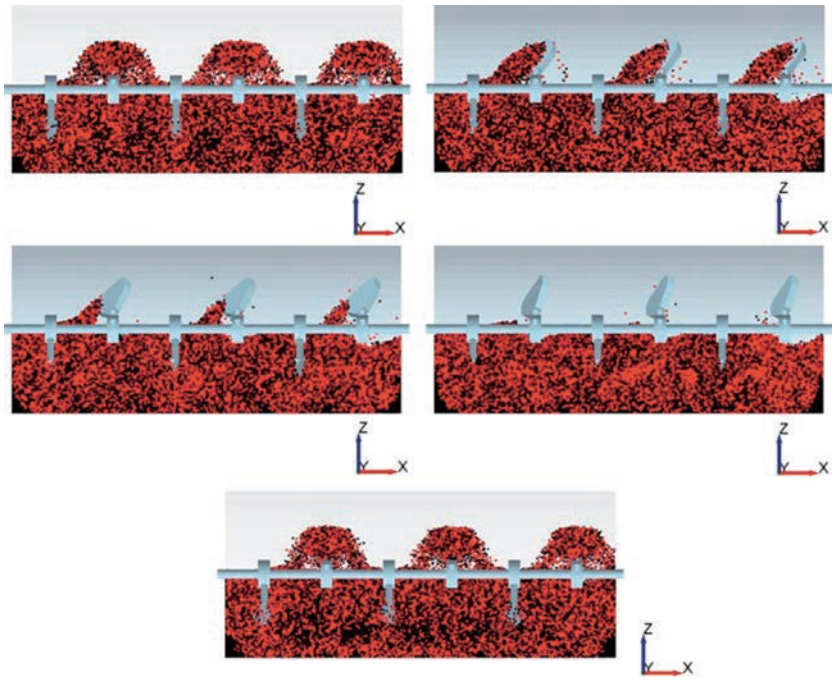


Fig. 16 A snapshot of particle mixing after 10 revolutions of mixing from the front view sliced at the centre of the mixer, reprinted with permission from Ref. (Ebrahimi et al., 2018). Copyright: (2018) Elsevier B.V.

cohesion in both two-bladed and four-bladed ribbon mixers, each possessing a horizontal cylindrical vessel. Beyond that, the mixing rate was observed to decline. In particular, the mixing rate of cohesive particles was found to deteriorate at higher impeller speeds in the 2-bladed mixer. The results showed that with an increase in fill level, the flow behavior of non-cohesive particles changed from sliding flow to recirculation flow and eventually to cascading flow. The comparison results can be seen in **Fig. 17**. Chandratilleke et al. conducted a numerical investigation of the impact of blade-supporting spokes on the overall mixing performance in a ribbon mixer using DEM. This study analysed the effect of several key variables, including the number of spokes, the cohesiveness of particles, and the fill level on the mixing performance. The results indicated that, in the case of non-cohesive particles, increasing the number of spokes was advantageous for improving the overall mixing rate when the fill level was substantial. However, this improvement came with the cost of increased contact forces.

In contrast, the best overall mixing performance was observed with a no-spoke impeller for cohesive particles. The critical findings are depicted in **Fig. 18**. Subsequently, DEM was used to examine the impact of particle size and density on particle mixing in a laboratory-scale ribbon mixer (Chandratilleke et al., 2021). The study conducted by Basinskas and Sakai (2016) employed numerical simulations to examine the impact of various factors on the degree of mixing in a laboratory-scale ribbon mixer. The results indicated that the mixing rate decreased as the particle size was reduced with the fill level fixed, and the density effect

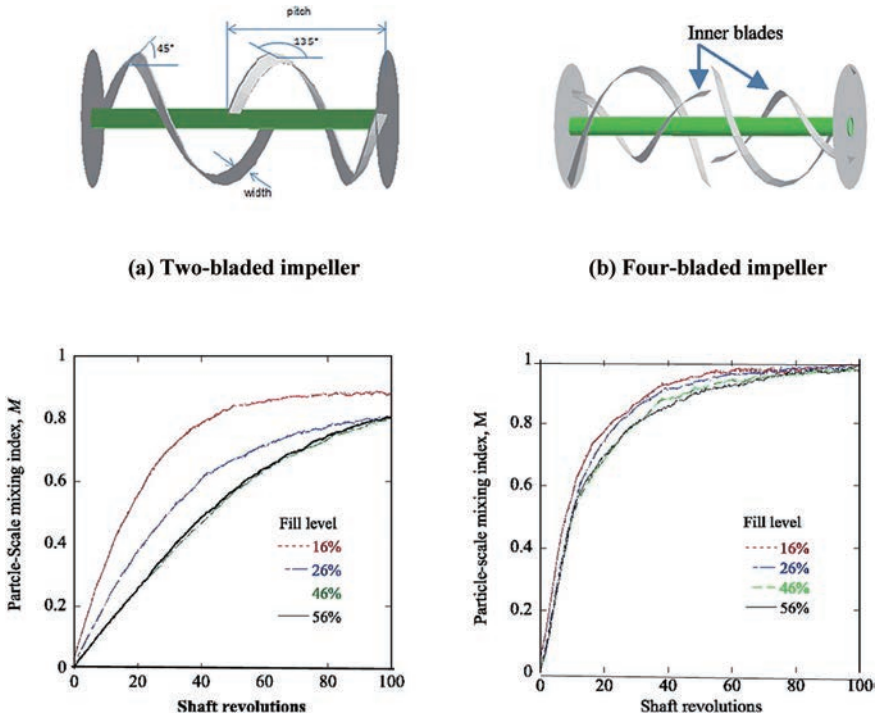


Fig. 17 Effect of fill level on the mixing performance of a 2-bladed mixer at different Bond numbers (shaft speed = 100 rpm), reprinted with permission from Ref. (Halidan et al., 2018). Copyright: (2018) Elsevier B.V.

was negligible for small particle sizes. An empirical equation was formulated to describe the particle-size effect, which was also extrapolated to consider much smaller particles. The present investigation employed numerical methods to assess the impact of powder quantity, blade speed, and initial loading on the degree of mixing in a ribbon mixer (See **Fig. 19**). The degree of mixing in the axial direction was found to be relatively less variable than that in the perpendicular direction. The results indicated that the amount of powder and the blade speed positively influenced the mixing performance. However, the study found that only the initial loading and powder quantity had a significant impact on the quality of mixing in the ribbon mixer, with only modest variations observed in the axial direction compared to the perpendicular direction. Recently, several noteworthy DEM studies on the mixing processes in convective mixers have been reviewed and summarized in **Table 3**.

4. Current progress and future perspectives

The mixing of particles is a common practice in several industries, including ceramics, pharmaceuticals, food, and chemicals, where a high-quality end product is crucial. The quality of powder products, which are composed of particulate ingredients that must be thoroughly mixed, is heavily influenced by the design of the mixer and its operating conditions. Various types of mixers, such as rotating drums, orbiting screw mixers, and ribbon mixers, are used for this purpose. However, the mechanism of particle mixing in these mixers is still not well understood due to the complex nature of particle behavior in the mixing system. Understanding and controlling particle behavior during mixing remains a significant challenge for improving the operation and optimization of mixers. Up to date, the design of solid mixers is generally limited to first selecting qualitatively the equipment that might be suitable and then arranging tests with potential suppliers, where unified theory and criteria are still not available due to insufficient knowledge of the mixing mechanism. An extensive understanding of particle mixing is crucial both from a scientific perspective and a practical standpoint to optimise industrial processes related to it.

Despite the prevalence of powder mixing in various industries, there remains a lack of robust and systematic methods for characterizing mixing quality and determining the optimum mixing conditions. This has motivated researchers to focus on developing more advanced experimental techniques to better understand the underlying physics and mechanics of particle mixing. By improving our understanding of the mechanisms and principles that govern particle mixing, researchers aim to improve the efficiency and quality of powder processing. Therefore, there is a growing need for improved experimental techniques and advanced simulation methods to better understand particle mixing behaviors and incorporate the particles' microscopic properties into the models. This would lead to a more accurate prediction of mixing performance and could aid in the design and optimization of industrial solid mixing processes. Additionally, the integration of experimental data and simulation results can help to establish a

Table 3 Summary of representative DEM work for the mixing processes in the convective flow in recent years. (Continued on next page)

Reference	Solid properties	Operating condition	Research Descriptions	Reported results
(Xiao et al., 2023)	Particle size: 4.75–8 mm Particle density 2837 kg/m^3	Fill level 45 % Rotating speed 40 rpm	The mixing processes of gravel materials.	・The introduction of rods into a drum has been found to enhance the mixing degree of particles. ・The diameter of the cylindrical rods appears to have a minimal effect on the particle mixing degree. ・The smaller the distance between the rods, the better the mixing degree.
(Yu et al., 2022)	Particle size: 3, 4, 5 and 6 mm Particle density 2500 kg/m^3 Particle number: 88379, 101005 and 113630	Fill level 35 %, 40 % and 45 % Rotating speed 5.4, 8.5 and 11.6 rpm	The flow behavior of polydisperse particles in a rolling mode rotating drum.	・The behaviour of particle flow in a drum was investigated through the examination of particle velocity, duration of residence, mixing intensity, and axial dispersion in various regions within the drum. The objective was to reveal the flow behaviour of polydisperse particles. ・Propositions are put forth to enhance the rotating drum's efficiency in the rolling mode. ・The distinction in flow behaviour between polydisperse and monodisperse particles is presented.
(Xu et al., 2023)	Particle size: 3 mm Particle density 1414 kg/m^3 Particle number: 20000, 30000, 35000 and 40000	Fill level 15 %, 23 %, 26 % and 31 % Rotating speed 5, 8, 10 and 15 rpm	Effect of drum structure on particle mixing behavior.	・The contact number between particles and wall is improved in LC and LLC compared to the cylinder drum.
(Miao et al., 2022)	Particle size: 6 and 12 mm Particle density 2500 kg/m^3 Particle number: 20000, 30000, 35000 and 40000	Fill level 20 % Rotating speed ±40 rpm	Particle mixing and segregation behaviors in the rotating drums with adjacent axial segmentations in different speed directions.	・Alternating axial segregation bands can be formed in adjacent axial segmentations with the same velocity direction, while the overall mixing degree is improved under conditions of the opposite velocity direction.
(Liu et al., 2022)	Particle size: 3 mm Particle density 2700 kg/m^3 Particle number: 10000	Fill level 50 % Rotating speed 3 rpm	Effect of baffles on mixing and heat transfer in drums is studied.	・The optimal length-to-diameter ratio of central baffles varies between 0.4 and 0.7. ・The peripheral baffles perform best at a high length-to-radius ratio of 0.9.
(Wu et al., 2022)	Particle size: 3 mm Particle density 1358.8 kg/m^3 Particle number: 37600	Fill level 20 % Rotating speed 15 rpm	Prediction of particle mixing time in a rotary drum by 2D DEM simulations and cross-correlation.	Compared to machine learning approaches, the cross-correlation method has the advantage of interpretability, expandability, and relatively high accuracy for limited data size.
(Ebrahimi et al., 2021)	Particle size: 3 and 5 mm Particle density 2500 kg/m^3 Particle number: 153,780 for 3 mm, 38,446 for 5 mm	Fill level 40 % and 60 % Rotating speed 40, 70 and 100 rpm	The mixing of bi-disperse particles in a horizontal paddle mixer.	・r_n had the most significant effect on the mixing performance. The study's results revealed that the mechanism of diffusion was predominant over that of convection. Furthermore, when the values of the diffusion coefficients for 5 mm and 3 mm particles were found to be comparable, the optimal mixing performance was achieved.
(Deng et al., 2021)	Particle size: 0.6 mm Particle density 2500 kg/m^3 Particle number: 100,000, 200,000 and 300,000	Rotating speed 20, 40 and 60 rpm	The effects of various operational parameters on the mixing performance.	・Factors such as rotational speed, filling level, liquid viscosity, and paddle obliquity can significantly impact the mixing performance. The identification of various mixing mechanisms can be achieved through the utilization of the probability distribution function.

Table 3 Summary of representative DEM work for the mixing processes in the convective flow in recent years. (Continued from previous page)

Reference	Solid properties	Operating condition	Research Descriptions	Reported results
(Horváth et al., 2019)	Particle size: 6, 10 and 20 mm Particle density 7750 kg/m^3 Particle number: 43,200, 54,000, and 63,837	Fill level 10 %–25 %, Rotating speed 0.63; 0.95; 1.58 r/s	Create a DEM model suitable for determining the mixing power requirements of an agitated drum dryer pilot plant, which can be applied to the modeling of mixing granular materials of various moisture content.	・The results of the study showed that the moisture content of the material and the rotational speed of the mixing unit have a significant impact on the mixing power requirement. In addition, the mixing torque requirement was found to decrease as the rotational speed increased.
(Yaraghi et al., 2018)	Particle diameter: 3 mm Particle density 2500 kg/m^3 Particle number: 120,000	Fill level 40 % Rotating speed 40 rpm	The influence of impeller configuration on the mixing performance of free-flowing mono-disperse spherical particles in a horizontal agitating paddle mixer.	・The alterations in impeller configurations had minimal effect on the particle-particle contact forces. ・The simulation with the 0° angle paddle resulted in higher granular temperature values than the rectangular one. This observation partially explains the improved mixing performance obtained for the former impeller compared to the latter impeller.
(Pasha et al., 2015)	Particle diameter: 4.52 mm Particle density 1000 kg/m^3 Particle number: 60000	NA	Simulate PEPT experiments for a paddle mixer using DEM.	・It takes 251 seconds for a tracer to traverse the entire active space of the system. ・The average velocity distribution remains unaffected by an increase in the number of tracers in the paddle mixer system.
(Sarkar and Wassgren, 2015)	Particle diameter: 1.5 mm–12 mm Particle density 1000 kg/m^3 Particle number: 113,152	Fill level 30 % Rotating speed 30 rpm	The influence of the modelled particle size on flow and mixing in a bladed granular mixer.	The effect of particle size on the macroscopic advective flow was found to be significant, particularly in dilute flow regions. These findings indicate that particle size should be taken into consideration when performing DEM mixing simulations with larger particles.
(Chandratilleke et al., 2021)	Particle diameter: 5–15 mm Particle density 417–2500 kg/m^3	Fill level 40 % Rotating speed 100 rpm	The effects of the particle size and density on particle mixing on a laboratory-scale ribbon mixer.	・When the fill level was kept constant, a reduction in particle size resulted in a slower mixing rate at a given density. However, for particles with small sizes, the effect of density on mixing was negligible. The particle size effect was described by an empirical equation and was extrapolated for even smaller particle sizes.
(Tsugeno et al., 2021)	Particle diameter: 4 mm Particle density 2500 kg/m^3 Particle number: 120,000 80,000	Rotating speed 20 and 60 rpm	An effective parameter for better mixing in the ribbon mixer using DEM.	・The blade width is identified as a critical aspect for optimizing mixing performance. ・The relationship between the swept volume and the mixing index remained consistent despite changes in the paddle design.
(Gao et al., 2019)	Particle density 3948 kg/m^3 Particle diameter: 40, 50 and 60 mm Particle number: 52348 and 104549	Rotating speed 15, 25 and 35 rpm	The effects of the operational and geometrical parameters, including initial loading, particle size, impeller rotational speed, and inner blades on the mixing quality of particles with a double U-shaped vessel.	・The initial loading and the rotational speed of the impeller have a significant impact on the quality of particle mixing, while the effect of the other two parameters was relatively small. A numerical investigation on the ribbon mixer equipped with a double U-shaped vessel indicates that better mixing performance is achieved under top–bottom and front–back initial loadings, whereas inferior mixing performance is observed under side–side initial loading.
(Halidan et al., 2016)	Particle diameter: 15 mm Particle density 417 kg/m^3 Particle number: 18000	Rotating speed 100 rpm	The effect of interparticle cohesion on powder mixing in a ribbon mixer was studied by means of the discrete element method.	・With increased cohesion, mixing rate and uniformity deteriorate. The coordination number increases, indicating a loss in free-flowing motion ability, and many particles have more vital tangential velocity for bulk angular motion.

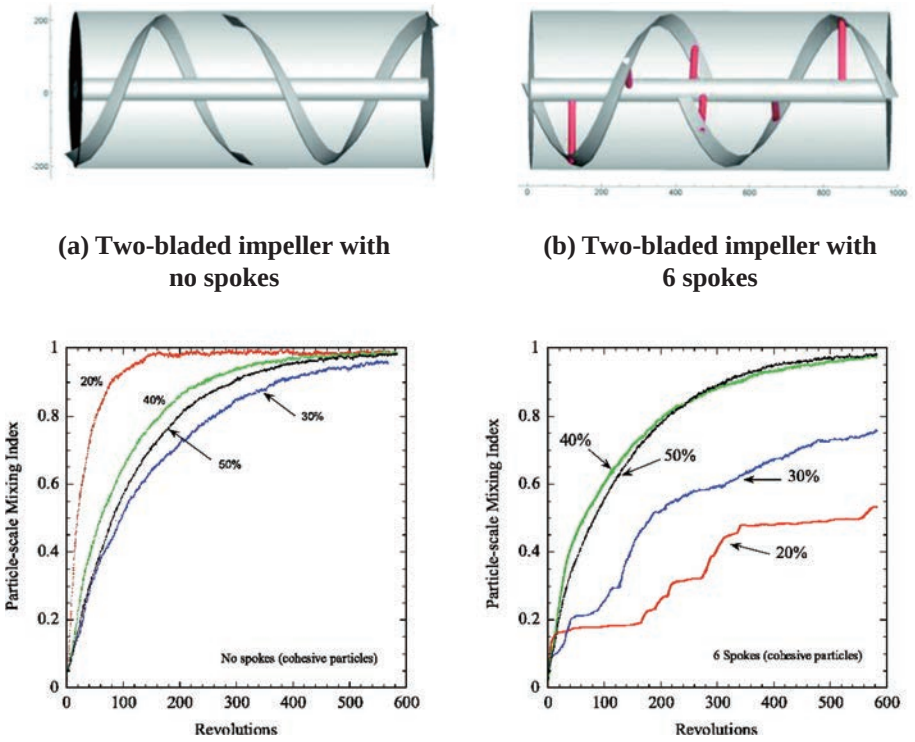


Fig. 18 The effect of blade-supporting spokes of the impeller on overall mixing performance in a ribbon mixer, reprinted with permission from Ref. (Chandratilleke et al., 2018). Copyright: (2018) Elsevier B.V.

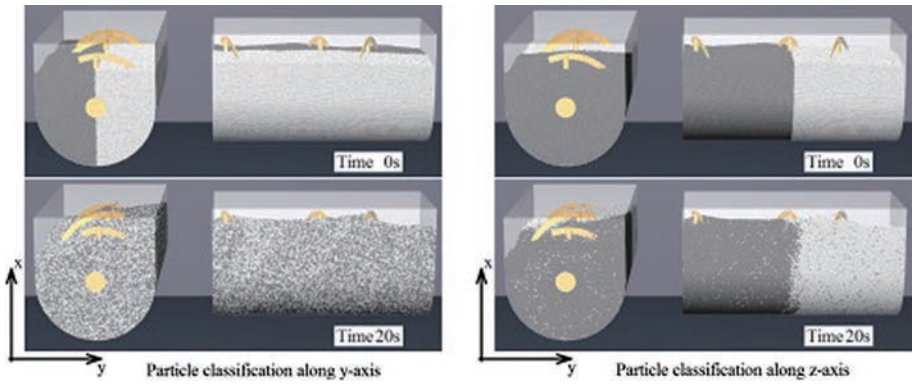


Fig. 19 Mixing states at different times for different loading methods, reprinted with permission from Ref. (Basinskas and Sakai, 2016). Copyright: (2016) Elsevier B.V.

more comprehensive understanding of particle mixing, which is crucial for the continuous improvement of the powder processing industry. Additionally, developing more advanced computational models that consider the microscopic properties of particles will be critical to understanding and improving the efficiency of solid mixing processes in the industry (Ghadiri, 2020). This, in turn, can lead to significant advances in the quality and consistency of a wide range of powder products, as well as reduced energy consumption, lower costs, and reduced environmental impact associated with the production of these products.

Moreover, the integration of Industry 4.0 technologies, such as the Internet of Things (IoT) and artificial intelligence (AI), can further enhance the accuracy and efficiency of measurement and control systems, thereby enabling more effective and efficient solid mixing processes in the future (Bowler et al., 2020). It is also worth focusing on the recently developed soft sensors, expected to gain popularity as they provide a low-cost and simple-to-implement method of predicting final product qualities.

Acknowledgments

We sincerely acknowledge the financial support from the Australian Research Council (DP220100306 and FT190100361).

References

Alexander A., Shinbrot T., Johnson B., Muzzio F.J., V-blender segregation

patterns for free-flowing materials: effects of blender capacity and fill level, International Journal of Pharmaceutics, 269 (2004) 19–28. DOI: 10.1016/S0378-5173(03)00296-5

Arratia P., Duong N.-h., Muzzio F., Godbole P., Reynolds S., A study of the mixing and segregation mechanisms in the Bohle Tote blender via DEM simulations, Powder Technology, 164 (2006) 50–57. DOI: 10.1016/j.powtec.2006.01.018

Basinskas G., Sakai M., Numerical study of the mixing efficiency of a ribbon mixer using the discrete element method, Powder Technology, 287 (2016) 380–394. DOI: 10.1016/j.powtec.2015.10.017

Berntsson O., Danielsson L.-G., Lagerholm B., Folestad S., Quantitative in-line monitoring of powder blending by near infrared reflection spectroscopy, Powder Technology, 123 (2002) 185–193. DOI: 10.1016/S0032-5910(01)00456-9

Bowler A.L., Bakalis S., Watson N.J., A review of in-line and on-line measurement techniques to monitor industrial mixing processes, Chemical Engineering Research & Design, 153 (2020) 463–495. DOI: 10.1016/j.cherd.2019.10.045

Brandao R.J., Lima R.M., Santos R.L., Duarte C.R., Barrozo M.A., Experimental study and DEM analysis of granular segregation in a rotating drum, Powder Technology, 364 (2020) 1–12. DOI: 10.1016/j.powtec.2020.01.036

Bridgwater J., Mixing of powders and granular materials by mechanical means—A perspective, Particuology, 10 (2012) 397–427. DOI: 10.1016/j.partic.2012.06.002

Brone D., Alexander A., Muzzio F., Quantitative characterization of mixing of dry powders in V-blenders, AIChE journal, 44 (1998) 271–278. DOI: 10.1002/aic.690440206

Brone D., Muzzio F., Enhanced mixing in double-cone blenders, Powder Technology, 110 (2000) 179–189. DOI: 10.1016/S0032-5910(99)00204-1

Chandratilleke G., Jin X., Shen Y., DEM study of effects of particle size and density on mixing behavior in a ribbon mixer, Powder Technology, 392 (2021) 93–107. DOI: 10.1016/j.powtec.2021.06.058

Chen Q., Yang H., Li R., Xiu W., Zheng G., Kong P., Rearrangement of irregular sand particles in a rotary drum after avalanche flow, Powder Technology, 360 (2020) 549–554. DOI: 10.1016/j.powtec.2019.10.083

Cho J., Zhu Y., Lewkowicz K., Lee S., Bergman T., Chaudhuri B., Solving granular segregation problems using a biaxial rotary mixer, Chemical Engineering and Processing: Process Intensification, 57 (2012) 42–50. DOI: 10.1016/j.cep.2012.04.002

Chung Y.-C., Liao C.-C., Zhuang Z.-H., Experimental investigations for the effect of fine powders on size-induced segregation in binary granular mixtures, Powder Technology, 387 (2021) 270–276. DOI: 10.1016/j.powtec.2021.04.034

Crouter A., Briens L., Passive acoustic emissions from particulates in a V-blender, Drug Development and Industrial Pharmacy, 41 (2015) 1809–1818. DOI: 10.3109/03639045.2015.1009913

Cullen P., Bakalis S., Sullivan C., Advances in control of food mixing operations, Current Opinion in Food Science, 17 (2017) 89–93. DOI: 10.1016/j.cofs.2017.11.002

Deng S., Wen Z., Su F., Wang Z., Lou G., Liu X., Dou R., Radial mixing of metallurgical slag particles and steel balls in a horizontally rotating drum: a discussion of particle size distribution and mixing time, Powder Technology, 378 (2021) 441–454. DOI: 10.1016/j.powtec.2020.10.022

Ding Y., Seville J., Forster R., Parker D., Solids motion in rolling mode rotating drums operated at low to medium rotational speeds, Chemical Engineering Science, 56 (2001) 1769–1780. DOI: 10.1016/S0009-2509(00)00468-1

Duran J., Sands, Powders, And Grains: An Introduction to the Physics of Granular Materials, Springer New York, 2012, ISBN: 978-1461204992. DOI: 10.1007/978-1-4612-0499-2

Ebrahimi M., Yaraghi A., Ein-Mozaffari F., Lohi A., The effect of impeller configurations on particle mixing in an agitated paddle mixer, Powder Technology, 332 (2018) 158–170. DOI: 10.1016/j.powtec.2018.03.061

Ebrahimi M., Yaraghi A., Jadidi B., Ein-Mozaffari F., Lohi A., Assessment of bi-disperse solid particles mixing in a horizontal paddle mixer through experiments and DEM, Powder Technology, 381 (2021) 129–140. DOI: 10.1016/j.powtec.2020.11.041

Forterre Y., Pouliquen O., Flows of dense granular media, Annual Review of Fluid Mechanics, 40 (2008) 1–24. DOI: 10.1146/annurev.fluid.40.111406.102142

Gao W., Liu L., Liao Z., Chen S., Zang M., Tan Y., Discrete element analysis of the particle mixing performance in a ribbon mixer with a double U-shaped vessel, Granular Matter, 21 (2019) 12. DOI: 10.1007/s10035-018-0864-4

Ghadiri M., Pasha M., Nan W., Hare C., Vivacqua V., Zafar U., Nezamabadi S., Lopez A., Pasha M., Nadimi S., Cohesive powder flow: trends and challenges in characterisation and analysis, KONA Powder and Particle Journal, 37 (2020) 3–18. DOI: 10.14356/kona.2020018

Gijón-Arreortúa I., Tecante A., Mixing time and power consumption during blending of cohesive food powders with a horizontal helical double-ribbon impeller, Journal of Food Engineering, 149 (2015) 144–152. DOI: 10.1016/j.jfoodeng.2014.10.013

Halidan M., Chandratilleke G.R., Dong K., Yu A., The effect of interparticle cohesion on powder mixing in a ribbon mixer, AIChE Journal, 62 (2016) 1023–1037. DOI: 10.1002/aic.15101

Halidan M., Chandratilleke G.R., Dong K., Yu A., Mixing performance of ribbon mixers: effects of operational parameters, Powder Technology, 325 (2018) 92–106. DOI: 10.1016/j.powtec.2017.11.009

He S., Gan J., Pinson D., Yu A., Zhou Z., Particle shape-induced axial segregation of binary mixtures of spheres and ellipsoids in a rotating drum, Chemical Engineering Science, 235 (2021) 116491. DOI: 10.1016/j.ces.2021.116491

Horváth D., Poós T., Tamás K., Modeling the movement of hulled millet in agitated drum dryer with discrete element method, Computers, Electronics in Agriculture, 162 (2019) 254–268. DOI: 10.1016/j.ces.2021.116491

Huang A., Cheng T., Hsu W., Huang C., Kuo H., DEM study of particle segregation in a rotating drum with internal diameter variations, Powder Technology, 378 (2021a) 430–440. DOI: 10.1016/j.powtec.2020.10.019

Huang A., Wang X., Hsu W., Kuo H., Particle segregation in a rotating drum with inner segmentation ring pair, Powder Technology, 394 (2021b) 891–900. DOI: 10.1016/j.powtec.2021.09.015

Huang P., Miao Q., Ding Y., Sang G., Jia M., Research on surface segregation and overall segregation of particles in a rotating drum based on stacked image, Powder Technology, 382 (2021) 162–172. DOI: 10.1016/j.powtec.2020.12.063

Jadidi B., Ebrahimi M., Ein-Mozaffari F., Lohi A., Mixing performance analysis of non-cohesive particles in a double paddle blender using DEM and experiments, Powder Technology, 397 (2022) 117122. DOI: 10.1016/j.powtec.2022.117122

Jiang S., Long X., Ye Y., Liu J., Yang S., Xiao X., Liu S., Experimental research on the motion behavior of particles in a rotating drum based on similarity, Powder Technology, (2021) 117046. DOI: 10.1016/j.powtec.2021.117046

Jin X., DEM study on the mixing behavior of U-shaped ribbon mixers, doctoral thesis, UNSW Sydney, 2022. DOI: 10.26190/unsworks/24134

Kato Y., Kushimoto K., Ishihara S., Kano J., Development of a method for estimating particles mixing curves in short DEM simulation time, Advanced Powder Technology, 33 (2022) 103841. DOI: 10.1016/j.apt.2022.103841

Kumar S., Khatoon S., Yogi J., Verma S.K., Anand A., Experimental investigation of segregation in a rotating drum with non-spherical

particles, Powder Technology, 411 (2022) 117918. DOI: 10.1016/j.powtec.2022.117918

Kuo H., Knight P., Parker D., Seville J., Solids circulation and axial dispersion of cohesionless particles in a V-mixer, Powder Technology, 152 (2005) 133–140. DOI: 10.1016/j.powtec.2004.12.003

Kuo H.-P., Tseng W.-T., Huang A.-N., Controlling of segregation in rotating drums by independent end wall rotations, KONA Powder and Particle Journal, 33 (2016) 239–248. DOI: 10.14356/kona.2016004

Lee S., Henthorn K.H., Particle Technology and Applications, 1st edition, CRC Press, 2012, ISBN: 9780429184949. DOI: 10.1201/b11904

Lemieux M., Léonard G., Doucet J., Leclaire L.-A., Viens F., Chaouki J., Bertrand F., Large-scale numerical investigation of solids mixing in a V-blender using the discrete element method, Powder Technology, 181 (2008) 205–216. DOI: 10.1016/j.powtec.2006.12.009

Li D., Xu X., Chen J., Yang K., Liu X., Yang L., Numerical study on the effect of drum on the flow behavior of binary-size particles in rotating drums, Powder Technology, 386 (2021) 108–119. DOI: 10.1016/j.powtec.2021.03.013

Li M., Wu Y., Qian Y., An X., Li H., DEM simulation on mixing characteristics and macroscopic/microscopic flow behaviors of different-shaped sphero-cylinders in a rotating drum, Industrial & Engineering Chemistry Research, 60 (2021) 8874–8887. DOI: 10.1021/acs.iecr.1c00962

Li R., Xiu W., Liu B., Zheng G., Yang H., Velocity distribution of rice particles in a rotating drum, Powder Technology, 386 (2021) 394–398. DOI: 10.1016/j.powtec.2021.03.050

Liao C.-C., Huang Y.-Y., Experimental investigate the effect of liquid distribution state on size segregation of wet granular materials in rotating drums, Powder Technology, 381 (2021) 561–566. DOI: 10.1016/j.powtec.2020.12.032

Liao C.-C., Ou S.-F., Chen S.-L., Chen Y.-R., Influences of fine powder on dynamic properties and density segregation in a rotating drum, Advanced Powder Technology, 31 (2020) 1702–1707. DOI: 10.1016/j.apt.2020.02.006

Liao C.-C., Tsai C.-C., Behavior of density-induced segregation with multi-density granular materials in a thin rotating drum, Granular Matter, 22 (2020) 65. DOI: 10.1007/s10035-020-01034-w

Liu B., Wang Q., Zhou Z., Zou R., Influence of baffles on mixing and heat transfer characteristics in an internally heated rotating drum, Powder Technology, 398 (2022) 117129. DOI: 10.1016/j.powtec.2022.117129

Ma H., Zhao Y., Modelling of the flow of ellipsoidal particles in a horizontal rotating drum based on DEM simulation, Chemical Engineering Science, 172 (2017) 636–651. DOI: 10.1016/j.ces.2017.07.017

Marigo M., Stitt E.H., Discrete element method (DEM) for industrial applications: comments on calibration and validation for the modelling of cylindrical pellets, KONA Powder and Particle Journal, 32 (2015) 236–252. DOI: 10.14356/kona.2015016

MArczuk A., Caban J., Savinykh P., Turubanov N., Zyryanov D., Maintenance research of a horizontal ribbon mixer, Eksploatacja i Niezawodność, 19 (2017) 121–125. DOI: 10.17531/ein.2017.1.17

Miao Q., Huang P., Ding Y., Guo J., Jia M., Particle mixing and segregation behaviors in the rotating drums with adjacent axial segmentations in different speed directions, Powder Technology, (2022) 117534. DOI: 10.1016/j.powtec.2022.117534

Mori Y., Sakai M., Advanced DEM simulation on powder mixing for ellipsoidal particles in an industrial mixer, Chemical Engineering Journal, 429 (2022) 132415. DOI: 10.1016/j.cej.2021.132415

Musha H., Dong K., Chandratilleke G.R., Bridgwater J., Yu A., Mixing behavior of cohesive and non-cohesive particle mixtures in a ribbon mixer, AIP Conference Proceedings, 1542 (2013) 731–734. DOI: 10.1063/1.4812035

Muzzio F.J., Llusa M., Goodridge C.L., Duong N.-H., Shen E., Evaluating the mixing performance of a ribbon blender, Powder Technology, 186 (2008) 247–254. DOI: 10.1016/j.powtec.2007.12.013

Nijssen T.M., van Dijk M.A., Kuipers H.A., van der Stel J., Adema A.T., Buist K.A., Experiments on floating bed rotating drums using magnetic particle tracking, AIChE journal, 68 (2022) e17627. DOI: 10.1002/aic.17627

Ottino J., Khakhar D., Mixing and segregation of granular materials, Annual Review of Fluid Mechanics, 32 (2000) 55–91. DOI: 10.1146/annurev.fluid.32.1.55

Page M.J., Lourenço A.L., David T., LeBeau A.M., Cattaruzza F., Castro H.C., VanBrocklin H.F., Coughlin S.R., Craik C.S., Non-invasive imaging and cellular tracking of pulmonary emboli by near-infrared fluorescence and positron-emission tomography, Nature Communications, 6 (2015) 8448. DOI: 10.1038/ncomms9448

Pasha M., Hassanpour A., Ahmadian H., Tan H., Bayly A., Ghadiri M., A comparative analysis of particle tracking in a mixer by discrete element method and positron emission particle tracking, Powder Technology, 270 (2015) 569–574. DOI: 10.1016/j.powtec.2014.09.007

Rahmanian N., Ng B., Hassanpour A., Ding Y., Antony J., Jia X., Ghadiri M., van der Wel P., Krug-Polman A., York D., Bayly A., Tan H.S., Scale-up of high-shear mixer granulators, KONA Powder and Particle Journal, 26 (2008) 190–204. DOI: 10.14356/kona.2008017

Ren X., Xu J., Qi H., Cui L., Ge W., Li J., GPU-based discrete element simulation on a tote blender for performance improvement, Powder Technology, 239 (2013) 348–357. DOI: 10.1016/j.powtec.2013.02.019

Rhodes M.J., Introduction to Particle Technology, John Wiley & Sons, 2008, ISBN: 9780470014271. DOI: 10.1002/9780470727102

Rong W., Feng Y., Schwarz P., Yurata T., Witt P., Li B., Song T., Zhou J., Sensitivity analysis of particle contact parameters for DEM simulation in a rotating drum using response surface methodology, Powder Technology, 362 (2020) 604–614. DOI: 10.1016/j.powtec.2019.12.004

Sakai M., How should the discrete element method be applied in industrial systems?: a review, KONA Powder and Particle Journal, 33 (2016) 169–178. DOI: 10.14356/kona.2016023

Sakai M., Mori Y., Sun X., Takabatake K., Recent progress on mesh-free particle methods for simulations of multi-phase flows: a review, KONA Powder and Particle Journal, 37 (2020) 132–144. DOI: 10.14356/kona.2020017

Santomaso A., Olivi M., Canu P., Mechanisms of mixing of granular materials in drum mixers under rolling regime, Chemical Engineering Science, 59 (2004) 3269–3280. DOI: 10.1016/j.ces.2004.04.026

Sarkar A., Wassgren C.R., Effect of particle size on flow and mixing in a bladed granular mixer, AIChE journal, 61 (2015) 46–57. DOI: 10.1002/aic.14629

Shenoy P., Viau M., Tammel K., Innings F., Fitzpatrick J., Ahrné L., Effect of powder densities, particle size and shape on mixture quality of binary food powder mixtures, Powder Technology, 272 (2015) 165–172. DOI: 10.1016/j.powtec.2014.11.023

Silveira J.C., Lima R.M., Brandao R.J., Duarte C.R., Barrozo M.A., A study of the design and arrangement of flights in a rotary drum, Powder Technology, 395 (2022) 195–206. DOI: 10.1016/j.powtec.2021.09.043

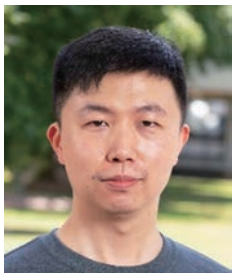
Tahvildarian P., Ein-Mozaffari F., Upreti S.R., Circulation intensity and axial dispersion of non-cohesive solid particles in a V-blender via DEM simulation, Particuology, 11 (2013) 619–626. DOI: 10.1016/j.partic.2012.12.010

Tanabe S., Gopireddy S.R., Minami H., Ando S., Urbanetz N.A., Scherließ R., Influence of particle size and blender size on blending performance of bi-component granular mixing: a DEM and experimental study, European Journal of Pharmaceutical Sciences, 134 (2019) 205–218. DOI: 10.1016/j.ejps.2019.04.024

Tsugeno Y., Sakai M., Yamazaki S., Nishinomiya T., DEM simulation for optimal design of powder mixing in a ribbon mixer, Advanced Powder Technology, 32 (2021) 1735–1749. DOI: 10.1016/j.apt.2021.

03.026
Volpato S., Scanferla L., Santomaso A., Experimental and computational investigation of segregation during tumblers unloading, Powder Technology, 338 (2018) 538–547. DOI: 10.1016/j.powtec.2018.07.066
Wang S., Zhou Z., Ji S., Radial segregation of a gaussian-dispersed mixture of superquadric particles in a horizontal rotating drum, Powder Technology, 394 (2021) 813–824. DOI: 10.1016/j.powtec.2021.09.012
Wu W., Chen K., Tsotsas E., Prediction of particle mixing time in a rotary drum by 2D DEM simulations and cross-correlation, Advanced Powder Technology, 33 (2022) 103512. DOI: 10.1016/j.apt.2022.103512
Xiao X., Li Y., Peng R., Gao J., Hu C., Parameter calibration and mixing uniformity of irregular gravel materials in a rotating drum, Powder Technology, 414 (2023) 118074. DOI: 10.1016/j.powtec.2022.118074
Xu G., Zhang Y., Yang X., Chen G., Jin B., Effect of drum structure on particle mixing behavior based on DEM method, Particuology, 74 (2023) 74–91. DOI: 10.1016/j.partic.2022.05.008
Yamamoto M., Ishihara S., Kano J., Evaluation of particle density effect for mixing behavior in a rotating drum mixer by DEM simulation, Advanced Powder Technology, 27 (2016) 864–870. DOI: 10.1016/j.apt.2015.12.013
Yang S., Cahyadi A., Wang J., Chew J.W., DEM study of granular flow characteristics in the active and passive regions of a three-dimensional rotating drum, AIChE journal, 62 (2016) 3874–3888. DOI: 10.1002/aic.15315
Yaraghi A., Ebrahimi M., Ein-Mozaffari F., Lohi A., Mixing assessment of non-cohesive particles in a paddle mixer through experiments and discrete element method (DEM), Advanced Powder Technology, 29 (2018) 2693–2706. DOI: 10.1016/j.apt.2018.07.019
Yazdani E., Hashemabadi S.H., The influence of cohesiveness on particulate bed segregation and mixing in rotating drum using DEM, Physica A: Statistical Mechanics its Applications, 525 (2019) 788–797. DOI: 10.1016/j.physa.2019.03.127
Yeow S.T., Shahar A., Aziz N.A., Anuar M.S., Yusof Y.A., Taip F.S., The influence of operational parameters and feed preparation in a convective batch ribbon powder mixer, Drug Design, Development and Therapy, 5 (2011) 465–469. DOI: 10.2147/DDDT.S25047
Yu M., Zhang H., Guo J., Zhang J., Han Y., Three-dimensional DEM simulation of polydisperse particle flow in rolling mode rotating drum, Powder Technology, 396 (2022) 626–636. DOI: 10.1016/j.powtec.2021.10.058
Zhang L., Jiang Z., Mellmann J., Weigler F., Herz F., Bück A., Tsotsas E., Influence of the number of flights on the dilute phase ratio in flighted rotating drums by PTV measurements and DEM simulations, Particuology, 56 (2021) 171–182. DOI: 10.1016/j.partic.2020.09.010
Zhang L., Jiang Z., Weigler F., Herz F., Mellmann J., Tsotsas E., PTV measurement and DEM simulation of the particle motion in a flighted rotating drum, Powder Technology, 363 (2020) 23–37. DOI: 10.1016/j.powtec.2019.12.035
Zhang L., Weigler F., Idakiev V., Jiang Z., Mörl L., Mellmann J., Tsotsas E., Experimental study of the particle motion in flighted rotating drums by means of Magnetic Particle Tracking, Powder Technology, 339 (2018) 817–826. DOI: 10.1016/j.powtec.2018.08.057

Authors' Short Biographies



Xin Jin

Dr Jin is a Postdoctoral fellow in Prof. Yansong Shen's lab in the Department of Chemical Engineering at the University of New South Wales. He received a PhD in Chemical Engineering in 2022 from the same university. His research interests include the numerical simulation and process optimisation of industrial mixing and segregation systems.



Yansong Shen

Yansong Shen is a full Professor (tenured) and ARC Future Fellow (A/Prof, 2019–2021, Senior Lecturer, 2016–2018, UNSW; Lecturer, 2014–2016, Monash). He is the director of a vibrant research lab - Process Modelling and Optimisation of Reacting Flows "ProMO Lab" (www.promo.unsw.edu.au), with applications to a range of complex reactive flow processes in traditional and emerging industries particularly resource and energy sectors, including process metallurgy, solid fuel preparation/utilisation, water treatment, recycling processes of e.g. solar panels, plastic, and renewable energy processes e.g. solar cell/biomass/hydrogen. His research interests range from understanding fundamentals to optimising & developing new, cleaner and more efficient technologies, powered by advanced numerical and experimental approaches. He is a member of the editorial boards of "Advanced Powder Technology" and "Metallurgical and Materials Transactions B".

KONA Powder and Particle Journal

KONA Powder and Particle Journal No. 41 (2024) 172–182/https://doi.org/10.14356/kona.2024001 Review Paper

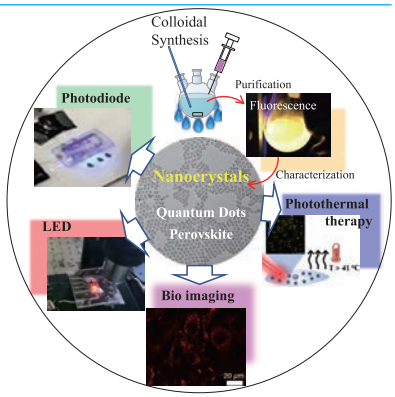
Recent Progress in Controlled Nanostructure of Colloidal Nanocrystal Powders for Efficient Light Emission†

Naoto Shirahata

[1] *Research Center for Materials Nanoarchitectonics (MANA), National Institute for Materials Science (NIMS), Japan*
[2] *Graduate School of Chemical Sciences and Engineering, Hokkaido University, Japan*
[3] *Department of Physics, Chuo University, Japan*
[4] *CNRS–Saint-Gobain–NIMS, IRL3629, Laboratory for Innovative Key Materials and Structures, Japan*

The application of semiconductor nanocrystals containing cadmium, lead, selenium and mercury as constituent elements is strictly limited by concerns about environmental pollution and health effects. Nanocrystals free of these toxic elements are being pushed to the forefront of nanocrystal research because of their environmentally friendly advantages and attractive photophysical properties on recent advances in colloidal synthesis, excellent optical properties, optoelectronic device applications, and biological applications of these environmentally friendly fluorescent nanocrystals. In this context, the first topic in this review paper introduces group IV semiconductors. In particular, the unique light emitting properties generated in silicon nanocrystals of diameters smaller than bulk exciton Bohr radius are highlighted. Next the topic turns to the nanocrystals of group III–V semiconductors. After that, attentions are paid to the lead-free perovskite nanocrystals such as tin-based halide perovskite and double perovskite structures. Recent efforts on how to control nanostructures to enhance photoluminescence quantum yields is highlighted for each semiconductor nanocrystal. Finally, the remaining challenges that must be overcome to realize nontoxic optoelectronic devices will be discussed.

Keywords: quantum dot, perovskite nanocrystals, photoluminescence, optoelectronics, bioimaging, photothermal effect



1. Introduction

Colloidal semiconductor nanocrystals have attracted huge interests over 30 years. The nanocrystals contain hundreds to thousands of atoms and are covered with organic molecules (i.e., ligands) to make them stabilize in solution (Calvin et al., 2022), providing high accessibility to printable technology. They are called "quantum dots (QDs)", "artificial atoms" or "zero-dimensional quantum boxes". The effect of quantum confinement happens for the nanocrystals of diameter smaller than the bulk exciton Bohr radius for the bulk crystal. QDs are usually larger than the conventional organic dyes but comparable to fluorescent proteins and other large biomolecules. Their optical properties are unique and can be adjusted with diameter, chemical composition, shape, and surface state. Therefore, the QDs as optically active sources have a strong potential for use in a variety of optoelectronic applications including light-emitting diodes, photodiodes and photovoltaics as well as in biomedical detection such as fluorescence cellular imaging. In a typical, a single QD contains atoms of group IV elements (e.g., Si, C or Ge), group II–VI elements (e.g., CdS, CdSe, CdTe, ZnS, ZnSe or ZnTe), group III–V elements (e.g., InP, InSb or InAs), group I–III–VI_2 elements (e.g., $CuInS_2$, $CuInSe_2$, $AgInS_2$ or $AgInSe_2$), group IV–VI elements (e.g., PbS, PbSe or PbTe), ZnS–$AgInS_2$ (ZAIS) or $AgInSe_2$–ZnSe (ZAISe). The QD as a core could be often encapsuled with additional protective shells of ZnS and/or ZnSe, which are well-known wide-band-gap semiconductors, to form core/shell structures.

Metal-halide perovskite nanocrystals are optically active materials whose chemical compositions and structural spaces are constantly expanding for successive tuning of optical absorption and emission spectra. Lead halide perovskite has emerged as an attractive semiconductor material due to its excellent optical and electronic properties and is expected to find applications in a wide range of optoelectronic fields, including light-emitting diodes (LEDs). Until now, many efforts have been made to increase photoluminescence quantum yield (PLQY) to nearly 100 % in the visible and near-infrared regions by optimizing synthesis parameters, impurity doping, alloying and surface passivation (Chen et al., 2021a). Various high-performance optoelectronic devices with the lead perovskite nanocrystals as active layers have been investigated by taking advantage of these excellent properties (Quan et al., 2019). Thus, the

† Received 25 July 2022; Accepted 19 October 2022
J-STAGE Advance published online 29 December 2022
[1, 4] Add: 1-1 Namiki, Tsukuba, Ibaraki 305-0044, Japan
[2] Add: Kita 13, Nishi 8, Kita-ku, Sapporo 060-0814, Japan
[3] Add: 1-13-27 Kasuga, Bunkyo, Tokyo 112-8551, Japan
E-mail: SHIRAHATA.Naoto@nims.go.jp
TEL: +81-29-859-2743 FAX: +81-29-859-2401

Copyright © 2024 The Author. Published by Hosokawa Powder Technology Foundation. This is an open access article under the CC BY license (https://creativecommons.org/licenses/by/4.0/).

lead halide perovskite nanocrystals are expected to be the next generation of light emitting devices, and the external quantum efficiency of lead-based LEDs exceeds 20 % (Lin et al., 2018). There are concerns of environmental pollution and health problems due to the toxicity of Pb. Recent studies have shown that the bioavailability of lead from lead halide perovskite is stronger than other sources of lead and that as the concentration of lead halide perovskite in plants increases, the capacity for lead uptake increases (Li et al., 2020). To overcome this short coming, lead-free perovskite nanocrystals such as tin halide perovskite or double perovskite nanostructures have attracted attention over the years. However, the luminescence performances of the lead-free perovskite nanocrystals currently far inferior to the lead perovskite ones.

Controlling the fate of free-charge carriers generated in nanocrystals of semiconductor through sequential absorption of photons in the photoexcited state determines optical performance (Chen et al., 2021b). For example, radiative recombination between electrons and holes should be strengthened to increase the PLQY. Furthermore, defective surface serving as electron trapper should be removed to decrease the nonradiative recombination rate (Ghosh et al., 2020). On the other hand, the formation of shallow energy level is key to synthesize long persistent phosphors, which are a class of optical batteries, allowing emission of luminescence continuously for a long time after the removal of excitation sources (Liu Q. et al., 2021a). In this review, recent efforts on defect control to improve PLQY of typical non-toxic nanocrystals for optical applications such as light-emitting diodes with emission layer of QD (QLED), namely, electrically driven luminescent (EL) devices will be presented.

2. Group IV QDs

QDs in group IV semiconductors such as carbon, silicon (Si), and germanium have attracted attention in the applications of abundant and nontoxic fluorescence materials, with an emphasis on their role in optoelectronics and nanomedicine. This chapter presents the research advances in fluorescent SiQD on controlled nanostructures giving a strong light emission and various photonic applications such as light-emitting diodes, biomarkers for cellular imaging and photothermal therapy of cancer cells.

2.1 Improved PLQYs

Bulk Si crystal has an indirect band structure, which results in very low PLQY (<10^{-4} %). However, the situation changes drastically when crystals are nanosized to nanoparticles of 5 nm or less in diameter. In the electronic structure of 2–5 nm crystals, the quantum confinement effect of photoexcited carriers relaxes the momentum conservation based on the uncertainty principle ($\Delta\chi\Delta\rho \geq \hbar/2$) and interface scattering-induced Γ–X coupling, leading to the zero-phonon optical interband transitions (Lee et al., 2016). In the 1.1–1.7 nm crystal size range, a diamond cubic crystalline Si can behave like a molecule in terms of energy structure (Shirahata et al., 2020). The most conventional Si surface is terminated with hydrogen atoms (H-SiQD) as known from the wafer chemistry (Shirahata et al., 2005). Photoluminescence (PL) properties are dependent of the size of diamond cubic nanocrystal of Si. First, the peak position of the PL spectrum depends on the size of the H-SiQD and can be modulated over a wide wavelength range of 530–1050 nm as shown in **Fig. 1(a)–(c)**. Second, the PLQYs monotonically increase with decrease in size of H-SiQD based on the quantum confinement effect (see **Fig. 1(d)**). PL peak positions at 1050 nm for the 5-nm diameter SiQD and does not shift to a longer wavelength side anymore for the diameter range between 5 and 8 nm. The hydrogen atoms may cover 99 % of the Si atoms in the outermost layer. In the oxidized SiQD,

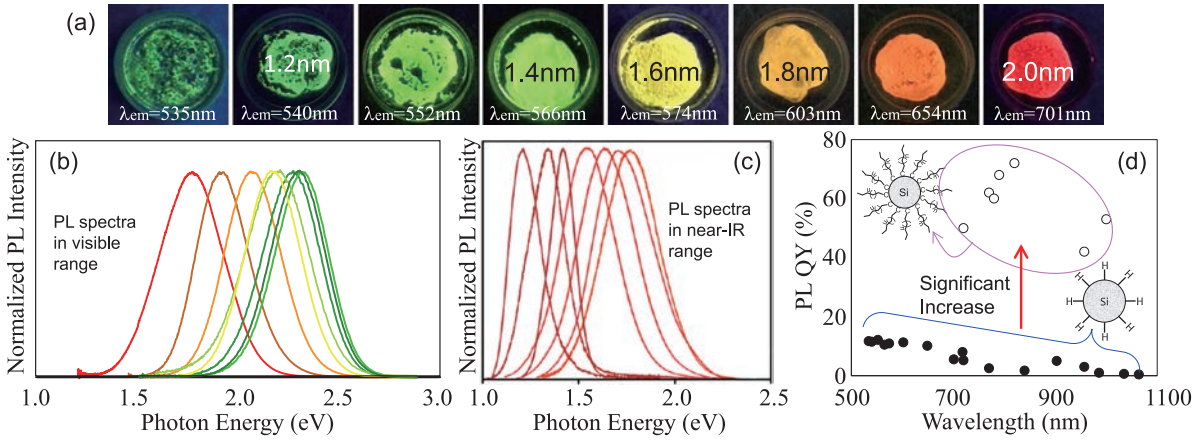


Fig. 1 Optical properties of SiQD powders: **(a)** photographs of visible-light emitting H-SiQD powders excited at UV light (λ = 365 nm), **(b)** PL spectra of the H-SiQD powders listed in the Panel **(a)**, **(c)** near-infrared PL spectra of the H-SiQDs excited at UV light (λ = 365 nm), **(d)** PLQYs of the H-SiQDs before and after hydrosilylation of 1-decene. The PL spectral tuning could be realized by controlling diameters of SiQDs in the 1–5 nm range. Adapted with permission from Ref. (Shirahata et al., 2020). Copyright 2020, American Chemical Society.

the electron-hole recombination involves O-related defect centers (Dohnalová et al., 2013). In contrast, the hydrogen termination minimizes surface oxidation that forms SiO*x*. Nevertheless, the resultant PLQYs are still less than 15 % as shown in **Fig. 1(d)**. A significant increase in PLQY is realized by replacement of surface hydrogen atom with alkyl monolayer through the hydrosilylation reaction (see **Fig. 1(d)**). The best value of PLQY is more than 73 % for the near-infrared light emitting QD (Jurbergs et al., 2006). Two possible mechanisms have been proposed to explain the improved PLQY. Dohnalová et al. reported the theoretical study of the change in radiation rate and recombination process due to the attachment of alkyl monolayers, which switches SiQD from an indirect-bandgap-like material to a direct-one, leading to the phonon-less character of excitonic recombination close to band edges (Poddubny and Dohnalová, 2014). The increase in radiative recombination rate resulting from the alkylation of surface Si atoms has also been reported (Mastronardi et al., 2012), consistent with the theoretical prediction (Lee et al., 2016). Furthermore, alkyl monolayers work to inhibit the formation of defects as a nonradiative channel in the outermost layer of QD. Specifically, combining scanning transmission electron microscopic (STEM) observation with Raman spectroscopy demonstrated that the hydrogenated surface layer is distorted under structural reconstruction to generate an amorphous phase (Ghosh et al., 2016), whereas the passivation with alkyl monolayers suppresses the surface reconstruction to hold a bulk-like geometry (i.e., a diamond cubic lattice structure) in a broad range from the center toward the near-surface in QD (Ghosh et al., 2018a). The amorphous region might have many dangling bonds as a nonradiative relaxation channel, resulting in a low PLQY, but there are few defects around the surface terminated with alkyl monolayers. This suggests that the passivation with alkyl monolayers works to prevent any undesired surface reconstruction, leading to high PLQY.

2.2 Optoelectronic devices

The tremendous improvement in PLQY has attracted interests of scientists and encouraged the fabrication of devices such as current-driven QLEDs in which alkyl terminated SiQD works as an active layer. The reported device architectures have a multilayer structure where SiQD are sandwiched between hole and electron transportation layers as shown in **Fig. 2(a)–(c)**. The electroluminescence (EL) signals are observed under low applied voltage. **Fig. 2(d)–(f)** demonstrates that the EL spectral peak shape and broadness are similar with those of PL spectra. Besides, the photocurrent depends on applied voltage, leading to the increase of luminance at high device current density. The EL spectral peak position precisely tuned by diameter of SiQD. To date, the highest values of external quantum efficiency (EQE) at present were 4.8 %, 8.6 %, 3.36 %, 6.2 %, for the EL spectral peaking at 1000 nm (Watanabe et al., 2021), 853 nm (Cheng et al., 2011), 755 nm (Yamada et al., 2020), 720 nm (Ghosh et al., 2018), 700 nm (Liu X. et al., 2018), respectively. The EQEs of EL spectra peaking at the wavelength shorter than 700 nm are less than 1.2 % (Yamada et al., 2020). These values are still lower than

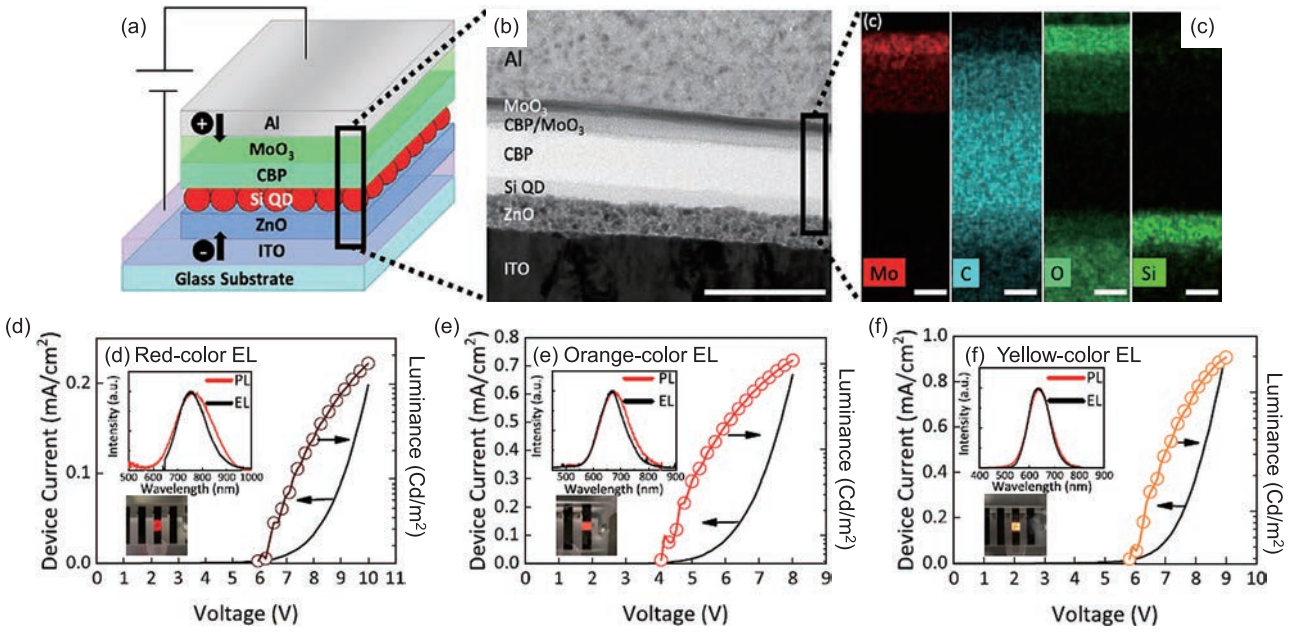


Fig. 2 **(a)** Schematic representation, **(b)** a cross-sectional TEM image with **(c)** EDS maps of the area indicated in the image **(b)** of the Si-QLED. Scale bars are 200 nm for the image **(b)** and 20 nm for the image **(c)**. **(d–f)** Device current-voltage and luminance-voltage characteristics for each QLED. Inset figure shows comparison of EL and PL spectra and photograph demonstrates a representative EL emission during operation. Adapted with permission from Ref. (Yamada et al., 2020). Copyright 2020, American Chemical Society.

20 % which is commonly employed as a benchmark. Further improved EQE requires both improvement of carrier mobility and charge balance (Watanabe et al., 2021).

By taking advantage of the large Stokes shift between optical absorption and emission derived from SiQDs, a white-light EL is realized with a superimposed spectrum of a red EL peak and a blue–green EL peak without loss of optical energy (Ghosh et al., 2014). The high PLQYs are realized by various method such as nonthermal plasma (Kortshagen et al., 2016), annealing of Si-rich borophosphosilicate (Kano et al., 2018) and thermal disproportionation of hydrogen silsesquioxane (Dasog et al., 2016) or silicon monoxide (Sun et al., 2015). Hydrogen silsesquioxane are commercially available from Dow Corning Corporation (trade name FOx-17) but could be synthesized by hydrolysis and condensation of triethoxysilane (Chandra et al., 2017) or trichlorosilane (Sun et al., 2016).

2.3 Bio imaging and analysis

Inherently nontoxic element such as Si is expected to use for fluorescence labeling of cells or tissues. Wang et al. reported the first ever biomedical use of SiQDs as a fluorescence label for DNA (Wang et al., 2004). Since then, many papers have been reported on modifying the surface of QDs to give them water solubility (Xu et al., 2016). Swihart et al. further studied the labeling of cells with SiQDs and found that SiQDs can be used for in vivo imaging (Erogbogbo et al., 2010). Si as an element shows cell cytotoxicity but the toxicity is strongly influenced by surface terminal groups (Ruizendaal et al., 2009). Specifically, amine-terminated surfaces are known to have low cell viability, while carboxyl-terminated surfaces are less toxic to cells than amine-terminated ones, since most living cells are negatively charged. In many cases, amphiphilic molecules such as Pluronic F127 or PEG are employed to encapsulate the core of SiQDs because the PEGylated surface is electronically neutralized due to hydroxyl groups exposed on the QD surface (Chinnathambi et al., 2019) resulting in high hydrophilicity and biocompatibility (Hessel et al., 2010). Such a biologically inert surface demonstrates a potential for medical diagnosis without major conformational change of human blood plasma proteins in the bloodstream (Chinnathambi et al., 2020). Thus, water-soluble SiQDs have the potential to be used as fluorescent labeling materials for cells and tissues due to their low cytotoxicity, but there are still challenging topics in terms of optical properties. Specifically, PL spectra are dependent of QD size in the near-infrared (NIR) wavelength range, but SiQDs exhibit low absorption efficiency for NIR light. Therefore, it is difficult to realize NIR–NIR excitation-emission bioimaging in a single-photon excitation environment. There are two methods to overcome this difficulty. First one is the fluorescence imaging under multiphoton excitation conditions (He et al., 2008). The first multiphoton-excited fluorescence imaging of cells labeled with SiQD was reported in 2016 (Chandra et al., 2016). Second one takes advantage of long radiative decay time (~μs scale) originating from energy structure of SiQD. That is, the time-gated fluorescence imaging in the NIR wavelength range was investigated for the observation of biological tissues labeled with SiQDs (Sakiyama et al., 2018).

The Si surface exhibits high chemical affinity for covalent bonding with carbon, oxygen, and nitrogen, and can produce a variety of organic derivatives hybridized at the molecular level (Shirahata, 2011). Their bonding ability can be used for post-synthesis purification by gel permeation chromatography (Shirahata et al., 2010). During purification, QDs can be separated according to differences in PLQY (Watanabe et al., 2021).

2.4 Photothermal effect

The photothermal effect refers to the ability to convert photon energy from light absorption into heat. Thermal conversion by photoexcited nanostructures can take place by different mechanisms depending on the nature of the material. Unlike metallic nanoparticles, for semiconductor QDs, photothermal conversion is explained by excess carriers undergoing nonradiative recombination, which is enhanced by maximizing the nonradiative decay rates and manipulating nonradiative channels. Controlling the heat of the QDs expands their availability for applications including phototheranostics and photoacoustic bioimaging. The photothermal responses of crystalline Si have been investigated for various forms, including nanoribbons, nanowires, films, porous particles, and nanoparticles. Multiple structural parameters such as size, surface configuration, and shape affect the photothermal response, but size is the most influential parameter. The temperature trend for larger crystals is explained by the Mie resonances (Ishii et al., 2016). As shown in **Fig. 3(a)**, the photothermal response was dependent of size of QD even in the narrow range of 2–5 nm because the presence of a relatively high density of defect states for nonradiative thermal dissipation for larger QDs (Özbilgin et al., 2021). The photothermal conversion efficiency values of SiQDs are dependent of their sizes and estimated to be 25–37 % which are comparable to the nanoparticles of mesoporous Si (33.6 %), Au (13–21 %), CuSe (21 %) Fe/Fe_3O_4 (20.3 %), black phosphorus (24.8 %), Bi_2S_3 (28.1 %) or CdTe (14 %), suggesting a potential of SiQD available in photothermal applications. One example is demonstrated in the thermotherapeutic study where carboxy-terminated SiQDs internalized in the HeLa cell generates the heat to kill the cells under laser irradiation (Özbilgin et al., 2022). **Fig. 3(b)** shows the fluorescence image of HeLa cells labeled with the water-soluble red-light-emitting SiQDs, confirming the cellular internalization of the QDs. Furthermore, there is no

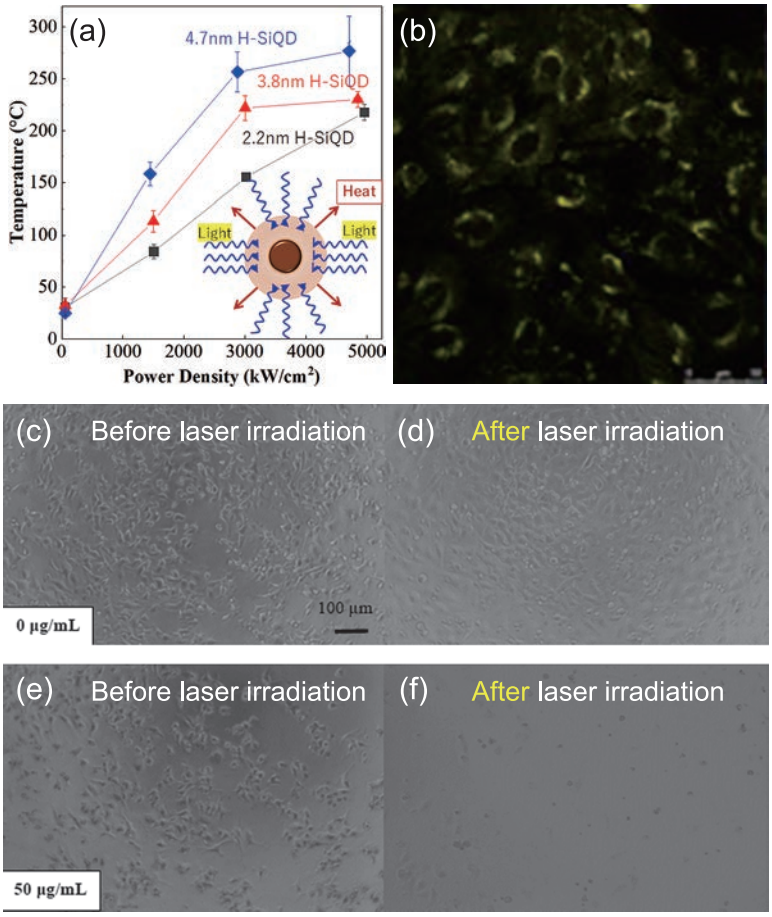


Fig. 3 **(a)** Summary of temperature rise traces of SiQDs of different sizes and forms as a function of incident green-laser power. **(b)** HeLa cellular uptake of QDs terminated with undecanoic acid under confocal fluorescence microscopy. **(c–f)** Observation of HeLa cells before and after laser irradiation: **(c, d)** HeLa cells without QDs and **(e, f)** HeLa cells with 50 μg/mL QDs. Adapted with permission from Ref. (Özbilgin et al., 2022). Copyright 2022, American Chemical Society.

significant change in cell morphology. **Fig. 3(c)** and **3(d)** show the differential interference contrast (DIC) image where HeLa cells are observed throughout the microscope field of view. Without QDs, the cells remained the same even after laser irradiation as shown in **Fig. 3(d)**. However, there was a noticeable decrease in the number of cells observed for the irradiated cells in which the QDs with even the concentration as low as 50 μg/mL are internalized. As evidenced in **Fig. 3(f)**, the HeLa cells that take up the QDs detached from the glass substrate. A few cells remaining on the glass surface have also changed their morphology to round and have lost their adhesive ability. This result indicates that QDs can be effectively used for photothermal therapy. Controlling the nonradiative channels allows surgeons and medical/healthcare professions to manipulate the photothermal heating in a relatively lower temperature range, contributing to the development of therapeutic thermal phononics.

3. Group III–V QDs

Group III–V semiconductors are compounds formed between group III and group V of the periodic table and contain InN, GaN, GaAs, InP, InAs and InSb. Group III–V semiconductor devices are used as high electron mobility transistors due to their high electron mobility and electron density, which are essential for high-speed device operation. For example, InN is a semiconductor with a narrow band gap of about 0.7 eV at room temperature. When combined with gallium to make the ternary alloy InGaN, the band gap is tuned in the range of 0.7–3.4 eV, covering the infrared to the UV. GaN offers a wide energy bandgap and attract the development of nitride based blue LEDs and ultraviolet laser diodes. Bulk crystal of InP has a 1.35 eV of bandgap at room temperature, and its bulk exciton Bohr radius and exciton binding energy are 11 nm and 6 meV, respectively. Therefore, QD of InP crystal has attracted attention for the spectral tunability of the emission and the first exciton peak of absorption in a wide visible wavelength range. This chapter describe recent strategies for structural control of InP QDs to obtain high PLQY for optoelectronic applications.

3.1 Improved PLQYs

To improve PL performance, it is necessary to eliminate

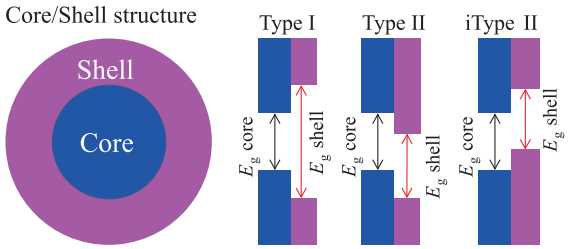


Fig. 4 Types of Core/Shell energy structure.

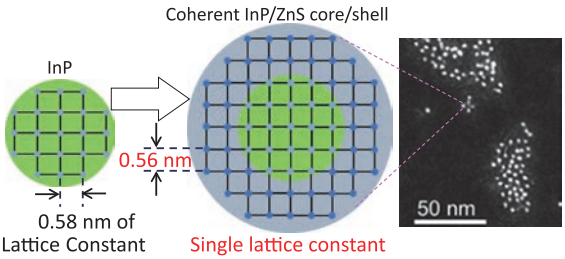


Fig. 5 Illustration and HAADF-STEM image of InP/ZnS QDs of coherent core/shell structure with a single lattice parameter of 0.56 nm. Adapted with permission from Ref. (Nemoto et al., 2022). Copyright 2022, Royal Society of Chemistry.

surface defects, which work as nonradiative exciton recombination centers (Coughlan et al., 2017). In a typical, a semiconductor core/shell structure is employed to reduce defects such as electron traps at the interface as depicted in **Fig. 4** (Reiss et al., 2009). A core QD (e.g., indium phosphide, InP) is encapsulated by another semiconductor shell whose band gap (E_g) is large enough for sandwiching that of the core QD. Such a core/shell heterostructure is referred to as a Type I band alignment. In this configuration, excitons are spatially confined to the core, minimizing their interaction with surface states, and preventing their diffusion throughout the core/shell QD due to high energy barrier of shell E_g (Tamang et al., 2016). This confinement strength allows for enhanced radiative recombination rates and high PLQY. A good example of Type I architecture is InP/ZnSe/ZnS core/shell/shell structure. In the bulk state, direct deposition of ZnS (lattice constant, a_{ZnS} = 0.541 nm) on InP (a_{InP} = 0.587 nm) results in a large lattice mismatch of 7.8 %, sufficient to cause defect formation at the heterogeneous core/shell interface and relaxation of the mismatch by lattice distortion is no longer thermodynamically feasible because of lattice mismatch relaxation. There are three approaches to solve this problem. First is to use the ZnSe (a_{ZnSe} = 0.566 nm) as the shell material; the lattice mismatch (≤3.5 %) between ZnSe and InP is reduced compared to the case of ZnS, so an energy-graded core/shell interface is constructed, and defect generation is suppressed. As a result, PLQY is significantly enhanced up to unity (Wu et al., 2020). Second, multielement alloying for the core (e.g., In_xZn_yP) is effective to mediate the lattice strain at the heterogeneous core/shell interface, leading to the improved PLQY. As expected, the strategy of alloying core has inspired the concept of compositional alloying between Se and S or Mg and Zn for shell materials (Lim et al., 2013). In the InP/GaP/ZnS core/shell/shell system, the strain energy that would have been induced at the interface between the inner shell and core is relaxed by cation exchange. During high-temperature synthesis for shell formation, Ga^{3+} ions diffuse into the core and are alloyed by replacing In^{3+} ions. This alloying QD achieves a PLQY as high as 80 % by continuously changing the chemical composition and reducing the strain energy at the interface (Srivastava et al., 2018). Third, Nemoto et al. reported an interesting idea of using material strain to build a QD with a coherent core/shell structure (Nemoto et al., 2022). Specifically, the core/shell QD allowed both epitaxial growth of the shell layer and distortion of the spherical core, changing the intrinsic interatomic distance of each crystal for coherency, where the core crystal is elastically compressed, and the shell crystal is stretched by lattice distortion to a lattice constant similar with that of the core. As depicted in **Fig. 5**, the coherent growth of ZnS on a InP core QD yields InP/ZnS core/shell structure with *a single lattice constant* of 0.563 nm. Compared to the bulk crystal of zinc-blend (cubic) InP, the lattice of the core QD is compressed by 4.1 %. In contrast, the lattice of the shell expands by 4.1 % relative to the bulky ZnS crystal throughout the core/shell QD. This could be because the change in lattice constant due to stress is thermodynamically more favorable than the formation of defect trapping sites at the core/shell interface to release strain energy. As expected, PLQY is enhanced up to 70 % and PL spectrum is also as narrow as 36 nm.

3.2 Optoelectronic devices

The first QLED that exceeded the benchmark was reported in winter of 2014 and used CdSe as the active layer of the device, emitting red light (Dai et al., 2014). The second QLED exhibited the green EL with 20 % EQE and had $CsPbBr_3$/MABr quasi-core/shell structure as the active layer (Lin et al., 2018). InP-based QDs as optically active layers are the most promising alternative Cd- and Pb-free QLEDs. Since the innovative work of the first InP-QLED in 2011, intensive efforts have produced visible light emitting QLEDs. Finally, in 2019, Jang et al. reported blue, green, and red emitting QLEDs with 20 % of EQE using InP/ZnSe/ZnS QDs as active layers (Won et al., 2019).

Photoelectrode is also one of the optoelectronic applications. It is expected to realize the wavelength tunability of detected light by taking advantage of size dependence of the first exciton peak in the optical absorption spectrum, but not yet reported before due to possible difficulty in dissociation of photogenerated carriers into electrons and holes. Do-Hyun Kwak et al. reported a phototransistor with a light absorbing layer of InP QD in the hybrid structure of InP QD/black phosphorus. They replaced the oleylamine

on the QD surface with 1,2-ethanedithiol (EDT), which has a shorter alkyl length, by ligand exchange to improve the carrier mobility and enhance device characteristics (Kwak et al., 2019). Under violet-light illumination, the photogenerated electrons from the InP QD layers are quickly transferred to the BP transport layer, resulting in a high photo response of 10^9 A/W and a high detectivity of 4.5×10^{16} Jones.

4. Lead-free perovskite nanocrystals

Lead halide perovskites are increasingly gaining attention for advanced optoelectronic applications due to their excellent optoelectronic properties, but there are two serious concerns for commercial use. First, metallic lead ions are readily soluble in water to cause ecological threats. Second, the current lead perovskite nanocrystals have been found to have low stability to UV irradiation, moisture, and heat. These disadvantages have stimulated the development of research into the colloidal synthesis of lead-free perovskite nanocrystals. This chapter presents recent progress in synthesis methods to enhance the PLQY of lead-free perovskite nanocrystals.

4.1 Cesium tin halide perovskite nanocrystals

Inorganic metal halide perovskites have a general chemical formula ABX_3, where A is a monovalent cation (e.g., cesium, Ce^+), B is a divalent metal ion (typically tin, germanium or copper), and X is a halide anion (Cl^-, Br^-, or I^-). Tin halide perovskite exhibits a band gap of 1.2–1.4 eV, high carrier mobilities, and long carrier diffusion lengths (Pitaro et al., 2022). Therefore, nanocrystals of cesium tin halide perovskite structure (i.e., Cs_2SnX_3) are expected to be a representative of Pb-free perovskite nanocrystals. Owing to a large absorption coefficient and a wide bandgap-tunability between 1.3 and 2.8 eV, Cs_2SnX_3 has a potential of their use in various applications such as photovoltaics, photoelectrode and light-emitting devices (Chen J. K., 2021c). So far, the synthetic development of its nanocrystals lags far behind lead perovskite nanocrystals. As a result, their optical properties are also inferior to those of Pb-based materials; Jellicoe et al. reported that a higher density of trapped states results in lower PLQY (Jellicoe T. C. et al., 2016); Wong et al. pointed that Sn vacancies as the trap states work to lower PLQY (Wong et al., 2018). How to reduce defect density to obtain high PLQY? To answer this conundrum, Sun et al. proposed that precisely adjusting the ratios of starting precursors corresponding to Cs, Sn, and X over a wide range is crucial for suppressing the formation of lattice defects in $CsSnX_3$ nanocrystals because the defect formation energy is closely related to the chemical potential of each component. Wang et al. tuned the molar ratios of precursors in a wide range to suppress the formation of defects contributing to nonradiative charge-carrier recombination and found that addition of the small amount of zwitterionic phosphatidylcholine as a surfactant in the reaction is crucial for controlling the growth rate of the nanocrystals (Wang et al., 2021). According to their experimental study, the growth rate of $CsSnX_3$ nanocrystals was controlled by the formation of an intermediate complex between the zwitterionic phosphatidylcholine and the precursor and the steric hindrance effect of the branched fatty acid side chain of phosphatidylcholine. The resultant nanocrystal exhibited PLQY of 12.5 %.

Great attention has more recently been paid to the colloidal synthesis guiled by theoretical study using machine learning. In this context, Sun et al. investigated the formation energy and the thermodynamical charge-transition levels of typical point defects, as well as the influence of Sn vacancy on the photophysical properties based on density functional theory (DFT) calculations and molecular dynamics (MD) simulations (Liu et al., 2021b). Specifically, the stability regions of different compounds vs. I and Sn chemical potentials of $CsSnI_3$ was calculated at the outset (see **Fig. 6(a)**). The result implied that the defect formation energy of $CsSnI_3$ is sensitive to the chemical potentials of reactants. Then, the defect formation energies and defect charge-transition levels were calculated to show **Fig. 6(b)** and **6(c)**. Clearly, tin vacancies (V_{Sn}) introduced deep trap levels. Guided by this calculation result, $CsSnI_3$ nanocrystals were colloidally synthesized through the careful tuning of the ratio of precursors. It was found that suppressing the Sn vacancy strengthens the increase of radiative recombination rate for enhanced PLQY along with a narrow emission spectral peak. By intentionally adopting a Sn-rich reaction condition, along with judicious choice of precursors with suitable reactivity, the resulting narrow-band-emissive $CsSnI_3$ nanocrystals exhibit a record PLQY of 18.4 %. The development of synthetic methods, guided by computational science, will facilitate the study of tin-based perovskite nanocrystals and accelerate their application in high-performance optoelectronic devices such as solar cells, light-emitting diodes, and lasers.

4.2 Double perovskite nanocrystals

Inorganic double perovskite crystals have a chemical formula, $A_2B(I)B(III)X_6$ where A is a monovalent cation (typically Ce^+), B(I) is a monovalent cation (Ag^+ or Na^+), B(III) is trivalent cation (In^{3+}, Bi^{3+} or Sb^{3+}). Since the first report on the synthesis of lead-free double perovskite crystals, various chemical compositions of compound $A_2B(I)B(III)X_6$ have been investigated to tune the bandgap. For example, when Cl^- (2.77 eV), Br^- (1.95 eV), and I^- (1.75 eV) are introduced as X sites in the Cs_2AgBiX_6 structure, the band gap decreases in that order (Creutz et al., 2018). Among the reported lead-free double perovskite structures, a bulk crystal of white-light emitting $Cs_2Ag_xNa_{1-x}In_yBi_{1-y}Cl_6$ double perovskite structure was reported to show a high PLQY of 86 ± 5 % (Luo et al., 2018). After that, the PLQY

of Bi^{3+}-doped $Cs_2Ag_{0.4}Na_{0.6}InCl_6$ microcrystals of about 10 μm in diameter was improved up to 97.33 % (Peng K. et al., 2022). From now on, the double perovskite crystals become a potential material for single-emitter layer applied in optical applications (Zhang et al., 2022). However, a dramatic decrease in PLQY resulting from nanostructuration happens due to the formation of defective structures.

Research to increase PLQY in nanocrystals has been intensively pursued recently. Here, a typical method to find the underlying mechanism of the enhancement of the PLQY is demonstrated using $Cs_2Ag_{0.65}Na_{0.35}InCl_6$ nanocrystal as an example. HR-TEM image shown in **Fig. 7(a)** demonstrates $Cs_2Ag_{0.65}Na_{0.35}InCl_6$ nanocrystals having a square shape and an average diameter of about 10 nm. The estimated PLQY was 3 %. Improvement of PLQY was realized by impurity doping of Bi^{3+} ions. **Fig. 7(b)** shows a typical HR-TEM image of the Bi-doped nanocrystals. When the 1 % Bi^{3+} ion was doped, the PLQY was enhanced up to 33.2 % (see **Table 1**). **Fig. 7(c)** shows PL spectra of the undoped sample measured in the temperature range from 20 K to 300 K. As clearly seen, the integrated PL intensity decreases with the increasing temperature monotonously possibly due to the thermal activation of the nonradiative channels present in the nanocrystals. Doping of 1 % Bi^{3+} ions suppressed the decreasing rate in PL intensity with temperature compared

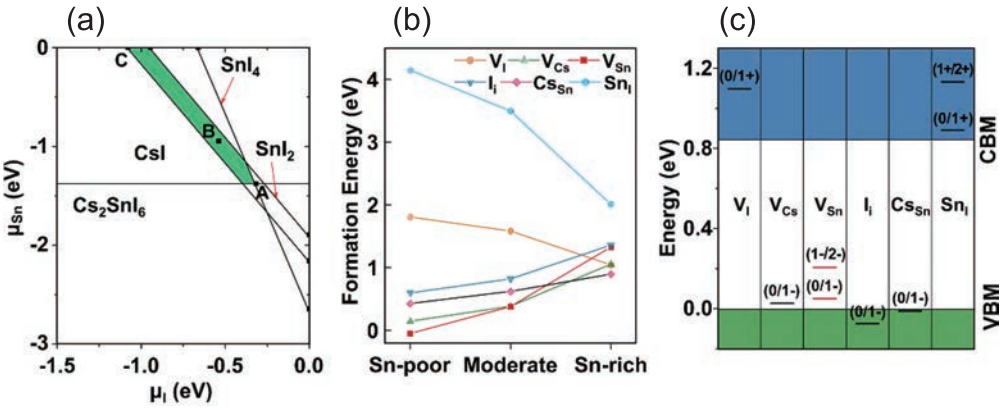


Fig. 6 **(a)** Stability regions of different compounds vs I and Sn chemical potentials of $CsSnI_3$. The shaded region indicates the equilibrium chemical potential region. The representative points (A: Sn-poor/I-rich, B: moderate, C: Sn-rich/I-poor conditions) are chosen for the defect formation energy calculations. **(b)** Calculated defect formation energies for 2 × 2 × 2 orthorhombic $CsSnI_3$ supercell at Sn-poor/I-rich, moderate, and Sn-rich/I-poor conditions, corresponding to the A, B, and C point in **(a)**, respectively. **(c)** Defect charge-transition levels of $CsSnI_3$. Adapted with permission from Ref. (Liu Q. et al., 2021b). Copyright 2021, American Chemical Society.

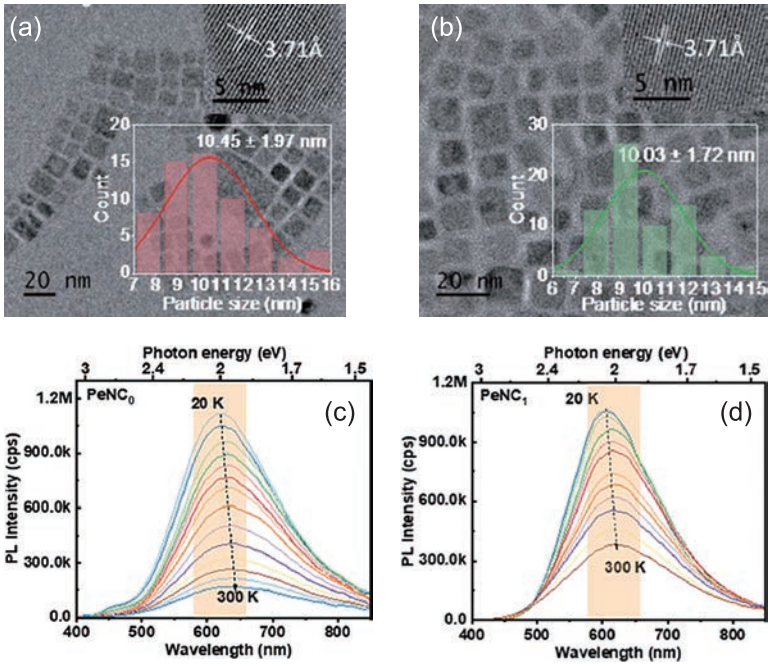


Fig. 7 TEM images and temperature dependent PL spectra of $Cs_2Ag_{0.65}Na_{0.35}InCl_6$ nanocrystals **(a, c)** without and **(b, d)** with 1 % Bi^{3+} ions. Adapted with permission from Ref. (Huang et al., 2022). Copyright 2022, Royal Society of Chemistry.

Table 1 PL decay parameters * of the $Cs_2Ag_{0.65}Na_{0.35}InCl_6$ doped with and without Bi^{3+} ions.

Sample	PLQY (%)	k_r [a] (μs^{-1})	k_{nr} [b] (μs^{-1})	R^2
Undoped	3.0	0.13	4.20	0.99
Doped	33.2	0.14	0.28	0.97

[a] k_r is the radiative recombination rate calculated by the formula: k_r = PLQY/τ(avg). τ(avg) means the value of average PL lifetime.
[b] k_{nr} is the nonradiative recombination rate calculated by the formula: $k_{nr} = 1/\tau(avg) - k_r$.
* Other parameters for calculation are reported in the published paper (Huang et al., 2022).

to undoped ones as shown in **Fig. 7(d)**, suggesting the decrease of nonradiative channels. As summarized in **Table 1**, the nonradiative recombination rate (k_{nr}) was reduced by a factor of 15 in the doped sample compared to the undoped sample. The possible defects as the nonradiative channel identified by investigating the temperature-dependence of PL spectral linewidth combined with chemical composition analysis were indium vacancies generated in the crystal growth (Huang et al., 2022). The possible mechanism of enhanced PLQY was that Bi^{3+} ions occupy the indium vacancy to relax the strained lattice, yielding the decreasing number of nonradiative channels. Thus, spectroscopic studies at low temperatures provide structural insight into the cause of low PLQY.

5. Summary

Driven by the toxicity concerns of cadmium, lead, mercury, and selenium, research on the synthesis of colloidal nanocrystals composed of nontoxic elements has made significant progress over the last decade. While previous studies have already detailed the synthesis and excellent properties of Cd- and Pb-based nanocrystals, non-toxic nanocrystals, the subject of this review, have not yet been fully described. The review was structured as follows: First, optical properties of SiQD were summarized. Due to their low absorption coefficients, they do not work as strong phosphors, but they find an application in the deice field of current driven LED because carriers are given from electrode and does not need absorbing the light. Second, InP was topicalized among III–V semiconductors. Metallic In is a small amount of constituent element on earth but does not exclude it from the discussion here. The pioneering work on red−green−blue (RGB) LEDs with beyond 20 % EQE spurs a lot of interests. Next target is narrowing of their EL spectra (<30 nm). For Pb-free perovskite nanocrystals, recent advances in colloidal chemical method were presented here. The journey to find experimental parameters to reduce defects has just begun. Much research is still needed to advance the field of non-toxic semiconductor nanocrystals. Although technological advances in synthesis methods, reports of prototype devices using light emission from nanocrystals, and even induced emission and nanobio applications have progressed over the past decade, it is safe to say that nanophotonics is still in its infancy.

Acknowledgments

This work was supported by WPI program, JSPS KAKENHI Grant-in-Aid for Scientific Research (B) Grant Number 21H01910 and The Murata Science Foundation.

References

Calvin J.J., Brewer A.S., Alivisatos A.P., The role of organic ligand shell structures in colloidal nanocrystal synthesis, Nature Synthesis, 1 (2022) 127–137. DOI: 10.1038/s44160-022-00025-4

Chandra S., Ghosh B., Beaune G., Nagarajan U., Yasui T., Nakamura J., Tsuruoka T., Baba Y., Shirahata N., Winnik F.M., Functional double-shelled silicon nanocrystals for two-photon fluorescence cell imaging: spectral evolution and tuning, Nanoscale, 8 (2016) 9009–9019. DOI: 10.1039/C6NR01437B

Chandra S., Masuda Y., Shirahata N., Winnik F.M., Transition metal doped NIR emitting silicon nanocrystals, Angewandte Chemie International Edition, 56 (2017) 6157–6160. DOI: 10.1002/anie.201700436

Chen J.-K., Zhao Q., Shirahata N., Yin J., Bakr O.M., Mohammed O.F., Sun H.-T., Shining light on the structure of lead halide perovskite nanocrystals, ACS Materials Letters, 3 (2021a) 845–861. DOI: 10.1021/acsmaterialslett.1c00197

Chen J.-K., Shirahata N., Sun H.-T., Metal-free scintillators excite X-ray community, Nature Photonics, 15 (2021b) 171–172. DOI: 10.1038/s41566-020-00751-1

Chen J.-K., Zhang B.-B., Liu Q., Shirahata N., Mohammed O.F., Bakr O.M., Sun H.-T., Advances and challenges in tin halide perovskite nanocrystals, ACS Materials Letters, 3 (2021c) 1541–1557. DOI: 10.1021/acsmaterialslett.1c00444

Cheng K.-Y., Anthony R., Kortshagen U.R., Holmes R.J., High-efficiency silicon nanocrystal light-emitting devices, Nano Letters, 11 (2011) 1952–1956. DOI: 10.1021/nl2001692

Chinnathambi S., Karthikeyan S., Hanagata N., Shirahata N., Molecular interaction of silicon quantum dot micelles with plasma proteins: hemoglobin and thrombin, RSC Advances, 9 (2019) 14928–14936. DOI: 10.1039/C9RA02829C

Chinnathambi S., Hanagata N., Yamazaki T., Shirahata N., Nano-bio interaction between blood plasma proteins and water-soluble silicon quantum dots with enabled cellular uptake and minimal cytotoxicity, Nanomaterials, 10 (2020) 2250. DOI: 10.3390/nano10112250

Coughlan C., Ibáñez M., Dobrozhan O., Singh A., Cabot A., Ryan K.M., Compound copper chalcogenide nanocrystals, Chemical Reviews, 117 (2017) 5865–6109. DOI: 10.1021/acs.chemrev.6b00376

Creutz S.E., Crites E.N., De Siena M.C., Gamelin D.R., Colloidal nanocrystals of lead-free double-perovskite (elpasolite) semiconductors: synthesis and anion exchange to access new materials, Nano Letters, 18 (2018) 1118–1123. DOI: 10.1021/acs.nanolett.7b04659

Dai X., Zhang Z., Jin Y., Niu Y., Cao H., Liang X., Chen L., Wang J., Peng X., Solution-processed, high-performance light-emitting diodes based on quantum dots, Nature, 515 (2014) 96–99. DOI: 10.1038/nature13829

Dasog M., Kehrle J., Rieger B., Veinot J.G.C., Silicon nanocrystals and silicon-polymer hybrids: synthesis, surface engineering, and applications, Angewandte Chemie International Edition, 55 (2016) 2322–2339. DOI: 10.1002/anie.201506065

Dohnalová K., Poddubny A.N., Prokofiev A.A., de Boer W.D.A.M., Umesh C.P., Paulusse J.M.J., Zuilhof H., Gregorkiewicz T., Surface brightens up Si quantum dots: direct bandgap-like size-tunable emission, Light: Science & Applications, 2 (2013) e47. DOI: 10.1038/

lsa.2013.3

Erogbogbo F., Yong K.-T., Hu R., Law W.-C., Ding H., Chang C.-W., Prasad P.N., Swihart M.T., Biocompatible magnetofluorescent probes: luminescent silicon quantum dots coupled with superparamagnetic iron(III) oxide, ACS Nano, 4 (2010) 5131–5138. DOI: 10.1021/nn101016f

Ghosh B., Takeguchi M., Nakamura J., Nemoto Y., Hamaoka T., Chandra S., Shirahata N., Origin of the photoluminescence quantum yields enhanced by alkane-termination of freestanding silicon nanocrystals: temperature-dependence of optical properties, Scientific Reports, 6 (2016) 36951. DOI: 10.1038/srep36951

Ghosh B., Hamaoka T., Nemoto Y., Takeguchi M., Shirahata N., Impact of anchoring monolayers on the enhancement of radiative recombination in light-emitting diodes based on silicon nanocrystals, The Journal of Physical Chemistry C, 122 (2018a) 6422–6430. DOI: 10.1021/acs.jpcc.7b12812

Ghosh B., Masuda Y., Wakayama Y., Imanaka Y., Inoue J.-i., Hashi K., Deguchi K., Yamada H., Sakka Y., Ohki S., Shimizu T., Shirahata N., Hybrid white light emitting diode based on silicon nanocrystals, Advanced Functional Materials, 24 (2014) 7151–7160. DOI: 10.1002/adfm.201401795

Ghosh B., Shirahata N., Influence of oxidation on temperature-dependent photoluminescence properties of hydrogen-terminated silicon nanocrystals, Crystals, 10 (2020) 143. DOI: 10.3390/cryst10030143

Ghosh B., Yamada H., Chinnathambi S., Özbilgin İ.N.G., Shirahata N., Inverted device architecture for enhanced performance of flexible silicon quantum dot light-emitting diode, The Journal of Physical Chemistry Letters, 9 (2018b) 5400–5407. DOI: 10.1021/acs.jpclett.8b02278

He G.S., Zheng Q., Yong K.-T., Erogbogbo F., Swihart M.T., Prasad P.N., Two- and three-photon absorption and frequency upconverted emission of silicon quantum dots, Nano Letters, 8 (2008) 2688–2692. DOI: 10.1021/nl800982z

Hessel C.M., Rasch M.R., Hueso J.L., Goodfellow B.W., Akhavan V.A., Puvanakrishnan P., Tunnel J.W., Korgel B.A., Alkyl passivation and amphiphilic polymer coating of silicon nanocrystals for diagnostic imaging, Small, 6 (2010) 2026–2034. DOI: 10.1002/smll.201000825

Huang X., Matsushita Y., Sun H.-T., Shirahata N., Impact of bismuth-doping on enhanced radiative recombination in lead-free double-perovskite nanocrystals, Nanoscale Advances, 4 (2022) 3091–3100. DOI: 10.1039/D2NA00238H

Ishii S., Sugavaneshwar R.P., Chen K., Dao T.D., Nagao T., Solar water heating and vaporization with silicon nanoparticles at Mie resonances, Optical Materials Express, 6 (2016) 640–648. DOI: 10.1364/OME.6.000640

Jellicoe T.C., Richter J.M., Glass H.F.J., Tabachnyk M., Brady R., Dutton S.E., Rao A., Friend R.H., Credgington D., Greenham N.C., Böhm M.L., Synthesis and optical properties of lead-free cesium tin halide perovskite nanocrystals, Journal of the American Chemical Society, 138 (2016) 2941–2944. DOI: 10.1021/jacs.5b13470

Jurbergs D., Rogojina E., Mangolini L., Kortshagen U., Silicon nanocrystals with ensemble quantum yields exceeding 60 %, Applied Physics Letters, 88 (2006) 233116. DOI: 10.1063/1.2210788

Kano S., Tada Y., Matsuda S., Fujii M., Solution processing of hydrogen-terminated silicon nanocrystal for flexible electronic device, ACS Applied Materials & Interfaces, 10 (2018) 20672–20678. DOI: 10.1021/acsami.8b04072

Kortshagen U.R., Sankaran R.M., Pereira R.N., Girshick S.L., Wu J.J., Aydil E.S., Nonthermal plasma synthesis of nanocrystals: fundamental principles, Materials, and Applications, Chemical Reviews, 116 (2016) 11061–11127. DOI: 10.1021/acs.chemrev.6b00039

Kwak D.-H., Ramasamy P., Lee Y.-S., Jeong M.-H., Lee J.-S., High-performance hybrid InP QDs/black phosphorus photodetector, ACS Applied Materials & Interfaces, 11 (2019) 29041–29046. DOI: 10.1021/acsami.9b07910

Lee B.G., Luo J.-W., Neale N.R., Beard M.C., Hiller D., Zacharias M., Stradins P., Zunger A., Quasi-direct optical transitions in silicon nanocrystals with intensity exceeding the bulk, Nano Letters, 16 (2016) 1583–1589. DOI: 10.1021/acs.nanolett.5b04256

Li J., Cao H.-L., Jiao W.-B., Wang Q., Wei M., Cantone I., Lü J., Abate A., Biological impact of lead from halide perovskites reveals the risk of introducing a safe threshold, Nature Communications, 11 (2020) 310. DOI: 10.1038/s41467-019-13910-y

Lim J., Park M., Bae W.K., Lee D., Lee S., Lee C., Char K., Highly efficient cadmium-free quantum dot light-emitting diodes enabled by the direct formation of excitons within InP@ZnSeS quantum dots, ACS Nano, 7 (2013) 9019–9026. DOI: 10.1021/nn403594j

Lin K., Xing J., Quan L.N., de Arquer F.P.G., Gong X., Lu J., Xie L., Zhao W., Zhang D., Yan C., Li W., Liu X., Lu Y., Kirman J., Sargent E.H., et al., Perovskite light-emitting diodes with external quantum efficiency exceeding 20 per cent, Nature, 562 (2018) 245–248. DOI: 10.1038/s41586-018-0575-3

Liu Q., Feng Z.-Y., Li H., Zhao Q., Shirahata N., Kuroiwa Y., Moriyoshi C., Duan C.-K., Sun H.-T., Non-rare-earth UVC persistent phosphors enabled by bismuth doping, Advanced Optical Materials, 9 (2021a) 2002065. DOI: 10.1002/adom.202002065

Liu Q., Yin J., Zhang B.-B., Chen J.-K., Zhou Y., Zhang L.-M., Wang L.-M., Zhao Q., Hou J., Shu J., Song B., Shirahata N., Bakr O.M., Mohammed O.F., Sun H.-T., Theory-guided synthesis of highly luminescent colloidal cesium tin halide perovskite nanocrystals, Journal of the American Chemical Society, 143 (2021b) 5470–5480. DOI: 10.1021/jacs.1c01049

Liu X., Zhao S., Gu W., Zhang Y., Qiao X., Ni Z., Pi X., Yang D., Light-emitting diodes based on colloidal silicon quantum dots with octyl and phenylpropyl ligands, ACS Applied Materials & Interfaces, 10 (2018) 5959–5966. DOI: 10.1021/acsami.7b16980

Luo J., Wang X., Li S., Liu J., Guo Y., Niu G., Yao L., Fu Y., Gao L., Dong Q., Zhao C., Leng M., Ma F., Liang W., Wang L., et al., Efficient and stable emission of warm-white light from lead-free halide double perovskites, Nature, 563 (2018) 541–545. DOI: 10.1038/s41586-018-0691-0

Mastronardi M.L., Maier-Flaig F., Faulkner D., Henderson E.J., Kübel C., Lemmer U., Ozin G.A., Size-dependent absolute quantum yields for size-separated colloidally-stable silicon nanocrystals, Nano Letters, 12 (2012) 337–342. DOI: 10.1021/nl2036194

Nemoto K., Watanabe J., Sun H.-T., Shirahata N., Coherent InP/ZnS core@shell quantum dots with narrow-band green emissions, Nanoscale, 14 (2022) 9900–9909. DOI: 10.1039/D2NR02071H

Özbilgin İ.N.G., Ghosh B., Yamada H., Shirahata N., Size-dependent photothermal performance of silicon quantum dots, The Journal of Physical Chemistry C, 125 (2021) 3421–3431. DOI: 10.1021/acs.jpcc.0c10027

Özbilgin İ.N.G., Yamazaki T., Watanabe J., Sun H.-T., Hanagata N., Shirahata N., Water-soluble silicon quantum dots toward fluorescence-guided photothermal nanotherapy, Langmuir, 38 (2022) 5188–5196. DOI: 10.1021/acs.langmuir.1c02326

Peng K., Yu L., Min X., Hu M., Yang Y., Huang S., Zhao Y., Deng Y., Zhang M., The synthesis of lead-free double perovskite Cs2Ag0.4Na0.6InCl6 phosphor with improved optical properties via ion doping, Journal of Alloys and Compounds, 891 (2022) 161978. DOI: 10.1016/j.jallcom.2021.161978

Pitaro M., Tekelenburg E.K., Shao S., Loi M.A., Tin halide perovskites: from fundamental properties to solar cells, Advanced Materials, 34 (2022) 2105844. DOI: 10.1002/adma.202105844

Poddubny A.N., Dohnalová K., Direct band gap silicon quantum dots achieved via electronegative capping, Physical Review B, 90 (2014) 245439. DOI: 10.1103/PhysRevB.90.245439

Quan L.N., Rand B.P., Friend R.H., Mhaisalkar S.G., Lee T.-W., Sargent E.H., Perovskites for next-generation optical sources, Chemical Reviews, 119 (2019) 7444–7477. DOI: 10.1021/acs.

chemrev.9b00107
Reiss P., Protière M., Li L., Core/shell semiconductor nanocrystals, Small, 5 (2009) 154–168. DOI: 10.1002/smll.200800841
Ruizendaal L., Bhattacharjee S., Pournazari K., Rosso-Vasic M., de Haan L.H.J., Alink G.M., Marcelis A.T.M., Zuilhof H., Synthesis and cytotoxicity of silicon nanoparticles with covalently attached organic monolayers, Nanotoxicology, 3 (2009) 339–347. DOI: 10.3109/17435390903288896
Sakiyama M., Sugimoto H., Fujii M., Long-lived luminescence of colloidal silicon quantum dots for time-gated fluorescence imaging in the second near infrared window in biological tissue, Nanoscale, 10 (2018) 13902–13907. DOI: 10.1039/C8NR03571G
Shirahata N., Colloidal Si nanocrystals: a controlled organic–inorganic interface and its implications of color-tuning and chemical design toward sophisticated architectures, Physical Chemistry Chemical Physics, 13 (2011) 7284–7294. DOI: 10.1039/C0CP02647F
Shirahata N., Hirakawa D., Sakka Y., Interfacial-related color tuning of colloidal Si nanocrystals, Green Chemistry, 12 (2010) 2139–2141. DOI: 10.1039/C0GC00502A
Shirahata N., Hozumi A., Yonezawa T., Monolayer-derivative functionalization of non-oxidized silicon surfaces, The Chemical Record, 5 (2005) 145–159. DOI: 10.1002/tcr.20041
Shirahata N., Nakamura J., Inoue J.-i., Ghosh B., Nemoto K., Nemoto Y., Takeguchi M., Masuda Y., Tanaka M., Ozin G.A., Emerging atomic energy levels in zero-dimensional silicon quantum dots, Nano Letters, 20 (2020) 1491–1498. DOI: 10.1021/acs.nanolett.9b03157
Srivastava V., Kamysbayev V., Hong L., Dunietz E., Klie R.F., Talapin D.V., Colloidal chemistry in molten salts: synthesis of luminescent $In_{1-x}Ga_xP$ and $In_{1-x}Ga_xAs$ quantum dots, Journal of the American Chemical Society, 140 (2018) 12144–12151. DOI: 10.1021/jacs.8b06971
Sun W., Qian C., Cui X.S., Wang L., Wei M., Casillas G., Helmy A.S., Ozin G.A., Silicon monoxide—a convenient precursor for large scale synthesis of near infrared emitting monodisperse silicon nanocrystals, Nanoscale, 8 (2016) 3678–3684. DOI: 10.1039/C5NR09128D
Sun W., Qian C., Wang L., Wei M., Mastronardi M.L., Casillas G., Breu J., Ozin G.A., Switching-on quantum size effects in silicon nanocrystals, Advanced Materials, 27 (2015) 746–749. DOI: 10.1002/adma.201403552
Tamang S., Lincheneau C., Hermans Y., Jeong S., Reiss P., Chemistry of InP nanocrystal syntheses, Chemistry of Materials, 28 (2016) 2491–2506. DOI: 10.1021/acs.chemmater.5b05044
Wang L., Reipa V., Blasic J., Silicon nanoparticles as a luminescent label to DNA, Bioconjugate Chemistry, 15 (2004) 409–412. DOI: 10.1021/bc030047k
Wang L.-M., Chen J.-K., Zhang B.-B., Liu Q., Zhou Y., Shu J., Wang Z., Shirahata N., Song B., Mohammed O.F., Bakr O.M., Sun H.-T., Phosphatidylcholine-mediated regulation of growth kinetics for colloidal synthesis of cesium tin halide nanocrystals, Nanoscale, 13 (2021) 16726–16733. DOI: 10.1039/D1NR04618G
Watanabe J., Yamada H., Sun H.-T., Moronaga T., Ishii Y., Shirahata N., Silicon quantum dots for light-emitting diodes extending to the NIR-II window, ACS Applied Nano Materials, 4 (2021) 11651–11660. DOI: 10.1021/acsanm.1c02223
Won Y.-H., Cho O., Kim T., Chung D.-Y., Kim T., Chung H., Jang H., Lee J., Kim D., Jang E., Highly efficient and stable InP/ZnSe/ZnS quantum dot light-emitting diodes, Nature, 575 (2019) 634–638. DOI: 10.1038/s41586-019-1771-5
Wong A.B., Bekenstein Y., Kang J., Kley C.S., Kim D., Gibson N.A., Zhang D., Yu Y., Leone S.R., Wang L.-W., Alivisatos A.P., Yang P., Strongly quantum confined colloidal cesium tin iodide perovskite nanoplates: lessons for reducing defect density and improving stability, Nano Letters, 18 (2018) 2060–2066. DOI: 10.1021/acs.nanolett.8b00077
Wu Z., Liu P., Zhang W., Wang K., Sun X.W., Development of InP Quantum Dot-Based Light-Emitting Diodes, ACS Energy Letters, 5 (2020) 1095–1106. DOI: 10.1021/acsenergylett.9b02824
Xu G., Zeng S., Zhang B., Swihart M.T., Yong K.-T., Prasad P.N., New generation cadmium-free quantum dots for biophotonics and nanomedicine, Chemical Reviews, 116 (2016) 12234–12327. DOI: 10.1021/acs.chemrev.6b00290
Yamada H., Saitoh N., Ghosh B., Masuda Y., Yoshizawa N., Shirahata N., Improved brightness and color tunability of solution-processed silicon quantum dot light-emitting diodes, The Journal of Physical Chemistry C, 124 (2020) 23333–23342. DOI: 10.1021/acs.jpcc.0c06672
Zhang Y., Zhang Z., Yu W., He Y., Chen Z., Xiao L., Shi J.-j., Guo X., Wang S., Qu B., Lead-free double perovskite $Cs_2AgIn_{0.9}Bi_{0.1}Cl_6$ quantum dots for white light-emitting diodes, Advanced Science, 9 (2022) 2102895. DOI: 10.1002/advs.202102895

Author's Short Biography



Naoto Shirahata

Naoto Shirahata is Group Leader of Nanoparticle Group of National Institute for Materials Science (NIMS) in Japan, and Guest Professors of Hokkaido University and Chuo University. He earned his Ph.D. in materials science from Kyoto Institute of Technology in 2001. He worked as postdoc researchers at Nagoya University, AIST, and NIMS from 2001 to 2006. Since 2006 he has been permanent researcher at NIMS. He was holder of JST-PRESTO in 2009–14. He was visiting scientist at University of Toronto in 2015–16. He has received awards for his research from the Division of Colloid and Surface Chemistry, the Chemical Society of Japan, the Ceramic Society of Japan, and Japan Society of Powder and Powder Metallurgy.

KONA Powder and Particle Journal

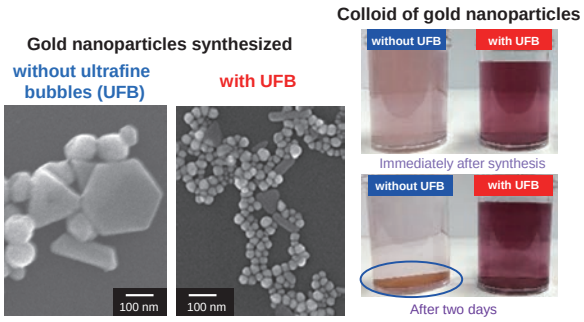
KONA Powder and Particle Journal No. 41 (2024) 183–196/https://doi.org/10.14356/kona.2024004 Review Paper

Characteristics of Ultrafine Bubbles (Bulk Nanobubbles) and Their Application to Particle-Related Technology†

Keiji Yasuda

Department of Chemical Systems Engineering, Nagoya University, Japan

Ultrafine bubbles (bulk nanobubbles), small bubbles with a diameter of less than 1 μm, have attracted academic and industrial attention because of their numerous advantages, including their chemical-free nature and extraordinarily long lifetime. The long lifetime is related to the much higher Brownian motion velocity compared to buoyancy. The reason why ultrafine bubbles can endure under stable conditions is still unclear, even though their inside is highly pressured. They have several characteristics, such as pH-dependent surface charge and reduced friction. They are also closely related to ultrasound. Ultrafine bubbles are generated and removed by selecting the ultrasonic frequency. Reaction and separation using ultrasonic cavitation and atomization, respectively, are enhanced by ultrafine bubbles. They can produce hollow nanoparticles, enhance adsorption on activated carbon, and clean solid surfaces. This review discusses the fundamental and ultrasonic characteristics of ultrafine bubbles and their application in particle-related technology, encompassing fine particle synthesis, adsorption, desorption, extraction, cleaning, and prevention of fouling.



Keywords: ultrafine bubbles, bulk nanobubbles, ultrasound, sonochemistry, fine particle synthesis, cleaning

1. Introduction

Submicron-sized bubbles have attracted academic and industrial interest lately. Although these floating bubbles in a liquid have previously been referred to as "nanobubbles" or "bulk nanobubbles," the International Organization for Standards (ISO) decided in 2017 that these bubbles less than 1 μm in diameter be termed "ultrafine bubbles" (ISO 20480-1, 2017). Therefore, this review will refer to nanobubbles and bulk nanobubbles as ultrafine bubbles. Furthermore, bubbles between 1 and 100 μm in diameter are termed microbubbles, and ultrafine bubbles and microbubbles are collectively termed fine bubbles.

Ultrafine bubbles and microbubbles are liquid-floating bubbles with the entire bubble interface surrounded by liquid. Microbubbles in water appear cloudy, like milk, while ultrafine bubbles are transparent because they do not scatter visible light. Surface nanobubbles, on the other hand, are small bubbles with one side of the bubble interface in contact with liquid and the other side attached to the solid wall (Lohse and Zhang, 2015). The surface nanobubbles are spherical caps with heights ranging from a few nanometers to tens of nanometers and widths of about 1 μm. They do not move from a solid wall.

The rising velocity U of fine bubbles (microbubbles and ultrafine bubbles) in liquid due to buoyancy depends on the diameter of fine bubbles d and the physical properties of liquid and is expressed by the following Stokes equation (Stokes, 1851),

$$U = \frac{d^2(\rho_L - \rho_G)g}{18\mu} \tag{1}$$

where ρ_L and ρ_G are liquid and gas densities, respectively, μ is the liquid viscosity, and g is the gravitational acceleration. The Stokes equation is known to accurately represent the setting motion of a solid sphere in a liquid when the Reynolds number is less than 2. Experimental results of the rising velocity of microbubbles agree with those calculated using **Eqn. (1)** (Takahashi, 2005; Lee and Kim, 2005). However, ultrafine bubbles are subject to intense Brownian motion, like solid colloidal particles, due to collisions caused by the thermal motion of liquid molecules. The following Stokes–Einstein equation expresses the displacement of spherical particles using Brownian motion at low Reynolds numbers (Einstein, 1905).

$$\langle \Delta x^2 + \Delta y^2 + \Delta z^2 \rangle = \frac{2kTt}{\pi\mu d} \tag{2}$$

where $\langle \Delta x^2 + \Delta y^2 + \Delta z^2 \rangle$ is the mean square displacement of the fine particles, k is the Boltzmann constant, T is the temperature, and t is the observation time. **Fig. 1** shows the comparison between the rising velocity using **Eqn. (1)** and the average velocity of Brownian motion per 1 s and 100 s

† Received 17 October 2022; Accepted 19 December 2022
J-STAGE Advance published online 25 March 2023
Add: Furo-cho, Chikusa-ku, Nagoya 464-8603, Japan
E-mail: yasuda.keiji@material.nagoya-u.ac.jp
TEL: +81-52-789-3623

Copyright © 2024 The Author. Published by Hosokawa Powder Technology Foundation. This is an open access article under the CC BY license (https://creativecommons.org/licenses/by/4.0/).

by Eqn. (2) in the range of bubbles diameters from 10 nm to 10 μm. When the temperature is 298.15 K, the liquid and gas are considered to be water and air, respectively, and the bubbles are expected to be perfectly spherical. In the case of ultrafine bubbles less than 100 nm, the average velocity of Brownian motion is much greater than the rising velocity. This means that the ultrafine bubbles are dominated by random motion in all directions compared to the rising motion. Due to this interesting behavior, the removal of ultrafine bubbles from the liquid surface is nearly negligible. If there is no collision between the bubbles or dissolution into the liquid, ultrafine bubbles remain for a long time.

Thus, ultrafine bubbles have various interesting properties, such as a very long lifetime in liquid, a charged surface, and controllable bubble concentration using ultrasound. Therefore, they have been applied in many fields, including water treatment, medicine, and the food industry (English, 2022). This review explains the fundamental and ultrasonic characteristics of ultrafine bubbles and describes their applications to particle-related technologies.

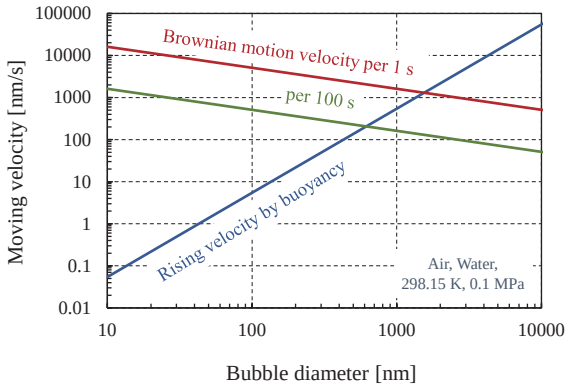


Fig. 1 Velocity comparison between Brownian motion and buoyancy.

2. Fundamental characteristics

2.1 Size, concentration, and zeta potential

Like colloidal particles in solution, the surface of ultrafine bubbles is charged. The size and concentration of ultrafine bubbles in a liquid are closely related to the zeta potentials of ultrafine bubbles. They are mainly affected by the pH of solution, concentration, and several types of inorganic ions and surfactants in water.

Nirmalkar et al. (2018b) prepared air-filled ultrafine bubbles from pure water at pH = 6.5 using hydrodynamic cavitation methods and then changed the pH of ultrafine bubbles water by HCl and NaOH. The size distribution and zeta potential of ultrafine bubbles were measured using nanoparticle tracking analysis (Patois et al., 2012) and electrophoresis, respectively. Fig. 2 shows the effects of pH on (a) size distribution, (b) number density (concentration), (c) mean diameter, and (d) zeta potential of ultrafine bubbles. When pH was higher than 4, the bubble size distribution did not significantly change. However, at pH below 4, the peak of the bubble size distribution decreased sharply. This is reflected in the sharp drop in the bubble

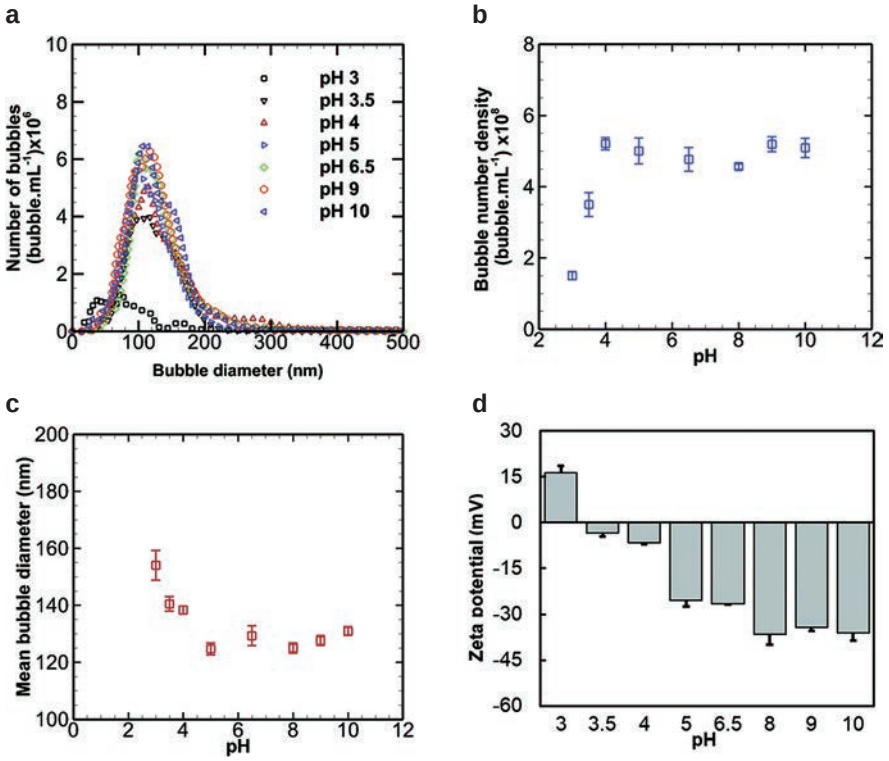


Fig. 2 Effects of pH on **(a)** size distribution, **(b)** concentration, **(c)** mean diameter, and **(d)** zeta potential of ultrafine bubbles. Reproduced with permission from Ref. (Nirmalkar et al., 2018b). Copyright: (2018) The Royal Society of Chemistry.

number concentration (density) as the pH decreased from 4 to 3. The mean bubble diameter increased significantly as the pH decreased below 4. The negative zeta potential of bubbles approached 0 with decreasing pH and became positive below the isoelectric point between pH 3 and 3.5. This is because the electrostatic repulsive force between ultrafine bubbles becomes weaker, bubbles agglomerate, and the bubble diameter increases, as the zeta potential is close to the isoelectric point. At the same time, excessively large bubbles rise and collapse at the gas–liquid interface, and the bubble concentration decreases. Other researchers have reported similar results with isoelectric points between pH 3 and 5 (Calgaroto et al., 2014; Azevedo et al., 2016; Bui et al., 2019; Ma et al., 2022).

Effects of NaCl concentration on properties of ultrafine bubbles have been widely reported (Millare and Basilia, 2018; Nirmalkar et al., 2018a, 2018b; Meegoda et al., 2018, 2019; Ke et al., 2019). Most of the data indicated that as the NaCl concentration increased, the bubble concentration decreased, the mean diameter increased, and the zeta potential approached zero. This is because sodium ions are adsorbed at the surface of the ultrafine bubble, and the zeta potential is close to zero. In the case of $AlCl_3$, a trivalent cation, the zeta potential first approached zero and then changed to positive with increasing $AlCl_3$ concentration (Nirmalkar et al., 2018b). Hewage et al. (2021a) investigated the mean diameter and zeta potential of ultrafine bubbles in aqueous solutions for several inorganic salts.

The addition of cetyltrimethylammonium bromide, a cationic surfactant, changed the zeta potential from negative to positive, as in the case of $AlCl_3$ (Nirmalkar et al., 2018b; Agarwal et al., 2022). On the other hand, adding sodium dodecyl sulfate, an anionic surfactant, further decreased the zeta potential (Phan et al., 2021b). The addition of nonionic surfactants had a little significant effect on the zeta potential (Nirmalkar et al., 2018b). These experimental results of surfactant addition were explained using the adsorption of surfactants on ultrafine bubbles due to hydrophobic attraction. Effects of gas types inside ultrafine bubbles have been reported (Meegoda et al., 2018; Zhou et al., 2021). For air, nitrogen, oxygen, and ozone gases, it was explained that the bubble size increased with increasing gas solubility in water and the zeta potential depended on the ability of the gas to produce OH^- ions at the water–gas interface (Meegoda et al., 2018).

The ultrafine bubbles in water were concentrated without loss and size change when water was evaporated from ultrafine bubble water under reduced pressure using a rotary evaporator (Tanaka et al., 2020). Additionally, ultrafine bubbles in water were diluted by gently adding pure water without loss and size change of ultrafine bubbles. A facile membrane-based physical sieving method was developed to make the ultrafine bubbles in targeting size (Zhang R. et al., 2022b). They used several membranes consisting of six different materials with pore diameters of 0.22 and 0.45 μm. The size distribution of the ultrafine bubbles could be intentionally adjusted by selecting the membrane and filtration rate. The ability to control the concentration and size of ultrafine bubble will be important for future application development.

2.2 Stability

The unique property of ultrafine bubbles is their unusually long lifetime. Ultrafine bubbles, once formed, are highly persistent (Zimmerman et al., 2011) and stable for days (Ohgaki et al., 2010; Ushikubo et al., 2010; Liu et al., 2013) and even months (Duval et al., 2012; Nirmalkar et al., 2018a; Kanematsu et al., 2020; Soyluoglu et al., 2021; Tanaka et al., 2021b).

Tanaka et al. (2021b) generated air-filled ultrafine bubbles from ultrapure water using the pressurized dissolution method and stored the ultrafine bubble water at 298 K for 74 days. The results showed little difference in the stability of ultrafine bubbles between 30 mL glass vials, 1 L glass bottles, and 20 L high-density polyethylene containers. **Fig. 3** shows the effect of storage temperature on the stability of ultrafine bubbles in 30 mL glass vials. Although number concentration decreased with time, ultrafine bubbles still existed on day 74. This is because the translational velocity due to Brownian motion is considerably

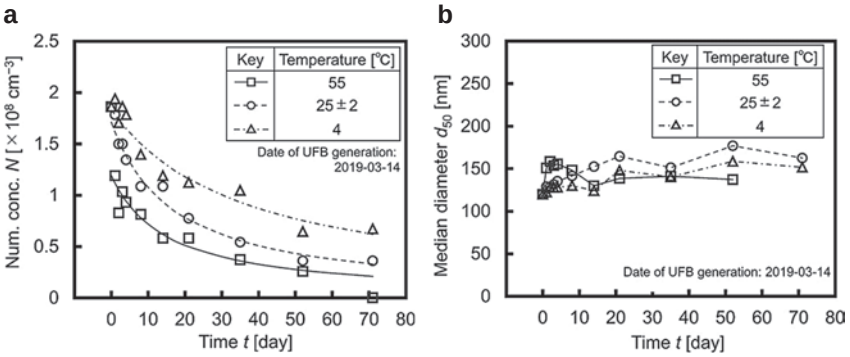


Fig. 3 Effect of storage temperature on the stability of ultrafine bubbles in 30 mL glass vials: **a)** number concentration and **b)** median diameter of ultrafine bubbles. Reprinted with permission from Ref. (Tanaka et al., 2021b). Copyright: (2021) John Wiley and Sons.

higher than the rising velocity due to buoyancy, as shown in Fig. 1. The stability became higher as the temperature decreased, and median diameter slightly increased with time. They explained that the Brownian motion of ultrafine bubbles became more active at higher temperatures and ultrafine bubbles tended to aggregate more easily. They expressed the stability of the ultrafine bubbles in terms of a second-order flocculation rate equation. Kanematsu et al. (2020) investigated the stability of ultrafine bubbles for 9 months at 298 K and reported that ultrafine bubbles were stable and zeta potential did not change significantly for 9 months.

Effects of additives on the long-term stability of oxygen ultrafine bubbles were investigated for 60 days (Soyluoglu et al., 2021). The bubble stability decreased with decreasing pH in the range of 3 to 9. The addition of Na^+ and Ca^{2+} ions reduced the stability. This is because the zeta potential of the ultrafine bubbles became close to 0, and the ultrafine bubbles tended to aggregate. Furthermore, the stability became low when the concentration of organic substances was high, but the effect of chlorine was small.

The boundary layer structure of ultrafine bubbles has been studied to elucidate the reason for their stability. Ohgaki et al. (2010) used attenuated total reflectance infrared spectroscopy to analyze and reported that the surfaces of the ultrafine bubbles contain hard hydrogen bonds that may reduce the diffusivity of gases through the interfacial film. Weijs et al. (2012) used molecular dynamics and concluded that ultrafine bubbles within a cluster of bubbles protect each other from diffusion by a shielding effect. Zhang X. et al. (2016) performed quantum computations and Raman spectrometric measurements. They proposed that an ultrafine bubble is more dynamically stable because the bubble is surrounded by a layer of supersolid skin. Hirai et al. (2019) studied the structure of ultrafine bubbles using small- and wide-angle X-ray scattering and explained that an ultrafine bubble is surrounded by a diffusive boundary, and the electron density differs between the diffusive boundary and the bulk solution. Zhang R. et al. (2022a) quantified the boundary layer thickness of the ultrafine bubbles using solvent relaxation of nuclear magnetic resonance. For effective gas diameters of 243.5, 358.5, and 412.8 nm, the determined boundary layer thicknesses were 41.5, 44.8, and 35.9 nm, and the ratios of the boundary layer thickness to the effective gas diameter were 0.17, 0.125, and 0.087, respectively.

The bubble was surrounded by water, which has high intermolecular forces, and the inner bubble was pressurized because it is a gas with a sparse density compared to the liquid. The pressure difference Δp is expressed using the Young–Laplace equation as follows (Attard, 2014),

$$\Delta p = p_{in} - p_{out} = \frac{2\sigma}{r} \tag{3}$$

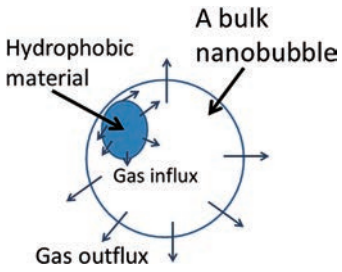


Fig. 4 Dynamic equilibrium model. Reprinted with permission from Ref. (Yasui et al., 2016). Copyright: (2016) American Chemical Society.

where p_{in} and p_{out} are the inner and outer pressure of the bubble, respectively and σ is the interfacial surface tension, and r is the bubble radius. Assuming that the interfacial tension at the macroscale and nanoscale is the same, the internal pressure of a bubble increases with decreasing bubble radius and becomes significantly high in the case of ultrafine bubbles. The inner pressure of bubbles becomes 2.98 MPa, when the bubble radius is 50 nm, the interfacial tension of water is 72 mN/m, and the outer pressure of the bubble is 0.1 MPa. The inner pressure of surface nanobubbles obtained using electrochemical measurement (German et al., 2016) and that of ultrafine bubbles estimated from the measurement of gas content in water (Kim E. et al., 2020) were consistent with the theoretical pressure values in Eqn. (3).

However, ultrafine bubbles are expected to dissolve immediately into the surrounding liquid because the pressure of the gas dissolved in a liquid is usually in the order of 0.1 MPa. The time for the complete dissolution of a bubble with 100 nm in radius is only about 80 μs according to the Epstein–Plesset theory (Epstein and Plesset, 1950; Yasui, 2015, 2018). Therefore, the lifetime of ultrafine bubbles should theoretically be very short, but in practice, as previously mentioned, it is very long.

Several stabilization models of ultrafine bubbles have been proposed to explain this discrepancy. Yasui et al. (2018) reviewed these models and supported the dynamic equilibrium model (Yasui et al., 2015, 2016; Brenner and Lohse, 2008; Petsev et al., 2013) because images of the transmission electron microscope showed stable ultrafine bubbles partly covered with hydrophobic materials in aqueous solutions (Sugano et al., 2017). Fig. 4 illustrates the dynamic equilibrium model. This model shows that a hydrophobic substance adheres to the bubble surface, and the gas concentrated on the surface of the hydrophobic substance flows into the bubble and is balanced by the amount of gas flowing out of the bubble in the rest of the bubble. However, the high stability of ultrafine bubbles must be investigated further, both experimentally and theoretically, to obtain a consistent conclusion in the future.

2.3 Other characteristics

Other characteristics of ultrafine bubbles include a

reduction in solution viscosity (Phan et al., 2021a), a reduction in friction (Ushida et al., 2012a; Nakagawa et al., 2022), and the generation of radicals.

Viscosities of apple juice concentrate and canola oil were examined after they were injected with CO_2 ultrafine bubbles with sizes ranging from 50 to 850 nm (Phan et al., 2021a). A significant viscosity reduction was observed by up to 18 % and 10 % in apple juice concentrate and canola oil, respectively. The pressure drop across a micro-orifice was measured using water and glycerol aqueous solutions containing ultrafine bubbles (Ushida et al., 2012a). The friction reduction was observed for orifice diameters of 50 μm or less. This was because the ultrafine bubbles adhered to the wall surface, forming a gas phase that resulted in wall slip. The reduction of friction factor in an acrylic pipe with glass beads increased with an increasing number of ultrafine bubbles (Nakagawa et al., 2022). They explained that ultrafine bubbles filled more undulated space and made the rough surface smoother.

Free radicals, including hydroxyl radicals, were detected in ultrafine bubble water (Minamikawa et al., 2015; Liu et al., 2016a, b; Atkinson et al., 2019). Free radicals are believed to be formed through the collapse of ultrafine bubbles (Takahashi et al., 2021). Soyluoglu et al. (2021) reported that hydroxyl radicals in oxygen ultrafine bubble solutions were detected at pH 3 but were little detected at pH 6.5. Yasui et al. (2018) discussed the generation possibility of hydroxyl radicals from air ultrafine bubbles using numerical simulations. They suggested that hydroxyl radicals formed due to hydrodynamic cavitation in producing ultrafine bubbles.

3. Ultrasonic characteristics

3.1 Ultrasonic cavitation

When water is irradiated with ultrasound, fine bubbles are generated from bubble nuclei, grow to a resonance size through rectified diffusion (Ashokkumar et al., 2007; Crum, 1980) and collapse by semi-adiabatic compression (Leighton, 1994; Yasui, 2015). This phenomenon is called ultrasonic cavitation. By collapsing fine bubbles, the field inside the fine bubbles becomes high temperature and pressure, generating various radical species, which produces chemical effects (Suslick, 1990). Simultaneously, the collapse of fine bubbles generates jet flow and shock wave (Lauterborn and Ohl, 1997), producing mechanical effects.

Examples of the chemical effects include the decomposition of harmful substances (Pétrier et al., 1994; Yasuda, 2021) and the synthesis of metal nanoparticles (Gedanken, 2004; Sakai et al., 2009). However, examples of the mechanical effects include ultrasonic cleaning (Muthukumaran et al., 2005; Mason, 2016), ultrasonic emulsification (Beal and Skauen, 1955; Yasuda et al., 2012), and ultrasonic atomization (Wood and Loomis, 1927; Sato et al., 2001). Mechanical effects have been used to develop commercial products such as cleaners, homogenizers, and atomizers. Usually, plate-type transducers are used for ultrasonic cleaners and atomizers, while horn-type transducers are used for ultrasonic homogenizers. Thus, ultrasound is closely related to ultrafine bubbles, and many studies using ultrasound have been reported.

3.2 Generation and removal of ultrafine bubbles

Ultrafine bubbles were generated using ultrasonic cleaner at 42 kHz (Kim J.-Y. et al., 2000) and ultrasonic homogenizer at 20 kHz (Cho et al., 2005; Nirmalkar et al., 2018a, 2019; Li et al., 2021; Lee and Kim, 2022b; Ma et al., 2022). Their generation rate increased with increased dissolved air content in pure water (Nirmalkar et al., 2018a). Studies have used several plate-type transducers to change ultrasonic frequencies ranging from 20 kHz to 1 MHz and to generate ultrafine bubbles in ultrapure water (Yasuda et al., 2019). **Figs. 5(a)** and **(b)** show the effect of ultrasonic frequency on the generation rate and mode diameter of ultrafine bubbles. The generation rate increased with decreasing frequency because cavitation collapse became stronger at lower frequencies. However, the mode diameters of ultrafine bubbles were 90–100 nm regardless of the frequency. The diameter, zeta potential, and stability of ultrafine bubbles generated using ultrasound are almost identical to those generated by hydrodynamic cavitation (Jadhav and Brigou, 2020), which is a commonly used method. The ultrasound method has the advantage of small sample volumes and the ability to generate ultrafine bubbles in variety of liquids, including organic solvents (Nirmalkar et al., 2019), inorganic solutions (Ma et al., 2022), and surfactant solutions (Lee and Kim, 2022a).

Removing ultrafine bubbles from liquid media is important to distinguish them from nanoparticles. The freeze–thawing method is often used to remove ultrafine bubbles in pure water. However, this method little removes ultrafine bubbles in the surfactant solution (Nirmalkar et al., 2018a), and it is time-consuming. Ultrasound has been irradiated at various frequencies to highly concentrated ultrafine bubble water produced using the pressurized dissolution method (Yasuda et al., 2019). **Fig. 5(c)** shows the effect of ultrasonic frequency on the removal rate of ultrafine bubbles. The removal rate increased with increasing frequency because the secondary Bjerknes force, an attraction between bubbles, increased. We modeled the formation and removal of ultrafine bubbles using ultrasound and discovered that ultrafine bubbles reach a frequency-dependent equilibrium concentration (**Fig. 5(d)**), regardless of the ultrasound intensity. Tanaka et al. (2021a) confirmed the ultrasonic removal of ultrafine bubbles using indirect irradiation. The ultrasonic frequency was 1.6 MHz, and ultrafine bubbles dispersions were prepared using two different bubble generator methods: pressurized dissolution and swirling liquid flow. Results showed that the indirect ultrasonic irradiation

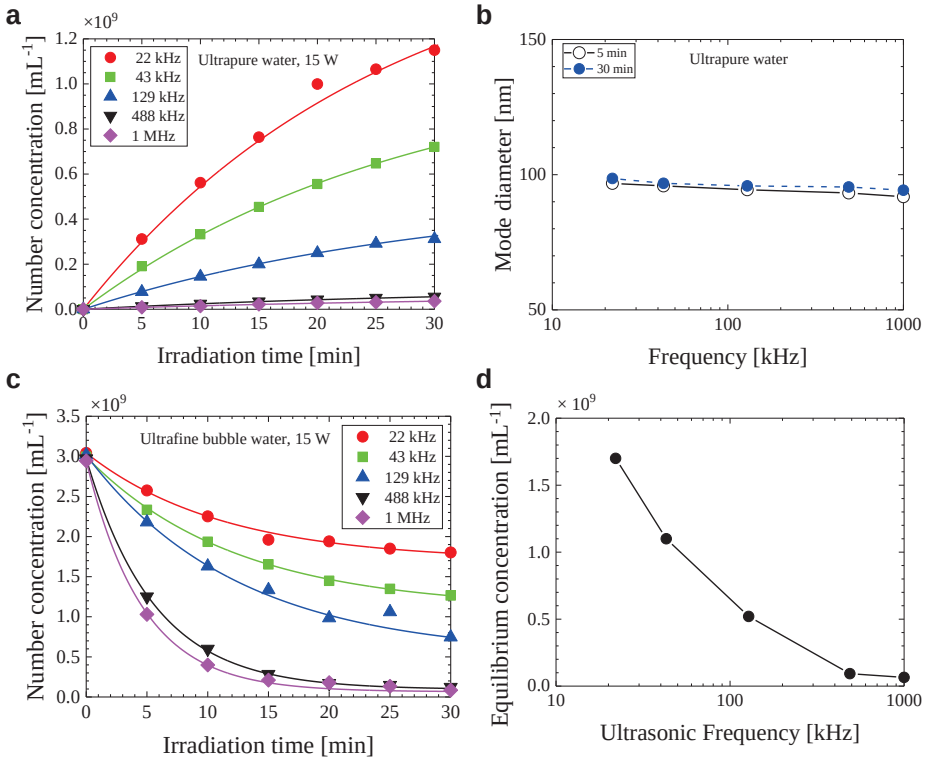


Fig. 5 Effect of ultrasonic frequency on **(a)** generation rate, **(b)** mode diameter, **(c)** removal rate, and **(d)** equilibrium concentrations of ultrafine bubbles.

for 30 min reduced the number concentration of ultrafine bubbles by 90 % regardless of the generation method. Feasibility studies were also conducted for ultrafine bubbles in an aqueous surfactant solution or solid particle dispersion. The ultrasonic method selectively destabilized ultrafine bubbles in the solutions. Ultrafine bubble removal using ultrasound has been adopted as an international standard by the International Organization for Standardization (ISO 24261-2, 2021) because of its simplicity and quickness of operation.

3.3 Sonochemical characteristics

Sonochemistry is a field in chemistry, physics, and biology related to ultrasonic cavitation. Some reports have shown that ultrafine bubbles promote ultrasonic cavitation (Tuziuti et al., 2020, 2021; Tsuchida et al., 2022). Sonoluminescence, which is light emission from a liquid due to ultrasonic cavitation (Brenner et al., 2002; Ashokkumar, 2011), was enhanced by ultrafine bubbles when ultrasound was applied at 54 kHz with high intensity (Tuziuti et al., 2020). This phenomenon was observed for various bubble concentrations (Tuziuti et al., 2021). They considered that ultrafine bubbles had the potential to provide nucleation sites for ultrasonic cavitation. The sonochemical degradation of acid orange was accelerated when the microbubble solution was irradiated with ultrasound at 45 kHz (Tsuchida et al., 2022). They concluded that ultrafine bubbles played an important role in improving sonochemical reactions.

An in-situ sediment remediation method using a combination of ultrasound and ozone ultrafine bubbles was investigated to remediate both organic (p-terphenyl) and inorganic (chromium) materials in contaminated sediments of the lower Passaic River in United States (Batagoda et al., 2019; Hewage et al., 2020, 2021b). The ozone ultrafine bubbles increased the solubility of ozone in water and reduced wastage. Also, the high-ozone concentration in water also increases chromium oxidation (Batagoda et al., 2019). This proposed treatment method showed sufficient remediation success with removing these combined contaminants, on average, 60 % and 71 % for p-terphenyl and chromium, respectively. The chromium removal was directly influenced by the chemical oxidation and sonication for chromium desorption from sediments. However, p-terphenyl degradation was more likely influenced by the combined effects of chemical oxidation and ultrasound-assisted pyrolysis (Hewage et al., 2021b). Dark green Rit dye was effectively decolored by combining ultrafine bubbles and ultrasonic irradiation (Bui and Han, 2020). The color removal mechanisms were due to the electrostatic attraction between the ultrafine bubble and dye and the oxidation of the dye using reactive species such as hydroxy radicals generated through ultrasonic cavitation.

Ultrasonic atomization generates a mist, such as fine droplets at room temperature (Wood and Loomis, 1927; Yasuda et al., 2011). When an aqueous ethanol solution is atomized using ultrasound, the ethanol is enriched in the

mist (Sato et al., 2001; Yasuda et al., 2003; Matsuura et al., 2007). Ethanol enrichment is attributed to the hydrophobic interaction of ethanol molecules in water (Yasuda et al., 2014). Separation using ultrasonic atomization has also been reported on ketones (Yasuda et al., 2004), amino acids (Suzuki et al., 2006), surfactants (Jimmy et al., 2008), fine particles (Nii and Oka, 2014), and ion liquid (Mai et al., 2019). The advantages of ultrasonic atomization separation include simple operation, maintenance-free, and suitability for heat sensitive materials. Ultrafine bubbles water was used as a solvent to improve the enrichment performance using ultrasonic atomization (Yasuda et al., 2020b; 2022). The ethanol concentration in the collected mist with ultrafine bubbles was higher than that without ultrafine bubbles (Yasuda et al., 2020b). When the ethanol concentration in the solution was low and the carrier gas velocity was slow, the enrichment effect of ultrafine bubbles was particularly remarkable. Next, the enrichment characteristics of amino acids were investigated using ultrasonic atomization (Yasuda et al., 2022). **Fig. 6** shows the effect of the concentration of amino acids in solution on the enrichment factor with and without ultrafine bubbles for L-phenylalanine and L-tyrosine. Here, the ratio of the solute concentration in the mist to that in the solution is defined as the enrichment factor. The enrichment factor increased with decreasing solution concentration and was enhanced by adding ultrafine bubbles. The authors explained the reason for this enhancement as follows. Amino acid bonds to the surface of ultrafine bubbles in a solution because of their hydrophobic affinity. Under ultrasonic fields, ultrafine bubbles containing amino acids aggregate or coalesce by secondary Bjerknes force (Leighton, 1994), rise in the solution by buoyancy force and burst at the solution surface. The concentration of amino acids increases at the solution surface, and many amino acids are contained in the droplets.

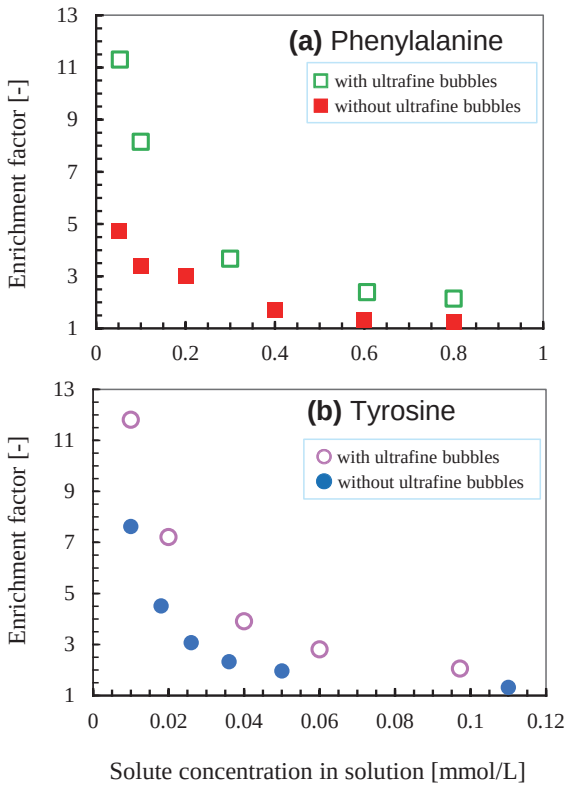


Fig. 6 Effect of solute concentration in solution on enrichment factor with and without ultrafine bubbles for **(a)** phenylalanine and **(b)** tyrosine.

Freezing of foods is a complicated and time-consuming process that requires the aggregation of molecules from a liquid to a solid crystal network (Kiani and Sun, 2011). The influences of CO_2 ultrafine bubbles and ultrasound on the crystallization behavior of water during freezing of model sugar solutions were examined (Adhikari et al., 2019). The combination treatment facilitated in reducing the supercooling degree, resulting in faster nucleation during the freezing process. This method may improve the characteristics of frozen products such as ice cream and frozen desserts.

4. Application to particle-related technologies

4.1 Fine particle synthesis

Synthesis of fine particles using ultrafine bubbles has been reported in several papers. Authors (Yasuda et al., 2020a) used $HAuCl_4$ aqueous solutions and synthesized gold nanoparticles by ultrasonic irradiation at 500 kHz with the aid of ultrafine bubbles without any capping and reducing agents. **Figs. 7(a)** and **(b)** show the electron micrographs and size distribution of gold nanoparticles synthesized with and without ultrafine bubbles. The particle sizes prepared with ultrafine bubbles were much smaller than those of the gold nanoparticles prepared without ultrafine bubbles. The mean diameter of the spherical gold nanoparticles synthesized with ultrafine bubbles decreased with increasing concentration of ultrafine bubbles. This is because ultrafine bubbles accelerate the sonochemical reduction of gold ions and suppress the aggregation between gold nanoparticles. Moreover, the gold nanoparticles were stable in a solution containing ultrafine bubbles (**Fig. 7(c)**) because gold nanoparticles were electrostatically adsorbed on ultrafine bubbles (**Fig. 7(d)**), which have a very long lifetime in water.

Nanocomposites of $CaCO_3$ and pulp fiber were prepared by injecting ultrafine bubbles of CO_2 into an aqueous $Ca(OH)_2$ solution containing pulp fibers (Fuchise-Fukuoka et al., 2020). The precipitated $CaCO_3$ nanoparticles formed on the pulp fiber surfaces were more stably attached to the pulp fiber surfaces against shear force. Compared with mixing method, the specific surface area and surface smoothness of nanosized $CaCO_3$-containing handsheets increased. Water containing ultrafine bubbles of hydrogen at high concentrations was used as the blending solvent for preparing cement mortar (Kim W.-K. et al., 2021). The cement mortar had greater flexural and compressive strengths

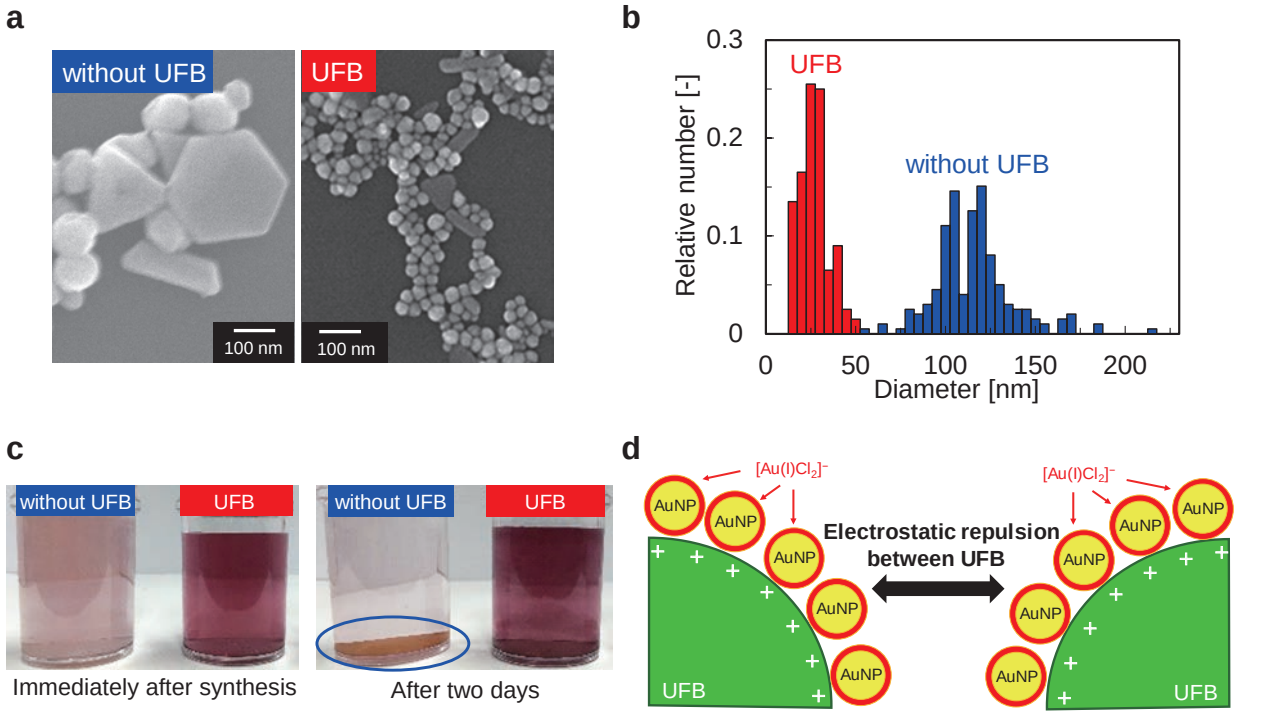


Fig. 7 Effect of ultrafine bubbles (UFB) on sonochemical synthesis and colloidal stability of gold nanoparticles: **(a)** Electron micrograph and **(b)** the size distribution of particles; **(c)** Photograph of colloids immediately and 2 days after synthesis; **(d)** Stabilization mechanism by ultrafine bubbles.

than plain water-based mortars. This was because ultrafine bubbles enhanced the collision between the solvent and cement particles, accelerating the hydration and pozzolanic reactions.

Jadhav and Brigou (2020) formed the hollow zinc phosphate nanoparticles using ultrafine bubbles as shown in **Fig. 8**. First, zinc nitrate was added to the ultrafine bubble water to adsorb Zn^{2+} ions on the negatively charged surface of ultrafine bubbles. Next, by adding diammonium phosphate, the ultrafine bubbles served as nucleation sites for the subsequent reaction of Zn^{2+} with PO_4^{3-} ions. Finally, the pH of the solution was adjusted to 8.5 to precipitate zinc phosphate on the ultrafine bubble surfaces, forming hollow particles. The advantages of using ultrafine bubbles for fine particle synthesis are safety, low environmental loads, and no impurities in fine particles. Ultrafine bubbles, in particular, are optimal for creating fine hollow fine particles since there is no need to remove the core templates, which are generally employed with solid or liquid particles.

4.2 Adsorption, desorption, and extraction

Studies have been reported on the use of ultrafine bubbles to promote adsorption onto particles, as well as desorption and extraction from particles. The effect of ultrafine bubbles on the adsorption of lead ions onto activated carbon was investigated with and without agitation (Kyzas et al., 2019; 2020). In the case of agitation, the effect of ultrafine bubbles on the adsorption capacity of lead ions was small. However, in the case without agitation, the

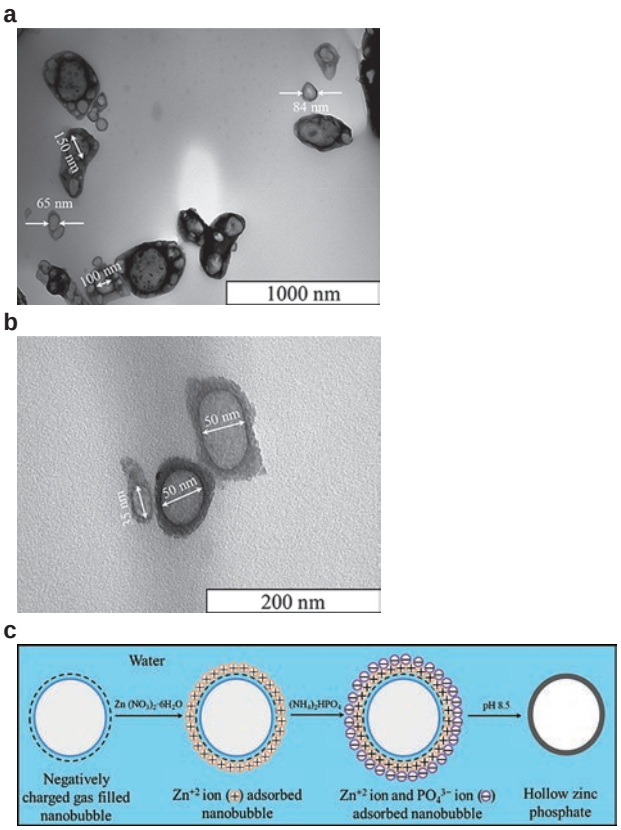


Fig. 8 Images of transmission electron microscopy of hollow zinc phosphate nanoparticles obtained by encapsulation of ultrafine bubbles shown on different scales: **(a)** 1000 nm; **(b)** 200 nm; **(c)** schematic representation of the formation of the hollow nanoparticles. Reprinted with permission from Ref. (Jadhav and Brigou, 2020). Copyright: (2020) American Chemical Society.

adsorption capacity in the presence of ultrafine bubbles became much higher than that in the absence of ultrafine bubbles. Moreover, ultrafine bubbles largely accelerated the adsorption rate with and without agitation. They explained that the ultrafine bubbles accepted positively charged lead ions onto their interface and assisted the diffusion and penetration phenomena of lead ions into the activated carbon pores. The influence of ultrafine bubbles on the adsorption of sodium oleate on calcite surface was examined (Wang et al., 2019). Ultrafine bubbles had a certain inhibitory effect on the adsorption of sodium oleate on the calcite surface, and it significantly promoted the flocculation between particles of sodium oleate.

Hydrogen ultrafine bubbles were applied to soils contaminated with copper to desorb copper (Kim and Han, 2020). Ultrafine bubbles improved the desorption of copper. Additionally, when the ultrafine bubbles were used as desorption enhancers in electrokinetic experiments, they had better remediation effects than distilled water.

Ettoumi et al. (2022) generated ultrafine bubbles in ion liquid using compression–decompression method and extracted polyphenols from Chinese Hickory. Compared to the extract using ion liquid without ultrafine bubbles, the extract of this method showed significantly higher antioxidant activity and polyphenol yields. Electron micrographs confirmed that nanojets due to ultrafine bubbles caused morphological destruction of the husk powder. Their group also extracted phytochemical compounds from Camellia Oleifera shells using water with CO_2 ultrafine bubbles (Javed et al., 2022). Compared with ethanol extraction, ultrafine bubble water led to a higher extraction yield of total phenolic and flavonoid content. Collagen was extracted from tilapia scales by bubbling ultrafine bubbles of three different gases (O_2, CO_2, and O_3) into an acetic acid solution (Kuwahara, 2021). Using CO_2 in the acetic acid solution was the most effective method to obtain collagen in a relatively high yield. The ultrafine bubble method is a simple, mild, cost-effective, and environmentally friendly method for adsorption onto particles, as well as desorption and extraction from particles.

4.3 Cleaning and prevention of fouling

The most typical application of ultrafine bubbles is cleaning. There are several reports on the use of ultrafine bubbles to remove contaminants from solid surfaces. Minute particles with a diameter of about 50 nm were successfully removed from the wafer surfaces by impinging a jet of ultrapure water containing ultrafine bubbles (Morimatsu et al., 2004). Removal of protein from the solid–liquid interface was investigated using a quartz crystal microbalance to evaluate the removal amount (Liu et al., 2008; Liu and Craig, 2009). Bovine serum albumin was completely removed from both hydrophobic and hydrophilic surfaces using ultrafine bubbles. The cleaning efficiency compared to sodium dodecyl sulfate, a typical surfactant (Liu et al., 2008). Lysozyme was completely removed from hydrophobic surfaces by combing ultrafine bubbles and sodium dodecyl sulfate (Liu and Craig, 2009). Ushida et al. (2012b) investigated the washing rate of cloth in an alternating flow system. The ultrafine bubble water achieved a washing rate greater than that of ion-exchanged water. Moreover, the mixture with ultrafine bubbles and anionic surfactant exhibited a washing rate higher than that of an aqueous anionic surfactant solution without ultrafine bubbles. The ceramic membrane completely clogged by humic acid fouling was effectively cleaned using ultrafine bubbles (Ghadimkhani et al., 2016). Dyed cotton towels were washed without soap using oxygen-rich ultrafine bubbles and with soap using the conventional method (Anis et al., 2022). The lowest color strength and highest fastness were obtained after washing with ultrafine bubbles. Chemical oxygen demand measurements of washing baths revealed that ultrafine bubble washing was more environmentally friendly than conventional methods.

Terasaka (2021) investigated the cleaning process of salt adhering to wall surfaces when ultrafine bubble water was passed through a sample surface at a constant flow rate. The cleaning rate was determined using the dissolved salt concentration in water. **Fig. 9(a)** shows the progress of the cleaning rate when "hard deposits," such as salts, were washed with running water, as opposed to paste-like "soft deposits," such as biofilm and starch. The cleaning process consists of adhesion, dissolution, peeling, and dissolution. The starting time of the peeling step is promoted by ultrafine bubbles, and consequently, the cleaning is completed in a shorter time with ultrafine bubble water. **Fig. 9(b)** shows a hypothesis of the cleaning mechanism. It explains that the cleaning mechanism using ultrafine bubbles uses the high permeability of ultrafine bubbles accompanying water and the metastability of ultrafine bubbles that shift to a stable state when the specific potential is exceeded. In 2011, West Nippon Expressway Company Limited started cleaning toilets in expressway service stations and parking areas using ultrafine bubbles. Ultrafine bubbles have been successfully used to remove salts from bridge surfaces. The necessary time for removing salt from the surface has shortened to less than one-fourth using a water jet containing ultrafine bubbles (Yabe, 2021).

Ultrafine bubbles were found to prevent surface fouling of bovine serum albumin (Wu et al., 2008) and lysozyme (Zhu et al., 2016). Farid et al. (2022) demonstrated the benefits of introducing ultrafine bubbles into the feed for alleviating flux reduction and membrane pore wetting associated with mineral scaling in membrane distillation. Introducing ultrafine bubbles reduced membrane scaling propensity and offered excellent resistance to pore wetting associated with scaling. This is attributed to high surface shear forces due to flow turbulence and electrostatic

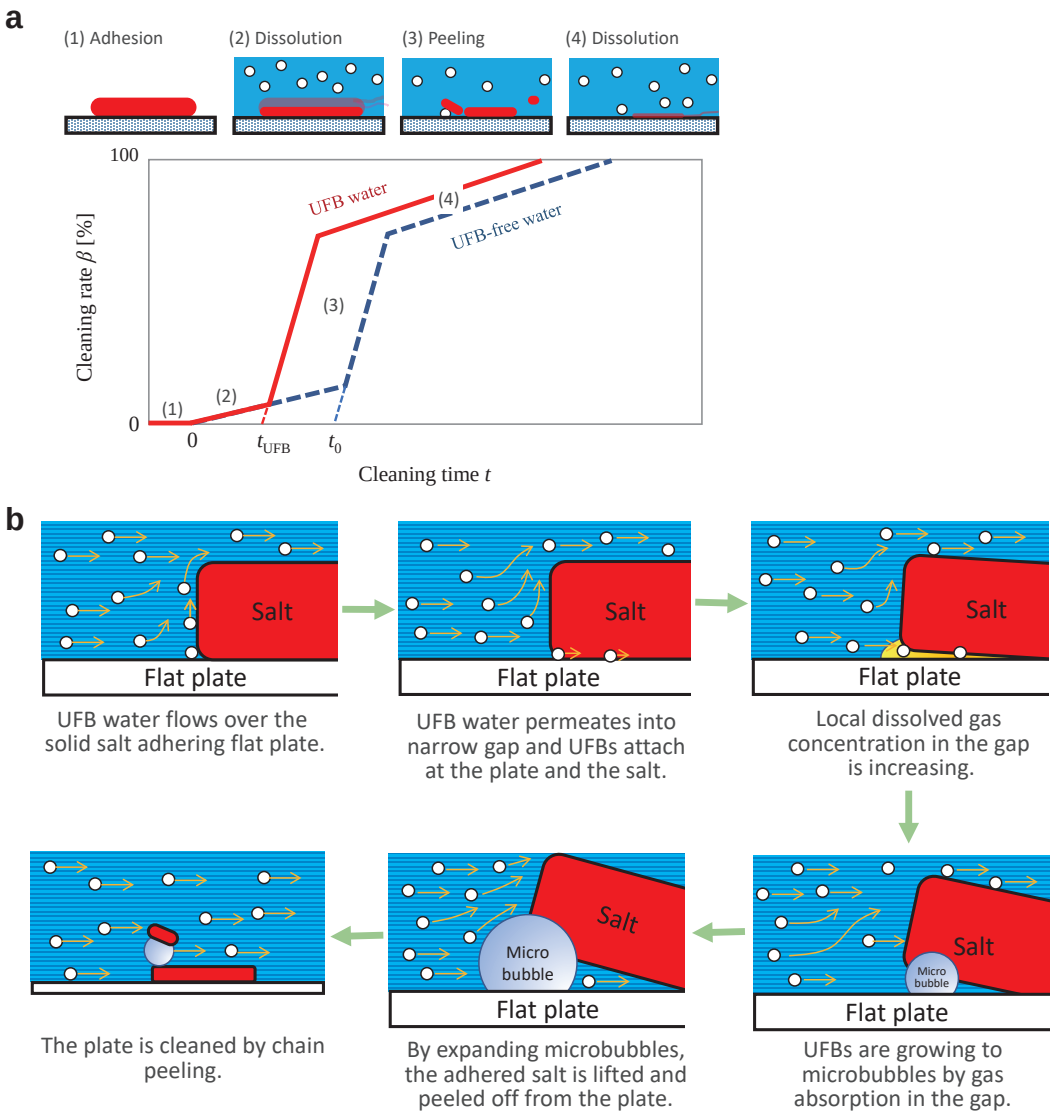


Fig. 9 **(a)** Cleaning process of salt adhering to wall surface with ultrafine bubble water and **(b)** hypothesis of removal mechanism of wall-attached salt by flowing ultrafine bubble water. Reprinted with permission from Ref. (Terasaka, 2021). Copyright: (2021) Jenny Stanford Publishing.

attractions between the negatively charged ultrafine bubbles and the counterions. The potential use of ultrafine bubbles as corrosion and scale inhibitors for geothermal power plants was discussed (Kioka and Nakagawa, 2021). The crystal growth rate of calcite, which causes scaling, was found to be more retarded as the concentration of ultrafine bubbles increased (Tagomori et al., 2022). Ultrafine bubbles inhibit the corrosion of low-carbon steels, with an inhibition efficiency of 20–50 % in the acidic geothermal fluid (Aikawa et al., 2021). They concluded that ultrafine bubbles could act as a nanoscopic coating material in mitigating corrosion, increasing the slip length on the solid interface and preventing exposing the interface to acidic geothermal fluids by (1) behaving as a bubble mattress covering most of the steel surface or (2) promoting nucleation and aggregation of an insignificant quantity of silica precipitation on the steel surface. Compared to commonly used chemical products, ultrafine bubbles have shown to be a potent, chemically benign, environmentally friendly, and inexpensive corrosion and scale inhibitor of calcium carbonate.

5. Conclusions

This review discussed the fundamental and ultrasonic characteristics of ultrafine bubbles (bulk nanobubbles) and introduced their application to particle-related technology. The diameter of ultrafine bubbles is less than 1 μm, and the bubble surface is highly charged. The rising velocity due to buoyancy is much smaller than the Brownian motion velocity. The diameter and concentration are closely related to zeta potential. The diameter, concentration, and zeta potential of ultrafine bubbles depend on pH of solution, concentration, and several types of inorganic ions and surfactants in water. Additionally, the concentration can be increased using a rotary evaporator. They are stable in water for several months; however, there is no model

to fully explain the stabilization mechanism. They formed hydroxy radicals at strong acid conditions and reduced in friction in the orifice.

Ultrafine bubbles can be generated and removed using ultrasonic irradiation at low and high frequencies, respectively. Chemical and physical effects of ultrasonic cavitation, such as luminescence and degradation, were enhanced by ultrafine bubbles. It was considered that ultrafine bubbles became the nucleation of cavitation. Separation performance of ethanol and amino acids from aqueous solutions using ultrasonic atomization was improved by ultrafine bubbles.

Ultrafine bubbles have been applied to fine particle synthesis, adsorption, desorption, extraction, cleaning, and prevention of fouling. Fine gold nanoparticles, $CaCO_3$/pulp fiber nanocomposites, and hollow zinc phosphate nanoparticles were synthesized by ultrafine bubbles. Adsorption of lead ions to activated carbon and desorption of copper from soil were enhanced by ultrafine bubbles due to electrostatic interaction between ultrafine bubbles and metal ions. Bubbling CO_2 ultrafine bubbles effectively extracted collagen from tilapia scales. Ultrafine bubble water without surfactant efficiently cleaned the protein, dye, and salt on solid surfaces and prevented surface fouling. Thus, ultrafine bubbles have been shown to be powerful, environmentally friendly, safe, clean, simple, and inexpensive methods.

Currently, ultrafine bubbles have many theoretically unexplained characteristics, such as high stability and chargeability, and a great deal of academic research is still being conducted. Clarifying the various characteristics of ultrafine bubbles is expected to lead to academic development and further social and industrial diffusion of ultrafine bubbles through applied research, such as developing new applications in various fields and reducing production costs.

Acknowledgments

This work was partly supported by JSPS KAKENHI Grant Numbers JP16H04560 and JP19H02505.

References

Adhikari B.M., Tung V.P., Truong T., Bansal N., Bhandari B., Water crystallisation of model sugar solutions with nanobubbles produced from dissolved carbon dioxide, Food Biophysics, 14 (2019) 403–414. DOI: 10.1007/s11483-019-09590-2

Agarwal K., Trivedi M., Nirmalkar N., Bulk nanobubbles in aqueous salt solution, Materials Today: Proceedings, 57 (2022) 1789–1792. DOI: 10.1016/j.matpr.2021.12.477

Aikawa A., Kioka A., Nakagawa M., Anzai S., Nanobubbles as corrosion inhibitor in acidic geothermal fluid, Geothermics, 89 (2021) 101962. DOI: 10.1016/j.geothermics.2020.101962

Anis P., Toprak-Cavdur T., Çalışkan N., Oxygen-enriched nanobubbles for a green reactive washing process, AATCC Journal of Research, 9 (2022) 152–160. DOI: 10.1177/24723444221084396

Ashokkumar M., Lee J., Kentish S., Grieser F., Bubbles in an acoustic field: an overview, Ultrasonics Sonochemistry, 14 (2007) 470–475. DOI: 10.1016/j.ultsonch.2006.09.016

Ashokkumar M., The characterization of acoustic cavitation bubbles—an overview, Ultrasonics Sonochemistry, 18 (2011) 864–872. DOI: 10.1016/j.ultsonch.2010.11.016

Atkinson A.J., Apul O.G., Schneider O., Garcia-Segura S., Westerhoff P., Nanobubble technologies offer opportunities to improve water treatment, Account of Chemical Research, 52 (2019) 1196–1205. DOI: 10.1021/acs.accounts.8b00606

Attard P., The stability of nanobubbles, The European Physical Journal Special Topics, 223 (2014) 893–914. DOI: 10.1140/epjst/e2013-01817-0

Azevedo A., Etchepare R., Calgaroto S., Rubio J., Aqueous dispersions of nanobubbles: generation, properties and features, Minerals Engineering, 94 (2016) 29–37. DOI: 10.1016/j.mineng.2016.05.001

Batagoda J.H., Hewage S.D.A., Meegoda J.N., Remediation of heavy-metal-contaminated sediments in USA using ultrasound and ozone nanobubbles, Journal of Environmental Engineering and Science, 14 (2019) 130–138. DOI: 10.1680/jenes.18.00012

Beal H.M., Skauen D.M., A study of emulsification with ultrasonic waves II, Journal of the American Pharmaceutical Association, 44 (1955) 490–493. DOI: 10.1002/jps.3030440810

Brenner M.P., Hilgenfeldt S., Lohse D., Single-bubble sonoluminescence, Reviews of Modern Physics, 74 (2002) 425–484. DOI: 10.1103/RevModPhys.74.425

Brenner M.P., Lohse D., Dynamic equilibrium mechanism for surface nanobubble stabilization, Physical Review Letters, 101 (2008) 214505. DOI: 10.1103/PhysRevLett.101.214505

Bui T.T., Nguyen D.C., Han M., Average size and zeta potential of nanobubbles in different reagent solutions, Journal of Nanoparticles Research, 21 (2019) 173. DOI: 10.1007/s11051-019-4618-y

Bui T.T., Han M., Decolorization of dark green Rit dye using positively charged nanobubbles technologies, Separation and Purification Technology, 233 (2020) 116034. DOI: 10.1016/j.seppur.2019.116034

Calgaroto S., Wilberg K.Q., Rubio J., On the nanobubbles interfacial properties and future applications in flotation, Minerals Engineering, 60 (2014) 33–40. DOI: 10.1016/j.mineng.2014.02.002

Cho S.-H., Kim J.-Y., Chun J.-H., Kim J.-D., Ultrasonic formation of nanobubbles and their zeta-potentials in aqueous electrolyte and surfactant solutions, Colloids and Surfaces A: Physicochemical and Engineering Aspects, 269 (2005) 28–34. DOI: 10.1016/j.colsurfa.2005.06.063

Crum L.A., Measurements of the growth of air bubbles by rectified diffusion, The Journal of the Acoustical Society of America, 68 (1980) 203–211. DOI: 10.1121/1.384624

Duval E., Adichtchev S., Sirotkin S., Mermet A., Long-lived submicrometric bubbles in very diluted alkali halide water solutions, Physical Chemistry Chemical Physics, 14 (2012) 4125–4132. DOI: 10.1039/c2cp22858k

Einstein A, Über die von der molekularkinetischen Theorie der Wärme geforderte Bewegung von in ruhenden Flüssigkeiten suspendierten Teilchen, Annalen der Physik, 322 (1905) 549–560. DOI: 10.1002/andp.19053220806

English N.J., Environmental exploration of ultra-dense nanobubbles: rethinking sustainability, Environments, 9 (2022) 33. DOI: 10.3390/environments9030033

Epstein P.S., Plesset M.S., On the stability of gas bubbles in liquid-gas solutions, The Journal of Chemical Physics, 18 (1950) 1505–1509. DOI: 10.1063/1.1747520

Ettoumi F.-E., Zhang R., Belwal T., Javed M., Xu Y., Li L., Weide L., Luo Z., Generation and characterization of nanobubbles in ionic liquid for a green extraction of polyphenols from Carya cathayensis Sarg, Food Chemistry, 369 (2022) 130932. DOI: 10.1016/j.foodchem.2021.130932

Farid M.U., Kharraz J.A., Lee C.-H., Fang J.K.-H., St-Hilaire S., An A.K., Nanobubble-assisted scaling inhibition in membrane distillation for the treatment of high-salinity brine, Water Research, 209 (2022) 117954. DOI: 10.1016/j.watres.2021.117954

Fuchise-Fukuoka M., Oishi M., Goto S., Isogai A., Preparation of $CaCO_3$ nanoparticle/pulp fiber composites using ultrafine bubbles, Nordic

Pulp & Paper Research Journal, 35 (2020) 279–287. DOI: 10.1515/npprj-2019-0078

Gedanken A., Using sonochemistry for the fabrication of nanomaterials, Ultrasonics Sonochemistry, 11 (2004) 47–55. DOI: 10.1016/j.ultsonch.2004.01.037

German S.R., Edwards M.A., Chen Q., White H.S., Laplace pressure of individual H_2 nanobubbles from pressure-addition electrochemistry, Nano Letters, 16 (2016) 6691–6694. DOI: 10.1021/acs.nanolett.6b03590

Ghadimkhani A., Zhang W., Marhaba T., Ceramic membrane defouling (cleaning) by air nano bubbles, Chemosphere, 146 (2016) 379–384. DOI: 10.1016/j.chemosphere.2015.12.023

Hewage S.A., Batagoda J.H., Meegoda J.N., In situ remediation of sediments contaminated with organic pollutants using ultrasound and ozone nanobubbles, Environmental Engineering Science, 37 (2020) 521–534. DOI: 10.1089/ees.2019.0497

Hewage S.A., Kewalramani J., Meegoda J.N., Stability of nanobubbles in different salts solutions, Colloids and Surfaces A, 609 (2021a) 125669. DOI: 10.1016/j.colsurfa.2020.125669

Hewage S.A., Batagoda J.H., Meegoda J.N., Remediation of contaminated sediments containing both organic and inorganic chemicals using ultrasound and ozone nanobubbles, Environmental Pollution, 274 (2021b) 116538. DOI: 10.1016/j.envpol.2021.116538

Hirai M., Ajito S., Takahashi K., Iwasa T., Li X., Wen D., Kawai-Hirai R., Ohta N., Igarashi N., Shimizu N., Structure of ultrafine bubbles and their effects on protein and lipid membrane structures studied by small- and wide-angle X-ray scattering, The Journal of Physical Chemistry B, 123 (2019) 3421–3429. DOI: 10.1021/acs.jpcb.9b00837

ISO 20480-1:2017, Fine bubble technology—General principles for usage and measurement of fine bubbles—Part 1: Terminology, (2017). <https://www.iso.org/standard/68187.html> accessed 20.12.2022.

ISO 24261-2:2021, Fine bubble technology—Elimination method for sample characterization—Part 2: Fine bubble elimination techniques, (2021). <https://www.iso.org/standard/80020.html> accessed 20.12.2022.

Jadhav A.J., Brigou M., Bulk nanobubbles or not nanobubbles: that is the question, Langmuir, 36 (2020) 1699–1708. DOI: 10.1021/acs.langmuir.9b03532

Javed M., Belwal T., Ruyuan Z., Xu Y., Li L., Luo Z., Optimization and mechanism of phytochemicals extraction from Camellia Oleifera shells using novel biosurfactant nanobubbles solution coupled with ultrasonication, Food and Bioprocess Technology, 15 (2022) 1101–1114. DOI: 10.1007/s11947-022-02793-5

Jimmy B., Kentish S., Grieser F., Ashokkumar M., Ultrasonic nebulization in aqueous solutions and the role of interfacial adsorption dynamics in surfactant enrichment, Langmuir, 24 (2008) 10133–10137. DOI: 10.1021/la801876s

Kanematsu W., Tuziuti T., Yasui K., The influence of storage conditions and container materials on the long term stability of bulk nanobubbles—consideration from a perspective of interactions between bubbles and surroundings, Chemical Engineering Science, 219 (2020) 115594. DOI: 10.1016/j.ces.2020.115594

Ke S., Xiao W., Quan N., Dong Y., Zhang L., Hu J., Formation and stability of bulk nanobubbles in different solutions, Langmuir, 35 (2019) 5250–5256. DOI: 10.1021/acs.langmuir.9b00144

Kiani H., Sun D-.W., Water crystallization and its importance to freezing of foods: a review, Trends in Food Science & Technology, 22 (2011) 407–426. DOI: 10.1016/j.tifs.2011.04.011

Kim D., Han J., Remediation of copper contaminated soils using water containing hydrogen nanobubbles, Applied Sciences, 10 (2020) 2185. DOI: 10.3390/app10062185

Kim E., Choe J.K., Kim B.H., Kim J., Park J., Choi Y., Unraveling the mystery of ultrafine bubbles: establishment of thermodynamic equilibrium for sub-micron bubbles and its implications, Journal of Colloid and Interface Science, 570 (2020) 173–181. DOI: 10.1016/j.jcis.2020.02.101

Kim J.-Y., Song M.-G., Kim J.-D., Zeta potential of nanobubbles generated by ultrasonication in aqueous alkyl polyglycoside solutions, Journal of Colloid and Interface Science, 223 (2000) 285–291. DOI: 10.1006/jcis.1999.6663

Kim W.-K., Hong G., Kim Y.-H., Kim J.-M., Kim J., Han J.-G., Lee J.-Y., Mechanical strength and hydration characteristics of cement mixture with highly concentrated hydrogen nanobubble water, Materials, 14 (2021) 2735. DOI: 10.3390/ma14112735

Kioka A., Nakagawa M., Theoretical and experimental perspectives in utilizing nanobubbles as inhibitors of corrosion and scale in geothermal power plant, Renewable and Sustainable Energy Reviews, 149 (2021) 111373. DOI: 10.1016/j.rser.2021.111373

Kuwahara J., Extraction of type I collagen from tilapia scales using acetic acid and ultrafine bubbles, Processes, 9 (2021) 288. DOI: 10.3390/pr9020288

Kyzas G.Z, Bomis G., Kosheleva R.I., Efthimiadou E.K., Favvas E.P., Kostoglou M., Mitropoulos A.C., Nanobubbles effect on heavy metal ions adsorption by activated carbon, Chemical Engineering Journal, 356 (2019) 91–97. DOI: 10.1016/j.cej.2018.09.019

Kyzas G.Z, Favvas E.P., Kostoglou M., Mitropoulos A.C., Effect of agitation on batch adsorption process facilitated by using nanobubbles, Colloids and Surfaces A, 607 (2020) 125440. DOI: 10.1016/j.colsurfa.2020.125440

Lauterborn W., Ohl C.-D., Cavitation bubble dynamics, Ultrasonics Sonochemistry,4(1997)65–75.DOI:10.1016/S1350-4177(97)00009-6

Lee J.I., Kim J.-M., Role of anionic surfactant in the generation of bulk nanobubbles by ultrasonication, Colloid and Interface Science Communications, 46 (2022a) 100578. DOI: 10.1016/j.colcom.2021.100578

Lee J.I., Kim J.-M., Influence of temperature on bulk nanobubble generation by ultrasonication, Colloid and Interface Science Communications, 49 (2022b) 100639. DOI: 10.1016/j.colcom.2022.100639

Lee S.J., Kim S., Simultaneous measurement of size and velocity of microbubbles moving in an opaque tube using an X-ray particle tracking velocimetry technique, Experiments in Fluids, 39 (2005) 492–497. DOI: 10.1007/s00348-005-0956-x

Leighton T.G., The Acoustic Bubble, Academic Press, London, 1994, ISBN: 0-12-441921-6.

Li M., Ma X., Eisener J., Pfeiffer P., Ohl C.-D., Sun C., How bulk nanobubbles are stable over a wide range of temperatures, Journal of Colloid and Interface Science, 596 (2021) 184–198. DOI: 10.1016/j.jcis.2021.03.064

Liu G., Wu Z., J. Craig V.S.C., Cleaning of protein-coated surfaces using nanobubbles: an investigation using a quartz crystal microbalance, The Journal of Physical Chemistry C, 112 (2008) 16748–16753. DOI: 10.1021/jp805143c

Liu G., J. Craig V.S.C., Improved cleaning of hydrophilic protein-coated surfaces using the combination of nanobubbles and SDS, Applied Materials and Interfaces, 1 (2009) 481–487. DOI: 10.1021/am800150p

Liu S., Kawagoe Y., Makino, Y., Oshita, S., Effects of nanobubbles on the physicochemical properties of water: the basis for peculiar properties of water containing nanobubbles, Chemical Engineering Science, 93 (2013) 250–256. DOI: 10.1016/j.ces.2013.02.004

Liu S., Oshita S., Makino Y., Wang Q., Kawagoe Y., Uchida T., Oxidative capacity of nanobubbles and its effect on seed germination, ACS Sustainable Chemistry & Engineering, 4 (2016a) 1347–1353. DOI: 10.1021/acssuschemeng.5b01368

Liu S., Oshita S., Kawabata S., Makino Y., Yoshimoto T., Identification of ROS produced by nanobubbles and their positive and negative effects on vegetable seed germination, Langmuir, 32 (2016b) 11295–11302. DOI: 10.1021/acs.langmuir.6b01621

Lohse D., Zhang X., Surface nanobubbles and nanodroplets, Reviews of Modern Physics, 87 (2015) 981–1035. DOI: 10.1103/RevModPhys.87.981

Ma X., Li M., Pfeiffer P., Eisener J., Ohl C.-D., Ion adsorption stabilizes bulk nanobubbles, Journal of Colloid and Interface Science, 606 (2022) 1380–1394. DOI: 10.1016/j.jcis.2021.08.101

Mai N.L., Koo Y.-M., Ha S.H., Separation characteristics of hydrophilic ionic liquids from ionic liquids-water solution by ultrasonic atomization, Ultrasonics Sonochemistry, 53 (2019) 187–191. DOI: 10.1016/j.ultsonch.2019.01.004

Mason T.J., Ultrasonic cleaning: an historical perspective, Ultrasonics Sonochemistry, 29 (2016) 519–523. DOI: 10.1016/j.ultsonch.2015.05.004

Matsuura K., Fukazu T., Abe F., Sekimoto T., Tomishige T., Efficient separation coupled with ultrasonic atomization using a molecular sieve, AIChE Journal, 53 (2007) 737–740. DOI: 10.1002/aic.11113

Meegoda J.N., Hewage S.A., Batagoda J.H., Stability of nanobubbles, Environmental Engineering Science, 35 (2018) 1216–1227. DOI: 10.1089/ees.2018.0203

Meegoda J.N., Hewage S.A., Batagoda J.H., Application of the diffused double layer theory to nanobubbles, Langmuir, 35 (2019) 12100–12112. DOI: 10.1021/acs.langmuir.9b01443

Millare C.J., Basilia B.A., Nanobubbles from ethanol-water mixtures: generation and solute effects via solvent replacement method, Chemistry Select, 3 (2018) 9268–9275. DOI: 10.1002/slct.201801504

Minamikawa K., Takahashi M., Makino T., Tago K., Hayatsu M., Irrigation with oxygen-nanobubble water can reduce methane emission and arsenic dissolution in a flooded rice paddy, Environmental Research Letters, 10 (2015) 084012. DOI: 10.1088/1748-9326/10/8/084012

Morimatsu T., Goto M., Kohno M., Yabe A., Cleaning effect of nanobubbles (1st report: minute particle contamination), Thermal Science and Engineering, 12 (2004) 67–68.

Muthukumaran S., Kentish S., Lalchandani S., Ashokkumar M., Mawson R., Stevens G.W., Grieser F., The optimisation of ultrasonic cleaning procedures for dairy fouled ultrafiltration membranes, Ultrasonics Sonochemistry, 12 (2005) 29–35. DOI: 10.1016/j.ultsonch.2004.05.007

Nakagawa M., Kioka A., Tagomori K., Nanobubbles as friction modifier, Tribology International, 165 (2022) 107333. DOI: 10.1016/j.triboint.2021.107333

Nii S., Oka N., Size-selective separation of submicron particles in suspensions with ultrasonic atomization, Ultrasonics Sonochemistry, 21 (2014) 2032–2036. DOI: 10.1016/j.ultsonch.2014.03.033

Nirmalkar N., Pacek A.W., Barigou M., On the existence and stability of bulk nanobubbles, Langmuir, 34 (2018a) 10964–10973. DOI: 10.1021/acs.langmuir.8b01163

Nirmalkar N., Pacek A.W., Barigou M., Interpreting the interfacial and colloidal stability of bulk nanobubbles, Soft Mater, 14 (2018b) 9643–9656. DOI: 10.1039/c8sm01949e

Nirmalkar N., Pacek A.W., Barigou M., Bulk nanobubbles from acoustically cavitated aqueous organic solvent mixtures, Langmuir, 35 (2019) 2188–2195. DOI: 10.1021/acs.langmuir.8b03113

Ohgaki K., Khanh N.Q., Joden Y., Tsuji A., Nakagawa T., Physicochemical approach to nanobubble solutions, Chemical Engineering Science, 65 (2010) 1296–1300. DOI: 10.1016/j.ces.2009.10.003

Patois E., Capelle M.A.H., Palais C., Gurny R., Arvinte T., Evaluation of nanoparticle tracking analysis (NTA) in the characterization of therapeutic antibodies and seasonal influenza vaccines: pros and cons, Journal of Drug Delivery Science and Technology, 22 (2012) 427–433. DOI: 10.1016/S1773-2247(12)50069-9

Pétrier C., Lamy M.-F., Francony A., Benahcene A., David B., Sonochemical degradation of phenol in dilute aqueous solutions: comparison of the reaction rates at 20 and 487 kHz, Journal of Physical Chemistry, 98 (1994) 10514–10520. DOI: 10.1021/j100092a021

Petsev N.D., Shell M.S., Leal L.G., Dynamic equilibrium explanation for nanobubbles' unusual temperature and saturation dependence, Physical Review E, 88 (2013) 010402. DOI: 10.1103/PhysRevE.88.010402

Phan K., Truong T., Wang Y., Bhandari B., Effect of CO_2 nanobubbles incorporation on the viscosity reduction of fruit juice concentrate and vegetable oil, International Journal of Food Science and Technology, 56 (2021a) 4278–4286. DOI:10.1111/ijfs.15240

Phan K., Truong T., Wang Y., Bhandari B., Effect of electrolytes and surfactants on generation and longevity of carbon dioxide nanobubbles, Food Chemistry, 363 (2021b) 130299. DOI: 10.1016/j.foodchem.2021.130299

Sakai T., Enomoto H., Torigoe K., Sakai H., Abe M., Surfactant- and reducer-free synthesis of gold nanoparticles in aqueous solutions, Colloids and Surfaces A: Physicochemical and Engineering Aspects, 347 (2009) 18–26. DOI: 10.1016/j.colsurfa.2008.10.037

Sato M., Matsuura K., Fujii T., Ethanol separation from ethanol-water solution by ultrasonic atomization and its proposed mechanism based on parametric decay instability of capillary wave, The Journal of Chemical Physics, 114 (2001) 2382–2386. DOI: 10.1063/1.1336842

Soyluoglu M., Kim D., Zaker Y., Karanfil T., Stability of oxygen nanobubbles under freshwater conditions, Water Research, 206 (2021) 117749. DOI: 10.1016/j.watres.2021.117749

Stokes G.G, On the effect of the internal friction of fluids on the motion of pendulums, Transactions of the Cambridge Philosophical Society, 9 (1851) 8–106.

Sugano K., Miyoshi Y., Inazato S., Study of ultrafine bubble stabilization by organic material adhesion, Japanese Journal of Multiphase Flow, 31 (2017) 299–306. DOI: 10.3811/jjmf.31.299

Suslick K.S., Sonochemistry, Science, 247 (1990) 1439–1445. DOI: 10.1126/science.247.4949.1439

Suzuki A., Maruyama H., Seki H., Matsukawa Y., Inoue N., Enrichment of amino acids by ultrasonic atomization, Industrial & Engineering Chemistry Research, 45 (2006) 830–833. DOI: 10.1021/ie0506771

Tagomori K., Kioka A., Nakagawa M., Ueda A., Sato K., Yonezu K., Anzai S., Air nanobubbles retard calcite crystal growth, Colloids and Surfaces A: Physicochemical and Engineering Aspects, 648 (2022) 129319. DOI: 10.1016/j.colsurfa.2022.129319

Takahashi M., ζ potential of microbubbles in aqueous solutions: electrical properties of the gas-water interface, Journal Physical Chemistry B, 109 (2005) 21858–21864. DOI: 10.1021/jp0445270

Takahashi M., Shirai Y., Sugawa S., Free-radical generation from bulk nanobubbles in aqueous electrolyte solutions: ESR spin-trap observation of microbubble-treated water, Langmuir, 37 (2021) 5005–5011. DOI: 10.1021/acs.langmuir.1c00469

Tanaka S., Naruse Y., Terasaka K., Fujioka S., Concentration and dilution of ultrafine bubbles in water, Colloids and Interfaces, 4 (2020) 50. DOI: 10.3390/colloids4040050

Tanaka S., Kobayashi H., Ohuchi S., Terasaka K., Fujioka S., Destabilization of ultrafine bubbles in water using indirect ultrasonic irradiation, Ultrasonics Sonochemistry, 71 (2021a) 105366. DOI: 10.1016/j.ultsonch.2020.105366

Tanaka S., Terasaka K., Fujioka S., Generation and long-term stability of ultrafine bubbles in water, Chemie Ingenieur Technik, 93 (2021b) 168–179. DOI: 10.1002/cite.202000143

Terasaka K., Chapter 7—Cleaning with ultrafine bubble water, in: Terasaka K., Yasui K., Kanematsu W., Aya N. (Eds.), Ultrafine Bubbles (1st ed.), Jenny Stanford Publishing, 2021, pp. 179–190, ISBN: 9781003141952. DOI: 10.1201/9781003141952

Tsuchida K., Maruyama A., Kobayashi Y., Sato G., Atsumi R., Murakami Y., Influence of microbubbles on free radical generation by ultrasound in aqueous solution: implication of the important roles of nanobubbles, Research on Chemical Intermediates, 48 (2022) 1045–1061. DOI: 10.1007/s11164-021-04612-6

Tuziuti T., Yasui K., Kanematsu W., Variations in the size distribution of bulk nanobubbles in response to static pressure increases, Japanese Journal of Applied Physics, 59 (2020) SKKD03. DOI: 10.35848/1347-4065/ab78e5

Tuziuti T., Yasui K., Kanematsu W., Influence of bulk nanobubble concentration on the intensity of sonoluminescence, Ultrasonics Sonochemistry, 76 (2021) 105646. DOI: 10.1016/j.ultsonch.2021.105646

Ushida A., Hasegawa T., Nakajima T., Uchiyama H., Narumi T., Drag reduction effect of nanobubble mixture flows through micro-orifices and capillaries, Experimental Thermal and Fluid Science, 39 (2012a) 54–59. DOI: 10.1016/j.expthermflusci.2012.01.008

Ushida A., Hasegawa T., Takahashi N., Nakajima T., Murao S., Narumi T., Uchiyama H., Effect of mixed nanobubble and microbubble liquids on the washing rate of cloth in an alternating flow, Journal

of Surfactants and Detergents, 15 (2012b) 695–702. DOI: 10.1007/s11743-012-1348-x

Ushikubo F.Y., Furukawa T., Nakagawa R., Enari M., Makino Y., Kawagoe Y., Shiina T., Oshita S., Evidence of the existence and the stability of nano-bubbles in water, Colloids Surface A: Physicochemical and Engineering Aspects, 361 (2010) 31–37. DOI: 10.1016/j.colsurfa.2010.03.005

Wang Y., Pan Z., Luo X., Qin W., Jiao F., Effect of nanobubbles on adsorption of sodium oleate on calcite surface, Minerals Engineering, 133 (2019) 127–137. DOI: 10.1016/j.mineng.2019.01.015

Weijs J.H., Seddon J.R.T., Lohse D., Diffusive shielding stabilizes bulk nanobubble clusters, Chem Phys Chem, 13 (2012) 2197–2204. DOI: 10.1002/cphc.201100807

Wood R.W., Loomis A.L., XXXVIII. The physical and biological effects of high-frequency sound-waves of great intensity, The London, Edinburgh, and Dublin Philosophical Magazine and Journal of Science, 4 (1927) 417–436. DOI: 10.1080/14786440908564348

Wu Z., Chen H., Dong Y., Mao H., Sun J., Chen S., Craig V.S.J., Hu J., Cleaning using nanobubbles: defouling by electrochemical generation of bubbles, Journal of Colloid and Interface Science, 328 (2008) 10–14. DOI: 10.1016/j.jcis.2008.08.064

Yabe A., Chapter 1—History of ultrafine bubbles, in: Terasaka K., Yasui K., Kanematsu W., Aya N. (Eds.), Ultrafine Bubbles, Jenny Stanford Publishing, 2021, pp. 1–16, ISBN: 9781003141952. DOI: 10.1201/9781003141952

Yasuda K., Tanaka N., Rong L., Nakamura M., Li L., Oda A., Kawase Y., Effects of carrier gas conditions on concentration of alcohol aqueous solution by ultrasonic atomization, Japanese Journal of Applied Physics, 42 (2003) 2956–2957. DOI: 10.1143/JJAP.42.2956

Yasuda K., Bando Y., Yamaguchi S., Nakamura M., Fujimori E., Oda A., Kawase Y., The effects of the solute properties in aqueous solutions on the separation characteristics in ultrasonic atomization, Journal of Chemical Engineering of Japan, 37 (2004) 1290–1292. DOI: 10.1252/jcej.37.1290

Yasuda K., Honma H., Xu Z., Asakura Y., Koda S., Ultrasonic atomization amount for different frequencies, Japanese Journal of Applied Physics, 50 (2011) 07HE23. DOI: 10.1143/JJAP.50.07HE23

Yasuda K., Nakayama S., Asakura Y., Characteristics of nanoemulsion prepared by tandem acoustic emulsification at a high frequency, Journal of Chemical Engineering of Japan, 45 (2012) 734–736. DOI: 10.1252/jcej.12we057

Yasuda K., Mochida K., Asakura Y., Koda S., Separation characteristics of alcohol from aqueous solution by ultrasonic atomization, Ultrasonics Sonochemistry, 21 (2014) 2026–2031. DOI: 10.1016/j.ultsonch.2014.02.011

Yasuda K., Matsushima H., Asakura Y., Generation and reduction of bulk nanobubbles by ultrasonic irradiation, Chemical Engineering Science, 195 (2019) 455–461. DOI: 10.1016/j.ces.2018.09.044

Yasuda K., Sato T., Asakura Y., Size-controlled synthesis of gold nanoparticles by ultrafine bubbles and pulsed ultrasound, Chemical Engineering Science, 217 (2020a) 115527. DOI: 10.1016/j.ces.2020.115527

Yasuda K., Nohara Y., Asakura Y., Effect of ultrafine bubbles on ethanol enrichment using ultrasonic atomization, Japanese Journal of Applied Physics, 59 (2020b) SKKD09. DOI: 10.35848/1347-4065/ab83d9

Yasuda K., Sonochemical green technology using active bubbles: degradation of organic substances in water, Current Opinion in Green and Sustainable Chemistry, 27 (2021) 100411. DOI: 10.1016/j.cogsc.2020.100411

Yasuda K., Hamada K., Asakura Y., Enrichment of amino acids from its aqueous solution by ultrasonic atomization and ultrafine bubbles, Japanese Journal of Applied Physics, 61 (2022) SG1009. DOI: 10.35848/1347-4065/ac43e5

Yasui K., Chapter 3—Dynamics of acoustic bubbles, in: Grieser F., Choi P.-K., Enomoto N. et al. (Eds.), Sonochemistry and the Acoustic Bubble, Elsevier, Amsterdam, 2015, pp. 41–83, ISBN: 9780128015308. DOI: 10.1016/B978-0-12-801530-8.00003-7

Yasui K., Tuziuti T., Kanematsu W., Kato K., Advanced dynamic-equilibrium model for a nanobubble and a micropancake on a hydrophobic or hydrophilic surface, Physical Review E, 91 (2015) 033008. DOI: 10.1103/PhysRevE.91.033008

Yasui K., Tuziuti T., Kanematsu W., Kato K., Dynamic equilibrium model for a bulk nanobubble and a microbubble partly covered with hydrophobic material, Langmuir, 32 (2016) 11101–11110. DOI: 10.1021/acs.langmuir.5b04703

Yasui K., Acoustic Cavitation and Bubble Dynamics, Springer, Cham, Switzerland, 2018, ISBN: 9783319682372. DOI: 10.1007/978-3-319-68237-2

Yasui K., Tuziuti T., Kanematsu W., Mysteries of bulk nanobubbles (ultrafine bubbles); stability and radical formation, Ultrasonics Sonochemistry, 48 (2018) 259–266. DOI: 10.1016/j.ultsonch.2018.05.038

Zhang R., Gao Y., Chen L., Ge G., Nanobubble boundary layer thickness quantified by solvent relaxation NMR, Journal of Colloid and Interface Science, 609 (2022a) 637–644. DOI: 10.1016/j.jcis.2021.11.072

Zhang R., Gao Y., Chen L., Ge G., Controllable preparation of monodisperse nanobubbles by membrane sieving, Colloids and Surfaces A: Physicochemical and Engineering Aspects, 642 (2022b) 128656. DOI: 10.1016/j.colsurfa.2022.128656

Zhang X., Liu X., Zhong Y., Zhou Z., Huang Y., Sun C.Q., Nanobubble skin supersolidity, Langmuir, 32 (2016) 11321–11327. DOI: 10.1021/acs.langmuir.6b01660

Zhou Y., Han Z., He C., Feng Q., Wang K., Wang Y., Luo N., Dodbiba G., Wei Y., Otsuki A., Fujita T., Long-term stability of different kinds of gas nanobubbles in deionized and salt water, Materials, 14 (2021) 1808. DOI: 10.3390/ma14071808

Zhu J., An H., Alheshibri M., Liu L., Terpstra P.M.J., Liu G., Craig V.S.J., Cleaning with bulk nanobubbles, Langmuir, 32 (2016) 11203–11211. DOI: 10.1021/acs.langmuir.6b01004

Zimmerman W.B., Tesař V., Bandulasena H.C.H., Towards energy efficient nanobubble generation with fluidic oscillation, Current Opinion in Colloid & Interface Science, 16 (2011) 350–356. DOI: 10.1016/j.cocis.2011.01.010

Author's Short Biography



Keiji Yasuda

Keiji Yasuda is currently an Associate Professor of the Department of Chemical Systems Engineering, Nagoya University. He received Doctor degree of Engineering from Nagoya University in 1997. His research interests are in the area of fundamentals of fine bubbles and sonochemistry, and their application to material and environmental fields.

KONA Powder and Particle Journal

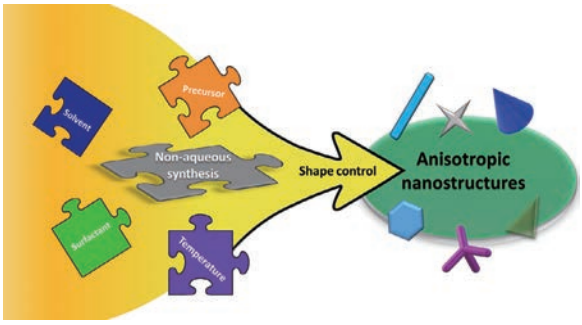
KONA Powder and Particle Journal No. 41 (2024) 197–220/https://doi.org/10.14356/kona.2024014 Review Paper

Synthesis of Anisotropic Metal Oxide Nanoparticles via Non-Aqueous and Non-Hydrolytic Routes†

Sherif Okeil[1,4], Julian Ungerer[2], Hermann Nirschl[2] and Georg Garnweitner[1,3]*

[1] *Institute for Particle Technology, Technische Universität Braunschweig, Germany*
[2] *Institute for Mechanical Process Engineering and Mechanics, Karlsruhe Institute of Technology (KIT), Germany*
[3] *Laboratory for Emerging Nanometrology, Technische Universität Braunschweig, Germany*
[4] *Pharmaceutical Analytical Chemistry Department, Faculty of Pharmacy, Ain Shams University, Egypt*

Due to their low cost, high stability and low toxicity, metal oxide nanomaterials are widely used for applications in various fields such as electronics, cosmetics and photocatalysis. There is an increasing demand thereby for nanoparticles with highly defined properties, in particular a narrow particle size distribution and a well-defined morphology. Such products can be obtained under high control via bottom-up synthesis approaches. Although aqueous processes are largely found in literature, they often lead to particles with low crystallinity and broad size distribution. Thus, there has been a growing trend towards the use of non-aqueous and non-hydrolytic synthesis routes. Through variation of the reaction medium and the use of adequate additives, such non-aqueous systems can be tuned to adapt the product properties, and especially to yield anisotropic nanoparticles with peculiar shapes and even complex architectures. Anisotropic particle growth enables the exposure of specific facets of the oxide nanocrystal, leading to extraordinary properties such as enhanced catalytic activity. Thus, there is an increasing demand for anisotropic nanoparticles with tailored morphologies. In this review, the non-aqueous and non-hydrolytic synthesis of anisotropic metal oxide nanoparticles is presented, with a particular focus on the different parameters resulting in anisotropic growth to enable the rational design of specific morphologies. Furthermore, secondary phenomena occurring during anisotropic particle growth, such as oriented attachment mechanisms, will be discussed.



Keywords: non-aqueous synthesis, non-hydrolytic synthesis, anisotropic nanoparticles, metal oxides, oriented attachment

1. Introduction

Metal oxides emerged as an indispensable class of materials due to the wide range of properties they can exhibit according to their composition, degree of crystallinity and morphology. Thus, they are employed in various technological fields such as catalysis (Védrine, 2017), electronics, including transistors (Yu et al., 2016) and gas sensors (Arafat et al., 2012; Chavali and Nikolova, 2019; Yu et al., 2022), as well as energy storage (Ellis et al., 2014; Fleischmann et al., 2022; Su et al., 2016) and solar cells (Chen et al., 2012). These diverse applications of metal oxides often require the use of particles with defined properties. In particular, due to their advantages such as high specific surface area providing high surface activity or small size providing a high degree of homogeneity, nanoparticles of metal oxides are desired. Hence, synthesis routes which enable the synthesis of metal oxides with tailored properties and which at the same time are reliable, cost-effective, versatile and scalable are important prerequisites for many of these applications.

In the past decades, scientists have always been working on different synthesis techniques to access metal oxide nanomaterials. Therefore, various synthesis methods exist, ranging from top-down methods such as ball milling and laser ablation to bottom-up methods like gas-phase synthesis and solution-based methods (Chavali and Nikolova, 2019; Parashar et al., 2020). While gas-phase synthesis is often expensive and requires large instrumentation, the solution-based synthesis of metal oxide nanoparticles is simple, comparatively less expensive, easily scalable and still enables precise control of the formed nanoparticles. To date, the solution-based synthesis of metal oxides is carried out mainly via aqueous synthesis, although non-aqueous and non-hydrolytic synthesis routes offer interesting advantages for nanoparticle synthesis.

In the case of aqueous synthesis, the precursor compound—which often is a metal alkoxide or other reactive metal compound—reacts with water directly in a hydrolysis step. This usually results in very high reaction rates,

† Received 7 September 2022; Accepted 4 May 2023
J-STAGE Advance published online 31 August 2023
* Corresponding author: Georg Garnweitner;
[1] Add: Volkmaroder Str. 5, 38104 Braunschweig, Germany
[3] Add: Langer Kamp 6A, 38106 Braunschweig, Germany
E-mail: g.garnweitner@tu-braunschweig.de
TEL: +49 (531) 391-65371 FAX: +49 (531) 391-9633

Copyright © 2024 The Authors. Published by Hosokawa Powder Technology Foundation. This is an open access article under the CC BY license (https://creativecommons.org/licenses/by/4.0/).

which decreases the homogeneity of the resulting product and leads to difficulty in adjusting or controlling the product properties (Chang and Doong, 2006). Many reaction parameters such as the rate of addition of precursor or water, the type and intensity of mixing, as well as solution parameters like pH, ionic strength, the type and concentration of chelating agents must be precisely controlled to obtain reproducible results. Concerning crystallinity of the resulting nanoparticles, the aqueous sol-gel synthesis at low temperatures usually results in amorphous or low-crystallinity oxides, and requires further heat treatment of the obtained product to obtain crystallinity (Wu et al., 2007a; Zhang et al., 2005). However, calcination at high temperatures results in an increase of crystallite size, neck formation and thus aggregate formation, and eventually even decomposition or phase transformation (Satapathy et al., 2014; Wang et al., 2002). In contrast, in the non-aqueous or non-hydrolytic synthesis, highly crystalline metal oxides are obtained directly in many cases (Wang et al., 2005). Moreover, the crystal phase can even be tuned by varying the reaction conditions of the non-aqueous synthesis (Wu et al., 2007a). This makes the non-aqueous and non-hydrolytic synthesis an attractive pathway for the simplified production of certain nanomaterials (Buonsanti et al., 2008; Niederberger and Garnweitner, 2006).

In non-aqueous synthesis routes, no water is added to the reaction mixture. Usually, an organic solvent is employed as a reaction medium but it can also act as a stabilizing agent, which results in a simpler reaction procedure and enables the synthesis of nanomaterials with uniform properties and a lower amount of strongly bound organics due to the absence of surfactants in the case of solvent-directed syntheses (Mutin and Vioux, 2013; Niederberger and Pinna, 2009). In contrast, the synthesis of nano-sized particles in aqueous media often requires the addition of various surfactants and capping agents that limit the growth of the inorganic particles and stabilize the resulting dispersion. While enabling a precise control over the resulting shape and particle size distribution, this also leads to coverage of the surface of the resulting particles by a large amount of surface organics (Niederberger and Pinna, 2009). In non-aqueous synthesis, alcohols are often used as reaction media, and water may be formed in situ during the synthesis process. On the other hand, non-hydrolytic synthesis proceeds in the absence of hydroxyl groups and thus requires the use of an aprotic medium.

In the past few decades, there was an immense increase of interest in crystal engineering, where a huge spectrum of anisotropic particle shapes has been reported for nanoparticles of different materials (Görke and Garnweitner, 2021). A general classification of nanomaterials can be made according to their dimensionality into one-dimensional nanostructures, like nanorods and nanowires, two-dimensional nanostructures such as nanoplatelets and sheet-like structures, and finally more complex three-dimensional nanostructures such as nanocubes, nanopyramids, nanostars, tetrapods or multipods. Small nanoparticles, in contrast, are often referred to as zero-dimensional nanodots. Each of these morphologies can lead to distinct anisotropic properties which are in most cases unique and make them suitable for specific applications rather than spherical nanoparticles which lack the direction-dependent properties (Burrows et al., 2016; Sajanlal et al., 2011). For example, the exposure of specific crystal planes was found to have a drastic effect on the photocatalytic efficiency of metal oxide nanoparticles (Chang and Waclawik, 2012). Anisotropic iron oxide nanoparticles show magnetic behavior which is highly dependent on its shape anisotropy, resulting in enhanced performance in different biomedical applications (Andrade et al., 2020). Metal oxide nanotube structures expose outer and inner surfaces as well as edges, which results in an increased surface area that proved to be highly beneficial for energy storage applications and can be used to embed other materials to form nanocomposites (Ellis et al., 2014; Patzke et al., 2002). All this shows the importance of anisotropic metal oxide nanoparticles. Generally, anisotropic shapes can be formed either through seed-mediated growth which usually results in monocrystalline nanoparticles, through oriented attachment or controlled aggregation (Burrows et al., 2016). Interestingly, non-aqueous synthesis routes can feature chemical species formed in situ that can direct anisotropic growth (Djerdj et al., 2008a) or even form inorganic-organic hybrid nanostructures through self-assembly (Pinna and Niederberger, 2008). Thus, the non-aqueous or non-hydrolytic synthesis routes show a high potential in obtaining anisotropic shapes in a simple manner.

Understanding the formation mechanisms of metal oxide nanoparticles is crucial for predicting anisotropic growth and enabling the rational design of new non-aqueous synthesis routes capable of producing such anisotropic shapes. There are several review articles (Deshmukh and Niederberger, 2017; Jun et al., 2006; Mutin and Vioux, 2013, 2009; Niederberger and Garnweitner, 2006; Niederberger and Pinna, 2009; Pinna and Niederberger, 2008; Styskalik et al., 2017) presenting the different non-aqueous or non-hydrolytic synthesis routes for metal oxides and discussing the reaction mechanisms leading to particle formation. Additionally, several general reviews have been published on the wet chemical synthesis of metal oxide nanoparticles (Jun et al., 2006; Nikam et al., 2018) or their applications (Chavali and Nikolova, 2019; Yu et al., 2016). In contrast to these, this contribution will be limited to the synthesis of anisotropic metal oxides in non-aqueous and non-hydrolytic systems. In this way, we aim to provide a deeper insight into the formation of anisotropic metal oxide nanoparticles or nanostructures, and discuss the different factors and mechanisms involved in the emergence

of anisotropic particle shapes in the different non-aqueous and/or non-hydrolytic reaction systems. This should help in the design of new tailored non-aqueous synthesis routes for anisotropic metal oxide nanoparticles.

In the following paragraphs, an overview of the synthesis of anisotropic particles of the most important metal oxides via non-aqueous and/or non-hydrolytic synthesis routes will be presented. Each oxide is discussed separately as the interaction of the different solvents and surfactants with the nanocrystal surface differs according to the crystal properties of the metal oxide. This will be followed by a discussion of the unique mechanisms, especially oriented attachment, encountered in the formation of anisotropic metal oxides in non-aqueous and non-hydrolytic synthesis routes. Then, the formation of anisotropic metal oxides in some special solvents, like benzyl alcohol is reviewed. The review is finally concluded by an outlook on possible future directions.

2. Titanium dioxide

The synthesis of titanium dioxide as the most-used photocatalytic material has been the focus of research for decades (Liu et al., 2014). Many studies were devoted to the synthesis of TiO_2 nanoparticles with distinct morphologies due to the increased surface-to-volume ratio where the increased interface permits enhanced catalytic activity (Fattakhova-Rohlfing et al., 2014). **Table S1** in the supplementary material provides a list of non-aqueous and non-hydrolytic synthesis approaches resulting in different anisotropic TiO_2 nanocrystal morphologies in chronological order of their publication. The main factors affecting the anisotropic growth in non-aqueous systems will be discussed in the following text. Although the main factors are presented, it must be considered that interconnections between the different factors exist, which makes it hard to isolate the effect of single factors completely.

2.1 Effect of solvent

Non-aqueous sol-gel synthesis routes were shown as being capable of controlling the size and shape, thus achieving different anisotropic TiO_2 structures with simple one-pot synthesis by simply changing the solvent used. The first non-aqueous synthesis procedure to well-defined anisotropic titania particles was reported by Wang et al., using titanium tetrachloride ($TiCl_4$) as the precursor in a solvent mixture of absolute ethanol and acetic acid (Wang et al., 2001). In this work, different organic solvent mixtures were tested for the synthesis of titania nanoparticles, with only the combination of absolute ethanol with acetic acid yielding anisotropic rutile titania structures (tenuous fiber and rod-like structures, **Table S1**). Ethylene glycol or glycerol as alternatives for ethanol yielded spherical nanoparticles, which was evident from the corresponding TEM and XRD analysis. The authors suggested that the titania formation in these systems mainly proceeds via a hydrolytic mechanism due to the water formed in the system from the esterification reaction between ethanol and acetic acid. The use of solely ethanol as a solvent also resulted in isotropic nanoparticles (Wang et al., 2001; 2002). The difference in the obtained morphologies by changing the alcohol type was rationalized by the preferential surface binding of the ethanol molecules to specific lattice planes, slowing down their growth (Doxsee et al., 1998). The investigation of a series of other alcohols as solvents for the non-aqueous synthesis of titania from $TiCl_4$ at a low temperature showed that fibrous structures could also be obtained in the case of using isopropanol and *n*-butyl alcohol as solvents (Wang et al., 2002).

2.2 Effect of precursor concentration (precursor-to-solvent ratio)

Investigating the influence of the precursor concentration, it was found that the $TiCl_4$/butanol ratio plays an important role in determining the phase and morphology of the formed TiO_2 nanocrystals. Only a low $TiCl_4$/butanol ratio resulted in the formation of rutile-phase nanorods, while higher ratios resulted in isotropic particles (Cao et al., 2011). While the sol-gel reaction of titanium tetrachloride and benzyl alcohol normally yields spherical particles (Niederberger et al., 2002a), nanorod particles have been obtained by Abazović et al. (Abazović et al., 2006; 2008) using the same reaction system, which underlines the importance of the applied reaction conditions. The formation of anatase TiO_2 nanorods in this reaction system has been attributed to the prolonged aging time at an elevated temperature (75 °C for 3 days) , which is longer than that used for spherical particles (24 h only at 75 °C). Rutile-phase TiO_2 nanofibers were also synthesized in a non-aqueous system from $TiCl_4$ in acetone at 110 °C, where the ratio of the precursor to acetone was found to be crucial for tuning the phase and morphology of the synthesized TiO_2. A 1:10 ratio of precursor to acetone was required to obtain rutile-phase nanofibers, while lower precursor concentrations resulted in anatase-phase isotropic and irregular-shaped particles (Wu et al., 2007a; 2007b). The same behavior was also observed with other ketones like butanone, 4-methylpentanone, and acetophenone (Wu et al., 2007b). In contrast, the reaction of titanium isopropoxide in ketones generally results in spherical anatase nanoparticles (Garnweitner et al., 2005).

2.3 Effect of surfactants

While it is evident that changing the solvent can control the morphology of the resulting metal oxide, the addition of a surfactant can further tune and direct the nanoparticle growth and can be used to obtain new particle shapes. Surfactants can preferentially bind to certain facets of a crystal changing its surface-free energy and thus changing

the growth rate of the different facets resulting in anisotropic growth (Bakshi, 2016). Alivisatos et al. used two different surfactants, namely lauric acid (LA), which selectively binds to the anatase {001} facets, and trioctylphosphine oxide (TOPO), which nonselectively coordinates to the TiO_2 surface. By variation of the ratio of these surfactants, it is possible to obtain different anisotropic TiO_2 particles ranging from bullet-shaped and rod-shaped nanocrystals to more complex branched nanocrystal shapes (Jun et al., 2003). At low LA concentrations, anisotropic crystal growth along the [001] direction takes place, eliminating the {001} faces and exposing {101} faces forming bullet-shaped (**Fig. 1(a)**) and diamond-shaped (**Fig. 1(b)**) nanocrystals. Increasing the amount of the LA surfactant slows down the growth along the [001] direction, leading to the formation of facetted nanorods (**Fig. 1(c)** and **(d)**). At very high LA concentrations, further inhibition of the growth in the [001] direction favors the growth of the {101} crystal faces and results in the branching-out of the {101} faces, yielding branched nanorod structures (**Fig. 1(e)**) (Jun et al., 2003).

The use of oleic acid as a surfactant in the non-aqueous titania synthesis in anhydrous toluene yielded dumbbell-shaped nanorods at 250 °C only when the amount of titanium isopropoxide (TIP) precursor was high, using a constant surfactant/precursor ratio of 3:1. At lower precursor concentrations, an increase of the surfactant/precursor ratio above 3:1 was necessary to obtain the dumbbell-shaped nanorods (Kim et al., 2003). This shows that not only the surfactant/precursor ratio is crucial for obtaining anisotropic structures but also the relative amount of precursor to the non-aqueous solvent used.

A reaction of TIP with oleic acid at lower temperatures (80 °C) results in the derivatization of the titanium precursor forming a titanium oleate complex. This can be used as an alternative precursor for the TiO_2 synthesis due to its lower reactivity, which can enable better control of the nanoparticle formation. Adapting the chemical reactivity of the precursor, further control of the nanoparticle synthesis can be achieved. The injection of oleylamine into the non-coordinating solvent 1-octadecene at 260 °C starts the decomposition of the titanium oleate complex through aminolysis, resulting in the formation of TiO_2 which is capped by carboxylate ions. The higher reactivity of the (001) planes leads to the facilitated aminolysis of the capping oleate at these planes, which enables anisotropic growth of the titania nanocrystals in the [001] direction. Thus, titania nanorods are formed whose length can be easily tuned through variation of the injected oleylamine amount. An increase in the oleylamine amount from 1 to 2 mmol increases the titania nanorod length in this system. A further increase was found to suppress anisotropic growth where 3 mmol oleylamine leads to a decrease in the resulting nanorod length; finally for 4 mmol oleylamine, isotropic titania nanoparticles were achieved. The observed suppression of anisotropic growth could be due to the accelerated aminolysis and increased consumption of surface-coordinated oleate by the high oleylamine concentration. Even the diameter of the titania nanorods formed could be tuned in this system through the use of the more weakly binding surfactant cetyltrimethylammonium bromide (CTAB) (Zhang et al., 2005). Thus, variation of the oleylamine/oleic acid ratio represents a powerful tool to tune the morphology of titania nanocrystals.

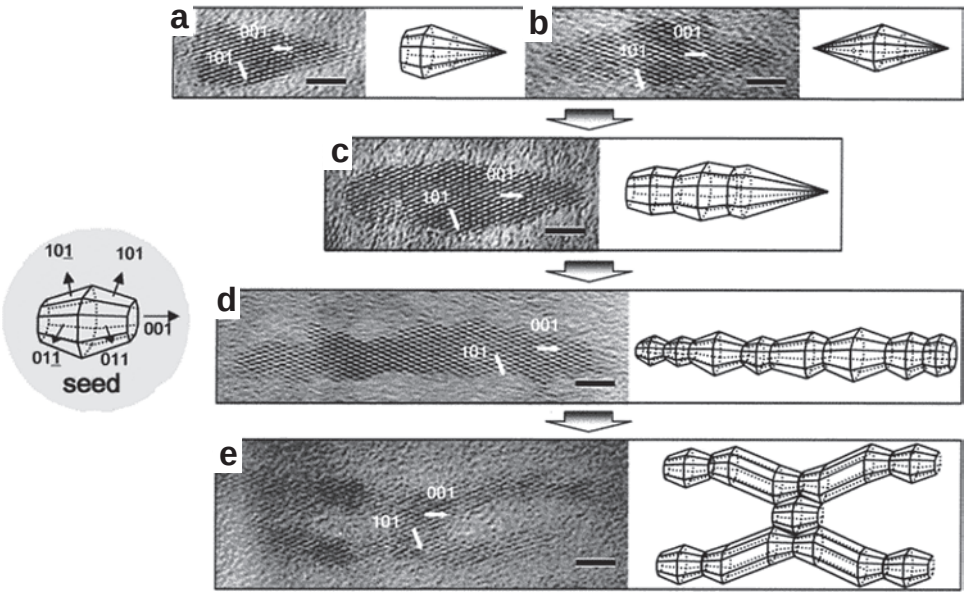


Fig. 1 High-resolution TEM images showing the evolution of different shapes of TiO_2 with varying relative ratio of LA and TOPO surfactants: **(a)** bullet-shaped, **(b)** diamond-shaped, **(c)** short nanorod, **(d)** long nanorod and **(e)** branched nanorod structures (Scale bar = 3 nm). Adapted with permission from Ref. (Jun et al., 2003). Copyright 2003 American Chemical Society.

Through variation of the oleylamine/oleic acid ratio it is also feasible to finely control the shape of the obtained nanorods. Buonsanti et al. observed that at a lower oleylamine/oleic acid ratio of 26, brookite-phase TiO_2 nanorods with tapered tips were obtained, whereas at much higher ratios of about 104, rectangular endings of the TiO_2 nanorods were observed (Buonsanti et al., 2008). It has to be noted that the precursor used is $TiCl_4$ instead of TIP and a seeded-growth technique has been adopted for the synthesis.

A similar system was used by Hyeon et al. for the large-scale non-aqueous synthesis of TiO_2 nanorods, where the TIP precursor was allowed to react with oleic acid at 270 °C for 2 hours, assuming that an ester elimination reaction results in the formation of the titania nanorods growing along the [001] direction (**Fig. 2(a)**). The addition of controlled amounts of 1-hexadecylamine (HDA) enabled control of the resulting nanorod diameter as, according to the authors, HDA strongly coordinates to the (101) anatase faces slowing down its growth. Thus, an increase of the HDA amount leads to a decrease in the titania nanorod diameter from 3.4 nm to 2.0 nm (Joo et al., 2005b). Although it was noted by Zhang et al. that the use of oleic acid or oleylamine alone did not result in particle formation (Zhang et al., 2005), the reaction system of Joo et al. enabled the formation of particles by solely reacting TIP with oleic acid (Joo et al., 2005b).

It was also feasible to obtain ultrathin TiO_2 nanosheets upon heating of $TiCl_4$ precursor in oleylamine alone, which in this case serves as both the solvent and surfactant (**Fig. 2(b)**) (Yang et al., 2015). This shows that the concentration of the precursor and surfactant plays an important role in the particle formation, along with the reaction temperature and synthesis time. It is noteworthy that the synthesis of TiO_2 in oleic acid results in preferential growth in the [001] direction, resulting in nanorods (**Fig. 2(a)**) (Joo et al., 2005b), while the synthesis in oleylamine results in an inhibition of the growth in the [001] direction (*c*-axis) where the preferred growth along the *a*- and *b*-axis yields in the formation of nanosheets (**Fig. 2(b)**) (Yang et al., 2015), which could indicate the different roles of these surfactants.

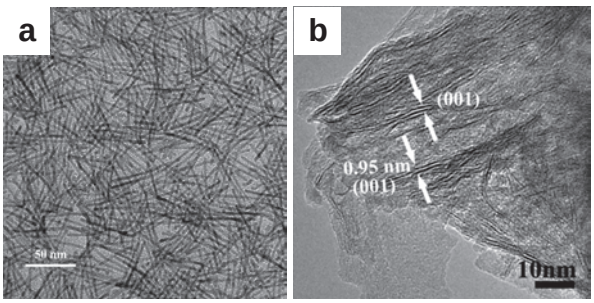


Fig. 2 TEM images of **(a)** TiO_2 nanorods synthesized in oleic acid (adapted with permission from Ref. (Joo et al., 2005b). Copyright 2005 American Chemical Society) and **(b)** ultrathin TiO_2 nanosheets synthesized in oleylamine (adapted with permission from Ref. (Yang et al., 2015). Copyright 2015 The Royal Society of Chemistry).

Detailed investigations of the parameters leading to the anisotropic growth of TiO_2 nanocrystals using a solvothermal synthesis in cyclohexane with titanium butoxide as a precursor and linoleic acid as a surfactant at a low temperature (150 °C for 48 h) were performed by Li et al. The influence of surfactant amount, reaction temperature, reaction time and type of surfactant were studied, where an increase in surfactant amount promoted the anisotropic growth. The nanorods formed also showed spherical tips similar to the dumbbell-shaped nanorods previously obtained in the work by Kim et al. (2003). GC-MS analysis determined the side products formed during the solvothermal synthesis, which indicated an ester elimination reaction mechanism. Checking the effect of carboxylic acid surfactants revealed that ester elimination alone is not sufficient for particle formation; a long-chain organic acid is also crucial for TiO_2 particle formation (Li et al., 2006).

2.4 Effect of doping and precursor addition rate

Alkyl halide elimination for the synthesis of Zr-doped TiO_2 nanocrystals, using a non-hydrolytic, non-aqueous synthesis route, was adopted by using a mixture of a metal halide and a metal alkoxide. TOPO was used as the coordinating solvent. The formation of anisotropic facetted Zr-doped TiO_2 nanorods was only possible at high temperatures (400 °C), with an increase in Zr-doping leading to a subsequent enlargement of the nanorods (Chang and Doong, 2006). The same titania precursors also yielded anisotropic structures at a lower temperature of 300 °C in the non-coordinating solvent 1-octadecene when using oleylamine as the surfactant. The morphology and even the phase of the evolving TiO_2 nanostructures could be precisely controlled through the slow addition of the precursors to hot oleylamine via a syringe pump. A comparably high injection rate of 30 mL/h of the precursors yielded anatase TiO_2 nanorods of 6 nm in diameter and 50 nm in length (**Fig. 3(a)**). Lowering the precursor addition rate to 2.5 mL/h enables the formation of larger anatase nanorods of 9 nm in diameter and 100 nm in length together with rutile-phase star-shaped nanostructures (25 × 200 nm in dimension) (**Fig. 3(b)**). Reducing the flow rate to 1.25 mL/h yields pure rutile star-shaped TiO_2 of 25 nm × 450 nm in size (**Fig. 3(c)**). Consequently, a slower precursor addition rate enabled the formation of fewer nuclei which continuously grew with continuous precursor addition. In contrast, one-shot injection of these precursors into the hot oleylamine resulted in the formation of a mixture of polydisperse nanoparticles and nanorods, which underlines the importance of the addition rate of the precursors in controlling particle morphology (Koo et al., 2006).

3. Zinc oxide

Zinc oxide, as a relatively cheap and non-toxic semiconductor with a wide range of functional properties, has attracted broad attention in various application fields such as gas sensing, piezoelectric devices, photocatalysis, optoelectronic devices and even biomedicine (Bharat et al., 2019; Kolodziejczak-Radzimska and Jesionowski, 2014; Zhang et al., 2013). In all of these applications, shape control can open the door for better integration of ZnO nanostructures into the selected application to reach the desired outcome. Using non-aqueous and non-hydrolytic synthesis routes, unique morphologies such as teardrop-like shape (Zhong and Knoll, 2005), hexagonal pyramid shape (Choi S.H. et al., 2005) and nanowires (Yuhas et al., 2006) were achieved. Supplementary **Table S2** lists the different ZnO particle shapes reported to be obtained from non-aqueous and non-hydrolytic synthesis routes in chronological order of their publication. In the following paragraphs, the effects of different factors on ZnO particle morphology will be discussed in more detail.

3.1 Effect of solvent

Through the use of solvents with different coordinating powers, it was possible to control the shape of evolving ZnO nanoparticles. Thin zinc oxide nanorods (2 nm in diameter) were obtained in trioctylamine (TOA) with oleic acid as a surfactant. The self-assembly of the synthesized nanorods in stacks was observed in this system, with the nanorods being arranged parallel to each other (**Fig. 4(a)**) (Andelman et al., 2005; Yin et al., 2004). The use of the less coordinating solvent 1-hexadecanol (HD) resulted in the formation of less elongated ZnO nanoparticles in the form of nanotriangles (**Fig. 4(b)**). Using the non-coordinating solvent 1-octadecene (OD) results in the loss of anisotropic growth, yielding spherical ZnO nanoparticles (**Fig. 4(c)**) (Andelman et al., 2005). Thus, the choice of solvent, in combination with the surfactant, played an important role in stabilizing the different crystal planes and determining the resulting nanoparticle morphology.

Zhang et al. also tested the influence of different non-coordinating and coordinating solvents on the morphology of the evolving ZnO nanoparticles formed from zinc carboxylate precursors using oleylamine as reagent and surfactant. It is interesting to note that in this work, when employing oleylamine as both a reagent and surfactant, the use of non-coordinating solvents such as dioctyl ether,

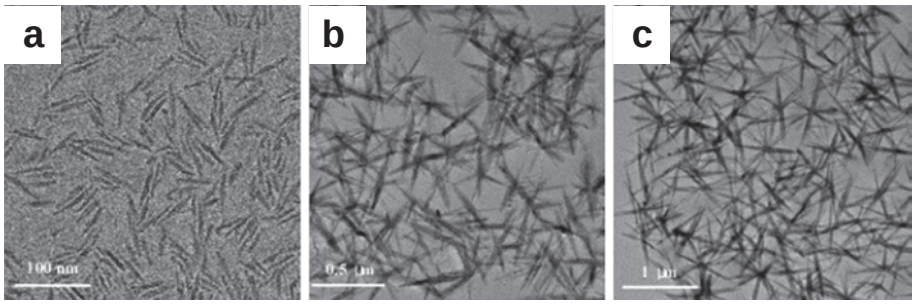


Fig. 3 TEM images of **(a)** anatase TiO_2 nanorods formed at 30 mL/h, **(b)** mixture of anatase nanorods and rutile star-shaped TiO_2 structures formed at 2.5 mL/h and **(c)** pure star-shaped rutile TiO_2 formed at 1.25 mL/h precursor addition rate. Adapted with permission from Ref. (Koo et al., 2006). Copyright 2006 American Chemical Society.

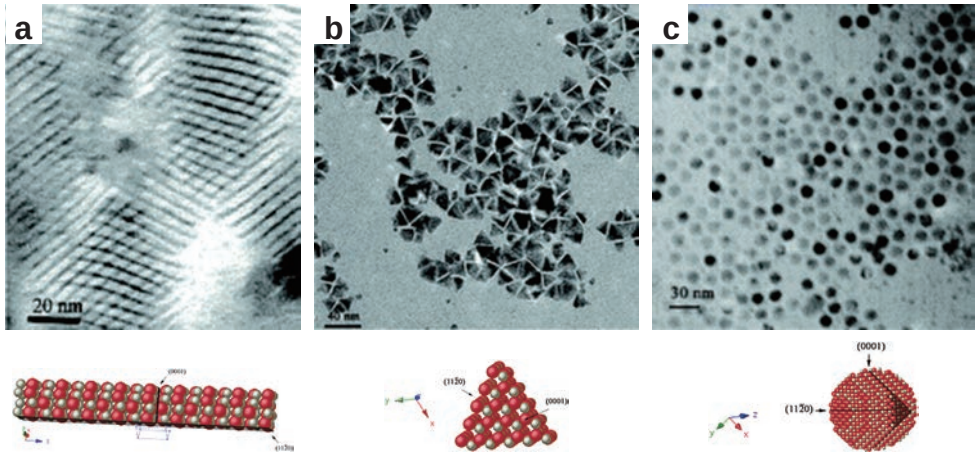


Fig. 4 TEM images with the corresponding crystal structures of **(a)** ultrathin ZnO nanorods self-assembled in stacks, **(b)** ZnO nanotriangles and **(c)** spherical ZnO nanoparticles formed in solvents with different coordinating power. Adapted with permission from Ref. (Andelman et al., 2005). Copyright 2005 American Chemical Society.

diphenyl ether and OD yielded ZnO nanorods (Zhang Z. et al., 2006), which shows that the control of anisotropic growth is a complex interplay between different factors, including the combination of solvent and surfactant used. In this particular system, the use of the coordinating solvent trioctylphosphine (TOP) led to the formation of nanotetrahedrons, similar to the nanotriangles obtained in the work of Andelman et al. (Andelman et al., 2005; Zhang Z. et al., 2006). Increasing the coordinating power by using TOPO as a solvent results in the formation of irregularly shaped particles, which was attributed to the very strong coordination of TOPO to the zinc acetate precursor and the steric effect of the bulky alkyl chains hindering the access for oleylamine to the nanocrystal surface, thus drastically decreasing the kinetics of the aminolytic reaction essential for particle growth in this system (Zhang Z. et al., 2006).

It also has to be mentioned that the role of solvent and surfactant cannot be separated as the solvent itself usually shows some coordination and thus surface activity in covering certain facets of the evolving nanocrystal.

A study of the effect of solvent alone was conducted by Kunjara Na Ayudhya et al., where the influence of different glycols, alcohols, *n*-alkanes and aromatic solvents on the morphology of ZnO nanoparticles was investigated (Kunjara Na Ayudhya et al., 2006). The formation of ZnO from the zinc acetate precursor in glycols and alcohols was achieved at 250 °C, while in non-polar and non-coordinating solvents (*n*-alkanes and aromatic solvents), the precursor decomposition temperature increased to 300 °C. The decomposition temperature of the zinc acetate precursor in the corresponding solvent was related to the dielectric constant of the latter. When the highly polar glycols were used as a solvent, low anisotropic particles of polyhedral shape were obtained, while alcohols yielded nanorods of moderate aspect ratio. The use of *n*-alkanes and aromatic solvents resulted in nanorods with a high-aspect ratio (Kunjara Na Ayudhya et al., 2006). Thus, the aspect ratio of the ZnO nanorods formed was found to be tunable depending on the polarity of the solvent used: the higher the polarity of the solvent, the less the preferential growth of ZnO in the [001] direction. Thus, alcohols with increasing chain length resulted in an increase of the aspect ratio of the ZnO nanorods formed (Cheng and Samulski, 2004; Kunjara Na Ayudhya et al., 2006; Rai et al., 2013; Tonto et al., 2008). Similar observations were made when benzyl alcohol was replaced by the non-polar anisole as a solvent in ZnO synthesis from zinc acetate, where a substantial increase in the nanorod aspect ratio could be observed (Clavel et al., 2007). Other studies reported similar but still deviating behavior using a different precursor and different reaction conditions (Ramya et al., 2019; Šarić et al., 2019). The synthesis of ZnO nanoparticles through a precipitation reaction from zinc acetate and sodium hydroxide in a series of alcohols at low temperatures resulted in isotropic nanoparticles in methanol, mixed nanoparticles and short nanorods in ethanol and nanorods with increasing aspect ratio from butanol to octanol. In octanol, isotropic particles were also observed together with the high-aspect-ratio nanorods. Finally, isotropic particles were obtained again in decanol. In this system, the growth behavior was found to be related to the zeta potential of the formed colloids, which results in different aggregation rates where a lower zeta potential increases the aggregation rate of the colloid and leads to an increased growth rate (Šarić et al., 2019).

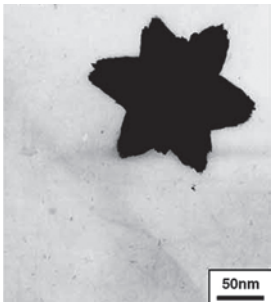


Fig. 5 TEM image of a ZnO nanostar formed from zinc acetate in a mixture of ethanol and ethylene glycol at 80 °C. Adapted with permission from Ref. (Wang et al., 2005). Copyright 2005 Elsevier.

Solvent mixtures are also capable of producing interesting anisotropic structures through selectively enhancing or retarding the growth of specific crystal planes. For example, a mixture of ethanol and ethylene glycol resulted in the formation of ZnO nanostars from a zinc acetate precursor at a low temperature (80 °C) without the need for a surfactant, as can be seen in **Fig. 5** (Wang et al., 2005). In this case, the anisotropic structure formed could be an aggregate of smaller primary particles which possibly resulted in a hierarchical structure, which, however, was not investigated in this work.

3.2 Effect of surfactant and reaction temperature

The ester elimination reaction, similar to that used for the large-scale synthesis of TiO_2 nanorods, has also been applied for the synthesis of different ZnO nanoparticles. The Hyeon Group demonstrated thereby that the use of different surfactants resulted in strong changes in morphology. TOPO, OA, HDA and TDPA in dioctyl ether as solvents resulted in the formation of wedge-shaped ZnO nanocones self-assembled in spherical nanostructures (**Fig. 6(a)**), cone-shaped ZnO nanocrystals (**Fig. 6(b)**), hexagonal cone-shaped ZnO nanocrystals (**Fig. 6(c)**) and ZnO nanorods (**Fig. 6(d)**), respectively (Joo et al., 2005a). Changing the alcohol used to 1,2-dodecanediol and the solvent to the higher-boiling-point-solvent benzyl ether to perform the synthesis at higher temperatures while using TOPO as the surfactant yielded similarly pyramidal or cone-shaped particles (Kachynski et al., 2008).

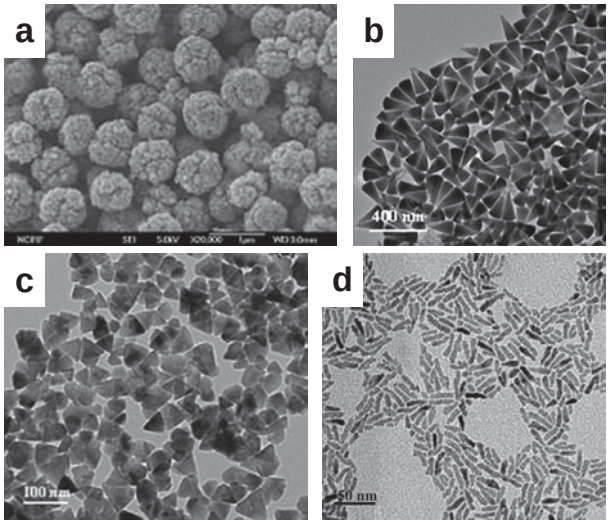


Fig. 6 TEM micrographs of **(a)** spherical hierarchical structures composed of wedge-shaped ZnO nanocones synthesized using TOPO, **(b)** ZnO nanocones synthesized using oleic acid, **(c)** hexagonal ZnO nanocones synthesized using HAD and **(d)** ZnO nanorods synthesized using TDPA as surfactant. Adapted with permission from Ref. (Joo et al., 2005a). Copyright 2005 Wiley-VCH.

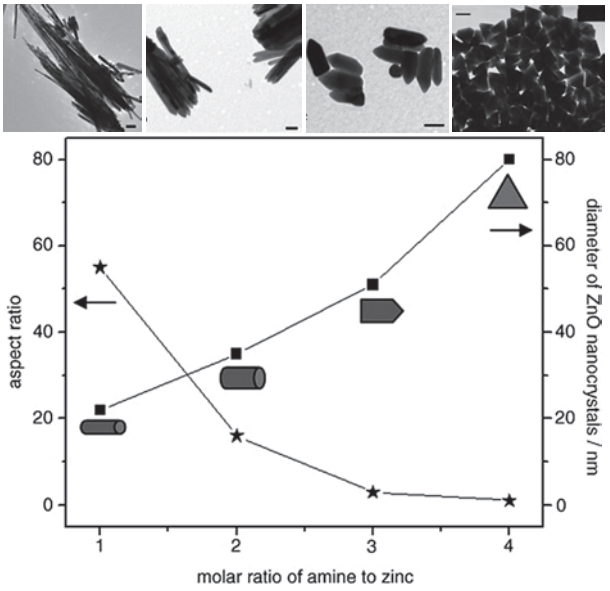


Fig. 7 Diagram showing the relation between the molar ratio of oleylamine to zinc acetate used and the resulting aspect ratio as well as the diameter of the ZnO nanocrystals. Above, for each morphology in the diagram (long nanorods, short nanorods, bullet-shaped nanocrystals and nanoprisms), the corresponding TEM image proving the formation of such ZnO nanomaterial is shown (scale bar: 100 nm). Adapted with permission from Ref. (Zhang et al., 2007). Copyright 2007 Wiley-VCH.

Increasing the concentration of the surfactant also has an influence on the particle shape and can even result in the self-assembly of anisotropic particles to various complex nanostructures. For example, a rise in the concentration of oleylamine used in the synthesis of ZnO in TOP led to the formation of nanotetrahedrons that self-assembled into so-called nanofans. A further increase in the oleylamine concentration resulted in larger dumbbell-shaped nanostructures (Zhang Z. et al., 2006).

The decomposition of zinc acetylacetonate ($Zn(acac)_2$) in oleylamine, which in this case had the role of solvent and surfactant, yielded different particle shapes by varying the oleylamine/precursor molar ratio together with the reaction time and temperature. A ratio of 10:1 at a reaction temperature of 205 °C for 1 h yielded short nanorods arranged in belt-like structures. A lower precursor concentration (ratio 100:1 of oleylamine/precursor) resulted in heart-shaped nanoparticles at 205 °C for 24 h (Liu et al., 2007).

Similarly, the influence of oleylamine on the particle morphology was also investigated by Zhang et al., however, using zinc acetate as the precursor. In this system, the amine was able to attack the precursor in an amide elimination reaction or aminolysis yielding ZnO. In that case, it was found that increasing the molar ratio of oleylamine to precursor decreases the anisotropic growth along the [001] direction, leading to the formation of nanorods with a lower aspect ratio and finally nanoprisms in the case of ratios greater than 3 (**Fig. 7**). A further increase of the oleylamine/precursor ratio up to 24:1 had no significant effect on the resulting morphology (Zhang et al., 2007). It has to be noted that in this work, the precursor used is different, which affects the rate of monomer generation and partly explains the difference to the shapes obtained in the work by Liu et al. (2007). Nevertheless, both works showed a decrease in anisotropic growth with an increasing amount of oleylamine (Liu et al., 2007; Zhang et al., 2007), which was related to an increased reaction rate, leading to rapid nucleation and leaving fewer monomers available for further particle growth. On the other hand, a low amine-to-precursor ratio resulted in a low reaction rate, leading to the formation of fewer initial nuclei and leaving more monomers for further particle growth, where the growth of faster-growing planes becomes apparent, forming highly anisotropic nanocrystals (Zhang et al., 2007).

The testing of other amines (hexadecylamine, dioctylamine and dodecylamine) showed that the longer the alkyl chain of the amine used, the thinner and longer are the ZnO nanowires or nanorods produced when all other reaction parameters are kept constant (Zhang et al., 2007). Correlating these results with other studies where the effect of the solvent was investigated (Clavel et al., 2007; Kunjara Na Ayudhya et al., 2006), it can be deduced that the amines with longer-chain lengths result in higher aspect ratios due to their lower polarity. Using other amines like benzylamine as a reagent to initiate the aminolysis reaction of zinc acetate in benzyl ether also resulted in different anisotropic shapes such as nanocones, nanobullets, nanorods and nanoplates depending on the molar ratio of benzylamine to the zinc precursor as well as the reaction temperature used (Ahmad et al., 2013; Chang and Waclawik, 2012). By

adjusting the amount of benzylamine and the reaction temperature, the reaction rate was controlled which resulted in different nucleation and growth mechanisms. It was found that zinc acetate does not decompose in pure benzyl ether at temperatures below 210 °C unless a reagent initiating an aminolysis reaction is added. Thus, performing a reaction at 170 °C using a benzylamine/Zn ratio of 10 would be a pure aminolysis reaction resulting in the formation of ZnO nanocones. On the other hand, keeping the same amine-to-Zn ratio while using a higher reaction temperature of 210 °C would result in a mixed thermal decomposition and aminolysis reaction, together with an increased reaction rate due to the increased temperature. Thus, the reaction at 210 °C resulted in the formation of ZnO nanobullets where the top cone shape of the nanobullets was explained by the capping effect of the excess benzylamine. This underlines the dual role of the amine reagent, where on the one hand it is a reagent for the aminolysis reaction, and on the other hand, any excess not involved in the aminolysis reaction acts as a capping agent for the polar ZnO facets. This is further proved by decreasing the benzylamine/Zn ratio to 1 while keeping the reaction temperature at 210 °C, resulting in the formation of nanorods without the cone-shaped tip due to the absence of excess benzylamine, which would take the function of a capping agent. An increase of the ratio to 40 resulted in nanoplate formation due to the strong coordination of excess benzylamine to the polar Zn^{2+} surface, inhibiting growth along the [001] direction. It has to be mentioned that the heating rate was also found to have a pronounced effect on the resultant morphology in this system, where rapid heating resulted in the ZnO nanoplates, while slow heating (~ 5 °C/min) to the same reaction temperature led to the formation of "uncompleted" ZnO nanocones (Chang and Waclawik, 2012).

While oleylamine has been widely used as a surfactant and morphology-controlling agent in the synthesis of ZnO nanostructures, oleic acid would be another possible interesting surfactant for morphology control due to its strong coordination ability with the ZnO surface. Usually, however, OA was used in combination with amines (Choi S.H. et al., 2005; Yin et al., 2004) during the synthesis of ZnO, which makes it hard to determine the role of each in the formation of the anisotropic structure. Zhong et al. used a mixture of OA and oleyl alcohol to synthesize ZnO nanostructures from zinc acetate by the well-known ester elimination reaction. In this system, the alcohol acts as a solvent and reagent for the formation of ZnO from zinc acetate through an "esterification alcoholysis reaction", while the OA acts as a surfactant and structure-directing agent. By adjusting the relative amount of oleic acid to oleyl alcohol, while keeping the total volume of the mixture constant, it was possible to obtain a range of complex nanostructures such as spiked ZnO nanostructures (**Fig. 8(a)**) and ZnO tetrapods of various dimensions (**Fig. 8(b)** and **(c)**). By increasing the relative amount of oleyl alcohol and decreasing the relative amount of oleic acid, smaller-sized ZnO tetrapods were obtained due to the increased reaction rate of the alcohol with the precursor, which results in a large number of initial nuclei in a short time (Zhong et al., 2007). Similarly, Zhang et al. also obtained Mn-doped ZnO tetrapods and multipods from bulk ZnO using OA and oleyl alcohol in the non-coordinating solvent 1-octadecene (Zhang and Li, 2009). The use of other alcohols like 1,12-dodecanediol and 1-hexadecanol with oleic acid and zinc acetate yielded ZnO nanocones (Joo et al., 2005a) and nanotriangles (Andelman et al., 2005), respectively.

Oleic acid was also used as a capping agent without any other additives in the non-polar solvent *n*-octadecene. In this medium, previously prepared zinc oleate was used as a precursor with further addition of oleic acid as the surfactant, and the mixture reacted under reflux. Interestingly, defined triangular and hexagonal two-dimensional plate-like structures were formed with prolonged reflux time (**Fig. 9(a)**). The formation of these two-dimensional thin plate-like ZnO structures of about 10 nm in thickness is attributed to the strong binding affinity of oleic acid to the chemically active Zn^{2+} terminated (0001) surface, which prevents further growth in this direction (*c*-direction) (Chiu et al., 2008). While a longer synthesis time yielded more defined shapes, it was also observed that a thinning of the central area of the ZnO platelets took place (**Fig. 9(b)**), which was correlated to an etching activity of the bound

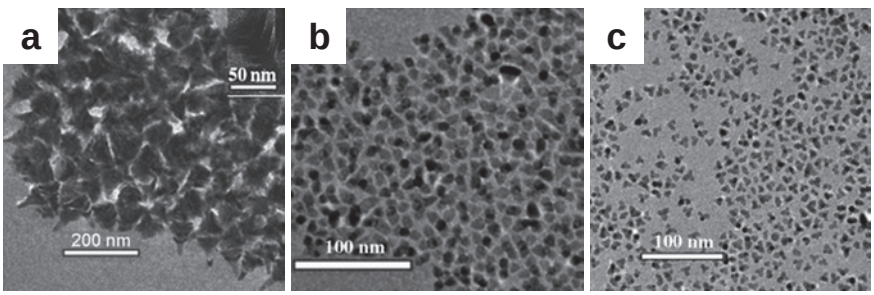


Fig. 8 TEM images of **(a)** ZnO spiked clusters formed using a volume ratio of 1:2 oleic acid to oleyl alcohol, **(b)** large ZnO tetrapods formed using a volume ratio of 1:3.5 oleic acid to oleyl alcohol and **(c)** small ZnO tetrapods formed using a volume ratio of 1:8 oleic acid to oleylamine while keeping the total volume constant. Adapted with permission from Ref. (Zhong et al., 2007). Copyright 2007 Wiley-VCH.

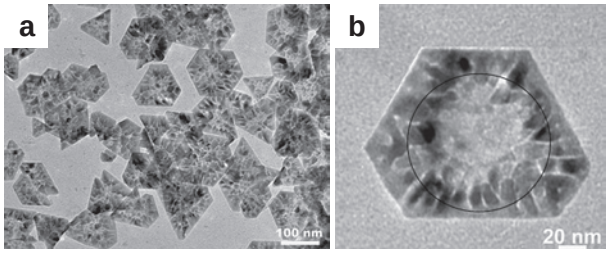


Fig. 9 TEM images of two-dimensional ZnO platelets **(a)** showing the different triangular and hexagonal platelet structures formed after 90 min synthesis time and **(b)** an individual ZnO platelet formed after 120 min synthesis time showing a thinning effect in the center with increased synthesis time. Adapted with permission from Ref. (Chiu et al., 2008). Copyright 2008 Elsevier.

oleic acid. Thus, it was predicted that even longer reflux times could yield ring-like ZnO structures (Chiu et al., 2008).

The use of ethylene diamine as a short-chain diamine was reported to yield micrometer-long ZnO nanorods in alcohols (Panchakarla et al., 2007). Hexamethylenetetramine (HMTA) was also used as a surfactant for the synthesis of ZnO nanorods from $Zn(acac)_2$ in the coordinating solvent trioctylamine at a low temperature, where an increase in the surfactant-to-precursor ratio resulted in well-defined nanorods with a higher aspect ratio. However, increasing the reaction temperature from 70 °C to 140 °C while maintaining the HMTA to $Zn(acac)_2$ constant resulted in a decrease in the aspect ratio, forming less anisotropic structures (Devarepally et al., 2012). Alternatively, polyvinylpyrrolidone (PVP) in ethanol was reported to result in nanorods at a low temperature (80 °C) with good crystallinity (Wang et al., 2005), showing that strongly coordinating ligands such as amines are not necessary for nanorod growth.

The formation of ZnO from zinc acetate and a hydroxide is a typical precipitation reaction that can also be performed in organic media, and as no water was added to the system, this can still be interpreted as a non-aqueous synthesis. Alcohols like methanol and ethanol have been mainly used as solvents, where usually an alcoholic solution of NaOH or KOH is added to a zinc salt dissolved in the same alcohol. While ZnO nanorods have been mainly obtained at higher temperatures (Cheng and Samulski, 2004; Pacholski et al., 2002; Rai et al., 2013), interwoven ZnO nanosheets were obtained when the reaction was performed at room temperature (Khokhra et al., 2015) which shows that the reaction temperature is also a crucial factor for tuning the shape of the nanostructures obtained.

3.3 Effect of precursor type

The type of metal oxide precursor used also has a significant influence on the nanostructure obtained. Heating different zinc alkylcarboxylate precursors in TOP using

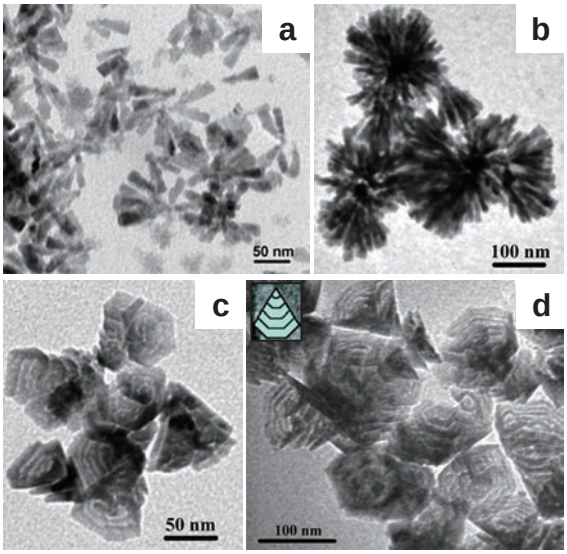


Fig. 10 TEM micrographs of ZnO nanostructures formed from different zinc carboxylate precursors: **(a, b)** multiarmed ZnO nanostructures formed of nanotetrahedrons obtained from **(a)** zinc acetate and **(b)** zinc hexanoate, **(c, d)** squamous ZnO nanostructures produced from **(c)** zinc octanoate and **(d)** zinc oleate. The inset of **(d)** shows a schematic of the structure of the squamous nanocrystals. Adapted with permission from Ref. (Zhang Z. et al., 2006). Copyright 2006 American Chemical Society.

oleylamine as a surfactant results in various types of nanostructures. Zinc salts of short alkyl chain carboxylic acids, such as zinc acetate and zinc hexanoate, resulted in the formation of multiarmed ZnO nanostructures formed of nanotetrahedrons, while precursors containing longer-chain carboxylates like zinc octanoate and zinc oleate produced "squama-like" (fish scale-like) nanostructures (**Fig. 10**) (Zhang Z. et al., 2006). In these non-aqueous synthesis methods, the oleylamine attacks the carboxylates in an aminolytic reaction resulting in amide elimination and ZnO formation. The change in morphology with precursor type was attributed to the difference in the reactivity of the precursor to the oleylamine, thus modulating the rate of the aminolytic reaction. With an increasing chain length of the carboxylate in the precursor, the steric hindrance increased, resulting in a decrease of the aminolysis rate at the coordinated {110} planes but leaving the growth in the [001] direction unhindered. Thus, precursors containing shorter-chain carboxylates formed nanotetrahedrons, while the longer-chain carboxylate precursors formed squamous-like nanocrystals, where the strong binding affinity and steric effects of the longer-chain carboxylates such as oleate to the (110) plane leads to further suppression of the growth in the [110] direction, forming very thin "nanosquamas" (Zhang Z. et al., 2006).

In a separate study by Xu et al., different precursors also resulted in a good variation of particle morphology when used in tetrahydrofuran (THF). While zinc acetate resulted in hexagonal-based pyramidal particles, using $Zn(acac)_2$

instead led to isotropic particles arranged in a cauliflower-like morphology (Xu et al., 2009). The decomposition temperature of each precursor in the same solvents already gives a clue about the different behavior of different precursors. Kunjara Na Ayudha et al. found that the solvothermal synthesis of ZnO from zinc acetate in the non-polar solvents decane and toluene was not feasible at 250 °C, and the synthesis temperature needed to be increased to 300 °C to obtain ZnO nanorods (Kunjara Na Ayudhya et al., 2006). On the other hand, it was possible to obtain ZnO from $Zn(acac)_2$ in decane and toluene at the much lower temperature of 120 °C. In that case, completely different morphologies were obtained where the synthesis in decane resulted in truncated hexagonal pyramidal particles, while in toluene hourglass-like particles were obtained (Xu et al., 2009).

3.4 Effect of precursor concentration

It is generally known from different reaction systems that nanocrystal growth is highly dependent on the monomer concentration. A low monomer concentration usually results in isotropic growth while a high monomer concentration results in an anisotropic growth profile due to the different growth rates of the diverse crystal facets (Manna et al., 2000; Peng and Peng, 2002). In the synthesis of ZnO nanoparticles in a basic methanolic solution of zinc acetate dihydrate, it was observed that by simply increasing the Zn precursor concentration (10-fold compared to the concentration yielding spherical particles), anisotropic ZnO nanorods could be obtained (Pacholski et al., 2002). Similar observations were also made for the microwave-assisted synthesis of ZnO from zinc acetylacetonate in 1-butanol, where an increase of the precursor concentration increased the aspect ratio of the formed nanoparticles, resulting in ZnO nanorods (Ambrožič et al., 2011).

While in some systems, no effect of the precursor concentration on the resulting morphology of the nanoparticles was detected—although an increase of the overall particle size was still observed (Ambrožič et al., 2010; Tonto et al., 2008)—the influence of precursor concentration was more pronounced in other systems (Ambrožič et al., 2011; Pacholski et al., 2002), which underlines the fact that it is an interplay of the precursor type used and overall synthesis conditions used. In this context, Ambrožič et al. observed a concentration-dependent morphology change when using microwave irradiation, whilst a concentration-independent behavior was observed for the same reaction system using reflux conditions with conventional heating (Ambrožič et al., 2010; 2011).

3.5 Effect of doping

It was also observed that doping could affect the anisotropic growth of metal oxide nanoparticles. Co- and Mn-doping of ZnO nanorods synthesized in benzyl alcohol was found to decrease the aspect ratio of the resulting ZnO nanorods, with the effect of Co-doping on the nanorod aspect ratio being more pronounced (Djerdj et al., 2008b).

3.6 Other factors

There are different non-trivial factors that can significantly affect the growth behavior of nanocrystals in the reaction system studied but they are usually overlooked. While the effects of solvents, ligands or surfactants, types of metal oxide precursors, solvent/surfactant/precursor ratios, reaction temperature and synthesis time are the most-studied factors, some other factors can still significantly affect anisotropic crystal growth. Zhao et al. investigated the influence of the mixing time of the precursor, dicyclohexyl zinc, with the ligand, dodecylamine, on the anisotropic growth of ZnO particles (Zhao et al., 2021). A mixing time of more than 6 hours before the start of the actual hydrolysis reaction was found to inhibit the anisotropic particle growth, which was ascribed to the increasing viscosity of the reaction mixture with increasing mixing time, subsequently hindering the anisotropic growth of ZnO through the oriented attachment mechanism (Zhao et al., 2021). Thus, whilst many different factors have been identified that facilitate the synthesis of ZnO nanostructures with anisotropic morphologies, a particular reaction system must always be understood in detail to enable proper control of the particle properties.

4. Iron oxide

Iron oxide is one of the most important magnetic materials, and iron oxide nanocrystals with defined properties are used in manifold applications such as magnetic storage media and magnetic resonance imaging (MRI) (Ajinkya et al., 2020; Teja and Koh, 2009). Anisotropy can be used to modulate the magnetic properties of such nanoparticles where it was found that anisotropic iron oxide nanoparticles possess improved magnetic properties (Zhang et al., 2009). Tuning the shape of the iron oxide nanoparticles results in the exposure of different crystal facets that could be used to vary the T_1 and T_2 proton relaxation time shortening effects, which in turn is important for the design of efficient MRI contrast agents (Zhou et al., 2015). **Table S3** in the supplementary material summarizes the state of the literature on the synthesis of anisotropic iron oxide nanocrystals in non-aqueous media in chronological order.

Whilst typically, magnetite (Fe_3O_4) is the desired material, maghemite (γ-Fe_2O_3) shows similar ferromagnetic behavior and is obtained under more oxidative conditions. As magnetite particles may oxidize during extended storage, particularly in aqueous media, the direct synthesis of maghemite might thus provide a more stable product (Grabs et al., 2012; Masthoff et al., 2014). In non-aqueous reaction systems for the synthesis of iron oxide, surfactants are typically required to obtain particle shapes other than

spheres. The use of long-chain amines such as dodecylamine was found to result in the formation of large hexagon-shaped γ-Fe_2O_3 particles from iron pentacarbonyl ($Fe(CO)_5$) at a surfactant-to-precursor ratio of at least 10. Lower ratios resulted in a mixture of spherical, triangular and diamond-shaped nanocrystals (Cheon et al., 2004). Unique star-shaped Fe_3O_4 nanocrystals were obtained by the use of the bulky 1-adamantanecarboxylic acid instead of the linear oleic acid as the surfactant together with oleylamine (**Fig. 11**) (Zhang L. et al., 2006). It was proposed that the growth mechanism resulting in the anisotropic star shape is based on the bulkiness of the 1-adamantanecarboxylic acid surfactant molecules. Due to their bulkiness, some sites were not covered by the surfactant molecules and led to their further growth, which resulted in the observed spikes of the star-shaped nanocrystals. Further substitution of oleylamine with the bulky 1-adamantaneamine so that the surfactant system is composed of 1-adamantanecarboxylic acid and 1-adamantaneamine instead of the traditional oleic acid/oleylamine surfactant system resulted in a certain anisotropy where irregular-shaped particles were obtained forming flower-like aggregates (Zhang L. et al., 2006). With a ternary surfactant mixture of oleic acid, oleylamine and hexadecane-1,2-diol in a ratio of 3:3:5, it was even possible to produce tetrapod-shaped maghemite nanocrystals from $Fe(CO)_5$ (**Fig. 12**) (Cozzoli et al., 2006). Increasing the precursor concentration of resulted in an increase in anisotropic growth that led to longer tetrapod arms. It was also found that a significant deviation from the optimized 3:3:5 ratio of the three-component surfactant system—or omitting any of these surfactants from the reaction system—resulted in a loss of the tetrapod geometry, which shows the important role of all surfactants in this specified ratio in forming the unique tetrapod geometry (Cozzoli et al., 2006). Analogous tripods, or shamrock-shaped particles, of nickel manganese ferrite were interestingly obtained in a much more facile synthesis without surfactants via an oriented attachment mechanism (Masthoff et al., 2015). Hofmann et al. also investigated the influence of the surfactant ratio of the surfactant system of trioctylamine and oleic acid on the morphology of iron oxide nanoparticles and found that the nanocrystal shape is significantly influenced by the surfactant ratio used. Increasing the trioctylamine to oleic acid ratio resulted in the formation of cubic wüstite iron oxide nanocrystals with concave faces which were referred to as nanotetracubes (Hofmann et al., 2008).

Fatty acid surfactants such as oleic acid were used in several studies, often in the form of its oleate anion as part of the iron oxide precursor. Typically, iron(III) oleate is first synthesized in a separate step and the purified precursor is then mixed with the solvent and heated for the actual synthesis. In this case the oleate already present in the precursor can act as a surfactant and structure-directing agent. Heating the iron oleate complex in 1-octadencene at 320 °C for one hour resulted in cubic iron oxide nanocrystals (Kwon et al., 2007). In another study, the controlled decomposition of the iron oleate precursor at a low temperature of 150 °C in the same solvent formed iron oxide nanowhiskers. At temperatures higher than 300 °C, spherical particles were formed, as commonly reported in the literature. Thermogravimetric analysis (TGA) and density functional theory (DFT) calculations revealed the dissociation of two of the three oleate ligands from the complex at 150 °C, and the third bound oleate ligand was assumed to act as a structure-directing agent for the formation of the one-dimensional nanowhiskers (Palchoudhury et al., 2011a). The addition of the weakly binding surfactant TOPO to a system of iron oleate and oleic acid at a ratio of 6.3:1 (TOPO/OA) resulted in the formation of iron oxide nanoworms, which was attributed to the controlled aggregation of spherical nanoparticles (Palchoudhury et al., 2011b).

A plethora of different iron oxide nanocrystal shapes were accessed by the use of oleate salts instead of oleic acid as the surfactant. Although the oleate ligands in the

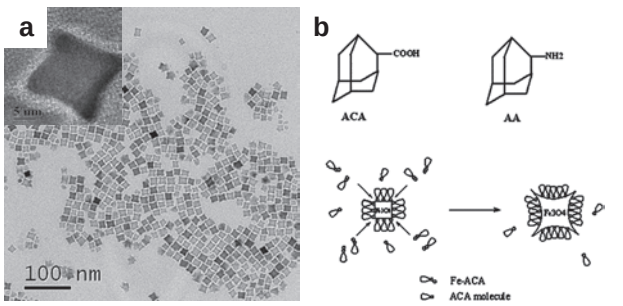


Fig. 11 **(a)** TEM image of iron oxide nanostars obtained using the bulky 1-adamantanecarboxylic acid as a surfactant. The inset shows the HRTEM image of a single iron oxide nanostar. **(b)** Schematic illustration showing the proposed formation mechanism of iron oxide nanostars. Adapted with permission from Ref. (Zhang L. et al., 2006). Copyright 2006 Elsevier.

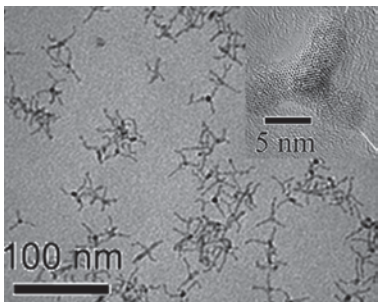


Fig. 12 TEM image of tetrapod maghemite nanocrystals formed through a 3:3:5 surfactant ratio of oleic acid, oleylamine and hexadecane-1,2-diol. The inset shows a HRTEM image of a single tetrapod nanocrystal viewed along the <111> zone axis. Adapted with permission from Ref. (Cozzoli et al., 2006). Copyright 2006 American Chemical Society.

precursor can act as a surfactant, further addition of oleic acid and sodium oleate to the reaction mixture has a significant influence on the shape evolution of the iron oxide nanocrystals. Kovalenko et al. observed that replacing the surfactant oleic acid with its sodium or potassium salt in a reaction system containing iron oleate as a precursor results in the formation of cubic instead of spherical iron oxide nanocrystals. Decreasing the sodium oleate-to-iron oleate precursor ratio even resulted in bipyramidal nanocrystals. From conductivity measurements, it was inferred that the oleate salts in octadecene dissociate at temperatures above 220–230 °C, resulting in ionic oleate species, which is not the case for oleic acid; this difference was related to the different shape evolution (Kovalenko et al., 2007). Similarly, Bao et al. synthesized iron oxide nanorods from iron oleate in benzyl ether by replacing oleic acid with sodium oleate as surfactant, whereby the aspect ratio of the product could be carefully tuned by varying the synthesis temperature (Bao et al., 2012).

A broad range of different iron oxide nanocrystal shapes was also synthesized by Gao's group through variation of the sodium oleate-to-iron oleate molar ratio and using 1-octadecene or trioctylamine as a solvent (**Fig. 13**) (Zhou et al., 2015). Increasing this ratio in 1-octadecene resulted in an increased exposure of the {111} facets, which led to the shape evolving from spherical particles (in the absence of sodium oleate) to hexagonal plates, truncated octahedrons, and finally to tetrahedrons (**Fig. 13(b)–(d)**). Accordingly, it was assumed that the oleate ions preferentially attached to the {111} facets, thus stabilizing them and retarding their growth, which resulted in an increased exposure of the {111} facets with an increasing sodium oleate amount. Using trioctylamine as the solvent, in which higher synthesis temperatures are possible, iron oxide nanocubes (**Fig. 13(e)**) were obtained at low sodium oleate-to-iron oleate ratios (NaOL/FeOL ≤ 1:10), while at a ratio of 2:10, spikes started to emerge at the cube corners forming what the authors called "concave" nanocrystals (**Fig. 13(f)**). A further increase of the sodium oleate amount (NaOL/FeOL = 5:10) resulted in assembled nanostructures which were supposedly formed through the oriented attachment of smaller building blocks (**Fig. 13(g)**). Using low NaOL to FeOL ratios (NaOL/FeOL = 1:10) that previously resulted in nanocubes formed multibranched iron oxide nanoparticles when higher dilutions were used (i.e. lower concentrations of NaOL and FeOL in the system) (**Fig. 13(h)**) (Zhou et al., 2015).

In addition, the use of long-chain quaternary ammonium salts such as tetraoctylammonium bromide was found to induce anisotropic iron oxide nanocrystal growth where nanooctahedra were obtained from the iron oleate precursor. In this system, the authors also addressed the fact that chemical species formed in situ during the synthesis can play an important role in determining the shape of the synthesized nanoparticles (Shavel et al., 2009).

Besides the amount of surfactant or the surfactant-to-precursor ratio, some other non-trivial factors were described to influence the anisotropic growth during the non-aqueous and non-hydrolytic synthesis. Recently, the effect of nitrogen purging on the anisotropic growth of iron oxide nanoparticles was investigated by AbuTalib et al. (2021). Through testing different configurations for nitrogen flow, it was found that bubbling the reaction mixture with nitrogen induced anisotropic growth in their system, while applying nitrogen flow over the reaction mixture reduced the anisotropic growth, and finally the use of only a

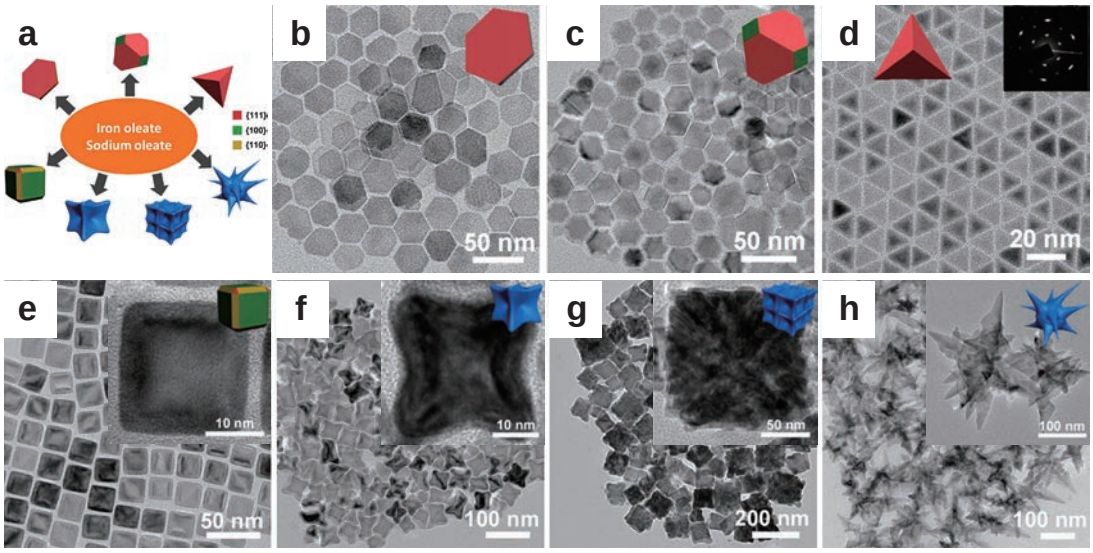


Fig. 13 **(a)** Overview of the different iron oxide particle morphologies obtained using iron oleate as a precursor and sodium oleate as a surfactant; TEM images showing iron oxide **(b)** nanoplates, **(c)** truncated octahedrons, **(d)** tetrahedrons obtained in 1-octadecene and **(e)** nanocubes, **(f)** concave particles, **(g)** assembled structures and **(h)** multibranched nanocrystals obtained in trioctylamine using different sodium oleate-to-iron oleate ratios. Adapted with permission from Ref. (Zhou et al., 2015). Copyright 2015 American Chemical Society.

"nitrogen blanket" (i.e. positive pressure of nitrogen in the system without steady flow) favored isotropic crystal growth. The nitrogen flow rate did not play a significant role in the extent of anisotropic growth. It is assumed that the reason for this anisotropy observed in the nitrogen-bubbling system arises from increased turbulence, the bubbles acting as nucleation sites and inducing aggregation, or the improved removal of volatile by-products from the system which otherwise influence the particle morphology (AbuTalib et al., 2021). Additionally, a significant influence of the amount of the oleylamine surfactant relative to the $Fe(acac)_3$ precursor on the morphology of the product was found in this system. While at very high oleylamine-to-precursor ratios (above 40 equivalents), isotropic particles were observed, decreasing the oleylamine amount to 25 equivalents resulted in anisotropic nuclei which formed iron oxide nanocrystals with two branches (bipods). A further decrease in the oleylamine amount to 17 equivalents resulted in multiply branched nanocrystals and finally branched nanocrystals with a flower-like appearance at 15 equivalents of oleylamine. An investigation of the evolution of the branched iron oxide nanocrystals over time revealed the formation of small anisotropic nuclei in most cases, which further aggregate in the initial stages of the synthesis forming polycrystalline nanocrystals. The defects and misalignments in the formed aggregates are then removed through rearrangement and ordering over the course of the reaction, and finally monocrystalline branched iron oxide nanocrystals are obtained.

Prolongation of the synthesis time also has an influence on the product morphology. While the decomposition of iron oleate in 1-octadecane at 320 °C results in the formation of monodisperse spherical nanocrystals for a synthesis time up to 30 minutes (Park et al., 2004a), an increase of the synthesis time to one hour resulted in monodisperse cubic nanocrystals (Kwon et al., 2007). The spherical iron oxide nanocrystals are converted to cubic nanocrystals upon prolonged aging at 320 °C, forming the thermodynamically most stable shape for the iron oxide spinel structure with only {100} planes exposed (Kwon et al., 2007). A change of shape with reaction time was also observed during the synthesis of iron oxide from iron(II) acetate in trioctylamine using oleic acid as the surfactant at 255 °C. While at shorter synthesis times (10–25 min) cubic nanocrystals were formed, the particles transformed into truncated octahedrons when the reaction time was prolonged further (Redl et al., 2004).

Two-dimensional iron oxide nanocrystals obtained from non-aqueous and non-hydrolytic synthesis are still rare and the parameters and conditions required for their synthesis are still not well understood. Examples of such two-dimensional iron oxide nanocrystals were presented by Casula et al., where circular nanodisks were obtained from iron pentacarbonyl in octyl ether using tridecanoic acid as the surfactant (Casula et al., 2006). It is important to note that the disk form of the obtained nanoparticles has been confirmed through AFM height measurements. In general, even if TEM investigations reveal a spherical nanocrystal appearance, it is important to investigate the true height of the nanoparticles to prove their isotropy or anisotropy, but this is usually not performed in most of the published works so far. In another work, hexagonal and triangular iron oxide nanoplates were obtained in diethylene glycol from iron(III) chloride without the use of any surfactant (Zhang et al., 2009).

5. Other metal oxides

A number of other metal oxides and mixed-metal oxides have been synthesized as anisotropic nanocrystals via non-aqueous synthesis routes. As there are only a few reports about each, they are discussed in this section in combined form. **Table S4** in the supplementary material provides an overview of the materials and morphologies obtained and the respective synthesis conditions. In the following paragraphs, some more insight will be given for some of these reaction systems.

Zirconia nanocrystals synthesized in benzyl alcohol using sodium lauryl sulfate as a surfactant showed one-dimensional growth when $ZrOCl_2 \cdot 8H_2O$ was used as the precursor, while $Zr(SO_4)_2 \cdot H_2O$ yielded only isotropic nanoparticles (Siddiqui et al., 2012). The reaction of zirconium *n*-propoxide in benzyl alcohol was reported to lead to fractal nanostructures, in particular at lower reaction temperatures and extended reaction times (Stolzenburg et al., 2016).

The synthesis of V_2O_3 from $VOCl_3$ in benzyl alcohol led to ellipsoidal-shaped nanorods (Niederberger et al., 2002b; Ohayon and Gedanken, 2010), whereby doping with the rare earth metals Gd and Nd resulted in an alteration of the morphology to nanoflakes and nanocubes, respectively (Venkatesan et al., 2015).

Due to the great potential of tungsten oxide in different fields, such as for batteries, gas sensing, as well as photocatalytic and electrochromic applications, different non-aqueous synthesis procedures for tungsten oxide nanorods or nanowires have been developed (Choi H.G. et al., 2005; Lee et al., 2003; Polleux et al., 2006; Woo et al., 2005). Woo et al. conducted a systematic study which revealed that the aspect ratio of tungsten oxide nanorods could be tuned through the coordinating power of the surfactant system used. Increasing the coordinating power was thereby found to decrease the tungsten oxide nanorod length, which was attributed to the increased inhibition of growth in the [010] direction resulting from the stronger ligand binding (Woo et al., 2005). In a different approach, Choi et al. were able to tune the aspect ratio of tungsten oxide nanorods by adjusting the precursor concentration in an ethanolic solution, without the need for any surfactant.

Using lower WCl_6 precursor concentrations resulted in higher aspect ratios and even in the growth of tungsten oxide nanowires (Choi H.G. et al., 2005). To obtain more complex structures, Zhao et al. added urea to the ethanolic WCl_5 precursor solution to act as a ligand and structure-directing agent due to its strong hydrogen bonding ability. This enabled the formation of tungsten oxide nanotubes using a template-free non-aqueous synthesis for the first time, whereby the as-synthesized product was identified as tungstic acid hydrate ($H_2W_{1.5}O_{5.5}\cdot H_2O$) and was transformed to WO_3 through calcination without loss of the hollow structure (Zhao and Miyauchi, 2008). Variation of the synthesis parameters, such as the urea amount and reaction time, yielded further hollow tungstic acid hydrate nanostructures (hollow spheres and boxes), which were converted to tungsten trioxide upon calcination. Interestingly, a broad range of morphologies was obtained thereby, which was attributed to different self-assembly processes of smaller nanoparticles and nanorods due to the presence of urea in the reaction system (Zhao and Miyauchi, 2009).

There has also been an interest in synthesizing manganese oxide due to its magnetic properties, especially at the nanoscale (Park et al., 2004b). Uniform MnO nanorods were obtained by Park et al. through injecting a previously prepared manganese oleylamine complex into trioctylphosphine or triphenylphosphine at high temperatures (330 °C) (Park et al., 2004b). Zitoun et al. were able to prepare MnO multipods via the decomposition of $Mn(oleate)_2$ in *n*-trioctylamine in the presence of oleic acid at 320 °C, where the arms showed an arrow-like ending and a zigzag structure which indicated an oriented attachment process of the initially formed cube-shaped or truncated octahedral nuclei (Zitoun et al., 2005). Similar anisotropic MnO nanoparticle shapes termed as “dumbbell-shaped” MnO nanocrystals were obtained by Zhong et al. through the use of manganese formate hydrate as a precursor (Zhong et al., 2006). Anisotropic shapes for manganese cobalt oxide ($MnCoO_x$) ternary mixed-metal oxides were obtained through the decomposition of $Mn(oleate)_2$ and $Co(oleate)_2$ precursors in 1-octadecene in the presence of oleic acid (Gliech et al., 2020). Interestingly, the use of a single metal oxide precursor in this system yielded cubic or octahedral shapes for manganese oxide and aggregated octahedral shapes for cobalt oxide, while for the mixed-metal oxide, rod-, T-, cross- and hexapod-shaped nanocrystals were obtained with decreasing cobalt concentrations. A new solution-solid-solid (SSS) oxide mechanism was suggested for the anisotropic growth of the mixed-metal oxide nanoparticles, which is a good example of the influence of other metal ions on the anisotropic growth of metal oxides. In the suggested SSS growth mechanism, first MnO nuclei are formed, followed by the deposition of Co monomers to form Co-rich regions which serve as sites for outward growth in the <100> directions, thus forming the arms. At low Co concentration, the Co has time to accumulate on different facets of the MnO nuclei, thus forming several starting points for the branching, resulting in multiarmed structures such as hexapods. Increasing the Co concentration decreases the cobalt accumulation time and less branched structures occur, thus leading to nanorod structures at high concentrations (Gliech et al., 2020).

Even more exotic metal oxides such as actinide oxides have been synthesized using the non-aqueous and non-hydrolytic synthesis route. In several cases, the use of certain surfactants and certain synthesis conditions yielded anisotropic shapes for those oxides. For example, anisotropic thorium oxide (ThO_2) has been obtained from thorium acetylacetonate in benzyl ether using a ternary surfactant mixture of TOPO, OA and trioctylamine at 280 °C (Hudry et al., 2012).

6. Oriented attachment mechanisms resulting in anisotropic structures

Different mechanisms have been reported to potentially lead to the formation of anisotropic nanoparticles or nanostructures such as controlled aggregation (for example via oriented attachment), etching and branching (AbuTalib et al., 2021). According to the classical crystallization model, anisotropic growth in metal oxides can be mainly achieved via kinetic control through the use of surfactants or by the selective formation of nuclei of specific crystal phases featuring different surface energies (Jun et al., 2006; Sajanlal et al., 2011). Besides the classical crystallization theory, oriented attachment has been proven to represent an important pathway to result in anisotropic metal oxide nanocrystals.

The oriented attachment mechanism is based on the controlled aggregation of nanoparticle building blocks showing an aligned crystal orientation towards each other and thus, in principle, leads to one larger crystal. Thereby, isotropic metal oxide nanoparticles can also be used as building blocks for larger anisotropic and more complex three-dimensional structures. This process can be observed in the absence of organic surfactants which delimits this process from usual self-assembly phenomena that occur due to organic building blocks. This phenomenon was identified to represent an important non-classical crystal growth mechanism and was found in many systems including non-aqueous and/or non-hydrolytic metal oxide synthesis (Chen et al., 2022; Pacholski et al., 2002; Xue et al., 2014). Kinetic models describing the oriented attachment process have been developed by Ribeiro et al. (2005; 2006).

The general mechanism for the formation of anisotropic nanoparticles or nanostructures from smaller (usually isotropic) nanoparticles was identified to consist of the following steps: 1) Collisions of nanoparticles leading to their loose attachment where sometimes the crystal planes are

already aligned, 2) Rotation of the attached nanoparticles takes place to eliminate some misorientation, 3) Smoothening of the surface occurs due to further monomer addition and eventually Ostwald ripening (**Fig. 14**) (Lee et al., 2005; Xue et al., 2014). Interestingly, this process can occur in some systems even at room temperature without the addition of specific ligands (Leite et al., 2003), while higher temperatures usually enhance the particle coalescence and thus the oriented attachment process (Lee et al., 2005). The presence of some crystal defects or misalignments such as twinning, stacking faults or dislocations in the final product can give a hint on the crystal evolution through the oriented attachment mechanism (Chen et al., 2022). The oriented attachment process can even give rise to anisotropic growth directions that are generally not accessible through traditional monomer deposition or classical crystal growth (Lee et al., 2005; Leite et al., 2003). The use of selective surfactants can facilitate and direct the oriented attachment process and inhibit Ostwald ripening (Xue et al., 2014). This makes the oriented attachment process a very effective mechanism for achieving novel and even more complex anisotropic structures.

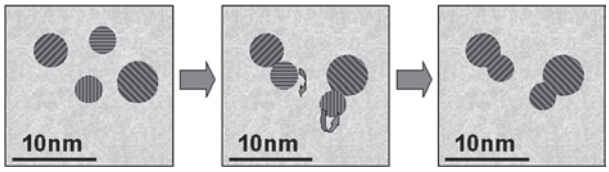


Fig. 14 Schematic showing the collision, attachment and rotation steps involved in the oriented attachment process. Adapted with permission from Ref. (Leite et al., 2003). Copyright 2003 American Institute of Physics.

A good example showing the formation of anisotropic zinc oxide nanorods from quasi-spherical ZnO nanoparticles via oriented attachment in non-aqueous systems was presented by Pacholski et al. (2002). Thereby, a sol of the ZnO nanoparticles previously prepared from a dilute basic methanolic solution of zinc acetate dihydrate (**Fig. 15(a)**) was first concentrated through solvent evaporation. Refluxing of the resulting sol resulted in ZnO nanorods where the dimensions of the nanorods increased with increasing reflux time, yielding excellent monocrystalline ZnO nanorods after one day (**Fig. 15(b)**). Sampling at different time intervals showed the arrangement of the quasi-spherical particles into chains where neck formation and coalescence with excellent alignment of the particle crystal planes was observed in high-resolution TEM images (**Fig. 15(c)–(g)**) (Pacholski et al., 2002). Similar observations were made by Peukert et al. through an in-depth investigation of ZnO nanorod formation kinetics in the same

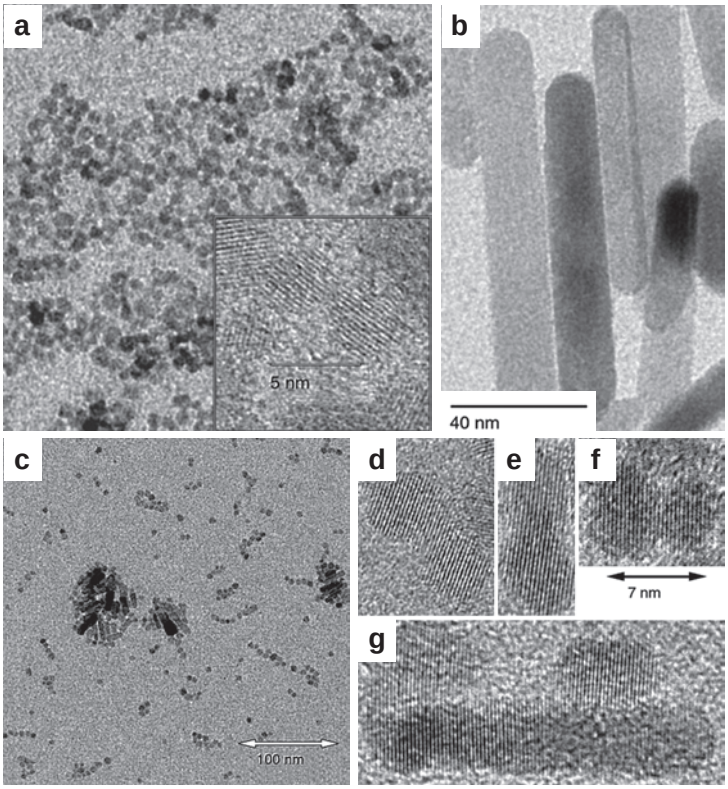


Fig. 15 TEM images of **(a)** quasi-spherical ZnO nanoparticles used as starting sol for the synthesis of ZnO nanorods, **(b)** final monocrystalline ZnO nanorods formed by oriented attachment of the quasi-spherical ZnO particles, **(c)** sample of the reaction mixture after 2 h showing some ZnO nanorods and quasi-spherical ZnO particles arranged in shorter and longer chains, **(d–g)** high-resolution TEM micrographs of differently attached particles showing neck formation and coalescence with aligned crystal planes. Adapted with permission from Ref. (Pacholski et al., 2002). Copyright 2002 Wiley-VCH.

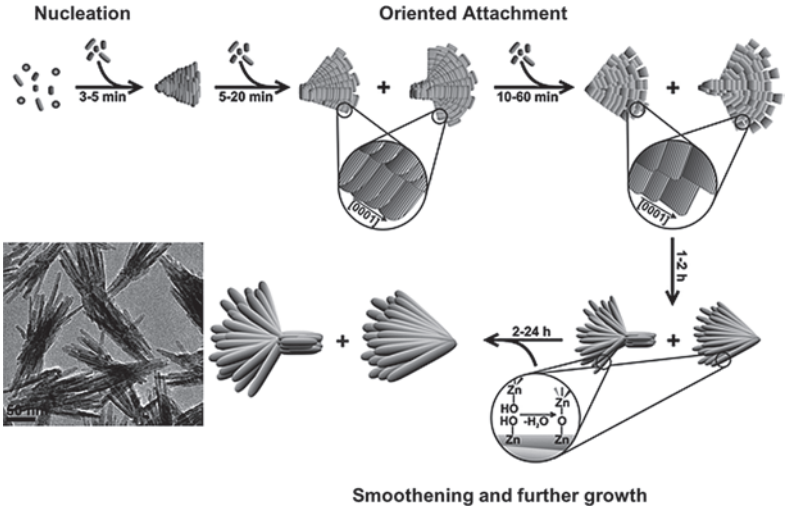


Fig. 16 Schematic showing the steps involved in the temporal evolution of ZnO fan- and bouquet-like nanostructures in benzyl alcohol. Adapted with permission from Ref. (Ludi et al., 2012). Copyright 2012 The Royal Society of Chemistry.

system (Voigt et al., 2010). Buha et al. observed the formation of hexagonal ZnO nanoplatelets from $Zn(acac)_2$ in acetonitrile, which was identified in high-resolution TEM to be a mesocrystal formed of perfectly aligned crystal domains, so that the final hexagonal nanocrystal behaves as a single crystal (Buha et al., 2007). Similarly, the formation of hexagonal Al-doped ZnO (AZO) in benzylamine was observed and investigated via small-angle X-ray scattering (SAXS), where time-resolved analysis revealed oriented aggregation forming hexagonal mesocrystals (Ungerer et al., 2019; 2020). Oriented attachment was also observed for the formation of TiO_2 nanorods when the reaction system of Joo et al. (2005b) (synthesis of TiO_2 from TIP using oleic acid as a surfactant, **Table S1**) was reinvestigated by Dalmaschio and Leite, where even the detachment of well-faceted nanoparticles was observed for longer reaction times and this was interpreted as Rayleigh instability of the TiO_2 originally formed through oriented attachment (Dalmaschio and Leite, 2012). Although Joo et al. (2005b) already observed the presence of spherical nanoparticles along with the synthesized TiO_2 nanorods, the reason behind their presence in the product was not further investigated.

Oriented attachment can also be the reason for the formation of ordered aggregates as was observed in the formation of ZnO nanorod bundles (Zhang et al., 2007). More complex geometries could even be obtained due to oriented-attachment mechanisms such as hollow hexagonal ZnO mesocrystals which form via the oriented attachment of trapezoidal ZnO nanosheets (Wang et al., 2013), interwoven ZnO nanosheets (Khokhra et al., 2015) and fan- and bouquet-like ZnO nanostructures (Ludi et al., 2012). Khokhra et al. proposed that the aggregation of ZnO nanosheets to form an interwoven structure was induced by the interaction of the solvent used with the adsorbed hydroxide and acetate ions on the surface of the ZnO nanocrystals via hydrogen bonds (Khokhra et al., 2015). In a detailed study, the temporal evolution of the fan- and bouquet-like ZnO nanostructures was followed from platelet-like ZnO nanoparticles formed in benzyl alcohol (**Fig. 16**). Overlapping stages of classical nucleation, oriented attachment followed by further growth and surface smoothening could be observed in this reaction system (Ludi et al., 2012).

7. Benzyl alcohol route for anisotropic particle growth

The “benzyl alcohol route” has emerged as a unique non-aqueous synthesis route for multiple metal oxides. The advantage of this route lies in the fact that it is mainly a solvent-directed route which makes it possible to synthesize metal oxides and control their morphology through the variation of different experimental parameters without the need of any surfactants. This is achieved via the coordinating ability of benzyl alcohol to the metal oxide surface, however, compared to surfactants, a relatively low amount of surface organics results, rendering a “clean surface” that is accessible for small molecules, which is important for catalytic or sensing applications (Clavel et al., 2007; Pinna and Niederberger, 2008).

Benzyl alcohol can act as a solvent, reducing agent and structure-directing agent for many metal oxides (Pinna et al., 2011; Qamar et al., 2017). The fact that it can also act as a reducing agent was successfully applied to synthesize several non-stoichiometric metal oxide nanoparticles, which is very useful for catalytic applications where these defects can act as catalytic centers (Qamar et al., 2017). The structure-directing properties of benzyl alcohol are revealed in the formation of different anisotropic metal oxides. Qamar et al. synthesized a series of non-stoichiometric

metal oxides (TiO_x, ZnO_x, SnO_x, CeO_x, In_2O_x and Ga_2O_x) at a high temperature of 245 °C, where for several metal oxides, a square or rectangular plate-like morphology was obtained (Qamar et al., 2017). ZnO nanorods were successfully synthesized in benzyl alcohol from $Zn(acac)_2$ hydrate without the need of any surfactant (Djerdj et al., 2008b). Moreover, Al-doped ZnO formed with a rod-like shape in benzyl alcohol, in contrast to the synthesis in benzylamine where no elongated growth was observed (Zellmer et al., 2015). Similarly, TiO_2 nanorods were obtained in benzyl alcohol from $TiCl_4$ at a temperature as low as 70 °C (Abazović et al., 2008; 2006). While shorter synthesis times of some hours up to one day yielded spherical anatase TiO_2 nanoparticles (Garnweitner and Grote, 2009; Niederberger et al., 2002a), longer synthesis times of three days resulted in the formation of nanorods (Abazović et al., 2008; Jia et al., 2009). The use of TIP as a precursor together with minor amounts of silanes in the benzyl alcohol route yielded platelet-like TiO_2 particles (Koziej et al., 2009), while the use of OLA as a surfactant even resulted in two-dimensional TiO_2 nanosheets (Wu et al., 2008). Interestingly, the analogous synthesis in benzylamine also results in nanosheets that are evenly stacked, proving the tendency of amines to guide the reaction towards the formation of 2-D structures (Garnweitner et al., 2008).

Zirconia nanocrystals synthesized in benzyl alcohol using sodium lauryl sulfate as a surfactant showed one-dimensional growth when $ZrOCl_2{\cdot}8H_2O$ was used as the precursor while $Zr(SO_4)_2{\cdot}H_2O$ yielded only isotropic nanoparticles (Siddiqui et al., 2012). The reaction of zirconium *n*-propoxide in benzyl alcohol was reported to lead to fractal nanostructures, in particular at lower reaction temperatures and extended reaction times (Stolzenburg et al., 2016).

In several cases, the synthesis of metal oxides via the benzyl alcohol route yielded nanoparticles of narrow size distribution together with a surprising tendency of forming well-defined aggregates, sometimes even with two-dimensional or complex three-dimensional anisotropic morphologies. In situ formed organics were often judged to exert a pronounced effect on the nanoparticle and aggregate morphology formed. An in-depth analysis of the organics present on the particle surface as well as organic by-products in the reaction mixture revealed the in-situ formation of benzoate species that adsorb on the nanocrystal surface and thus act as a capping and structure-directing agent (Pinna et al., 2005; Pucci et al., 2012). In another study, the formation of WO_3 nanowire bundles was attributed to the partial oxidation of benzyl alcohol to benzaldehyde which contributed to the formation of nanowire bundles as an inorganic-organic hybrid nanostructure (Polleux et al., 2005; 2006).

The use of additives other than surfactants could also have a significant effect on the formed nanostructures in the "benzyl alcohol route", giving access to novel shapes. For example, the addition of HCl to $Ti(OBu)_4$ in benzyl alcohol enabled the formation of walnut-like aggregate structures composed of rutile-phase nanorods as building blocks. An increase in the amount of HCl added allowed tuning the size of the nanorods and thus, of the formed aggregate structure. It was proposed that the presence of chloride ions supports the anisotropic growth of rutile TiO_2 through selective adsorption to the (110) plane of rutile TiO_2 suppressing its growth, thus favoring the growth in the [001] direction (Kim et al., 2013). In the synthesis of tungsten oxide from WCl_6 in benzyl alcohol, the formation of tungstite ($WO_3{\cdot}H_2O$) nanoplatelets was observed. Upon the addition of the siderophore deferoxamine mesylate as an additive, a fundamental change in the morphology of the resulting tungsten oxide was observed. Tungsten oxide nanowires were obtained, which were arranged in bundles to form inorganic-organic hybrid superstructures (Polleux et al., 2005).

8. Summary and outlook

In this article, the different non-aqueous and/or non-hydrolytic reaction systems used for the synthesis of simple and complex anisotropic metal oxide nanocrystals and nanostructures were summarized. Many examples for the most common metal oxides, in particular titania, zinc and iron oxide as well as for more specialized systems were summarized, showing that there are many parameters controlling the resultant morphology. Moreover, the common theories resulting in anisotropic crystal growth in these non-aqueous systems were elaborated. While some general mechanisms and concepts have been developed for the anisotropic crystal growth in non-aqueous media, some reaction systems are still found to possess some unique features and mechanisms for anisotropic nanostructure formation, such as unique aggregation behavior, and need to be investigated in detail for each system on its own.

To date, the synthesis of anisotropic metal oxides has still largely focused on low-dimensional nanoparticles, and more complex anisotropic structures remain relatively uncommon and need further investigation of the reaction parameters that can yield such structures in a single step or through multi-step approaches. It should be noted that anisotropic metal oxide nanoparticles or nanostructures can be formed directly through either the "truly" anisotropic growth of a single crystal or via an oriented-attachment or controlled-aggregation process, usually leading to polycrystalline anisotropic structures or mesocrystals with certain misalignments and defects. A deeper understanding of the factors governing the controlled aggregation and oriented attachment of nanoparticles in non-aqueous media would help to engineer more complex anisotropic metal oxide nanostructures formed from smaller isotropic or anisotropic building blocks.

Different parameters have been identified to play an important role in anisotropic growth, where surfactants represent a cornerstone in regulating anisotropic particle growth. However, the solvent can also fulfill this function and additionally act as a structure-directing agent. Moreover, the precursor type and its ratio to the solvent, as well as possibly the surfactant, can influence the growth processes and induce the formation of anisotropic structures. This can be attributed to specific precursor decomposition mechanisms, as well as the presence of certain counter ions or ligands from the precursor in the system. The precursor may also contain water from crystallization which can also influence the nanoparticle formation process in various ways. It has to also be taken into consideration that side products formed during the non-aqueous synthesis can coordinate to the nanoparticle surface, resulting in strong modification of the nanoparticle growth and triggering aggregation, even though they might only be formed in very small amounts. The reaction temperature is another substantial factor that affects nanocrystal nucleation and the subsequent reaction rate, which can result in different crystal growth mechanisms. While most of the studies concentrate on factors such as the surfactant used, surfactant concentration, reaction solvent and metal oxide precursor, attention should also be paid to several uncommon factors which need more in-depth investigation in non-aqueous systems such as the heating rate, cooling rate, mixing of reaction components, rate and order of reagent addition, hot-injection of the precursor, etc.

As presented in this contribution, the synthesis of metal oxides in organic media has been intensively studied in the literature, while the preparation of other metal oxides has been only rarely investigated in non-aqueous media. It is important to note that different metal oxide precursors exhibit different reactivity and reaction kinetics, even in similar reaction media, which makes it important to study the shape evolution of each metal oxide in non-aqueous media separately. There is still a high potential for the development of non-aqueous and non-hydrolytic synthesis routes capable of synthesizing various anisotropic metal oxide nanostructures because of the almost infinite possibilities of combining different organic reaction media, metal oxide precursors and surfactants, as well as varying the corresponding reaction parameters.

Supplementary information

The online version contains supplementary material available at https://doi.org/10.14356/kona.2024014.

Acknowledgments

The authors acknowledge funding by the German Research Foundation (Deutsche Forschungsgemeinschaft, DFG), grants GA 1492/9-2 and NI 414/24-2.

References

Abazović N.D., Čomor M.I., Dramićanin M.D., Jovanović D.J., Ahrenkiel S.P., Nedeljković J.M., Photoluminescence of anatase and rutile TiO_2 particles, Journal of Physical Chemistry B, 110 (2006) 25366–25370. DOI: 10.1021/jp064454f

Abazović N.D., Ruvarac-Bugarčić I.A., Čomor M.I., Bibić N., Ahrenkiel S.P., Nedeljković J.M., Photon energy up-conversion in colloidal TiO_2 nanorods, Optical Materials, 30 (2008) 1139–1144. DOI: 10.1016/j.optmat.2007.05.038

AbuTalib N.H., LaGrow A.P., Besenhard M.O., Bondarchuk O., Sergides A., Famiani S., Ferreira L.P., Cruz M.M., Gavriilidis A., Thanh N.T.K., Shape controlled iron oxide nanoparticles: Inducing branching and controlling particle crystallinity, CrystEngComm, 23 (2021) 550–561. DOI: 10.1039/d0ce01291b

Ahmad M.Z., Chang J., Ahmad M.S., Waclawik E.R., Wlodarski W., Non-aqueous synthesis of hexagonal ZnO nanopyramids: gas sensing properties, Sensors and Actuators B: Chemical, 177 (2013) 286–294. DOI: 10.1016/j.snb.2012.11.013

Ajinkya N., Yu X., Kaithal P., Luo H., Somani P., Ramakrishna S., Magnetic iron oxide nanoparticle (IONP) synthesis to applications: Present and future, Materials, 13 (2020) 4644. DOI: 10.3390/ma13204644

Ambrožič G., Orel Z.C., Žigon M., Microwave-assisted non-aqueous synthesis of ZnO nanoparticles, Materiali in Tehnologije, 45 (2011) 173–177.

Ambrožič G., Škapin S.D., Žigon M., Orel Z.C., The synthesis of zinc oxide nanoparticles from zinc acetylacetonate hydrate and 1-butanol or isobutanol, Journal of Colloid and Interface Science, 346 (2010) 317–323. DOI: 10.1016/j.jcis.2010.03.001

Andelman T., Gong Y., Polking M., Yin M., Kuskovsky I., Neumark G., O'Brien S., Morphological control and photoluminescence of zinc oxide nanocrystals, Journal of Physical Chemistry B, 109 (2005) 14314–14318. DOI: 10.1021/jp050540o

Andrade R.G.D., Veloso S.R.S., Castanheira E.M.S., Shape anisotropic iron oxide-based magnetic nanoparticles: synthesis and biomedical applications, International Journal of Molecular Sciences, 21 (2020) 2455. DOI: 10.3390/ijms21072455

Arafat M.M., Dinan B., Akbar S.A., Haseeb A.S.M.A., Gas sensors based on one dimensional nanostructured metal-oxides: a review, Sensors, 12 (2012) 7207–7258. DOI: 10.3390/s120607207

Bakshi M.S., How surfactants control crystal growth of nanomaterials, Crystal Growth and Design, 16 (2016) 1104–1133. DOI: 10.1021/acs.cgd.5b01465

Bao L., Low W.-L., Jiang J., Ying J.Y., Colloidal synthesis of magnetic nanorods with tunable aspect ratios, Journal of Materials Chemistry, 22 (2012) 7117–7120. DOI: 10.1039/c2jm16401a

Bharat T.C., Shubham, Mondal S., S. Gupta H., Singh P.K., Das A.K., Synthesis of doped zinc oxide nanoparticles: a review, Materials Today: Proceedings, 11 (2019) 767–775. DOI: 10.1016/j.matpr.2019.03.041

Buha J., Djerdj I., Niederberger M., Nonaqueous synthesis of nanocrystalline indium oxide and zinc oxide in the oxygen-free solvent acetonitrile, Crystal Growth and Design, 7 (2007) 113–116. DOI: 10.1021/cg060623+

Buonsanti R., Grillo V., Carlino E., Giannini C., Kipp T., Cingolani R., Cozzoli P.D., Nonhydrolytic synthesis of high-quality anisotropically shaped brookite TiO_2 nanocrystals, Journal of the American Chemical Society, 130 (2008) 11223–11233. DOI: 10.1021/ja803559b

Burrows N.D., Vartanian A.M., Abadeer N.S., Grzincic E.M., Jacob L.M., Lin W., Li J., Dennison J.M., Hinman J.G., Murphy C.J., Anisotropic nanoparticles and anisotropic surface chemistry, Journal of Physical Chemistry Letters, 7 (2016) 632–641. DOI: 10.1021/acs.jpclett.5b02205

Cao T., Li Y., Wang C., Shao C., Liu Y., One-step nonaqueous synthesis of pure phase TiO_2 nanocrystals from $TiCl_4$ in butanol and their photo-

catalytic properties, Journal of Nanomaterials, 2011 (2011) 267415. DOI: 10.1155/2011/267415

Casula M.F., Jun Y., Zaziski D.J., Chan E.M., Corrias A., Alivisatos A.P., The concept of delayed nucleation in nanocrystal growth demonstrated for the case of iron oxide nanodisks, Journal of the American Chemical Society, 128 (2006) 1675–1682. DOI: 10.1021/ja056139x

Chang J., Waclawik E.R., Facet-controlled self-assembly of ZnO nanocrystals by non-hydrolytic aminolysis and their photodegradation activities, CrystEngComm, 14 (2012) 4041–4048. DOI: 10.1039/c2ce25154j

Chang S.M., Doong R.A., Characterization of Zr-doped TiO_2 nanocrystals prepared by a nonhydrolytic sol-gel method at high temperatures, Journal of Physical Chemistry B, 110 (2006) 20808–20814. DOI: 10.1021/jp0626566

Chavali M.S., Nikolova M.P., Metal oxide nanoparticles and their applications in nanotechnology, SN Applied Sciences, 1 (2019) 607. DOI: 10.1007/s42452-019-0592-3

Chen R., Nguyen Q.N., Xia Y., Oriented attachment: a unique mechanism for the colloidal synthesis of metal nanostructures, ChemNanoMat, 8 (2022). DOI: 10.1002/cnma.202100474

Chen S., Manders J.R., Tsang S.-W., So F., Metal oxides for interface engineering in polymer solar cells, Journal of Materials Chemistry, 22 (2012) 24202–24212. DOI: 10.1039/c2jm33838f

Cheng B., Samulski E.T., Hydrothermal synthesis of one-dimensional ZnO nanostructures with different aspect ratios, Chemical Communications, 4 (2004) 986–987. DOI: 10.1039/b316435g

Cheon J., Kang N.-J., Lee S.-M., Lee J.-H., Yoon J.-H., Oh S.J., Shape evolution of single-crystalline iron oxide nanocrystals, Journal of the American Chemical Society, 126 (2004) 1950–1951. DOI: 10.1021/ja038722o

Chiu W.S., Khiew P.S., Isa D., Cloke M., Radiman S., Abd-Shukor R., Abdullah M.H., Huang N.M., Synthesis of two-dimensional ZnO nanopellets by pyrolysis of zinc oleate, Chemical Engineering Journal, 142 (2008) 337–343. DOI: 10.1016/j.cej.2008.04.034

Choi H.G., Jung Y.H., Kim D.K., Solvothermal synthesis of tungsten oxide nanorod/nanowire/nanosheet, Journal of the American Ceramic Society, 88 (2005) 1684–1686. DOI: 10.1111/j.1551-2916.2005.00341.x

Choi S.H., Kim E.G., Park J., An K., Lee N., Kim S.C., Hyeon T., Large-scale synthesis of hexagonal pyramid-shaped ZnO nanocrystals from thermolysis of Zn-oleate complex, Journal of Physical Chemistry B, 109 (2005) 14792–14794. DOI: 10.1021/jp052934l

Clavel G., Willinger M.G., Zitoun D., Pinna N., Solvent dependent shape and magnetic properties of doped ZnO nanostructures, Advanced Functional Materials, 17 (2007) 3159–3169. DOI: 10.1002/adfm.200601142

Cozzoli P.D., Snoeck E., Garcia M.A., Giannini C., Guagliardi A., Cervellino A., Gozzo F., Hernando A., Achterhold K., Ciobanu N., Parak F.G., Cingolani R., Manna L., Colloidal synthesis and characterization of tetrapod-shaped magnetic nanocrystals, Nano Letters, 6 (2006) 1966–1972. DOI: 10.1021/nl061112c

Dalmaschio C.J., Leite E.R., Detachment induced by Rayleigh-instability in metal oxide nanorods: insights from TiO_2, Crystal Growth and Design, 12 (2012) 3668–3674. DOI: 10.1021/cg300473u

Deshmukh R., Niederberger M., Mechanistic aspects in the formation, growth and surface functionalization of metal oxide nanoparticles in organic solvents, Chemistry—A European Journal, 23 (2017) 8542–8570. DOI: 10.1002/chem.201605957

Devarepally K.K., Cox D.C., Fry A.T., Stolojan V., Curry R.J., Munz M., Synthesis of linear ZnO structures by a thermal decomposition method and their characterisation, Journal of Materials Science, 47 (2012) 1893–1901. DOI: 10.1007/s10853-011-5978-6

Djerdj I., Arčon D., Jagličić Z., Niederberger M., Nonaqueous synthesis of metal oxide nanoparticles: short review and doped titanium dioxide as case study for the preparation of transition metal-doped oxide nanoparticles, Journal of Solid State Chemistry, 181 (2008a) 1571–1581. DOI: 10.1016/j.jssc.2008.04.016

Djerdj I., Garnweitner G., Arčon D., Pregelj M., Jagličić Z., Niederberger M., Diluted magnetic semiconductors: Mn/Co-doped ZnO nanorods as case study, Journal of Materials Chemistry, 18 (2008b) 5208–5217. DOI: 10.1039/b808361d

Doxsee K.M., Chang R.C., Chen E., Myerson A.S., Huang D., Crystallization of solid-state materials in nonaqueous gels. 1. Silver Bromide, Journal of the American Chemical Society, 120 (1998) 585–586. DOI: 10.1021/ja9704343

Ellis B.L., Knauth P., Djenizian T., Three-dimensional self-supported metal oxides for advanced energy storage, Advanced Materials, 26 (2014) 3368–3397. DOI: 10.1002/adma.201306126

Fattakhova-Rohlfing D., Zaleska A., Bein T., Three-dimensional titanium dioxide nanomaterials, Chemical Reviews, 114 (2014) 9487–9558. DOI: 10.1021/cr500201c

Fleischmann S., Kamboj I., Augustyn V., Nanostructured transition metal oxides for electrochemical energy storage, in: Transition Metal Oxides for Electrochemical Energy Storage, Wiley-VCH, ISBN: 9783527344932, 2022, pp. 183–212. DOI: 10.1002/9783527817252.ch8

Garnweitner G., Antonietti M., Niederberger M., Nonaqueous synthesis of crystalline anatase nanoparticles in simple ketones and aldehydes as oxygen-supplying agents, Chemical Communications, 2005 (2005) 397–399. DOI: 10.1039/b414510k

Garnweitner G., Grote C., In situ investigation of molecular kinetics and particle formation of water-dispersible titania nanocrystals, Physical Chemistry Chemical Physics, 11 (2009) 3767–3774. DOI: 10.1039/b821973g

Garnweitner G., Tsedev N., Dierke H., Niederberger M., Benzylamines as versatile agents for the one-pot synthesis and highly ordered stacking of anatase nanoplatelets, European Journal of Inorganic Chemistry, 2008 (2008) 890–895. DOI: 10.1002/ejic.200700995

Gliech M., Görlin M., Gocyla M., Klingenhof M., Bergmann A., Selve S., Spöri C., Heggen M., Dunin-Borkowski R.E., Suntivich J., Strasser P., Solute incorporation at oxide–oxide interfaces explains how ternary mixed-metal oxide nanocrystals support element-specific anisotropic growth, Advanced Functional Materials, 30 (2020) 1909054. DOI: 10.1002/adfm.201909054

Görke M., Garnweitner G., Crystal engineering of nanomaterials: current insights and prospects, CrystEngComm, 23 (2021) 7916–7927. DOI: 10.1039/d1ce00601k

Grabs I.-M., Bradtmöller C., Menzel D., Garnweitner G., Formation mechanisms of iron oxide nanoparticles in different nonaqueous media, Crystal Growth and Design, 12 (2012) 1469–1475. DOI: 10.1021/cg201563h

Hofmann C., Rusakova I., Ould-Ely T., Prieto-Centurión D., Hartman K.B., Kelly A.T., Lüttge A., Whitmire K.H., Shape control of new Fe_xO-Fe_3O_4 and $Fe_{1-y}Mn_yO$-$Fe_{3-z}Mn_zO_4$ nanostructures, Advanced Functional Materials, 18 (2008) 1661–1667. DOI: 10.1002/adfm.200701119

Hudry D., Apostolidis C., Walter O., Gouder T., Courtois E., Kübel C., Meyer D., Non-aqueous synthesis of isotropic and anisotropic actinide oxide nanocrystals, Chemistry—A European Journal, 18 (2012) 8283–8287. DOI: 10.1002/chem.201200513

Jia H., Zheng Z., Zhao H., Zhang L., Zou Z., Nonaqueous sol-gel synthesis and growth mechanism of single crystalline TiO_2 nanorods with high photocatalytic activity, Materials Research Bulletin, 44 (2009) 1312–1316. DOI: 10.1016/j.materresbull.2008.12.016

Joo J., Kwon S.G., Yu J.H., Hyeon T., Synthesis of ZnO nanocrystals with cone, hexagonal cone, and rod shapes via non-hydrolytic ester elimination sol-gel reactions, Advanced Materials, 17 (2005a) 1873–1877. DOI: 10.1002/adma.200402109

Joo J., Kwon S.G., Yu T., Cho M., Lee J., Yoon J., Hyeon T., Large-scale synthesis of TiO_2 nanorods via nonhydrolytic sol-gel ester elimina-

tion reaction and their application to photocatalytic inactivation of E. coli, Journal of Physical Chemistry B, 109 (2005b) 15297–15302. DOI: 10.1021/jp052458z

Jun Y., Choi J., Cheon J., Shape control of semiconductor and metal oxide nanocrystals through nonhydrolytic colloidal routes, Angewandte Chemie International Edition, 45 (2006) 3414–3439. DOI: 10.1002/anie.200503821

Jun Y.W., Casula M.F., Sim J.H., Kim S.Y., Cheon J., Alivisatos A.P., Surfactant-assisted elimination of a high energy facet as a means of controlling the shapes of TiO_2 nanocrystals, Journal of the American Chemical Society, 125 (2003) 15981–15985. DOI: 10.1021/ja0369515

Kachynski A.V., Kuzmin A.N., Nyk M., Roy I., Prasad P.N., Zinc oxide nanocrystals for nonresonant nonlinear optical microscopy in biology and medicine, Journal of Physical Chemistry C, 112 (2008) 10721–10724. DOI: 10.1021/jp801684j

Khokhra R., Singh R.K., Kumar R., Effect of synthesis medium on aggregation tendencies of ZnO nanosheets and their superior photocatalytic performance, Journal of Materials Science, 50 (2015) 819–832. DOI: 10.1007/s10853-014-8642-0

Kim C.S., Moon B.K., Park J.H., Choi B.C., Seo H.J., Solvothermal synthesis of nanocrystalline TiO_2 in toluene with surfactant, Journal of Crystal Growth, 257 (2003) 309–315. DOI: 10.1016/S0022-0248(03)01468-4

Kim D.H., Min K.-M., Park K.-S., Park I.J., Cho I.S., Seong W.M., Kim D.-W., Hong K.S., Controlled synthesis and Li-electroactivity of rutile TiO_2 nanostructure with walnut-like morphology, Dalton Transactions, 42 (2013) 4278–4284. DOI: 10.1039/c2dt32251j

Kolodziejczak-Radzimska A., Jesionowski T., Zinc oxide-from synthesis to application: a review, Materials, 7 (2014) 2833–2881. DOI: 10.3390/ma7042833

Koo B., Park J., Kim Y., Choi S.H., Sung Y.E., Hyeon T., Simultaneous phase- and size-controlled synthesis of TiO_2 nanorods via non-hydrolytic sol-gel reaction of syringe pump delivered precursors, Journal of Physical Chemistry B, 110 (2006) 24318–24323. DOI: 10.1021/jp065372u

Kovalenko M.V., Bodnarchuk M.I., Lechner R.T., Hesser G., Schäffler F., Heiss W., Fatty acid salts as stabilizers in size- and shape-controlled nanocrystal synthesis: the case of inverse spinel iron oxide, Journal of the American Chemical Society, 129 (2007) 6352–6353. DOI: 10.1021/ja0692478

Koziej D., Fischer F., Kränzlin N., Caseri W.R., Niederberger M., Nonaqueous TiO_2 nanoparticle synthesis: a versatile basis for the fabrication of self-supporting, transparent, and UV-absorbing composite films, ACS Applied Materials and Interfaces, 1 (2009) 1097–1104. DOI: 10.1021/am9000584

Kunjara Na Ayudhya S., Tonto P., Mekasuwandumrong O., Pavarajarn V., Praserthdam P., Solvothermal synthesis of ZnO with various aspect ratios using organic solvents, Crystal Growth & Design, 6 (2006) 2446–2450. DOI: 10.1021/cg050345z

Kwon S.G., Piao Y., Park J., Angappane S., Jo Y., Hwang N.-M., Park J.-G., Hyeon T., Kinetics of monodisperse iron oxide nanocrystal formation by "heating-up" process, Journal of the American Chemical Society, 129 (2007) 12571–12584. DOI: 10.1021/ja074633q

Lee E.J.H., Ribeiro C., Longo E., Leite E.R., Oriented attachment: an effective mechanism in the formation of anisotropic nanocrystals, Journal of Physical Chemistry B, 109 (2005) 20842–20846. DOI: 10.1021/jp0532115

Lee K., Seo W.S., Park J.T., Synthesis and optical properties of colloidal tungsten oxide nanorods, Journal of the American Chemical Society, 125 (2003) 3408–3409. DOI: 10.1021/ja034011e

Leite E.R., Giraldi T.R., Pontes F.M., Longo E., Beltrán A., Andrés J., Crystal growth in colloidal tin oxide nanocrystals induced by coalescence at room temperature, Applied Physics Letters, 83 (2003) 1566–1568. DOI: 10.1063/1.1605241

Li X.L., Peng Q., Yi J.X., Wang X., Li Y., Near monodisperse TiO_2 nanoparticles and nanorods, Chemistry—A European Journal, 12 (2006) 2383–2391. DOI: 10.1002/chem.200500893

Liu G., Yang H.G., Pan J., Yang Y.Q., Lu G.Q.M., Cheng H.-M., Titanium dioxide crystals with tailored facets, Chemical Reviews, 114 (2014) 9559–9612. DOI: 10.1021/cr400621z

Liu J.F., Bei Y.Y., Wu H.P., Shen D., Gong J.Z., Li X.G., Wang Y.W., Jiang N.P., Jiang J.Z., Synthesis of relatively monodisperse ZnO nanocrystals from a precursor zinc 2,4-pentanedionate, Materials Letters, 61 (2007) 2837–2840. DOI: 10.1016/j.matlet.2007.03.028

Ludi B., Süess M.J., Werner I.A., Niederberger M., Mechanistic aspects of molecular formation and crystallization of zinc oxide nanoparticles in benzyl alcohol, Nanoscale, 4 (2012) 1982–1995. DOI: 10.1039/c1nr11557j

Manna L., Scher E.C., Alivisatos A.P., Synthesis of soluble and processable rod-, arrow-, teardrop-, and tetrapod-shaped CdSe nanocrystals, Journal of the American Chemical Society, 122 (2000) 12700–12706. DOI: 10.1021/ja003055+

Masthoff I.C., Gutsche A., Nirschl H., Garnweitner G., Oriented attachment of ultra-small $Mn_{(1-x)}ZnxFe_2O_4$ nanoparticles during the non-aqueous sol-gel synthesis, CrystEngComm, 17 (2015) 2464–2470. DOI: 10.1039/c4ce02068e

Masthoff I.C., Kraken M., Mauch D., Menzel D., Munevar J.A., Baggio Saitovitch E., Litterst F.J., Garnweitner G., Study of the growth process of magnetic nanoparticles obtained via the non-aqueous sol-gel method, Journal of Materials Science, 49 (2014) 4705–4714. DOI: 10.1007/s10853-014-8160-0

Mutin P.H., Vioux A., Nonhydrolytic processing of oxide-based materials: simple routes to control homogeneity, morphology, and nanostructure, Chemistry of Materials, 21 (2009) 582–596. DOI: 10.1021/cm802348c

Mutin P.H., Vioux A., Recent advances in the synthesis of inorganic materials via non-hydrolytic condensation and related low-temperature routes, Journal of Materials Chemistry A, 1 (2013) 11504–11512. DOI: 10.1039/c3ta12058a

Niederberger M., Bartl M.H., Stucky G.D., Benzyl alcohol and titanium tetrachloride-a versatile reaction system for the nonaqueous and low-temperature preparation of crystalline and luminescent titania nanoparticles, Chemistry of Materials, 14 (2002a) 4364–4370. DOI: 10.1021/cm021203k

Niederberger M., Bartl M.H., Stucky G.D., Benzyl alcohol and transition metal chlorides as a versatile reaction system for the nonaqueous and low-temperature synthesis of crystalline nano-objects with controlled dimensionality, Journal of the American Chemical Society, 124 (2002b) 13642–13643. DOI: 10.1021/ja027115i

Niederberger M., Garnweitner G., Organic reaction pathways in the nonaqueous synthesis of metal oxide nanoparticles, Chemistry—A European Journal, 12 (2006) 7282–7302. DOI: 10.1002/chem.200600313

Niederberger M., Pinna N., Metal Oxide Nanoparticles in Organic Solvents—Synthesis, Formation, Assembly and Application, Springer London, London, 2009, ISBN: 9781848826700. DOI: 10.1007/978-1-84882-671-7

Nikam A.V., Prasad B.L.V., Kulkarni A.A., Wet chemical synthesis of metal oxide nanoparticles: a review, CrystEngComm, 20 (2018) 5091–5107. DOI: 10.1039/C8CE00487K

Ohayon E., Gedanken A., The application of ultrasound radiation to the synthesis of nanocrystalline metal oxide in a non-aqueous solvent, Ultrasonics Sonochemistry, 17 (2010) 173–178. DOI: 10.1016/j.ultsonch.2009.05.015

Pacholski C., Kornowski A., Weller H., Self-assembly of ZnO: from nanodots to nanorods, Angewandte Chemie International Edition, 41 (2002) 1188–1191. DOI: 10.1002/1521-3773(20020402)41:7<1188::AID-ANIE1188>3.0.CO;2-5

Palchoudhury S., An W., Xu Y., Qin Y., Zhang Z., Chopra N., Holler R.A.,

Turner C.H., Bao Y., Synthesis and growth mechanism of iron oxide nanowhiskers, Nano Letters, 11 (2011a) 1141–1146. DOI: 10.1021/nl200136j

Palchoudhury S., Xu Y., Goodwin J., Bao Y., Synthesis of iron oxide nanoworms, Journal of Applied Physics, 109 (2011b) 07E314. DOI: 10.1063/1.3549600

Panchakarla L.S., Govindaraj A., Rao C.N.R., Formation of ZnO nanoparticles by the reaction of zinc metal with aliphatic alcohols, Journal of Cluster Science, 18 (2007) 660–670. DOI: 10.1007/s10876-007-0129-6

Parashar M., Shukla V.K., Singh R., Metal oxides nanoparticles via sol–gel method: a review on synthesis, characterization and applications, Journal of Materials Science: Materials in Electronics, 31 (2020) 3729–3749. DOI: 10.1007/s10854-020-02994-8

Park J., An K., Hwang Y., Park J.-G., Noh H.-J., Kim J.-Y., Park J.-H., Hwang N.-M., Hyeon T., Ultra-large-scale syntheses of monodisperse nanocrystals, Nature Materials, 3 (2004a) 891–895. DOI: 10.1038/nmat1251

Park J., Kang E., Bae C.J., Park J.-G., Noh H.-J., Kim J.-Y., Park J.-H., Park H.M., Hyeon T., Synthesis, characterization, and magnetic properties of uniform-sized MnO nanospheres and nanorods, Journal of Physical Chemistry B, 108 (2004b) 13594–13598. DOI: 10.1021/jp048229e

Patzke G.R., Krumeich F., Nesper R., Oxidic nanotubes and nanorods—anisotropic modules for a future nanotechnology, Angewandte Chemie International Edition, 41 (2002) 2446–2461. DOI: 10.1002/1521-3773(20020715)41:14<2446::AID-ANIE2446>3.0.CO;2-K.

Peng Z.A., Peng X., Nearly monodisperse and shape-controlled CdSe nanocrystals via alternative routes: nucleation and growth, Journal of the American Chemical Society, 124 (2002) 3343–3353. DOI: 10.1021/ja0173167

Pinna N., Garnweitner G., Beato P., Niederberger M., Antonietti M., Synthesis of yttria-based crystalline and lamellar nanostructures and their formation mechanism, Small, 1 (2005) 112–121. DOI: 10.1002/smll.200400014

Pinna N., Karmaoui M., Willinger M.-G., The “benzyl alcohol route”: an elegant approach towards doped and multimetal oxide nanocrystals: Short review and $ZnAl_2O_4$ nanostructures by oriented attachment, Journal of Sol-Gel Science and Technology, 57 (2011) 323–329. DOI: 10.1007/s10971-009-2111-2

Pinna N., Niederberger M., Surfactant-free nonaqueous synthesis of metal oxide nanostructures, Angewandte Chemie International Edition, 47 (2008) 5292–5304. DOI: 10.1002/anie.200704541

Polleux J., Gurlo A., Barsan N., Weimar U., Antonietti M., Niederberger M., Template-free synthesis and assembly of single-crystalline tungsten oxide nanowires and their gas-sensing properties, Angewandte Chemie International Edition, 45 (2006) 261–265. DOI: 10.1002/anie.200502823

Polleux J., Pinna N., Antonietti M., Niederberger M., Growth and assembly of crystalline tungsten oxide nanostructures assisted by bioligation, Journal of the American Chemical Society, 127 (2005) 15595–15601. DOI: 10.1021/ja0544915

Pucci A., Willinger M.-G., Liu F., Zeng X., Rebuttini V., Clavel G., Bai X., Ungar G., Pinna N., One-step synthesis and self-assembly of metal oxide nanoparticles into 3D superlattices, ACS Nano, 6 (2012) 4382–4391. DOI: 10.1021/nn3010735

Qamar M., Adam A., Azad A.-M., Kim Y.-W., Benzyl alcohol-mediated versatile method to fabricate nonstoichiometric metal oxide nanostructures, ACS Applied Materials and Interfaces, 9 (2017) 40573–40579. DOI: 10.1021/acsami.7b09515

Rai P., Kwak W.K., Yu Y.T., Solvothermal synthesis of ZnO nanostructures and their morphology-dependent gas-sensing properties, ACS Applied Materials and Interfaces, 5 (2013) 3026–3032. DOI: 10.1021/am302811h

Ramya M., Nideep T.K., Nampoori V.P.N., Kailasnath M., Understanding the role of alcohols in the growth behaviour of ZnO nanostructures prepared by solution based synthesis and their application in solar cells, New Journal of Chemistry, 43 (2019) 17980–17990. DOI: 10.1039/c9nj03212f

Redl F.X., Black C.T., Papaefthymiou G.C., Sandstrom R.L., Yin M., Zeng H., Murray C.B., O’Brien S.P., Magnetic, electronic, and structural characterization of nonstoichiometric iron oxides at the nanoscale, Journal of the American Chemical Society, 126 (2004) 14583–14599. DOI: 10.1021/ja046808r

Ribeiro C., Lee E.J.H., Longo E., Leite E.R., A Kinetic model to describe nanocrystal growth by the oriented attachment mechanism, ChemPhysChem, 6 (2005) 690–696. DOI: 10.1002/cphc.200400505

Ribeiro C., Lee E.J.H., Longo E., Leite E.R., Oriented attachment mechanism in anisotropic nanocrystals: a “polymerization” approach, ChemPhysChem, 7 (2006) 664–670. DOI: 10.1002/cphc.200500508

Sajanlal P.R., Sreeprasad T.S., Samal A.K., Pradeep T., Anisotropic nanomaterials: structure, growth, assembly, and functions, Nano Reviews, 2 (2011) 5883. DOI: 10.3402/nano.v2i0.5883

Šarić A., Despotović I., Štefanić G., Alcoholic solvent influence on ZnO synthesis: a joint experimental and theoretical study, Journal of Physical Chemistry C, 123 (2019) 29394–29407. DOI: 10.1021/acs.jpcc.9b07411

Satapathy S., Ahlawat A., Paliwal A., Singh R., Singh M.K., Gupta P.K., Effect of calcination temperature on nanoparticle morphology and its consequence on optical properties of $Nd:Y_2O_3$ transparent ceramics, CrystEngComm, 16 (2014) 2723–2731. DOI: 10.1039/c3ce42529k

Shavel A., Rodríguez-González B., Pacifico J., Spasova M., Farle M., Liz-Marzán L.M., Shape control in iron oxide nanocrystal synthesis, induced by trioctylammonium ions, Chemistry of Materials, 21 (2009) 1326–1332. DOI: 10.1021/cm803201p

Siddiqui M.R.H., Al-Wassil A.I., Al-Otaibi A.M., Mahfouz R.M., Effects of precursor on the morphology and size of ZrO_2 nanoparticles, synthesized by sol-gel method in non-aqueous medium, Materials Research, 15 (2012) 986–989. DOI: 10.1590/S1516-14392012005000128

Stolzenburg P., Freytag A., Bigall N.C., Garnweitner G., Fractal growth of ZrO_2 nanoparticles induced by synthesis conditions, CrystEngComm, 18 (2016) 8396–8405. DOI: 10.1039/c6ce01916a

Styskalik A., Skoda D., Barnes C.E., Pinkas J., The power of non-hydrolytic sol-gel chemistry: a review, Catalysts, 7 (2017) 168. DOI: 10.3390/catal7060168

Su H., Jaffer S., Yu H., Transition metal oxides for sodium-ion batteries, Energy Storage Materials, 5 (2016) 116–131. DOI: 10.1016/j.ensm.2016.06.005

Teja A.S., Koh P.-Y., Synthesis, properties, and applications of magnetic iron oxide nanoparticles, Progress in Crystal Growth and Characterization of Materials, 55 (2009) 22–45. DOI: 10.1016/j.pcrysgrow.2008.08.003

Tonto P., Mekasuwandumrong O., Phatanasri S., Pavarajarn V., Praserthdam P., Preparation of ZnO nanorod by solvothermal reaction of zinc acetate in various alcohols, Ceramics International, 34 (2008) 57–62. DOI: 10.1016/j.ceramint.2006.08.003

Ungerer J., Thurm A.-K., Garnweitner G., Nirschl H., Formation of aluminum-doped zinc oxide nanocrystals via the benzylamine route at low reaction kinetics, Chemical Engineering and Technology, 43 (2020) 797–803. DOI: 10.1002/ceat.201900466

Ungerer J., Thurm A.-K., Meier M., Klinge M., Garnweitner G., Nirschl H., Development of a growth model for aluminum-doped zinc oxide nanocrystal synthesis via the benzylamine route, Journal of Nanoparticle Research, 21 (2019) 106. DOI: 10.1007/s11051-019-4547-9

Védrine J.C., Heterogeneous catalysis on metal oxides, Catalysts, 7 (2017) 341. DOI: 10.3390/catal7110341

Venkatesan A., Krishna Chandar N.R., Kandasamy A., Karl Chinnu M., Marimuthu K.N., Mohan Kumar R., Jayavel R., Luminescence and electrochemical properties of rare earth (Gd, Nd) doped V_2O_5 nano-

structures synthesized by a non-aqueous sol-gel route, RSC Advances, 5 (2015) 21778–21785. DOI: 10.1039/c4ra14542a

Voigt M., Klaumünzer M., Thiem H., Peukert W., Detailed analysis of the growth kinetics of ZnO nanorods in methanol, Journal of Physical Chemistry C, 114 (2010) 6243–6249. DOI: 10.1021/jp911258d

Wang C., Deng Z.X., Li Y., The synthesis of nanocrystalline anatase and rutile titania in mixed organic media, Inorganic Chemistry, 40 (2001) 5210–5214. DOI: 10.1021/ic0101679

Wang C., Deng Z., Zhang G., Fan S., Li Y., Synthesis of nanocrystalline TiO_2 in alcohols, Powder Technology, 125 (2002) 39–44. DOI: 10.1016/S0032-5910(01)00523-X

Wang C., Shen E., Wang E., Gao L., Kang Z., Tian C., Lan Y., Zhang C., Controllable synthesis of ZnO nanocrystals via a surfactant-assisted alcohol thermal process at a low temperature, Materials Letters, 59 (2005) 2867–2871. DOI: 10.1016/j.matlet.2005.04.031

Wang H., Xin L., Wang Hai, Yu X., Liu Y., Zhou X., Li B., Aggregation-induced growth of hexagonal ZnO hierarchical mesocrystals with interior space: nonaqueous synthesis, growth mechanism, and optical properties, RSC Advances, 3 (2013) 6538–6544. DOI: 10.1039/c3ra23010d

Woo K., Hong J., Ahn J.-P., Park J.-K., Kim K.-J., Coordinatively induced length control and photoluminescence of $W_{18}O_{49}$ nanorods, Inorganic Chemistry, 44 (2005) 7171–7174. DOI: 10.1021/ic0504644

Wu B., Guo C., Zheng N., Xie Z., Stucky G.D., Nonaqueous production of nanostructured anatase with high-energy facets, Journal of the American Chemical Society, 130 (2008) 17563–17567. DOI: 10.1021/ja8069715

Wu Y., Liu H.-M., Xu B.-Q., Solvothermal synthesis of TiO_2: anatase nanocrystals and rutile nanofibres from $TiCl_4$ in acetone, Applied Organometallic Chemistry, 21 (2007a) 146–149. DOI: 10.1002/aoc.1184

Wu Y., Liu H.-M., Xu B.-Q., Zhang Z.-L., Su D.-S., Single-phase titania nanocrystallites and nanofibers from titanium tetrachloride in acetone and other ketones, Inorganic Chemistry, 46 (2007b) 5093–5099. DOI: 10.1021/ic070199h

Xu L., Hu Y.-L., Pelligra C., Chen C.-H., Jin L., Huang H., Sithambaram S., Aindow M., Joesten R., Suib S.L., ZnO with different morphologies synthesized by solvothermal methods for enhanced photocatalytic activity, Chemistry of Materials, 21 (2009) 2875–2885. DOI: 10.1021/cm900608d

Xue X., Penn R.L., Leite E.R., Huang F., Lin Z., Crystal growth by oriented attachment: kinetic models and control factors, CrystEngComm, 16 (2014) 1419–1429. DOI: 10.1039/c3ce42129e

Yang Y., Yao Y., He L., Zhong Y., Ma Y., Yao J., Nonaqueous synthesis of TiO_2-carbon hybrid nanomaterials with enhanced stable photocatalytic hydrogen production activity, Journal of Materials Chemistry A, 3 (2015) 10060–10068. DOI: 10.1039/c5ta00638d

Yin M., Gu Y., Kuskovsky I.L., Andelman T., Zhu Y., Neumark G.F., O'Brien S., Zinc oxide quantum rods, Journal of the American Chemical Society, 126 (2004) 6206–6207. DOI: 10.1021/ja031696+

Yu H.X., Guo C.Y., Zhang X.F., Xu Y.M., Cheng X.L., Gao S., Huo L.H., Recent development of hierarchical metal oxides based gas sensors: from gas sensing performance to applications, Advanced Sustainable Systems, 6 (2022) 2100370. DOI: 10.1002/adsu.202100370

Yu X., Marks T.J., Facchetti A., Metal oxides for optoelectronic applications, Nature Materials, 15 (2016) 383–396. DOI: 10.1038/nmat4599

Yuhas B.D., Zitoun D.O., Pauzauskie P.J., He R., Yang P., Transition-metal doped zinc oxide nanowires, Angewandte Chemie International Edition, 45 (2006) 420–423. DOI: 10.1002/anie.200503172

Zellmer S., Kockmann A., Dosch I., Temel B., Garnweitner G., Aluminum zinc oxide nanostructures with customized size and shape by non-aqueous synthesis, CrystEngComm, 17 (2015) 6878–6883. DOI: 10.1039/c5ce00629e

Zhang L., Dou Y.-H., Gu H.-C., Sterically induced shape control of magnetite nanoparticles, Journal of Crystal Growth, 296 (2006) 221–226. DOI: 10.1016/j.jcrysgro.2006.08.010

Zhang W.-D., Xiao H.-M., Zhu L.-P., Fu S.-Y., Template-free solvothermal synthesis and magnetic properties of novel single-crystalline magnetite nanoplates, Journal of Alloys and Compounds, 477 (2009) 736–738. DOI: 10.1016/j.jallcom.2008.10.105

Zhang Y.-L., Li X.-F., Containing manganese DMSs nanostructures via a nonaqueous route, Advanced Materials Research, 79–82 (2009) 533–536. DOI: 10.4028/www.scientific.net/AMR.79-82.533

Zhang Y., Nayak T.R., Hong H., Cai W., Biomedical applications of zinc oxide nanomaterials, Current Molecular Medicine, 13 (2013) 1633–1645. DOI: 10.2174/15665240136661311111300058

Zhang Z., Liu S., Chow S., Han M.Y., Modulation of the morphology of ZnO nanostructures via aminolytic reaction: from nanorods to nanosquamas, Langmuir, 22 (2006) 6335–6340. DOI: 10.1021/la060351c

Zhang Z., Lu M., Xu H., Chin W.S., Shape-controlled synthesis of zinc oxide: a simple method for the preparation of metal oxide nanocrystals in non-aqueous medium, Chemistry—A European Journal, 13 (2007) 632–638. DOI: 10.1002/chem.200600293

Zhang Z., Zhong X., Liu S., Li D., Han M., Aminolysis route to monodisperse titania nanorods with tunable aspect ratio, Angewandte Chemie, 117 (2005) 3532–3536. DOI: 10.1002/ange.200500410

Zhao Z.-G., Miyauchi M., Nanoporous-walled tungsten oxide nanotubes as highly active visible-light-driven photocatalysts, Angewandte Chemie International Edition, 47 (2008) 7051–7055. DOI: 10.1002/anie.200802207

Zhao Z.G., Miyauchi M., Shape modulation of tungstic acid and tungsten oxide hollow structures, Journal of Physical Chemistry C, 113 (2009) 6539–6546. DOI: 10.1021/jp900160u

Zhao Z., Wang Y., Delmas C., Mingotaud C., Marty J.D., Kahn M.L., Mechanistic insights into the anisotropic growth of ZnO nanoparticles deciphered through 2D size plots and multivariate analysis, Nanoscale Advances, 3 (2021) 6696–6703. DOI: 10.1039/d1na00591j

Zhong X., Feng Y., Zhang Y., Lieberwirth I., Knoll W., Nonhydrolytic alcoholysis route to morphology-controlled ZnO nanocrystals, Small, 3 (2007) 1194–1199. DOI: 10.1002/smll.200600684

Zhong X., Knoll W., Morphology-controlled large-scale synthesis of ZnO nanocrystals from bulk ZnO, Chemical Communications, (2005) 1158–1160. DOI: 10.1039/b414948c

Zhong X., Xie R., Sun L., Lieberwirth I., Knoll W., Synthesis of dumbbell-shaped manganese oxide nanocrystals, The Journal of Physical Chemistry B, 110 (2006) 2–4. DOI: 10.1021/jp056064j

Zhou Z., Zhu X., Wu D., Chen Q., Huang D., Sun C., Xin J., Ni K., Gao J., Anisotropic shaped iron oxide nanostructures: controlled synthesis and proton relaxation shortening effects, Chemistry of Materials, 27 (2015) 3505–3515. DOI: 10.1021/acs.chemmater.5b00944

Zitoun D., Pinna N., Frolet N., Belin C., Single crystal manganese oxide multipods by oriented attachment, Journal of the American Chemical Society, 127 (2005) 15034–15035. DOI: 10.1021/ja0555926

Authors' Short Biographies



Sherif Okeil

Sherif Okeil is currently working as a competence team leader for nanomaterial synthesis in Georg Garnweitner's group at the Institute for Particle Technology, Technical University of Braunschweig. He received his bachelor's degree in Pharmacy at Ain Shams University in Cairo, Egypt in 2009. In 2013, he obtained his masters in Pharmaceutical Analytical Chemistry from the same university. In 2014, he was awarded a scholarship from the German Academic Exchange Service (DAAD) through which he obtained his Ph.D. in Inorganic Chemistry at the Technical University of Darmstadt in 2020. His current research interests are inorganic nanomaterial synthesis and their electronic applications.



Julian Ungerer

Julian Ungerer obtained his bachelor's degree in applied mechanics in 2013 and his master's degree in the process engineering machines group of Prof. Dr.-Ing Hermann Nirschl at the Karlsruhe Institute of Technology in 2016, where he also continued his academic research in the field of functional nanomaterials for renewable energy systems before receiving his Ph.D. in 2022.



Hermann Nirschl

Hermann Nirschl received his Ph.D. in Fluid Mechanics from the Technical University of Munich in 1994. For his habilitation in 1997 he worked on the numerical simulation of the particle-laden flows. He entered the 3M company in the dental division as the head of process engineering in the years between 1997 and 2002 where he worked as a project manager for different projects in Munich and St. Paul/Minnesota. Since 2003 he is Professor for Mechanical Process Engineering at the KIT in Karlsruhe. The focus of the research is on particle technology with a special emphasis on separation processes, numerical simulations and the development of particle analysis technologies.



Georg Garnweitner

Georg Garnweitner received a Diploma in Technical Chemistry at Vienna University of Technology, Austria, in 2003 and then moved to the Max Planck Institute of Colloids and Interfaces, Potsdam, Germany, where he obtained his Ph.D. in Colloids Chemistry in 2005. He was appointed as Professor at Technische Universität Braunschweig, Germany, in 2007. His research is centered on the synthesis of inorganic nanoparticles and hybrid materials, in particular via nonaqueous approaches. In addition, the surface modification and functionalization of nanomaterials are studied in his group, targeting diverse application fields such as solid-state and lithium-sulfur batteries, lightweight composites and drug delivery.

KONA Powder and Particle Journal

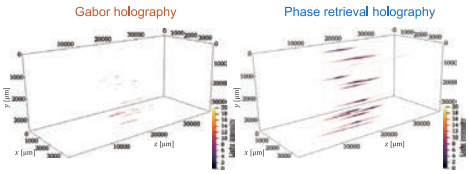
KONA Powder and Particle Journal No. 41 (2024) 221–228/https://doi.org/10.14356/kona.2024002 Original Research Paper

Particle Size Measurement Using a Phase Retrieval Holography System with a GPU-Equipped SBC†

Yohsuke Tanaka[1]* and Dai Nakai[2]

[1] *Faculty of Mechanical Engineering, Kyoto Institute of Technology, Japan*
[2] *Graduate School of Mechanical Engineering, Kyoto Institute of Technology, Japan*

We have developed a phase retrieval holography system using a single-board computer (SBC) with a graphics processing unit (GPU) for particle size measurement. The system comprises two cameras connected to the SBC with a GPU (Jetson Nano™, NVIDIA®), a diode-pumped solid-state green laser, and a beam splitter. The GPU enables us to reconstruct holograms in real-time and measure particle size. The system can record the shapes and positions of particles falling in a static flow in a three-dimensional volume as two holograms generating an interference pattern. Two holograms solve the twin image problem that arises because of the lack of phase information using phase retrieval holography. We also present the requirement of this system for experimentally recording and numerically reconstructing holograms of particles. Finally, we compare the particle size distribution obtained by the system to that of conventional two-dimensional image measurement.



Keywords: particle size measurement, phase retrieval holography, single-board computer, graphics processing unit

1. Introduction

Digital transformation (Stolterman and Fors, 2004) has changed society as a whole, as evidenced by the spread of telework and other online activities due to the COVID-19 pandemic. The use of Internet of Things (IoT) (Mattern and Floerkemeier, 2010) has also been advancing. In particular, Malik et al. (2021) reported that the use of Industrial IoT in industry has brought significant improvements and profitability in process visualization using the Raspberry Pi, an inexpensive single-board computers (SBC). In powder production, big data aggregated from each process are used for trouble detection, quality control, and determination of production conditions through artificial intelligence technology (Fujita et al., 2020).

As the processing speed of computers has improved, the amount of information obtained by optical measurement, which is used in powder production, has increased from point measurement with phase Doppler anemometry (Durst et al., 1981) to image measurement (Lichti and Bart, 2018). In addition, holography, invented by Gabor (1948), has been used for measuring particles in three-dimensional space. Gabor holography can be realized easily with a light source and a complementary metal oxide semiconductor (CMOS) camera and is insensitive to vibration because the reference and object waves are on the same optical axis.

Gabor holography is a three-dimensional microparticle measurement with a deep focal depth, involving size (Nayak et al., 2021), position (Memmolo et al., 2015), and velocity (Katz and Sheng, 2010). However, only the light intensity of the complex amplitude is recorded by the camera, which causes the twin image problem that degrades the contrast of reconstructed particles (Latychevskaia and Fink, 2007). To solve this problem, phase retrieval holography using two or more cameras has been proposed (Liu and Scott, 1987; Zhang et al., 2003). The present authors have used this method to measure microparticles (Tanaka et al., 2016), microbubbles (Kubonishi et al., 2018), and microdroplets (Nakatani et al., 2019; Tanaka et al., 2019b). However, practical usage of Gabor holography and phase retrieval holography is limited by the huge execution time for volumetric reconstruction.

Parallel processing by a graphics processing unit (GPU) accelerates holography processing (Tian et al., 2010) to be much faster than that by a central processing unit (CPU). In particle measurements, the CPU to GPU execution time ratio has been shown to be higher than 100 times (Tanaka et al., 2019a). Since 2014, NVIDIA® has released GPU-equipped SBCs for AI and IoT applications, and in 2019 it released the Jetson Nano™ as an inexpensive SBC.

This paper proposes particle size measurement using a phase retrieval holography system with a GPU-equipped SBC with theoretical and fabrication considerations. We also confirm the effectiveness of the system by comparing particle size distributions measured by it and conventional two-dimensional image measurement.

† Received 20 August 2022; Accepted 19 October 2022
J-STAGE Advance published online 28 January 2023
* Corresponding author: Yohsuke Tanaka;
Add: Matsugasaki, Sakyo-ku, Kyoto 606-8585, Japan
E-mail: tyohsuke@kit.ac.jp
TEL: +81-75-724-7355 FAX: +81-75-724-7355

Copyright © 2024 The Authors. Published by Hosokawa Powder Technology Foundation. This is an open access article under the CC BY license (https://creativecommons.org/licenses/by/4.0/).

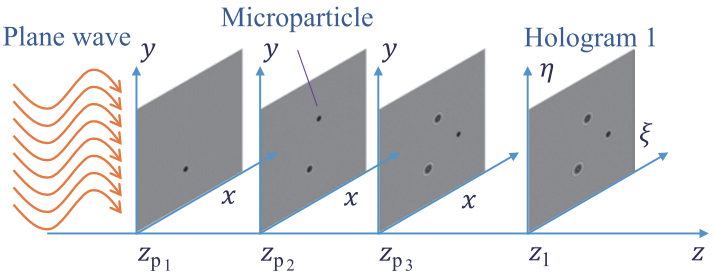


Fig. 1 Recording hologram in particle measurement.

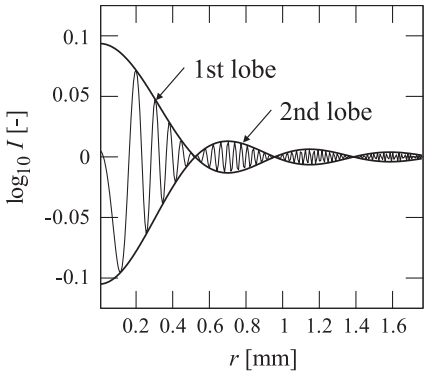


Fig. 2 Hologram intensity of a particle from **Eqn. (3)** for z_p = 50 mm, d_p = 62 μm, and λ = 532 nm.

2. Recording and reconstruction of holograms in particle measurement

First, we focus on the principles of recording and reconstructing particles in three-dimensional space using Gabor holography. In particular, we discuss hologram recording conditions, the twin image problem, and particle elongation in the optical direction. Moreover, we explain the principle of phase retrieval holography used in the proposed system to suppress the twin image problem.

2.1 Recording holograms using Gabor holography

We consider the case in which particles illuminated by a plane wave of wavelength λ as shown in **Fig. 1**. The complex amplitude Ψ_z at a distance z is formulated as

$$\Psi_z = \frac{\exp\left(\mathrm{j}\frac{2\pi z}{\lambda}\right)}{\mathrm{j}\lambda z}\iint_{-\infty}^{\infty}(1-b_i)\exp\left\{\mathrm{j}\frac{\pi}{\lambda z}\left[(x-\xi)^2 + (y-\eta)^2\right]\right\}\mathrm{d}x\mathrm{d}y \tag{1}$$

where $\mathrm{j}^2 = -1$ is the imaginary unit. The diffracting aperture b_i for the ith particle is defined as the transmittance function, namely,

$$b_i\left(x_{pi}, y_{pi}, z_{pi}\right) = \begin{cases} 1\left(\sqrt{(x-x_{pi})^2+(y-y_{pi})^2} \le d_p/2\right) \\ 0\left(\sqrt{(x-x_{pi})^2+(y-y_{pi})^2} > d_p/2\right) \end{cases} \tag{2}$$

where d_p is the diameter of the particle, x_{pi} and y_{pi} are its center position.

Because this aperture has circular symmetry, the intensity distribution is derived by performing the integration

$$I_{z_{pi}} = 1 - \frac{\pi {d_p}^2}{\lambda z_{pi}}\sin\left(\frac{\pi r^2}{\lambda z_{pi}}\right)\frac{J_1\left(\frac{\pi d_p r}{\lambda z_{pi}}\right)}{\frac{\pi d_p r}{\lambda z_{pi}}} + \left(\frac{\pi {d_p}^2}{4\lambda z_{pi}}\right)^2\left[\frac{2J_1\left(\frac{\pi d_p r}{\lambda z_{pi}}\right)}{\frac{\pi d_p r}{\lambda z_{pi}}}\right]^2 \tag{3}$$

where J_1 represents the first-order Bessel function. The particle information is contained mostly in the first lobe (Vikram, 1992) as shown in **Fig. 2**. The recording distance of a particle is limited to the range in which the lobe can be resolved, that is,

$$\frac{{d_p}^2}{\lambda} < z_1 < \frac{d_p W/2}{1.22\lambda} \tag{4}$$

where $W/2$ is the half width of the CMOS elements. Additionally, the pixel pitch Δx of the elements is also limited by the relation,

$$\Delta x < \frac{d_p}{2.44} \tag{5}$$

2.2 Reconstruction of holograms using Gabor holography

We reconstruct holograms explained in **sec. 2.1** by introducing the convolution kernel defined as (Onural and Scott, 1987)

$$h_z = \frac{1}{\lambda z}\exp\left[\mathrm{j}\frac{2\pi}{\lambda z}(x^2+y^2)\right] \tag{6}$$

Eqn. (1) can be expressed compactly using the two-dimensional convolution ** as

$$\Psi_{z_i} = \exp\left(\mathrm{j}\frac{2\pi}{\lambda}z_i\right)[1-b_i] ** h_{z_i} \tag{7}$$

The hologram intensity is recorded on a hologram as

$$I_{z_i} = \left|\Psi_{z_i}\right| \approx 1 - b_i^{*}{**}h^{*}{}_{z_i} - b_i{**}h_{z_i} \tag{8}$$

where a superscript * denotes complex conjugate, and the complex amplitude of particles are reconstructed as

$$\Psi_{z_{pi}} = I_{z_i}{**}h_{-z_{pi}} = 1 - b_i^{*}{**}h_{-2z_{pi}} - b_i{**}h_{z_{pi}} \tag{9}$$

The second and third terms on the right-hand side of **Eqn. (9)** lead to the virtual and real particle images. The virtual particle image causes the out-of-focus particle, as shown in the intensity line profile of **Fig. 3**. This is known as the twin image problem (Latychevskaia and Fink, 2007) due to the loss of phase information when the complex amplitude of the hologram is recorded by the CMOS camera.

2.3 Suppression of twin image problem using phase retrieval holography

We use phase retrieval holography, which requires two holograms separated by a distance Δz to obtain the phase information as shown in **Fig. 4** (Liu and Scott, 1987; Zhang et al., 2003). This iterative phase retrieval algorithm is based on the Gerchberg–Saxton algorithm (Gerchberg and Saxton, 1972) using two holograms as intensity constraint conditions. The distance Δz between the two holograms with good convergence of the iterative process is given by Tanaka et al. (2016)

$$\Delta z = \frac{z_1}{m} \quad (m = 1, 2, \ldots,\ m \in \mathbb{N}) \tag{10}$$

This method has an iterative process with four steps as shown in **Fig. 5(a)**.

Step 1. Reconstruct the complex amplitude of the first hologram to the second hologram with the distance:

$$\Psi_{z_{2k}} = \exp(\mathrm{j}\Delta z)\Psi_{z_{1k}}{**}h_{\Delta z} = \left|\Psi_{z_{2k}}\right|\exp(\mathrm{j}\phi_2) \tag{11}$$

Step 2. Replace the absolute value of $\left|\Psi_{z_{2k}}\right|$ with $\sqrt{I_2}$:

$$\Psi_{z_{2k}} = \sqrt{I_2}\,\exp(\mathrm{j}\phi_2) \tag{12}$$

Step 3. Back-reconstruct the amplitude of step 2 to the first hologram:

$$\Psi_{z_{1k}} = \exp(\mathrm{j}\Delta z)\Psi_{z_{2k}}{**}h_{-\Delta z} = \left|\Psi_{z_{1k}}\right|\exp(\mathrm{j}\phi_2) \tag{13}$$

Step 4. Replace the absolute value of $\left|\Psi_{z_{1k}}\right|$ with $\sqrt{I_1}$:

$$\Psi_{z_{1k}} = \sqrt{I_1}\,\exp(\mathrm{j}\phi_1) \tag{14}$$

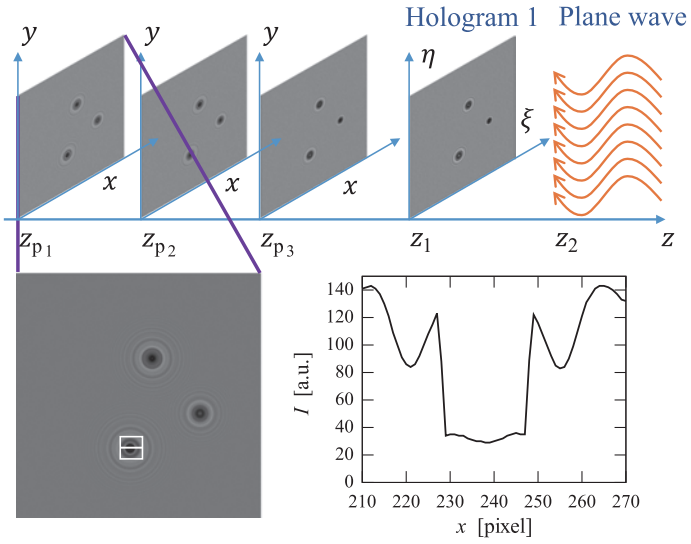


Fig. 3 Reconstruction of a hologram in particle measurement.

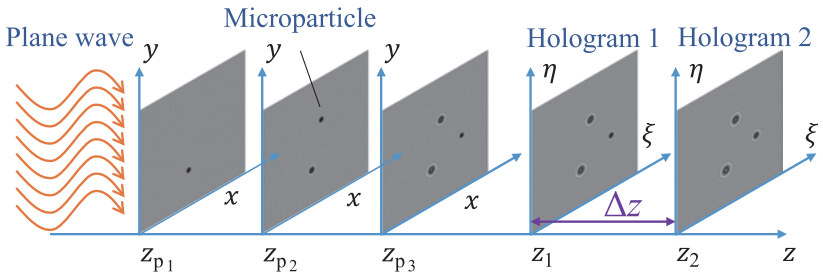


Fig. 4 Phase retrieval holography using two holograms.

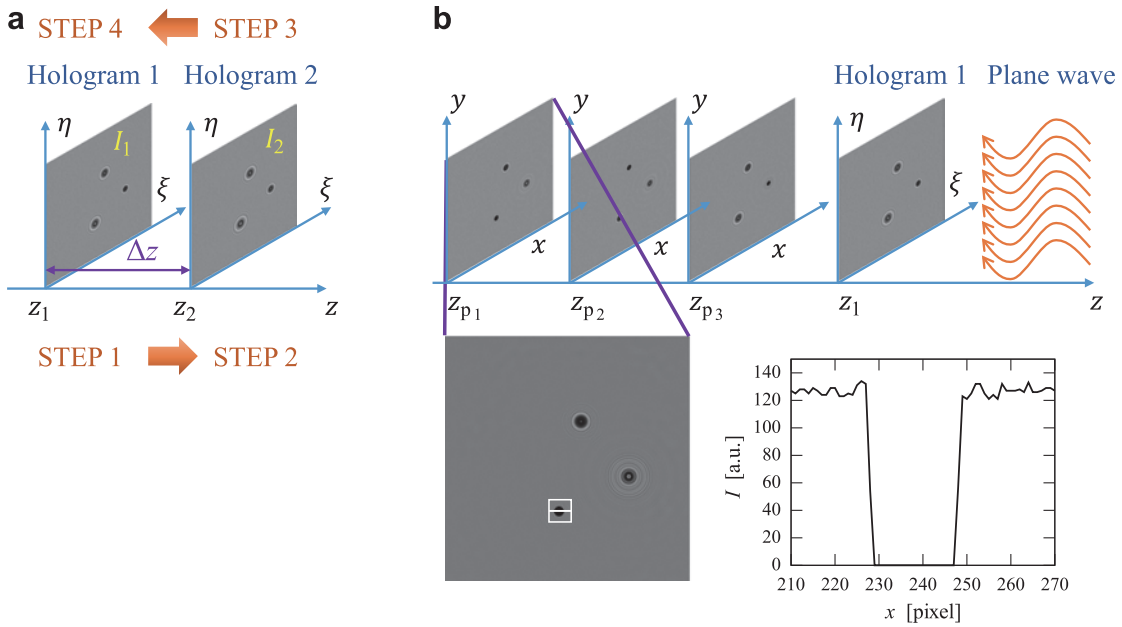


Fig. 5 Phase retrieval holography: **(a)** iterative process and **(b)** reconstruction of a hologram with retrieved phase information.

where ϕ_1 and ϕ_2 are the retrieved phases at the first and second hologram, respectively. The iterative loop exits when the mode of the reconstructed image at z_{p3} becomes the maximum value (Tanaka et al., 2016). The virtual particle image has been removed by phase retrieval holography, as shown in the intensity line profile of **Fig. 5(b)** compared with **Fig. 3**.

2.4 Particle elongation in the optical axis direction

In addition to the twin image problem, another problem is that the reconstructed particle is elongated in the optical axis direction. To understand this problem, the complex amplitude reconstructed from the hologram formed by one particle at $(x_p, y_p) = (0,0)$ on the z axis can be considered as a circular aperture on a screen (Yang et al., 2006), that is,

$$\psi_{za}(0,0,z) \approx 1 - \exp(j\phi) \tag{15}$$

where ϕ is $\pi r_p^2/(\lambda z)$. On the other hand, the amplitude ψ_{zo} of an opaque disk is derived by using Babinet's principle ($\psi_{za} + \psi_{zo} = 0$) (Born et al., 1970) as

$$\psi_{zo}(0,0,z) \approx (1+\cos\phi) - j\sin(\phi) \tag{16}$$

whereupon we obtain the intensity as

$$I_z = |\psi_{zo}| \approx \left[1+\cos\left(\frac{\pi r_p^2}{\lambda z}\right)\right]^2 + \sin^2\left(\frac{\pi r_p^2}{\lambda z}\right) \tag{17}$$

Fig. 6 shows that the intensity oscillates, with the frequency increasing toward the position of the particle. In practice, the oscillations are limited owing to the finite sensor size, as shown in the numerical plots in **Fig. 6**.

Particle elongation is defined by a zero-valued position that oscillates symmetrically about $z = 0$ in the following equation (Nakatani et al., 2019):

$$\Delta L = \frac{d_p^2}{2(2n-1)\lambda'} (n = 1,2,\cdots, n \in N) \tag{18}$$

Particle elongation can be expressed as $d_p^2/(6\lambda)$ by substituting $n = 2$ into **Eqn. (18)** under the conditions of **Fig. 2**. Furthermore, taking this elongation into account, the recording range of **Eqn. (4)** can be extended as

$$\frac{d_p^2}{6\lambda} < z_1 < \frac{d_p W/2}{1.22\lambda} \tag{19}$$

3. Holographic particle size measurement system using a GPU-equipped single-board computer

In this section, we illustrate the details of the holographic particle size measurement system using a GPU-equipped SBC (Jetson Nano, NVIDIA). **Fig. 7** shows the optical setup for the phase retrieval holography system with two holograms. The laser beam (532 nm, 5 mW, Edmund®) is magnified using an objective lens (40/0.65) and converted to a collimated beam using a beam expander (TS Scorpii®, 8×, Edmund). After passing through the measurement volume (6.9 mm × 6.9 mm × 40 mm) where the particles (SP20SS, Mitsubishi Chemical Corporation) fall at their terminal velocity, the collimated light is split by a beam splitter and recorded by two CMOS cameras (BFS-U3-31S4C-BD2, FLIR, processing rates: 0.4 fps (Gabor holography) and 0.5 fps (phase retrieval holography), shutter speed: 200 µs, image size: 512 pixels × 512 pixels, cell pitch: 3.45 µm) fitted with telecentric lenses (VS-TCT05-65/S, 0.5×, WD: 65.7 mm, VS Technology®). Two cameras

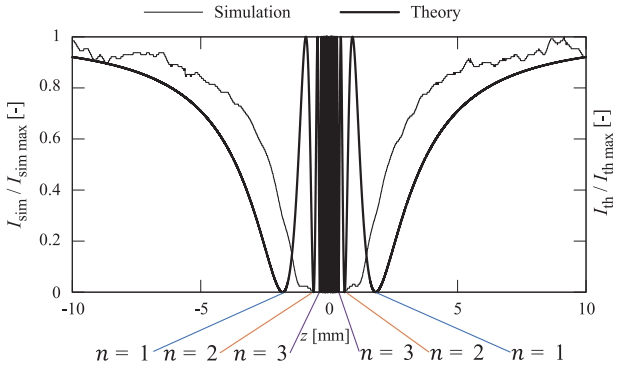


Fig. 6 Theoretical and numerical distribution of light intensity of **Fig. 2** through the center of the particle.

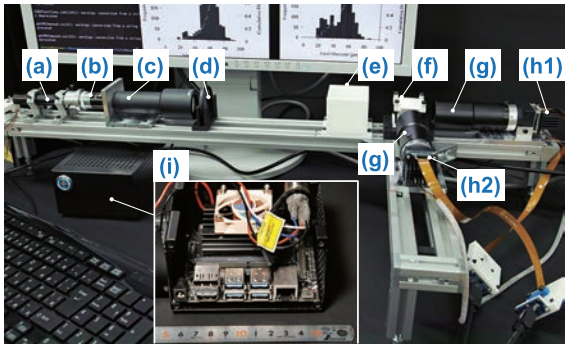


Fig. 7 Optical setup for particle size measurement using phase retrieval holography system with a GPU-equipped SBC: **(a)** laser; **(b)** objective lens; **(c)** collimator lens; **(d)** ND filter; **(e)** observation box; **(f)** beam splitter; **(e)** telecentric lens; **(h1)** CMOS camera 1; **(h2)** CMOS camera 2; **(i)** NVIDIA Jetson Nano as GPU-equipped SBC.

are installed at positions z_1 = 10 mm and z_2 = 20 mm under the condition of m = 1. The misalignment of a rotation and a shift in the xy plane between the two cameras was calibrated numerically within one pixel by bundle adjustment of the image distortion correction (Russ and Neal, 2016) using a calibration plate printed with random dots.

The holograms recorded by the two cameras are processed by the NVIDIA Jetson Nano with JetPack® SDK 4.6.1. Camera control and image acquisition are conducted with the Spinnaker® SDK C++ v2.5.0.80 library. The CUDA C/C++ 10.2 library and Thrust API are used for image processing and hologram reconstruction calculation using the GPU. The textbook by Shimobaba and Ito (2019) is informative, detailing GPU programming of hologram recording and reconstruction. OpenCV 4.5.4 is used to display images in GUI windows during processing. The application for bundle adjustment of the two cameras is implemented in Julia® 1.7.2.

Table 1 gives the CPU and GPU execution times for reconstruction processes using Gabor and phase retrieval holography. The CPU to GPU execution time ratio indicates that a GPU-equipped SBC is essential for early-time processing.

For comparison with holographic measurement, we used image measurement to determine the sizes of particles stuck to a glass plate, as shown in **Fig. 8(a)**. We used image analysis software (Fiji 2.3.0: Schindelin et al., 2012) to apply dynamic thresholding (Prewitt et al., 1966) to the recorded image to obtain a binarized image, and we measured the particle size as the Feret diameter, as shown in **Fig. 8(b)**.

Table 1 Comparison of execution time comparison between CPU and GPU for Gabor and phase retrieval holography.

	[s]		[Ratio]
	CPU	GPU	CPU/GPU
Gabor	82.5	2.0	41.2
Phase retrieval	101.7	2.6	39.1

4. Results

In this section, we report use of the fabricated system to measure particle size distributions in three-dimensional space using Gabor holography and phase retrieval holography. The effectiveness of the system is confirmed by comparing its measured distributions with that measured conventionally by two-dimensional image measurement.

Reconstructed volumes (6.9 mm × 6.9 mm × 40 mm) of Gabor and phase retrieval holography are shown in **Figs. 9(a)** and **10(a)**, respectively. Particles are elongated along the optical axis, as shown in **Eqn. (18)** and **Fig. 6**. Although particle size can be measured from the elongation (Nakatani et al., 2019), to reduce the computational load for real-time processing, we measure the size by using the binarized image with the minimum value in the optical axis direction in the volume.

The obtained minimum-intensity image, binarized image, and intensity histogram are shown in **Figs. 9(b)** and **9(c)** and **Figs. 10(b)** and **10(c)**, respectively. As compared in **Figs. 3** and **5**, phase retrieval holography, which suppresses the twin image problem, has a histogram peak at the value of zero light intensity as focused particles. In contrast, Gabor holography, which is affected by the twin image problem, has no peak in the histogram at the zero value. Consequently, Gabor holography has a larger threshold value than that of phase retrieval holography, and its binarized particle size is smaller than that of phase retrieval holography.

The Feret diameter is measured from the binarized images as in the image measurement of **Fig. 8(b)**, and the particle size distributions of Gabor and phase retrieval holography are shown in **Figs. 11(a)** and **11(b)**, respectively. Gabor and phase retrieval holography have peaks of similar size. However, as mentioned above, Gabor holography has more particles below 40 μm than does phase retrieval holography because of the smaller size due to the twin image problem.

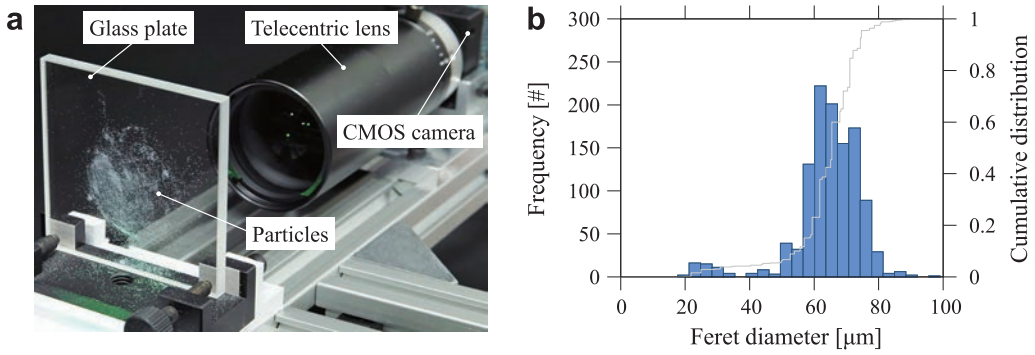


Fig. 8 Particle size distribution by image measurement: **(a)** observation of particles with telecentric lens; **(b)** histogram of particle size distribution (number of particles N_p = 1147).

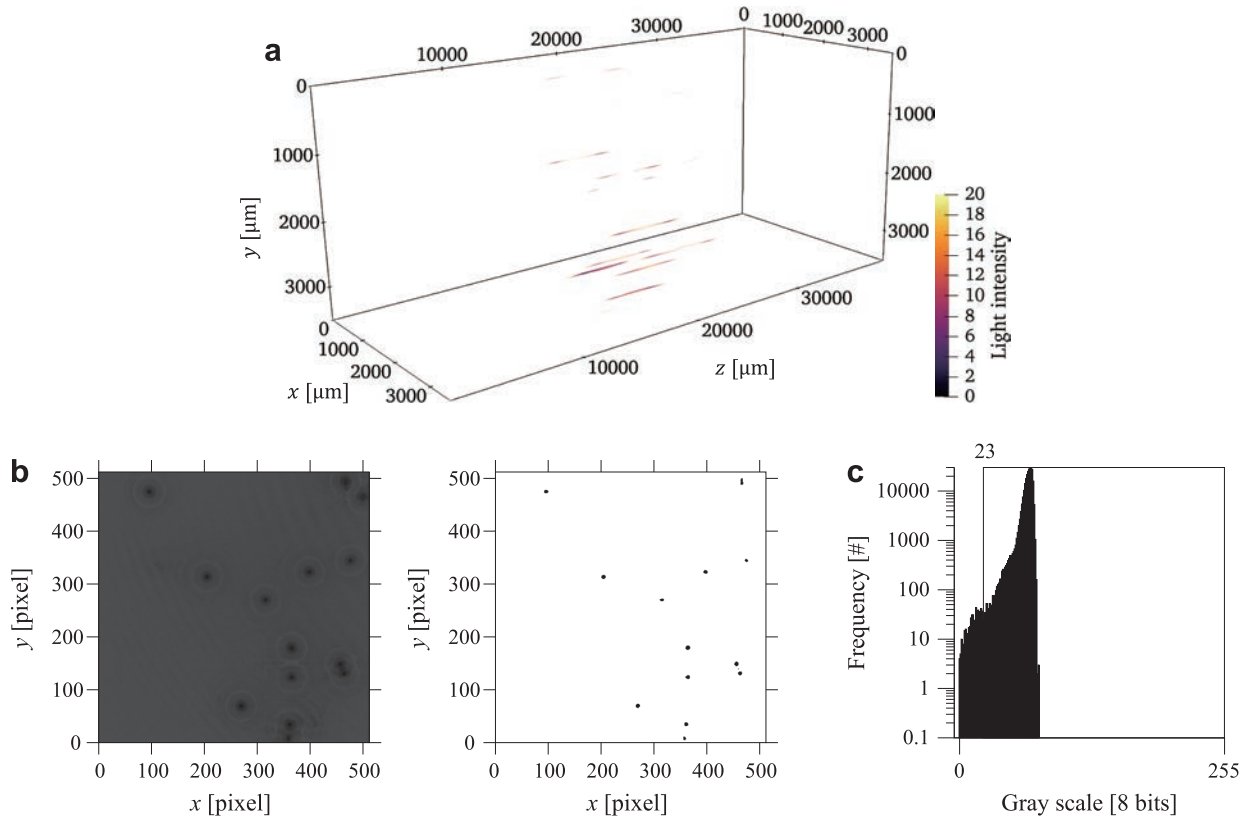


Fig. 9 Gabor holography: **(a)** reconstructed particles in measurement volume; **(b)** imposed volume and binarized image (threshold number: 23); **(c)** intensity histogram.

The cumulative frequency distribution functions are generated from the particle size distribution of image measurement, phase retrieval, and Gabor holography. The distributions determine the sizes corresponding to the 10th, 50th, 90th percentiles, and the span, labeled d_{10}, d_{50}, d_{90}, and d_{span} respectively. From the values in **Table 2**, unlike Gabor holography, phase retrieval holography enables the measurement of almost the same distribution levels as those of image measurement.

5. Conclusion

We have illustrated a phase retrieval holography system with a GPU-equipped SBC with theoretical and fabrication considerations. This system enables real-time measurements of particle size distributions in a three-dimensional space with almost the same accuracy as that of conventional two-dimensional image measurement. The results show that the fabricated system has reached the stage of practical particle-size measurements in three-dimensional space.

Data Availability Statement

The data on particle distributions by image measurement, Gabor holography, and phase retrieval holography is available publicly in J-STAGE Data (https://doi.org/10.50931/data.kona.22002518).

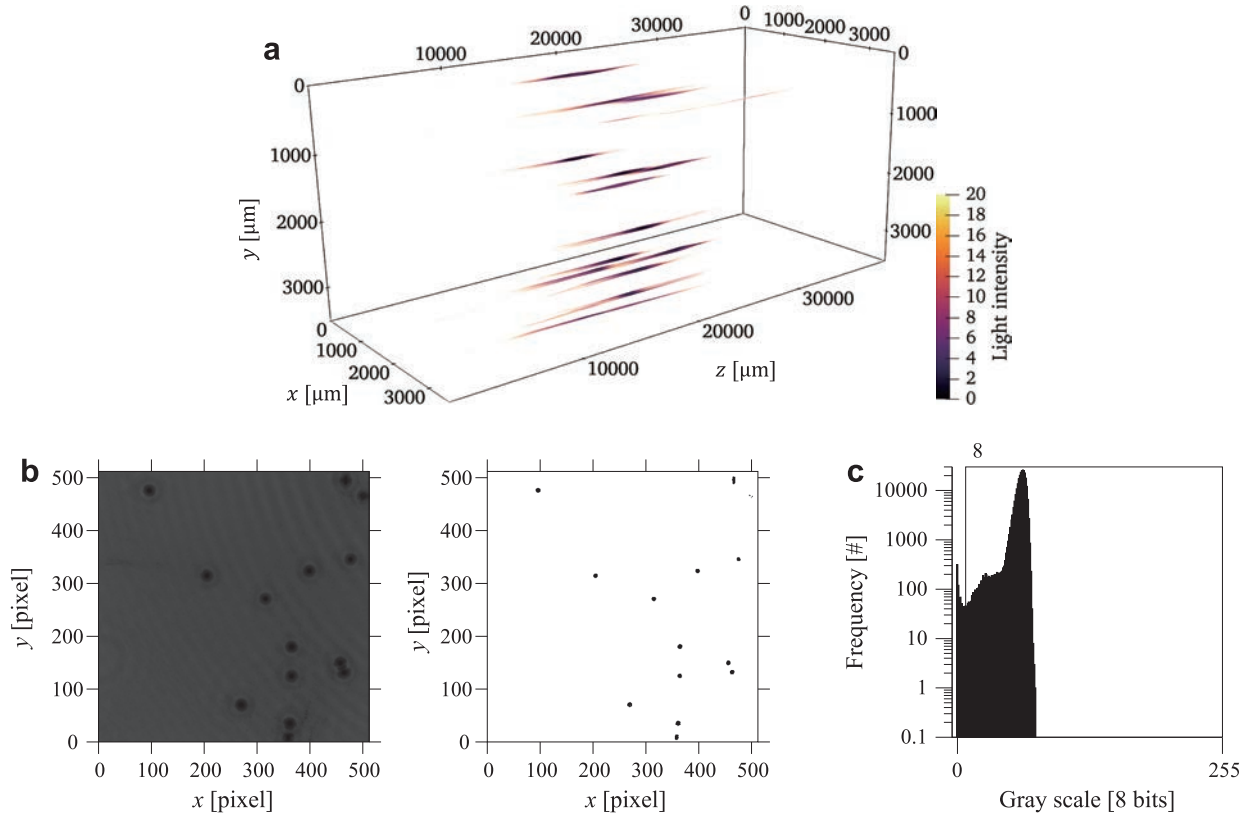


Fig. 10 Phase retrieval holography: **(a)** reconstructed particles in measurement volume; **(b)** imposed volume and binarized image (threshold number: 8); **(c)** intensity histogram.

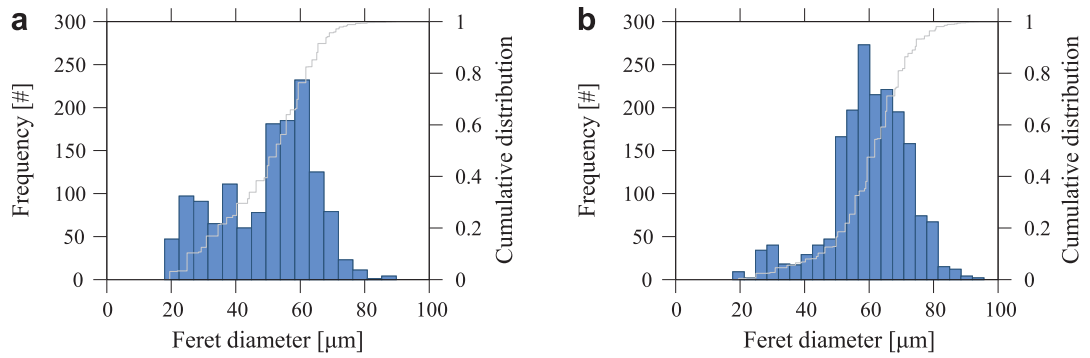


Fig. 11 Particle size distributions by **(a)** Gabor holography (number of particles N_p = 1390) and **(b)** Phase retrieval holography (number of particles N_p = 1837).

Table 2 Particle size distributions of Feret diameter.

	[μm]			[-]
	d_{10}	d_{50}	d_{90}	d_{span}*
Image measurement	53.9	65.4	74.3	0.3
Phase retrieval	44.1	61.7	74.3	0.5
Gabor	24.8	52.5	65.4	0.8

* $d_{span} = (d_{90} - d_{10})/d_{50}$

Acknowledgments

Our research on the phase retrieval holography system for measuring particle size distribution was supported by the Hosokawa Powder Technology Foundation (Grant Number HPTF20108).

References

Born M., Wolf E., Bhatia A.B., Clemmow P.C., Principles of Optics: Electromagnetic Theory of Propagation, Interference and Diffraction of Light, fourth ed., Pergamon Press, Oxford, 1970, ISBN: 0521642221.

Durst F., Melling A., Whitelaw J.H., Principles and Practice of Laser-Doppler Anemometry, Academic Press, 1981, ISBN: 0122252500.

Fujita S., Kitamura T., Murata K., Innovation of powder process using IoT, AI, The Micromeritics, 63 (2020) 90–96. DOI: 10.24611/micromeritics.2020016

Gabor D., A new microscopic principle, Nature, 161 (1948) 777–778. DOI: 10.1038/161777a0

Gerchberg R.W., Saxton W.O., A practical algorithm for the determination

of phase from image and diffraction plane pictures, Optik, 35 (1972) 237–246.
Katz J., Sheng J., Applications of holography in fluid mechanics and particle dynamics, Annual Review of Fluid Mechanics, 42 (2010) 531–555. DOI: 10.1146/annurev-fluid-121108-145508
Kubonishi A., Tanaka Y., Murata S., Observing bubbles using phase-retrieval holography, Journal of Flow Visualization and Image Processing, 25 (2018) 25–32. DOI: 10.1615/JFlowVisImageProc.2018026686
Latychevskaia T., Fink H.W., Solution to the twin image problem in holography, Physical Review Letters, 98 (2007) 233901. DOI: 10.1103/PhysRevLett.98.233901
Lichti M., Bart H.-J., Particle measurement techniques in fluid process engineering, ChemBioEng Reviews, 5 (2018) 79–89. DOI: 10.1002/cben.201800001
Liu G., Scott P.D., Phase retrieval and twin-image elimination for in-line Fresnel holograms, Journal of the Optical Society of America A, 4 (1987) 159–165. DOI: 10.1364/JOSAA.4.000159
Malik P.K., Sharma R., Singh R., Gehlot A., Satapathy S.C., Alnumay W.S., Nayak J., Industrial Internet of Things and its applications in industry 4.0: state of the art, Computer Communications, 166 (2021) 125–139. DOI: 10.1016/j.comcom.2020.11.016
Mattern F., Floerkemeier C., From the internet of computers to the internet of things, in: Sachs K., Petrov I., Guerrero P. (Eds.), From Active Data Management to Event-Based Systems and More, Springer Berlin Heidelberg, Berlin, Heidelberg, 2010, pp. 242–259, ISBN: 978-3-642-17226-7. DOI: 10.1007/978-3-642-17226-7_15
Memmolo P., Miccio L., Paturzo M., Di Caprio G., Coppola G., Netti P.A., Ferraro P., Recent advances in holographic 3D particle tracking, Advances in Optics and Photonics, 7 (2015) 713–755. DOI: 10.1364/AOP.7.000713
Nakatani Y., Tanaka Y., Murata S., Estimation of spray droplet-size distribution based on droplet elongations reconstructed by phase retrieval holography, Japanese Journal of Multiphase Flow, 33 (2019) 63–70. DOI: 10.3811/jjmf.2019.004
Nayak A.R., Malkiel E., McFarland M.N., Twardowski M.S., Sullivan J.M., A review of holography in the aquatic sciences: in situ characterization of particles, plankton, and small scale biophysical interactions, Frontiers in Marine Science, 7 (2021) 572147. DOI: 10.3389/fmars.2020.572147
Onural L., Scott P.D., Digital decoding of in-line holograms, Optical Engineering, 26 (1987) 1124–1132. DOI: 10.1117/12.7974205
Prewitt J.M., Mendelsohn M.L., The analysis of cell images, Annals of the New York Academy of Sciences, 128 (1966) 1035–1053. DOI: 10.1111/j.1749-6632.1965.tb11715.x
Russ J.C., Neal F.B., The Image Processing Handbook, seventh ed., CRC Press, 2016, ISBN: 9781138747494.
Schindelin J., Arganda-Carreras I., Frise E., Kaynig V., Longair M., Pietzsch T., Cardona A., Fiji: an open-source platform for biological-image analysis, Nature Methods, 9 (2012) 676–682. DOI: 10.1038/nmeth.2019
Shimobaba T., Ito T., Computer Holography: Acceleration Algorithms and Hardware Implementations, 1st ed., CRC Press, 2019, ISBN: 9781482240498.
Stolterman E., Fors A.C., Information technology and the good life, in: Kaplan B., Truex D.P., Wastell D., Wood-Harper A.T., DeGross J.I. (Eds.), Information Systems Research: Relevant Theory and Informed Practice, Springer US, Boston, MA, 2004, pp. 687–692, ISBN: 978-1-4020-8095-1. DOI: 10.1007/1-4020-8095-6_45
Tanaka Y., Matsushi H., Murata S., Phase retrieval holography for particle measurement with GPU acceleration, Proceedings of the ASME-JSME-KSME 2019 8th Joint Fluids Engineering Conference, (2019a) V004T04A030. DOI: 10.1115/AJKFluids2019-5204
Tanaka Y., Nakatani Y., Murata S., Visualization of spray droplets using phase retrieval holography, Proceedings of the SPIE 11051, 32nd International Congress on High-Speed Imaging and Photonics, (2019b) 69–74. DOI: 10.1117/12.2524601
Tanaka Y., Tani S., Murata S., Phase retrieval method for digital holography with two cameras in particle measurement, Optics Express, 24 (2016) 25233–25241. DOI: 10.1364/OE.24.025233
Tian L., Loomis N., Domínguez-Caballero J.A., Barbastathis G., Quantitative measurement of size and three-dimensional position of fast-moving bubbles in air-water mixture flows using digital holography, Applied Optics, 49 (2010) 1549–1554. DOI: 10.1364/AO.49.001549
Vikram C.S., Particle Field Holography, 1st ed., Cambridge University Press, 1992, ISBN: 9780521018302.
Yang W., Kostinski A.B., Shaw R.A., Phase signature for particle detection with digital in-line holography, Optics Letters, 31 (2006) 1399–1401. DOI: 10.1364/OL.31.001399
Zhang Y., Pedrini G., Osten W., Tiziani H.J., Whole optical wave field reconstruction from double or multi in-line holograms by phase retrieval algorithm, Optics Express, 11 (2003) 3234–3241. DOI: 10.1364/OE.11.003234

Authors' Short Biographies



Yohsuke Tanaka

Yohsuke Tanaka is an Associate Professor at the Faculty of Mechanical Engineering, Kyoto Institute of Technology. He worked for 3 years as a field engineer at Kyocera Corporation after receiving his Master's Degree in 2002 from the Kyoto Institute of Technology. He received his Ph.D. in Engineering from Osaka University in 2008. He received fellowships (DC2) from the Japan Society for Promotion of Science from 2007 to 2008. His research interests include optical, flow, and sound measurements.



Dai Nakai

Dai Nakai received his Bachelor of Engineering from the Kyoto Institute of Technology in 2022. He has since been researching particle measurement using holography as a Master's student at the Kyoto Institute of Technology. He is currently researching development of a machine learning-based holographic collision detection system to observe microdroplet collision in precipitation processes.

KONA Powder and Particle Journal

KONA Powder and Particle Journal No. 41 (2024) 229–241/https://doi.org/10.14356/kona.2024016 Original Research Paper

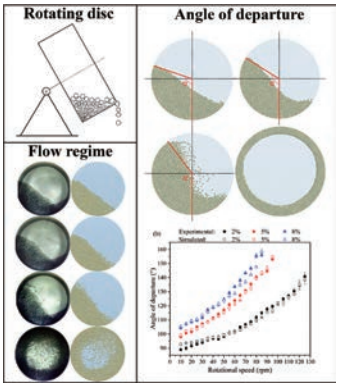
Effects of DEM Parameters and Operating Conditions on Particle Dynamics in a Laboratory Scale Rotating Disc†

Rondinelli M. Lima, Gisele M. Souza, Rodolfo J. Brandão, Claudio R. Duarte and Marcos A.S. Barrozo*

School of Chemical Engineering, Federal University of Uberlândia, Brazil

Rotating discs are usually used as granulators in many industrial processes. The efficiency of the granulation process in this device is directly related to the particle motion behavior in different flow regimes. In this work, the granular flow in a rotating disc was investigated experimentally and numerically. The Discrete Element Method (DEM) was used in the simulations, while Central Composite Designs (CCD) were employed to quantify the effects of DEM input parameters and operating conditions (filling degree (FD), angle of inclination (AI), and rotational speed) on the contacts between particles. The results showed that the particle–wall static friction coefficient had the most significant impact on the studied response. Additionally, the effect of operating variables on the collision force between particles, the angle of departure and particle velocities were successfully investigated, with corresponding DEM simulation predictions. It was also verified that the simulations performed with experimentally measured DEM input parameter values were able to reproduce the flow regimes in the rotating disc.

Keywords: rotating disc, flow regimes, DEM, DEM parameters, number of contacts



1. Introduction

The granulation process is widely employed in different industries, such as fertilizer, pharmaceutical, food, chemical, steel, and ceramics. This particle size enlargement technique allows the production of useful structural forms, modifies the material rheology, increases its flowability, reduces material loss and dust emissions, and controls porosity (Capes, 1980; Litster and Ennis, 2004).

Industrial granulators promote agglomeration through particle mixing and collision. Compared to other types of equipment, rotating discs stand out due to their pronounced segregation ability and flexibility to operate different types of materials (Litster and Ennis, 2004). Moreover, their geometry is relatively simple, consisting of a disc with a certain diameter (D), an angle of inclination (θ) and a rim (L) that rotates around its axis (**Fig. 1**).

Although rotating discs have been widely used as a granulator (Azrar et al., 2016; Ball, 1959; Chadwick and Bridgwater, 1997), only qualitative descriptions of solids flow have been usually made, with little quantitative information on particle dynamics (Chadwick and Bridgwater, 1997). The effects of different operating variables, such as rotational speed, filling degree (FD) and angle of inclination (AI), on the motion and contacts of particles are still not fully understood (Lima et al., 2022). Furthermore, as granulation is a dynamic process, investigating both the responses that are directly related to the granule formation (i.e., particle velocity, and number and force of contacts between particles) and flow regimes can also be a potential tool to optimize the granulation process in rotating discs (Gladky et al., 2021).

Depending on the operating conditions, different regimes of solids motion can be identified in a rotating disc: slipping, rolling, cascading, cataracting, and centrifuging, each with a specific flow behavior. Detailed descriptions of these flow regimes can be found in Mellmann (2001).

In the rolling regime, the granular bed can be divided into two distinct regions: the passive layer, where the particles are dragged up by the disc wall as a rigid body, and the active layer, where the particles roll over the bed surface downwards. For higher velocities, a kidney-shaped curve develops on the bed surface and a larger area of the disc is used, corresponding to the cascading regime. Regarding the granulation process, the rolling and cascading regimes in particular have the advantage of promoting more effective contacts between particles than the others (Azrar et al., 2016; Salman et al., 2006).

In addition to experimental studies, numerical simulations have become a complementary tool in granular flow analysis. Introduced by Cundall and Strack (1979), the Discrete Element Method (DEM) has been extensively applied to investigate granular dynamics in different types of equipment. In this method, each particle is described

† Received 30 March 2023; Accepted 1 May 2023
J-STAGE Advance published online 31 August 2023
* Corresponding author: Marcos A.S. Barrozo;
Add: Bloco K, Campus Santa Mônica, 38400-902, Uberlandia, MG, Brazil
E-mail: masbarrozo@ufu.br
FAX: +55-34-32394188

Copyright © 2024 The Authors. Published by Hosokawa Powder Technology Foundation. This is an open access article under the CC BY license (https://creativecommons.org/licenses/by/4.0/).

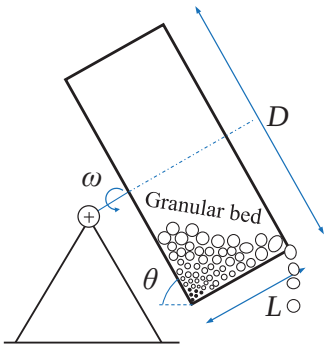


Fig. 1 Schematic diagram of a rotating disc.

individually through the application of a balance of forces and contact laws. The precision of the DEM model for predicting the granular flow relies on the selected contact model and the input parameters, which depend on both the particle properties and the particle-contact properties.

DEM simulations provide microscopic results at the particle level, such as trajectories of particles and forces that act on them, making it possible to obtain important information about particle dynamics. In this context, the knowledge of the solids flow in rotating discs is crucial for their design and applicability. However, there are a limited number of studies on the fluid dynamics of rotating discs using numerical analysis in conjunction with experimental results. Thus, through the use of DEM simulations and experimental data the present work aims to investigate how numerical parameters and different operating conditions influence particle dynamics in a rotating disc. The flow regimes and particle velocity distributions were also studied.

2. Discrete element method

DEM uses a time-stepping algorithm where the modeling is repeated in each time interval. Each particle is tracked contact by contact and its positions are updated based on the results of the previous time step (Nascimento et al., 2022; O'Sullivan, 2011). During each time step, Newton's second law is applied to determine the particle trajectory, while the particle–particle and particle–wall contact forces are evaluated based on the force–displacement law (Brandao et al., 2020; Cundall and Strack, 1979; Potyondy and Cundall, 2004). The motion of individual particles is determined by **Eqns. (1)** and **(2)**:

$$m_i \frac{\mathrm{d}v_i}{\mathrm{d}t} = \sum_j F_{ij} \tag{1}$$

$$I_i \frac{\mathrm{d}\omega_i}{\mathrm{d}t} = \sum_j \tau_{ij} \tag{2}$$

where t, m_i, I_i, v_i, and ω_i are the time, mass, moment of inertia, linear velocity, and angular velocity of particle i, respectively, and F_{ij} and τ_{ij} are the force and torque between particles i and j, respectively.

Table 1 Nonlinear Hertz–Mindlin model equations (Cundall and Strack, 1979; Di Maio and Di Renzo, 2005; Tsuji et al., 1992).

Normal force	$F_\mathrm{n} = \frac{4}{3} E^* \sqrt{R^*}\, \delta_\mathrm{n}^{\frac{3}{2}}$	(3)
Damping normal force	$F_\mathrm{n}^\mathrm{d} = -2\sqrt{\frac{5}{6}}\beta\sqrt{S_\mathrm{n} m^*}\, v_\mathrm{n}^\mathrm{rel}$	(4)
Equivalent contact radius	$\frac{1}{R^*} = \frac{1}{R_i} + \frac{1}{R_j}$	(5)
Equivalent mass	$\frac{1}{m^*} = \frac{1}{m_i} + \frac{1}{m_j}$	(6)
Equivalent Young's modulus	$\frac{1}{E^*} = \frac{1-\upsilon_i^2}{E_i} + \frac{1-\upsilon_j^2}{E_j}$	(7)
Normal stiffness	$S_\mathrm{n} = 2E^*\sqrt{R^*\delta_\mathrm{n}}$	(8)
Damping coefficient	$\beta = \frac{\ln e}{\sqrt{\ln^2 e + \pi^2}}$	(9)
Tangential force	$F_\mathrm{t} = -\delta_\mathrm{t} S_\mathrm{t}$	(10)
Tangential damping force	$F_\mathrm{t}^\mathrm{d} = -2\sqrt{\frac{5}{6}}\beta\sqrt{S_\mathrm{t} m^*}\, v_\mathrm{t}^\mathrm{rel}$	(11)
Tangential stiffness	$S_\mathrm{t} = 8G^*\sqrt{R^*\delta_\mathrm{n}}$	(12)
Equivalent shear modulus	$\frac{1}{G^*} = \frac{2-\upsilon_i}{G_i} + \frac{2-\upsilon_j}{G_j}$	(13)

The contact model used herein was the nonlinear Hertz–Mindlin. The main equations of this model are summarized in **Table 1**.

The equations in the **Table 1** involve normal and tangential overlaps (δ_n, δ_t), normal and tangential relative velocities $\left(v_\mathrm{n}^\mathrm{rel}, v_\mathrm{t}^\mathrm{rel}\right)$, restitution coefficient (e), and Poisson's ratio (υ).

3. Materials and methods

Laboratory tests and numerical simulations were conducted using a disc granulator made of stainless steel with a smooth surface and diameter of 35 cm, length of 20 cm, and variable angle of inclination. The granular material used was glass beads with a diameter of 6.35 ± 0.01 mm, density of 2455 ± 24 kg/m^3, and sphericity of 0.99 ± 0.01.

The DEM simulations were performed on the commercial EDEM® software. To ensure the numerical stability of the simulation, a time step of 4×10^{-5} s, which is equivalent to 20 % of the Rayleigh time, was adopted. The simulation conditions are listed in **Table 2**.

3.1 Measurement of DEM input parameters

The restitution coefficient (e), which quantifies the energy conserved in shocks between solid bodies, can be experimentally measured by the ratio between the relative velocities after (V_1) and before (V_0) the impact of two colliding bodies (Lima et al., 2021; Machado et al., 2017; Marinack Jr. et al., 2013), as shown in **Eqn. (14)**:

$$e = \frac{V_1}{V_0} \tag{14}$$

To determine the velocity before and after collision, the experimental apparatus described in previous studies was employed (Bharadwaj et al., 2010; Hastie, 2013; Marinack Jr. et al., 2013). It consists of a vacuum pump responsible for a suction pressure that holds particles at a height of 50 mm from the plate. In this procedure, the pump is switched off to allow particles to fall, while their trajectory is filmed by a high-speed video camera (Fastec IL5—up to 44,000 frames/s).

In order to measure the static friction coefficient (μ_S), the inclined plane method was applied (ASTM G115-10, 2013). In this method, the plane is gradually inclined and the angle of inclination (Φ) from which the particles start to slide is used to calculate the μ_S (**Eqn. (15)**).

$$\mu_S = \tan(\Phi) \tag{15}$$

To replicate the particle–wall interactions, the surface of the inclined plane was covered with a stainless steel plate. The particle–particle interaction behavior was studied by covering the surface of the plane with a fixed granular bed of glass beads (Brandao et al., 2020; Lima et al., 2021).

To calculate the rolling friction coefficient (μ_R), a measurement procedure based on that described in Lima et al. (2022) was adopted. The particle was placed on the top of the launching device (**Fig. 2**) at a certain height (h_0), and then allowed to travel through the entire device. The distance traveled by the particle after leaving the launching device until its resting point (D_r) was subsequently measured. The rolling friction coefficient was calculated using **Eqn. (16)**:

$$\mu_R = \frac{h_0}{D_r} \tag{16}$$

The experimental parameter values were used herein as inputs to the DEM model. Brandao et al. (2020) showed that the simulations performed with experimentally measured parameters were in good agreement with the experimental responses.

Table 2 DEM simulation conditions.

Model	Hertz–Mindlin
Time step (s)	4×10^{-5}
Poisson's ratio (-)	
Glass beads	0.22
Stainless steel	0.30
Shear modulus (Pa)	
Glass beads	1×10^{6}
Stainless steel	7×10^{10}

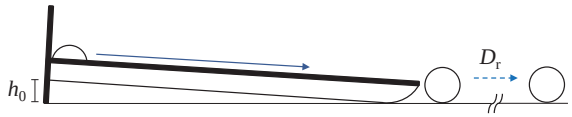


Fig. 2 Rolling friction coefficient apparatus.

3.2 Sensitivity analysis of DEM parameters

In order to quantify the effect of DEM parameters (i.e., restitution, static, and rolling friction coefficients) on the contact between particles in the rotating disc, a fractional Central Composite Design (CCD) (2^{6-1}, with 2x6 axial points and one central point) was used for the DEM calibration procedure. The CCD levels are shown in **Table 3**.

The CCD data was used to better understand the influence of the DEM parameters on the rotating disc simulation. Therefore, the CCD can help in both the calibration process and the development of new disc designs.

This CCD was applied to angles of inclination of 40°, 50° and 60°, and the rotating disc was filled with glass beads (2 % per volume). The rotational speed was set at 10 rpm. The dependent variable (response) was the average number of contacts between particles (N_{Cpp}), since it is a relevant parameter in the granulation process. The greater the contact between particles, the more effective the granulation process.

For each CCD run, the real-time simulation was 30 s. The N_{Cpp} average was obtained in the last 10s of simulation, since the rotating disc was operating in steady state. The steady-state condition was considered when the granular bed reached a constant height.

Table 3 CCD levels used in the sensitivity analysis of DEM parameters.

Factor coding	e_{pp}, e_{pw}, μ_{Spp}, μ_{Spw}	μ_{Rpp}, μ_{Rpw}
$-\alpha$ (–1.78)	0.054	0.005
–1	0.250	0.025
0	0.500	0.050
1	0.750	0.075
$+\alpha$ (+1.78)	0.946	0.095

*e_{pp}, e_{pw}, μ_{Spp}, μ_{Spw}, μ_{Rpp}, μ_{Rpw} correspond to the restitution, static, and rolling friction coefficients, respectively. The subscripts pp and pw indicate the particle–particle and particle–wall interactions, respectively.

Table 4 CCD levels used in the sensitivity analysis of operating conditions.

Coded Factor	*FD* (%)	*AI* (°)	*RS* (rpm)
$-\alpha$ (–1.47)	0.59	35.29	5.29
–1	2.00	40.00	10.00
0	5.00	50.00	20.00
+1	8.00	60.00	30.00
$+\alpha$ (+1.47)	9.41	64.71	34.71

**FD*: filling degree, *AI*: angle of inclination, *RS*: rotational speed.

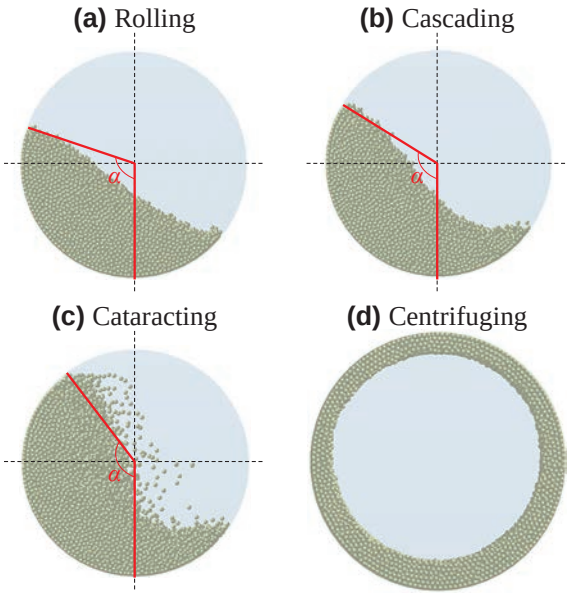


Fig. 3 Analyzed flow regimes and angle of departure measurement.

3.3 Sensitivity analysis of operating conditions

Another CCD was applied to evaluate the sensitivity of operating conditions on the number of contacts between particles. For these simulations the DEM parameters were kept constant following the values defined in **Section 3.1**. The analyzed operating conditions and the corresponding CCD levels are listed in **Table 4**.

3.4 Simulation of flow regimes

The flow regimes (i.e., rolling, cascading, cataracting, and centrifuging) were numerically investigated and compared with experimental results of our previous work (Lima et al., 2022). The angle of departure (α) was defined as the angle at which the particles detached from the equipment wall; it was measured using the Meazure software (**Fig. 3**).

The analyses were carried out at filling degrees of 2 %, 5 % and 8 % and angles of inclination of 40°, 50° and 60°. The flow regimes were simulated using experimental values of DEM parameters.

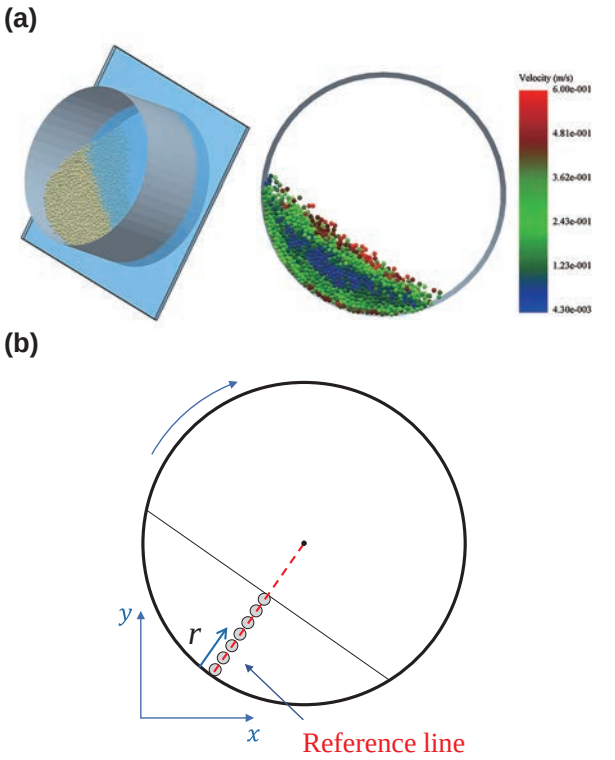


Fig. 4 Determination of particle velocity distribution: **(a)** cross-section representation parallel to the base of the rotating disc; and **(b)** schematic representation for particle velocity measurement.

3.5 Simulation of particle velocity distributions

In order to determine the passive and active layers of the rolling regime, the particle velocities were measured. Due to the inclination of the rotating disc, these layers were located in the inner part of the granular bed. Therefore, it was necessary to perform a cross-sectional cut parallel to the base of the rotating disc, as illustrated in **Fig. 4(a)**.

The particle velocity was determined along the reference line drawn in the middle of the granular bed (**Fig. 4(b)**) under different conditions (Delele et al., 2016; Resende et al., 2017; Santos et al., 2013, 2015). The reference line was discretized and normalized at evenly distributed points, and at each point the velocity of five different particles was determined.

The conditions used to investigate the velocity profiles of glass beads in the rotating disc were filling degrees of 2 % and 5 %, angles of inclination of 50° and 60°, and rotational speeds of 10 rpm, 15 rpm and 20 rpm.

4. Results and discussions

4.1 Sensitivity analysis of DEM parameters

A CCD (see levels in **Table 3**) was employed to evaluate the influence of DEM parameters on the number of contacts between particles (N_{Cpp}) in a rotating disc. To this end, a total of 45 simulations were performed for the rotating disc operating at angles of inclination of 40°, 50°, and 60°, a filling degree of 2 %, and a rotational speed of 10 rpm.

The obtained results are depicted in **Appendix A** (Supplementary material: **Table A1**).

From these results, it was possible to quantify such effects for each angle of inclination by regression techniques. The prediction equations (**Eqns. (17)–(19)**) resulted in correlation coefficients (R^2) of 0.94, 0.95 and 0.95 for angles of inclination of 40°, 50° and 60°, respectively.

$$N_{\text{Cpp-40°}} = 1.17 - 0.05x_1 + 0.05x_1^2 + 0.05x_2^2 - 0.09x_3 - 0.36x_4 + 0.16x_4^2 + 0.06x_5^2 + 0.05x_6^2 \quad (17)$$

$$N_{\text{Cpp-50°}} = 1.18 - 0.05x_1 + 0.06x_1^2 + 0.06x_2^2 - 0.12x_3 + 0.06x_3^2 - 0.40x_4 + 0.17x_4^2 + 0.07x_5^2 + 0.06x_6^2 - 0.04x_1x_4 \quad (18)$$

$$N_{\text{Cpp-60°}} = 1.19 - 0.05x_1 + 0.06x_1^2 + 0.06x_2^2 - 0.13x_3 + 0.06x_3^2 - 0.41x_4 + 0.18x_4^2 + 0.07x_5^2 + 0.06x_6^2 - 0.03x_1x_4 \quad (19)$$

The DEM parameters of these equations are presented in coded form as follows:

$$x_1 = \frac{e_{\text{pp}} - 0.50}{0.25} \qquad x_2 = \frac{e_{\text{pw}} - 0.50}{0.25}$$

$$x_4 = \frac{\mu_{\text{Spw}} - 0.50}{0.25} \qquad x_3 = \frac{\mu_{\text{Spp}} - 0.50}{0.25}$$

$$x_5 = \frac{\mu_{\text{Rpp}} - 0.050}{0.025} \qquad x_6 = \frac{\mu_{\text{Rpw}} - 0.050}{0.025}$$

where x_1 = particle–particle restitution coefficient, x_2 = particle–wall restitution coefficient, x_3 = particle–particle static friction coefficient, x_4 = particle–wall static friction coefficient, x_5 = particle–particle rolling friction coefficient, and x_6 = particle–wall rolling friction coefficient, all in coded form.

In **Eqns. (17)–(19)**, only the statistically significant parameters were included. It was possible to observe that all DEM parameters had a significant effect on N_{Cpp} at a significance level of 5 %.

The coefficients of **Eqns. (17)–(19)** show that e_{pw} (x_2 in coded form), μ_{Rpp} (x_5 in coded form), and μ_{Rpw} (x_6 in coded form) were only influenced by the quadratic term. On the other hand, μ_{Spw} (x_4 in coded form) was the parameter that most influenced N_{Cpp}, with an effect four times greater than that of μ_{Spp} (x_3 in coded form)—the second most relevant parameter—and eight times greater than that of e_{pp} (x_1 in coded form). In addition, the change in the angle of inclination of the rotating disc practically did not influence the intensity of the parameter effects.

In order to obtain accurate simulations based on the DEM approach, a correct set of input parameter values is required. Several studies have used the calibration process to determine such values (Cunha et al., 2016; El Kassem et al., 2021; Marigo and Stitt, 2015; Nascimento et al., 2022; Santos et al., 2016). One of the disadvantages of the calibration process is the high number of simulations required to find the parameter values. Therefore, the analysis of the effects of DEM parameters becomes essential to quantify the influence of each parameter on the rotating disc. As μ_{Spw} has a much greater influence than the other parameters, an alternative is to only calibrate this parameter, thus reducing the number of simulations.

Another factor to be analyzed is that μ_{Spw} has a negative effect, i.e., the number of contacts between particles decreases as the coefficient value increases. This information is necessary for the design and optimization of rotating discs, because depending on the interaction between the granular material and the equipment wall, the contact between particles can decrease, thus hindering the granulation process.

Rong et al. (2020) used a 3^k factorial design to evaluate the sensitivity of particle–particle DEM parameters in a rotating drum. The authors found that the sliding friction coefficient, when compared with the rolling friction coefficient and the restitution coefficient, was the determining parameter on the mean power draw of the rotating drum. With the increase in the sliding friction coefficient, more power was required due to the increased resistance of particles when they come into contact with other particles.

Table 5 CCD used to analyze the influence of operating conditions on N_{Cpp}.

Run	*FD* (%)	*AI* (°)	*RS* (rpm)	N_{Cpp}
1	2.00	40.00	10.00	1.31
2	2.00	40.00	30.00	0.79
3	2.00	60.00	10.00	1.34
4	2.00	60.00	30.00	0.86
5	8.00	40.00	10.00	1.59
6	8.00	40.00	30.00	1.15
7	8.00	60.00	10.00	1.65
8	8.00	60.00	30.00	1.26
9	0.59	50.00	20.00	0.71
10	9.41	50.00	20.00	1.42
11	5.00	35.29	20.00	1.19
12	5.00	64.71	20.00	1.28
13	5.00	50.00	5.29	1.73
14	5.00	50.00	34.71	1.03
15	5.00	50.00	20.00	1.29

4.2 Analysis of the effects of operating conditions

Table 5 shows the results of the CCD used to analyze the influence of filling degree (*FD*), angle of inclination (*AI*) and rotational speed (*RS*) on N_{Cpp} (see levels in **Table 4**).

The data in **Table 5** were subjected to regression analysis to quantify the effects of each independent variable and its corresponding interactions on the response (N_{Cpp}). The variables *FD*, *AI* and *RS* were coded as x_7, x_8, and x_9, respectively. The obtained equation (**Eqn. (20)**) has a correlation coefficient (R^2) equal to 0.97.

$$N_{Cpp} = 1.27 + 0.19x_7 - 0.09x_7^2 + 0.03x_8 - 0.23x_9 + 0.06x_9^2 \quad (20)$$

where: $x_7 = \dfrac{FD - 5\%}{3\%}$; $x_8 = \dfrac{AI - 50°}{10°}$;

and $x_9 = \dfrac{RS - 20\text{rpm}}{10\text{rpm}}$

All operating conditions analyzed had a significant effect on N_{Cpp} at a significance level of 5 %. It is noteworthy that there was no interaction between the variables, i.e., each variable alone had a direct influence on N_{Cpp}.

As it can be seen in **Eqn. (20)**, the effect of *FD* was positive, that is, the number of contacts between particles increased as a function of the number of particles in the rotating disc. An opposite effect was observed for rotational speed, i.e., the *RS* increased with decreasing N_{Cpp}. According to Capes (1980), during the granulation process the particle residence time can be lengthened by increasing the rotational speed. However, at high rotational speeds the rotating disc tends to operate in the cataracting regime, which can result in agglomerate degradation and breakage depending on the agitation intensity. A strict control of the rotational speed is then necessary for the rotating disc to operate in the rolling and cascading regimes, consequently improving the efficiency of the granulation process (Pietsch, 1997; Salman et al., 2006).

The change in the disc inclination had little influence on N_{Cpp} when compared to the other variables. This result confirms what was observed in the sensitivity analysis of DEM parameters.

Other variables such as size distribution of feed, liquid content in the feed powder, and liquid surface tension can also influence the granulation process (Capes, 1980). Nevertheless, **Eqn. (20)** can elucidate the granulation process, assisting in the operation, design and optimization of rotating discs.

Table 6 DEM parameter values obtained experimentally.

DEM parameters	Values
e_{pp}	0.900
e_{pw}	0.690
μ_{Spp}	0.620
μ_{Spw}	0.330
μ_{Rpp}	0.014
μ_{Rpw}	0.013

4.3 Simulation of flow regimes

DEM simulations were also used to predict the behavior of flow regimes in a rotating disc. In these simulations, the input parameters obtained from the experimental procedure described in **Section 3.1** were employed. **Table 6** shows the values of DEM parameters obtained by the respective experimental measurement. To verify the validity of these DEM input parameters, the numerical and experimental results were compared. Two analyses were carried out: a qualitative one, where images of the flow regimes were confronted, and a quantitative one, where the angle of departure values were compared.

Figs. 5 to **7** compare the images of the experimental and simulated results for the different flow regimes in the rotating disc, operating at different angles of inclination (*AI*). As it can be seen, the DEM simulations accurately predicted each flow regime.

Regarding the quantitative analysis, **Fig. 8** compares the numerical and experimental angles of departure for the studied disc inclinations. As observed, the experimental and simulated results were very similar for the entire range of flow regimes (i.e., rolling, cascading, cataracting, and centrifuging). The average percentage deviation of the angle of departure was less than 2 %. Therefore, both qualitative (**Figs. 5** to **7**) and quantitative (**Fig. 8**) analyses confirmed that the direct experimental measurements of the DEM input parameters were able to reproduce the bulk behavior of particles in the rotating disc. For this reason, it was not necessary to perform the calibration of DEM parameters, allowing the preservation of their physical meanings.

Barrios et al. (2013) verified that experimental measurements of DEM parameters for a single particle proved to be a viable alternative to estimate the parameter values of iron ore pellets. According to the authors, the computational effort is reduced since the parameter values are obtained directly, without requiring a calibration process.

Brandao et al. (2020) used DEM Simulations to study the mixing and segregation of materials in a rotating drum. The authors measured the DEM parameters experimentally and performed a calibration approach. They verified that the parameter values obtained by the calibration process were similar to the experimental ones.

From the validation of the DEM model it can be verified that the DEM parameters successfully represent the evaluated experimental results. Therefore, it is possible to analyze the influence of the experimental operating conditions on the maximum collision force ($F_{C,max}$). To determine the maximum collision force, all particles were tracked along

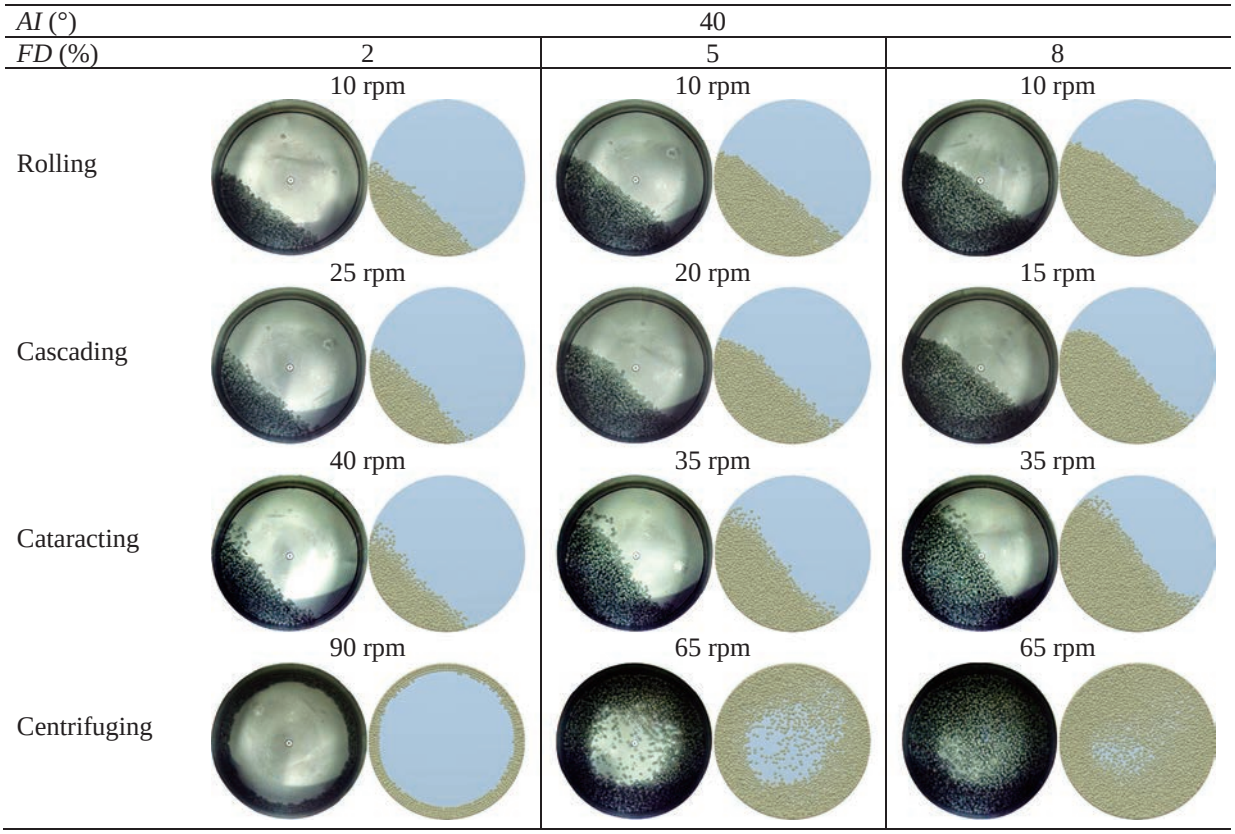


Fig. 5 Experimental and numerical results of the qualitative analysis of flow regimes for an angle of inclination of 40°.

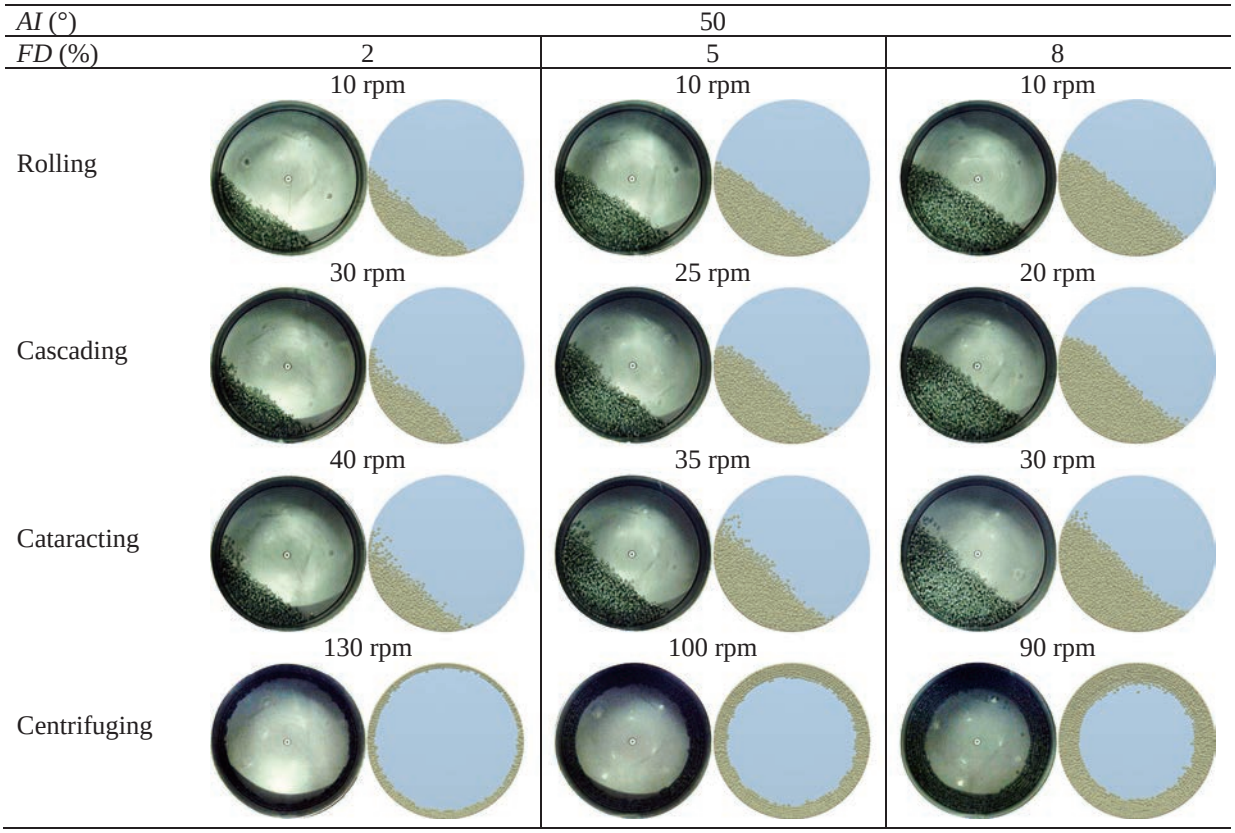


Fig. 6 Experimental and numerical results of the qualitative analysis of flow regimes for an angle of inclination of 50°.

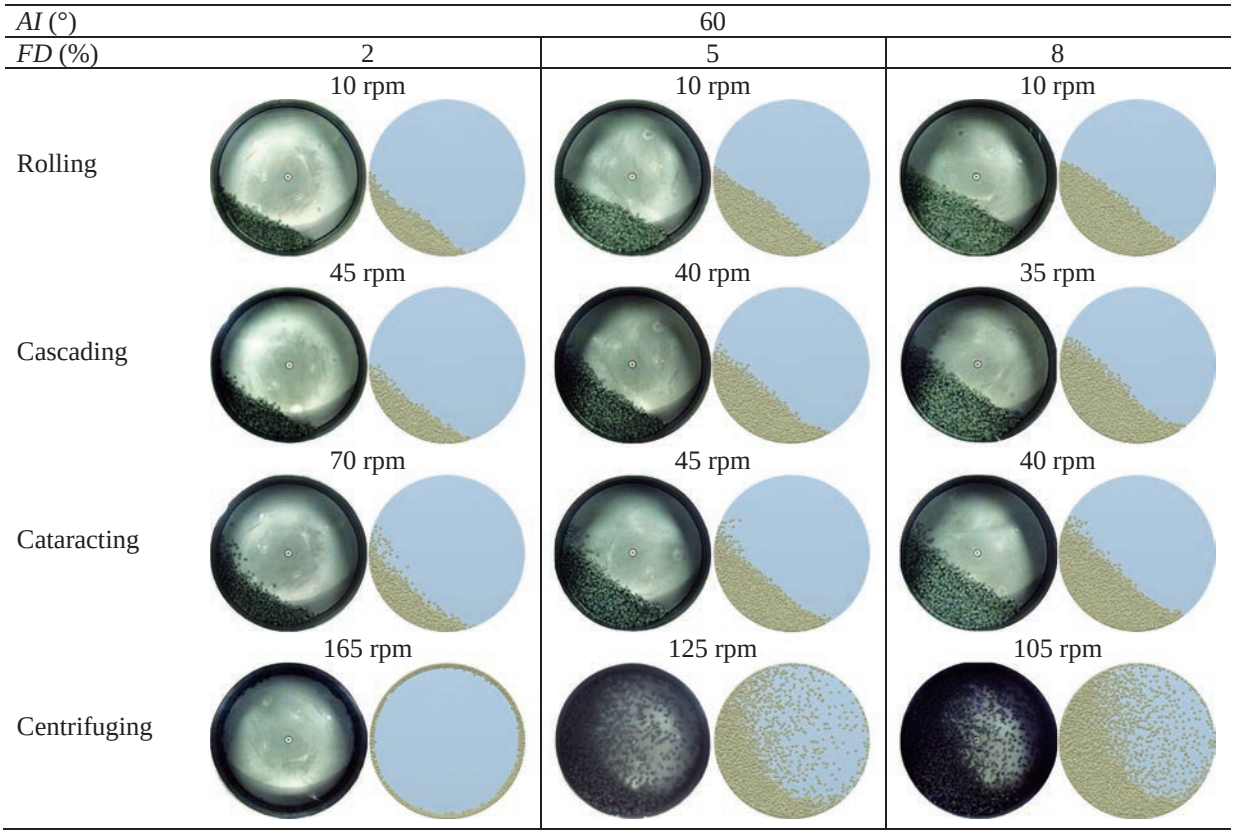


Fig. 7 Experimental and numerical results of the qualitative analysis of flow regimes for an angle of inclination of 60°.

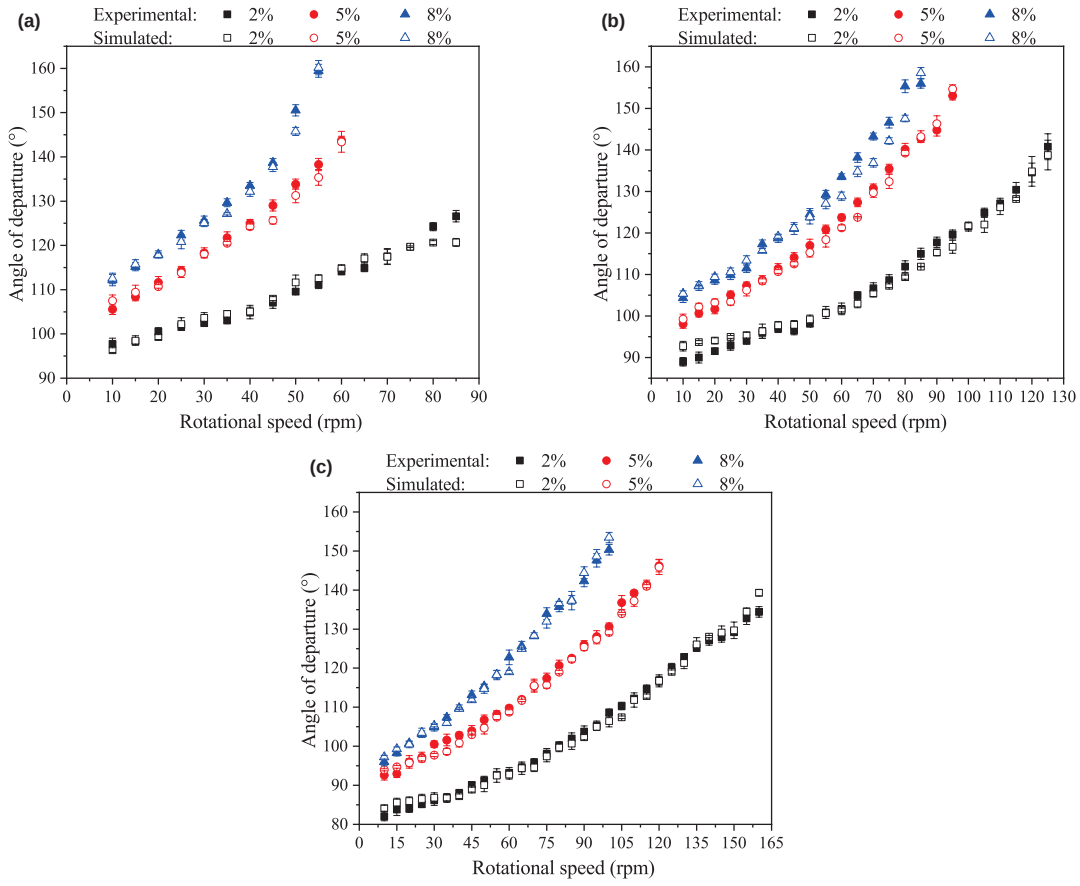


Fig. 8 Experimental and numerical results of the quantitative analysis of angles of departure for angles of inclination of **(a)** 40°, **(b)** 50° and **(c)** 60°.

the simulation time.

A 3^k factorial design was used to evaluate the effects of the following operating conditions on $F_{C,max}$: filling degree (*FD*), angle of inclination (*AI*) and rotational speed (*RS*). The levels used for the independent variables (*FD*, *AI*, and *RS*) were the same as the experimental ones. This analysis can be used to help prevent agglomerate degradation and breakage.

Table 7 shows the conditions and results ($F_{C,max}$) of the 3^k factorial design.

The effects of *FD*, *AI* and *RS* on $F_{C,max}$ were quantified by regression techniques using the experimental data in **Table 7**. From **Eqn. (21)**, which has a correlation coefficient (R^2) equal to 0.82, it is possible to predict the maximum collision force between particles ($F_{C,max}$) as a function of the operational variables and quantify its respective effects. The independent variables *FD*, *AI*, and *RS* are presented in coded forms (x_{10}, x_{11} and x_{12}, respectively).

Table 7 3^k factorial design used to analyze the influence of operating conditions of a rotating disc on $F_{C,max}$.

Run	*FD* (%)	*AI* (°)	*RS* (rpm)	$F_{C,max}$ (N)
1	2	40	10	1.10
2	2	40	30	1.52
3	2	40	50	1.98
4	2	50	10	1.21
5	2	50	30	1.33
6	2	50	50	1.62
7	2	60	10	1.18
8	2	60	30	1.72
9	2	60	50	1.93
10	5	40	10	1.24
11	5	40	30	1.46
12	5	40	50	2.31
13	5	50	10	1.21
14	5	50	30	1.43
15	5	50	50	1.80
16	5	60	10	1.45
17	5	60	30	1.91
18	5	60	50	1.72
19	8	40	10	1.35
20	8	40	30	1.74
21	8	40	50	2.91
22	8	50	10	1.55
23	8	50	30	1.49
24	8	50	50	1.68
25	8	60	10	1.52
26	8	60	30	1.50
27	8	60	50	1.75

All operating conditions had a positive effect on $F_{C,max}$ at a significance level of 5 %. $F_{C,max}$ increased as a function of both *FD* (x_{10} in coded form) and *RS* (x_{12} in coded form), with the latter affecting this variable three times more than the former. This analysis highlights the care that must be taken when operating rotating discs at high rotational speeds, as this can result in degradation of the agglomerates formed, thus impairing the granulation process. On the other hand, *AI* (x_{11} in coded form) had a negative effect on $F_{C,max}$, and although it did not affect linearly the collision force, it interacted with other variables.

$$F_{C,max} = 1.61 + 0.10x_{10} - 0.10x_{11}^2 + 0.33x_{12} - 0.12x_{10}x_{11} - 0.19x_{11}x_{12} + 0.09x_{11}x_{12}^2 - 0.10x_{11}^2x_{12} \quad (21)$$

where: $x_{10} = \frac{FD - 5\%}{3\%}$; $x_{11} = \frac{AI - 50°}{10°}$;

and $x_{12} = \frac{RS - 30\text{rpm}}{20\text{rpm}}$

The effect of operating conditions on $F_{C,max}$ was similar to that observed for the angle of departure and this result is

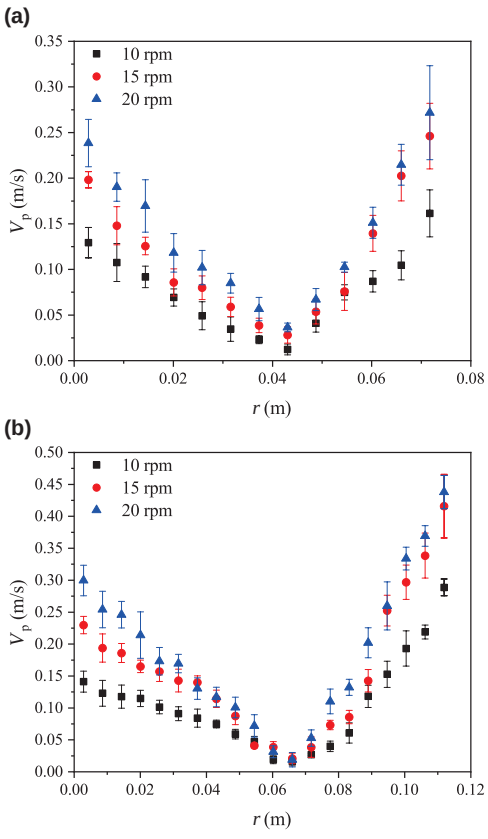


Fig. 9 Velocity profiles of glass beads for an angle of inclination of 50°: **(a)** 2 % and **(b)** 5 %.

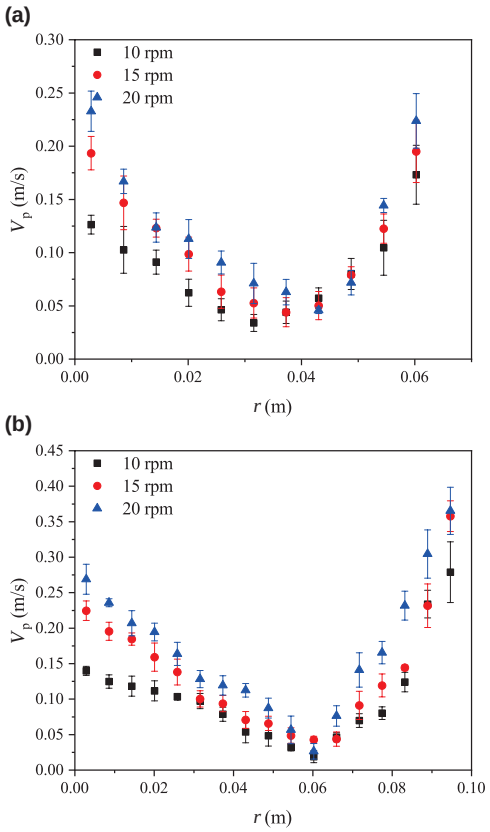


Fig. 10 Velocity profiles of glass beads for an angle of inclination of 60°: **(a)** 2 % and **(b)** 5 %.

in agreement with the behavior observed by Lima et al. (2022).

4.4 Simulation of particle velocity distributions

Due to the rotating disc inclination, the active and passive layers of the rolling regime were found to be located in the inner regions of the granular bed. Therefore, they could only be observed through simulations.

Figs. 9 and **10** display the particle velocity distributions, where *V*p is the particle velocity and *r* is the particle position along the reference line (**Fig. 4(b)**). The variable *r* starts from the disc wall and ends at the granular bed surface. In this work, only the cases in which the rotating disc was operating in the rolling regime were considered, i.e., at angles of inclination of 50 (**Fig. 9**) and 60° (**Fig. 10**), filling degrees of 2 and 5 %, and velocities of 10, 15 and 20 rpm.

The two different bed structure regions visualized in the **Figs. 9** and **10** demonstrate that as the value of *r* increased, the particle velocities decreased until reaching a minimum value (close to zero), evidencing the interface between the passive and active layers. This behavior is typical of the passive layer in the rolling regime, in which the particles move as a solid body and are dragged up by the disc wall. From the interface, the solids velocities started to increase along *r*, characterizing the active layer. In this region, the particles had a higher dynamics, moving in the opposite direction to the passive layer. As observed, the highest velocity values were found to be near the granular bed surface.

Table 8 Analysis of active and passive layer thicknesses.

Angle of inclination	Filling degree [%]	Layer thickness [m]		Ratio (*A*/*P*)
		Passive (*P*)	Active (*A*)	
50°	2	0.040	0.029	0.714
	5	0.063	0.046	0.727
60°	2	0.034	0.023	0.667
	5	0.057	0.034	0.600

It can also be seen that higher rotational speeds resulted in greater velocities in both layers, but without changing the interface position. When the rotational speed was kept constant and the filling degree was increased, the particle velocities also increased in both layers, and such effect was higher in the active layer. Regarding the angle of inclination, it can be observed that the disc operating at 50° achieved higher particle velocities in the active layer. In this case, the granular bed reached a higher angle of departure, increasing the potential energy of the particles and therefore their dynamics.

In contrast to the rotational speed, changes in the filling degree and angle of inclination modified the interface position, suggesting the significant impact of these variables on the active layer thickness. The correct prediction of the active and passive layers for a rotating disc operating in the rolling regime is very important for the granulation process. It is worth mentioning that the best particle interactions, mixing and segregation, as well as the highest rates of heat and mass transfer, occur in the active layer. **Table 8** presents the thicknesses of the active layers and their ratio to the passive layer thicknesses for angles of inclination of 50° and 60°.

For constant filling degrees, the change in the angle of inclination from 50° to 60° resulted in a reduced ratio between the layers of 6.58 % and 17.47 % for filling degrees of 2 % and 5 %, respectively, evidencing the movement of particles to the passive layer region.

Santos et al. (2015) found similar behavior, when studied, numerically and experimentally, the velocity profile of soybean particles in a rotating drum operating in the rolling regime. They observed that, keeping the filling degree constant and increasing the rotational speed, there was an increase in the velocity of the particles in both layers (passive and active), and the point where a reverse of the flow takes place was kept constant. On the other hand, when the rotational speed was kept constant and the filling degree was changed from 18.81 % to 31.40 %, the inflection point

changed from 4 cm to 5.5 cm, respectively.

5. Conclusions

In this work, DEM simulations were performed to study the influence of DEM parameters and operating conditions on particle dynamics in a rotating disc.

The methodology used herein allowed to analyze and quantify the effect of DEM parameters on the number of contacts between particles, an important variable in the granulation process. All DEM parameters had a significant influence on the analyzed response, with μ_{Spw} being the parameter with the greatest effect.

DEM simulations were also used to predict the behavior of flow regimes in a rotating disc. In these simulations, the input parameters obtained from the experimental procedure were used and successfully predicted the experimental behavior of all flow regimes.

With respect to the effects of the operating conditions of the rotating disc (i.e., filling degree, angle of inclination and rotational speed) on N_{Cpp} and $F_{C,max}$, it was observed that the increase in the filling degree had a positive effect on both responses. In contrast, the increase in the rotational speed led to a reduction in N_{Cpp}, but an increase in $F_{C,max}$, which can impair the efficiency of the granulation process. Lastly, in relation to the disc inclination, the change in this parameter had little influence on N_{Cpp}. Additionally it was verified that greater angles of inclination led to a reduction in the intensity of $F_{C,max}$.

In this study, it is also possible to verify the effect of the operating conditions of the rotating disc on the particle velocity distributions in the rolling regime. As the filling degree and rotational speed increased, the particle velocity was also raised in both layers, whilst the change in the angle of inclination affected the active layer. The disc operating at 50° showed the highest ratio between the active and passive layer thicknesses.

Supplementary information

The online version contains supplementary material available at https://doi.org/10.14356/kona.2024016.

Acknowledgments

The authors are grateful to the Minas Gerais Research Funding Foundation (FAPEMIG), the Brazilian National Council for Scientific and Technological Development (CNPq), and the Coordination for the Improvement of Higher Education Personnel (CAPES) for their financial support.

Nomenclature

D	diameter of disc granulator (m)
D_r	distance traveled by the particle (m)
e	restitution coefficient (-)
E	Young's modulus (Pa)
E^*	equivalent Young's modulus (Pa)
F	force (N)
G	shear modulus (Pa)
G^*	equivalent shear modulus (Pa)
h_0	device height (m)
I	moment of inertia (m s^{-2})
L	rim height of disc granulator (m)
m^*	equivalent mass (kg)
m	mass (kg)
N_c	number of contact (-)
R	radius (m)
R^*	equivalent contact radius (m)
S	stiffness (Pa m)
t	time (s)
v	linear velocity (ms^{-1})
V_0	velocity before impact (m s^{-1})
V_1	velocity after impact (m s^{-1})
V_p	particle velocity (m s^{-1})

Greek Symbol

α	angle of departure (°)
β	damping coefficient (kg s^{-1})
δ	overlap distance of two particles (m)
θ	angle of inclination of disc granulator (°)
μ_R	rolling friction coefficient (-)
μ_S	static friction coefficient (-)
τ	torque (N m^{-1})
υ	Poisson ratio (-)
Φ	angle of inclination used in the friction coefficient measurement (-)
ω	angular velocity (s^{-1})

Indexes

C	contact
d	damping
i and j	particle identification index
n	normal direction
pp	particle–particle interaction
pw	particle–wall interaction
t	tangential direction

References

ASTM G115 - 10, Standard guide for measuring and reporting friction coefficients, American Society for Testing and Materials (ASTM), (2013). DOI: 10.1520/G0115-10R13.2

Azrar H., Zentar R., Abriak N.E., The effect of granulation time of the pan granulation on the characteristics of the aggregates containing Dunkirk sediments, Procedia Engineering, 143 (2016) 10–17. DOI:

10.1016/j.proeng.2016.06.002

Ball F.D., Pelletizing before sintering: some experiments with a disc, Journal of the iron and steel institute, 192 (1959) 40–55.

Barrios G.K.P., de Carvalho R.M., Kwade A., Tavares L.M., Contact parameter estimation for DEM simulation of iron ore pellet handling, Powder Technology, 248 (2013) 84–93. DOI: 10.1016/j.powtec.2013.01.063

Bharadwaj R., Ketterhagen W.R., Hancock B.C., Discrete element simulation study of a Freeman powder rheometer, Chemical Engineering Science, 65 (2010) 5747–5756. DOI: 10.1016/j.ces.2010.04.002

Brandao R.J., Lima R.M., Santos R.L., Duarte C.R., Barrozo M.A.S., Experimental study and DEM analysis of granular segregation in a rotating drum, Powder Technology, 364 (2020) 1–12. DOI: 10.1016/j.powtec.2020.01.036

Capes C.E., Particle Size Enlargement, 1st ed, Elsevier, Elsevier, Amsterdam, 1980, ISBN: 9781483275079.

Chadwick P.C., Bridgwater J., Solids flow in dish granulators, Chemical Engineering Science, 52 (1997) 2497–2509. DOI: 10.1016/S0009-2509(97)00068-7

Cundall P.A., Strack O.D.L., A discrete numerical model for granular assemblies, Géotechnique, 29 (1979) 47–65. DOI: 10.1680/geot.1979.29.1.47

Cunha R.N., Santos K.G., Lima R.N., Duarte C.R., Barrozo M.A.S., Repose angle of monoparticles and binary mixture: an experimental and simulation study, Powder Technology, 303 (2016) 203–211. DOI: 10.1016/j.powtec.2016.09.023

Delele M.A., Weigler F., Franke G., Mellmann J., Studying the solids and fluid flow behavior in rotary drums based on a multiphase CFD model, Powder Technology, 292 (2016) 260–271. DOI: 10.1016/j.powtec.2016.01.026

Di Maio F.P., Di Renzo A., Modelling particle contacts in distinct element simulations: linear and non-linear approach, Chemical Engineering Research and Design, 83 (2005) 1287–1297. DOI: 10.1205/cherd.05089

El Kassem B., Salloum N., Brinz T., Heider Y., Markert B., A semi-automated dem parameter calibration technique of powders based on different bulk responses extracted from auger dosing experiments, KONA Powder and Particle Journal, 38 (2021) 235–250. DOI: 10.14356/kona.2021010

Gladky A., Lieberwirth H., Lampke J., Schwarze R., Numerical modeling of bulk flow on a pelletizing disc in different rotational regimes, Granular Matter, 23 (2021) 1–9. DOI: 10.1007/s10035-021-01121-6

Hastie D.B., Experimental measurement of the coefficient of restitution of irregular shaped particles impacting on horizontal surfaces, Chemical Engineering Science, 101 (2013) 828–836. DOI: 10.1016/j.ces.2013.07.010

Lima R.M., Brandao R.J., Santos R.L., Duarte C.R., Barrozo M.A.S., Analysis of methodologies for determination of DEM input parameters, Brazilian Journal of Chemical Engineering, 38 (2021) 287–296. DOI: 10.1007/s43153-021-00107-4

Lima R.M., Brandão R.J., Souza G.M. De, Silveira J.C., Potenza F., Duarte C.R., Barrozo M.A.S., Analysis of particle dynamics in a rotating dish, Powder Technology, 409 (2022) 117827. DOI: 10.1016/j.powtec.2022.117827

Litster J., Ennis B., The Science and Engineering of Granulation Processes, Springer Netherlands, Dordrecht, 2004, ISBN: 9781402018770. DOI: 10.1007/978-94-017-0546-2

Machado M.V.C., Santos D.A., Barrozo M.A.S., Duarte C.R., Experimental and numerical study of grinding media flow in a mall mill, Chemical Engineering and Technology, 40 (2017) 1835–1843. DOI: 10.1002/ceat.201600508

Marigo M., Stitt E.H., Discrete element method (DEM) for industrial applications: comments on calibration and validation for the modelling of cylindrical pellets, KONA Powder and Particle Journal, 32 (2015) 236–252. DOI: 10.14356/kona.2015016

Marinack Jr. M.C., Musgrave R.E., Higgs C.F., Experimental investigations on the coefficient of restitution of single particles, Tribology Transactions, 56 (2013) 572–580. DOI: 10.1080/10402004.2012.748233

Mellmann J., The transverse motion of solids in rotating cylinders-forms of motion and transition behavior, Powder Technology, 118 (2001) 251–270. DOI: 10.1016/S0032-5910(00)00402-2

Nascimento S.M., Lima R.M., Brandão R.J., Santos D.A., Duarte C.R., Barrozo M.A.S., Comparison between the Eulerian (CFD) and the Lagrangian (DEM) approaches in the simulation of a flighted rotary drum, Computational Particle Mechanics, 9 (2022) 251–263. DOI: 10.1007/s40571-021-00407-z

O'Sullivan C., Particulate Discrete Element Modelling, Particulate Discrete Element Modelling, CRC Press, London, 2011, ISBN: 9780429077517. DOI: 10.1201/9781482266498

Pietsch W, Size Enlargement by Agglomeration, in: Fayed M.E., Otten L.(eds.), Handbook of Powder Science & Technology, Springer New York, 1997, pp. 202–377 ISBN: 9780412996214. DOI: 10.1007/978-1-4615-6373-0

Potyondy D.O., Cundall P.A., A bonded-particle model for rock, International Journal of Rock Mechanics and Mining Sciences, 41 (2004) 1329–1364. DOI: 10.1016/j.ijrmms.2004.09.011

Resende I.A., Machado M.V.C., Duarte C.R., Barrozo M.A.S., An experimental analysis of coffee beans dynamics in a rotary drum, Canadian Journal of Chemical Engineering, 95 (2017) 2239–2248. DOI: 10.1002/cjce.22961

Rong W., Feng Y., Schwarz P., Yurata T., Witt P., Li B., Song T., Zhou J., Sensitivity analysis of particle contact parameters for DEM simulation in a rotating drum using response surface methodology, Powder Technology, 362 (2020) 604–614. DOI: 10.1016/j.powtec.2019.12.004

Salman A.D., Hounslow M.J., Seville J.P.K., Granulation, Handbook of Powder Technology, 1st edition, Elsevier Science, 2006, ISBN: 9780080467887.

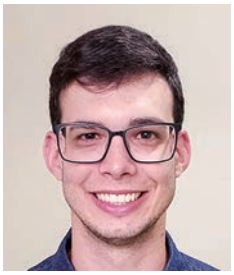
Santos D.A., Barrozo M.A.S., Duarte C.R., Weigler F., Mellmann J., Investigation of particle dynamics in a rotary drum by means of experiments and numerical simulations using DEM, Advanced Powder Technology, 27 (2016) 692–703. DOI: 10.1016/j.apt.2016.02.027

Santos D.A., Dadalto F.O., Scatena R., Duarte C.R., Barrozo M.A.S., A hydrodynamic analysis of a rotating drum operating in the rolling regime, Chemical Engineering Research and Design, 94 (2015) 204–212. DOI: 10.1016/j.cherd.2014.07.028

Santos D.A., Petri I.J., Duarte C.R., Barrozo M.A.S., Experimental and CFD study of the hydrodynamic behavior in a rotating drum, Powder Technology, 250 (2013) 52–62. DOI: 10.1016/j.powtec.2013.10.003

Tsuji Y., Tanaka T., Ishida T., Lagrangian numerical simulation of plug flow of cohesionless particles in a horizontal pipe, Powder Technology, 71 (1992) 239–250. DOI: 10.1016/0032-5910(92)88030-L

Authors' Short Biographies



Rondinelli Moulin Lima

Dr. Rondinelli Moulin Lima received his Ph. D. in Chemical Engineering from the Federal University of Uberlândia in 2021. He has experience in Chemical Engineering, with emphasis on Computational Fluid Dynamics and Discrete Element Method in the area of particulate systems and separation processes. He is currently a researcher at the Institutional Training Program at the Center for Mineral Technology (CETEM), with the development of agglomerated stones.



Gisele Márcia de Souza

MSc. Gisele Márcia de Souza received her master's degree in Metallurgical and Mining Engineering from the Federal University of Minas Gerais. Currently, she is a Ph. D. candidate at the Federal University of Uberlândia in the area of particulate systems and separation processes. She has experience in Chemical Engineering, with emphasis on Transport Phenomena, Unit Operations, Computational Fluid Dynamics and Discrete Element Method.



Rodolfo Junqueira Brandão

Dr. Rodolfo Junqueira Brandão is Adjunct Professor I at the Technology Center at the Federal University of Alagoas. He received his Ph. D. in Chemical Engineering from the Federal University of Uberlândia in 2019. He is currently Coordinator of the Technology Center and Tutor of the Special Engineering Training Program. He works mainly in the area of particulate systems, separation processes and numerical simulation.



Claudio Roberto Duarte

Dr. Claudio Roberto Duarte is a Full Professor at the Federal University of Uberlândia in Brazil. He received his Ph. D. in Chemical Engineering from the Federal University of Uberlândia in 2006. He served as the Coordinator of the Postgraduate Program in Chemical Engineering at the Federal University of Uberlândia from 2019 to 2022. He works mainly on the following topics: granulation, rotating drums, mills, drying, pyrolysis, solid-liquid separation, spouted bed, modelling, computational fluid dynamics, and cyclone.



Marcos Antonio de Souza Barrozo

Dr. Marcos Antonio de Souza Barrozo is a Full Professor at the Federal University of Uberlândia in Brazil. He received his Ph. D. in Chemical Engineering from the Federal University of São Carlos in 1995. He is an A1 researcher at the National Council for Scientific and Technological Development (CNPq) and a member of the Standing Committee of the Brazilian Congress of Particulate Systems. He has experience in Particulate Systems, working mainly on the following topics: fluid dynamics of particulate systems, solid-fluid separation, drying, coating, granulation, flotation, pyrolysis, and hydrothermal carbonization.

KONA Powder and Particle Journal

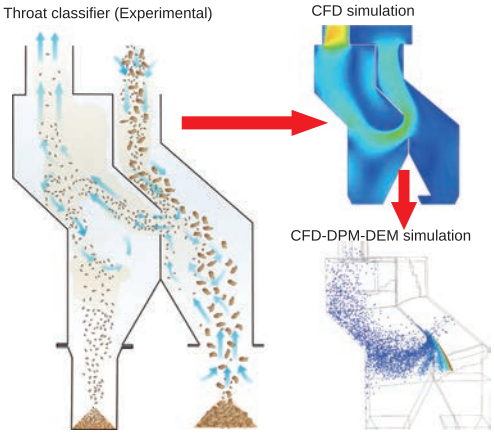
KONA Powder and Particle Journal No. 41 (2024) 242–253/https://doi.org/10.14356/kona.2024006 Original Research Paper

Simulation of the Classification of Manufactured Sands in the Throat Air Classifier†

Horacio A. Petit* and Edgardo Fabián Irassar

The Center for Research in Physics and Engineering of the Center of the Province of Buenos Aires (CIFICEN), Argentina

The scarcity of natural sands has triggered a considerable increase in the consumption of manufactured sands for concrete production. In this regard, particle flaking and excessive fines are the main problems that should be addressed when utilizing manufactured sands. The throat classifier is an air classifier designed for the elimination of fine particles (smaller than 75 micrometers) from manufactured sands. The main features of the classifier have been presented in the literature, but the mechanism that drives the classification has not been studied in detail. Therefore, this work explores the mechanism of classification of the throat classifier by using CFD-DPM and CFD-DEM simulations. The accuracy and limitations of the methodologies were evaluated by comparing the results against experimental data obtained at the pilot scale. The simulations presented fair results in the representation of the airflow and the particle classification inside the throat classifier. Differences between the predictions using CFD-DPM and CFD-DEM methodologies under the simulated conditions were found to be negligible. The results of the simulations allowed for a more detailed understanding of the classification mechanism that occurs inside the device and the influence of operational variables on the equipment performance.



Keywords: manufactured sands, air classification, CFD-DEM, stone dust, aggregates

1. Introduction

The worldwide growth of population and wealth has triggered an increase in the construction of housing, facilities, service cities, and infrastructure. The new urban building environment (drinking water and sanitation, public transport, roads, etc.) is demanding large volumes of building materials such as aggregates, cement, ceramics, lime, gypsum, glass, wood, steel, aluminum, and plastic. The demand for such enormous volumes of natural resources is affecting the sustainability of these industrial sectors (OECD, 2019). Among the building materials, concrete and mortar are the most widely used, both consisting of cement, aggregates, and water. Cement production represents about 5 % of the global CO_2 emissions worldwide. Therefore, the cement and concrete industries are developing new approaches to increase production with a lower carbon footprint and less usage of natural resources. The main goal is to achieve net zero emission by 2050 (GCCA, 2022). Despite cement, aggregates also play an essential role in the eco-efficiency of concrete; nearly 75 % of the concrete volume is represented by coarse and fine aggregates (Tatari and Kucukvar, 2012). Aggregates can be natural (gravel or river sand) or manufactured (crushed stone or manufactured sand). At the beginning of this century, governments and academic communities were on alert about the depletion of natural sources of sand and its increasing scarcity (Torres et al., 2017; UNEP, 2014). Manufactured sands had been found to be an alternative for river sands (Donza et al., 2002; Goncalves et al., 2007); thus, the replacement of natural sands by manufactured sands became an intense research subject ever since.

There are two main shortcomings for the application of manufactured sands in concrete: the particle shape and the high content of dust. Manufactured sands are produced by crushing and sieving during coarse aggregate production. The angular shape (sometimes flaky) of manufactured sand particles causes a low packing density, increasing the water demand and affecting the rheology of the mortar or concrete (Cepuritis et al., 2016; 2017). The content of dust is defined as the percentage of particles smaller than 75 μm in the sands. It increases the water demand for mortar and concrete and enhances other problems such as particulate matter emissions during handling (Petit et al., 2021) and inhomogeneity of the stock due to humidity. The performance of mortar and concrete constituted by manufactured sands can be improved by reducing the content of dust and the

† Received 14 September 2022; Accepted 25 October 2022
J-STAGE Advance published online 3 June 2023
* Corresponding author: Horacio A. Petit;
Add: Pinto 399, 7000, Tandil, Argentina
E-mail: hpetit@fio.unicen.edu.ar
TEL: +54-2284-451055

Copyright © 2024 The Authors. Published by Hosokawa Powder Technology Foundation. This is an open access article under the CC BY license (https://creativecommons.org/licenses/by/4.0/).

flakiness of the sand particles (Ramos et al., 2013). Water-washers are generally used for the elimination of dust. Although water-washers are effective, they have several problems such as unwanted sewage in the quarries, unsellable wastes, final wet products, and a large water footprint (Aasly et al., 2014).

New dry processes, such as magnetic (André et al., 2019) or air classification (Peng et al., 2022), can avoid the use of water for dedusting manufactured sands. A novel classifier, the throat classifier, was explicitly developed for the dedusting of manufactured sands (Petit and Irassar, 2021). Its design focuses on simplicity of operation, reduction of energy consumption, and low maintenance. In this machine, the manufactured sand is fed using a conveyor belt and classified into three products with different gradations. The advantage of this classifier is that the dust extracted from the manufactured sand remains dry and can be stored in a silo for later use as filler in cement, mortar, and concrete (Di Salvo Barsi et al., 2020), or other industrial applications such as filler in the plastic industry (Passaretti et al., 2019; Tawfik et al., 2022). The throat classifier was tested at pilot scale as a replacement for water-washers, giving excellent results (Petit et al., 2018a). However, detailed knowledge about the airflow and particle classification occurring inside the device is needed to improve its design. In this regard, Computational Fluid Dynamics (CFD) and the Discrete Phase Method (DPM) can be used to simulate the airflow and classification mechanism inside the chamber (Petit et al., 2020; Stone et al., 2019). However, this approach has limitations for systems where the concentration of solids is high and particle–particle interactions are of critical importance. The Discrete Element Method (DEM) is similar to the DPM method but takes into account the particle–particle interactions at the micro level, thus representing the bulk behavior of the granular flow (da Cunha et al., 2013).

In this paper, the airflow and particle classification inside the throat classifier were simulated using the CFD-DPM approach. The accuracy and limitations of the simulation methodology were evaluated. Elements of the DEM method were incorporated into the CFD-DPM methodology to compare the results and assess the necessity of modeling particle–particle interactions. The airflow behavior and classification mechanisms inside the throat classifier were studied and visualized by analyzing the simulation results, improving the understanding of the influence of the main operational variables on the classification mechanisms and complementing the knowledge obtained by previous experimental studies.

2. Materials and methods

2.1 Experimental set-up

A scheme of the throat classifier is presented in **Fig. 1** (Petit, 2018; Petit and Irassar, 2021). The classifier presents two classification chambers separated by an inclined plate and a vertical deflector. The right-side chamber is the primary chamber, while the left-side chamber is the secondary chamber. The space between the vertical deflector and the edge of the inclined plate is called the throat and is the region where the primary classification takes place. The primary classification at the throat is performed by an air stream that classifies particles according to its aerodynamic diameter. The airflow that passes through the throat is composed of a main airflow and an auxiliary airflow. The main airflow enters the classifier through the primary inlet at the top of the primary chamber, while the auxiliary airflow enters the classifier through the auxiliary air inlet located at the bottom of the primary chamber. Both, the main and auxiliary airflows, merge at the throat and flow towards the secondary classification chamber. The auxiliary airflow is used to improve the performance of the classifier and its use is optional. Therefore, the auxiliary air inlet can be closed using the adaptable hopper. The manufactured sand enters the classifier through the main air inlet at the top. Sand particles fall by gravity and impact against the inclined plate. Coarse particles bounce after the impact, while fine particles slide over the inclined plate. All particles reach the edge of the inclined plate with different inertia, depending on the segregation and percolation that takes place on the inclined plate. Particles are then classified by the airflow at the throat. Coarse particles are less sensitive to the drag force and fall to the bottom of the primary chamber, while fine particles are dragged by the airflow to the secondary chamber. If the auxiliary airflow is used, coarse particles exit the classifier as the primary product through the primary product outlet. Otherwise, the primary product is collected in the adaptable hopper. The fine particles that were dragged to the secondary chamber experience a secondary classification. The airflow reduces its velocity in the secondary chamber, causing some of the particles to settle at the bottom and to be collected in the secondary hopper as the secondary product of the classification. Particles that did not settle in the secondary chamber exit the classifier with the air and are collected in an auxiliary equipment such as a cyclone classifier or a bag filter. These particles represent the tertiary product of the classification. The performance of the classifier is controlled by adjusting the velocity of the airflow and the position of the vertical deflector. The position of the deflector is characterized by a set of coordinates (d and D) set on the edge of the inclined plate with the y-axis direction pointing downwards, as shown in **Fig. 1**.

2.2 Case studies

Two experimental studies are presented in this work. The first study was performed to characterize the airflow inside the equipment and to obtain validation data to be compared to the results of the CFD simulations. In this regard, the

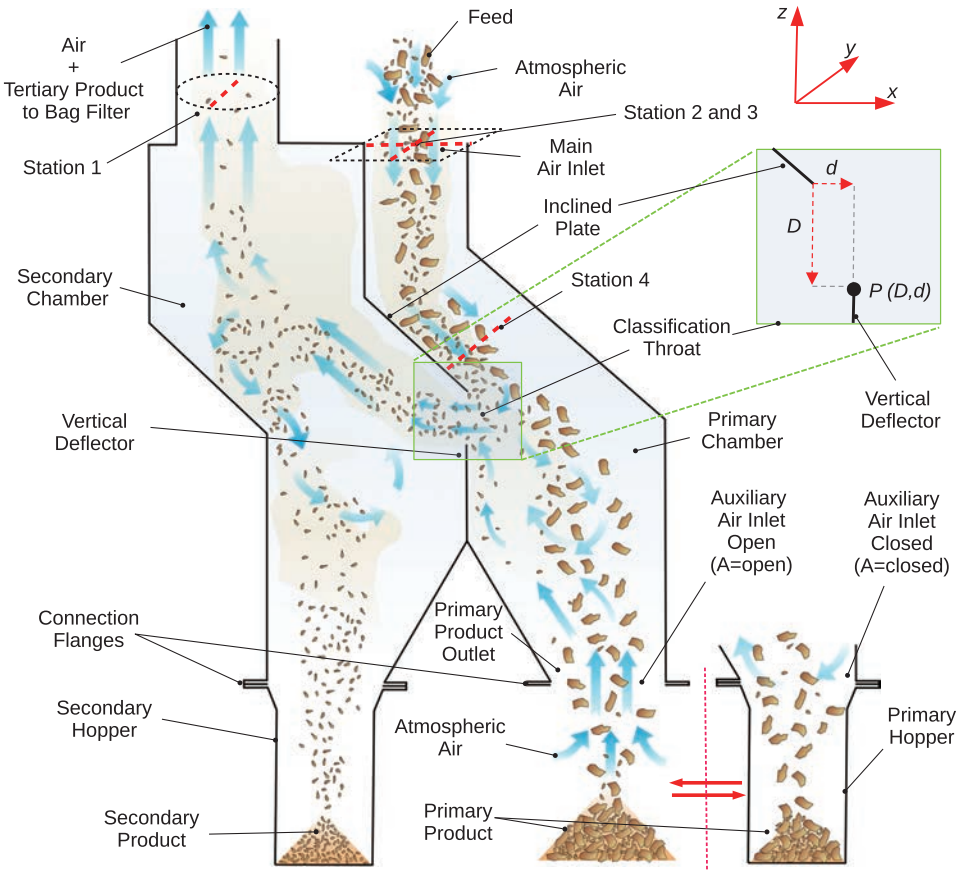


Fig. 1 Scheme of the throat classifier (Petit et al., 2019), and illustration of its main classification mechanism. Stations 1–4 locate the measurements of the air velocity profiles.

main variables of interest are the pressure loss and the air velocity at specific positions inside the equipment. The pressure loss was measured with a differential manometer; the first measurement point was set at the exit tube of the classifier and the second at an arbitrary point outside the equipment. Hence, the pressure loss accounts for the loss of energy inside the equipment and the loss due to the acceleration of the atmospheric air while entering the classifier. The velocity inside the equipment was measured using a Pitot tube. Velocity profiles for the air were measured at four different stations, as presented in **Fig. 1**. Station 1 was set to measure the velocity profile inside the exit tube. Stations 2 and 3 were set at the inlet of the classifier. Station 4 was set perpendicular to the inclined plate, near the throat, in order to study the velocity profile near the classification zone. The measurement of the velocity profile at the throat was not possible due to the relatively large dimensions of the Pitot tube, so only the mean air velocity was measured at the throat.

The second study was carried out to characterize the classification of sand particles using different set-ups for the operational variables of the classifier. The obtained data was then used to validate the results of the CFD-DPM and CFD-DEM simulations. The classification study consisted of three classification cases that differed in the position of the vertical deflector (P), the velocity at the throat (u_{th}), and the utilization of the auxiliary air inlet (A), as presented in **Table 1**. Two different positions were used for the vertical deflector. Position P = 1 is determined by the coordinates D = 0.08 m and d = 0.02 m and position P = 2 by the coordinates D = 0.02 m and d = –0.02 m (**Fig. 1**). Case 1 and 2 differ in the utilization of the auxiliary air inlet, A = closed for case 1, while A = open for case 2. Granitic manufactured sand was used for the study, presenting a solid density of 2630 kg/m^3, a dust content of 14.59 %, and a moisture content of 0.24 %. Compared to the standard limits for fine aggregates in concrete (ASTM C33, 2018) (**Fig. 2**), the manufactured sand presents an excess of material passing the 300 μm. For each case of study, 1 kg of granitic manufactured sand was fed to the classifier at a constant rate of 80 kg/h. After the classification, the primary and secondary products of the classification were characterized by sieving

Table 1 Cases of study for the classification experiences.

Case	Position (P)	u_{th} [m/s]	Aux. Inlet (A)
1	$P1$	3.80	closed
2	$P1$	3.20	open
3	$P2$	7.75	closed

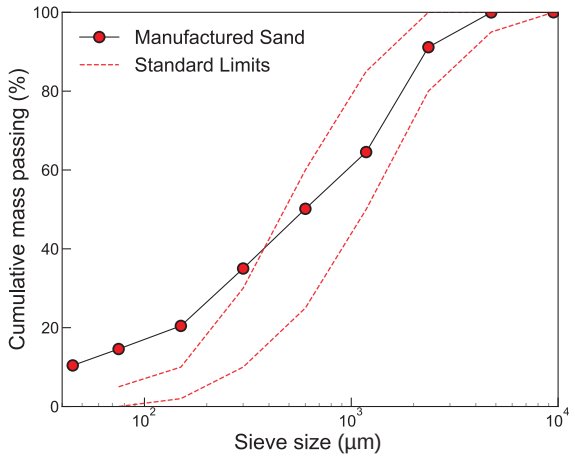


Fig. 2 PSD of the granitic manufactured sand and comparison against the standard limits (ASTM C33, 2018).

analysis. The partition curve and the cut sizes were computed by comparing the particle size distribution (PSD) of the products and the feed. These cases were selected from a more complete study that the reader may find in previous works by the authors (Petit, 2018; Petit and Irassar, 2021).

2.3 Numerical set-up

The numerical method used for the simulation has been used previously by the authors in the simulation of similar air classifiers (Petit and Barbosa, 2017; Petit et al., 2018b, 2020). An overall description of the simulation methodology is presented here, but the reader may find the full description of the model in the supplementary materials. The air was treated as a continuum phase, and the turbulent flow was simulated by solving the Unsteady Reynolds Averaged Navier-Stokes equations. These equations require a closure model for the computation of turbulence, so two different turbulence models were assessed in this work. The first model is the realizable $k - \varepsilon$ model which uses conservation equations for the kinetic turbulent energy (k) and the turbulent dissipation rate (ε). The second model is the Reynolds Stress Model, which is defined by a transport equation for the Reynolds stress tensor.

Particles were modeled as a discrete phase using a Lagrangian reference frame. Particles were grouped to form what is known as parcels, groups of particles with the same size. The trajectory of each parcel was computed in a similar manner as that of a single particle, using the common particle size of the parcel. The positions of all particles that form the parcel were updated based on this trajectory, thus reducing computation time. The mass flow rate of the parcel is given by the number of particles times the mass of the component particles. The trajectories of the parcels were predicted by integrating the force balance, accounting for the gravity and drag forces. Manufactured sand particles present irregular and flaky particles (Rolny et al., 2015; Johansson and Evertsson, 2014); therefore, the drag coefficient was computed using the Haider and Levenspiel model (Haider and Levenspiel, 1989). The shape factor (ratio between the surface area of a sphere having the same volume as the particle and the actual surface area of the particle) was computed using an optical microscope, presenting the mean value of $\phi = 0.7$. The effect of turbulence on the particle trajectories was taken into account by using the Random Walk–Eddy Lifetime model. The discrete phase exchanges momentum with the continuum phase through a momentum source term in the momentum equations of the fluid phase.

Air classifiers are generally operated at low solid concentrations. However, in the case of the throat air classifier, the concentration of particles is high near the inclined plate and the throat. Particle–particle interactions may present an additional influence on the classification mechanism. If relevant, a proper model for the particle–particle interaction should be used. One way to assess the relevance of the particle–particle interactions was proposed by Elghobashi (1994) and then used by Greifzu et al. (2016). The assessment is carried out by defining the volume fraction occupied by the particles (α_p) and the ratio between the particle reaction time (τ_p) to the Kolmogorov (τ_κ). However, the particle-laden flow inside the throat classifier cannot be easily labeled based on these parameters. The concentration of particles is high in the incline plate where most particle–particle collision occurs. The concentration of solids diminishes away from the throat and becomes negligible further away from this region. Moreover, the sizes of the manufactured sand particles range from a few microns to a few millimeters, changing the values of the particle reaction time by four orders of magnitude. The reader may find more details about this assessment in the supplementary materials or in Petit (2018). To summarize: a DEM model was used in order to account for particle–particle interactions and to assess the necessity of a four-way coupled simulation under the tested conditions.

Collisions between particles were computed based on the work of Cundall and Strack (1979). The normal force acting on a particle experiencing a collision was represented by a spring-dashpot model, which is defined by a spring constant (K) and a damping coefficient (γ). The force acting on the second particle was computed using the Newton's third law. On the other hand, the tangential forces were computed by using the Coulomb law of friction, defined by a friction coefficient (μ_f). Collisions between the particles and the geometry were modeled by assuming a coefficient of restitution for the impact, which was decomposed into a normal (C_N) and tangential contribution (C_T). The methodology proposed for the modeling of the particle–particle interactions is an extension of the DPM method that was solved using the built-in capabilities of the CFD solver and presents several limitations such as the lack of particle rotation and rolling friction effects. However, these effects

can be considered secondary when particles are inside a high-velocity flow. Moreover, the calibration of the DEM parameters is not as simple as the calibration of a full DEM method due to the influence of the continuum phase. Therefore, the values of the DEM parameters (**Table 2**) were estimated based on reported values for similar systems (Chu and Yu, 2008; Traoré et al., 2015; Zhou et al., 2014; Boemer and Ponthot, 2016). These values were used in the simulations of different air classifiers, giving fairly realistic results (Petit and Barbosa, 2017; Petit et al., 2018b, 2020).

A mesh independence study was carried out using a coarse, a medium and a fine mesh. Each structured mesh consisted of approximately 3×10^5, 5×10^5, and 7×10^5 elements, respectively. Mesh refinement was done progressively, paying special attention to the region near the throat where the largest gradients of velocity and pressure are present. The pressure-inlet condition was used at the inlet, the air outside the classifier was set to an arbitrary relative static pressure of $P_R = 0$. The same boundary condition was applied at the auxiliary air inlet when it was open. The pressure-outlet boundary condition was used on the outlet face where a negative static pressure was set according to the measured pressure loss of the current case study. The no-slip boundary condition and standard wall functions were used at the walls of the classifier. All simulations were carried out by following the same procedure. First, the CFD simulation of the airflow was performed using a second-order transient solver. The time step used for the fluid equations was $\Delta t = 2 \times 10^{-4}$ s. The simulations were continued until the airflow inside the classifier reached a steady state condition. Secondly, particles were injected into the fluid using the DPM or DEM method. The simulations were resumed, and the trajectories of the particles were updated for every fluid time step using the trapezoidal rule for the temporal integration. In the case of the DEM method, the particle time step was set two orders of magnitude smaller than the fluid time step. The simulations were continued until all particles in the domain escaped or settled in the hoppers. Finally, the positions of the remaining particles were used to calculate the classification efficiency.

Table 2 DEM parameters used in the present work.

Parameter	Units	Value
Spring constant (K)	N/m	1×10^{-5}
Damping coefficient (γ)	—	0.9
Friction coefficient (μ_f)	—	0.3
Normal restitution (C_N)	—	0.3
Tangential restitution (C_T)	—	0.7

3. Results and discussion

3.1 CFD results

The results of the CFD simulations for case 1 are presented in **Fig. 3**, and compared against the measured velocity profiles measured at the four stations. The overall results present a fair agreement with the experimental values. It can be observed that the velocity profile of Station 1 is underpredicted, the utilization of a more refined mesh or a different turbulence model did not improve the results. Compared to the values of Station 1, the profiles obtained in Station 2 and 3 present a better agreement with the experimental values and a better estimation of the velocity. However, the value of the velocity near the walls presents differences with the experimental values, which can be attributed to the limitations of the Pitot tube used for the measurements for such low velocities. In the case of Station 3, the positive values of the velocity near the walls could not be measured with the available measurement device. Similarly to Station 1, the utilization of a refined mesh or the RSM turbulence model did not improve the results in Station 2 and 3. The results for Station 4 present the worst agreement between simulations and experiments. The velocity near the inclined plate is severely underpredicted and the same occurs for distances from the plate ($\ell_\perp$) greater than 0.03 m. A slight improvement in the results is obtained by using a refined mesh but is not sufficient to compensate for the increase in the computational effort. This region of the classifier is of great importance for an accurate modeling of the classification mechanism. The results show that the boundary layer of the flow near the throat, at the end of the inclined plate, is not accurately modeled by using the proposed approach. In addition, the utilization of a more complex turbulence model does not correct this major limitation of the simulation set-up. Other alternatives such as the utilization of different coupling algorithms (PISO instead of SIMPLEC), or different discretization schemes (QUICK scheme instead of second-order upwind scheme) were tested without any improvements (Petit, 2018). A more accurate approach may be to switch the first cell height from $y^+ \approx 30$ to $y^+ \approx 1$ and to resolve the boundary layer instead of modeling it by using wall functions. However, this approach would demand a computational effort that could not be matched by the available computational power at the time of the study. The same stands for the utilization of more complex turbulence models such as LES. Therefore, the limitations of the current methodology were assumed and further simulations were performed using the coarse mesh and the realizable $k - \varepsilon$ model.

The results of the CFD simulations, in terms of the pressure loss for the classifier, are presented in **Fig. 4**. The simulations were performed using the two different positions of the vertical deflector, with and without the auxiliary airflow. For each condition, the simulations were run using: –200, –115, –70, –35 and –10 Pa for the outlet

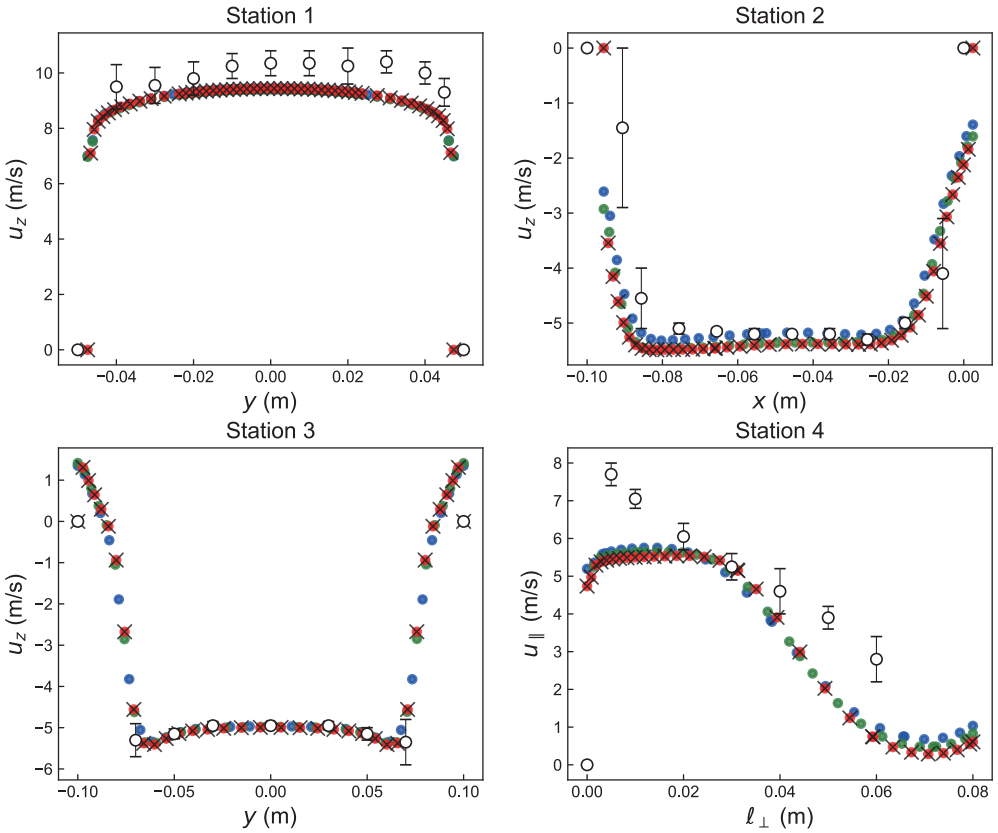


Fig. 3 Comparison between the experimental data (○) and the CFD predictions for case 1, using the coarse (•), medium (•), and fine (•) meshes and the realizable $k-\varepsilon$ turbulence model. Values obtained with the Reynolds stress model and the fine mesh (×) are also presented. Error bars represent minimum and maximum values while $\ell_\perp$ and $u_\parallel$ represent the normal distance to the wall and the velocity parallel to the wall, respectively.

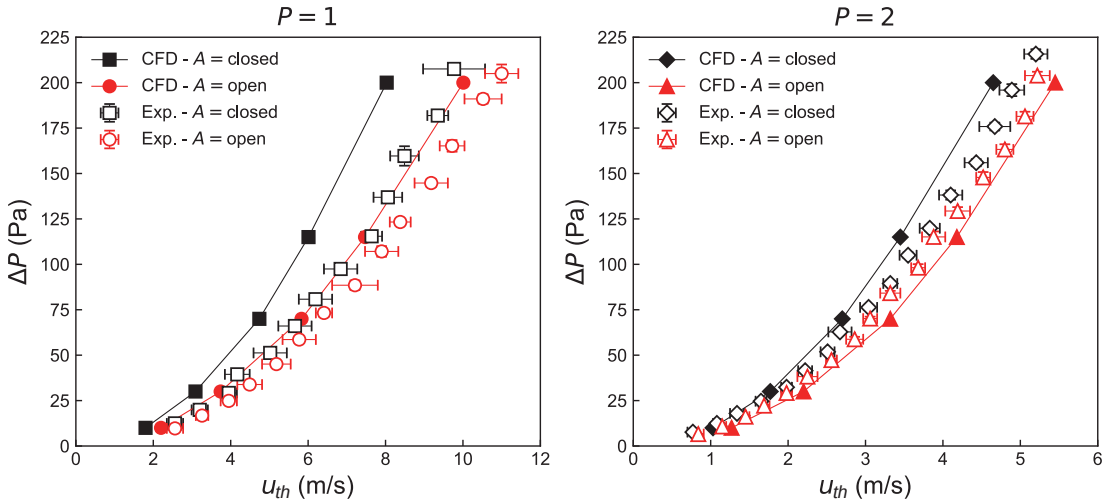


Fig. 4 Comparison between the experimental data and the CFD predictions for the pressure loss for different conditions.

boundary condition. Then, the velocity at the throat was computed for comparison against the experimental values. The simulations results present a fair agreement with the experimental values. Both the experimental and numerical results predict a higher pressure loss when the auxiliary air inlet is closed. The pressure loss obtained by simulations is overpredicted in almost all conditions. For $P = 1$, the pressure loss predicted by CFD is considerably higher than that observed experimentally. These differences are higher when the auxiliary air inlet is closed with errors as high as 20 %. For the same position, the error committed when the auxiliary air inlet is open is smaller, being as high as 14 %. For position $P = 2$, the error is smaller than that observed for position $P = 1$, as high as 5 %. In this position, the simulations overestimate the pressure drop when the auxiliary air inlet is closed and underestimate the loss when

the auxiliary air inlet is open. Fig. 3 shows that the simulation cannot represent in full extent the acceleration of the flow near the throat, which impacts on the conversion of mechanical energy in the flow and the computation of the energy losses. Other sources of error can be attributed to the numerical diffusion, the unresolved boundary layer near the wall and the effect of adverse pressure gradients.

Despite the limitations of the methodology, the utilization of the CFD simulations can be used to gain valuable insights about the behavior of the flow field inside the classifier. Contours of velocity magnitude for different conditions for the airflow inside the classifier are presented in Fig. 5. The results are presented for a pressure boundary condition of –200 Pa, and velocity contours for different pressure conditions presented a self-similar behavior. The trajectory of the airflow inside the classifier can be clearly identified. It can be observed that the behavior of the airflow is different depending on the position of the vertical deflector and the utilization of the auxiliary airflow. Therefore, differences in the classification of particles are expected due to the different flow behavior. For position $P = 1$ and the auxiliary air inlet closed, the airflow enters at the primary inlet and accelerates towards the throat. The airflow reaches the end of the inclined plate and changes its direction almost 180°, describing a U-shaped trajectory and entering the secondary chamber. Secondary flows can be observed near the main flow on both sides of the vertical deflector, which are stronger in the secondary chamber and may affect the secondary classification. For position $P = 2$, the velocity patterns are similar to those observed for position $P = 1$. However, the change of direction at the throat for position $P = 2$ is more abrupt. The air still changes its direction about 180° but the radius of the swirl is smaller than that observed for position $P = 1$. The flow area of the throat is smaller for position $P = 2$; therefore, the air velocity is higher.

The utilization of the auxiliary airflow modifies the flow pattern, as the contribution of the ascending stream of air in the primary chamber decreases the contribution of the primary airflow entering at the top. Both streams merge at the throat as expected. However, the trajectory of the airflow entering the secondary chamber changes with the presence of the auxiliary airflow. In the case of position $P = 1$, the air entering the secondary chamber describes a smoother trajectory when the auxiliary airflow is present. In addition, the presence of secondary flows in the secondary chamber is reduced, thus expecting a cleaner secondary classification. These changes are not as clear for position $P = 2$; nonetheless, the influence of the auxiliary airflow on the velocity pattern at the throat can still be observed. The upward auxiliary airflow at the bottom of the primary chamber suggests that particles that could not be classified at the throat may experience a second counter-current classification in this region; therefore, improving the classifier performance.

The velocity contours show that the main pressure loss is due to the strangulation of the airflow at the throat. Therefore, position $P = 2$, with a smaller flow area presents higher pressure drops than that observed for position $P = 1$. The utilization of the auxiliary airflow reduces the swirl intensity of the flow at the throat; therefore, cases with the auxiliary air inlet open present less energy dissipation and lower pressure losses. In this regard, the conclusions drawn from the observation of the velocity contours match the trends in the experimental values presented in Fig. 4.

3.2 CFD-DPM and CFD-DEM results

Snapshots of the position of the particles, obtained by CFD-DPM simulations, for the three case studies are presented in Fig. 6. It can be observed that the feed (sand) falls

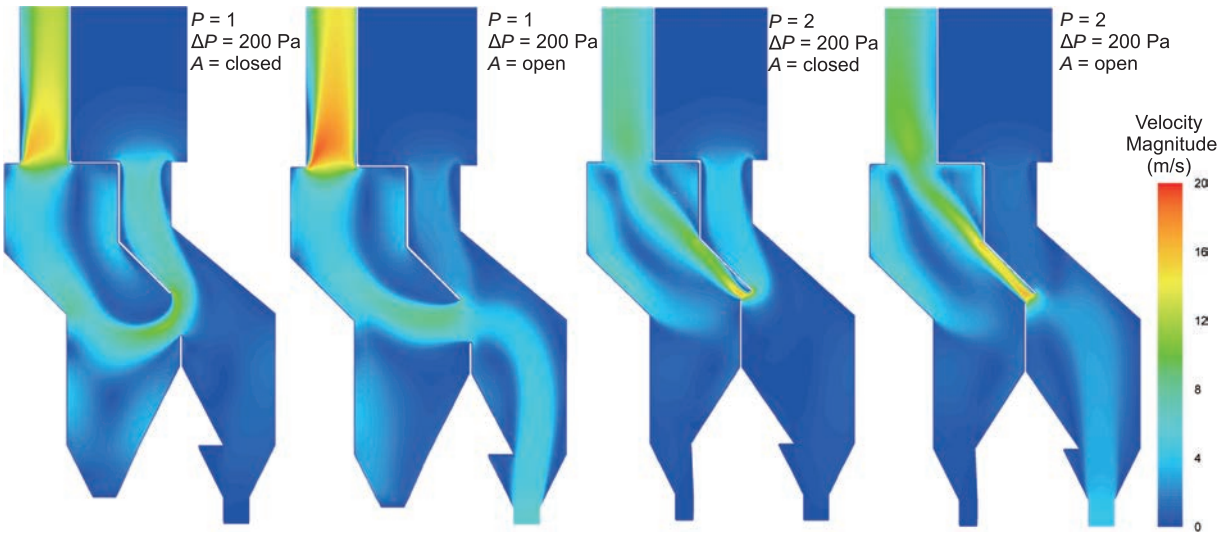


Fig. 5 Contours of velocity magnitude for the throat classifier for two different positions of the vertical deflector ($P = 1$ and $P = 2$), with and without the utilization of the secondary air inlet (A = open and A = closed, respectively).

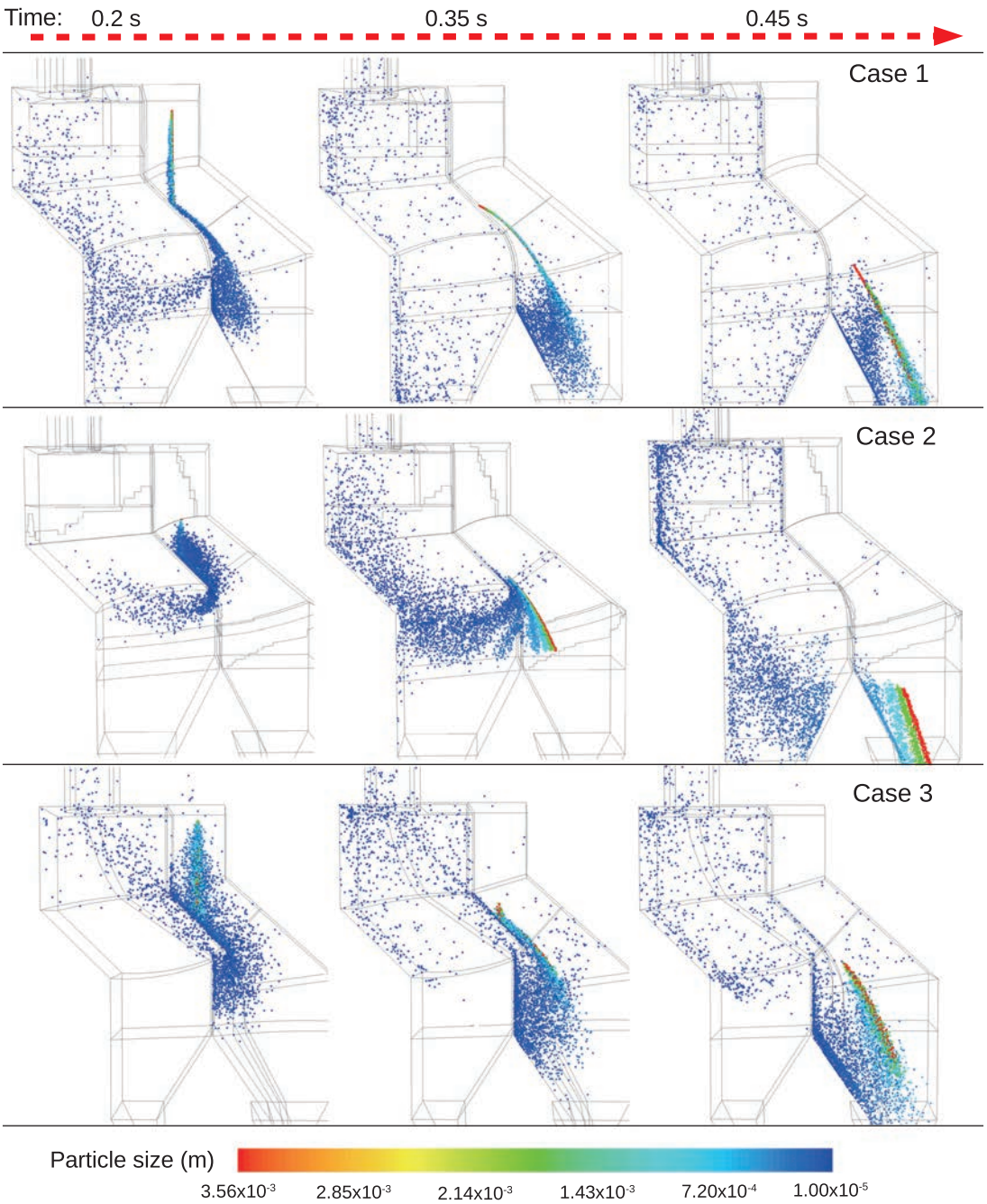


Fig. 6 Snapshots of the particle positions inside the classifier at different times after the injection.

through the inlet creating a curtain of particles. The behavior of the feed varies depending on the flow conditions. It can be observed in cases 1 and 3 that after entering the classifier, fine particles are dragged by the airflow and reach the end of the inclined plate before coarse particles. This behavior is observed in cases 1 and 3 where the auxiliary air inlet is closed and the primary airflow moves downward with high velocity. On the other hand, the auxiliary air inlet is open in case 2 and the contribution of the primary air inlet is less intense. Thus, the segregation of fine particles due to the high velocity of the primary airflow in case 2 is not as clear as in cases 1 and 3.

After falling, particles bounce against the inclined plate and change the direction of their trajectories. It was found experimentally that the trajectory after the impact depends on the particle size and shape. Coarse particles present more inertia than fine particles and are less affected by the drag force (Petit and Irassar, 2021; Petit, 2018). Moreover, fine particles present more flaky shapes, increasing the drag force and forcing them to follow the airflow. This behavior is only partially represented in the simulations. The main issue regarding the current simulation set-up is that particles of different sizes share a single coefficient of restitution and shape factor. However, the effect of the drag on the particle is modeled sufficiently well to recreate the different trajectories after the impact. The differences in

the trajectories for different particle sizes are more clearly observed in case 2, where the auxiliary air inlet is open.

The classification of particles at the throat can be observed in the three simulated cases. Fine particles near the throat are dragged by the air and pass to the secondary chamber. Particles that cannot follow the air impact against the vertical deflector, which agrees with the large amount of particles found in the deflector after the experimental runs (Petit, 2018). Cases 1 and 3, where only the primary airflow is used, present a more abrupt change in the flow direction, and fewer particles are able to pass to the secondary chamber. On the other hand, the presence of the auxiliary airflow modifies the flow at the throat (as seen in **Fig. 5**), reducing the intensity of the swirl and forcing more particles to pass to the secondary chamber. Therefore, the utilization of the auxiliary air inlet increases the cut size of the primary classification. After passing to the secondary chamber, some particles settle into the secondary hopper, while others exit the classifier. As expected from the flow visualizations presented in **Fig. 5**, the auxiliary airflow allows a more ordered classification in the secondary chamber. On the other hand, the strong secondary flows in cases 1 and 3 disperse the particles, making the settlement more difficult. The effect of the auxiliary airflow can also be observed at the bottom of the primary chamber in case 2. The auxiliary airflow enters the classifier at the bottom and flows upwards, dragging fine particles that were kept in the bulk of the coarser particles and could not pass through the throat to the secondary chamber.

The prediction of the CFD-DPM and CFD-DEM simulations in terms of the particle size distribution of the products is presented in **Fig. 7**, where the standard limits are presented in the plot for reference. The yield of the products and the values of the cut sizes for the three cases of study are presented in **Fig. 8** and **Fig. 9**, respectively. It can be observed that the PSD of the primary product is accurately estimated by the simulations, with a slight under prediction observed in case 2. On the contrary, the PSD of the secondary and tertiary products is not as well described as for the primary products. An exception occurs in case 2 where the overall results for the PSD are in fair agreement with experimental values for all products. The results indicate that the simulation methodologies are able to describe the main classification mechanism that takes place in the primary chamber but not the secondary classification in the secondary chamber. The results in **Fig. 8** support this affirmation, the yield of the primary product is well estimated in all the three cases, while errors appear for the yields of the secondary and tertiary products. The same can be observed in **Fig. 9**, where the primary cut size (x_{50}) is in better agreement with the experimental values than that observed for the secondary cut size (y_{50}).

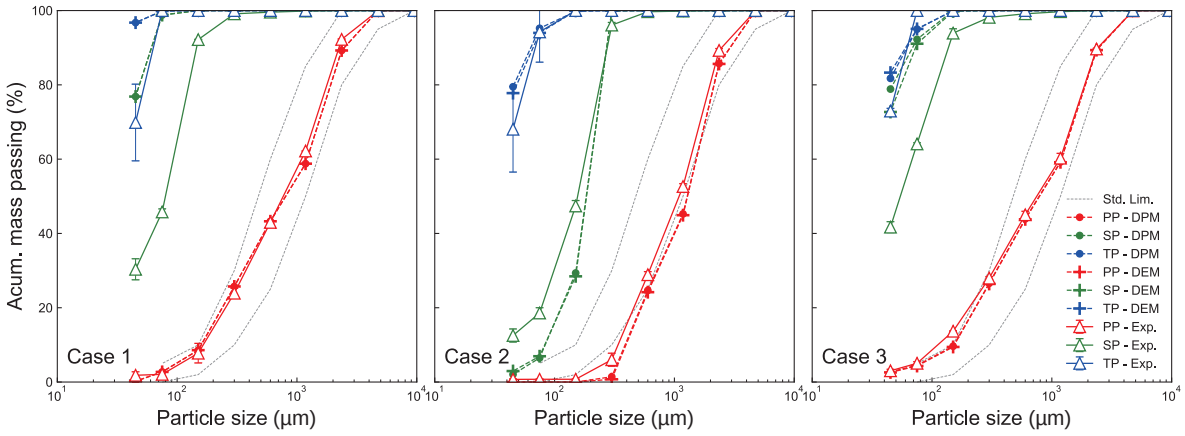


Fig. 7 PSDs of the primary (PP), secondary (SP), and tertiary (PP) products obtained experimentally or by simulations.

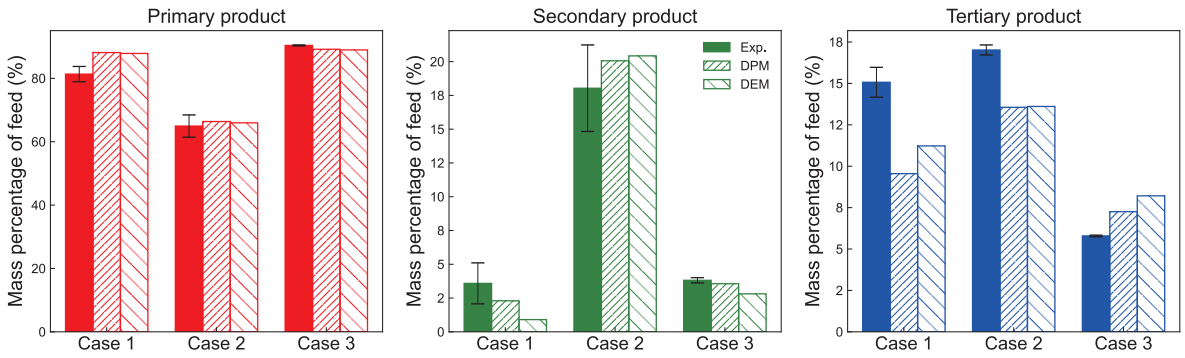


Fig. 8 Yield of the products of classification and comparison against the CFD-DPM and CFD-DEM results.

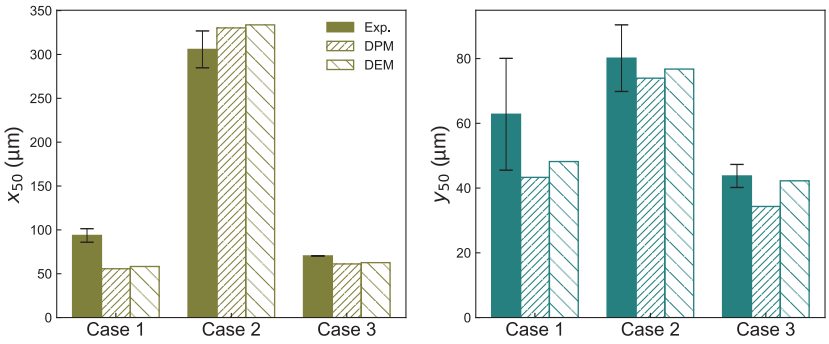


Fig. 9 Cut sizes of the classification and comparison against the CFD-DPM and CFD-DEM results. Variables x_{50} and y_{50} represents the primary and secondary cut sizes, respectively.

The limitations of the CFD-DPM methodology were tested by fine-tuning some parameters such as the coefficient of restitution (C_N), the shape factor (ϕ), and the Lagrangian time coefficient (C_L) of the particles. The results of the procedure are omitted here for brevity but can be found in Petit (2018). In summary, reducing the values of the coefficient of restitution and increasing the value of the Lagrangian time coefficient slightly improved the results. However, it was found that the increase in the accuracy of the representation of the secondary classification deprecated the representation of the primary classification. This shows that one of the major limitations of the methodology is the impossibility of using size-dependent parameters. In addition, the utilization of more classes to represent the PSD of the feed was tested without any significant changes with the exception of more computational effort. The influence of the Lagrangian coefficient, which dominates the particle dispersion due to turbulent effects, suggests that the turbulent dispersion of the particles is not correctly modeled. The results support this assumption, as case 2 presents the best agreement with the experimental values, being the case that was found to present a less turbulent airflow in the secondary chamber (**Fig. 5**) and a more ordered secondary classification (**Fig. 6**).

The utilization of the CFD-DEM methodology does not present any improvements over the CFD-DPM methodology. Only minor differences in the PSD of the products, the cut sizes, and the yield of the products were observed between the two methodologies. In the case of the cut sizes, all predictions using the CFD-DEM method present a coarser cut size, for both the primary and secondary classifications. In any case, the increase in the computational demand for the utilization of the DEM method does not bring an increase in the accuracy of the simulations for the concentrations of solid used in this study. It is clear that the limitations of the simulation are associated with the modeling of the fluid–particle interaction and not with the particle–particle interactions.

Despite the limitations, the simulations gave a good description of the primary classification in the different cases and offered predictions of the influence of the position of the deflector and the auxiliary airflow. Regarding the auxiliary airflow, the simulations showed that the upstream airflow at the bottom of the primary chamber in case 2 (**Fig. 5**) enables a better classification of the particles (**Fig. 6**), resulting in a coarser primary product (**Fig. 7**) and a greater primary cut size (**Fig. 9**). Regarding the position of the vertical deflector, the CFD simulation described the complexity of the swirl that occurs in the throat in case 3 (**Fig. 5**) and the finer classification that occurs due to the more abrupt change of direction in the airflow (**Fig. 6**). Thus, resulting in finer particles in the primary product (**Fig. 7**) and a lower primary cut size (**Fig. 9**).

4. Conclusions

The airflow inside the throat classifier was simulated by using the CFD methodology. The overall results showed that the simulation provided fair predictions of the airflow behavior with some limitations regarding the description of velocity profiles in some locations. Changing the turbulence models or numerical schemes did not improve the results.

Simulations of particle classification were performed using both CFD-DPM and CFD-DEM methodologies. The simulations showed reasonable results in the representation of the overall performance of the classifier and excellent results in describing the primary classification products. The utilization of the DEM method did not bring any improvements in the accuracy of the simulations. The major limitations of the simulation methodology, for the concentration of solids used in this study, reside in the modeling of the fluid–particle interactions.

Despite these limitations, the simulation methodology allowed for an explanation of the previously collected experimental results. Valuable information was gathered regarding the description of the airflow inside the classifier which explains the mechanisms of particle classification that occur inside the device. In addition, the utilization of the simulations allowed to study in detail the influence of operational variables on the performance of the classifier,

such as the position of the vertical deflector and the utilization of the auxiliary air inlet.

Nomenclature

CFD	Computational Fluid Dynamics
DEM	Discrete Element Method
DPM	Discrete Phase Method
PP	Primary product
PSD	Particle size distribution
SP	Secondary product
TP	Tertiary product
A	Opening of the auxiliary air inlet (-)
C_L	Lagrangian time constant (-)
C_N	Normal coef. of restitution (-)
C_T	Tangential coef. of restitution (-)
D	Vertical position of deflector (m)
d	Horizontal position of deflector (m)
K	Spring constant (N/m)
k	Turbulent kinetic energy (m^2/s^2)
$\ell_\perp$	Normal distance to the wall (m)
P	Position of the vertical deflector (-)
P_R	Relative static pressure (Pa)
u_i	Velocity components (m/s)
u_{th}	Fluid velocity at the throat (m/s)
$u_\parallel$	Velocity parallel to the wall (m/s)
x, y, z	Cartesian coordinates (m)
x_{50}	Primary cut size (m, μm)
y^+	Wall dimensionless distance (-)
y_{50}	Secondary cut size (m, μm)
α_p	Volume fraction of particles (-)
Δt	Time step (s)
ΔP	Pressure loss (Pa)
γ	Damping coefficient (kg/s)
ε	Turbulent dissipation rate (m^2/s^3)
ϕ	Particle shape factor (-)
τ	Particle relaxation time (s)
τ_p	Particle reaction time (s)
τ_κ	Kolmogorov time scale (s)

Data Availability Statement

The data from the comparison between experimental and numerical investigation of the throat air classifier is available publicly in J-STAGE Data (https://doi.org/10.50931/data.kona.23272763).

References

Aasly A.K., Danielsen S., Wigun J., Norman S.H., Cepuritis R., Onnela T., Review report on dry and wet classification of filler materials for concrete, COIN Project report, 52 (2014).

André F.P., Miceli H., Moura L.C., Neumann R., Tavares L.M., Upgrading a manufactured fine aggregate for use in concrete using dry rare-earth magnetic separation, Minerals Engineering, 143 (2019) 105942. DOI: 10.1016/j.mineng.2019.105942

ASTM C33, Standard Specification for Concrete Aggregates, ASTM International, 2018. DOI: 10.1520/C0033_C0033M-18

Boemer D., Ponthot J.P., DEM modeling of ball mills with experimental validation: influence of contact parameters on charge motion and power draw, Computational Particle Mechanics, (2016) 1–15. DOI: 10.1007/s40571-016-0125-4

Cepuritis R., Jacobsen S., Pedersen B., Mørtsell E., Crushed sand in concrete – effect of particle shape in different fractions and filler properties on rheology, Cement and Concrete Composites, 71 (2016) 26–41. DOI: 10.1016/j.cemconcomp.2016.04.004

Cepuritis R., Jacobsen S., Smeplass S., Mørtsell E., Wigum B.J., Ng S., Influence of crushed aggregate fines with micro-proportioned particle size distributions on rheology of cement paste, Cement and Concrete Composites, 80 (2017) 64–79. DOI: 10.1016/j.cemconcomp.2017.02.012

Chu K., Yu A., Numerical simulation of complex particle–fluid flows, WCPT5 Papers presented at the 5th World Conference of Particle Technology (WCPT5), Orlando, Florida, April 23–27 2006, 5th World Conference of Particle Technology (WCPT5), 179 (2008) 104–114. DOI: 10.1016/j.powtec.2007.06.017

Cundall P.A., Strack O.D.L., A discrete numerical model for granular assemblies, Géotechnique, 29 (1979) 47–65. DOI: 10.1680/geot.1979.29.1.47

da Cunha E.R., de Carvalho R.M., Tavares L.M., Simulation of solids flow and energy transfer in a vertical shaft impact crusher using DEM, Minerals Engineering, 43–44 (2013) 85–90. DOI: 10.1016/j.mineng.2012.09.003

Di Salvo Barsi A., Trezza M.A., Irassar E.F., Comparison of dolostone and limestone as filler in blended cements, Bulletin of Engineering Geology and the Environment, 79 (2020) 243–253. DOI: 10.1007/s10064-019-01549-4

Donza H., Cabrera O., Irassar E., High-strength concrete with different fine aggregate, Cement and Concrete Research, 32 (2002) 1755–1761. DOI: 10.1016/S0008-8846(02)00860-8

Elghobashi S., On predicting particle-laden turbulent flows, Applied Scientific Research, 52 (1994) 309–329. DOI: 10.1007/BF00936835

GCCA (Global Cement and Concrete Association) , 2050 Net Zero Roadmap Accelerator Program, 2022. <https://gccassociation.org/netzeroaccelerator/> accessed11052023.

Gonçalves J., Tavares L., Toledo Filho R., Fairbairn E., Cunha E., Comparison of natural and manufactured fine aggregates in cement mortars, Cement and Concrete Research, 37 (2007) 924–932. DOI: 10.1016/j.cemconres.2007.03.009

Greifzu F., Kratzsch C., Forgber T., Lindner F., Schwarze R., Assessment of particle-tracking models for dispersed particle-laden flows implemented in OpenFOAM and ANSYS FLUENT, Engineering Applications of Computational Fluid Mechanics, 10 (2016) 30–43. DOI: 10.1080/19942060.2015.1104266

Haider A., Levenspiel O., Drag coefficient and terminal velocity of spherical and nonspherical particles, Powder Technology, 58 (1989) 63–70. DOI: 10.1016/0032-5910(89)80008-7

Johansson R., Evertsson M., CFD simulation of a centrifugal air classifier used in the aggregate industry, Computational Modelling, 63 (2014) 149–156. DOI: 10.1016/j.mineng.2014.03.013

OECD, Global Material Resources Outlook to 2060 Economic Drivers and Environmental Consequences, OECD publishing, 2019. DOI: 10.1787/9789264307452-en

Passaretti M.G., Ninago M.D., Paulo C.I., Petit H.A., Irassar E.F., Vega D.A., Villar M.A., López O.V., Biocomposites based on thermoplastic starch and granite sand quarry waste, Journal of Renewable

Materials, 7 (2019) 393–402. DOI: 10.32604/jrm.2019.04281
Peng S., Wu Y., Tao J., Chen J., Airflow velocity designing for air classifier of manufactured sand based on CPFD method, Minerals, 12 (2022) 90. DOI: 10.3390/min12010090
Petit A., Cordoba G., Paulo C.I., Irassar E.F., Novel air classification process to sustainable production of manufactured sands for aggregate industry, Journal of Cleaner Production, 198 (2018a) 112–120. DOI: 10.1016/j.jclepro.2018.07.010
Petit H., Barbosa M., Simulación de un clasificador de polvo de flujo cruzado con altos contenidos de polvo, Revista Internacional de Métodos Numéricos para Cálculo y Diseño en Ingeniería, 33 (2017) 262–270. DOI: 10.1016/j.rimni.2016.06.003
Petit H.A., Diseño de separadores de partículas finas empleando modelización de flujos complejos, Ph.D. thesis, Universidad Nacional del Centro de la Provincia de Buenos Aires, 2018. Olavarría - Argentina. http://hdl.handle.net/11336/93493
Petit H.A., Irassar E.F., The throat classifier: a novel air classifier for the control of dust in manufactured sands, Powder Technology, 390 (2021) 417–427. DOI: 10.1016/j.powtec.2021.05.049
Petit H.A., Irassar E.F., Barbosa M.R., Evaluation of the performance of the cross-flow air classifier in manufactured sand processing via CFD-DEM simulations, Computational Particle Mechanics, 5 (2018b) 87–102. DOI: 10.1007/s40571-017-0155-6
Petit H.A., Irassar E.F., Barbosa M.R., Desempolvador de arena triturada mediante via seca, Patent (2019) AR110376A1. https://patents.google.com/patent/AR110376A1
Petit H.A., Paulo C.I., Cabrera O.A., Irassar E.F., Modelling and optimization of an inclined plane classifier using CFD-DPM and the Taguchi method, Applied Mathematical Modelling, 77 (2020) 617–634. DOI: 10.1016/j.apm.2019.07.059
Petit H.A., Paulo C.I., Cabrera O.A., Irassar E.F., Evaluation of the dustiness of fugitive dust sources using gravitational drop tests, Aeolian Research, 52 (2021) 100724. DOI: 10.1016/j.aeolia.2021.100724
Ramos T., Matos A.M., Schmidt B., Rio J., Sousa-Coutinho J., Granitic quarry sludge waste in mortar: effect on strength and durability, Construction and Building Materials, 47 (2013) 1001–1009. DOI: 10.1016/j.conbuildmat.2013.05.098
Rolny D., Sovarso L., Cruz Palma J., Coyoupetrou L., Cremaschi G., Etcheverry R., Forte L., Estudio Preliminar de la Forma, Textura Superficial y Distribución del Tamaño de Partículas de Arenas de trituración, in: Actas del Segundo Congreso Argentino de Aridos, San Isidro, 2015, pp. 233–240.
Stone L., Hastie D., Zigan S., Using a coupled CFD–DPM approach to predict particle settling in a horizontal air stream, Advanced Powder Technology, 30 (2019) 869–878. DOI: 10.1016/j.apt.2019.02.001
Tatari O., Kucukvar M., Eco-efficiency of construction materials: data envelopment analysis, Journal of Construction Engineering and Management, 138 (2012) 733–741. DOI: 10.1061/(ASCE) CO.1943-7862.0000484
Tawfik M.E., Eskander S.B., Ahmed N.M., Potential applications of granite waste powder as an add-value polymer composite product, Polymers and Polymer Composites, 30 (2022) 09673911221110138. DOI: 10.1177/09673911221110138
Torres A., Brandt J., Lear K., Liu J., A looming tragedy of the sand commons, Science, 357 (2017) 970–971. DOI: 10.1126/science.aao0503
Traoré P., Laurentie J.C., Dascalescu L., An efficient 4 way coupling CFD–DEM model for dense gas–solid particulate flows simulations, Computers & Fluids, 113 (2015) 65–76. DOI: 10.1016/j.compfluid.2014.07.017
UNEP (United Nations Environment Programme), Sand, rarer than one thinks: UNEP global environmental alert service (GEAS) , 2014. <https://wedocs.unep.org/20.500.11822/8665> accessed11052023.
Zhou F., Hu S., Liu Y., Liu C., Xia T., CFD–DEM simulation of the pneumatic conveying of fine particles through a horizontal slit, Particuology, 16 (2014) 196–205. DOI: 10.1016/j.partic.2014.03.015

Authors' Short Biographies



Horacio A. Petit

Horacio Andrés Petit is a Chemical Engineer and obtained a Ph.D. in Engineering at the Universidad Nacional del Centro de la Provincia de Buenos Aires. Worked as a postdoc research assistant at the Universidade Federal de Rio de Janeiro (UFRJ). Now works as a researcher at the CIFICEN research unit (UNCPBA - CICPBA - CONICET). His research interests are the design and simulation of mineral processing units. His works focuses on the utilization of CFD and DEM methods for the simulation of air classifiers and other mineral processing equipment.



Edgardo Fabián Irassar

Edgardo F Irassar is a Full Professor of Civil Engineering Department at the Universidad Nacional del Centro de la Provincia de Buenos Aires, Olavarria, Argentina. He is Head of the INMAT Research Group of the Engineering Faculty and Vice Chair of the CIFICEN Research Unit (UNCPBA - CICPBA - CONICET). His research interests are the cementitious building materials (Concrete, mortar, cement) for sustainable concrete including durability, new supplementary cementing materials, aggregates beneficiation, recarbonatation and LCA evaluation.

KONA Powder and Particle Journal

KONA Powder and Particle Journal No. 41 (2024) 254–264/https://doi.org/10.14356/kona.2024007 Original Research Paper

The Mechanism behind Vibration Assisted Fluidization of Cohesive Micro-Silica†

Rens Kamphorst*, P. Christian van der Sande, Kaiqiao Wu*, Evert C. Wagner, M. Kristen David, Gabrie M.H. Meesters and J. Ruud van Ommen

Department of Chemical Engineering, Delft University of Technology, The Netherlands

Vibro-assisted fluidization of cohesive micro-silica has been studied by means of X-ray imaging, pressure drop measurements, and off-line determination of the agglomerate size. Pressure drop and bed height development could be explained by observable phenomena taking place in the bed; slugging, channeling, fluidization or densification. It was observed that channeling is the main cause of poor fluidization of the micro-silica, resulting in poor gas-solid contact and little internal mixing. Improvement in fluidization upon starting the mechanical vibration was achieved by disrupting the channels. Agglomerate sizes were found to not significantly change during experiments.

Keywords: fluidized bed, X-ray imaging, agglomeration, assistance methods, cohesive powder



1. Introduction

Fluidization of cohesive powders has seen significant interest in the last decades, fueled by the increase in applications of powders with small particle sizes. Cohesive micro- and nanopowders find their use in medical applications (Prabhu and Poulose, 2012; Guo et al., 2013), catalysis (Li et al., 2003) and coatings (Mahato and Cho, 2016) for example.

Due to their small particle size, the attractive van der Waals forces between these particles are dominant, in the absence of moisture, making them hard to fluidize (Kamphorst et al., 2023). Two main complications are seen: channeling and agglomeration. Channeling is the phenomenon where a gas bypass, or channel, is formed through the bed in the vertical direction upon the introduction of gas. Gas mainly flowing through a channel has poor interaction with the powder bed, meaning less drag is created and no fluidization takes place. Agglomeration is the formation of particle clusters as a result of dominant cohesive forces. Whereas agglomerates can sometimes be fluidized without assistance (Morooka et al., 1988), gas-solid contact is reduced due to the surface area of particles being inside the agglomerate and gas mostly passing outside of it, with diffusion into the agglomerates pores. A phenomenon that is also sometimes observed, at startup, for cohesive powder is slugging or plugging, here the entire bed is pushed up through the fluidization column. While one could argue this to be a third complication of cohesive powder fluidization, we consider this an extreme form of agglomeration, where the entire bed acts as one large cluster. Slugging is typically not seen in industrial-scale beds.

In order to fluidize cohesive powders, assistance methods can be employed, which introduce an additional manipulation. For most assistance methods it was concluded, by one or more studies, mostly done on nano-particles, that the mechanism by which fluidization was improved is by breaking up agglomerates; mechanical vibration (Nam et al., 2004; Barletta and Poletto, 2012), acoustic vibration (Guo et al., 2006), magnetic field (Zhou et al., 2013), stirring (Zhang et al., 2021), micro-jet (Quevedo and Pfeffer, 2010; Nasri Lari et al., 2017) and pulsed flow (Al-Ghurabi et al., 2020; Ali et al., 2016; Ali and Asif, 2012). This conclusion is based on smaller agglomerate sizes being measured in beds that have been fluidized, using an assistance method, than one that could not be fluidized. However, the mechanism of agglomerate breakage should be taken into account. First of all, they can break as a result of collisions, either with other agglomerates or with the column wall. However, in an unfluidized bed, agglomerates will be (mostly) static, meaning no collisions take place. Another way for agglomerates to decrease in size is due to shear with the fluidizing gas, though simulations for nanoparticle fluidization have shown this effect to be minor, even at high gas velocities (van Ommen et al., 2010). For this to happen at a significant scale, there should be significant gas-solid contact, which is also absent before fluidization is initiated.

Based on this, we hypothesize that agglomerates break as a result of initiated fluidization, but this agglomerate

† Received 4 November 2022; Accepted 24 February 2023
J-STAGE Advance published online 17 June 2023
* Corresponding authors: Rens Kamphorst and Kaiqiao Wu;
Add: van der Maasweg 9, Delft, The Netherlands
E-mail: R.Kamphorst@tudelft.nl (R.K.); K.Wu-3@tudelft.nl (K.W.)
TEL: +31 (0)15 27 89806 (R.K.); +31 (0)15 27 89806 (K.W.)

Copyright © 2024 The Authors. Published by Hosokawa Powder Technology Foundation. This is an open access article under the CC BY license (https://creativecommons.org/licenses/by/4.0/).

breakage is not the cause of the improvement. Rather than agglomeration, we propose channeling is the major hurdle to overcome to achieve fluidization of cohesive powders. By introducing additional manipulation, from an assistance method, the channels can be destabilized and will collapse. Note that mechanical vibration, acoustic vibration, magnetic fields, pulsed flow, stirring, and a (micro-)jet all introduce additional motion of gas, column or internals into the bed, providing a mechanism by which the channeling can be disrupted. In the absence of channels, all fluidizing gas has to flow through the bed, creating drag. When sufficiently large drag is created, the particles or agglomerates will be fluidized. This reasoning leaves one to conclude that the best assistance methods are not the ones that are best at breaking agglomerates, but those which most effectively destroy channels. For further development and optimization of assistance methods, it is essential to have a complete understanding of the mechanism by which the fluidization is improved.

Characterization of the fluidization quality is often done by measuring bed height expansion and pressure drop (Nam et al., 2004; Barletta and Poletto, 2012; Mawatari et al., 2003). These two measurements alone are insufficient when it comes to analyzing the cause of poor fluidization. Visualization of the temporal evolution of hydrodynamics, going from poor fluidization with channeling to bubbling fluidization under the influence of an assistance method, could provide a better understanding of the mechanism. Simple optical techniques that are typically used to visualize hydrodynamics in two-phase systems are, however, limited to acquiring information close to the wall region, because the large solid fraction of the dispersion phase makes the dense flow opaque to visible light. X-ray imaging, on the other hand, has been demonstrated to be a valuable technique to study dynamics in opaque systems, such as fluidized beds with nanoparticles (Gómez-Hernández et al., 2017), irregular particles (Mema et al., 2020), sintering (Macrì et al., 2020) internals (Maurer et al., 2015; Helmi et al., 2017), and spouts (Barthel et al., 2015).

This study aims to characterize the hydrodynamics of a gas-solid fluidized bed, consisting of cohesive micro-silica, with and without vibration applied to it. This is done by means of X-ray imaging, pressure drop, and bed height extension measurements. Channel formation and disruption are shown and agglomerate sizes are measured to elucidate the mechanism behind the employed assistance method.

2. Experimental and methodology

2.1 Fluidization procedure

A Perspex column with an inner diameter of 9 cm and sample ports at 2.5, 6.5, and 13.5 cm from the distributor plate was used as the fluidized bed column. The pressure drop was measured from the surface of the distributor plate to the breakout box, using OMEGA PX409-10WG5V pressure transducers. The static pressure of the powder was 2.3 mbar (2.3×10^2 Pa) for all experiments. The column was mounted on a vibration table, a frequency of 30 Hz and a vertical amplitude of 1 mm was used for all experiments with vibration. For this study, two gas velocities were used, 1.8 and 3.1 cm s^{-1}. During the X-ray experiments, a remotely controlled camera was used to capture images of the column from which the bed height was measured.

The used powder, Köstropur 050818, consists of SiO_2 particles with a volume-averaged primary particle size of 9.7 µm (as measured by laser diffraction); particle size distribution is shown in **Fig. 1**. The powder was sieved beforehand (mesh size 1.25 mm). Note that this is orders of magnitude larger than the primary particle size, meaning it did not affect the size distribution of the powder, but was done to establish an equal state of aeration at the start of each experiment, ensuring reproducibility. The bulk density after sieving was measured to be 134 kg m^{-3}.

After each experiment, powder samples were taken from the plane center of the collapsed bed at heights 2.5, 6.5, and 13.5 cm from the distributor plate. A Zeiss Colibri 7 Axio Observer microscope, equipped with Orca Flash 4.0 Hamamatsu V2 camera was used for imaging. The images were analyzed using ImageJ. The equivalent circle diameter of the agglomerates was calculated from the projected area of the agglomerates on the image. To avoid including primary particles too, which will drastically shift the number-based distribution, agglomerates with a diameter smaller than 35 µm were excluded. A minimum of 800 agglomerates was measured for each sample.

To be able to distinguish between the effect of 1) agglomerate breaking and 2) disrupting of channels on the fluidization quality, three sets of experiments were conducted. One where no vibration was used, one where vibration was used for 8 min, and finally one where vibration was used for 5 s before the inlet gas and vibration were switched off, all at the two aforementioned gas velocities.

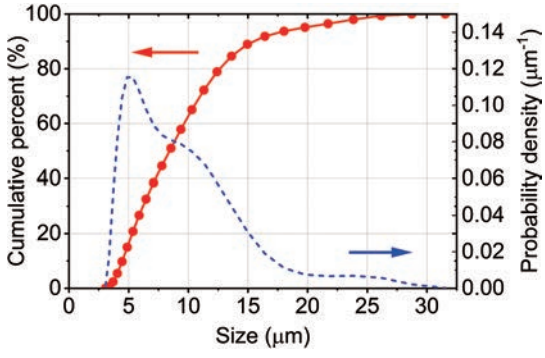


Fig. 1 Volume based size distribution of micro silica powder acquired with the Coulter LS230 particle size analyzer.

2.2 X-ray imaging setup

The gas-solids distribution inside the fluidized bed column was measured using an in-house fast X-ray analysis setup. The complete setup consists of three standard industrial-type X-ray sources (Yxlon International GmbH) with a maximum energy of 150 keV working in cone beam mode. The sources are placed at 120° around a common center, which forms the field of view. Three 2D detectors (Teledyne Dalsa Xineos) are placed opposite of the sources. The sources and detectors are attached to a hexagonal support frame that enables translation of the detectors. By changing the distance between the source and detector, or the relative position of the column, the magnification of the image of the column can be adjusted. In this study the experiments were performed with one X-ray source-detector pair to obtain a projected 2D output from the 3D column as shown in **Fig. 2**. The column was fixed to a vibration table which was positioned in the center of the setup. The distance between the source and the detector was 128.8 cm.

The experimental procedure was controlled from a workstation outside the setup room, guaranteeing a safe working environment. The workstation was used to trigger the X-ray source and read out the signals from the detector plate. The theoretical spatial resolution of the X-ray detector was 0.15 mm per pixel. During all experiments the X-ray images were recorded with a frequency of 50 Hz for a measurement time of 200 s for the channel-breaking experiments or 600 s for the full experiment, which corresponded to the acquisition of respectively 10,000 and 30,000 images per experiment. The measured data was stored for further digital image analysis.

2.3 X-ray image processing

For each experiment, the attenuation of the X-ray beam was measured at the detector plate to obtain the time-resolved projected 2D intensity map of the reactor. The raw images acquired were corrected for dead-pixels, originating from the construction of the detector plate, by means of interpolation to give pre-processed images.

In order to convert the measured X-ray attenuation to a solids concentration, a two points calibration protocol was performed. First, a reference image was acquired of the empty column. Then, the column was completely filled with the powder and vibrated for 10 minutes to approach the maximum packing density. After packing, the full reference image was acquired. The X-ray measurement principle is based on the attenuation of X-rays that travel through a material in a straight line from an X-ray source to a scintillation detector. The law of Lambert-Beer describes the transmission of a monochromatic beam of high energy photons with initial intensity I_0 through a material of constant density:

$$I(x) = I_0 \exp(-\mu x) \tag{1}$$

where $I(x)$ represents the intensity measured at the detector, μ the attenuation coefficient, and x the thickness. In the case of a varying attenuation, the measured intensity is the integral effect of the local attenuation with the local attenuation coefficient. By applying the Lambert-Beer law the measurement gas-fraction map was obtained from the measurement intensity map by using the empty and full reference. The normalized solids fraction α was calculated as follows:

$$\alpha = 1 - \frac{\log(I_{\text{measured}} / I_{\text{full}})}{\log(I_{\text{empty}} / I_{\text{full}})} \tag{2}$$

Note the range of normalized solid fraction used in this work is between 0 to 1, with 0 representing pure gas and 1 representing close packing of the solids. For the solid fraction map, low attenuation of X-rays is represented by light colors and indicates low solid concentrations. By

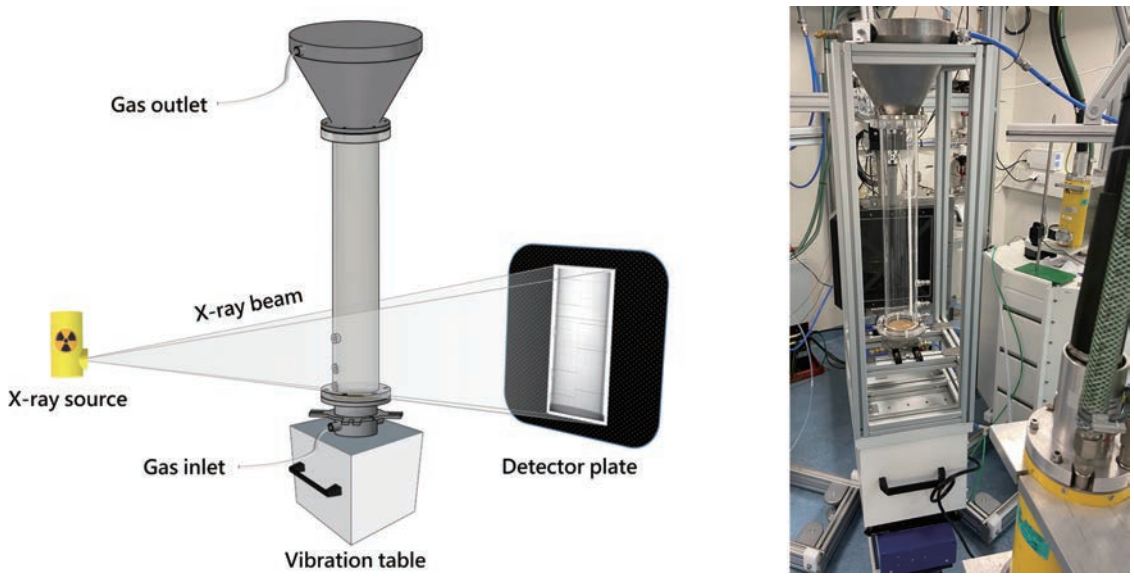


Fig. 2 Experimental X-ray imaging setup showing the X-ray source and detector plate, fluidized bed column and the vibration table.

contrast, high attenuation of X-rays is represented by the dark colors and indicates a high solids concentration. The acquired images obtain time-resolved, or dynamic, information of the gas-solids distribution in the column.

2.4 Pressure data processing

Pressure drop over the whole fluidized bed, or over part of it, is commonly used to evaluate fluidization. When mechanical vibration is applied, the periodic oscillation of mass and gas induced is significantly greater than that caused by rising bubbles and suspension of solids. These driven oscillations affect the measured time series of bed pressure drop, greatly complicating the analysis of fluidization state. For example, **Fig. 3(a)** plots the time series of bed pressure drop sampled over 600 s. The vibration was introduced at around 120 s, after which the measured signal (black) fluctuates largely with an amplitude of up to triple the theoretical bed pressure drop. To further determine the components of such oscillations, one could analyze the signal in the frequency domain (Wu et al., 2023). In **Fig. 3(b)** the power spectrum for the signal sampled between 120–600 s is demonstrated. The dominant peaks occur at 30 Hz, corresponding to the vibration frequency adopted in the experiment, as well as its sub-harmonic frequencies with reduced intensity. As a result, in the following sections, the 10 s time-averaged pressure drop is used to assess fluidization quality during vibration, such as the red lines in **Fig. 3(a)**, while its standard deviation mainly associated with the vibration is therefore neglected. For the experiments where vibration was only used for 5 s, averages over 1 s were taken.

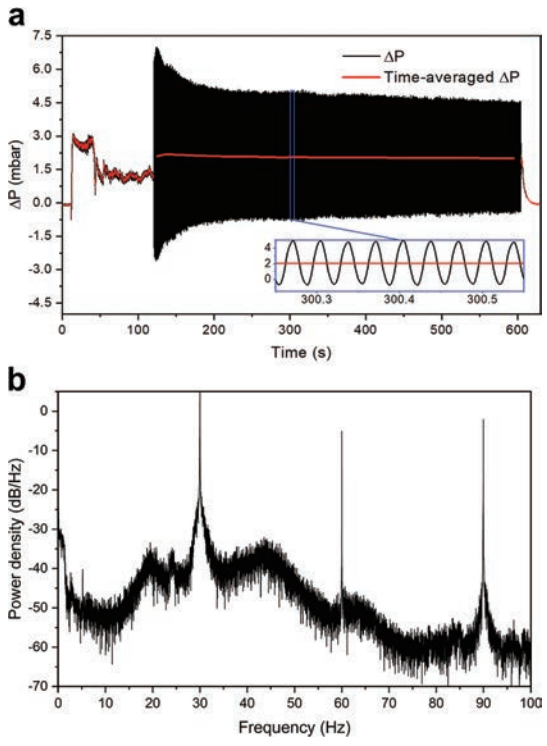


Fig. 3 **(a)** Pressure drop series and **(b)** power spectrum of the vibrated bed at 1.8 cm s^{-1}.

3. Results and discussion

3.1 Channel breakage by vibration

3.1.1 Pressure drop and X-ray images

In **Fig. 4** the pressure drop and X-ray images of the experiments where vibration was used are shown. Experiment 1 and 2 (under the same conditions) were terminated after 5 s of vibration. The third one was vibrated for 8 min after vibration started, in order to demonstrate the long-term fluidization behavior. The initial pressure drop fluctuations, seen in all pressure graphs, are caused by slugging which is discussed in detail in **Sections 3.2.1** and **3.2.3**. For each experiment, it can be seen that a semi-stable pressure drop was achieved after roughly 75 s. The $\Delta P/\Delta P_0$, the ratio of measured pressure drop over theoretical pressure drop (the static pressure of the powder; 2.3 mbar (2.3×10^2 Pa) for all experiments) of full fluidization, after 90 s, shown in **Fig. 4(b)-1**, **Fig. 4(d)-1** and **Fig. 4(f)-1**, was found to be low. The channeling, causing the low pressure drops, can clearly be seen. Comparing these images to **Fig. 4(b)-2**, **Fig. 4(d)-2** and **Fig. 4(f)-2** it can also be seen that these channels were stable with time, as the images with sub-labels 1 and 2 were taken 30 s apart. The relatively high and unstable pressure drop seen from 50 s to 120 s in **Fig. 4(e)** is explained by the collapse and reforming of unstable channels, in **Fig. 4(f)-2** the channel structure can be seen to have changed compared to **Fig. 4(f)-1**. We consider this occurs simply as a matter of chance, since up to 120 s there is no difference in operation between the three experiments. In the following images the effect of vibration, within the first seconds of initiation, can be seen. For all experiments, two types of channeling were observed: rat-holes and vein-like channels. Where rat-holes run almost vertically from bottom to top of the bed, creating a large gas bypass, vein-like channels branch out in several directions, resulting in a network of thinner interconnected channels. Not enough data was acquired to reliably assess what causes either type of channeling to occur. It was consistently observed that the vein-like channels disappear by merging together, due to the powder barriers, initially separating them, crumbling. The rat-holes, persist longer and are destroyed by powder falling into them, disrupting the gas flow and creating bubble-like gas pockets. In **Fig. 4(a)**, **Fig. 4(c)** and **Fig. 4(e)** it can be seen that the $\Delta P/\Delta P_0$ spiked to 0.89, 0.79 and 0.89 after 1 s, and kept increasing to 0.91, 0.88 and 0.94 after 5 s, of vibration respectively. Note that this increase over the first 5 s corresponds to more and more channels breaking, as seen in the X-ray images. The increase in the fluidized fraction of powder, as measured by pressure drop, is in all experiments clearly correlated to the breaking of channels.

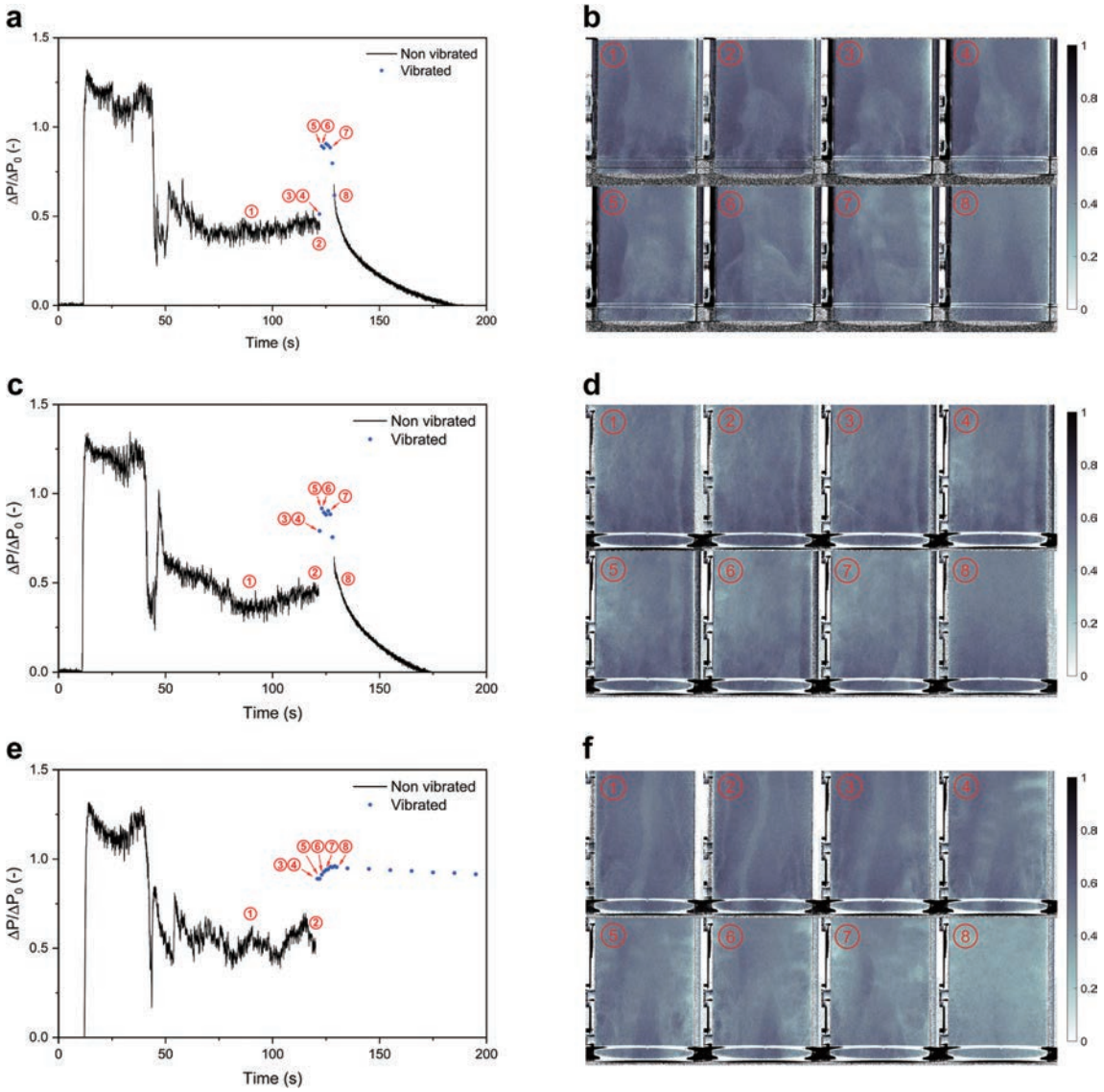


Fig. 4 Images corresponding to channel breakage experiments at 1.8 cm s^{-1} gas velocity, in all images: ①= 90 s, ②= 120 s, ③= 120.5 s, ④= 121 s, ⑤= 121.5 s, ⑥= 122 s, ⑦= 123 s and ⑧= 130 s into the experiment. **(a)** Pressure drop of experiment 1; **(b)** X-ray images of experiment 1; **(c)** Pressure drop of experiment 2; **(d)** X-ray images of experiment 2; **(e)** Pressure drop of experiment 3; **(f)** X-ray images of experiment 3.

3.1.2 Agglomerate sizes

For the experiments displayed in **Fig. 4**, the agglomerate sizes were measured after ending the experiment for the top, middle and bottom of the bed (as described in **Section 2.1**). The resulting number-based cumulative percentiles, d_{10}, d_{50} and d_{90}, are shown in **Fig. 5**. First comparing the two runs in which vibration only lasted for 5 s, labeled 1 and 2 in **Fig. 5**, no significant difference between them can be seen, showing the data is reproducible. Also, comparing the sizes in both of these experiments to the un-fluidized powder, no significant change is observed. Looking at the sizes found after 8 min of vibro-fluidizing, labeled 3 in **Fig. 5**, no big change in agglomerate sizes was found compared to the un-fluidized powder or compared to the other experiments.

It was hypothesized that channel disruption is the cause of initiated fluidization upon the introduction of vibration.

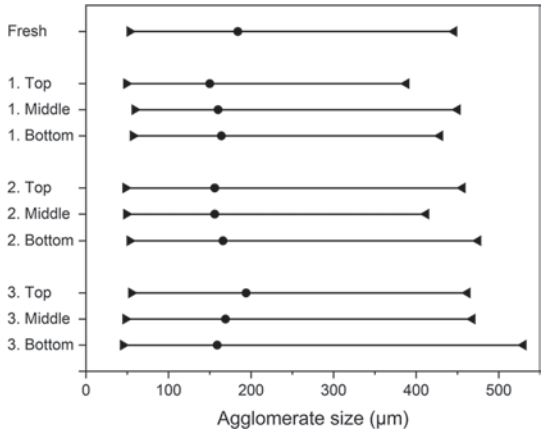


Fig. 5 Agglomerate sizes after vibration all with gas velocity of 1.8 cm s^{-1}; 1) vibrated for 5 s; 2) vibrated for 5 s; 3) vibrated for 8 min; ▶ = d_{10} ● = d_{50} ◀ = d_{90}, number based.

It was expected to find a decreased agglomerate size after 8 min of vibro-fluidization compared to 5 s, where virtually no decrease was expected. While no significant change in agglomerate sizes was found for any of the experiments, it can still be concluded that the break-up of agglomerates does not play a role in initiating fluidization of the cohesive powder.

3.2 Influence of vibration and gas velocity

3.2.1 No vibration, 1.8 cm s^{-1}

In **Fig. 6** the bed height, pressure drop and X-ray images from the experiment without vibration and 1.8 cm s^{-1} gas velocity are shown. It can be seen that the bed was initially lifted as a plug, which corresponded to a large pressure drop over the column. The plug eventually broke and fell down in pieces, as seen in **Fig. 6(c)-3**, which lead to heavy pressure swings in the system. Note that in this image most of the powder bed is still out of frame, higher up in the column. Right after, some fluidization took place, as seen by the pressure drop, significant bed height expansion and dilute X-ray image. Within 45 s after the plug fell down, stable channels had formed (**Fig. 6(c)-5**), that did not significantly change over time anymore. The pressure drop remained constant over this time with an average $\Delta P/\Delta P_0$ of 0.57. Bed height was decreasing slowly due to the bed compacting from its initial fluidized state. Still, an expansion ratio of 1.2 was maintained, caused by the added volume of the channels now present in the bed and the looser packing state of the powder. This experiment shows all the expected behavior of a cohesive powder upon the introduction of a gas flow.

3.2.2 Vibration, 1.8 cm s^{-1}

The results shown in **Fig. 7** are of the same experiment shown in **Fig. 4(e)** and **Fig. 4(f)**, but extended to the full experimental time to assess the effect of vibration over time. The bed initially rose as a plug again, the X-ray images corresponding to this were omitted since they are virtually identical to the experiment previously described in **Section 3.2.1** and the focus here is on the effect of vibration, which started at 120 s. In **Fig. 7(c)-1** to **Fig. 7(c)-5**, the initial stable channel collapsing and the initiation of fluidization are shown. Over time, compaction and partial de-fluidization took place. It can be seen that the bed height decreased, coupled with a decrease in $\Delta P/\Delta P_0$ from 0.93 in the first minute after vibration started to 0.87 in the last minute of the run. From the X-ray images, it could also be observed that the bed was densifying during this time, with a compacted region being present, dominantly at the bottom of the bed.

3.2.3 No vibration, 3.1 cm s^{-1}

The obtained results for the 3.1 cm s^{-1} experiment without vibration are shown in **Fig. 8**. As in the other experiments, the bed initially formed a plug. In **Fig. 8(c)-3** the fragments of the broken plug can be seen falling down, corresponding with the pressure swing seen at 30 s in **Fig. 8(b)**. This was followed by some degree of fluidization, giving a bed height expansion ratio of 1.5 and a $\Delta P/\Delta P_0$ of 0.89 at the peak, 115 s. The dip in bed height and pressure drop that followed is explained by the formation of two rat-holes, seen in **Fig. 8(c)-5**, which collapsed later leading to vein-like channel formation and some spouting

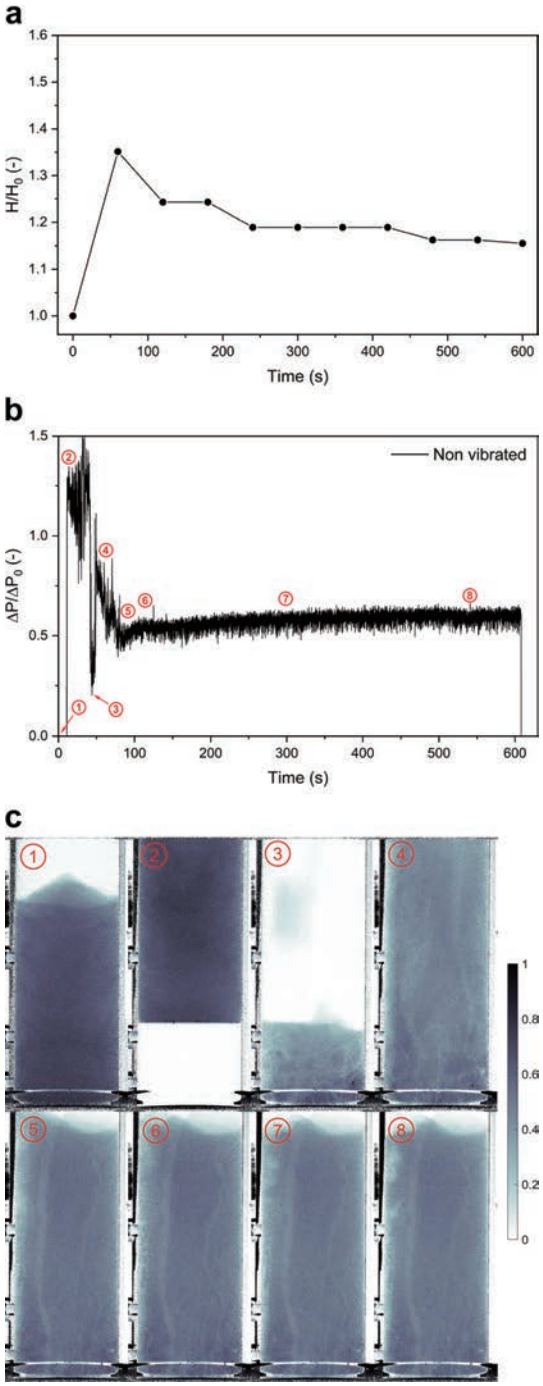


Fig. 6 Results of fluidization experiments, 1.8 cm s^{-1} without vibration, in all images: ①= 0 s, ②= 15 s, ③= 45 s, ④= 60 s, ⑤= 90 s, ⑥= 120 s, ⑦= 300 s and ⑧= 540 s into the experiment. **(a)** Bed height; **(b)** Pressure drop; **(c)** X-ray images.

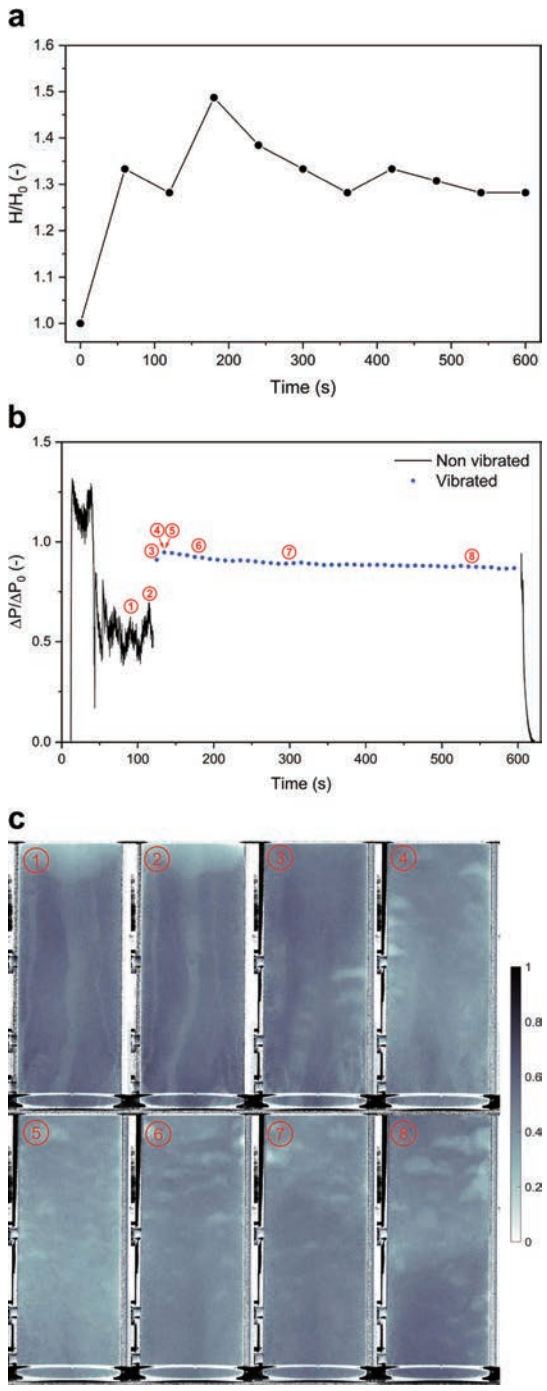


Fig. 7 Results of fluidization experiments, 1.8 cm s^{-1} with vibration, in all images: ①= 90 s, ②= 120 s, ③= 121 s, ④= 125 s, ⑤= 130 s, ⑥= 180 s, ⑦= 300 s and ⑧= 540 s into the experiment. **(a)** Bed height; **(b)** Pressure drop; **(c)** X-ray images.

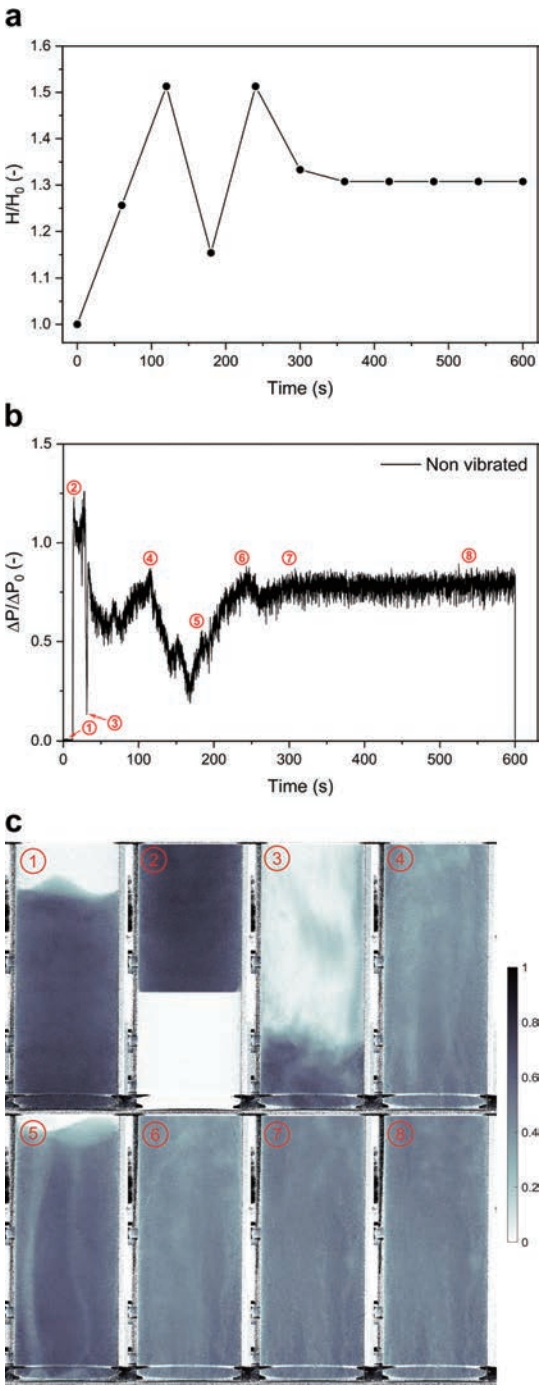


Fig. 8 Results of fluidization experiments, 3.1 cm s^{-1} without vibration, in all images: ①= 0 s, ②= 15 s, ③= 30 s, ④= 120 s, ⑤= 180 s, ⑥= 240 s, ⑦= 300 s and ⑧= 540 s into the experiment. **(a)** Bed height; **(b)** Pressure drop; **(c)** X-ray images.

and bubbling in top of the bed, coupled with stable $\Delta P/\Delta P_0$ of 0.77.

3.2.4 Vibration, 3.1 cm s^{-1}

Fig. 9 shows the data from the experiment at 3.1 cm s^{-1} with vibration. As for all experiments, slugging occurred initially, followed by some degree of fluidization before stable channels formed, which are seen in **Fig. 9(c)-1** and **Fig. 9(c)-2**. After 10 s of vibration (**Fig. 9(c)-5**), no long-term structures could be observed anymore and the bed was homogeneously fluidized. In the remaining time that the experiment was running, densification was observed, mainly at the bottom of the bed, as when 1.8 cm s^{-1} gas velocity was used. The densifying resulted in a lower bed height expansion ratio, eventually even lower than when no vibration was used at 3.1 cm s^{-1}, and a slight reduction in $\Delta P/\Delta P_0$ from 0.91 in the first minute after vibration started, to 0.87 after 8 min.

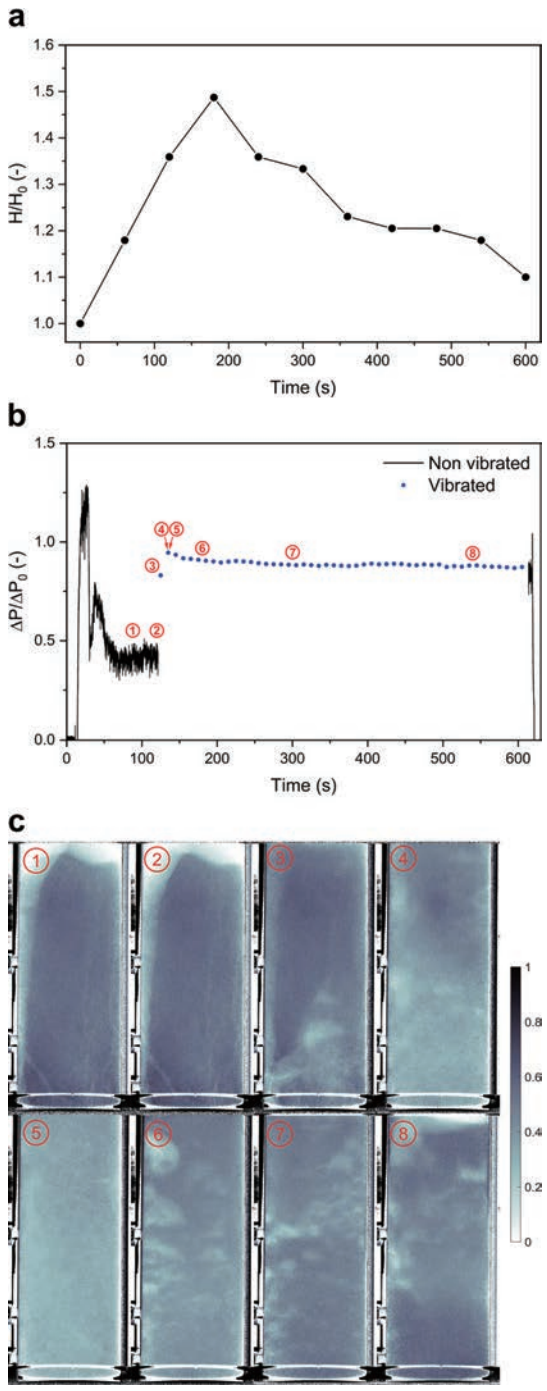


Fig. 9 Results of fluidization experiments, 3.1 cm s^{-1} with vibration, in all images: ①= 90 s, ②= 120 s, ③= 121 s, ④= 125 s, ⑤= 130 s, ⑥= 180 s, ⑦= 300 s and ⑧= 540 s into the experiment. **(a)** Bed height; **(b)** Pressure drop; **(c)** X-ray images.

3.2.5 Agglomerate sizes

For each 10 min experiment, the agglomerate sizes (d_{10}, d_{50} and d_{90}, number-based), at all sample heights, are shown in **Fig. 10**. Comparing the results, across gas velocities and with or without vibration to fresh powder, the differences are minor. The influence of vibration and gas velocities, within the ranges used in this study, on agglomerate sizes is therefore concluded to be insignificant. The

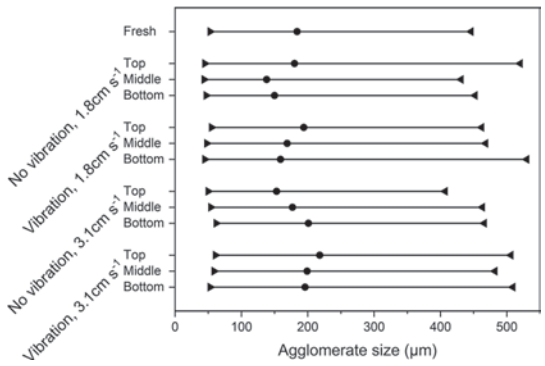


Fig. 10 Agglomerate sizes for experiments ran at 1.8 and 3.1 cm s^{-1}, with and without vibration for 8 min; ▶ = d_{10} ● = d_{50} ◀ = d_{90}, number based.

densification of the bottom bed—as observed after several minutes of vibration—is not reflected by the agglomerate size.

3.3 Channel formation

Channeling took place in all the experiments conducted, either without vibration or before vibration was switched on. From the X-ray images shown in the previous sections, the variety of the formed channels across different experiments is obvious. The diversity which is seen, even under identical conditions, underlines the random nature of channel formation. It also shows no bias from the used experimental method, since no preferential place for the channels to form is observed. The results also suggest that even the formation of rat-hole like or vein-like channeling is random and not affected by gas velocity within the range used for this study.

4. Conclusions

In this work, the mechanism behind the initiation of fluidization of cohesive micro-sized powder, by vibrations, was studied by means of X-ray imaging, pressure drop and bed height measurements. Agglomerate sizes were measured to decouple the phenomena of channel disruption and agglomerate breakage. When no vibration was used, the powder could not be properly fluidized at either 1.8 or 3.1 cm s^{-1} and severe channeling was observed, which was not always clearly reflected in the pressure drop or bed height, showcasing the limitations of these techniques when it comes to assessing the dynamics of complex systems. Gas velocity, vibration and vibration time were not found to have any significant effect on agglomerate sizes, within the parameter ranges applied in this work. From this, it is concluded that vibrations initiate fluidization not by breaking agglomerates, but by disrupting channels. Furthermore, it was found that narrow, vein-like channels are disrupted significantly faster than the larger rat-holes. Finally, when vibration was employed, bed compaction was observed over time, as a dense phase formed on top of

the distributor plate, causing a decrease in bed height and pressure drop. The study was carried out using a single micro-silica powder, meaning material- and size-specific influences, which might influence results, were not investigated. While variations are deemed likely when using other powders, based on the described mechanism by which assistance methods work and the absence of a mechanism by which agglomerates can be broken before fluidization is initiated, it is expected that the disruption of channels is the cause of initiated fluidization for other cohesive powders too. This study is a first step towards a better understanding of the mechanism behind vibro-assisted fluidization of cohesive powder and may contribute to the further development and optimization of assistance methods.

Supplementary information

The online version contains supplementary material available at https://doi.org/10.14356/kona.2024007.

Acknowledgments

We want to thank Stefan ten Hagen for his contribution to designing and manufacturing the column used in this study.

This work is part of the Advanced Research Center for Chemical Building Blocks, ARC CBBC, which is co-founded and co-financed by the Dutch Research Council (NWO) and the Netherlands Ministry of Economic Affairs and Climate Policy. The work has also received funding from the NWO under the grant number ENPPS. LIFT.019.027.

References

Al-Ghurabi E.H., Shahabuddin M., Kumar N.S., Asif M., Deagglomeration of ultrafine hydrophilic nanopowder using low-frequency pulsed fluidization, Nanomaterials, 10 (2020) 388. DOI: 10.3390/nano10020388

Ali S.S., Al-Ghurabi E.H., Ajbar A., Mohammed Y.A., Boumaza M., Asif M., Effect of frequency on pulsed fluidized beds of ultrafine powders, Journal of Nanomaterials, 2016 (2016) 23. DOI: 10.1155/2016/4592501

Ali S.S., Asif M., Fluidization of nano-powders: effect of flow pulsation, Powder Technology, 225 (2012) 86–92. DOI: 10.1016/j.powtec.2012.03.035

Barletta D., Poletto M., Aggregation phenomena in fluidization of cohesive powders assisted by mechanical vibrations, Powder Technology, 225 (2012) 93–100. DOI: 10.1016/j.powtec.2012.03.038

Barthel F., Bieberle M., Hoppe D., Banowski M., Hampel U., Velocity measurement for two-phase flows based on ultrafast X-ray tomography, Flow Measurement and Instrumentation, 46 (2015) 196–203. DOI: 10.1016/j.flowmeasinst.2015.06.006

Guo L., Yuan W., Lu Z., Li C.M., Polymer/nanosilver composite coatings for antibacterial applications, Colloids and Surfaces A: Physicochemical and Engineering Aspects, 439 (2013) 69–83. DOI: 10.1016/j.colsurfa.2012.12.029

Guo Q., Liu H., Shen W., Yan X., Jia R., Influence of sound wave characteristics on fluidization behaviors of ultrafine particles, Chemical Engineering Journal, 119 (2006) 1–9. DOI: 10.1016/j.cej.2006.02.012

Gómez-Hernández J., Sánchez-Delgado S., Wagner E., Mudde R.F., van Ommen J.R., Characterization of TiO_2 nanoparticles fluidization using X-ray imaging and pressure signals, Powder Technology, 316 (2017) 446–454. DOI: 10.1016/j.powtec.2016.11.068

Helmi A., Wagner E.C., Gallucci F., van Sint Annaland M., van Ommen J.R., Mudde R.F., On the hydrodynamics of membrane assisted fluidized bed reactors using X-ray analysis, Chemical Engineering and Processing: Process Intensification, 122 (2017) 508–522. DOI: 10.1016/j.cep.2017.05.006

Kamphorst R., Wu K., Salameh S., Meesters G.M.H., van Ommen J.R., On the fluidization of cohesive powders: differences and similarities between micro- and nano-sized particle gas–solid fluidization, The Canadian Journal of Chemical Engineering, 101 (2023) 227–243. DOI: 10.1002/cjce.24615

Li P., Miser D.E., Rabiei S., Yadav R.T., Hajaligol M.R., The removal of carbon monoxide by iron oxide nanoparticles, Applied Catalysis B: Environmental, 43 (2003) 151–162. DOI: 10.1016/S0926-3373(02)00297-7

Macrì D., Sutcliffe S., Lettieri P., Fluidized bed sintering in TiO_2 and coke systems, Chemical Engineering Journal, 381 (2020) 122711. DOI: 10.1016/j.cej.2019.122711

Mahato N., Cho M.H., Graphene integrated polyaniline nanostructured composite coating for protecting steels from corrosion: synthesis, characterization, and protection mechanism of the coating material in acidic environment, Construction and Building Materials, 115 (2016) 618–633. DOI: 10.1016/j.conbuildmat.2016.04.073

Maurer S., Wagner E.C., van Ommen J.R., Schildhauer T.J., Teske S.L., Biollaz S.M.A., Wokaun A., Mudde R.F., Influence of vertical internals on a bubbling fluidized bed characterized by X-ray tomography, International Journal of Multiphase Flow, 75 (2015) 237–249. DOI: 10.1016/j.ijmultiphaseflow.2015.06.001

Mawatari Y., Koide T., Ikegami T., Tatemoto Y., Noda K., Characteristics of vibro-fluidization for fine powder under reduced pressure, Advanced Powder Technology, 14 (2003) 559–570. DOI: 10.1163/156855203322448345

Mema I., Wagner E.C., van Ommen J.R., Padding J.T., Fluidization of spherical versus elongated particles - experimental investigation using X-ray tomography, Chemical Engineering Journal, 397 (2020) 125203. DOI: 10.1016/j.cej.2020.125203

Morooka S., Kusakabe K., Kobata A., Kato Y., Fluidization state of ultrafine powders, Journal of Chemical Engineering of Japan, 21 (1988) 41–46. DOI: 10.1252/jcej.21.41

Nam C.H., Pfeffer R., Dave R.N., Sundaresan S., Aerated vibrofluidization of silica nanoparticles, AIChE Journal, 50 (2004) 1776–1785. DOI: 10.1002/aic.10237

Nasri Lari H., Chaouki J., Tavares J.R., De-agglomeration of nanoparticles in a jet impactor-assisted fluidized bed, Powder Technology, 316 (2017) 455–461. DOI: 10.1016/j.powtec.2017.02.042

Prabhu S., Poulose E.K., Silver nanoparticles: mechanism of antimicrobial action, synthesis, medical applications, and toxicity effects, International Nano Letters, 2 (2012) 32. DOI: 10.1186/2228-5326-2-32

Quevedo J.A., Pfeffer R., In situ measurements of gas fluidized nanoagglomerates, Industrial & Engineering Chemistry Research, 49 (2010) 5263–5269. DOI: 10.1021/ie9015446

van Ommen J.R., King D.M., Weimer A., Pfeffer R., van Wachem B., Experiments and modelling of micro-jet assisted fluidization of nanoparticles, The 13th International Conference on Fluidization, (2010). <https://dc.engconfintl.org/fluidization_xiii/66> accessed 19042023.

Wu K., Galli F., de Tommaso J., Patience G.S., van Ommen J.R., Experimental methods in chemical engineering: Pressure, The Canadian Journal of Chemical Engineering, 101 (2023) 41–58. DOI: 10.1002/cjce.24533

Zhang X., Zhou Y., Zhu J., Enhanced fluidization of group A particles

modulated by group C powder, Powder Technology, 377 (2021) 684–692. DOI: 10.1016/j.powtec.2020.09.035
Zhou L., Zhang F., Zhou T., Kage H., Mawatari Y., A model for estimating agglomerate sizes of non-magnetic nanoparticles in magnetic fluidized beds, Korean Journal of Chemical Engineering, 30 (2013) 501–507. DOI: 10.1007/s11814-012-0170-5

Authors' Short Biographies



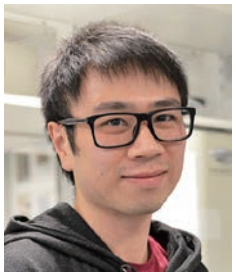
Rens Kamphorst

MSc Rens Kamphorst is a PhD researcher in the department of Chemical Engineering at Delft University of Technology (The Netherlands). In 2020 he completed his MSc in Chemical Engineering, also at this university. His research is focused on atomic layer deposition in a fluidized bed consisting of cohesive powders.



P. Christian van der Sande

MSc Christian van der Sande is a PhD researcher in the department of Chemical Engineering at Delft University of Technology (The Netherlands). He completed his MSc in Chemical Engineering with a specialization in process engineering at the same university. His research activities involve hydrodynamic studies with radiation-based imaging methods to study gas hold up, flow patterns and flow velocities inside multi-phase reactors. He has supervised over 10 BSc and MSc students for their thesis work.



Kaiqiao Wu

Dr. Kaiqiao Wu obtained his PhD from University College London in 2020. He has published several works of gas-solid fluidization in international journals, and has presented at conferences. He has won prizes for best talk in sessions, and placed second in the IChemE Young Researcher Awards at UK-China International PTF VII, 2019, and also received the Springer Theses Award for recognizing outstanding PhD research in 2021. He is currently a postdoctoral researcher at TU Delft.



Evert C. Wagner

Ing. Evert Wagner is a research assistant at Delft University of Technology, The Netherlands. He obtained a BSc degree in Applied Physics at the Technische Hogeschool, Rijswijk. Starting at TU Delft in 2006, he has been involved in most of the development of the X-ray setup used in this paper. He's a co-author of over 30 papers using this experimental technique.



Kristen David

Ing. Kristen David is a lab manager at Delft University of Technology (The Netherlands). She obtained her BSc degree in Chemical Engineering at De Haagse Hogeschool in Den Haag in 2019. She started at TU Delft on the same year and has been involved in managing the ML-1 labs of the Product and Process Engineering group of the Chemical Engineering department.

Authors' Short Biographies



Gabrie M.H. Meesters

Dr. Gabrie Meesters has 27 years of industrial formulations experience at Gistbrocades, Genencor International and DSM. He has 23 years of experience as a Part-Time Professor at TU Delft in particle technology and product design. From January 2019, he became a fulltime Assistant Professor at the TU Delft, Faculty of Applied Sciences, Product and Process Engineering. He is a contributor to several books on formulation. He is the editor of three books on product design and solids processing. He published over 70 refereed papers, has more than 20 patents and supervised more than 100 BSc, MSc and PhDs. He is a regular speaker at conferences and workshops. He was the organizer of the 2010 Partec and the 2010 World Congress on Particle Technology in Nuremberg, Germany.



J. Ruud van Ommen

Professor of Chemical Engineering at Delft University of Technology (The Netherlands). He obtained his PhD degree at Delft in 2001. He has been Visiting Professor at Chalmers University of Technology (Gothenburg, Sweden) and the University of Colorado (Boulder, USA). In recent years, he expanded his research from chemical reactor engineering to the scalable production of advanced, nanostructured materials. In 2011, he started an ambitious program (funded by an ERC Starting Grant) to investigate the interplay between agglomeration and coating of nanoparticles in the gas phase. He has published about 200 journal papers, of which a considerable part on powder technology.

KONA Powder and Particle Journal

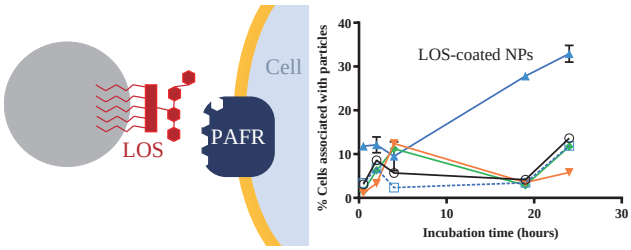
KONA Powder and Particle Journal No. 41 (2024) 265–279/https://doi.org/10.14356/kona.2024005 Original Research Paper

Lipooligosaccharide Ligands from Respiratory Bacterial Pathogens Enhance Cellular Uptake of Nanoparticles†

Mai H. Tu[1], Timothy M. Brenza[1], Margaret R. Ketterer[2], Morgan Timm[3], Benjamin M. King[4], Michael A. Apicella[2] and Jennifer Fiegel[1,4]*

[1] *Department of Pharmaceutical Sciences and Experimental Therapeutics, The University of Iowa, USA*
[2] *Department of Microbiology and Immunology, The University of Iowa, USA*
[3] *Department of Biochemistry and Molecular Biology, Gustavus Adolphus College, USA*
[4] *Department of Chemical and Biochemical Engineering, The University of Iowa, USA*

Several bacterial pathogens contain membrane ligands that facilitate their binding and internalization into human tissues. In this study, lipooligosaccharides (LOS) from the respiratory pathogen non-typeable *Haemophilus influenzae* (NTHi) were isolated from the bacterial surface and evaluated as a nanoparticle coating material to facilitate uptake into the respiratory epithelium. NTHi clinical isolates were screened to select a strain with high binding potential due to their elevated phosphorylcholine content. The association of particles with human bronchial epithelial cells was investigated as a function of particle surface chemistry and incubation time, and the uptake mechanism was evaluated via chemical inhibitor and receptor activation studies. A more than two-fold enhancement in particle uptake was achieved by coating the particles with LOS compared to uncoated or gelatin-coated particles, which was further increased by activating the platelet-activating factor receptor (PAFR). These findings demonstrate that bacterial-derived LOS ligands can enhance the targeting and binding of nanoparticles to lung epithelial cells.



Keywords: endocytosis, platelet-activating factor receptor, lipooligosaccharides, non-typeable *Haemophilus influenzae*, nanoparticle, bronchial epithelial cells

1. Introduction

Targeted drug delivery is a powerful strategy to treat diseases that affect human tissues, offering high drug concentrations at the target site with limited exposure of other tissues. Efficient delivery can be achieved using drug-loaded nanoparticles with chemical and physical properties tuned to avoid host defense mechanisms and inhibit non-specific distribution (Fenton et al., 2018; Patra et al., 2018). Active targeting can further enhance delivery to specific target organs or cells within the body. With appropriate surface functionality, such as through the attachment of ligands that recognize receptors on cellular surfaces, particulate carriers show improved efficiency in penetrating cells *in vitro*. One challenge in achieving active targeting has been the identification of cellular targets, which is limited by our knowledge of disease-specific cell receptors and their ligands. A potentially useful class of ligands is produced and used by human pathogenic organisms to infect the respiratory tract.

† Received 28 May 2022; Accepted 29 August 2022
J-STAGE Advance published online 25 March 2023
* Corresponding author: Jennifer Fiegel;
[1,4] Add: Iowa City, IA, 52242, USA
E-mail: jennifer-fiegel@uiowa.edu
TEL: +1-319-335-5162 FAX: +1-319-335-1415

Haemophilus influenzae (*H. influenzae*), a Gram-negative bacterium that colonizes the nasopharynx of up to 80 % of humans, is a leading cause for bacterial meningitis and other widespread bacteremic diseases (Cochi and Broome, 1986; Foxwell et al., 1998). While a polysaccharide conjugate vaccine is available for and is effective against *H. influenzae* serotype b, the vaccine is not effective against the subtype that lacks a capsule, called non-typeable *H. influenzae* (NTHi) (St. Geme, 1996). NTHi causes localized opportunistic infections including otitis media, sinusitis, conjunctivitis, bronchitis and pneumonia (Turk, 1984). It can infect cystic fibrosis (CF) patients early in childhood and prime the lungs for later infection with the bacterium *Pseudomonas aeruginosa*, which is correlated with higher morbidity and mortality in CF patients (Starner et al., 2006).

Diseases due to NTHi often start with colonization of the respiratory epithelium (Turk, 1984). The surface of NTHi is decorated with lipooligosaccharides (LOS) which contain a lipid structure that embeds in the outer leaf of the bacterial outer membrane and an oligosaccharide structure that facilitates bacterial pathogenesis. By expressing specific carbohydrates, such as phosphorylcholine (ChoP), as a terminal structure on the LOS, the bacteria are imbued with two important defenses. First, ChoP expression reduces the

Copyright © 2024 The Authors. Published by Hosokawa Powder Technology Foundation. This is an open access article under the CC BY license (https://creativecommons.org/licenses/by/4.0/).

ability of LOS-specific or bactericidal antibodies to bind to the bacteria through molecular mimicry of host structures, enabling the bacteria to evade the host immune system and limit their pulmonary clearance (Clark et al., 2012; Pang et al., 2008; Weiser et al., 1998). Second, the presence of ChoP on the NTHi surface enhances bacterial adherence to host cells by binding to the platelet-activating factor receptor (PAFR), effectively reducing mucociliary clearance of the bacteria and enhancing bacterial invasion of the respiratory epithelium (Swords et al., 2000, 2001; Turk, 1984). The effectiveness of OS in inducing cellular uptake is dependent on the specific LOS glycoform, with LOS containing higher ChoP content resulting in enhanced NTHi colonization and persistence in the lungs (Swords et al., 2000; Weiser et al., 1998). These findings suggest that isolated ChoP-containing LOS could be a potential targeting ligand for drug delivery particles to mimic bacterial entry into lung cells and thus deliver drugs directly to infected lung cells.

We hypothesized that LOS ligands naturally expressed on bacterial cell surfaces from NTHi could be utilized as targeting ligands to facilitate particle attachment and uptake into lung epithelial cells. The expression of ChoP on several clinical isolates of NTHi was measured and an NTHi strain with high ChoP content chosen for LOS isolation. Nanoparticle uptake was evaluated in 16HBEo- bronchial epithelial cells in the absence and presence of endocytosis pathway inhibitors and activators of PAFR.

2. Experimental

2.1 Culture of NTHi bacteria

NTHi clinical strains 2019 and 3198, isolated from patients with chronic obstructive pulmonary disease (Campagnari et al., 1987), and strain 956 were reconstituted from frozen glycerol stocks and propagated on chocolate agar (a non-selective, enriched growth medium) or brain heart infusion (BHI) agar (selective medium for NTHi) supplemented with 10 μg/mL hemin and 1 μg/mL nicotinamide adenine dinucleotide (NAD) at 37 °C and 5 % CO_2. All culture chemicals were obtained from Sigma Aldrich.

2.2 Detection of ChoP on NTHi cells via ELISA and dot immunoblot

The three NTHi strains were screened by enzyme-linked immunosorbent assay (ELISA) to identify bacterial strains and growth conditions that result in bacteria with high ChoP activity. An NTHi cell suspension (8.0×10^7 cells/mL) was added to each well of a 96-well plate (Corning Inc. product 3590; clear, flat-bottom polystyrene, high-binding). The plate was dried in an oven uncovered overnight at 40 °C. The wells were then washed three times with 200 μL ELISA wash solution (0.98 % w/v sodium acetate, 0.9 % w/v NaCl, 0.05 % v/v Tween 20 in purified water from NanoPure® Infinity UV Barnstead system). The primary monoclonal antibody 12D9, which was raised directly against ChoP, was diluted 1:25 and added to each well. The plate was incubated overnight at room temperature, then washed. Alkaline phosphatase-conjugated goat anti-mouse IgG AffiniPure F(ab')$_2$ (Jackson ImmunoResearch Inc.) diluted 1:2000 in ELISA buffer was added to each well and incubated for 1 h, after which the wells were again washed. The substrate, nitrophenyl phosphate bis (cyclohexyl ammonium) (pNPP), was prepared at 1 mg/mL in diethanolamine buffer (10 % w/v diethanolamine and 0.01 % w/v $MgCL_2$ in purified water, pH 9.8) immediately before use, added to all wells, and incubated in the dark. The substrate was then hydrolyzed by alkaline phosphatase to develop a yellow water-soluble product, p-nitrophenol. The relative absorbance of p-nitrophenol at 405 nm was read using a SpectraMax® M2 spectrophotometer (Molecular Devices) after 2 h incubation. Wells with no cells, no primary antibody, or no secondary antibody served as negative controls ($n = 4$). Dot immunoblot confirmed the relative high ChoP expression on NTHi 3198 cell surfaces.

2.3 Proteinase K/hot phenol method to isolate LOS from NTHi bacterial cells

Due to its relatively high ChoP expression, LOS was isolated from NTHi strain 3198 using the proteinase K digest, phenol-water extraction method (Apicella, 2008; Galanos et al., 1969). NTHi was cultured on supplemented BHI agar overnight, harvested, digested in ELISA buffer containing 1 % w/v sodium dodecyl sulfate (SDS, Sigma-Aldrich®) and 50 μg/mL proteinase K at 65 °C for 1 h, and incubated at 37 °C overnight to lyse the cells and digest the proteins. The mixture was washed three times via precipitation in 3 M sodium acetate and cold absolute ethanol overnight at –20 °C, then centrifuged at 3200 × g at 4 °C (Eppendorf centrifuge I810R). The precipitate was washed with ethanol to remove residual SDS. After the final precipitation, the pellets were air-dried at room temperature for 2 h and then suspended in 15 mL of DNase I buffer (10 mM Tris-HCl, 2.5 mM $MgCl_2$, 0.5 mM $CaCl_2$ in purified water, pH 7.6). Solutions of 10 μg/mL DNase (Roche) and 10 μg/mL RNase (Qiagen) were added and the solution incubated at 37 °C in a water bath for 2 h to digest residual nucleic acids. Finally, a phenol extraction of the LOS nuclease-treated mixture removed residual protein contamination. The LOS mixture was isolated from phenol soluble components using an equal volume of pre-heated phenol and incubated at 65 °C for 20 min, then on ice for 1 h. Upon cooling, the suspension was separated into a phenol phase containing proteins, an interphase containing cell-wall material, and an aqueous phase enriched in LOS. The top aqueous layer was collected and washed three times before lyophilization and storage at 4 °C in a desiccant box. The activity of the isolated LOS was confirmed using the colorimetric ELISA described above, except the

primary antibody 12D9 was prepared at 1:50 dilution in ELISA buffer, the secondary antibody was added at 1:2000 dilution in ELISA buffer, and the time for p-nitrophenol to develop was 3 h.

2.4 Preparation of LOS-functionalized particles

Polystyrene particles (0.2 μm plain white Polybead® or Fluoresbrite® polystyrene particles, Polysciences Inc.) were prepared for functionalization by washing twice with carbonate buffer (15.9 mg Na_2CO_3 and 25.9 mg $NaHCO_3$ in 100 mL purified water, pH 9.6) an centrifuging at 12,000 × g for 30 min, followed by resuspension at a concentration of 2×10^9 particles/mL. Particles with a nominal size of 0.2 μm were chosen to match the mean width of an NTHi bacterium.

To achieve particle functionalization, polystyrene particles were added to a solution containing NTHi 3198 LOS at either a low (5 ng/mL) or high (5 μg/mL) ligand concentration, mixed on a rotator for 2 h, washed twice with carbonate buffer, and resuspended in carbonate buffer. A subset of uncoated and high ligand coated polystyrene particles were exposed to a protein mixture of 0.1 % gelatin (Type B from bovine skin derived from lime-cured tissue, average MW 50,000–100,000 g/mol; Sigma G9382) solution in carbonate buffer. Particles were either stored in carbonate buffer at a final concentration of 2×10^9 particles/mL at 4 °C (cell association studies) or lyophilized overnight in a Labconco® FreeZone® 4.5-liter freeze dry system at a chamber pressure <0.02 mbar and collector temperature at or below –50 °C.

2.5 Particle characterization

Lyophilized polystyrene particles were prepared for size and zeta potential measurements by dispersion in water or serum-free medium (pH 7.4) via three cycles of vortexing for 90 s and sonication for 10 min in cold water bath at 4 °C. Particle suspensions were placed into folded capillary cells (DTS 1060C cuvettes, Malvern Instruments) and the average particle hydrodynamic diameter and zeta potential (n = 3) measured using a Zetasizer® Nano ZS (Malvern Panalytical LTD.). Particle size and morphology were confirmed via scanning electron microscopy using an S-4800 Field Emission Scanning Electron Microscope (FE-SEM). Lyophilized particles were tapped onto SEM stubs coated with double-sided black carbon tape and sputter coated with Au-Pl at 10 mA and pressure above 7×10^{-2} mbar for 3 min (K550 Emitech® sputter coater).

To prepare particles for surface chemical analysis, washed particles were dispersed in water, and 20 μL of the suspension was added and dried on clean silicon wafers. Chemical analysis was carried out using a Kratos® Axis Ultra X-ray photoelectron spectrometer (XPS) with concentric hemispherical electron energy analyzers combined with an established delay-line detector. The incident radiation from monochromatic Al Kα X-rays (1486.6 eV) at 150 W (accelerating voltage 15 kV, emission current 10 mA) was projected 45° to the sample surface and the photoelectron data was collected at a takeoff angle of θ = 90°. The base pressure in the analysis chamber was maintained at 1.0×10^{-9} torr. Survey scans were taken at a pass energy of 160 eV and carried out over a 1200 eV ~ –5 eV binding energy range with 1.0 eV steps and a dwell time of 200 ms. High resolution scans of C 1s, O 1s, N 1s, P 2p, and S 2p were taken at a pass energy of 20 eV with 0.1 eV steps and a dwell time of 2000 ms. Spectral analysis was conducted using CasaXPS software (version 2.3.17dev6.4k). Spectra were calibrated using the adventitious carbon C 1s peak at 285.0 eV.

2.6 Isothermal titration calorimetry (ITC)

ITC measures the heat released or absorbed during a biomolecular binding event, enabling accurate determination of the enthalpy of binding and the stoichiometry of each binding event at different concentrations of ligand, including proteins on nanoparticles. The GE MicroCal® iTC_{200} (GE Healthcare) was used in this study. The accuracy of the instrument was verified by titrating a 5 mM standard $CaCl_2$ solution into a 0.4 mM standard EDTA solution, both provided by the manufacturer. LOS and nanoparticle solutions were incubated in a 25 °C water bath for 15 min prior to use to ensure temperature equilibration. LOS solution at a concentration of either 20, 30, 50, or 100 μg/mL was loaded into the syringe and 625 μg/mL nanoparticle solution (the mass of nanoparticles in the original particle suspension was provided by the manufacturer) was loaded into the sample cell, then the system was equilibrated to 25 °C. Experimental parameters were set as follows: total number of injections = 20 (one 0.4 or 0.5 μL injection followed by nineteen 2 μL injections); cell temperature = 25 °C; initial delay = 60–200 s; syringe concentration = variable; mixing speed = 700 rpm. Accounting for the dilution in the ITC cell, the 30 and 50 μg/mL injections were equivalent to a final LOS concentration of about 4 and 7 μg/mL, respectively, interacting with the nanoparticles. Controls included carbonate buffer titrated into 625 μg/mL of nanoparticles and 50 μg/mL LOS titrated into carbonate buffer (to determine heat of dilution). Origin 7.0 software was used to convert all raw ITC data into DeltaH plots, and its regression function was used to calculate the stoichiometry, enthalpy, entropy and dissociation constant (K_d) of each titration.

2.7 Cultivation of immortalized bronchial epithelial cells

The 16HBE14o- cell line, generated by transformation of normal bronchial cells obtained from a heart-lung transplant patient, was generously provided by Professor Gruenert, Department of Otolaryngology, University of California, San Francisco (Gruenert et al., 1988). Cells

were propagated in cell culture medium composed of Eagle's minimum essential medium with Earle's salts (Life Technologies Co.) supplemented with 10 % fetal bovine serum (FBS, Atlanta Biologics Inc.), 2 mM L-glutamine (Life Technologies Co.), 100 µg/mL streptomycin and 100 units/mL penicillin G (Life Technologies Co.) in T-75 flasks (Greiner Bio-One). The cell culture medium was replaced every other day. At 80 % cell coverage (4–6 days), the cells were passaged by washing three times with biological buffer (prepared as a 10-times concentrated solution containing 3.795 g NaCl, 0.35 g Na_2HPO_4, 0.20 g KCl, 0.99 g glucose, and 1.265 g HEPES in 1 L of purified water, pH 7.4), detachment by treatment with Trypsin/EDTA (Life Technologies Co.) for 5–10 min at 37 °C and 5 % CO_2 with gentle agitation, and addition of the cell suspension to new flasks with 12 mL of media per flask. Passages 20 to 40 were used.

2.8 Immunofluorescent detection of PAFR on 16HBEo- cells

The expression of PAFR on the surface of 16HBEo- cells was determined using flow cytometry and confocal microscopy. Cells were prepared for flow cytometry by suspending cells in biological buffer containing 0.2 % Tween 20, centrifuging at 300 × g for 10 min, then incubating in cold methanol (–20 °C) for 10 min at –20 °C. The fixed cells were washed with biological buffer containing 0.2 % Tween 20 (Sigma) and incubated with 10 % normal goat serum in biological buffer containing 0.2 % Tween 20 at 4 °C overnight. Cells were then centrifuged, redispersed in biological buffer at a concentration of 1×10^7 cells/mL. To stain for PAFR expression, cells were incubated with 50 µL of 8 µg/mL solution of IgG2a PAFR (human) monoclonal antibody raised in mouse (product 160600, Cayman Chemical) in biological buffer for 30 min at room temperature. The controls were no stain, secondary antibody control, and isotype control using 8 µg/mL solution of mouse IgG2ak clone eBM2a (eBiosciences™) in biological buffer. Cells were then washed six times with cold biological buffer containing 0.2 % Tween 20 and incubated with 50 µL of either 6 % normal goat serum in biological buffer (no stain control) or 0.1 µg/mL solution of Alexa Fluor 647 Goat Anti-Mouse IgG (H+L) antibody (Life Technologies Co.) in biological buffer for 15 min. Cells were again washed six times with cold biological buffer containing 0.2 % Tween 20. After antibody treatment, cell suspensions were analyzed immediately using an LSR II flow cytometer (BD™ Biosciences).

To confirm and visualize PAFR expression, cells were cultured onto collagen-coated cover slips in 24-well plates and incubated overnight. The cells were washed three times with biological buffer containing 0.2 % Tween 20. Immunostaining of the cell membranes was conducted as described above, except 100 µL of each antibody solution was added to the cells and the secondary antibody Alexa Fluor 568 Goat Anti-Mouse IgG (H+L) antibody (Life Technologies Co.) was added at a concentration of 4 µg/mL. After cell washing, the glass coverslip containing the cell membrane was mounted to a microscope slide using antifade reagent with the nuclear stain DAPI, then kept at 4 °C until imaged. Cell layers were imaged using a Zeiss LSM 710 confocal microscope with 40× oil immersion objective lens.

2.9 Particle association with bronchial epithelial cells

To prepare cells for particle binding and uptake studies, 16HBEo- cells were propagated on collagen-coated glass coverslips. A volume of 100 µL of cells was dispensed, at 2×10^5 cells/well, onto dried collagen-coated coverslips and incubated one day until reaching 80 % confluency, as determined by visual inspection. Suspensions of fluorescent yellow particles with or without coating (0.22 µg/mL, 100 µL/well) were added to cells and incubated for 0.5, 2, 4, 18, or 24 h (n = 4 wells of cells per treatment) to quantify uptake with time. In each case, after incubation the cells were washed three times to remove unbound particles.

The number of cells associated with particles was quantified using an LSR II flow cytometer (BD Biosciences) with a 488 nm excitation source. Cells were processed for flow cytometry by incubating the cells with enzyme-free cell dissociation buffer (Life Technologies Co.) for 0.5–1 h at room temperature, centrifuging at 300 × g for 10 min at 4 °C, then dispersing in cold biological buffer by gentle pipetting to obtain a single cell suspension. Raw data was processed to gate the live cell population(s) based on cell size (forward scatter) and cell granularity (side scatter), effectively removing dead cells, cell debris and particle agglomerates. Gating was confirmed with controls, i.e. cells not treated with particles, particle alone, and cells and particles mixed briefly together. The population of cells containing particles were identified based on fluorescence intensity using the Probability Binning (PB) Chi(T) value (Roederer et al., 2001). The percentage of cells in the population was quantified using the Enhanced Normalization Subtraction (ENS) method in FlowJo® (Bagwell, 1996). Results were collected for at least 10,000 cells (n = 4).

Confocal microscopy was used to assess the location of particles within the cell cultures. After particle treatment, cell membranes were washed three times to remove unbound particles and secretions produced during the incubation period. Cell membranes were then stained with 1 µg/mL DiI D-282 (Life Technologies Co.), a lipophilic indocarbocyanine fluorescent red dye (549 nm/565 nm), in cell culture medium for 30 min, washed with biological buffer three times to remove excess dye, fixed with 2 % w/v paraformaldehyde for 30 min, blocked with 50 mM ammonia chloride for 10 min, and washed with

biological buffer once to remove excess reagents. Triton X-100 prepared at 0.05 % w/v in biological buffer was used to permeabilize the cell membrane for 10 min. The membranes were washed, the cover glass containing the membranes mounted to a microscope slide, and the cells exposed to ProLong® Gold antifade reagent with the blue-fluorescent nuclear 4',6-diamidino-2-phenylindole (DAPI 358 nm/461 nm; Life Technologies Co.) to stain the cell nuclei. The cells were kept at 4 °C until imaged. Z-stacks of cell layers were obtained using a LSM 710 upright confocal microscopy (Zeiss). A 40× oil immersion objective lens was used to take images with step size of 200 nm. Images were rendered in MATLAB.

2.10 Cell uptake inhibitor and activator studies

The toxicity of inhibitors to 16HBEo- cells was first determined using the MTS assay (CellTiter 96® Aqueous One Solution Cell Proliferation Assay; Promega Co.). Cells were seeded onto 96-well plates at 3×10^4 cells/well, incubated for 24 h, then treated for 0–5 h with one of the following inhibitors: 0.1 % NaN_3 with 50 mM 2-deoxyglucose, 5 μg/mL cytochalasin D, 80 μM dynasore, 200 μM genistein, 10 μg/mL chlorpromazine, or 5 mM methyl β-cyclodextrin. Negative and positive control were cells treated with biological buffer (absorbance normalized to 100 % cell viability) and cells treated with 2 % w/v SDS, respectively. Based on toxicity results, uptake studies in the presence of inhibitors were limited to time points less than 3 h, and studies with inhibitors of clathrin-mediated endocytosis were not conducted as cell viability with these inhibitors was 40–95 % at all time points.

To determine the mechanisms by which particles were taken up by cells, 16HBEo- cells were pre-treated with one of the following inhibitors one hour prior to particle treatment: 0.1 % NaN_3 with 50 mM 2-deoxyglucose, 5 μg/mL cytochalasin D, 80 μM Dynasore, 200 μM genistein, or 5 mM methyl β-cyclodextrin. The receptor PAFR was activated by pre-treating cells with PAF (10 μM) for 2 h. The treatment solutions were removed then replaced with the particle suspension containing fresh inhibitor or PAF and incubated. After incubation, cells were washed three times to remove unbound particles and secretions produced during the incubation period. Particle–cell association was measured by flow cytometry.

2.11 Statistical analysis

Significance ($p < 0.05$) of differences was determined by one-way ANOVA with Holm-Sidak's multiple comparison tests using GraphPad Prism software (version 6.05).

3. Results

3.1 Selection and characterization of NTHi bacteria

Since ChoP content is vital for epithelial cell binding, LOS with high ChoP content may enhance association with cells containing PAFR. Three NTHi strains were screened to select for the strain with a high activity of ChoP. NTHi strains 956 and 3198 expressed significantly higher ChoP activity, as measured by absorbance of p-nitrophenol, than the 2019 strain (**Fig. 1**). The higher level of ChoP activity on NTHi 3198 compared to NTHi 2019 was confirmed by dot immunoblot, with strain 3198 expressing more ChoP on its surface at shorter exposure times (1 s) than strain 2019 (30 s), as observed in the higher intensity and positive stained area of dark spots. This is in agreement with published literature that reports 78 % of strain 3198 expresses ChoP with high reactivity, compared to 9 % of strain 2019 (Swords et al., 2000; Weiser et al., 1997). Further, the expression of ChoP on strains 2019 and 3198 was higher when bacteria were cultured on BHI agar than on chocolate agar; in contrast, no statistical difference in ChoP expression was observed for strain 956 grown on the two substrates (**Fig. 1**). Strain 3198 cultured on supplemented BHI agar medium was chosen for LOS isolation and coating onto particles.

3.2 Physical and chemical characterization of uncoated and functionalized particles

Electron microscopy images of the uncoated polystyrene particles confirmed that particles were spherical, with smooth surfaces (**Fig. 2(a)**). Upon particle exposure to carbonate buffer, salt crystals were observed attached to the particle surfaces (**Fig. 2(b)**). Coating the polystyrene particles with 5 ng/mL LOS did not change their appearance compared to the carbonate buffer-washed particles (**Fig. 2(c)**), as salt crystals remained attached to the particle surface; however, upon coating with the higher concentration of LOS (5 μg/mL), salt crystals were no longer

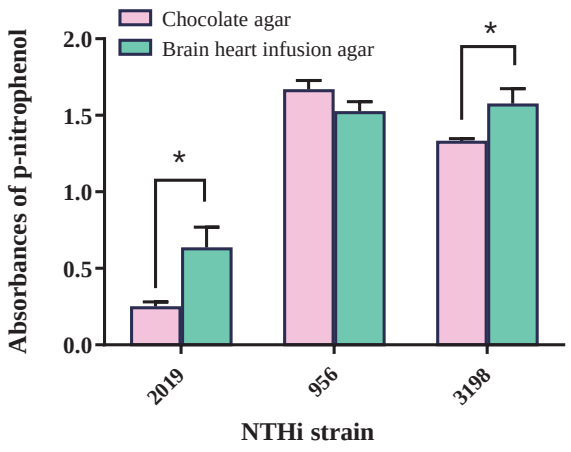


Fig. 1 Relative absorbance of p-nitrophenol at 405 nm from colorimetric ELISA indicating the expression of ChoP on NTHi bacterial strains 2019, 256, and 3198 in either chocolate agar or brain heart infusion agar growth medium ($n = 3$, mean ± SD). *indicates statistical difference between NTHi grown in different agar media ($p < 0.05$).

observed, suggesting LOS displaced the salt on the particle surface (**Fig. 2(d)**). Similarly, exposing uncoated particles with a protein solution (gelatin) resulted in visible residue on the particle surface (**Fig. 2(f)**); however, this residue was not observed on particles that were pre-coated with 5 μg/mL LOS prior to gelatin coating (**Fig. 2(e)**).

When suspended in water, uncoated particles exhibited low polydispersity with a hydrodynamic diameter of ~255 nm, and a zeta potential of about –50 mV (**Table 1**). When placed in carbonate buffer, the particles agglomerated slightly. Agglomeration was maintained with LOS coating and was intensified with gelatin coating. When placed in serum-free media for cell studies, particles generally de-agglomerated, except for the 5 μg/mL LOS coated particles which exhibited slightly higher agglomeration. In addition, particles suspended in media exhibited more neutral zeta potentials than the same particles in water. Serum-free media contains various salts that likely compressed the electrical double layer surrounding the particles, resulting in a reduction in the zeta potential. Particles coated with 5 μg/mL LOS exhibited the highest zeta potential in media at about –25 mV, suggesting significant surface coverage with the negatively charged LOS. LOS molecules have COOH groups on their carbohydrate structures which are negatively charged at physiologic pH, in addition to the ChoP moieties which are zwitterionic at physiologic pH.

The surface chemistry of uncoated and functionalized particles was investigated by XPS (**Table 2**). To confirm the existence of a coating on the functionalized particle surfaces, the raw coating materials were also analyzed. LOS contained mostly carbon (49.6 %) and oxygen (35.2 %), with the remaining composed of 9.3 % nitrogen, 5.6 % phosphate, and 0.3 % sulphur. Gelatin contained no phosphate, but was comprised of 65.8 % carbon, 18.7 %

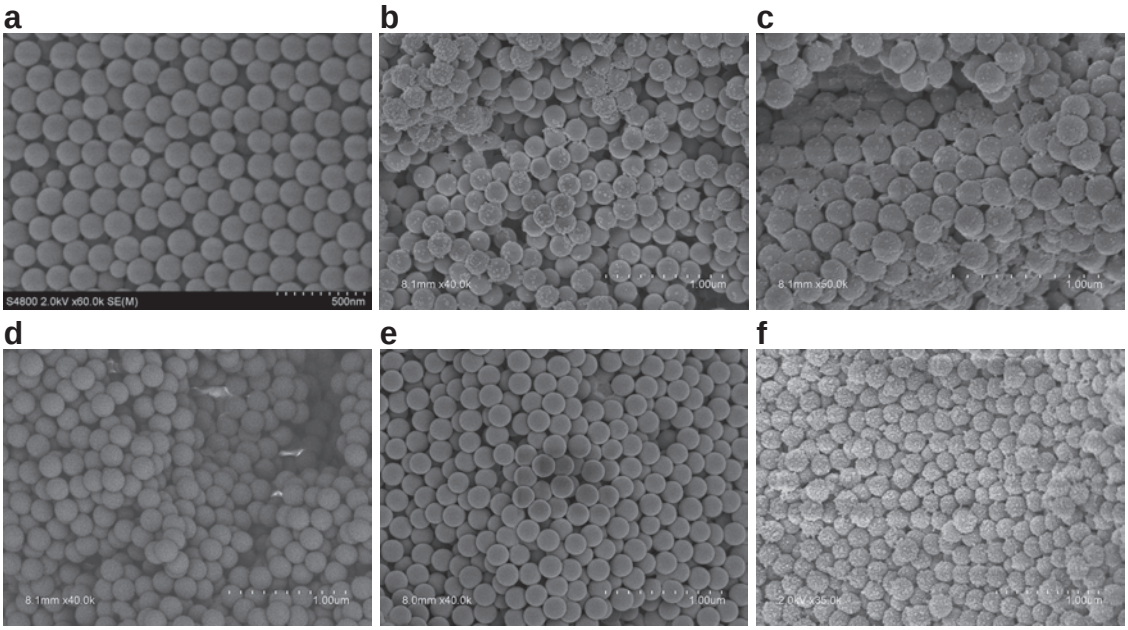


Fig. 2 Scanning electron microscopy images of **(a)** uncoated polystyrene particles, **(b)** particles washed with carbonate buffer, **(c)** particles coated with 5 ng/mL LOS, **(d)** particles coated with 5 μg/mL LOS, **(e)** particles coated with 5 μg/mL LOS and exposed to gelatin, **(f)** uncoated particles exposed to gelatin. Scale bar = 500 nm **(a)** or 1 μm **(b–f)**.

Table 1 Characterization of geometric size and zeta potential of polystyrene particles (200 nm nominal diameter) with various surface coatings in water and serum-free media. Values are reported as mean ± SD (n = 3).

Particle coating	Suspension in water		Suspension in serum-free media	
	Particle diameter (nm)	Zeta potential (mV)	Particle diameter (nm)	Zeta potential (mV)
Uncoated	255.15 ± 6.6	–50.0 ± 5.3	—	—
Carbonate buffer	381.0 ± 14.2	–40.9 ± 0.7	157.7 ± 9.9	–10.4 ± 1.2
5 ng/mL LOS	295.2 ± 6.4	–46.8 ± 2.2	183.7 ± 7.4	–8.8 ± 0.5
5 μg/mL LOS	351.6 ± 14.8	–47.8 ± 2.1	461.1 ± 7.8	–24.5 ± 2.2
5 μg/mL LOS and gelatin	555.4 ± 254.6	–39.5 ± 1.1	187.7 ± 13.8	–7.6 ± 0.9
Gelatin	1053.8 ± 372.5	–36.4 ± 4.9	165.7 ± 3.2	–7.3 ± 0.9

Table 2 Surface elemental analysis of LOS, gelatin, and polystyrene particles with various surface coatings via X-ray photoelectron spectroscopy.

Material		% Atomic concentration					C/O ratio
		C 1s	O 1s	N 1s	P 2p	S 2p	
LOS		49.6	35.2	9.3	5.6	0.3	1.4
Gelatin		65.8	18.7	15.3	0.0	0.2	3.5
Particles	Uncoated	19.5	54.3	0.0	6.7	19.5	0.36
	5 ng/mL LOS	38.6	40.8	1.0	5.0	14.6	0.9
	5 μg/mL LOS	57.7	29.2	0.5	3.1	9.6	2.0
	5 μg/mL LOS and gelatin	62.7	24.9	4.1	2.4	5.9	2.5
	Gelatin	75.9	16.7	4.5	0.6	2.3	4.5

oxygen, 15 % nitrogen and 0.2 % sulfur. Gelatin also had a higher C/O ratio at 3.5, compared to LOS at 1.4. In contrast, the uncoated particle surface contained carbon, oxygen, and sulfur since the polystyrene particles used in this study had a polystyrene backbone composed of carbon and oxygen, and sulfate function groups. The polystyrene particles had the smallest C/O ratio at 0.36. Some residual phosphate (7 %) was also observed on the uncoated particle surface, likely due to contamination from the water washes. Given these differences among the raw materials, the phosphate, nitrogen, and C/O ratio were used to confirm functionalization of the particles.

Particles coated with a 5 ng/mL LOS solution exhibited an elemental surface indicative of a mostly uncoated polystyrene surface with a small amount of LOS adsorbed (C/O ratio of 0.9, between that of LOS and polystyrene; with existence of N indicating some LOS adsorption). This suggests that LOS was on the particle surface but did not completely coat the entire surface. With a higher LOS coating solution concentration (5 μg/mL), the C/O ratio increased to 2.0, suggesting a higher concentration of LOS on the surface. In addition, the phosphorus and sulphur concentrations at the surface decreased to 3.1 % and 9.6 %, respectively, suggesting that these moieties were buried beneath the carbon and oxygen backbone of the LOS. When uncoated particles or LOS-coated particles were coated with gelatin, the nitrogen concentration and C/O ratio increased significantly compared to their uncoated counterparts, to values closer to that of pure gelatin. This suggests that gelatin partially masked the surface of the particles, even in the presence of LOS.

The LOS coating process was further analyzed by ITC to determine the stoichiometry of LOS binding to the polystyrene particles. ITC experiments were carried out using four different concentrations of LOS (**Fig. 3**). The regression lines for the 20 and 100 μg/mL titrations exhibited negligible slope and therefore not analyzed. For the 30 and 50 μg/mL titrations, the amount of LOS bound to the particle surface increased with an increase in LOS concentration resulting in an estimated 17.7 LOS binding sites per particle (titration with 30 μg/mL LOS) and 33.9 LOS binding sites per particle (titration with 50 μg/mL LOS). Enthalpies of binding were large and negative for all titrations (–2 kcal/mol to –10 kcal/mol), indicating strong binding of LOS to the particle surface.

3.3 Uptake of particles in 16HBEo- lung epithelial cells

PAFR expression in 16HBE14o- cells was confirmed via immunostaining (**Fig. 4**). The secondary and isotype controls exhibited low levels of staining due to non-specific receptor interactions (**Figs. 4(b)** and **4(c)**, respectively), which was quantified by flow cytometry via fluorescence intensity (**Fig. 4(e)**). PAFR expression on the cell surface was observed as diffuse staining across the entire cell surface (**Fig. 4(d)**). Flow cytometry confirmed that the entire population of 16HBEo- cells stained for PAFR exhibited higher intensity of fluorescence than controls, confirming the cells expressed PAFR (**Fig. 4(e)**).

Next, lung epithelial cells were exposed to uncoated, gelatin-coated, or functionalized particles for up to 24 h and the percentage of cells associated with particles quantified by flow cytometry. Uncoated particles and particles coated with 5 ng/mL LOS behaved similarly, with little uptake from 0–19 h (<10 % of cells were associated with particles) followed by a small increase at 24 h to 10 % (**Fig. 5(a)**). Gelatin coated particles were associated with at most 12 % of cells at 4 h, which was not statistically different than uncoated particles. However, particles coated with 5 μg/mL LOS were associated with about 12 % of cells at time 0 and this rose steadily to about 35 % at 24 h. Confocal microscopy confirmed that the 5 μg/mL LOS-coated particles were internalized into the 16HBEo- cells and not just attached to the cell surface (**Fig. 5(b)**).

The energy dependence of particle uptake in 16HBEo- cells was quantified after cell incubation with NaN_3/2-deoxyglucose, which inhibits all energy-dependent pathways (**Fig. 6**). Incubation of cells with NaN_3/2-

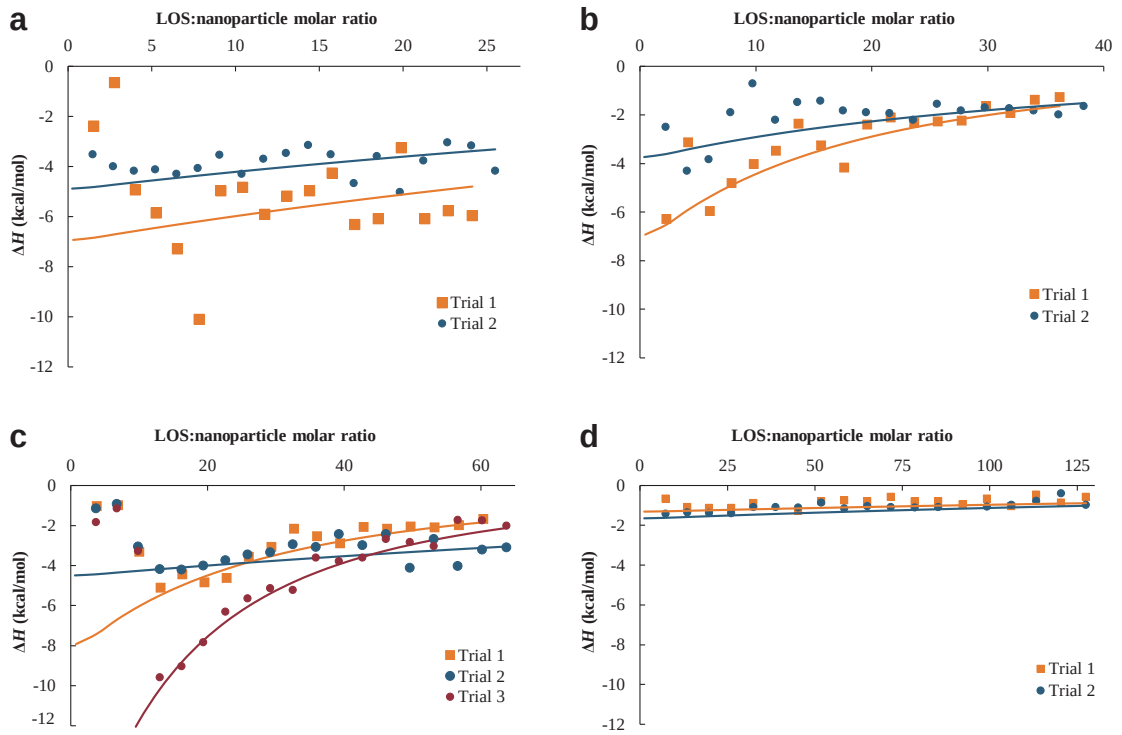


Fig. 3 Isothermal titration calorimetry (ITC) plots of Δ*H* versus LOS–nanoparticle molar ratio with single injections of **(a)** 20 μg/mL, **(b)** 30 μg/mL, **(c)** 50 μg/mL, or **(d)** 100 μg/mL of LOS. Colored symbols represent unique replicates. Lines represent regression curves originated by Origin software. A buffer–nanoparticle titration was used as a reference and subtracted from all data sets.

deoxyglucose resulted in complete loss of uptake of the 5 μg/mL LOS-coated particles, suggesting these particles are taken up by endocytosis. No other particle type experienced inhibited cell uptake after cell exposure to NaN_3/2-deoxyglucose and thus may be taken up by both energy-dependent and energy-independent pathways.

Further studies were conducted with specific pathway inhibitors to help elucidate specific uptake pathway for different particle types. Inhibitors of micropinocytosis (cytochalasin D) and caveolin-mediated endocytosis (genistein) did not inhibit the uptake of any particle type. Instead, particle uptake was sometimes enhanced with cell exposure to these inhibitors, suggesting that particles were taken up by multiple pathways. The inhibitor of cholesterol- dependent pathways (methyl β-cyclodextrin), which inhibits both caveolin-mediated and clathrin-mediated endocytosis, significantly reduced cell uptake of the 5 μg/mL LOS-coated particles. This suggest that the LOS-coated particles were primarily taken up by receptor-mediated endocytosis. However, due to the significant cell toxicity exhibited by the inhibitors of clathrin-mediated endocytosis, this could not be confirmed via chemical pathway inhibitors.

To prove that receptor-mediated endocytosis was the route by which LOS-coated particles were taken up into cells, we investigated whether PAFR-mediated endocytosis could be altered by the cognate ligand of the receptor (PAF). Upon cell incubation with PAF, the 5 μg/mL LOS-coated particles exhibited a 5- to 10-fold increase in uptake (**Fig. 7**). No significant change in the association of particles with lung cells was observed with the other particle types.

4. Discussion

Lipopolysaccharides (LPS), also known as endotoxins, are large lipid- and polysaccharide-containing molecules constituting the major component of the outer membrane of Gram-negative bacteria. They induce a strong immune response in animals and have been implicated in various pathogenic functions (Alexander and Rietschel, 2001; Simpson and Trent, 2019). Key studies have shown that isolating LPS from the bacterial surface and attaching it to a particle surface may not alter its functionality, enabling the particles to mimic some bacterial properties (Piazza et al., 2011). For example, titanium dioxide particles coated with LPS from *E-coli* induced pro-inflammatory signaling in primary human mononuclear phagocytes (Ashwood et al., 2007). LPS associated with polymeric and metallic components of orthopedic implants stimulate toll-like receptor (TLR) activation, which contributed to an inflammatory response (Greenfield et al., 2010; Hold and Bryant, 2011). However, the activation of the inflammatory response by LPS-coated particles was not desired for the current application.

Lipooligosaccharides (LOS) share a similar lipid A structure to LPS, but are lower in molecular weight, lack the O-antigens that allow serotyping, and have

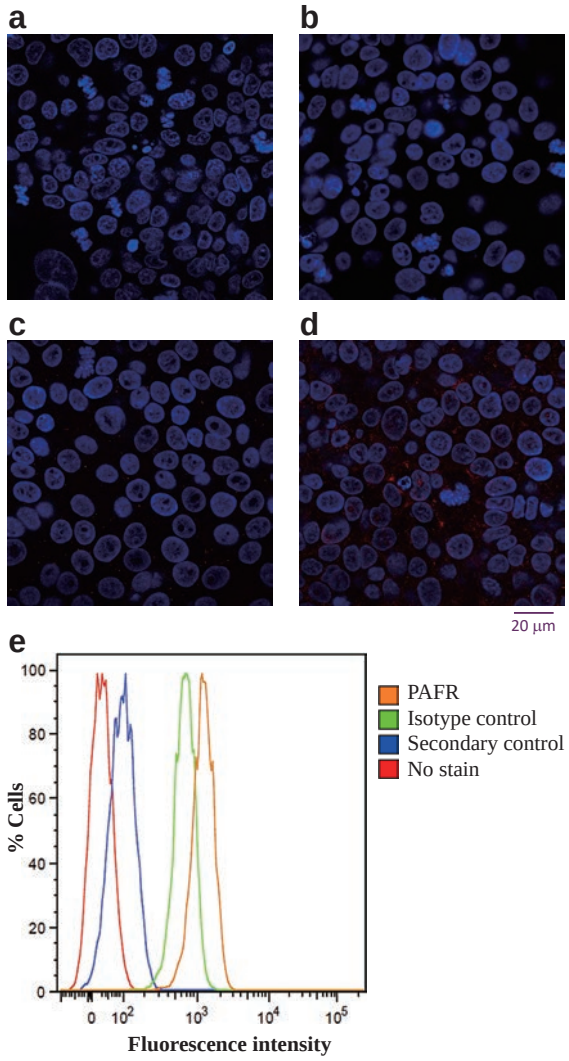


Fig. 4 **(a–d)** Confocal micrographs of 16HBE14o- cells with nuclei stained using DAPI (blue) and incubated with the **(b)** secondary antibody (secondary control, red stain), **(c)** fluorescent antibody IgG2ak to confirm the specificity of primary antibody binding (isotype control, red stain), or **(d)** the primary and secondary antibodies (red stain for PAFR). Scale bar = 20 µm. **(e)** Percent fluorescent cells as a function of fluorescence intensity for cells not stained (far left curve) or incubated with the secondary antibody (secondary control, second curve from left), IgG2ak (isotype control, third curve from left), or the primary and secondary antibodies (PAFR staining, far right curve).

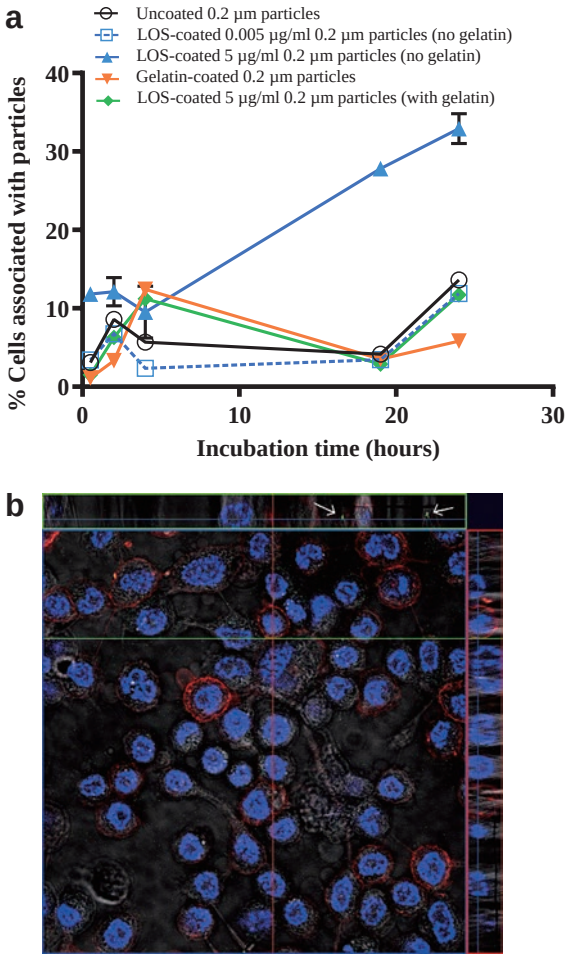


Fig. 5 **(a)** Percentage of 16HBE14o- cells associated with uncoated and functionalized particles as a function of incubation time at 37 °C (n = 4, mean ± SD). **(b)** Confocal microscopy image of 16HBEo- cells exposed to 5 µg/mL LOS-coated particles. Cell membranes were labeled by DiI (red fluorescence) and cellular nuclei were labeled by DAPI (blue fluorescence), and particles fluoresce green. Two representative cross-sections of the cell layer are displayed at top and right side of the micrograph, with green fluorescing particles denoted by the arrows.

significantly lower toxicity profiles (Preston et al., 1996). LOS is the major glycolipid expressed on mucosal Gram-negative bacteria, including members of the genera *Neisseria, Haemophilus, Bordetella, and Branhamella*. It is a heat stable, amphipathic glycolipid complex that covers up to 75 % of the outer membrane (Silipo et al., 2011), and is crucial for the viability and survival of Gram-negative bacteria as it helps maintain proper outer membrane structure. It also contributes to host-bacterium interactions related to adherence, colonization, internalization, and ultimately survival in host cells.

The oligosaccharide region of LOS is highly heterogeneous within and between bacterial strains, containing both the recognition structures for host cells and components of the immune system, as well as carbohydrate moieties that may camouflage the bacterial surface from the host through molecular mimicry of host structures (Mandrell and Apicella, 1993; Masoud et al., 1997; Moran et al., 1996; Murphy and Apicella, 1987; Risberg et al., 1999a, 1999b; Silipo et al., 2011). In some bacterial species, these carbohydrate structures further facilitate bacterial adherence to the respiratory epithelium (Clark et al., 2012; Jalalvand and Riesbeck, 2014; Swords et al., 2000, 2001). Phosphorylcholine (ChoP) expressed as a terminal structure of the OS region facilitates adherence of multiple bacterial pathogens, including NTHi, to the platelet-activating factor receptor (PAFR) on bronchial cells by molecularly mimicking the structure of the cognate ligand platelet-activating factor (PAF) (Cundell et al., 1995; Gillespie et al., 1996; Harvey et al., 2001; Lysenko et al., 2000; Rose-

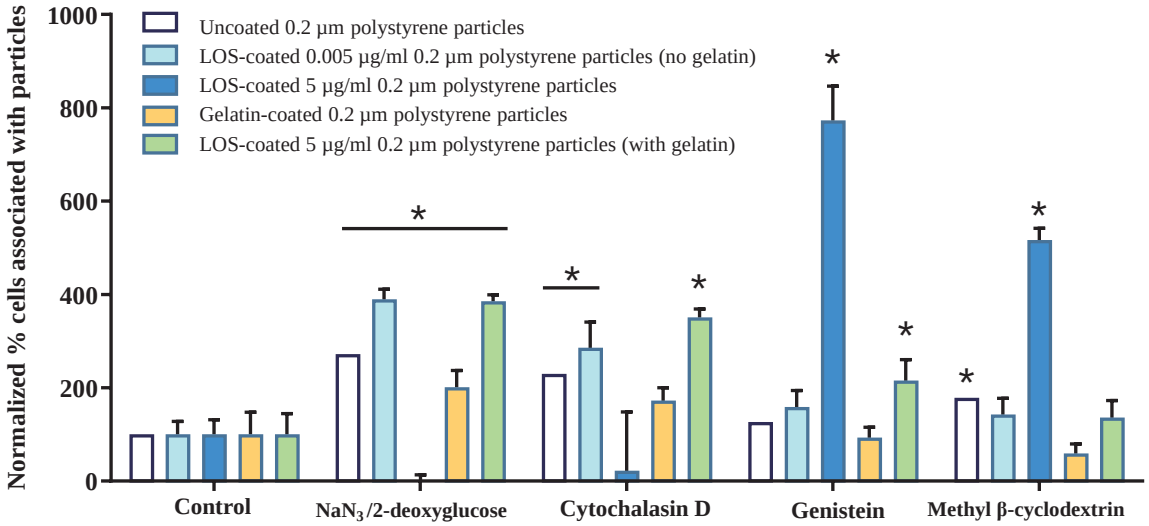


Fig. 6 Percentage of cells, as determined by flow cytometry, associated with 16HBEo- cells before (control) and after exposure to various inhibitors for 2 h. Data is reported as mean ± SD (n = 4). * indicates statistically significant differences compared to the absorbance of untreated cells.

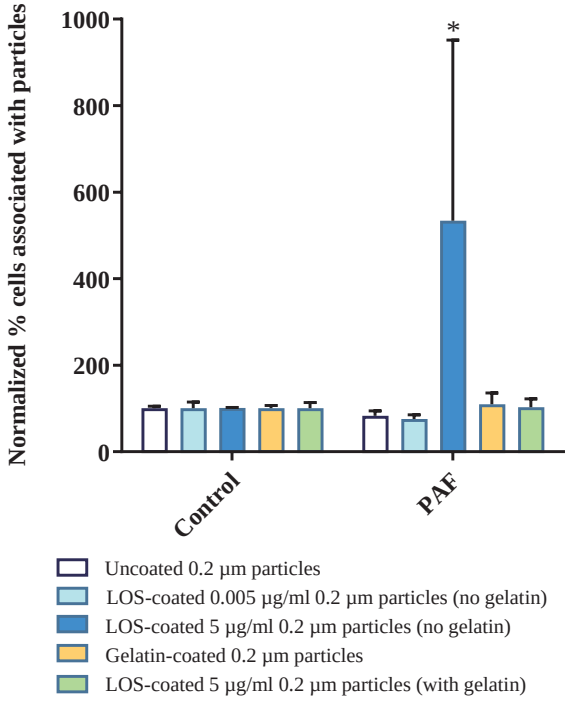


Fig. 7 Normalized percentage of 16HBE14o- cells associated with uncoated and functionalized polystyrene particles before (control) or after activation with PAF (n = 8, mean ± SD).

now et al., 1997; Schweda et al., 2000; Weiser et al., 1997, 1998). As a potential targeting ligand for particles, our previous studies indicated that coupling ChoP-containing LOS from NTHi (strain 2019) to the surface of 1 µm particles facilitated significantly more binding to the human bronchial epithelial surface compared to particles coated with gelatin or coated with truncated LOS lacking the oligosaccharide chains that contain ChoP (Swords et al., 2000). Here, we aimed to evaluate the ability of ChoP-containing LOS to facilitate the uptake of smaller nanoparticles into respiratory epithelial cells.

Given the heterogeneity of the OS expression between bacterial strains, a screening of clinically isolated NTHi strains was performed to select a strain with high ChoP content to facilitate particle adherence and uptake into lung cells. Two of the three NTHi clinical isolates tested (956 and 3198) exhibited high ChoP activity. While the ChoP content of strain 956 had not been previously reported, the observed differences between strains 3198 and 2019 agreed with published literature, which has reported that 78 % of strain 3198 expressed ChoP with high reactivity, compared to 9 % of strain 2019 (Swords et al., 2000; Weiser et al., 1997). Based on these results and the known ability of NTHi 3198 to associate with and invade primary lung epithelial cells (Ketterer et al., 1999), LOS from NTHi 3198 was chosen as the ligand for further studies.

LOS is a large molecule containing a lipid structure that embeds in the bacterial outer membrane and an oligosaccharide structure that is exposed on the surface. The polystyrene particles used in this study exhibit a hydrophobic, negatively charged surface containing sulfate ester functional groups. Due to the hydrophobicity of the particles and the lipophilicity of the LOS lipid tails, we anticipated that the lipid tails of the LOS molecules would readily adsorb to the hydrophobic particle surface. In this case, the carbohydrate heads on the LOS structure containing ChoP could be available for cell targeting. Based on analysis of the zeta potential and XPS data, LOS was indeed coated onto the surface of polystyrene particles, particularly with the more highly concentrated LOS coating solution. However, the XPS data also suggested that the phosphate groups were buried within a mostly carbon-oxygen LOS backbone. This would be undesirable if the ChoP functional groups were not available to function as a targeting ligand on the particle surface. As XPS studies

were conducted on dry particles, when the carbohydrate chains become hydrated, the LOS structure could open and give access to the ChoP moieties.

ITC further confirmed the ability of LOS to strongly adsorb to the nanoparticle surface. Typical enthalpies of binding for proteins to polystyrene nanoparticle surfaces has been reported to be on the order of 10 s to 100 s of kcal/mol (Porzeller et al., 2019), similar to the values obtained in this study. Using titration concentrations of 30 and 50 μg/mL, we estimated that there are about 34 LOS binding sites per particle. The titration concentration of 50 μg/mL (~7 μg/mL final concentration in the cell after titration), resulted in slightly more adsorbed LOS molecules than the 30 μg/mL titration concentration (~4 μg/mL final concentration in the cell after titration). This suggests that higher LOS concentrations enhance LOS adsorption to the particle surface. Previous work by Swords et al. reported a dose-response in which increasing the concentration of LOS coating resulted in more particle adherence to respiratory epithelium (Swords et al., 2000). LOS concentration is limited, though, as it readily forms micelles in aqueous solution at low concentrations due to its amphiphilic nature (Steimle et al., 2016). Thus, a higher LOS coating might be achieved by using a co-solvent to better solubilize the LOS. The ability of LOS to form micelles, as well as the complex structure of LOS, are potential reasons for the relatively high variability in the ITC data.

If the ChoP moieties on the LOS molecules remained accessible on the particle surface, we would expect the particles to exhibit better binding to and internalization into the respiratory epithelium. PAFR is expressed on human lung tissue membranes (Hwang et al., 1985; Shukla et al., 2016) and various lung epithelial cell lines (Chen et al., 2015). In the current study we confirmed PAFR expression in 16HBEo- bronchial epithelial cell monolayers via immuno-fluorescent staining and used these cells to evaluate the uptake of uncoated and coated particles. The 5 μg/mL LOS-coated particles exhibited the highest cell uptake of nanoparticles, with about 35 % uptake at the 24 h timepoint. All other particle types were taken up by less than 12 % of cells at any time. Confocal microscopy confirmed that particles were not just bound to the surface, but were internalized into the cell layers. While the ability of PAFR to mediate particle attachment to the respiratory epithelium had been previously established (Swords et al., 2000), this is the first time to our knowledge that bacterial-derived LOS has been used as a targeting ligand to facilitate particle uptake into cells.

We further investigated the uptake mechanism by blocking specific endocytic pathways using chemical inhibitors. NTHi bacteria have been shown to internalize into human lung epithelial cells by macropinocytosis and receptor-mediated endocytosis, so these pathways were likely candidates for LOS-coated nanoparticle uptake (Clementi and Murphy, 2011; Ketterer et al., 1999; Swords et al., 2000, 2001). Pre-incubation of the lung cells with NaN_3-2-deoxyglucose completely knocked out their ability to take up the 5 μg/mL LOS-coated particles, suggesting an energy-dependent pathway for these particles, but had no impact on the other particle types. We further saw no evidence of the LOS-coated particles being taken up by macropinocytosis. Due to significant cell toxicity upon cell incubation with inhibitors of the clathrin-mediated pathway, we were unable to confirm this pathway using chemical inhibitors of endocytic pathways. Thus, a different approach was chosen in which the impact of a PAFR activator on the cellular uptake of uncoated and functionalized particles was investigated. A549 cells were pre-treated with PAF, the natural substrate for PAFR (Chao and Olson, 1993). Prior studies have shown that PAFR stimulation is involved in bacterial entry and could assist the delivery of siRNA to airway epithelia (Krishnamurthy et al., 2014; Zhang et al., 2000). In the current study, PAF pre-treatment significantly enhanced cell uptake of the 5 μg/mL LOS-coated particles, suggesting that PAF activation aided their uptake. Activation of PAFR via PAF exhibited no significant change on the association of any other particle type, demonstrating receptor targeting with the LOS coating.

In summary, the functionalization of polystyrene nanoparticles with LOS bacterial ligands resulted in better cellular uptake in PAFR-expressing lung cells. This strategy could be extended to drug-containing nanoparticles to enhance the therapeutic efficacy of drug compounds that require cellular internalization. Further, receptor-ligand interactions could be enhanced by activating the cell receptor, suggesting that enhanced cellular uptake could be achieved in disease states where the receptor is already activated, such as in the instance of infection, COPD, asthma, and cancer.

Acknowledgments

Funding for this work was provided by the National Institutes of Health (R21HL113876 and P30 DK054759). M. Timm was supported through an NSF-REU program in Nanoscience and Nanotechnology (NSF 1359063). We thank the University of Iowa Central Microscopy Research Facility, a core resource supported by the Vice President for Research & Economic Development, the Holden Comprehensive Cancer Center, and the Carver College of Medicine, for access to and training on the confocal and electron microscopes. Flow cytometry data presented were obtained at the Flow Cytometry Facility, which is a Carver College of Medicine / Holden Comprehensive Cancer Center core research facility at the University of Iowa. The Facility is funded through user fees and the generous financial support of the Carver College of Medicine, Holden Comprehensive Cancer Center, and Iowa City Veteran's Administration Medical Center. Part of the study has been

published in the PhD thesis of author Mai Tu (Tu, 2015).

Nomenclature

BHI	Brain heart infusion
BSA	Bovine serum albumin
ChoP	Phosphorylcholine
ELISA	Enzyme-linked immunosorbent assay
ITC	Isothermal titration calorimetry
LOS	Lipooligosaccharide
LPS	Lipopolysaccharide
NAD	Nicotinamide adenine dinucleotide
NTHi	Non-typeable *Haemophilus influenzae*
PAF	Platelet-activating factor
PAFR	Platelet-activating factor receptor
pNPP	Nitrophenyl phosphate bis (cyclohexyl ammonium)
SDS	Sodium dodecyl sulfate
SEM	Scanning electron microscope
XPS	X-ray photoelectron spectrometer

References

Alexander C., Rietschel E.T., Bacterial lipopolysaccharides and innate immunity, Journal of endotoxin research, 7 (2001) 167–202. DOI: 10.1177/09680519010070030101

Apicella M.A., Isolation and characterization of lipopolysaccharides, in: DeLeo F.R., Otto M. (Eds.), Bacterial Pathogenesis: Methods and Protocols, Humana Press, Totowa, NJ, 2008, pp. 3–13, ISBN: 978-1-60327-032-8. DOI: 10.1007/978-1-60327-032-8_1

Ashwood P., Thompson R.P., Powell J.J., Fine particles that adsorb lipopolysaccharide via bridging calcium cations may mimic bacterial pathogenicity towards cells, Experimental Biology and Medicine, 232 (2007) 107–117. DOI: 10.3181/00379727-207-2320107

Bagwell B., A journey through flow cytometric immunofluorescence analyses—Finding accurate and robust algorithms that estimate positive fraction distributions, Clinical Immunology Newsletter, 16 (1996) 33–37. DOI: 10.1016/S0197-1859(00)80002-3

Campagnari A.A., Gupta M.R., Dudas K.C., Murphy T.F., Apicella M.A., Antigenic diversity of lipooligosaccharides of nontypable Haemophilus influenzae, Infection and Immunity, 55 (1987) 882–887. DOI: 10.1128/iai.55.4.882-887.1987

Chao W., Olson M.S., Platelet-activating factor: receptors and signal transduction, Biochemical Journal, 292 (1993) 617–629. DOI: 10.1042/bj2920617

Chen J., Lan T., Zhang W., Dong L., Kang N., Zhang S., Fu M., Liu B., Liu K., Zhan Q., Feed-forward reciprocal activation of PAFR and STAT3 regulates epithelial–mesenchymal transition in non–small cell lung cancer, Cancer Research, 75 (2015) 4198–4210. DOI: 10.1158/0008-5472.CAN-15-1062

Clark S.E., Snow J., Li J., Zola T.A., Weiser J.N., Phosphorylcholine allows for evasion of bactericidal antibody by Haemophilus influenzae, PLoS Pathogens, 8 (2012) e1002521. DOI: 10.1371/journal.ppat.1002521

Clementi C., Murphy T., Non-typeable Haemophilus influenzae invasion and persistence in the human respiratory tract, Frontiers in Cellular and Infection Microbiology, 1 (2011) DOI: 10.3389/fcimb.2011.00001

Cochi S.L., Broome C.V., Vaccine prevention of Haemophilus influenzae type b disease: past, present and future, Pediatric Infectious Disease, 5 (1986) 12–19. DOI: 10.1097/00006454-198601000-00003

Cundell D.R., Gerard N.P., Gerard C., Idanpaan-Heikkila I., Tuomanen E.I., Streptococcus pneumoniae anchor to activated human cells by the receptor for platelet-activating factor, Nature, 377 (1995) 435–438. DOI: 10.1038/377435a0

Fenton O.S., Olafson K.N., Pillai P.S., Mitchell M.J., Langer R., Advances in biomaterials for drug delivery, Advanced Materials, 30 (2018) 1705328. DOI: 10.1002/adma.201705328

Foxwell A.R., Kyd J.M., Cripps A.W., Nontypeable Haemophilus influenzae: pathogenesis and prevention, Microbiology and Molecular Biology Reviews, 62 (1998) 294–308. DOI: 10.1128/MMBR.62.2.294-308.1998

Galanos C., Lüderitz O., Westphal O., A new method for the extraction of R lipopolysaccharides, European Journal of Biochemistry, 9 (1969) 245–249. DOI: 10.1111/j.1432-1033.1969.tb00601.x

Gillespie S., Ainscough S., Dickens A., Lewin J., Phosphorylcholine-containing antigens in bacteria from the mouth and respiratory tract, Journal of Medical Microbiology, 44 (1996) 35–40. DOI: 10.1099/00222615-44-1-35

Greenfield E.M., Beidelschies M.A., Tatro J.M., Goldberg V.M., Hise A.G., Bacterial pathogen-associated molecular patterns stimulate biological activity of orthopaedic wear particles by activating cognate Toll-like receptors, Journal of Biological Chemistry, 285 (2010) 32378–32384. DOI: 10.1074/jbc.M110.136895

Gruenert D.C., Basbaum C.B., Welsh M.J., Li M., Finkbeiner W.E., Nadel J.A., Characterization of human tracheal epithelial cells transformed by an origin-defective simian virus 40, proceedings of the National Academy of Sciences of the United States of America, 85 (1988) 5951–5955. DOI: 10.1073/pnas.85.16.5951

Harvey H.A., Swords W.E., Apicella M.A., The Mimicry of human glycolipids and glycosphingolipids by the lipooligosaccharides of pathogenic Neisseria and Haemophilus, Journal of Autoimmunity, 16 (2001) 257–262. DOI: 10.1006/jaut.2000.0477

Hold G.L., Bryant C.E., The molecular basis of lipid a and Toll-like receptor 4 interactions, in: Knirel Y.A., Valvano M.A. (Eds.), Bacterial Lipopolysaccharides: Structure, Chemical Synthesis, Biogenesis and Interaction with Host Cells, Springer Vienna, Vienna, 2011, pp. 371–387, ISBN: 978-3-7091-0733-1. DOI: 10.1007/978-3-7091-0733-1_12

Hwang S.-B., Lam M.-H., Shen T., Specific binding sites for platelet activating factor in human lung tissues, Biochemical and Biophysical Research Communications, 128 (1985) 972–979. DOI: 10.1016/0006-291x(85)90142-1

Jalalvand F., Riesbeck K., Haemophilus influenzae: recent advances in the understanding of molecular pathogenesis and polymicrobial infections, Current Opinion in Infectious Diseases, 27 (2014) 268–274. DOI: 10.1097/qco.0000000000000057

Ketterer M.R., Shao J.Q., Hornick D.B., Buscher B., Bandi V.K., Apicella M.A., Infection of primary human bronchial epithelial cells by *Haemophilus influenzae*: Macropinocytosis as a mechanism of airway epithelial cell entry, Infection and Immunity, 67 (1999) 4161–4170. DOI: 10.1128/IAI.67.8.4161-4170.1999

Krishnamurthy S., Behike M.A., Apicella M.A., McCray P.B., Davidson B.L., Platelet activating factor receptor activation improves siRNA uptake and RNAi responses in well-differentiated airway epithelia, Molec Ther - Nucleic Acids, 3 (2014) e175. DOI: 10.1038/mtna.2014.26

Lysenko E., Richards J.C., Cox A.D., Stewart A., Martin A., Kapoor M., Weiser J.N., The position of phosphorylcholine on the lipopolysaccharide of *Haemophilus influenzae* affects binding and sensitivity to C-reactive protein-mediated killing, Molecular Microbiology, 35 (2000) 234–245. DOI: 10.1046/j.1365-2958.2000.01707.x

Mandrell R.E., Apicella M.A., Lipo-oligosaccharides (LOS) of mucosal pathogens: molecular mimicry and host-modification of LOS, Immunobiology, 187 (1993) 382–402. DOI: 10.1016/s0171-

2985(11)80352-9

Masoud H., Moxon E.R., Martin A., Krajcarski D., Richards J.C., Structure of the variable and conserved lipopolysaccharide oligosaccharide epitopes expressed by *Haemophilus influenzae* serotype b strain Eagan, Biochemistry, 36 (1997) 2091–2103. DOI: 10.1021/bi961989y

Moran A.P., Prendergast M.M., Appelmelk B.J., Molecular mimicry of host structures by bacterial lipopolysaccharides and its contribution to disease, FEMS Immunology and Medical Microbiology, 16 (1996) 105–115. DOI: 10.1111/j.1574-695X.1996.tb00127.x

Murphy T.F., Apicella M.A., Nontypable *Haemophilus influenzae*: a review of clinical aspects, surface antigens, and the human immune response to infection, Reviews of Infectious Diseases, 9 (1987) 1–15. DOI: 10.1093/clinids/9.1.1

Pang B., Winn D., Johnson R., Hong W., West-Barnette S., Kock N., Swords W.E., Lipooligosaccharides containing phosphorylcholine delay pulmonary clearance of nontypeable *Haemophilus influenzae*, Infection and Immunity, 76 (2008) 2037–2043. DOI: 10.1128/IAI.01716-07

Patra J.K., Das G., Fraceto L.F., Campos E.V.R., Rodriguez-Torres M.d.P., Acosta-Torres L.S., Diaz-Torres L.A., Grillo R., Swamy M.K., Sharma S., Habtemariam S., Shin H.-S., Nano based drug delivery systems: recent developments and future prospects, Journal of Nanobiotechnology, 16 (2018) 71. DOI: 10.1186/s12951-018-0392-8

Piazza M., Colombo M., Zanoni I., Granucci F., Tortora P., Weiss J., Gioannini T., Prosperi D., Peri F., Uniform lipopolysaccharide (LPS)-loaded magnetic nanoparticles for the investigation of LPS-TLR4 signaling, Angewandte Chemie International Edition, 50 (2011) 622–626. DOI: 10.1002/anie.201004655

Porzeller D., Morsbach S., Landfester K., Isothermal titration calorimetry as a complementary method for investigating nanoparticle-protein interactions, Nanoscale, 11 (2019) 19265–19273. DOI: 10.1039/C9NR05790K

Preston A., Mandrell R.E., Gibson B.W., Apicella M.A., The lipooligosaccharides of pathogenic gram-negative bacteria, Critical Reviews in Microbiology, 22 (1996) 139–180. DOI: 10.3109/10408419609106458

Risberg A., Alvelius G., Schweda E.K., Structural analysis of the lipopolysaccharide oligosaccharide epitopes expressed by *Haemophilus influenzae* strain RM. 118-126, European Journal of Biochemistry, 265 (1999a) 1067–1074. DOI: 10.1046/j.1432-1327.1999.00832.x

Risberg A., Masoud H., Martin A., Richards J.C., Moxon E.R., Schweda E.K., Structural analysis of the lipopolysaccharide oligosaccharide epitopes expressed by a capsule-deficient strain of Haemophilus influenzae Rd, European Journal of Biochemistry, 261 (1999b) 171–180. DOI: 10.1046/j.1432-1327.1999.00248.x

Roederer M., Treister A., Moore W., Herzenberg L.A., Probability binning comparison: a metric for quantitating univariate distribution differences, Cytometry, 45 (2001) 37–46. DOI: 10.1002/1097-0320(20010901)45:1<37::aid-cyto1142>3.0.co;2-e

Rosenow C., Ryan P., Weiser J.N., Johnson S., Fontan P., Ortqvist A., Masure H.R., Contribution of novel choline-binding proteins to adherence, colonization and immunogenicity of Streptococcus pneumoniae, Molecular Microbiology, 25 (1997) 819–829. DOI: 10.1111/j.1365-2958.1997.mmi494.x

Schweda E.K., Brisson J.R., Alvelius G., Martin A., Weiser J.N., Hood D.W., Moxon E.R., Richards J.C., Characterization of the phosphocholine-substituted oligosaccharide in lipopolysaccharides of type b Haemophilus influenzae, European Journal of Biochemistry, 267 (2000) 3902–3913. DOI: 10.1046/j.1432-1327.2000.01426.x

Shukla S.D., Muller H.K., Latham R., Sohal S.S., Walters E.H., Platelet-activating factor receptor (PAFr) is upregulated in small airways of alveoli of smokers and COPD patients, Respirology, 21 (2016) 504–510. DOI: 10.1111/resp.12709

Silipo A., Molinaro A., Lipid a structure, in: Knirel Y.A., Valvano M.A. (Eds.), Bacterial Lipopolysaccharides: Structure, Chemical Synthesis, Biogenesis and Interaction with Host Cells, Springer Vienna, Vienna, 2011, pp. 1–20, ISBN: 978-3-7091-0733-1. DOI: 10.1007/978-3-7091-0733-1_1

Simpson B.W., Trent M.S., Pushing the envelope: LPS modifications and their consequences, Nature Reviews Microbiology, 17 (2019) 403–416. DOI: 10.1038/s41579-019-0201-x

St. Geme J.W., Molecular determinants of the interaction between Haemophilus influenzae and human cells, American Journal of Respiratory and Critical Care Medicine, 154 (1996) S192–S196. DOI: 10.1164/ajrccm/154.4_Pt_2.S192

Starner T.D., Zhang N., Kim G., Apicella M.A., Paul B., McCray J., Haemophilus influenzae forms biofilms on airway epithelia: implications in cystic fibrosis, American Journal of Respiratory and Critical Care Medicine, 174 (2006) 213–220. DOI: 10.1164/rccm.200509-1459OC

Steimle A., Autenrieth I.B., Frick J.-S., Structure and function: lipid A modifications in commensals and pathogens, International Journal of Medical Microbiology, 306 (2016) 290–301. DOI: 10.1016/j.ijmm.2016.03.001

Swords W.E., Buscher B.A., Ver Steeg Ii K., Preston A., Nichols W.A., Weiser J.N., Gibson B.W., Apicella M.A., Non-typeable *Haemophilus influenzae* adhere to and invade human bronchial epithelial cells via an interaction of lipooligosaccharide with the PAF receptor, Molecular Microbiology, 37 (2000) 13–27. DOI: 10.1046/j.1365-2958.2000.01952.x

Swords W.E., Ketterer M.R., Shao J., Campbell C.A., Weiser J.N., Apicella M.A., Binding of the non-typeable *Haemophilus influenzae* lipooligosaccharide to the PAF receptor initiates host cell signalling, Cellular Microbiology, 3 (2001) 525–536. DOI: 10.1046/j.1462-5822.2001.00132.x

Tu M., Lipooligosaccharide-modified polymeric particles for targeted pulmonary drug delivery, Ph.D., University of Iowa, 2015. DOI: 10.17077/etd.21vj0y3n

Turk D.C., The pathogenicity of *Haemophilus influenzae*, Journal of Medical Microbiology, 18 (1984) 1–16. DOI: 10.1099/00222615-18-1-1

Weiser J.N., Goldberg J.B., Pan N., Wilson L., Virji M., The phosphorylcholine epitope undergoes phase variation on a 43-kilodalton protein in Pseudomonas aeruginosa and on pili of Neisseria meningitidis and Neisseria gonorrhoeae, Infection and Immunity, 66 (1998) 4263–4267. DOI: 10.1128/iai.66.9.4263-4267.1998

Weiser J.N., Shchepetov M., Chong S.T., Decoration of lipopolysaccharide with phosphorylcholine: a phase-variable characteristic of Haemophilus influenzae, Infection and Immunity, 65 (1997) 943–950. DOI: 10.1128/iai.65.3.943-950.1997

Zhang J.-R., Mostov K.E., Lamm M.E., Nanno M., Shimida S.-i., Ohwaki M., Tuomanen E., The polymeric immunoglobulin receptor translocates pneumococci across human nasopharyngeal epithelial cells, Cell, 102 (2000) 827–837. DOI: 10.1016/S0092-8674(00)00071-4

Authors' Short Biographies



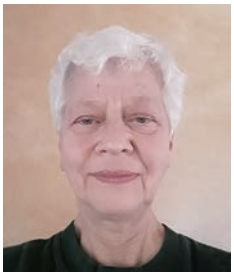
Mai H. Tu

Mai H. Tu earned a Ph.D. in pharmaceutics from the University of Iowa, USA under the guidance of Dr. Jennifer Fiegel. Her doctoral work focused on developing lipooligosaccharide-modified polymeric particles for targeted pulmonary drug delivery.



Timothy M. Brenza

Timothy M. Brenza completed a postdoctoral fellowship under the guidance of Dr. Jennifer Fiegel from 2008–2010. He is currently an Assistant Professor of chemical and biological engineering at South Dakota School of Mines and Technology.



Margaret R. Ketterer

Margaret R. Ketterer has worked at the University of Iowa Department of Microbiology and Immunology, in the laboratory of Dr. Michael Apicella, since 1993. Her research efforts have concentrated on the role of bacterial lipo-oligosaccharides in infections of human cells by *Neisseria* species and by *Haemophilus influenzae*.



Morgan Timm

Morgan Timm received a B.S. degree in biochemistry and molecular biology from Gustavus Adolphus College, USA and is currently an MD/PhD student at Washington University, USA. She conducted a summer research project in the laboratory of Dr. Jennifer Fiegel as part of the Nano NSF REU program at the University of Iowa.



Benjamin M. King

Benjamin M. King earned a Ph.D. in chemical and biochemical engineering from the University of Iowa, USA in 2018 under the guidance of Dr. Jennifer Fiegel. His doctoral work focused on interactions of environmental and therapeutics particles with the airway microenvironment.

Authors' Short Biographies



Michael A. Apicella

Michael A. Apicella is a Professor Emeritus of microbiology and immunology at the University of Iowa. His research focused on understanding the factors involved in human infections caused by Gram-negative bacterial pathogens.



Jennifer Fiegel

Jennifer Fiegel is a Professor of chemical and biochemical engineering at the University of Iowa (Iowa City, Iowa), with a secondary appointment in pharmaceutical sciences and experimental therapeutics. Her research expertise is in the design of improved therapeutic drug delivery strategies for the treatment and prevention of infections.

KONA Powder and Particle Journal No. 41 (2024) 280–281/https://doi.org/10.14356/kona.2024020 Information Article

The 55th Symposium on Powder Technology

The 55th Symposium on Powder Technology organized by the Hosokawa Powder Technology Foundation took place at the Hotel Tokyo Garden Palace in Japan on Monday, September 4, 2023. This event was held by the planning of the Council of Powder Technology, Japan and with the sponsorship of Hosokawa Micron Corporation. The theme of the symposium this year was “Powder Technology Contributing to a Sustainable Society”. There were seven lectures, including three KONA Award commemorative lectures, from basic and applied perspectives. This year’s symposium was held in a hybrid style, allowing both on-site and online participation.

At the beginning, Mr. Yoshio Hosokawa, the president of the Foundation, delivered the opening address mentioning that this symposium has been held almost annually in Osaka or Tokyo since 1968. However, due to the coronavirus pandemic, it was canceled for two years. Last year, a special event was held to commemorate the 30th anniversary of the foundation’s establishment in Osaka, and consequently, this event in Tokyo was for the first time in five years.

Prior to the lectures, the KONA Award presentation ceremony was held, and the plaques of the KONA Award were handed from the president to the two 2022 KONA Awardees; namely, Professor Hidehiro Kamiya, Director and Vice President of Tokyo University of Agriculture and Technology, and Professor Toshitsugu Tanaka of Osaka University. The contents of the symposium are shown below.

In the morning session, Prof. Kamiya and Prof. Tanaka gave the KONA Award 2022 commemorative lectures, in which they introduced their research results on particle adhesion and aggregation behavior in relation with the characterization and control, as well as on the development of discrete particle modeling and simulations of gas–solid two-phase flows, respectively.

The afternoon session began with the commemorative lecture for the KONA Award 2021 by Prof. Shuji Matsusaka of Kyoto University on advanced characterization of fine particles and the development of novel powder handling systems. Then, Prof. Toru Wakihara of the University of Tokyo and Prof. Tohru Sekino of Osaka University discussed a new preparation method for zeolite nanoparticles and its application, along with the creation of photo-physical-chemical functions by controlling the structure of the oxide nanoparticles, respectively, focusing on specific powder materials.

In the final session, Mr. Daisuke Ito of Murata Manufacturing Co., Ltd. and Dr. Aiko Sasai of Hosokawa Micron Corporation talked about the applications of powder technology and nanoparticle processing technology to the development of noteworthy products such as next-generation batteries, and regenerative medicine/cosmetics, respectively. After the end of the lectures, Prof. Hiroyuki Kage, Chairman of the Council of Powder Technology, Japan, gave the closing address, and the symposium concluded successfully.

Subsequently, in the reception hall, a social gathering was held for the first time in four years, allowing the lecturers and attendees to engage in meaningful exchanges in a relaxed atmosphere from beginning to end. The number of participants at this year’s venue was over 100, with nearly 240 in total, including online attendees. The following 56th Symposium is scheduled to be held in Osaka next year.



Opening address by President Yoshio Hosokawa.



For the memory of KONA Award presentation ceremony. (From left: 2022 KONA Awardee, Prof. Hidehiro Kamiya; President Yoshio Hosokawa; 2022 KONA Awardee, Prof. Toshitsugu Tanaka).

The 55th Symposium on Powder Technology

Theme: "*Powder Technology Contributing to a Sustainable Society*"
Date: Monday, September 4, 2023
Place: Hotel Tokyo Garden Palace

Opening address Mr. Yoshio Hosokawa (*President of Hosokawa Powder Technology Foundation, Chairman of Hosokawa Micron Corporation*)

・2022 KONA Award presentation ceremony

Session 1 Chaired by Prof. Masayoshi Fuji (*Nagoya Institute of Technology, Japan*)

・Lecture 1 (Special lecture by the 2022 KONA Awardee)

"Control of Nano and Fine Particles Adhesion and Aggregation Behaviors Based on Characterization and Analysis of Particle Interactions"

Prof. Hidehiro Kamiya (*Graduate School of Engineering, Tokyo University of Agriculture and Technology, Japan*)

・Lecture 2 (Special lecture by the 2022 KONA Awardee)

"Development of Discrete Element Model and Simulation Method to Predict Granular Flows"

Prof. Toshitsugu Tanaka (*Graduate School of Engineering, Osaka University, Japan*)

Session 2 Chaired by Emeritus Prof. Kikuo Okuyama (*Hiroshima University, Japan*)

・Lecture 3

"Advancements in Powder Characterization Methods and Developments in Advanced Powder Handling Technology"

Prof. Shuji Matsusaka (*Graduate School of Engineering, Kyoto University, Japan*)

・Lecture 4

"Novel Preparation Method of Nano-Sized Zeolite Using Pulverization Technology and Its Application"

Prof. Toru Wakihara (*School of Engineering, The University of Tokyo, Japan*)

・Lecture 5

"Creation of Photo-physical-chemical Functions of Nanostructured Materials via Various Structure Tuning"

Prof. Tohru Sekino (*SANKEN, Osaka University, Japan*)

Session 3 Chaired by Honorary Research Advisor, Dr. Hisao Makino (*CRIEPI, Japan*)

・Lecture 6

"Designs of Ceramic Powders: Toward Next-Generation Batteries"

Mr. Daisuke Ito (*Principal Researcher, Battery Development Department, Device Center, Murata Manufacturing Co., Ltd., Japan*)

・Lecture 7

"Development and Practical Use of Integrating Regenerative Medicine and Nanotechnology"

Dr. Aiko Sasai (*Pharmaceutical & Beauty Science Research Center, Material Business Division, Hosokawa Micron Corporation, Japan*)

Closing remarks Emeritus Prof. Hiroyuki Kage (*Kyushu Institute of Technology, President of Council of Powder Technology, Japan*)



Symposium on Powder Technology.



Get-acquainted Party.

KONA Powder and Particle Journal No. 41 (2024) 282–283/https://doi.org/10.14356/kona.2024021 Information Article

4th International Hosokawa Powder Technology Symposium Held in Germany

On September 14th, 2023, the 4th International Hosokawa Powder Technology Symposium took place at the Dorint An der Kongresshalle Hotel in Augsburg, Germany. The symposium was organized by the Hosokawa Powder Technology Foundation, in conjunction with KONA Europe e.V., the European / African Editorial Board of the academic journal KONA, and was co-hosted and sponsored by Hosokawa Alpine AG.

The International Hosokawa Powder Technology Symposium was first held in 2014 at Hosokawa Alpine AG to celebrate the Foundation's 20th anniversary. Subsequent symposia took place in the United States in 2017 and China in 2019, making this the fourth edition of the event.

The symposium began with a welcome speech by Dr. Kohei Hosokawa, Director of Hosokawa Powder Technology Foundation and President of Hosokawa Micron Corporation. The theme of the symposium was "Sustainable Production of Functional Particles," and it featured eight presentations highlighting collaborations between various companies, as well as the overviews by the academic researchers.

In the presentations, hot topics such as the future prospects of cultured meat production using continuous production facilities for cell culture media, dry and wet technology for efficient extraction of proteins from soybean, recycling technology and equipment for lithium-ion batteries, the relationship between processing techniques for rare earth materials and the performance of neodymium magnets, and the introduction of new spheronization equipment for graphite, a critical secondary battery material, were discussed.

Additionally, Dr. Akira Watanabe, General Manager of the Technology Development Department of Hosokawa Micron Corporation in Japan, shared insights into the differences in geopolitical and cultural perspectives between Japan and Germany, and the evolution of secondary battery material manufacturing equipment in Japan. At the end of the symposium, Dr. Fernández, President of Hosokawa Alpine AG, gave the closing remarks.

Participants came from various countries, including Germany, the host country, the Netherlands, and Lithuania. A welcome ceremony was held the day before the symposium. At the welcome ceremony, Dr. Steffen Sander, Secretary General of KONA Europe e.V. and head of the R&D center of Hosokawa Alpine AG, first explained about the company tour. Participants were then divided into small teams for a tour of the factory and the R&D center.

The guide explained that the company's factory has production lines segmented by application, such as minerals, chemicals, and films, allowing the company to produce products of the high quality for each application. After the factory tour, the group was guided through the R&D center from the top floor to the first floor. The R&D center is equipped not only with lab machines and small test machines, but also with test machines that are the same size as actual production facilities, which is expected to reduce the risk of scaling up test machines when users set up actual production facilities. A separate testing machine for pharmaceutical products is also available. With these well-equipped testing facilities, the company is able to respond to a variety of customer requests. After the company's tour, the group was divided into two teams: one team went on a tour of Augsburg, the famous walled city on the Romantic Road, while the other team toured the beer factory facilities. At the end of the tour, all the teams gathered once again to enjoy delicious German beer in a beer hall adjacent to the brewery, and international exchange was promoted.



Welcome speech by President Kohei Hosokawa.



Lecture scenery.

CC BY

4th International Hosokawa Powder Technology Symposium

Date: Tuesday, September 14, 2023

Place: Dorint Hotel An der Kongresshalle Augsburg, Germany

Theme: "***Sustainable Production of Functional Particles***"

Organizer: Hosokawa Powder Technology Foundation

Co-organizer: KONA Europe e.V., Hosokawa Alpine AG

➢**Welcome address** Dr. Kohei Hosokawa, Acting President of Hosokawa Powder Technology Foundation, President of Hosokawa Micron Corporation, Japan

➢**Lecture 1: Current trends in particle technology**
Ass. Prof. Gabrie Meesters, Department of Chemical Engineering, Delft University of Technology, The Netherlands

➢**Lecture 2: Leveraging AI in process engineering: Overview of multifaceted applications and synergetic integration opportunities**
Mr. Christoph Thon, Institute for Particle Technology (iPAT), Technische Universität Braunschweig, Germany

➢**Lecture 3: The future of cultivated meat and the continuous production of cell culture media**
Mr. Appachu Kodira, KCell Biosciences / JSBiosciences; Mr. Hermann Schmidt, Hosokawa Alpine AG, Germany

➢**Lecture 4: Deep Dive Pulses Protein: Combination of dry and wet extraction**
Mr. Remy Kriech, Bühler Technologies GmbH, Germany; Mr. Eric Emmert, Hosokawa Alpine AG, Germany

➢**Lecture 5: The difference between Germany and Japan from the viewpoint of the powder-related industry, and SDGs**
Dr. Akira Watanabe, Powder Technology Research Institute, Hosokawa Micron Corporation, Japan

➢**Lecture 6: Processing techniques for rare earth materials and the effect on magnetic materials performance**
Mr. Konrad Opelt, Department of Magnetic Materials, Fraunhofer IWKS, Germany

➢**Lecture 7: Comminution and classification as important processes for the circular production of lithium batteries**
Prof. Carsten Schilde, Institute for Particle Technology (iPAT), Technische Universität Braunschweig, Germany

➢**Lecture 8: Spheronization of natural graphite—background and novel process**
Dr. Marilena Mancini, Accumulators Materials Research (ECM) Department of ZSW, Germany; Mr. Benjamin Biber, Hosokawa Alpine AG, Germany

➢**Closing remarks** Dr. Antonio Fernández, President of Hosokawa Alpine AG., Germany



Lecture by Dr. Akira Watanabe, General Manager of Technical Development Dept.



Recess scenery.

The KONA Award 2022

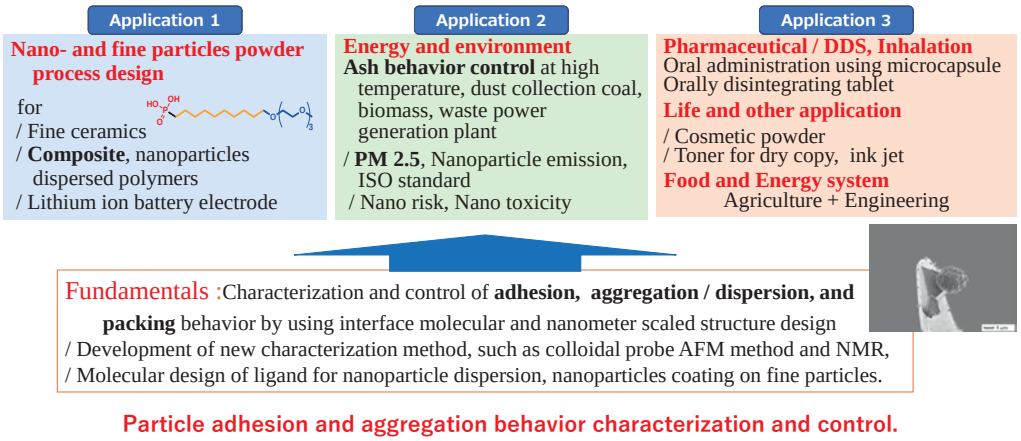
The KONA Award has been presented to researchers who have greatly contributed to research and development as well as education in the field of Powder and Particle Science and Technology since 1990. It was originally given by Hosokawa Micron Corporation, but now is presented to researchers from all over the world by the Hosokawa Powder Technology Foundation annually. The application for this award requires a specified recommendation form written in English to be submitted to the President of the Hosokawa Powder Technology Foundation. The award candidates are reviewed by the KONA Award Committee members, and the results are reported to the Selection Committee of the Foundation for the nomination of the awardee. It needs to be finally approved at the Board of Directors' meeting of the Foundation. The KONA Award is presented at a ceremony in or outside Japan with a plaque and a prize of one million yen. The KONA Award 2022 has been presented to two researchers this year, namely Prof. Hidehiro Kamiya and Prof. Toshitsugu Tanaka from Japan. The KONA Award plaques were presented to the awardees at the 55th Symposium on Powder Technology on September 4, 2023.

Dr. H. Kamiya has realized various achievements in powder technology, particularly those related to fine and nanoparticles, and has widely disseminated his activities overseas. Based on the characterization of the surface interaction and structure of nanoparticles, he investigated the fundamentals associated with the aggregation behavior of nanoparticles in liquid. He discovered an organic ligand structure with universal dispersibility of nanoparticles into various polar and nonpolar organic solvents. By synthesizing various ligands with different molecular structures, he discovered the optimum ligand molecular structure for universal dispersibility. Such surface-treated nanoparticles were applied to prepare new free-standing, rollable, and transparent silicone polymer films.

Utilizing fine particles and microcapsules measuring larger than 100 nm in diameter, he investigated the original molecular design of polymer structures on particles and capsules to characterize and control surface interaction via colloid probe AFM. In the gas phase, the adhesion of fine ash particles at high temperatures hindered the stable operation of various energy systems. Hence, he developed original systems for characterizing the particle adhesion force and shear strength of single ash at high temperatures based on a split-type tensile strength tester. Since real ash includes various chemical elements, he developed a model of ash particles prepared from pure silica as well as other metal oxide fine particles, with the addition of alkali metal or phosphorus. Based on the fundamental characterization method and ash model, he investigated the mechanism of increasing ash particles generated from different plant and fuel sources. To control the adhesion behavior of ash, he proposed the addition of alumina and other inorganic nanoparticles. The characterization,



At the KONA Award presentation ceremony,
President Yoshio Hosokawa (Left) and 2022 KONA Awardee Prof. Hidehiro Kamiya (Tokyo Univ. of Agriculture and Technology, Japan).



Selected research achievements for the KONA Award 2022 (Prof. Hidehiro Kamiya): Particle adhesion and aggregation behavior characterization and control.

simulation and modeling, and control of adhesion and aggregation have been expanded to various industrial fields, including pharmaceuticals, cosmetics, and pigments.

The results above have been published in 243 original papers (182 WoS papers) and 76 review papers. He has filed 23 patents, published 55 books, and presented 37 keynote lectures at international conferences. Additionally, he has contributed to the activities of the "Association of Powder and Particle Industry and Engineering in Japan, APPIE" as a coordinator of the "Fine Powder Nanotechnology" group from 2001 to 2021. Furthermore, he has served as a vice chair of the committee of "Nanoparticle Safety" and an editor for the book, "Safe Use of Nanoparticles."

Dr. T. Tanaka has been conducting research at Osaka University, focusing on fluid engineering and powder technology, particularly with regard to discrete particle modeling and simulations of gas–solid flows and granular flows, for 38 years. He began his career at the dawn of discrete particle simulation. When he started his numerical research, only the Lagrangian numerical simulation neglecting particle–particle collision or contact and the two-fluid-model simulation were available. He made pioneering works for modeling both collision-dominant flows and contact-dominant flows.

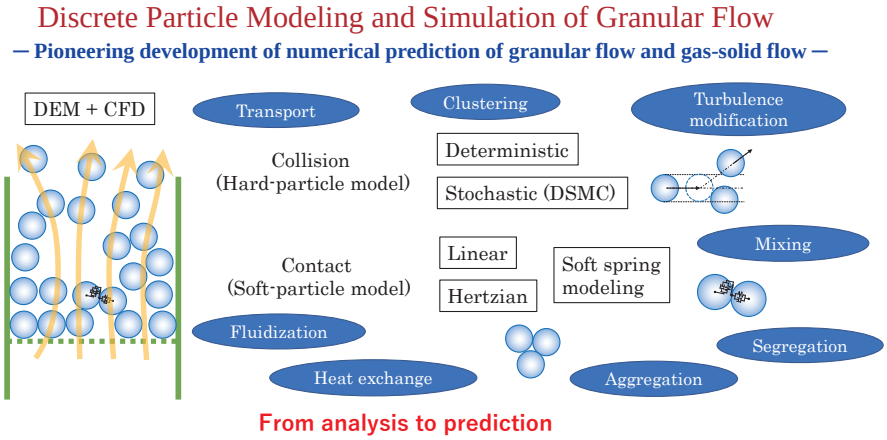
First, he proposed a deterministic method for calculating of particle–particle collision to study the effect of particle–particle collision on the diffusion of particles in dilute gas–solid flows, and to study the effect of particle–particle collision on the spatial structure of particles in gas–solid turbulent flow. To reduce the calculation cost, he proposed the utilization of DSMC method to gas–solid flows, and successfully predicted the particle cluster formation observed in the riser of circulating fluidized bed.

His most brilliant achievements were the developments of the DEM-CFD model and simulations. He made novel discrete simulation models and methods to reproduce a plug flow in a horizontal pipe and fluidized beds. Since then, his model and simulation method have been widely used for basic studies of dense gas–solid flows and applied for many industrial applications. The total number of citations of his pioneering papers on the DEM-CFD model is over 3400, demonstrating the excellence of his pioneering achievements. He extended his work to the large-scale DEM-CFD simulation of fluidized behavior in three-dimensional fluidized bed, and to a reduced spring constant model for cohesive particles.

For the above achievements, Dr. Tanaka was awarded the Best Paper Award of the Society of Powder Technology, Japan in 2012, JSME Fellow from JSME in 2011, and Distinguished Achievement Award of the Information Center of Particle Technology, Japan in 2004, among other awards. Dr. Tanaka is an acknowledged world leader, especially in the field of numerical modeling and simulations of gas-solid flows and granular flows, and has made significant contributions to the development of powder science and technologies worldwide



At the KONA Award presentation ceremony,
President Yoshio Hosokawa (Left) and 2022 KONA Awardee Prof. Toshitsugu Tanaka (Osaka University, Japan).



Selected research achievements for the KONA Award 2022 (Prof. Toshitsugu Tanaka): Development of discrete particle modeling and simulations of gas-solid flows and granular flows.

General Information

History of the Journal

The KONA journal (currently called "KONA Powder and Particle Journal") was first published as an open-accessed scientific journal in 1983 by the Council of Powder Technology, Japan (CPT), which was established in 1969 by Hosokawa Micron Corporation as a nonprofit organization to promote powder technology, in order to introduce excellent Japanese papers to the world. From issue No.8, the CPT changed its editorial policy to internationalize the KONA journal and to incorporate papers by authors throughout the world. In response to this change, three editorial blocks have been organized worldwide: Asian–Oceanian, American and European–African. Issues from No.1 (1983) to No.12 (1994) of the KONA journal were published by the CPT, and issues from No.13 (1995) and onwards by the Hosokawa Powder Technology Foundation. The policy and system have not changed even after the Hosokawa Foundation took over the publication from the CPT. From issue No.38 (2021), the KONA journal primarily publishes review articles by leading researchers, including established and recently Ph.D.-awarded young researchers in the field.

Aims and Scope

KONA publishes review and original research papers in a broad field of powder and particle science and technology, ranging from fundamental principles to practical applications. Papers on critical reviews of existing knowledge in special areas are particularly welcome.

The submitted papers are published only when they are judged by the Editor to contribute to the progress of powder science and technology, and approved by any of the three Editorial Committees.

The paper submitted to the Editorial Secretariat should not have been previously published.

Category of Papers

- Invited articles
  Review papers and feature articles invited by the KONA Editorial Committees.
- Contributed papers
  Original review papers and some limited number of original research papers of high quality submitted to the KONA Editorial Committees, and refereed by the reviewers and editors.

Submission of Papers

To submit your paper, please use the online Editorial Manager® for KONA Online Paper Submission and Peer Review System. For further information, please visit the journal's website at https://www.kona.or.jp/jp/journal/info.html

Publication in KONA is free of charge.

Publication Schedule

KONA is an annual publication with an expected release date around January 10th.

Subscription

KONA is distributed for free to senior researchers at universities and laboratories, as well as to institutions and libraries in the field throughout the world.

Instructions to Authors

(1) **Language**

All submissions should be written in good English. Authors may choose either British or American English, provided that the chosen style is used consistently. Authors from non-English-speaking countries are encouraged to use professional English editing services to proofread their manuscripts.

(2) **Data Repository Information**

In order to promote open data discoverability and use of research outputs, this journal encourages authors to submit data files supporting their manuscript work, which can be deposited in the journal's J-STAGE Data site <https://jstagedata.jst.go.jp/kona> after acceptance of the paper through the peer-review process.

These data may describe observations, experiments, modeling or analyses, and may take the form of databases, simulations, movies, large figures, or as otherwise appropriate.

For questions or more information, please contact the KONA Editorial Office (contact_zainq@hmc.hosokawa.com).

(3) **Manuscript format**

- Electric files should be submitted to the Editorial Secretariat via Online Submission System. Author's short biography with less than 100 words per person should be attached to the final version.
- The structure of manuscripts should follow the following order; title, authors, affiliations, abstract, graphical abstract, keywords, main text, (data availability statement), (acknowledgement), (nomenclature), references. The items with parentheses are not mandatory.
- Full postal addresses must be given for all the authors. Indicate the corresponding author by the asterisk mark"*" after the name. Telephone and fax numbers and e-mail address should be provided for the corresponding author.
- Abstract should not exceed 200 words.
- Graphical abstract should be a concise, visual summary of the article which will be displayed in the contents list both online and print.
- The appropriate number of keywords is 5 or 6.
- The maximum pages printed in KONA are supposed to be: 15 for an original research paper and 25 for a review paper.
- Symbols and units should be listed in alphabetical order with their definition and dimensions in SI units.
- The color figures will appear in color both on the KONA Website (https://www.kona.or.jp) and also in the paper version.
- Concerning references, the alphabetical system should be adopted. Please use reference management software such as Endnote to manage references as far as possible.

  List: References should be arranged first alphabetically and then further sorted chronologically if necessary. More than one reference from the same author(s) in the same year must be identified by the letters "a", "b", "c", etc., placed after the year of publication.

  Examples:

  - Reference to a book:
    Strunk Jr. W., White E.B., The Elements of Style, fourth ed., Longman, New York, 2000, ISBN: 9780205309023.
  - Reference to a chapter in an edited book:
    Mettam G.R., Adams L.B., How to prepare an electronic version of your article, in: Jones B.S., Smith R.Z. (Eds.), Introduction to the Electronic Age, E-Publishing Inc., New York, 2009, pp.281–304.
  - Reference to a journal publication:
    Tsuji Y., Tanaka T., Ishida T., Lagrangian numerical simulation of plug flow of cohesionless particles in a horizontal pipe, Powder Technology, 71 (1992) 239–250. DOI: 10.1016/0032-5910(92)88030-L

  Text: All citations in the text should refer to:

  1. Single author: the author's name (without initials, unless there is ambiguity) and the year of publication;
  2. Two authors: both authors' names and the year of publication;
  3. Three or more authors: first author's name followed by "et al." and the year of publication.

  Citations may be made directly (or parenthetically). Groups of references should be listed first alphabetically, then chronologically.

  Examples:

  "as demonstrated (Hidaka et al., 1995; Tsuji, 1992a, 1992b, 1993). Mori and Fukumoto (2002) have recently shown ...."

(4) **Copyright and permission**

- The original paper to be submitted to KONA has not been published before in any language or in any journals or media; it is not submitted and not under consideration for publication in whole or in part elsewhere.
- Authors are responsible for obtaining permission from the copyright holders to reproduce any figures, tables and photos for which copyright exists.
- The KONA Journal applies the Creative Commons Attribution License to all works published by the Journal. Copyright stays with the agreed copyright owner, and the Hosokawa Powder Technology Foundation is granted the exclusive right to publish and distribute the work, and to provide the work in all forms and media.
- Users of the journal will be able to reuse the contents in any way they like, provided they are accurately attributed. No permission is required from either the authors or the publisher.

Hosokawa Powder Technology Foundation (HPTF)

— Foundation Overview



HPTF was established by **Mr. Masuo Hosokawa** with his strong intention to contribute to the **worldwide promotion of the Powder Technology** on the occasion of the **75th anniversary of Hosokawa Micron Corporation (HMC) in 1991.** HPTF was based on his **private donation of one billion yen.**



Mr. Akihiko Hosokawa also donated additional **300 million yen** for the Foundation in 1994



Mr. Yoshio Hosokawa, President of Hosokawa Micron Corporation, has been the President of HTPF since 2010.

— Holding the Symposium on Powder Technology

1. Symposium on Powder Technology in Japan

The first one was held on the occasion of the completion of the new building of Hosokawa Micromeritics Lab. **in Hirakata, Osaka in 1968 and has been held annually since then.**



The 55th Symposium at Hotel Tokyo Garden Palace, Japan in 2023.

2. International Hosokawa Powder Technology Symposium

The First was held in Germany (2014), the Second in USA (2017), the Third in China (2019), and the Fourth in Germany (2023).



4th International Hosokawa Powder Technology Symposium held in Germany.

— Granting and Awarding

1. Granting the research projects at the universities in Japan

- **Funding research projects**
- **Supporting Ph.D. students**



Award Presentation Ceremony at HMC headquarters in Mar. 2019.

2. Awarding worldwide excellent researchers

- **KONA Award** (1 mil yen per person) Total since 1990: 38



— Publishing journal and books

1. KONA Powder and Particle Journal



No.41(2024)

1983	First publication
1990	3 editorial blocks worldwide
2009	Registered in Web of Science
	(2022 Impact Factor: 4.1)
2013	Registered and published on J-STAGE
2014	Started Advance Publication
2016	Introduced CC-BY license
2017	Adopted Editorial Manager®
2019	Registered in DOAJ
2021	Registered on J-STAGE Data repository

2. Nanoparticle Technology Handbook (Elsevier)

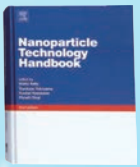
First edition	(2007)
Second edition	(2012)
Third edition	(2018)



1st edition (2007)
622 pages



2nd edition (2012)
703 pages



3rd edition (2018)
877 pages

Hosokawa Powder Technology Foundation

HOSOKAWA MICRON GROUP
Process technologies for tomorrow.

The new product line for processing systems to produce **ENERGY PERFORMANCE MATERIALS**



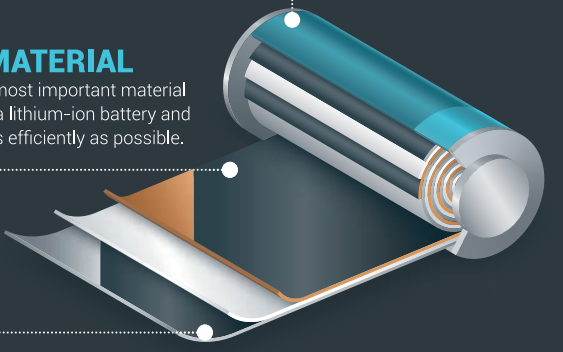
Advanced battery solutions for cathode and anode material

When charging and discharging a lithium-ion battery, the lithium ions move from the cathode to the anode and back again. The cathode and anode of a battery are made of different materials. A wide variety of lithium compounds (e. g. LCO, NMC, NCA or LFP) are used in the cathode. Graphite or lithium titanate form an essential component of the anode. On has developed special processes for lithium compounds as well as the rounding of graphite.

- Complete solutions for advanced battery manufacturing
- Technologies for advanced battery materials (cathode and anode)
- Contamination-free grinding with classifier mills and/or fluidised bed opposed jet mills
- Spheroidization of natural graphite and synthetic graphite
- Mixing, drying and coating of battery material

RECYCLING
Production scrap can be recycled directly during battery production.

ANODE MATERIAL
Graphite is the most important material in the anode of a lithium-ion battery and must be used as efficiently as possible.



CATHODE MATERIAL
Lithium is the most important active material in the cathode and determines the performance of your batteries.

On: Advanced battery materials for your commercial battery production

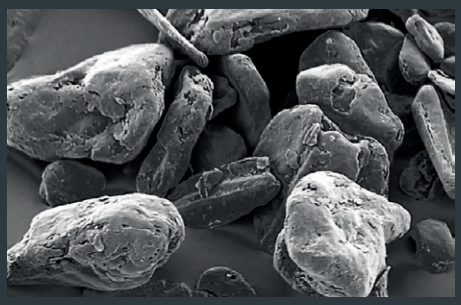
Whether in e-cars or e-bikes, smartphones or laptops, lithium-ion batteries have become an indispensable part of everyday life. Their performance depends crucially on the material for the cathode and anode of the batteries. On offers technologies for optimising lithium compounds and graphite, the most important battery materials. Manufacture your energy performance materials with us!

BATTERY PRODUCTION SYSTEMS



From R&D to industrial production: On develops production systems for battery material according to your specific requirements, including containment solutions.

OPTIMISED LITHIUM AND GRAPHITE



Technologies for advanced battery manufacturing: Optimise your cathode and anode material with machines and systems from On!

BATTERY RECYCLING SYSTEMS

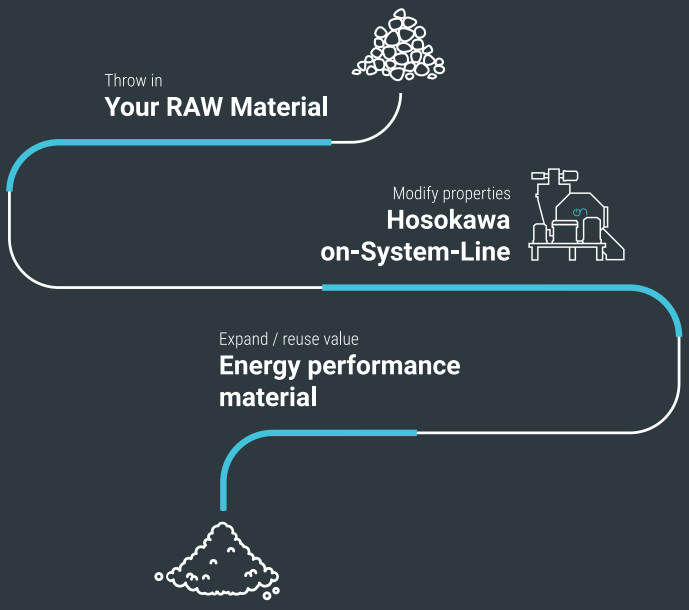


From direct-scrap recycling of material during the production process to end-of-life recycling: Take a look at our solutions for battery recycling!

THE ON SYSTEMS ARE PERFECTLY SUITED FOR YOUR ENERGY PERFORMANCE MATERIALS

We use the term energy performance materials for highly optimised powders whose particle properties improve end products in battery manufacturing. The charging time, storage capacity and service life of lithium-ion batteries can be specifically enhanced with our technologies.

On's solutions for advanced battery manufacturing include grinding, mixing, drying and other process steps. In the high-end industrial sector, most industries rely on our process engineering solutions. And for good reasons. Whether you are looking for a proven or a new solution for your advanced energy materials, the various companies of the Hosokawa Micron Group have coordinated their processes, systems and services to provide you with the perfect system for your requirements.



YOUR REQUEST IS IMPORTANT TO US

Would you like to improve your battery performance?
Then get in touch with us and let us know how we can help you!

+49 821 5906 0
energy@on-hosokawa.com

www.on-hosokawa.com

HOSOKAWA MICRON GROUP

The Hosokawa Micron Group will always be the leading global company covering the mountain range of Powder Technologies. The Group has been a pioneer in the filed of powder and particle processing and blown film processing. We provide R&D, engineering, manufacturing and services in various fields of the world's major industrial markets.



Measuring instruments for developing the powder science & engineering

Dynamic Particle Image Analyzer
Parshe Analyzer

Penetration speed
Peneto Analyzer, PNT-N

Carr's indicies
Powder characteristics tester, PT-X

Wet sieving
Viblette, VBL-F

Process Technologies for Tomorrow

HOSOKAWA MICRON CORPORATION

Headquaters Location :

HOSOKAWA MICRON CORPORATION

URL : www.hosokawamicron.com